Mapping petroleum migration pathways using magnetics, geochemistry and seismic mapping. Case study: Wessex Basin, southern England, UK.

Rabiu Abubakar

Imperial College London

Department of Earth Science and Engineering

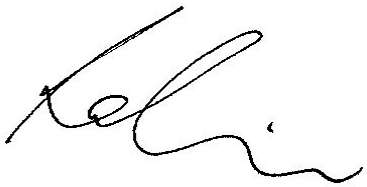
PhD Thesis

Statement of Copyright

The copyright of this thesis rests with the author and is made available under a Creative Commons Attribution Non-Commercial No Derivatives licence. Researchers are free to copy, distribute or transmit the thesis on the condition that they attribute it, that they do not use it for commercial purposes and that they do not alter, transform or build upon it. For any reuse or redistribution, researchers must make clear to others the licence terms of this work

Declaration

I declare that this thesis 'Mapping petroleum migration pathways using magnetics, geochemistry and seismic mapping. Case study: Wessex Basin' is entirely my own work and any materials sourced from somewhere have been duly cited and referenced.



Rabiu Abubakar

Supervisors: Dr. Adrian Muxworthy, Prof. Mark Sephton, Prof. Alastair Fraser

Abstract

This thesis presents, for the first time, direct evidence for the formation of magnetic minerals during hydrocarbon generation, it also reports on the nature and type of magnetic mineralogy formed during the generation of oil and gas. This thesis also reports experimental results that explain variations in magnetic mineralogy along potential crude oil migration paths in the Wessex Basin, southern England, UK.

Potential oil-source rocks from the Wessex Basin, England, were pyrolysed (artificial maturation) at various temperatures under conditions similar to those for hydrocarbon-generation to reveal the formation of nano-metre sized magnetic minerals, mainly magnetite and pyrrhotite, with traces of greigite. The potential of these magnetic minerals to migrate along with the generated crude oil is also reported in this thesis.

To assess the possibility of using magnetic characterisation to test for potential hydrocarbon migration, I examined the Wessex Basin, southern England, using 2D seismic data, geochemical analysis and mineral magnetic techniques. Potential hydrocarbon migration pathways from the hanging wall of the Purbeck fault into Sherwood Sandstone reservoir at Wytch Farm was identified via interpretation of 2D seismic data. Geochemical characterisation of oils extracted from core materials from the Wessex Basin revealed oils found at Stoborough and Waddock Cross are less mature than oils at Wytch Farm, which likely indicates spillage from the top of the reservoir at Wytch Farm due to regional tilting. In addition, the geochemical data from the core materials also show probable migration paths for oils found at Chickerell. Magnetic characterisation of reservoir core material (Bridport Sandstone and Inferior Oolite) revealed variations in magnetic signatures along potential migration routes, with variations also found with sampling depth. The magnetic signature was characterised using low-temperature magnetic remanence and hysteresis measurements, because much of the magnetic signature was found to be from nanoparticles that are thermally activated at room temperature (superparamagnetic). The study found magnetite predominates in the hydrocarbon proximal plume, pyrrhotite in the distal plume environment with mixed pyrrhotite and magnetite in shallow proximal plume environment. It is suggested that magnetic mineralogy has the potential to be used as a proxy for hydrocarbon migration identification in the future.

Acknowledgement

I would like thank the petroleum technology development fund (PTDF) for funding this PhD. I will also like to say thank you to Dr Adrian Muxworthy, Prof. Mark Sephton and Prof. Alastair Fraser for their wonderful supervision of this study. I would also want to say thank you to Dr Jonathan Watson, Dr Paul Southern, Dr Trevor Almeida, Dr Greig Paterson and Dr David Heslop for helping with instrument training and carrying out some of the measurements. I would also want to thank the British Geological Society (BGS) core store for granting me access to well core materials from the Wessex Basin.

I would also want to say a big thank you to my family, especially my parents, without whose guidance, this PhD would not have been possible. A special thank you to my brother, Lawal Garba, for seeing me through the most difficult periods of my life. A special thank you also goes to my wife, Amina Aliyu-Abubakar and my children Hindu and Mahmoud for making life easier for me, during this study.

Publication list

Abubakar, R. Muxworthy, A. R., Sephton, M. A., Fraser, A. J., Watson, J. and Almeida, T. P., 2015.Formation of magnetic minerals in hydrocarbon-generation conditions. *Marine and Petroleum Geology*.**68**, 509-519, http://dx.doi.org/10.1016/j.marpetgeo.2015.10.003

Contents

Declaration 2
Abstract 3
Acknowledgement 4
Publication list 5
Table of Figures 9
List of Tables 17
1. Introduction to thesis 20
1.2 Review of magnetisation 23
1.2.1 Basic magnetism 23
1.2.2 Magnetic properties of materials 25
1.2.3 Magnetic domain 27
1.2.4 Magnetic hysteresis 28
1.2.5 Magnetic Remanence 30
1.2.6 Magnetic minerals 30
1.2.7 Remagnetisation 33
1.3 Review of organic geochemistry 36
1.3.1 Sedimentary organic matter (SOM) 36
1.3.2 Chemical composition and accumulation of organic matter (OM) 37
1.3.3 Fate of organic matter is sedimentary successions 38
1.4 Composition of crude oils 39
1.5 Biomarkers 40
1.5.1 Source related biomarkers 42
1.6 Planned PhD Research 43
2.1 Introduction 45
2.1.1 Geological History 45
2.1.2 Megasequences 46
2.2 Sampling 51
2.2 Methodology 54
2.2.1 Geochemical experimentations 54
2.2.2 Magnetic experimentation 55
2.2.3 Seismic interpretation 59
2.2.4 Depth conversion and decompaction 62

3.1 Introduction....64
3.1.1 Magnetic mineral formation due to external fluids....66
3.1.2 Magnetic mineral formation due to burial....67
3.1.3 Organic formation of ferromagnetic minerals....67
3.1.4 Magnetic mineral formation and thermal metamorphism....67
3.1.5 Microbial action....68
3.1.6 Formation of magnetic minerals in hydrocarbon reservoirs....68
3.2 Samples....68
3.3 Magnetic characterisation of the rock samples....70
3.3.1 Magnetic hysteresis measurements....70
3.3.3 Low-temperature warming and cooling experiments....78
3.4 Transmission electron microscopy (TEM)....80
3.5 Relationship between oil generation and production of magnetic minerals....82
3.6 Magnetic minerals formed in hydrocarbon-generation conditions....84
3.7 Implications....86
3.8 Conclusions....86
4.1 Introduction....89
4.2 Hydrocarbon Plays....90
4.2.1 Sherwood Sandstone Group....90
4.2.2 Bridport Sandstone....91
4.2.3 Potential source rocks....93
4.3 Hydrocarbon generation and the Tertiary Inversion....94
4.4 Model....98
4.5 Discussion....108
4.5.1 Assumptions in the model....109
4.6 Conclusions....110
5.1 Introduction....112
5.2 Geochemical characterization....114
5.2.1 Biomarkers....114
5.2.1.1 Environment of deposition....114
5.2.1.2 Maturity parameters....126
5.2.1.3 Water column stratification....127
5.2.2 Are the oil samples genetically different?....132

5.2.2.1 Environment of deposition and maturation....132
5.4.2 Summary of geochemical characterisation....134
5.3 Magnetic Characterisation....134
5.3.1 Magnetic mineral abundance....134
5.3.2 Magnetic mineral grain sizes and remanence carrying materials....144
5.3.3 Magnetic mineralogy....152
5.4 Is there a relationship between oil staining and magnetism?....159
5.4.1 Are there variations in magnetic mineral abundance?....159
5.4.2 Are there variations in magnetic mineral grain sizes?....160
5.4.3 Are there variations in magnetic mineralogy?....161
5.4.4 Are the variations in magnetic mineralogy affected by intrinsic magnetic contributions or contamination?....162
5.5 Proposed model....163
5.6 Summary....165
6.1 Conclusion....167
6.1.1 Generation of magnetic materials in hydrocarbon-generation conditions....167
6.1.2 Seismic mapping and interpretations....168
6.1.3 Hydrocarbon and magnetic properties....**Error! Bookmark not defined.**
6.2 Future work....171
References....172
Appendix 1....182
RT-Hysteresis....183
LT-Hysteresis and ZFC warming experiments....201
Appendix 1.2204Appendix 2.1
....206
Appendix 2.2....252
Appendix 2.3....266

Table of Figures

Figure 1.1: (a) Magnetic HG′ map of a four-section (103-ha) part of the Alida (Mississippian limestone) field at North Pierson. The survey was completed prior to drilling of the wells shown. All five wells were drilled on HG′ anomalies and all encountered oil. Note the northwest southeast subcrop trend of erosional Mississippian cuesta reservoirs, seen also in Figure 1. HG′ contour values (proportional to nT/m2) greater than 2 were considered significant and are coloured. HG = high-resolution ground-magnetic From (LeSchack, 1997)……...…….22

Figure 1.2:a) A magnetic dipole made from a pair of magnetic charges. The magnetic charges are *p* and *-p* for the positive and negative ends respectively. *l*is the distance between the charges. b) A magnetic dipole made from a loop of electrical current. *I* is the current in the loop, *A* is area of the loop. Modified after Butler (1992) ……...……24

Figure 1.3: Figure 1.3 a) Magnetisation (M) vs magnetic field (H) for a diamagnetic substance. Magnetic susceptibility (χ) is negative. b) M vs H for a paramagnetic substance, magnetic susceptibility (χ) is positive. After Butler (1992)…….....25

Figure 1.4: Schematic representation of the distribution of magnetisation vectors in crystals, showing the resultant spontaneous magnetisation. After McElhinny (1973)……...26

Figure 1.5: Schematic representation of a) Single domain structure (SD), b) two domain magnetic structure (PSD) and c) four domain structure (MD), dashed lines represent domain walls and the arrows show the direction of saturation magnetisation (M_s) in each domain. After Dunlop and Özdemir (1997)…..28

Figure 1.6: M-H plot for ferromagnetic materials showing hysteresis parameters. After Walden *et al*. (1999)……...29

Figure 1.7: Ternary diagram of the main naturally occurring magnetic minerals and solid solution series. From Butler (1992)……30

Figure 1.8: The crystal structure of magnetite. Site A tetrahedral Fe2+, Site B octahedral Fe^{2+}/Fe^{3+}. From Banerjee and Moskowitz (1985)……..31

Figure 1.9: Magnetic mineral parageneses and magnetic susceptibilities (denoted relative to background: increased, +; neutral, 0; or decreased, -) predicted for non-plume conditions. Non-plume conditions in the left column define background magnetization prior to hydrocarbon seepage. Plume environments shown in centre and right columns. Environmental conditions in rows A = 25 °C, 1 bar; B = 50 °C, 150 bar; C = 100 °C 300 bar and D = 200 °C 600 bar. Levels of total aqueous sulphur denoted by LTS = low; MTS = intermediate; HTS = high. Fates of mineral denoted by U = unstable; S = stable. HEM= hematite; MAG= magnetite; PYRRH= pyrrhotite; SID= siderite. From Burton *et al*. (1993)……...33

Figure 1.10: Burial model for the formation of magnetic minerals in claystones. Central box represents a sedimentary column from the surface to 10km of depth. Formation of magnetic minerals depends on burial, presence and/or absence of oxygen and the availability of sulphur. From Aubourg *et al*. (2012)……...35

Figure 1.11: General schematic of the evolution of organic matter from time of deposition to onset of metamorphism. CH = carbohydrates, AA = amino acids, FA = fulvic acids, HA = humic acids, L = lipids, HC = hydrocarbon, Ro = vitrinite reflectance. From (Tissot and Welte, 1984)……...38

Figure 1.12: The class composition of crude oils in a triangular plot: Effects of maturation, oxidation and biodegradation. Modified from Tissot and Welte (1984)……40

Figure 2.1: Geological map of Wessex Basin showing sampling locations: (1) Blue Lias Fm (Lyme Regis), (2) Oxford Clay Fm (Chickerell), and (3) Kimmeridge Clay Fm (Kimmeridge Bay)……...46

Figure 2.2: Chronostratigraphic diagram depicting the main plate cycle seismic megasequences, their component sequences, relevant Jurassic lithostratigraphic elements and their respective reservoir, source, trap and charge potential. J = Jurassic megasequences R = potential reservoir rock S = potential source rock. After Hawkes *et al*. (1998)……..47

Figure 2.3: Late Norian (210 Ma), early Atlantic megasequence plate tectonic for northwest Europe……47

Figure 2.4: Early Aptian (125 Ma), Biscay megasequence plate tectonic reconstruction for northwest Europe. From Hawkes *et al*. (1998)……...50

Figure 2.5: Early Tertiary (Thanetian) (58 Ma), Alpine megasequence plate tectonic reconstruction for northwest Europe. From Hawkes *et al*. (1998)……50

Figure 2.6: Generalized stratigraphic column for the Wessex Basin showing the three mega-sequences. (JB= Junction Bed; CB= Cinder Bed; GAB= Green Ammonite Beds; PG= Penarth Group; BSPB= BudleighSalterton Pebble Beds). Modified from Underhill and Stoneley (1998)……..53

Figure 2.7: Core logger with high-resolution Bartington susceptibility meter. Some of the core measured and sampled cores measured (inset)……...57

Figure 2.8: polypropylene powder holder, a brass trough sample holder and a mounting station. Note the markings of sample centre position on the mounting station……...57

Figure 2.9: In-house built magnetic extractor used to extract magnetic materials present in the samples……59

Figure 2.10: Wessex Basin Tectonostratigraphy highlighting the key mapped seismic horizons……60

Figure 2.11: An image of section B92-40, showing the tops of the Chalk, Inferior Oolite, White Lias (Rheatic/Penarth) and Sherwood Sandstone……61

Figure 3.1: Crude oil generated from heating the Blue Lias Fm sample at 320 °C for 72 hrs. The other two samples (Kimmeridge and Oxford Clay Fms) heated at the same temperature for same duration also generated crude
oil…….……69

Figure 3.2: Hysteresis curves for the three unheated rock samples showing mainly paramagnetic behaviour. The curves are not slope corrected……..71

Figure 3.3: Magnetic hysteresis plots for the Kimmeridge Clay Fms heated (320 °C & 250 °C) and unheated showing changes in magnetic response after heating. The unheated sample response is almost flat and lies very close to the x-axis. The hysteresis loops do not have a paramagnetic correction…….71

Figure 3.4: Magnetic hysteresis plots for Oxford Clay Fms heated (320 °C & 250 °C) and unheated showing changes in magnetic response after heating. The hysteresis loops do not have a paramagnetic correction…….72

Figure 3.5: Magnetic hysteresis plots for Blue Lias Fm heated (320 °C & 250 °C) and unheated showing changes in magnetic response after heating. The immature sample response is almost flat and lies very close to the x-axis. The hysteresis loops do not have a paramagnetic correction…….....72

Figure 3.6: A) A plot of saturation remanent magnetization (Ms) versus pyrolysis temperature. Oxford Clay Fm showed a double peak Ms values first at 250 °C then a minimum at 300 °C and a secondary maximum at 320 °C. Kimmeridge Clay Fm showed the highest Ms at 320 °C pyrolysis temperature. B) Plot of the magnetic coercivity (Bc) against pyrolysis temperature for all three source materials……...73

Figure 3.7: Comparison of hysteresis measurements carried out at 5 K and at room temperature of a) Oxford Clay Fm 320 °C b) Blue Lias Fm 320 °C c) Kimmeridge Clay Fm 320 °C and d) Kimmeridge Clay Fm 250 °C…….74

Figure 3.8: First order reversal curves (FORC) diagrams for a) Oxford Clay Fm 200 °C showing narrow elongated contour distribution with peak at around 60 mT and b) Kimmeridge Clay Fm 320 °C showing narrow contour distribution with peak near the origin…….75

Figure 3.9: Multicycle thermomagnetic curves showing slight alteration and increase in magnetic moment (a, c & d) that indicates possible alterations from greigite and/or to possible magnetite. Panels b, e & f show an increase in moment after the first step, indicating alterations possibly to pyrrhotite and subsequent decrease in the moment in the 500 & 650 °C steps, indicating alterations to less magnetic mineral possibly pyrite and/or hematite. Insets: Continuous thermomagnetic curves indicating drop in magnetization on heating.(a, b, d & e) show drop of magnetization around 330 °C- 400 °C which might indicate the presence of pyrrhotite and at around 600 °C which indicates the presence of magnetite. (c& f) indicate the presence of 'mixed' pyrrhotite due to the shape of the curve and magnetite. All heating was carried out in helium atmosphere and a field of 100 mT…….77

Figure 3.10: Warming curves for the Kimmeridge Clay Fm (a & b) and the Blue Lias Fm (c) imparted with a saturation isothermal remanence in field of 7 T at 5 K. Two initial states are considered, zero-field cooling (ZFC) and (FC). ZFC samples were demagnetised at room-temperature before cooling in zero field to 5 K. FC samples were cooled in a field of 7 T from room-temperature to 5 K. Note the difference in scale of the magnetisation of both samples. (d) Shows RT-SIRM with no obvious drop in magnetization on cooling……..78

Figure 3.11: Bright field TEM images of magnetic extract from Kimmeridge Clay Fm (320 °C) showing (a) sheets of green rust, as identified by selected area electron diffraction (SAED) (inset); and (b) clusters of nanoparticles (< 50nm), with characteristic lattice fringes consistent with the presence of Fe3S4 (inset)……...79

Figure 3.12: (a) HAADF image of magnetic extract from Kimmeridge Clay Fm (320 °C) showing sheets of green rust; and (b-h) EDX chemical maps showing (b) aluminium; (c) carbon; (d) iron; (e) potassium; (f) magnesium; (g) oxygen; and (h) silicon, content…...……..80

Figure 3.13: (a) HAADF image of magnetic extract from Kimmeridge Clay Fm (320 °C) showing an individual nanoparticle; and (b, c) EDX chemical maps showing (b) iron; and (c) oxygen, content. (d) EDX spectrum acquired from the centre of the particle shown in (a)……...80

Figure 4.1: Satellite image of Dorset, showing the effects of the Tertiary inversion on the topography of the study area and seismic lines (red lines) and key wells (black dots) interpreted in this study. Modified from Underhill and Stoneley (1998)……87

Figure 4.2: Exposed section of the Sherwood Sandstone at Budleigh Salterton in Devon. (SY063817)……..88

Figure 4.3: Gross isopach map for the Triassic Sherwood Sandstone Group. Modified from (Hawkes *et al*., 1998)……..……..89

Figure 4.4: Exposed Bridport Sandstone section at West Bay in Dorset. (SY463903)…….89

Figure 4.5: Gross isopach map for the Bridport Sandstone showing structural control of deposition by the extensional faults. From Hawkes *et al*. (1998)…….90

Figure 4.6: Liassic – Monmouth Beach, Lyme Regis, Dorset ; Oxford Clay Fm – Weymouth Anticline, Dorset (SY703819); Kimmeridge Clay Fm – Kimmeridge Bay, Dorset (SY909790)……..91

Figure 4.7: Gross isopach map for Early Jurassic Lias Group showing structural control on deposition. Modified from Hawkes *et al*. (1998)……..……..91

Figure 4.8: Map showing the Tertiary inversion elements in the Wessex Basin. Modified from Butler (1998)……...94

Figure 4.9: Residual Bouguer gravity map showing the Wessex Basin and the English Channel. From Smith and Hatton (1998)……...…..94

Figure 4.10: Burial reconstruction showing a) Kimmeridge 5 with the Lias entering the oil generation window during the Early Cretaceous before uplift in Oligocene, b) Wytch Farm-2 showing the Lias briefly entering the oil window in Mid. Jurassic before uplift in the Late Jurassic. From Bray *et al*. (1998)……...95

Figure 4.11: Burial reconstruction showing a) Wytch Farm K1-25 with the Lias immature, b) Waddock Cross-1 with the Lias Immature, c) Radipole-1 showing the Lias entering the oil window during mid. Cretaceous, and d) Kimmeridge 5 showing the Lias entering the oil window in the Early Cretaceous. From Brau, 2015……..96

Figure 4.12: A multi-well one-way time (s) vs depth (m) showing a very strong correlation between the two……98

Figure 4.13: a) an image of seismic section B92-40, b) Interpretation of seismic section B92-40 showing tops of some of the geological formations identified and also the distribution and geometry of faults in the study area……..99

Figure 4.14: Seismic section B90-32 showing: a) Image of seismic section with faults and tops identified, b) Polygons generated using stratigraphic rock properties data, c) Depth converted and d) Decompacted section, note: an average of 150m increase in thickness……100

4.15: Seismic section B90-37 showing: a) Image of seismic section with tops identified, b) Polygons generated using stratigraphic rock properties data, c) Depth converted and d) Decompacted section……..101

Figure 4.16: a) a composite section running from the offshore Portland –South Wight Basin to the Wytch Farm area showing the structures and the stratigraphy, b) a geometrically restored section with hanging wall restored prior to Tertiary inversion……103

Figure 4.17: upheaval map, consisting of present day Inferior Oolite surface on the footwall of the Abbotsbury-Ridgeway and Purbeck faults, with the restored Inferior Oolite in the hanging wall superimposed on it (inset), showing potential migration routes……..105

Figure 4.18: upheaval map, consisting of present day Sherwood Surface (White Lias +300 m) surface on the footwall of the Abbotsbury-Ridgeway and Purbeck faults, with the restored Inferior Oolite in the hanging wall superimposed on it (inset), showing potential migration route from Bridport Sandstone to Sherwood Sandstone via Creech……106

Figure 5.1: Map of Wessex Basin with location of the 9 sampled wells…….111

Figure 5.2: Mass chromatogram (m/z 57) of aliphatic fractions of a and b) Bushey Farm A1 (3464) Kimmeridge 5 (872) respectively, stained probably by the drilling mud, and c and d) Chickerell 1 (262) and Wytch Farm A12 (2998) exhibiting typical *n*-Alkane distribution from crude oils…….115

Figure 5.3: Ratios of pristane/phytane (Pr/Ph) plotted to investigate redox conditions at the time of source rocks deposition. Samples Coomb1 and CH6 had anomalously low values……..116

Figure 5.4: Ratios of Ph/C_{18} against Pr/C_{17} plotted in tandem to investigate organic matter type, and environments of deposition (Lijmbach, 1975); nearly all the samples plotted within the type II kerogen, from algal organic matter in a strongly reducing environment……..116

Figure 5.5: A selection of samples measured using m/z 191 ion. BS9 and KM3 (a and b respectively) had low concentration of hopanes ($\leq C_{31}$ hopane), they belong to the 'P' marked group. CH1 and WC3 (c and d) on the other hand had a full suite of terpanes, up to C35 homohopane and they belong to the 'O' group……..118

Figure 5.6: A plot of C_{30}/C_{29} Ts showing two distinct groups of oils; Coomb1 and the CH oils in one group, and CR and WC oils in another, with MT2 and CR1 as outliers……..118

Figure 5.7: The distribution of well average values for C_{30}/C_{29} Ts, showing the biomarker mainly distributed along the main fault line of the study area…….119

Figure 5.8: A plot of C_{29}Ts/(C_{29} H+C_{29} Ts) with the CH oils plotting differently from CR and WC……121

Figure 5.9: The distribution of well average values for C_{29}Ts/(C_{29}H+ C_{29}Ts), showing the biomarker mainly distributed linearly along the main fault line of the study area……..121

Figure 5.10: A plot of C_{35}H/($C_3$1H – C_{35}H) showing the WX samples plotting separate from the rest of the samples……...122

Figure 5.11: The distribution of well average values for C_{35}H/(C_{31}H – C_{35}H), showing the biomarker mainly distributed on the eastern section of the study area with concentration getting less from Waddock Cross south-eastwards…….122

Figure 5.12: A plot C_{35}H/C_{34}H showing no distinct groupings from the different oil samples……..…123

Figure 5.13: A plot of C_{31} 22R/C_{30} H showing ST and WX grouped on one hand, and CH, CR and WC on the other……...124

Figure 5.14: The distribution of well average values for C_{31} 22R/C_{30} H biomarker, showing no particular pattern of distribution……126

Figure 5.15: A plot of 30-Norhopane/hopane index also not showing any groupings of the oil samples measured……126

Figure 5.16: The distribution of well average values for C_{29} H/C_{30} H biomarker showing a fair distribution across all wells except for B The distribution of well average values for C_{31} 22R/C_{30} H biomarker Bushey Farm (BS)…….….127

Figure 5.17: Plot of maturity biomarkers Ts/Tm versus C_{30}H…….……127

Figure 5.18: Plot of C_{29}steraneepimers, αββ/(αββ+ααα) versus (S/(S+R))…….…..128

Figure 5.19: Gammacerane indices plotted to using 10 × G/(G+C_{30} H) with all values plotting within 1.75 – 2.5……...…128

Figure 5.20: The distribution of 10 × G/(G + C_{30}) biomarker, showing increasing concentration of the biomarker away from the main fault of the basin……..…….129

Figure 5.21: A plot of G/C_{31} 22R biomarker with WX, CH, CR and WC having values between 0.6-1.0, indicating rocks deposited in stratified water due to hypersalinity……129

Figure 5.22: A plot of Gammacerane/C_{31} H, showing the concentration of the biomarker to the north and south of the main fault of the study area…….130

Figure 5.23: Plots of LT and RT magnetic hysteresis parameters showing plots of: a) M_s values, with 'O' samples having higher values than the 'P' samples in LT measurement, b) high-field susceptibility (χ_{hf})showing the 'O' samples having larger paramagnetic contributions both at LT and RT.……134

Figure 5.24: Plots of: a) LT- and RT-M_s values, showing lower LT value for BS9-O sample compared with the 'P' samples. b) χhf values, showing no trend either with respect to oil staining or depth of sample……...…….……134

Figure 5.25: Plots of: a) LT- and RT-Ms showing that the 'O' samples having higher LT-Ms values, except for CR7 and negative values for RT CR2 and CR6. b) χhf, showing no particular pattern with respect to depth of sampling or oil stain…….……135

Figure 5.26: Plots of: a) LT- and RT-Ms values, showing increasing values for LT-Ms and decreasing values for RT-Ms with sampling depth. b) LT- and RT-χhf with WC1 and WC2 having about equal paramagnetic contributions and WC3 slightly higher contribution.....……...139

Figure 5.27: a) LT- and RT-Ms, showing general increase in the LT-Ms values with depth of sampling, b) LT- and RT-χhf showing CH7 having the highest value……..139

Figure 5.28: Plots of: a) LT- and RT-Ms, showing random variations, b) LT- and RT-χhf, showing no one particular trend in variations……...……...140

Figure 5.29: Plots of: Plots of: a) LT- and RT-Ms showing WX2 having the value for the LT-Ms while decreasing with sampling depth for the RT-Ms, b) LT- and RT-χhf, showing WX2 having the largest paramagnetic contribution in both measurements……...….141

Figure 5.30: Plots of: Plots of: a) LT- and RT-Ms values, showing no variation with respect to depth of sampling, b) LT- and RT-χhf values showing no particular trend……..……...…141

Figure 5.31: Plots of a) LT- and RT-Ms values, showing no clear trend in variation, b) LT- and RT-χhf, showing paramagnetic contribution generally decreasing with depth sampling, except for MT3……...141

Figure 5.32: Plot of LT- and RT-Ms showing variations across all the wells sampled……...……142

Figure 5.33: Plot of well LT-Ms average values, showing increase in LT-Ms well averages from Kimmeridge to Wytch Farm and Waddock Cross, with Chickerell, Creech and Bushey Farm having similar averages……..143

Figure 5.34: Plots of: a) LT and RT Mrs measurements, with 'O' samples having lower values than the 'P' samples in the RT measurement, b) lower Bc values for the 'O' samples in the LT measurement…..144

Figure 5.35: Plots of: a) LT and RT Mrs values showing no clear trend in variations, b) Bc showing no clear variation or trend, c) Mrs/Ms ratios, with no apparent differences between the 'P' and the 'O' samples……..…….145

Figure 5.36: Plots of: a) LT- and RT-Mrs showing mixed results in LT-Mrs values with no clear trend. b) LT- and RT-Bc values with 'P' samples having lower LT-coercivity values than the 'O' samples except for CR1 and c) LT- and RT- Mrs/Ms with the 'P' samples having lower ratios in the LT-Mrs/Ms, CR2 and CR6 having negative ratios in the RT-Mrs/Ms with no apparent trend in the rest of the RT-Mrs/Ms ratios……..……..……141

Figure 5.37: Plots of: a) LT- and RT-Mrs values showing decreasing values with sampling depth in both LT- and RT-Mrs values, b) LT- and RT-Bc values, showing decreasing trend in values with sampling depth in the LT-Bc and no clear trend in the RT-Bc, c) LT- and RT-Mrs/Ms showing decreasing values for LT-Mrs/Ms with increasing depth of sampling but increasing values for RT-Mrs/Ms with increasing sampling depth…….……..146

Figure 5.38: Plots of: a) LT- and RT- Mrs, showing CH7 having highest value in both cases, b) LT- and RT-Bc values showing no particular pattern, with CH7 having highest and lowest values in the LT- and RT-Bc respectively, c) LT- and RT-Mrs/Ms with CH7 having the highest value……147

Figure 5.39: Plots of: a) LT- and RT- Mrs, with 'O' samples having higher Mrs values than their 'P' counterparts, b) LT- and RT- Bc, showing increase in Bc values for both measurements from ST1-ST3, with a decrease observed in ST4, c) LT- and RT-Mrs/Ms, with no one particular trend in both measurements……..……...148

Figure 5.40: Plots of: a) LT- and RT- Mrs values, with WX2 having the lowest value in both measurements, b) LT- and RT-Bc with WX2 having the lowest coercivity values in both measurements, c) LT- and RT-Mrs/Ms ratios, with WX2 again having the lowest value……148

Figure 5.41: Plots of: a) LT- and RT- Mrs values, the samples had near identical values in each of the measurements except for Coomb1 LT-Mrs, which is anomalously high, b) LT- and RT-Bc values, showing a general decrease in values with depth in the LT-Mrs but no particular trend in the RT-Mrs, c) LT- and RT-Mrs/Ms values showing a general decrease in value with sampling depth in the LT-Mrs values and no particular trend in the RT-Mrs…….……...……..149

Figure 5.42: Plots of a) LT- and RT-Mrs values, showing MT2 having the highest value in the RT-Mrs value and no clear trend in the RT-Mrs values, b) LT- and RT-Bc values, with MT2 having the highest RT-Bc, c) LT- and RT-Mrs/Ms values, showing a general decrease in the RT-Mrs/Ms values with depth of sampling and MT2 having a higher LT-Mrs/Ms value……..…….149

Figure 5.43: Figure 5.43: Plot of LT-Mrs for samples showing increase in values from Kimmeridge to Wytch Farm….....150

Figure 5.44: Plot of wells average LT-Mrs values, showing an increase from KM to WC through BS……...……151

Figure 5.45: Plots of a) LT-Mrs/Ms showing mixed relationship with 'O' samples and b) RT-Mrs/Ms nearly all samples had the same value…….……..….151

Figure 5.46: Plots of: a) LT-Bc, and b) RT-Bc values showing no clear trend in variations. Inset map shows the localities……..……...152

Figure 5.47: ZFC warming curves plot showing: a) KM1 with arrows showing magnetisations at 15, 30, 50 and 300 K whose ratios were used in this study to investigate the abundance of fine (<30 nm) and very fine (5-15 nm) ferromagnetic particles, b) KM2 showing higher magnetisation than KM1 with what appears to be a Verwey Transition at ~120 K, indicating the presence of magnetite in the sample, c) KM3 showing similar magnetisation to KM2 and possible Verwey Transition, d) KM4 showing a sharp drop in magnetisation around 120 K, which is indicative of magnetite……..…….153

Figure 5.48: Plots of: a & b) ratios of ZFC-FC LT-SIRM measurements showing the hyperfine magnetic ferromagnetic particles (30 K/15 K) decreasing with sampling depth and a decrease in larger ferromagnetic particles (300 K/50 K) from KM1 to KM3 and then increasing again at KM4……...153

Figure 5.49: Plots of a& b) ZFC warming curves showing pyrrhotite as the dominant magnetic phase and e & f) ratios of ZFC-FC warming curves also showing no particular trend……..……...……154

Figure 5.50: Plots of: a) ZFC warming curves for CR1 showing magnetite as the likely predominant mineral phase, due to its shape, b & c) ratios of FC and ZFC warming curves showing variation in amounts of large grains with sampling depth and oil staining in the 300 K/50 K ZFC (panel b).....154

Figure 5.51: a) ZFC warming curve for WC1 showing magnetite as the likely magnetic phase, b) and c) ratios of FC and ZFC warming curves showing variation in amounts of small/paramagnetic particles decreasing from WC1 to WC2 and increasing in WC3 in the FC curves (b)……..155

Figure 5.52: Plots of ZFC warming curve for Stoborough (ST), Waddock Cross (WX), Coombe Keynes (Coomb) and Martinstown (MT) all showing double crystallographic transitions (Besnus and Verwey) confirming the presence of pyrrhotite and magnetite in the samples……..……..155

Figure 5.53: a & b) 30 K/15 K FC and ZFC, values indicating two likely cycles of decrease in amounts of fine ferromagnetic particles from Kimmeridge to Wytch Farm and from Stoborough to Martinstown, c & d) 300 K/50 K FC and ZFC values showing no clear trend…….……..157

Figure 5.54: A plot of pseudo-κ values for the sampled intervals showing a fairly linear relationship between oil staining and low-field magnetic susceptibility. Note the gap at KM and CH, this is due to non-availability of data……...…….……..158

Figure 5.55: Map of study area showing mineralogical changes along migration paths; from mainly magnetite in KM area with arrows showing direction of increasing magnetic grain size and pyrrhotite content; ST, WX and Coomb and MT areas have mixed magnetite and pyrrhotite while there was mainly magnetite around CH……..162

List of Tables

Table 1: Properties of common magnetic minerals (After Evans and Heller (2003))……32

Table 2.1: Well core samples analysed during this study, showing sample depths, formation and lithology…...53

Table 3.1: Room-temperature hysteresis parameters carried out on the three rock samples used in this study. χhf= high-field susceptibility, Bcr= remanent coercivity, Bc= Coercivity, Mrs= saturation remanent magnetization, Mrs/Ms= ratio of saturation remanent magnetization to saturation magnetisation…….73

Table 4.1: List of 2D seismic lines used to produce surfaces during this study……97

Table 4.2: A selection of 2D seismic sections used to generate geometrically restored surfaces……104

Table 5.1: Distribution of gammacerane and homohopanes across all 45 samples analysed. Note the near total absence of any hydrocarbon in the Bushey Farm (BS) samples……113

Table 5.2: Summary of biomarkers and their interpretations used in this study…….…….115

Table 5.3a: mean, standard deviation and median of some of the biomarkers used in this Chapter……120

Table 5.3b: mean, standard deviation and median of some of the biomarkers used in this Chapter……...120

Table 5.4:Low (LT) and room-temperature (RT) hysteresis parameters for all samples analysed. See Table 2.1 for depth and lithological variations……...…...136

Table 5.5:Field-cooled (FC) and zero-field cooled ratios of magnetisation at 30 K/15 K and 300 K/50 K…...137

Table 5.6: mean, standard deviation and median for the low- and room-temperature magnetic measurements carried on the core samples……138

Table 5.7: Drilling mud types and composition for all the wells sampled……...…….…...163

Chapter 1

Introduction

1. Introduction to thesis

Petroleum is a complex material composed mainly of saturated and aromatic hydrocarbons with varying amounts of compounds containing nitrogen, sulphur and oxygen (NSO compounds), emulsified water and minerals. Petroleum also contains metals and metalloids in trace amounts either in organic or inorganic (organometallic) forms (Tissot and Welte, 1984). The possibility of exploration for petroleum using novel methods like magnetics by analysing data from aeromagnetic surveys was first suggested by Donovan *et al.* (1979). Donovan *et al.* (1979) linked the positive magnetic anomaly observed over the Cement oil fields in Oklahoma, to the presence of the underlying hydrocarbon accumulations. Later studies have not only successfully delineated oil and gas fields using aeromagnetic data but have also mapped out oil spills and micro-seepages (Donovan *et al.*, 1984; Foote, 1986, 1992; Foote and Sobehrad, 1997; Leblanc and Morris, 1999; LeSchack, 1994; LeSchack and Jackson, 2003; LeSchack and Van Alstine, 2002; Liu *et al.*, 2004; Liu *et al.*, 2006; Liu and Liu, 1999). For example, a study carried out by LeSchack and Van Alstine (2002) used a combination of ground magnetic and radiometric surveys to locate and delineate oil and gas fields with a recorded success of about 80% in Western Canada and LeSchack and Jackson (2003) carried out airborne measurement of transient electromagnetic pulses (EMP) in, Canada, USA, South Australia and New Zealand that has led to the discovery of several oil and gas fields some of which are now producing.

These studies have identified links between accumulation of hydrocarbons and the enhancement of rock magnetic properties either through the studies of aeromagnetic maps (Donovan *et al.*, 1979; Leblanc and Morris, 1999; LeSchack and Jackson, 2003; LeSchack and Van Alstine, 2002) or rock samples (Aldana *et al.*, 2003; Costanzo-Alvarez, 2006; Emmerton *et al.*, 2013) and the reported occurrence in amounts of metallic constituents in crude oils (Alberdi-Genolet and Tocco, 1999; Duyck *et al.*, 2002; Filby, 1994; Lewan, 1984; Lord, 1991; Sainbayar, 2012; Saunders *et al.*, 1991; Shirey, 1931). However, the origin of the chemical species residing either in the petroleum reservoir or along petroleum migration pathways that are responsible for the magnetic anomaly has been a subject of debate. Some authors (e.g., Burton *et al.*, 1993; Elmore *et al.*, 1994; Elmore *et al.*, 1987; Elmore *et al.*, 1993; Elmore *et al.*, 2001; Liu *et al.*, 2004; Liu *et al.*, 2006; Liu and Liu, 1999; Lu, 1990) argued that changes in redox conditions due to the presence of hydrocarbons could lead to a net positive or negative magnetic relief in an area while others (Aldana *et al.*, 2003; Costanzo-Alvarez, 2006; Díaz *et al.*, 2000; Emmerton *et al.*, 2013; McCabe *et al.*, 1987) stressed the importance of microbial

activity within the vicinity of hydrocarbon accumulations activities. Reynolds *et al.* (1991), however, argued that both biogenic and abiogenic magnetic materials are produced simultaneously in areas of hydrocarbon accumulation or seepages. The formation of secondary magnetic minerals, e.g. greigite, magnetite and pyrrhotite, has been reported to occur in sedimentary successions independent of the occurrence of hydrocarbon. Several authors (e.g., Aubourg and Pozzi (2010)) have reported the formation of secondary magnetic minerals due solely to the action of temperature and pressure.

The aim of this thesis is to address some of the uncertainties in the relationships between magnetic minerals and hydrocarbon formation, and to assess the potential use of magnetic methods in hydrocarbon exploration (see section 1.6). This thesis consists of six chapters; Chapter One deals with a general review of magnetism and geochemistry, two of the main subjects covered in this research. Chapter Two consists of reviews of geological history of the area of study and methods used in carrying out sampling, experimentation and modelling. Chapters Three, Four and Five are research chapters that cover the pyrolysis experiments (artificial maturation of source rocks to generate crude oils), basin models and magnetic/geochemical characterisation of sampled core materials respectively. Finally, Chapter Six is a summary of the three research chapters, i.e., chapters Three, Four and Five.

1.1 Magnetism as a tool for hydrocarbon exploration

As mentioned above Donovan *et al.* (1979)were the first to propose the use of aeromagnetic studies in the exploration of oil and gas due to magnetic anomalies observed over oil fields, and there have been later studies exploring this relationship(Burton *et al.*, 1993; Costanzo-Alvarez, 2006; Costanzo-Alvarez *et al.*, 2000; Díaz *et al.*, 2000; Donovan *et al.*, 1979; Donovan *et al.*, 1984; Ellwood and Crick, 1988; Ellwood and Pemberton, 1984; Elmore *et al.*, 1994; Elmore and Crawford, 1990; Elmore *et al.*, 1987; Elmore *et al.*, 1993; Foote, 1992; Foote and Sobehrad, 1997; Leblanc and Morris, 1999; LeSchack, 1994; LeSchack, 1997; LeSchack and Van Alstine, 2002). Working with well cuttings, Aldana *et al.* (1999) carried out rock magnetic measurements such as magnetic susceptibility, bulk magnetization coupled with X-ray diffraction analysis, scanning and transmission electron microscopy (SEM and TEM, respectively) on rock cuttings from La Victoria oil field in Venezuela. They found a correlation between regions with high magnetic susceptibility and bulk magnetization values with the presence of hydrocarbon. Similarly, Costanzo-Alvarez *et al.* (2000) carried out magnetic measurements on near-surface rock cuttings from Guafita oil field in Venezuela obtained from producer and non-producer wells. They identified two types of anomalies: anomaly A with

characteristic low-coercivity magnetic minerals and is restricted only to samples from the producer wells and is associated with the occurrence of spherical aggregates, and anomaly B which appears in most of the producer and non-producer wells and X-ray diffraction analysis revealed anomaly B was caused by magnetite and haematite. Another study carried out by Liu *et al.* (2006) examined rock cuttings from a producer and a non-producer well from Mawangmiao oil field in Hubei Province of China. They carried out measurements on rock samples that include magnetic susceptibility and hysteresis and made a plot of magnetic susceptibility/saturation remanent magnetisation (χ/M_{rs}) and saturation-remanent-magnetisation/saturation-magnetisation (M_{rs}/M_s) and discovered samples from the producer wells data from the two wells plotted separately with data from the producer well having higher M_{rs}/M_s values. The data indicated the presence of larger magnetic grains in the producer well. Sassen (1980) documented the evidence for microbial degradation of hydrocarbon that results in the formation of secondary minerals such as pyrite, calcite, magnetite and pyrrhotite and Garden *et al.* (2001) used such evidence to map hydrocarbon migration pathways in the Entrada Sandstone, southeast of Utah, USA.

Studies of aeromagnetic and ground magnetic data with interest in hydrocarbon exploration have been intensified in recent years. For example, Stone *et al.* (2004) carried out an aeromagnetic survey over Muglad Basin in South Sudan and discovered magnetic anomalies which clustered along a prospective structure and coincided with the Jarayan oil field. In addition, ground magnetic surveys have also been used to explore for oil and gas. LeSchack and Van Alstine (2002), discovered high-resolution ground magnetic (HRGM) anomalies occur above the most prolific reservoir in Western Canada, compared with smaller oil fields. Moreover, LeSchack and Van Alstine (2002) reported anomalous HRGM values for Leduc pinnacle-reef reservoir and also above Grand Canyon Formation Cuesta reservoir. LeSchack and Van Alstine (2002) argued the HRGM anomalies arise due to high concentrations of magnetic minerals in shallow magnetically enhanced zones within reservoirs. They argued that by using HRGM anomaly intensity and the residual magnetic anomaly azimuth, the reservoir responsible for the magnetic anomaly could be identified (Figure 1.1).

Moreover, airborne measurements using transient electromagnetic pulses have also been successfully used to identify hydrocarbon accumulations. LeSchack and Jackson (2003)argued transient pulses generated during lightning are trapped by the redox current currents in hydrocarbon reservoirs. LeSchack and Jackson (2003) carried out transient electromagnetic pulses measurements over known oil and gas producing fields in Alberta, Canada, and Texas,

USA, and compared with the surrounding area. This technique was used in Canada, USA, New Zealand and Australia with over 100,000 miles of lines flown. The technique has led to the expansion of known fields and also new discoveries that are now producing, e.g., oil fields at Pecos, Hidalgo and Shelby counties, Texas, USA.

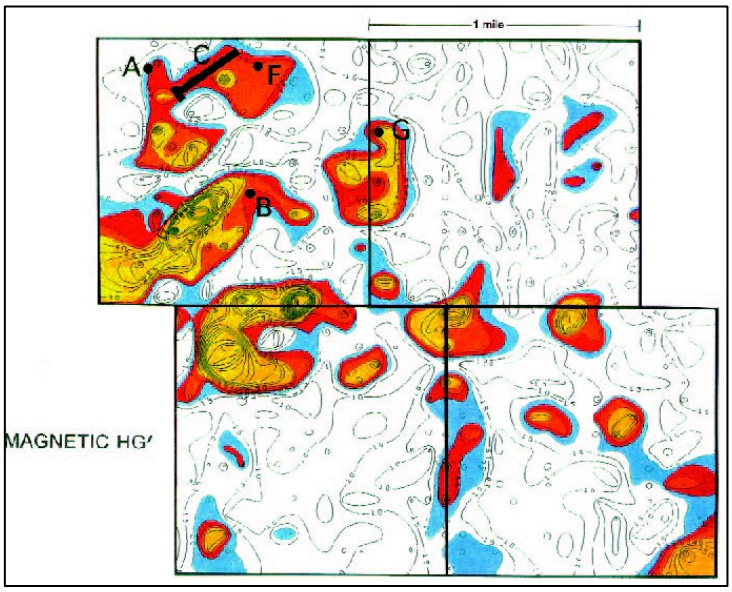


Figure 1.1: (a) Magnetic HG′ map of a four-section (103-ha) part of the Alida (Mississippian limestone) field at North Pierson. The survey was completed prior to drilling of the wells shown. All five wells were drilled on HG′ anomalies and all encountered oil. Note the northwest-southeast subcrop trend of erosional Mississippian cuesta reservoirs, seen also in Figure 1. HG′ contour values (proportional to nT/m2) greater than 2 were considered significant and are coloured. HG = high-resolution ground-magnetic anomaly. From (LeSchack, 1997).

1.2 Review of magnetisation

The concept of magnetism, the types of magnetic behaviours and minerals are briefly explained below.

1.2.1 Basic magnetism

The magnetic properties of materials lie within their constituent atoms. Atoms consist of electrons which orbit a central nucleus and also spin on their own axes (Butler, 1992).

The magnetic dipole moment **M** can be defined be either referring to a pair of magnetic charges (Figure 1.2a) or to a loop of electrical current (Figure 1.2b). For the pair of magnetic charges, the magnitude of charge is p, and the two opposing charges are separated by infinitesimal distance l. The magnetic moment **M** is thus:

$$\mathbf{m} = pl \qquad (1)$$

For a loop carrying a current I, with surface area A, magnetic moment is given as:

$\mathbf{m} = I\,A$ (2)

Magnetic field **H** is defined as the force experienced by a unit positive charge placed in a region.

The magnetic intensity or magnetization, **M**, of a material is the net magnetic dipole moment per unit volume.

$\mathbf{M} = \Sigma_i\, m/volume.$ (3)

There are basically two types of magnetizations; induced and remanent magnetizations. When a substance is exposed to a magnetic field H, it acquires an induced magnetization, M_i.

$M_i = K\,H$ (4)

Where K is the magnetic volume susceptibility of a substance which defines the magnetizability of a material (Butler, 1992). To obtain mass susceptibility, χ, volume susceptibility (K), is divided by the density (ρ) of the substance. Mass susceptibility has a dimension of m^3kg^{-1}.

$\chi = K/\rho$ (5)

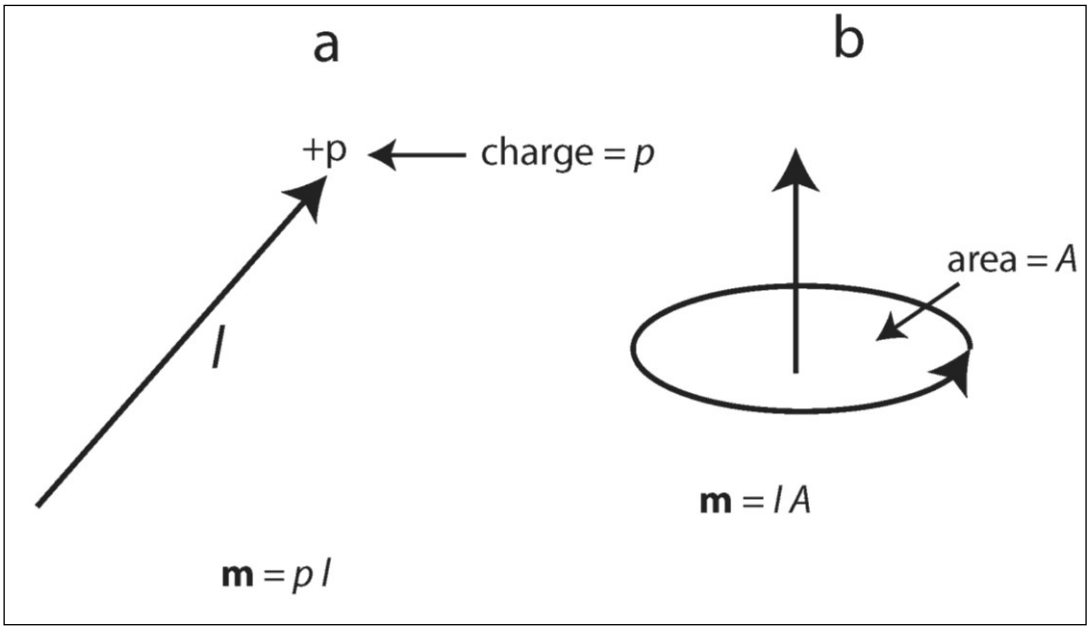


Figure 1.2: a) A magnetic dipole made from a pair of magnetic charges. The magnetic charges are *p* and *-p* for the positive and negative ends respectively. *l*is the distance between the charges. b) A magnetic dipole made from a loop of electrical current. *I* is the current in the loop, *A* is area of the loop. Modified from Butler (1992).

1.2.2 Magnetic properties of materials

Different materials respond in distinct ways to an external field. Below is a brief description of the fundamental types of magnetic properties of materials.

Diamagnetism

Diamagnetism is a property exhibited by all substances (Walden *et al.*, 1999). When a diamagnetic substance is placed in a magnetic field, H, it acquires a small-induced magnetization, M_i opposite to the applied field (Lenz's Law) (Figure 1.3a). The magnetization is linearly dependent on the applied field and it is lost when the field is removed. Diamagnetism is a property of all matter; it is weak and is often masked by the presence of other magnetic behaviours. A substance composed of atoms without permanent atomic magnetic moments exhibits only diamagnetic behaviour and has a negative magnetic susceptibility χ which is independent of temperature (Butler, 1992). Examples of materials with such behaviours are quartz (SiO_2) and water (H_2O).

Paramagnetism

This magnetic behaviour is exhibited by materials with permanent atomic magnetic moments (but no exchange interactions between adjacent atomic moments) (Butler, 1992). At any temperature above absolute zero, thermal energy excites paramagnetic materials' crystal lattices, causing a rapid and random oscillation of their atomic magnetic moments. In the

absence of an external field, the atomic moments are equally distributed in all directions with a resultant zero magnetization ($M_i = 0$) (Butler (1992).When such materials are subjected to an external field, H, the atomic magnetic moments in the material align parallel to the applied field (Fig. 1.3b). M_i is linearly dependent on the applied field until saturation and it reduces to zero once the field is removed.

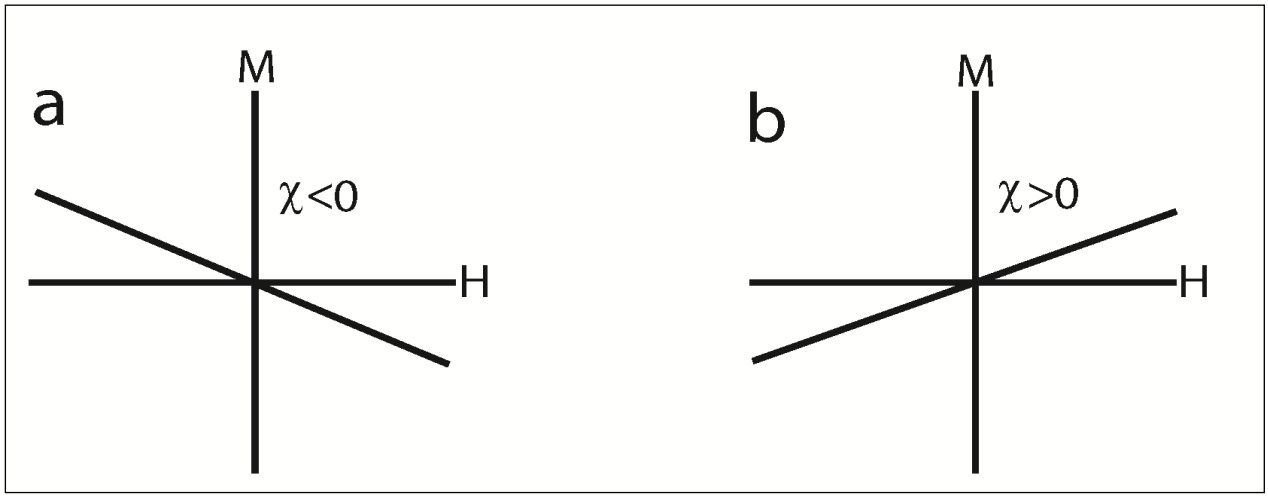


Figure 1.3: Figure 1.3 a) Magnetisation (M) vs magnetic field (H) for a diamagnetic substance. Magnetic susceptibility (χ) is negative. b) M vs H for a paramagnetic substance, magnetic susceptibility (χ) is positive. After Butler (1992).

Ferromagnetism

Ferromagnetism is a term used to refer to a group of related magnetic behaviours found in substances with permanent magnetic moments like paramagnetic materials, but unlike paramagnetic materials, adjacent atomic moments interact strongly through a quantum-mechanical exchange coupling(Butler, 1992; Walden *et al.*, 1999). The interaction between the adjacent unpaired electrons produces a spontaneous magnetisation (M_s) in ferromagnetic materials that exists in the absence of an externally applied magnetic field. Crystals of these metals whose atoms are organised in a fixed geometry have their spontaneous magnetisation aligned in preferred directions due to the intrinsic magnetocrystalline anisotropy. Due to variations in exchange coupling energies, there are four ferromagnetic behaviours (Figure 1.4) which arise due to different arrangement of atoms in the crystal lattices of the ferromagnetic materials (Walden *et al.*, 1999).

First, is the ferromagnetic (*sensustricto*) behaviour in which metals and their alloys have their unpaired electrons coupled parallel to one another and this results in the development of strong magnetisation e.g., metallic iron (Figure 1.4a). The second type of behaviour is found in the oxides of these metals, because coupling occurs via an intermediate oxygen atom, alternate

layers of the crystal become magnetised in opposite direction (anti-parallel). If the two opposing layers have equal numbers of unpaired electron sites, there will be no net magnetisation (Figure 1.4b) and it is called antiferromagnetism (Walden *et al*., 1999), but if on the other hand the two opposing layers have an unequal numbers of unpaired electrons, then this leads to a net spontaneous magnetisation and to a third behaviour called ferrimagnetism (Figure 1.4c), e.g., magnetite (Fe_3O_4). The fourth behaviour is when the sub-lattices of anti-ferromagnetic material are not perfectly anti-parallel; a weak spontaneous magnetism may develop. This is called canted or non-linear anti-ferromagnetism (Figure 1.4d), e.g., haematite (α-Fe_2O_3).

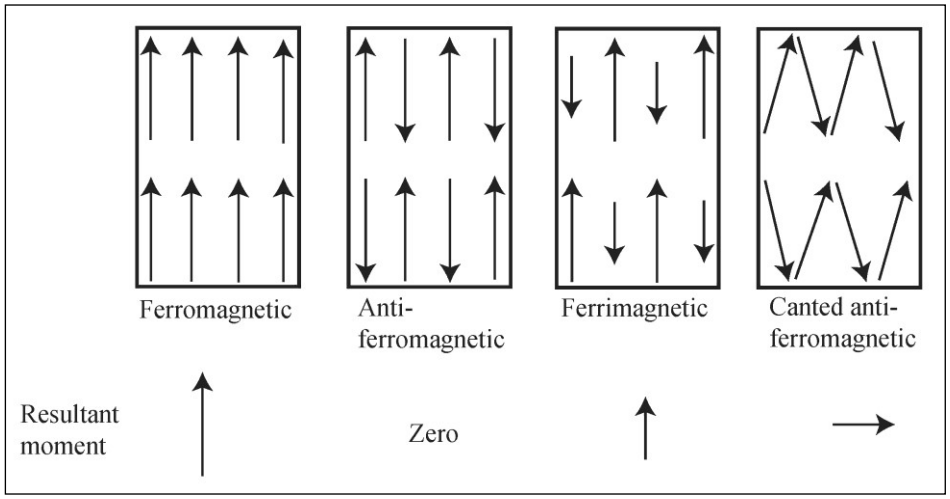


Figure 1.4: Schematic representation of the distribution of magnetisation vectors in crystals, showing the resultant spontaneous magnetisation. After McElhinny (1973).

1.2.3 Magnetic domain

Domain theory states that the magnetic moments within a domain are aligned parallel to one another (Kittel, 1949). Magnetic behaviour of materials is affected by the competing magnetic energies, the main energies are the demagnetisation energy (E_d), the anisotropy energy (E_{anis}), the exchange energy (E_{ex}) and the external field energy (E_h) (Kittel, 1949). A materials total magnetic energy is given by:

$$E_{tot} = E_d + E_{anis} + E_{ex} + E_h \quad (6)$$

where:

E_d: Self energy due to the interaction of magnetic field created by the magnetisation in some parts of the sample on other parts of the same sample. It is dependent on the volume occupied by the magnetic field extending outside the domain. This energy is reduced by minimizing the

magnetic flux outside the domain. Reducing this energy is the driving energy for the creation of multiple domains.

E_{anis}: Energy due to magnetic anisotropy, the crystal lattice is "easy" to magnetise in a given direction and "hard" to magnetise in others. Since the crystal lattice in separate grains of the material is usually oriented in different random directions, this causes the dominant domain magnetization in different grains to be pointed in different directions.

E_{ex}: Energy due to the exchange interaction between magnetic dipole molecules in ferromagnetic, ferromagnetic and antiferromagnetic materials.

E_h: Energy due to the interaction between the magnetic material and an externally applied magnetic field.

In ferromagnetic materials, it is energetically more favourable for the magnetic structure, at a temperature below the Curie temperature (T_c) and above a critical size (d_0), to break up into patterns called domains. A single domain structure (SD) is one in which all the magnetic moments are aligned in one direction only (Kittel, 1967). As ferromagnetic grains grow larger (e.g., 100 nm for magnetite) (Williams and Muxworthy, 2006), to reduce the demagnetisation energy (E_d) they break up into multiple domains, separated by narrow zones of rapidly changing spin directions called domain walls (Figure 1.5) and this cause the structure to act in an SD-like fashion termed pseudo-single domain (PSD) (Tipler, 1999).

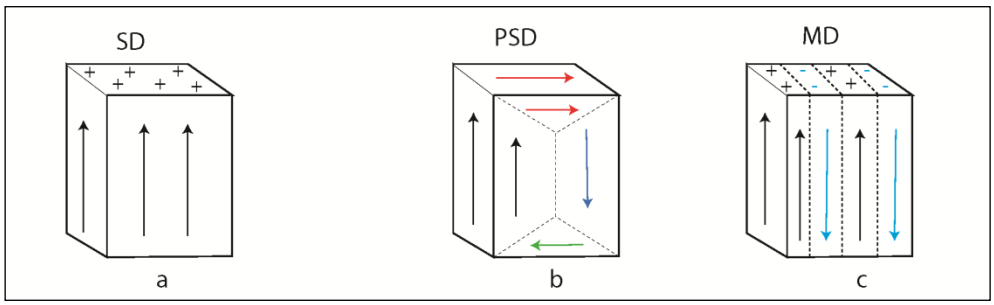


Figure 1.5: Schematic representation of a) single domain structure (SD), b) two domain magnetic structure (PSD) and c) four domain structure (MD), dashed lines represent domain walls and the arrows show the direction of saturation magnetisation (M_s) in each domain. After Dunlop and Özdemir (1997).

1.2.4 Magnetic hysteresis

By applying a magnetic field and measuring the magnetization in a sample, i.e. ferromagnetic, diamagnetic mineral etc., it is possible to distinguish between magnetic behaviours described above in section 1.2.3. Figure 1.3 describes a simple M-H relationship for diamagnetic and paramagnetic substances respectively. The M-H relationship for ferromagnetic substances is more complex and is shown in Figure 1.6. When a magnetic field is applied to a ferromagnetic

material, it increases the material's total energy (E_{tot}), this causes changes in magnetic domains within the material in order to accommodate for this increase in energy and the sample is said to be at least temporarily magnetised (Dunlop and Özdemir, 1997). Assuming we have a ferromagnetic substance that experiences zero field at point *a* (Figure 1.6), as the field strength is increased to H_g, a corresponding magnetisation (M_i) is induced in the sample at point *b*. The slope of *a*-*b* is called the initial, low-field magnetic susceptibility and is completely reversible. But once the applied field strength exceeds H_i, irreversible magnetisation of the sample occurs and the sample will not back to point *a* unless it is demagnetised. At field strength H_f, the sample produces a magnetization M_f and when the field is removed, and the sample retains a magnetisation at point *q*, this magnetisation is known as remanent magnetisation (M_r) and is less than M_f (Figure 1.6). At point *e* magnetisation tails off and will not increase even when the field intensity is increased, this is called the saturation magnetisation (M_s) and the field at which this is achieved is called the saturating field (H_s), when the field is removed the remanence is called saturation remanent magnetisation (M_{rs}). When a negative field is applied to M_{rs}, the sample will be demagnetised at the reverse field called the coercivity (H_c) or the coercive field (or force).

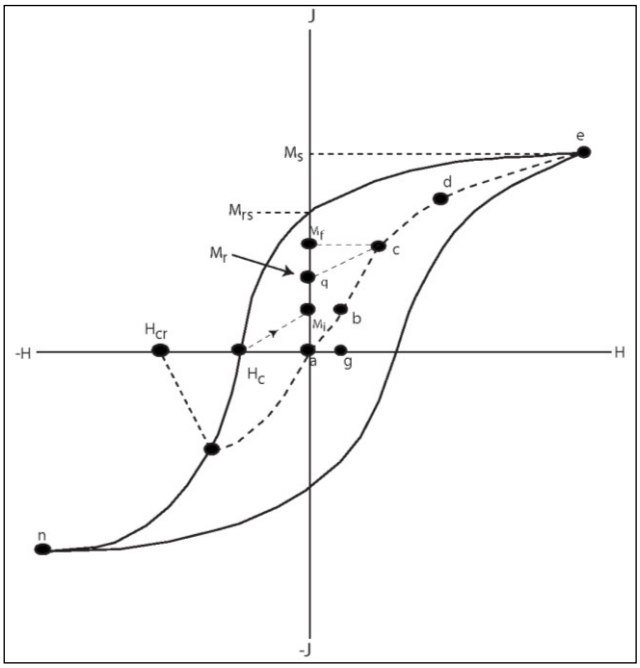


Figure 1.6: M-H plot for ferromagnetic materials showing hysteresis parameters. After Walden *et al.* (1999).

1.2.5 Magnetic Remanence

There are several types of magnetic remanence, e.g., thermoremanence magnetisation, chemical remanent magnetisation, detrital remanent magnetisation *etc.* the ones most relevant to this study are summarised below.

Isothermal remanent magnetization

An isothermal remanent magnetisation (IRM) can be induced in sample when the sample is exposed to strong magnetic field at constant temperature either in laboratory (e.g. hysteresis experiments) or during lightning. The acquisition of IRM depends on the presence of magnetic grains in the sample with coercive force less than the applied field (Butler, 1992). Stepwise IRM acquisition curves are used to study magnetic mineralogy in samples (Gong *et al.*, 2009).

Chemical remanent magnetization

A chemical remanent magnetisation (CRM) is produced when a new mineral crystallizes and has a volume larger than its blocking volume in the presence of a magnetic field. This typically occurs during sedimentary diagenesis, metamorphism or in the laboratory (Heider and Dunlop, 1987).

1.2.6 Ferromagnetic minerals

The most common naturally occurring ferromagnetic minerals are iron-titanium oxides, iron oxyhydroxides and iron sulphides (Table 1). Figure 1.7 shows a solid-solution series of titanium iron oxides and is referred to as TiO_2-FeO-Fe_2O_3 ternary plot. This ternary system can be divided into two structural groups; 1) Titanomagnetite and titanomaghaemite, these are strongly magnetic cubic oxides and 2) solid solution titanohaematites and haematite which are weakly magnetic rhombohedral minerals (Butler, 1992; Evans and Heller, 2003).

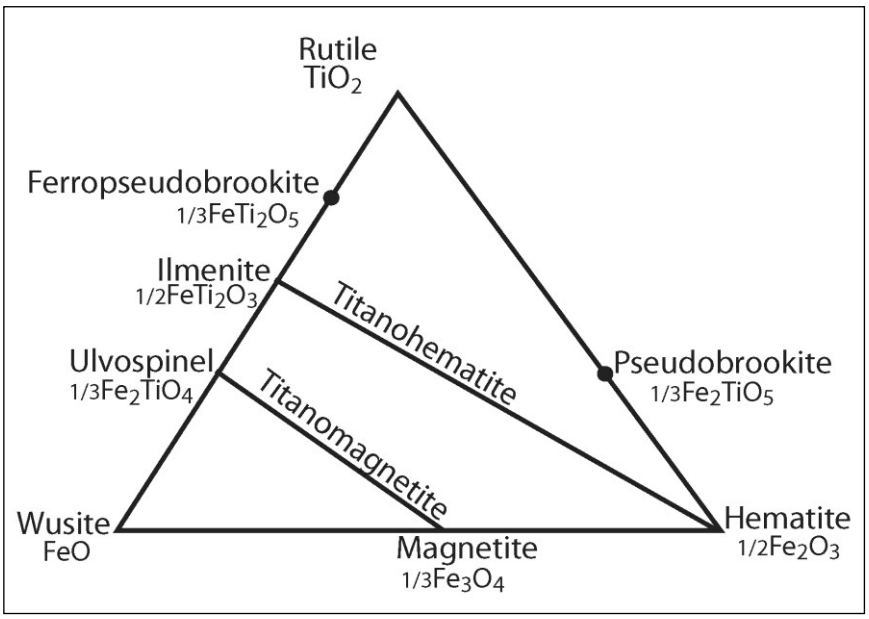


Figure 1.7: Ternary diagram of the main naturally occurring ferromagnetic minerals and solid solution series. From Butler (1992).

Magnetite (Fe_3O_4)

Magnetite is the single most important magnetic mineral on Earth because it is both abundant and highly magnetic (Dunlop and Özdemir, 1997). It occurs in igneous, sedimentary and metamorphic rocks and can also be synthesised biologically (Evans & Heller, 2003). It has a spinel structure with its oxygen atoms forming face-centred cubic framework. This framework consists of two kinds of interstitial spaces; a tetrahedral (A site) and an octahedral (B site) (Figure 1.8). This gives rise to two sublattices that are antiparallel and with an unequal magnetic moment and that makes magnetite ferrimagnetic (Evans and Heller, 2003). Site A contains only Fe^{3+} while site B has an equal number of Fe^{3+} plus additional Fe^{2+} cations. The trivalent cations cancel out leaving magnetite with a net moment arising from the divalent cations (Figure 1.8) with a Curie temperature of ~580 °C (Evans and Heller, 2003).

Haematite (α-Fe_2O_3)

Haematite occurs widely in all rock types and it is the most abundant ore of iron. It has a hexagonal crystal structure with alternating planes containing the trivalent (Fe^{3+}) ions arranged in (nearly) opposite direction. This near antiparallel arrangement makes haematite canted anti-ferromagnetic and is much weaker than Fe_3O_4. Haematite has a Curie temperature of ~675°C and a Morin transition of -15°C (Evans and Heller, 2003).

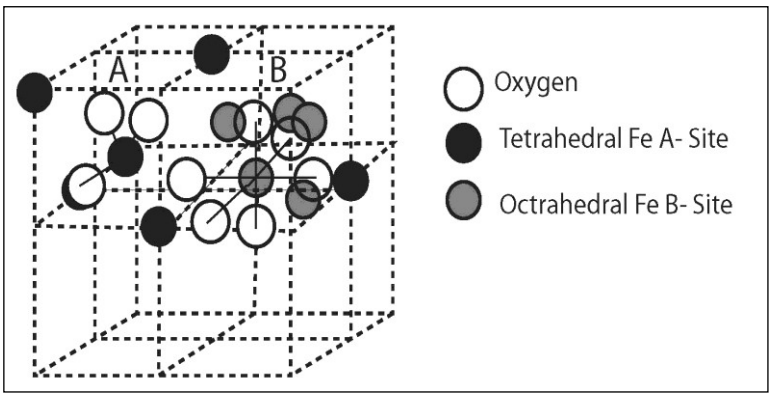


Figure 1.8: The crystal structure of magnetite. Site A tetrahedral Fe^{2+}, Site B octahedral Fe^{2+}/Fe^{3+}. From Banerjee and Moskowitz (1985).

Maghaemite (γ-Fe_2O_3)

Maghaemite also occurs widely in rocks and soils and is similar to Fe_3O_4; it has the same chemical formula as haematite but different crystal structure (it has a cubic crystal structure) and it is ferrimagnetic. Maghaemite is unstable at high temperatures hence its Curie temperature is difficult to be determined experimentally (Evans and Heller, 2003). At temperatures between 250 – 645 °C, it undergoes a permanent crystallographic (inversion) change to haematite (Dunlop and Özdemir, 1997).

Goethite (α-FeOOH)

Goethite is a product of weathering of other iron-rich minerals. It has a hexagonal crystal structure and it is antiferromagnetic in nature with a Curie temperature of about 120 °C. At temperatures higher than T_c ($\leq$300 °C) it dehydrates to form haematite via an intermediate non-stoichiometric magnetite phase(Dunlop and Özdemir, 1997).

Iron sulphides: Pyrrhotite (Fe_7S_8, Fe_9S_{10}), Greigite (Fe_3S_4) and pyrite

Pyrrhotite crystallizes in many forms but the monoclinic (Fe_7S_8)is the most common, it has Curie temperature of ~325°C and it is ferrimagnetic with a characteristic low temperature phase transition at ~35 K (Dekkers, 1988). The hexagonal pyrrhotite however is antiferromagnetic which undergoes a structural transition at 200 °C to a ferromagnet with much higher saturation magnetization (Dekkers, 1988). On the other hand, greigite has a cubic crystal structure and is ferrimagnetic with a Curie temperature of ~330 °C (Roberts *et al.*, 2011). Both pyrrhotite and greigite occur in reducing environments and they tend to oxidize to various iron oxides and paramagnetic pyrite (FeS_2) (Taylor and Tauxe, 2010).

Table 1: Properties of common ferromagnetic minerals (After Evans and Heller (2003))

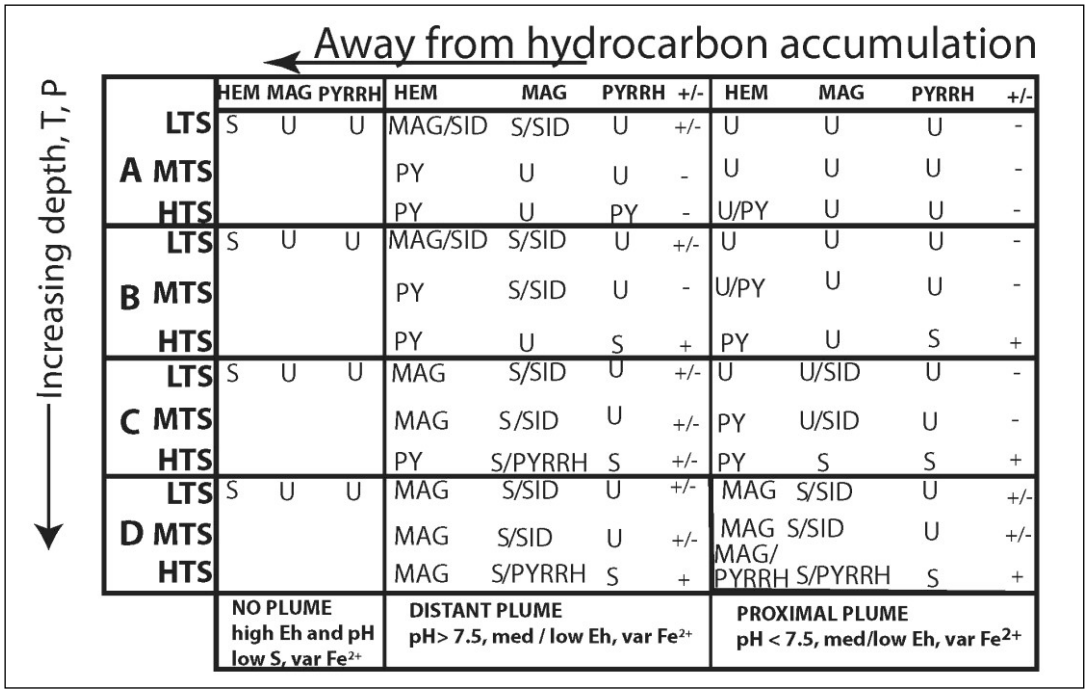
Mineral	Formula	M_s (A/m^2)	T_c (°C)
Magnetite	Fe_3O_4	480	580
Haematite	α-Fe_2O_3	~2.5	675
Maghaemite	γ-Fe_2O_3	380	590 – 675
Goethite	α-FeOOH	~2	120
Pyrrhotite	Fe_7S_8	~80	320
Greigite	Fe_3S_4	~125	~330

1.2.7 Remagnetisation and formation of secondary magnetic minerals

Remagnetisation or secondary magnetisation occurs when the natural remanent magnetisation (NRM) of the magnetic minerals is reset or overprinted. Secondary magnetisation is widespread and commonly observed within sedimentary successions (McCabe and Elmore, 1989) and occurs mainly through chemical remagnetisation (Elmore *et al.*, 2012). Chemical remagnetisation could be brought about by 1) action of externally derived fluids such as magmatic plumes, hydrothermal fluids and hydrocarbons, and 2) alterations due to burial diagenesis (Elmore *et al.*, 2012).

There has been number of studies which laid emphases on remagnetisation due to alterations caused by the physical-chemical changes in the environment as a result of clay mineral diagenesis (e.g., Curtis *et al.*, 1985; Katz *et al.*, 1998; Lu *et al.*, 1991; Moreau *et al.*, 2005; Tohver *et al.*, 2008), hydrocarbon presence (e.g., Burton *et al.*, 1993; Elmore *et al.*, 1993; Machel, 1995) or microbial activity during the biodegradation of hydrocarbons (e.g., Aldana *et al.*, 2003; Costanzo-Alvarez, 2006; Díaz *et al.*, 2000; Ellwood and Crick, 1988; Ellwood and Pemberton, 1984; Elmore *et al.*, 1987; Emmerton *et al.*, 2013; McCabe *et al.*, 1987; Peirce *et al.*, 1998; Richardson and Noltimier, 1980; Rijal *et al.*, 2010). Burton *et al.* (1993) proposed a theoretical model attempting to explain the thermodynamic stability of common magnetic mineral assemblages at different diagenetic settings with respect to proximity to hydrocarbon accumulation, depth, presence or absence of chemical species (HS^-, H_2S, or SO_4^{2-}), pH and Eh values (Figure 1.9). For example, Burton *et al.* (1993) proposed at point D (which equals about 6 km in depth, 200 °C and a pressure of ~600 bar) and proximal plume to hydrocarbon (right column), haematite will be unstable and will convert to magnetite at low-medium total sulphur (LTS-MTS) and to pyrrhotite at high total sulphur (HTS), this will lead to a net positive

magnetic relief. Magnetite will be mostly stable but could also be transformed into siderite, with a net negative magnetic anomaly or to pyrrhotite in high total sulphur conditions (Figure 1.9). In general, the model predicts increasing stability of magnetic mineral phases with increasing depth of burial and increasing magnetic susceptibility in distal plume environment (Figure 1.9).



		HEM	MAG	PYRRH	HEM	MAG	PYRRH	+/-	HEM	MAG	PYRRH	+/-
A	LTS	S	U	U	MAG/SID	S/SID	U	+/-	U	U	U	-
	MTS				PY	U	U	-	U	U	U	-
	HTS				PY	U	PY	-	U/PY	U	U	-
B	LTS	S	U	U	MAG/SID	S/SID	U	+/-	U	U	U	-
	MTS				PY	S/SID	U	-	U/PY	U	U	-
	HTS				PY	U	S	+	PY	U	S	+
C	LTS	S	U	U	MAG	S/SID	U	+/-	U	U/SID	U	-
	MTS				MAG	S/SID	U	+/-	PY	U/SID	U	-
	HTS				PY	S/PYRRH	S	+/-	PY	S	S	+
D	LTS	S	U	U	MAG	S/SID	U	+/-	MAG	S/SID	U	+/-
	MTS				MAG	S/SID	U	+/-	MAG	S/SID	U	+/-
	HTS				MAG	S/PYRRH	S	+	MAG/ PYRRH	S/PYRRH	S	+
		NO PLUME high Eh and pH low S, var Fe^{2+}			DISTANT PLUME pH> 7.5, med / low Eh, var Fe^{2+}				PROXIMAL PLUME pH < 7.5, med/low Eh, var Fe^{2+}			

Figure 1.9: Magnetic mineral parageneses and magnetic susceptibilities (denoted relative to background: increased, +; neutral, 0; or decreased, -) predicted for non-plume conditions. Non-plume conditions in the left column define background magnetization prior to hydrocarbon seepage. Plume environments shown in centre and right columns. Environmental conditions in rows A = 25 °C, 1 bar; B = 50 °C, 150 bar; C = 100 °C 300 bar and D = 200 °C 600 bar. Levels of total aqueous sulphur denoted by LTS = low; MTS = intermediate; HTS = high. Fates of mineral denoted by U = unstable; S = stable. HEM= haematite; MAG= magnetite; PYRRH= pyrrhotite; SID= siderite. From Burton *et al.* (1993).

Microbial degradation of hydrocarbons has also been put forward by many authors (Aldana *et al.*, 2003; Ellwood and Crick, 1988; Ellwood and Pemberton, 1984; Elmore *et al.*, 1987; Elmore *et al.*, 1993; Emmerton *et al.*, 2013; McCabe *et al.*, 1987) as one of the mechanisms for the generation of magnetic minerals. Scanning electron microscope (SEM) studies of carbonates, bitumen and speleotherms, and near surface soil samples in hydrocarbon habitat reveal the presence of authigenic magnetite formed as a result of the reduction of Fe^{3+} to Fe^{2+} by anaerobic microbial actions (Aldana *et al.*, 2003; Díaz *et al.*, 2000; Elmore and Crawford, 1990; Elmore *et al.*, 1987; Emmerton *et al.*, 2013; McCabe *et al.*, 1987). SEM images of the magnetic extracts reveal the presence of spherical crystal framboidal aggregates with aggregate sizes ranging 3-156 µm (Aldana *et al.*, 1999; Elmore *et al.*, 1987; Guzmán *et al.*, 2011; McCabe

et al., 1983; Wisniowiecki *et al.*, 1983). EDX analysis of these crystals confirmed the iron as the only cation present in these crystal aggregates. Framboidal magnetite are the only magnetic minerals found in this aggregate with the framboidal shapes argued to have come from pyrite replacement (Suk *et al.*, 1990) or from reduction of haematite (Elmore *et al.*, 1987; Machel, 1995; McCabe *et al.*, 1987). In both cases molecular oxygen and the presence of hydrocarbons play important roles as they control the redox conditions and also determine the type of microbial activity that can take place (Machel, 1995).

A number of studies (Aubourg and Pozzi, 2010; Kars *et al.*, 2012; Lu *et al.*, 1991) have proposed the formation of authigenic magnetite and pyrrhotite during burial diagenesis and also during the maturation of organic matter (Banerjee *et al.*, 1997; Blumstein *et al.*, 2004). The sole action of heat has been demonstrated to be responsible for the formation of magnetic minerals during laboratory burial simulation experiments (Aubourg and Pozzi, 2010; Kars *et al.*, 2012). Aubourg *et al.* (2012) proposed a model of schematic burial, based on atmospheric-pressure heating experiments with three magnetic burial-depth windows which greigite, magnetite and pyrrhotite occupy: <2 km, <6 km and >6 km respectively. They argued there is a continuous production of magnetite from depths >2 km to be replaced by pyrrhotite from burial depths of around 6 km (Figure 1.10). However, this model has limitations, as it does not take into account local environmental factors. It only considers temperature. In contrast, surface biodegradation of crude oils could result in the oxidation of ferrimagnetic minerals (e.g., magnetite) present within the vicinity of the crude oils to ferromagnetic ones (e.g., haematite) thereby by reducing the overall magnetic signals of the environment Emmerton *et al.* (2013).

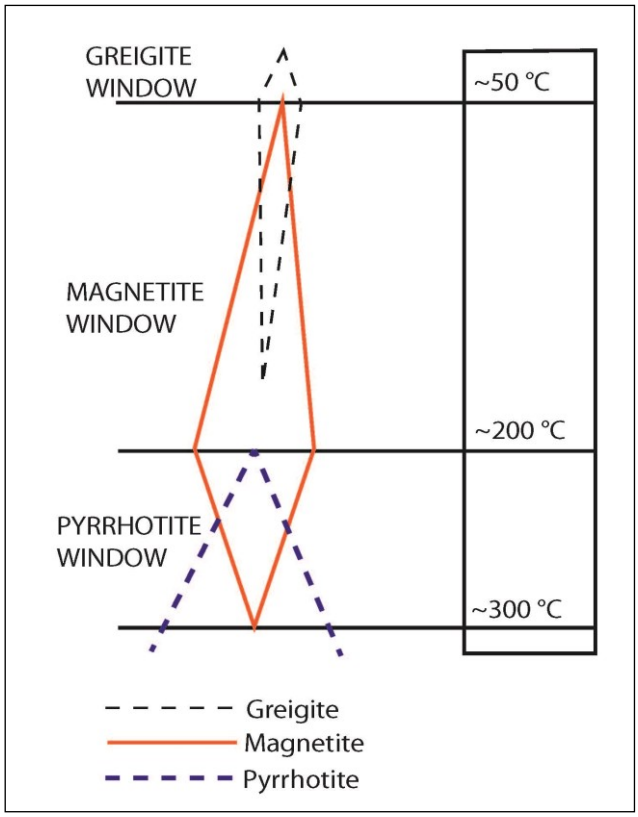


Figure 1.10: Burial model for the formation of magnetic minerals in claystones. Central box represents a sedimentary column from the surface to 10km of depth. Formation of magnetic minerals depends on burial, presence and/or absence of oxygen and the availability of sulphur. This model is based on experiments conducted at atmospheric pressure and in air. Modified from Aubourg *et al.* (2012).

1.3 Review of organic geochemistry

Petroleum is generated from the thermal decomposition of sedimentary organic matter. This organic matter is comprised of organic molecules in monomeric or polymeric forms which are derived from parts of living organism (Tissot and Welte, 1984).

1.3.1 Sedimentary organic matter (SOM)

The first stage in the production of organic matter begins with photosynthesis by plants. Photosynthesis, expressed in its most simple form, is the conversion of CO_2 and H_2O in the presence of sunlight into organic matter, oxygen and water based on the following simplified equation. The earlier forms of life were photosynthetic bacteria and blue-green algae during the Precambrian but by Ordovician and Silurian, a variety of phytoplankton appeared. Phytoplankton are the major contributors to organic sedimentary matter (Tissot and Welte, 1984). Higher plants also contribute significantly to sedimentary organic matter, their first appearance was recorded during the Silurian (Schwartz, 1980).

$$6CO_2 + 12H_2O \rightleftharpoons C_6H_{12}O_6 + 6O_2 + 6H_2O \qquad (7)$$

1.3.2 Chemical composition and accumulation of organic matter (OM)

The photosynthetic production of organic matter leading to other secondary metabolites, in addition to the simple sugars indicated in equation (7); some common types are highlighted below.

Carbohydrates

This is general name for sugars and their polymers; they include monosaccharides, oligosaccharides and polysaccharides. They have a generic empirical formula C_n $(H2O)_n$. Carbohydrates are the main energy source for many plants and animals (Schwartz, 1980).

Proteins

Proteins are highly ordered polymers made from amino acids and account for most of nitrogen compounds in living organisms. They constitute materials such as muscle fibres, silk and sponges (Tissot and Welte, 1984).

Lipids

Lipids are organism produced substances that are soluble only in chemical solvents (Breger, 1966). Lipids encompass compounds such as animal fat, vegetable oil and waxes. Lipids also include compounds such as terponoids, steroids and complex fats such as phospholipids (Tissot and Welte, 1984).

Lignin

Lignin is a high molecular weight polyphenol and is located between cellulose micelles of plant supporting tissues. It is commonly derived from plant woods and in some algae (Tissot and Welte, 1984).

Marine sedimentary organic matter is mainly made up of phytoplankton followed by phytobenthos that contribute significant amount in the shallow photic zones. Bacteria rework dead organisms in both deep and shallow marine and thereby constitute a part of the sedimentary organic matter (Tissot and Welte, 1984). In deltaic environments, however, sedimentary organic matter is dominated by allochthonous land-driven organic materials such as phytoclasts, pollen and spores. Most of the proteins and carbohydrates deposited on the sea

floor are degraded in a matter of days or weeks and the more resistant biopolymers such as lignin in months to a few years (Tyson, 2005), but where there is high organic matter productivity, the accumulation rate sometimes exceeds the degradation rate (sediments are added faster than microbes can oxidize them) even with rapid bacterial degradation. This lowers the oxygen levels to suboxic or even anoxic levels from where bacteria can only use nitrate (NO_3^{2-}) and sulphate (SO_4^{2-}) to metabolize the organic matter and once all oxygen is used up during denitrification and sulphate reduction, the bacteria turn to methanogenesis to metabolize the deposited organic matter. It is generally accepted that most of the sedimentary organic matter that survived the sulphate reduction stage is preserved (Tyson, 1987).

In marine sediments, the depths at which oxygen runs out varies from a few mm to about 0.1 m and the depth increases with decreasing organic matter flux (Tyson, 1987). In most cases however, rapidly deposited marine sediments are internally anoxic from a few mm of depth, even if biotubated, and although sulphate reduction and methanogenic metabolism of organic matter continues, the lipid-rich oil prone constituents are preserved and new ones may even form under these conditions thus enhancing the oil generating potential of the organic matter that survived.

1.3.3 Fate of organic matter is sedimentary successions

Sedimentary organic matter (SOM) undergoes transformational processes once deposited. Chemical composition of OM, interstitial water chemistry and the interaction between OM and inorganic rock matrix, temperature and pressure determine the fate of the deposited SOM (Tissot and Welte, 1984). Figure 1.11 shows a schematic evolution of SOM from time of deposition to the onset of metamorphism.

Diagenesis

Freshly deposited sediments in aquatic environments have porosities up to 80%. During diagenesis, the organic and the inorganic components of the sediments approach equilibrium through compaction, cementation and eventually lithification (Tissot and Welte, 1984). During diagenesis and under the right conditions geopolymers formed earlier are converted to kerogen (Figure 1.11). The most important hydrocarbon generated during diagenesis is biogenic methane, formed during methanogenesis (Tissot and Welte, 1984).

Catagenesis

At depths > 1000 m, at temperatures > 50 °C, the kerogen becomes unstable and begins to progressively degrade to produce petroleum. First to be produced are the N, S, O compounds together with the heavy oils (aromatic hydrocarbons), followed by the light fraction of the crude (naphthenic-paraffins and paraffins), then gas, which progressively gets drier until the last product, dry gas (methane) is present exclusively (Tissot and Welte, 1984).

Metagenesis

At this stage, the sediments have reached several kilometres deep and temperatures > 180 °C. All remaining organic carbon has been turned to graphite. This stage marks the onset of metamorphism (Figure 1.11) (Tissot and Welte, 1984).

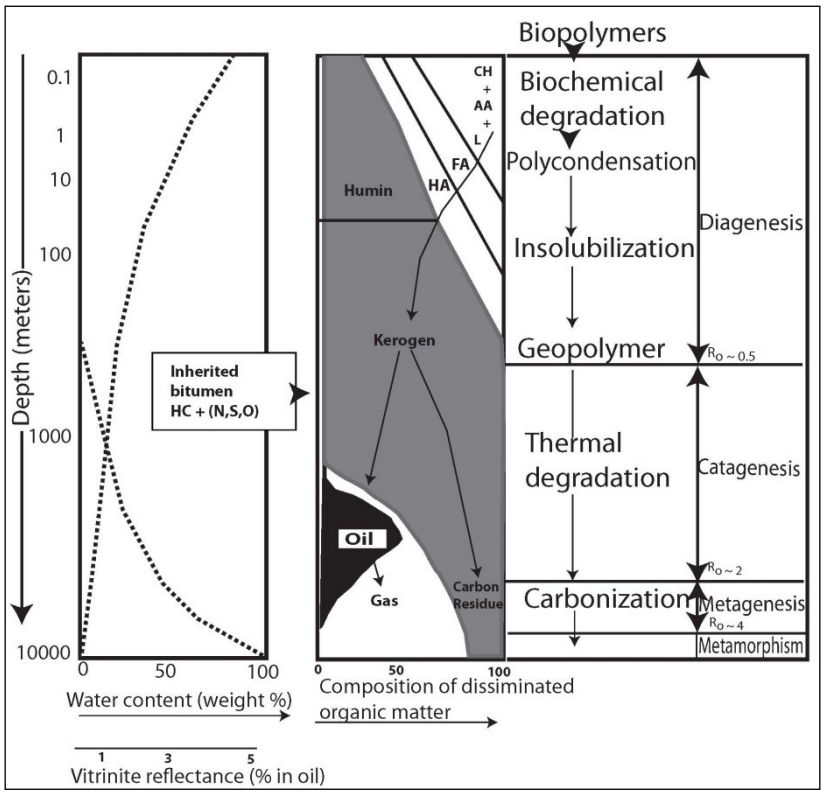


Figure 1.11: General schematic of the evolution of organic matter from time of deposition to onset of metamorphism. CH = carbohydrates, AA = amino acids, FA = fulvic acids, HA = humic acids, L = lipids, HC = hydrocarbon, R_o = vitrinite reflectance. From (Tissot and Welte, 1984).

1.4 Composition of crude oils

The overall composition of a crude oil can be classified as light or heavy (Tissot and Welte, 1984) based on the relative abundances of the following:

- Saturated (aliphatic) hydrocarbons
- Aromatic hydrocarbons
- Resins and asphaltenes

The following classification was proposed by Tissot and Welte (1984) based on concentration limits for the aliphatic, aromatic, resins and asphaltenes on oil fractions boiling at temperatures in excess of 2000 °C and 760 mmHg pressure. Figure 1.12 illustrates compositional limits of light, average and heavy crude oils and how biodegradation affects them.

Paraffinic: Usually very light oils with specific gravities <0.85, they contain >60% aliphatic compounds, about 20% aromatic compounds and usually <10% resin and asphaltenes. They also have low sulphur content.

Paraffinic – naphthenic: These are usually heavier and more viscous than paraffinic oils; they are composed of >50% aliphatic compounds, 25 – 40% aromatic compounds, 5 – 15% resin and asphaltenes with sulphur usually as benzothio-phenes in low amounts.

Naphthenic: Not very common, occur mostly with biodegraded oils with >50% saturated cyclics; < 20% n- and isoalkanes (from paraffins and paraffinic – naphthenic moieties).

Aromatic – intermediate: they contain 40 – 70% aromatic compounds with abundant sulphur in the form of thiophenes.

Aromatic – asphaltic: mostly biodegraded oils, probably of aromatic – intermediate in origin. They are composed of 30 – 60% asphaltenes and resins with sulphur <10%.

Naphthenic – aromatic: These are the products of biodegraded paraffinic and/or paraffinic – naphthenic oils and contain up to 25% resins.

1.5 Biomarkers

Biomarkers have been described as compounds that have unambiguous link to a biological precursor, whose basic skeletal structure has been preserved in recognizable form throughout diagenesis and much of catagenesis (Killops and Killops, 2004). Biomarkers can help to distinguish between oil source rocks and maturity; it is also used to determine the level of biodegradation in oils, correlate between oils, map out oil migration pathways, etc. Acyclic isoprenoids (pristane and phytane) and hopanes are the major biomarkers used during this study; below is a brief review of some of their indices.

Pristane (Pr) and phytane (Ph)

Pristane and phytane originated from the phytyl side chain of chlorophyll a in phototrophic organisms and also from bacteriochlorophyll a and b of purple sulphur bacteria (McKirdy and Powell, 1973). The phytyl side chain suffers from reduction in anoxic environments and it is transformed to phytane (Peters *et al.*, 2005). In contrast, the phytyl side chain undergoes transformation to phytenic acid in oxic environments, which undergoes further oxidation to yield pristene which is then reduced to pristane (Peters *et al.*, 2005)

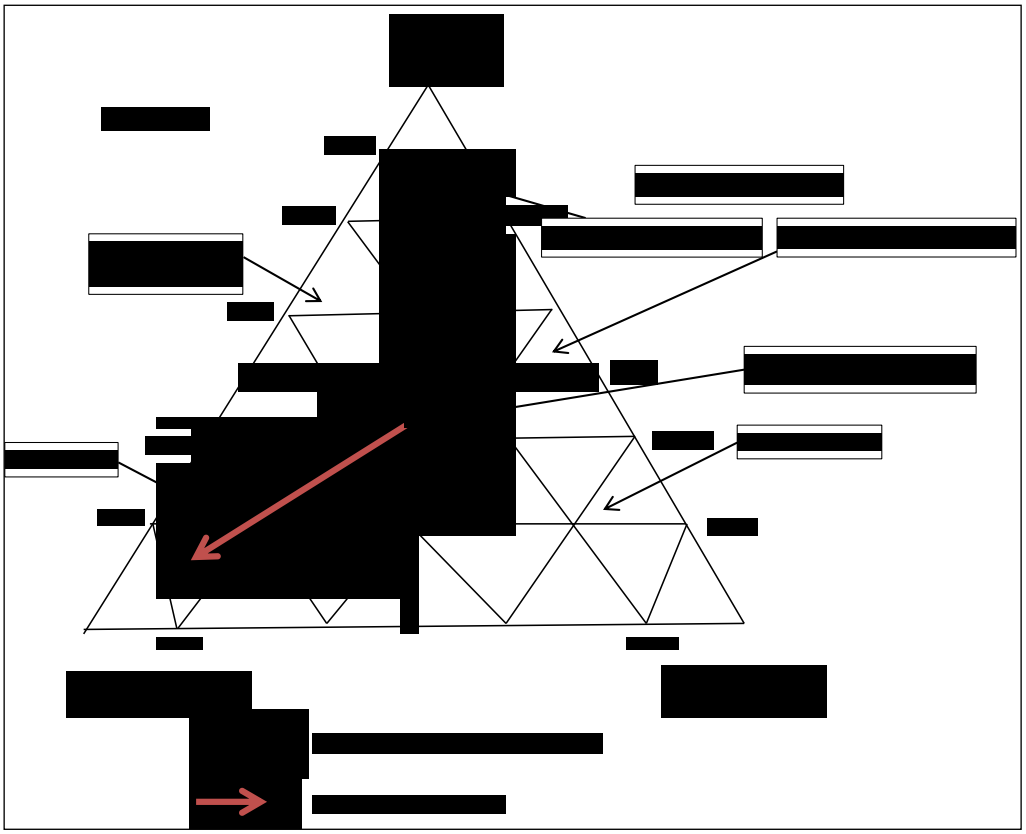


Figure 1.12: The class composition of crude oils in a triangular plot: Effects of maturation, oxidation and biodegradation. Modified from Tissot and Welte (1984).

Hopanes

These are pentacyclic triterpenoids that occur in prokaryotes and higher plants and believed to have originated from precursors in bacterial membranes (Ourisson *et al.*, 1987). They usually contain 27–35 carbon atoms and are characterised by three stereoisomeric series; the 17α, 21β (H), 17β, 21β (H), and 17β, 21α (H). They are usually measured using the *m/z* 191 ion in the aliphatic fraction of crude oils and the common ones include the C_{27} 17α-trisnorhopane (Tm), C_{27} 18α-trisnorhapane (Ts), the C_{30} hopane and the homohopanes (C_{31}-C_{35}hopanes).

1.5.1 Source related biomarkers

The source-specific indicators are useful in order to describe the type of organic matter input even when only crude oil samples are available. To determine crude oil source, information such as depositional environments, thermal maturity and age of source rocks are needed. Below is a brief description of the parameters used in this study

Ts/Tm

The ratio of Ts/Tm is a useful source indicator as it is based on the relative stability of C_{27} 17α-trisnorhopane (Tm) compared to more stable C_{27} 18α-trisnorhapane (Ts) and is measured using *m/z* 191 ion (Moldowan *et al.*, 1985). High Ts/Tm ratios are typically associated with shales deposited in anoxic environment, whereas low values are associated with carbonate rocks (McKirdy *et al.*, 1983).

17α-Diahopane/17α-hopane (C_{30}/C_{29}Ts)

This ratio is used to interpret the relationship between C_{30} and oxic-suboxic, clay rich depositional environment and is measured using the *m/z* 191 ion. The C_{30} is thought to have originated from bacterial inputs in clay rich rocks under oxic-suboxic conditions (Volkman, 1988a). The application of C_{30}/C_{29}Ts is not universal but there is strong evidence to suggest oils with high ratios are derived from shales deposited under oxic-suboxic conditions (Farrimond, 2005).

Homohopanes indices (C_{31}-C_{35})

The homohopanes (C_{31}-C_{35}) are believed to have originated from bacteriohopanetetrol and they are indicative reducing environment of deposition (Ourisson *et al.*, 1987). They are measured using the *m/z* 191 from the aliphatic fraction of the crude oils. Ratios of the homohopanes, such C_{31}/C_{30}, C_{35}/C_{34} and C_{35}/C_{34} v C_{29}/C_{30} have been used in this study to investigate redox conditions during the deposition of source rocks of the oils analysed.

Gammacerane indices

The gammacerane is a highly specific biomarker for water column stratification due to hypersalinity in both marine and non-marine environments and is measured using the *m/z* 191 ion (Damsté and De Leeuw, 1995). Gammacerane indices used in this study include 10 × Gammacerane / (Gammacerane + C_{30} αβ) and Gammacerane/C_{31} 22R.

1.6 Planned PhD Research

This research will try and establish an origin and implications of the magnetic minerals found within the vicinity of hydrocarbon accumulations using geochemical and geophysical techniques. This PhD has three main components. 1) Establishing an origin for the magnetic minerals by subjecting potential source rocks to oil generating conditions in the laboratory. 2) Magnetic and geochemical studies of samples of the reservoir rocks from the study area. 3) Combining magnetic and geochemical data coupled with seismic mapping generated of the study area to try and answer the following questions.

1. Can magnetic minerals form under hydrocarbon-generation conditions?

2. Are the magnetic minerals formed of right size to migrate alongside the crude oils generated?

3. Can these magnetic minerals be used to map-out crude oil migration pathways?

Chapter 2

Geological history, sampling and methodology

2.1 Introduction

For the purpose of this PhD, two rock sample sets and seismic data from the area of study (Wessex Basin) were acquired. The first rock sample set consisted of three potential oil source rocks (Kimmeridge Clay Fm, Oxford Clay Fm and the Blue Lias Fm) that were provided by Prof. Mark Sephton. The second sets were well cores, obtained from the British Geological Survey (BGS) Core Store in Keyworth, Nottinghamshire; the reservoir rock and potential cap rock were sampled. Finally, a 2D seismic data set that covers most of the sampled area was also acquired via an academic licence from the UK Onshore Geophysical Library (UKOGL). The Wessex Basin was chosen for this study because of its good sectional exposures, availability of seismic and core data. The Wessex is also the largest onshore oil field in Europe. These make the Wessex Basin ideal for this study. A detailed description of the samples and the various experimental techniques used in this study together with the geological history of the area are given below.

2.1.1 Geological History

The Wessex Basin lies in Southern England (Figure 2.1) and comprises a series of linked intra-cratonic basins that formed in the Jurassic and Early Cretaceous by extensional collapse of deep-seated Late Carboniferous Variscan thrusts. The complex structural and stratigraphic evolution of the Wessex Basin runs from Permian to Tertiary times. The basin is believed to have originated during the Permo-Triassic rifting events that affected most of north western Europe (Hawkes *et al.*, 1998) and its history is characterized by four major tectonic events; 1) Early Atlantic plate sequence (Late Permian-Triassic), 2) Atlantic plate sequence (Early Jurassic-Late Jurassic), 3) Biscay plate sequence (Late Jurassic-Late Cretaceous) and 4) Alpine plate sequence (Late Cretaceous-Tertiary) (Figure 2.2).

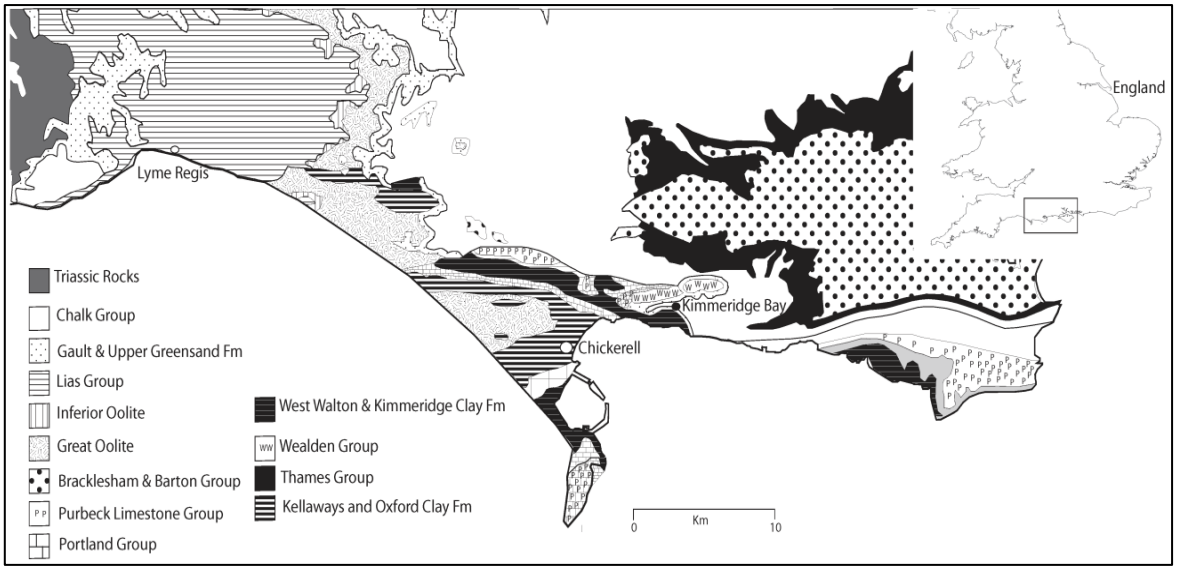


Figure 2.1: Geological map of Wessex Basin showing sampling locations: (1) Blue Lias Fm (Lyme Regis), (2) Oxford Clay Fm (Chickerell), and (3) Kimmeridge Clay Fm (Kimmeridge Bay). (Underhill and Stoneley, 1998).

2.1.2 Megasequences

The early Atlantic plate megasequence (Late Permian – Late Triassic)

The period from Late Permian to Late Triassic is marked by the stretching of the Pangea that is accompanied by the extension occurred in the North Sea and Norwegian-Greenland area of the interior Pangea Supercontinent. Meanwhile, the Neotethys started to consume the Paleotethys and the Central Atlantic started to rift at that time (Figure 2.3). Deposits during this time were mainly continental fluvial and aeolian red beds and they passed into playa facies at the top (Underhill and Stoneley, 1998). This was followed by the reddish brown mudstone of the Aylesbeare Mudstone Group (Figure 2.6). The Triassic witnessed the deposition of Sherwood Sandstone and the Murcia Mudstone Groups, with the former containing Budleigh Salterton Pebble Beds (BSPB) and the Otter Sandstone Formation (Figure 2.6), in a primarily North-South oriented rift system that linked fluvial systems originating in the Armorican Massif in northern France with the Wessex Basin, Worcester Graben and Cheshire, Manx-Furness and Irish Sea basins.

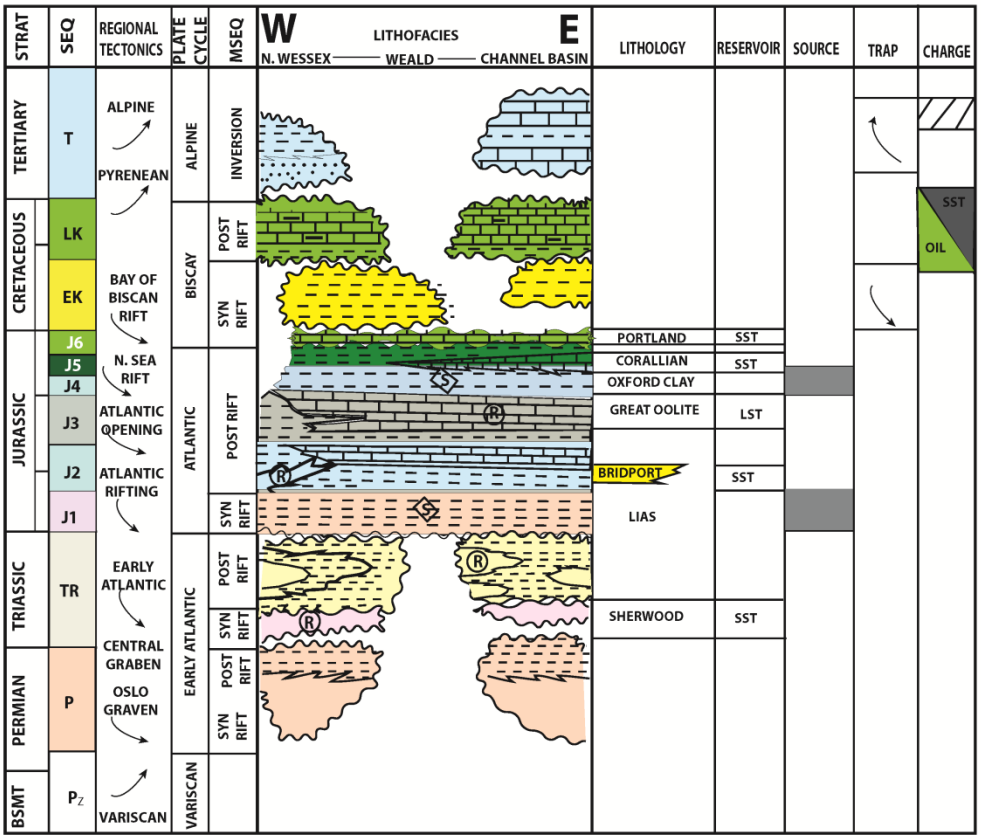


Figure 2.2: Chronostratigraphic diagram depicting the main plate cycle seismic megasequences, their component sequences, relevant Jurassic lithostratigraphic elements and their respective reservoir, source, trap and charge potential. J = Jurassic megasequences R = potential reservoir rock S = potential source rock. After Hawkes *et al.* (1998).

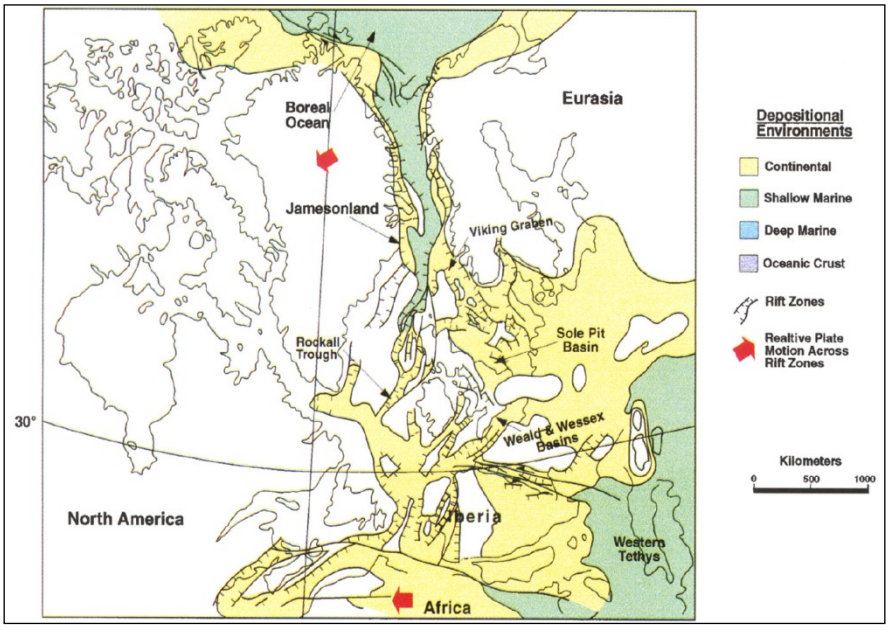


Figure 2.3: Late Norian (210 Ma), early Atlantic mega-sequence plate tectonic for northwest Europe.

The Atlantic rifting (Jurassic)

The Lower Jurassic witnessed a widespread rifting along a series of east-west trending faults in western Tethys, resulting in the formation of oceanic crust in the Central Atlantic and a rapid and extensive marine transgression in the area to the north of the Newfoundland-Azores Fracture Zone. The Atlantic rifting sequence has been divided into six shallowing-upwards depositional sequences (Figure 2.2) and Hawkes *et al.* (1998) argued that each cycle was initiated by pulsed northwards propagation of Atlantic rifting.

Sequence J1

Sequence J1 (Figure 2.2) represents a period of rifting and regional subsidence during the Early Jurassic that led to widespread marine transgression. The Lias Group were deposited during this period and this 'syn-rift' package forms the most important source rocks for liquid hydrocarbon in the southern England and the Paris Basin (Hawkes *et al.*, 1998). The boundary between J1 and J2 is marked by an unconformity at the top of the Junction Bed (Figure 2.2).

Sequence J2

At the top of the J2 sequence lays Inferior Oolite which is fairly well developed in the Wealden Basin but thin and sometimes difficult to identify in the Wessex Basin (Figure 2.2). Overlain by a thin (<5m) Inferior Oolite is the Bridport SandsFm, this forms an important reservoir horizon in the Wessex Basin (Hawkes *et al.*, 1998).

Sequence J3

The J3 sequence witnessed the deposition of Forest Marble in the Wessex Basin and this forms a secondary reservoir target in the Wytch Farm area where it is naturally fractured (Hawkes *et al.*, 1998).

Sequence J4

Sequence J4 represents a period of major marine transgression and this led to the deposition of Oxford Clay Fm Formation over the whole area. The Oxford Clay Fm Formation forms a major regional seal on Middle Jurassic Great Oolite reservoirs in the Weald Basin and is capped by the Corallian Sandstone Formation (Hawkes *et al.*, 1998).

Sequence J5

The J5 sequence represents a period that witnessed the deposition of the Kimmeridge Clay Fm Formation and is an organic rich mudstone that is largely immature in the Weald and Wessex basins of southern England (Hawkes *et al.*, 1998).

Sequence J6

The upper part of the Kimmeridge Clay Fm Formation was deposited during this period as a result of renewed marine transgression due to reactivation of rifting and regional subsidence. Facies deposited during this sequence showed an overall shallowing upwards from marine mudstones of the Kimmeridge Clay Fm Formation to marginal marine/brackish Purbeck Beds to Portland Sandstone Formation (Hawkes *et al.*, 1998).

Biscay plate sequence (Late Jurassic-Late Cretaceous)

During the Early Cretaceous the Wessex Basin was subjected to a major renewed extension, associated with successful rifting of the Bay of Biscay and Rockall areas north of the Biscay Fracture Zone (Figure 2.5). This led to the reactivation of faults formed earlier in the Lower Jurassic and a marked change from open marine conditions prevalent in the Late Jurassic to west-east trending fluvial deposition in the Early Cretaceous. Lacustrine-braidplain-alluvial fans (upper Purbeck Beds and the Wealden Group) were the predominant deposits during this period (Hawkes *et al.*, 1998). The Aptian witnessed a period of major continental break up and the onset of ocean spreading in the Bay of Biscay (Figure 2.5). This resulted in a regional sub aerial unconformity overlain by a widespread marine transgression into the Wessex and Weald area that persisted until the Late Cretaceous. The break-up unconformity is overlain by the transgressive Lower Greensand, Gault Clay and Upper Greensand (Figure 2.6) (Hawkes *et al.*, 1998). Further thermal subsidence in the Late Cretaceous resulted in the starvation of the Wessex region of clastic materials; this led to the deposition of pelagic carbonates (the Chalk).

Alpine plate sequence (Late Cretaceous-Tertiary)

The Alpine orogeny resulted from the northward collision of the African continent with Europe during the Late Maastrichtian. This event caused the inversion of the earlier east-west trending Early Jurassic and Early Cretaceous extensional faults (Hawkes *et al.*, 1998; Stoneley, 1982). Hawkes *et al.* (1998) argued for an uplift of more than 1500 m and subsequent erosion occurred during this period, based on evidence from vitrinite reflectance, shale velocity and back stripping studies of the Weald Basin (e.g., Law, 1998). The inversion caused a significant

change in depositional polarity of the basins (Weald and Wessex) with Tertiary sediments deposited on the footwalls of the original Mesozoic Weald and Wessex rifts forming the Hampshire and London Basins as mini-foreland basins (Hawkes *et al.*, 1998).

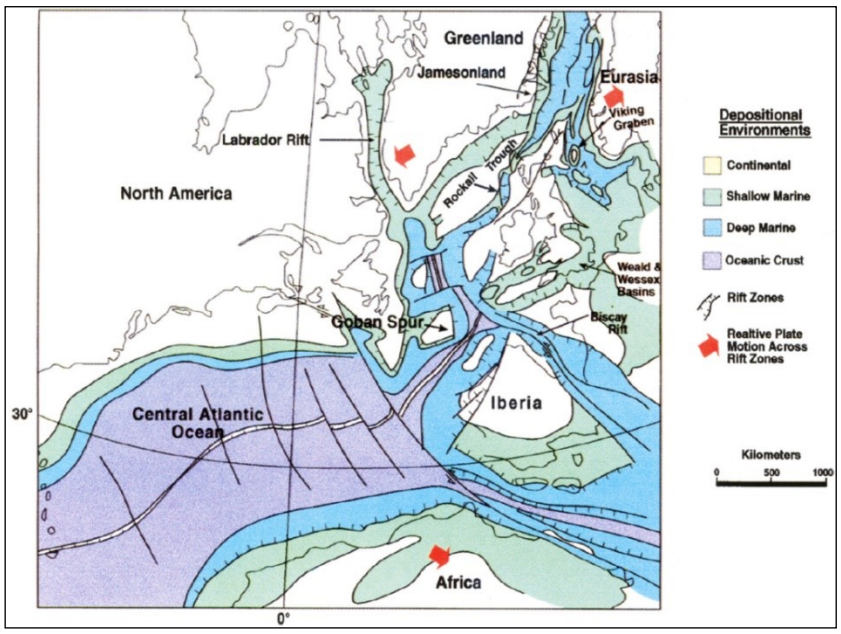


Figure 2.4: Early Aptian (125 Ma), Biscay megasequence plate tectonic reconstruction for northwest Europe. From Hawkes *et al.* (1998).

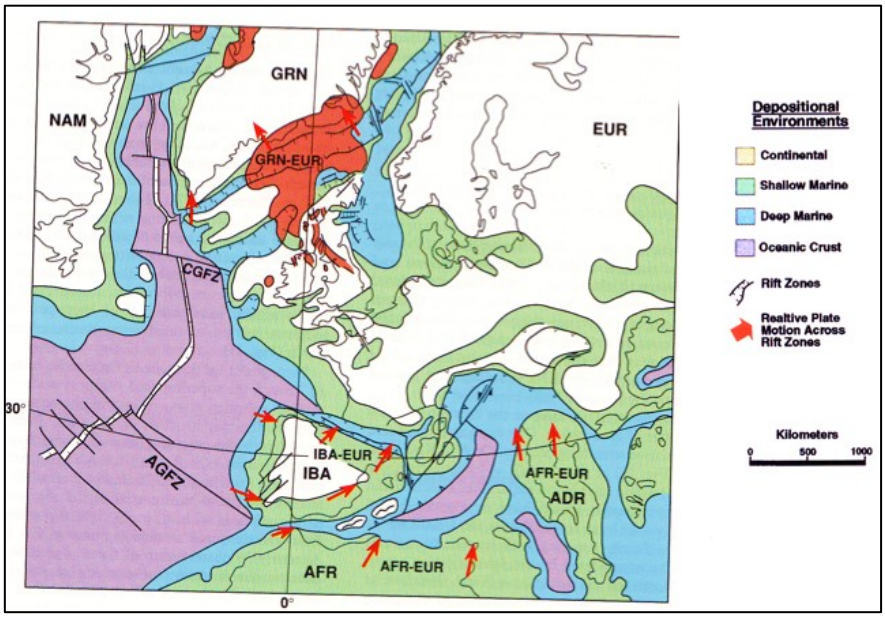


Figure 2.5: Early Tertiary (Thanetian) (58 Ma), Alpine megasequence plate tectonic reconstruction for northwest Europe. From Hawkes *et al.* (1998).

2.2 Sampling

Wessex Basin

The Kimmeridge Clay Fm was sampled from Kimmeridge Bay, Oxford Clay Fm from Chickerell and the Blue Lias Fm from Lyme Regis all by Prof. Mark Sephton (Fig. 2.1) representing the Upper, Middle and the Lower Jurassic respectively. Any of these three source rocks have the potential to have generated the hydrocarbon presently found in the study area (Underhill and Stoneley, 1998), hence the decision to sample these intervals (Fig. 2.6). All three samples are dark grey to black, fissile, marine shales containing Type II kerogen (Akande, 2012a; Ebukanson and Kinghorn, 1985).

Well Cores

Well cores from BGS core store at Keyworth, England, were also sampled. Cores were sampled from nine wells (Table 2.1) and the sampling was restricted to Bridport Sandstone and the Inferior Oolite formations of the Upper Lias (Fig. 2.6), which represent the reservoir rock and cap rock respectively (Hawkes *et al.*, 1998). Forty-five samples were collected in total for magnetic and geochemical characterization.

Table 2.1: Well-core samples analysed during this study, showing sample depths, formation and lithology.

Sample Name	Sample code	Depth (ft.)	Formation	Lithology
Bushey Fm SSK27620	BS1	3464	Bridport Sandstone Fm	Sandstone
Bushey Fm SSK27621	BS2	3468	Bridport Sandstone Fm	Sandstone
Bushey Fm SSK27622	BS3	3477.3	Bridport Sandstone Fm	Sandstone
Bushey Fm SSK27623	BS4	3485.1	Bridport Sandstone Fm	Sandstone
Bushey Fm SSK27624	BS5	3486	Bridport Sandstone Fm	Sandstone
Bushey Fm SSK27625	BS6	3504	Bridport Sandstone Fm	Sandstone
Bushey Fm SSK27626	BS7	3504.8	Bridport Sandstone Fm	Sandstone
Bushey Fm SSK27627	BS8	3518.1	Bridport Sandstone Fm	Sandstone
Bushey Fm SSK27628	BS9	3524	Bridport Sandstone Fm	Sandstone
Bushey Fm SSK27629	BS10	3526	Bridport Sandstone Fm	Sandstone
Coombe K. SSK35431	COOMB1	3443	Bridport Sandstone Fm	Sandstone
Coombe K. SSK35432	COOMB2	3475	Bridport Sandstone Fm	Sandstone
Coombe K. SSK36413	COOMB3	3498.75	Bridport Sandstone Fm	Sandstone
Coombe K. SSK36414	COOMB4	3522.9	Bridport Sandstone Fm	Sandstone
Martinstown 1 SSK35425	MT1	1514.6	Bridport Sandstone Fm	Sandstone
Martinstown 1 SSK35426	MT2	1534.12	Bridport Sandstone Fm	Sandstone
Martinstown 1 SSK35427	MT3	1516.83	Bridport Sandstone Fm	Sandstone
Martinstown 1 SSK35428	MT4	1534.12	Bridport Sandstone Fm	Sandstone
Stoborough 2 SSK36416	ST1	3536.75	Bridport Sandstone Fm	Sandstone
Stoborough 2 SSK36417	ST2	3561.3	Bridport Sandstone Fm	Sandstone
Stoborough 2 SSK36418	ST3	3562	Bridport Sandstone Fm	Sandstone
Stoborough 2 SSK36419	ST4	3569.23	Bridport Sandstone Fm	Sandstone
Waddock Cross SSK36415	WX1	2197.1	Bridport Sandstone Fm	Sandstone
Waddock Cross SSK35430	WX2	2203	Bridport Sandstone Fm	Sandstone
Waddock Cross SSK36415	WX3	2285	Bridport Sandstone Fm	Sandstone
Chickerell SSK27638	CH1	860.89	Bridport Sandstone Fm	Sandstone
Chickerell SSK27639	CH2	863.85	Bridport Sandstone Fm	Sandstone
Chickerell SSK27640	CH3	874.84	Bridport Sandstone Fm	Sandstone
Chickerell SSK27641	CH4	876.64	Bridport Sandstone Fm	Sandstone
Chickerell SSK27642	CH5	879.76	Bridport Sandstone Fm	Sandstone
Chickerell SSK27648	CH6	900.26	Bridport Sandstone Fm	Sandstone
Chickerell SSK27649	CH7	905.2	Bridport Sandstone Fm	Sandstone
Creech SSK27629	CR1	3451.4	Inferior Oolite Fm	Limestone
Creech SSK27630	CR2	3456	Inferior Oolite Fm	Limestone
Creech SSK27631	CR3	3452.76	Inferior Oolite Fm	Limestone
Creech SSK27632	CR4	3456.04	Bridport Sandstone Fm	Sandstone
Creech SSK27633	CR5	3456.92	Bridport Sandstone Fm	Sandstone
Creech SSK27634	CR6	3463.75	Bridport Sandstone Fm	Sandstone
Creech SSK27635	CR7	3470	Bridport Sandstone Fm	Sandstone
Kimmeridge SSK27636	KM1	2828.08	Bridport Sandstone Fm	Sandstone
Kimmeridge SSK27637	KM2	2854.66	Bridport Sandstone Fm	Sandstone
Kimmeridge SSK27643	KM3	2861.71	Bridport Sandstone Fm	Sandstone
Kimmeridge SSK27644	KM4	2870.57	Bridport Sandstone Fm	Sandstone
Wytch Fm SSK27645	WC1	2996	Bridport Sandstone Fm	Sandstone
Wytch Fm SSK27646	WC2	2997.25	Bridport Sandstone Fm	Sandstone
Wytch Fm SSK27647	WC3	2998.15	Bridport Sandstone Fm	Sandstone

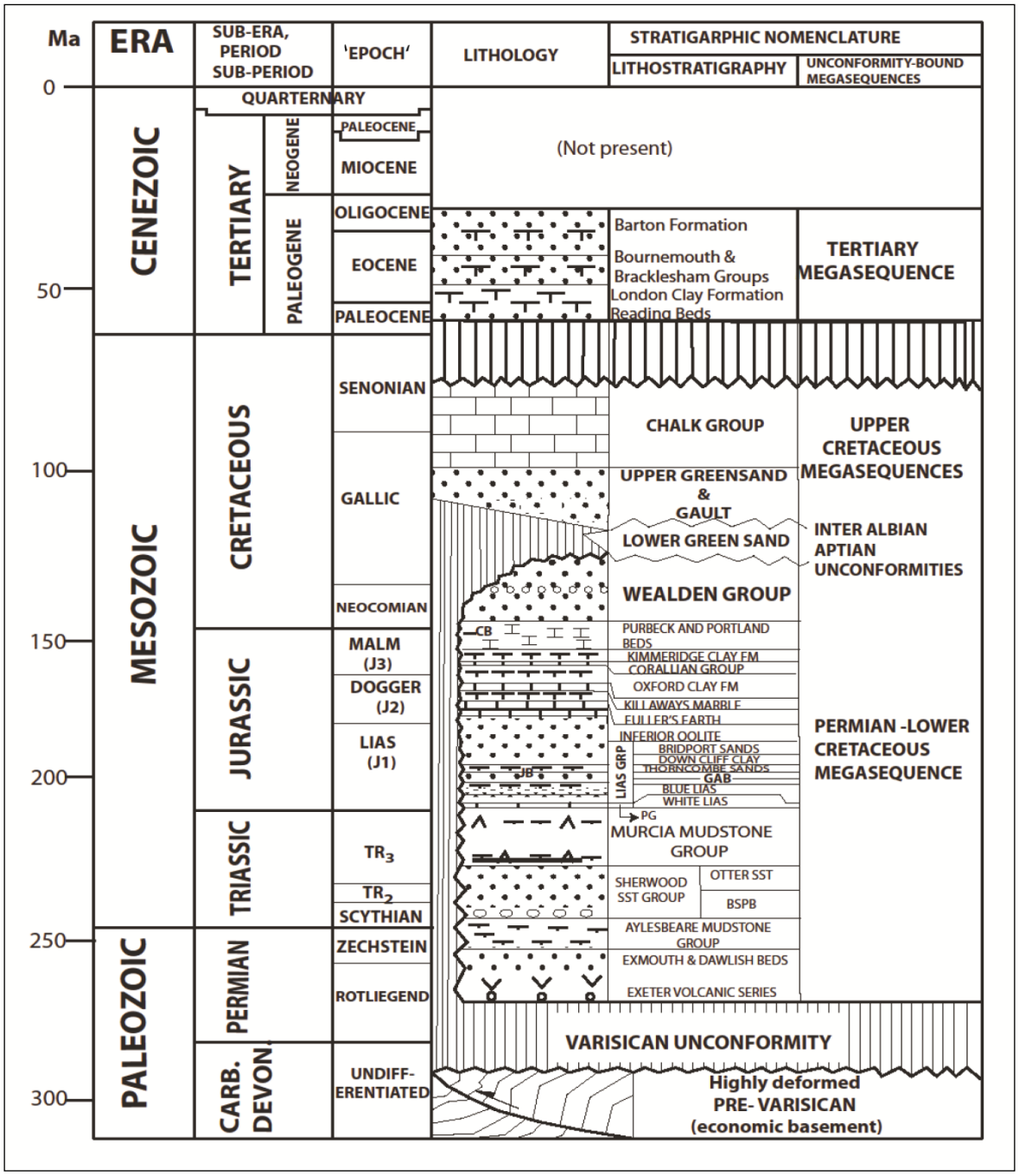


Figure 2.6: Generalized stratigraphic column for the Wessex Basin showing the three mega-sequences (JB= Junction Bed; CB= Cinder Bed; GAB= Green Ammonite Beds; PG= Penarth Group; BSPB= Budleigh Salterton Pebble Beds). Modified from Underhill and Stoneley (1998).

2.2 Methodology

A brief description of the all the laboratory techniques and seismic interpretation carried out during this study is given below.

2.2.1 Geochemical experimentations

Hydrous pyrolysis

Hydrous pyrolysis is a means through which rocks could be artificially matured. Samples from the Oxford Clay Fm, Kimmeridge Clay Fm, and the Blue Lias Fm were rinsed with dichloromethane (DCM) and then pulverised using a ceramic pestle and mortar. Two types of pyrolysis were carried out: 1) Thirty millilitres (30 ml) of deionized water was sonicated for 5 minutes to remove any dissolved gas and was added to the pressure vessel, 10 g of the powdered oil source rock sample was then added into vessel and the atmosphere purged with argon at 4 bar. The oven was set at the required temperature and the pressure within the vessel settled at around 100 bar after a couple of hours. After 72 hours the oven was switched off, the vessel allowed 24 hours to cool and the sample retrieved using a non-magnetic spatula. The pyrolysis temperatures used for this method were 250 and 320 °C and each sample was pyrolysed separately in this method. 2) The second involved pyrolysing the three rock samples simultaneously at a given temperature. Three millilitres of deionized water was put on a sonicator for 5 minutes and then fed into borosilicate glass tubes. The glass tube end containing the water was immersed in liquid nitrogen and then a 10 mg sample of the rocks was then introduced into the glass tube and dipped into liquid nitrogen again until frozen. The open end of the tube was attached to an Edwards vacuum system and the tube atmosphere evacuated to 10^{-4} bar and then sealed using a pencil torch. The vacuum-sealed tubes containing the samples were then pyrolysed in a 316 stainless steel pressure vessel at 150 °C, 200 °C and 300 °C with a calculated amount of water in the vessel used to equalize pressures across the glass tube walls. The main advantage of the tube method was to allow the processing of multiple samples simultaneously at desired pyrolysis temperatures and to rule out the possibility of any contamination coming from the steel-made pressure vessel. However, the two experiments are essentially the same as the amount of water required to ensure that samples in both types of experiments remain fully immersed in the liquid phase of the liquid-vapour system was carefully calculated. This is an important factor in hydrous pyrolysis. Throughout the experiments, pressure within the vessel was monitored via an external pressure gauge mounted on the vessel in order to avoid pressure/mass loss.

Column chromatography

Column chromatography is used to extract extractible organic matter (EOM) from samples by progressively adding various solvents that will elute the various fractions of EOM present in samples. This technique was used to extract EOM from the samples obtained from the BGS core store. A gram of the samples was fed into test tubes and a non-polar (pentane) solvent was gently added.

The test tubes containing the samples and the solvent were then placed on a mixer until the solvent and the sediment were thoroughly mixed and then placed in a beaker containing some water and placed in a sonicator for about five minutes; this was to enhance a full dissolution of the EOM by the solvent. The test tubes were then centrifuged at 2500 rpm for 5 minutes and the supernatants were carefully collected with a pipette into clean test tubes. This procedure was repeated until the mixture was clear and the collected EOM was blown down slowly using nitrogen. Secondly, alumina (Al_2O_3) was activated by heating it in an oven at 150 °C for about an hour and fed into a rinsed pipette plugged with quartz wool. DCM was then ran through the pipette for further rinsing. A small amount of the activated alumina was added into collected EOM and allowed to dry then gently fed into the pipette. Ten millilitres of hexane was run through the pipette to collect the aliphatic fractions followed by 10 ml of DCM to collect the aromatic fraction. The collected fractions were stored in labelled clean vials.

Gas chromatography mass spectroscopy (GC-MS)

The various fractions were analysed by GC-MS with an Agilent Technologies 6890 gas chromatograph coupled to a 5973 mass spectrometer. The gas chromatograph injector was held at 200 °C and operated in split mode (35:1) with a column flow rate of 2 ml min^{-1}. Separation was performed on a J&W GS-Q PLOT column (30 m · 0.32 mm). The gas chromatograph oven was held for 5 minutes at 35 °C and then ramped at a rate of 10 °C min^{-1} to 200 °C, where it was held for 4 min. Compounds present in the samples were identified based on elution order and mass spectrometric fragmentation patterns.

2.2.2 Magnetic experimentation

Well core sampling and magnetic susceptibility measurements

For sampling cores, an in-house core logger was used (Figure 2.7). Attached to the automated linear- slide was a Bartington susceptibility meter looped to provide volume susceptibility of cores as they pass through it. The core logger was attached to a computer with a program that

controls the movement of the motor pushing the 1 m long slide through the loop sensor and taking measurements at 5 cm intervals. The program also records the susceptibility values of the cores, make corrections for drifts and background noise. Sampling was made where the susceptibility reading was high or the sample was visibly oil stained. The rocks generally had weak magnetic signals; therefore, sections with a reasonably high magnetic susceptibility value were sampled for analysis (Appendix 2.3).

Quantum Design Magnetic Property Measurement System (MPMS) measurements

Rock magnetic properties of both the potential source rocks and the well core samples were measured using a Quantum Design MPMS at three localities: a SQUID vibrating sample magnetometer (VSM) at the Royal Institute of Great Britain (RI), London, and MPMS 2, at the Institute of Geology and Geophysics, Chinese Academy of Science, Beijing, China, and Research School of Earth Sciences, Australia National University (ANU), Australia. For the MPMS SQUID VSM at the RI, I carried out the experiments. About 10 mg of a powdered sample was fed into a polypropylene powder holder, which was then placed into a brass trough sample holder and the sample position centred using the mounting station (Figure 2.8). The brass trough sample holder was then attached to a carbon fibre sample rod, the assembly was inserted into the VSM at room temperature, and a field of 100 mT was applied afterwards. The VSM was used to locate the position of the sample with readjustments of sample positioning where needed. The sample chamber was then purged with helium and vacuum sealed.

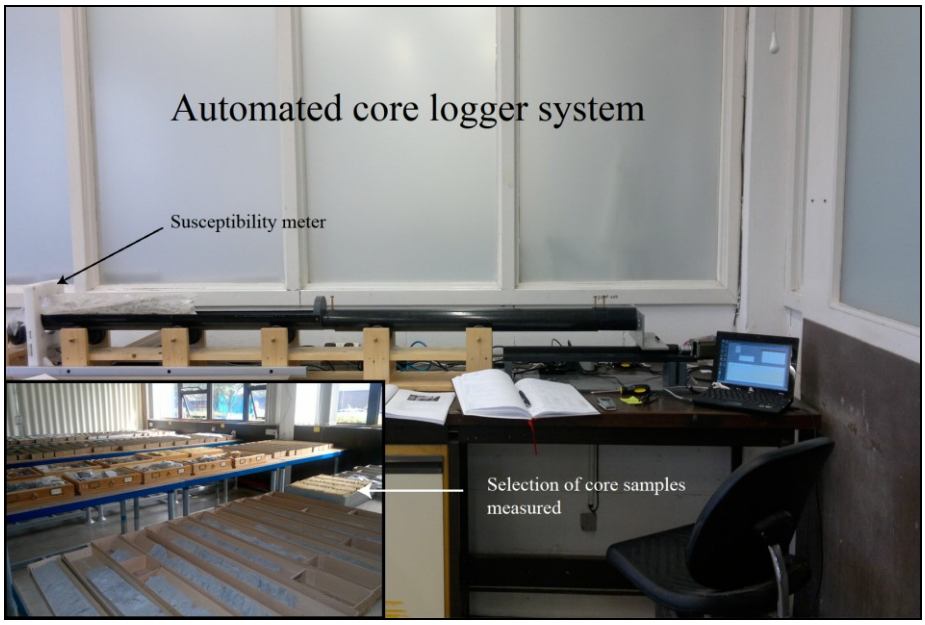


Figure 2.7: Core logger with high-resolution Bartington susceptibility meter. Some of the core measured and sampled cores measured (inset).

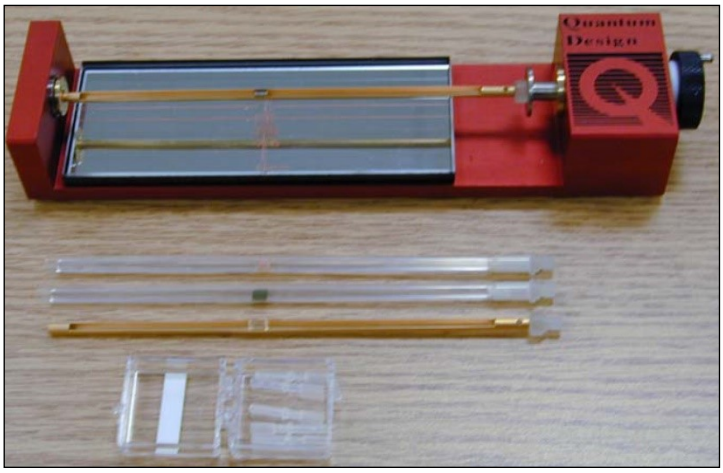


Figure 2.8: polypropylene powder holder, a brass trough sample holder and a mounting station. Note the markings of sample centre position on the mounting station.

Two types of measurements were carried out using the SQUID VSM: zero-field cooled/field cooled (ZFC/FC) measurements and hysteresis measurements. The zero-field cooled (ZFC) measurements were carried out with the samples cooled down from room temperature (300 K) to 5 K in 10 K/minute steps in a zero magnetic field. At 5 K, the samples were induced with saturation isothermal remanent magnetisation (SIRM) of 7 T and the magnetic moment of the samples was measured as the samples were warmed to 300 K whereas during the field cooled (FC) measurements, samples were cooled from room temperature to 5 K in a field of 7 T, the field was removed at 5 K and the magnetic moments of the samples were measured as they were warmed to room temperature. RT-SIRM experiments were also carried out using the SQUID VSM; the samples where induced with a saturating field (7 T) at room temperature and their magnetic moments measured as they cool down to 20 K. The methods allow identification of certain low-temperature crystallographic transitions and small particles, which are thermally activated (superparamagnetic) at room temperature.

The second type of measurement using the SQUID VSM was hysteresis at low (15 – 5 K) and room temperatures for all rock samples. Part of the well core samples were analysed at the RI, parts were sent to Beijing and ANU for measurements.

Princeton Vibrating Sample Magnetometer (VSM) measurements

Room-and high-temperature measurements were carried using a Princeton VSM at Imperial College London. Measurements carried out include room-temperature hysteresis measurements, first-order reversal curves (FORC) (Roberts *et al*., 2000), single and multicycle thermomagnetic measurements. During the hysteresis measurements, about 300 mg of the

powdered sample was placed into a gel cap with the open end fixed to a sample probe, which was screwed to the sample rod. Hysteresis and backfield curves were measured but only one sample displayed a good FORC diagram. In the thermomagnetic experiments, a few milligrams of Kimmeridge and Oxford Clay Formations pyrolysed at 250, 300 and 320 °C was mixed with a high temperature cement and a drop of glue, the mixture was placed on a ceramic sample holder and allowed 24 hours to dry before screwing it into a sample rod. Single and multicycle thermomagnetic measurements were then carried out to investigate the different magnetic mineral assembly present in the samples.

Imaging

For the purpose of imaging, the three potential source rocks pyrolysed at 320 °C were put through a magnetic extractor, built by former PhD-student Dr.Stacey Emmerton that consists of a large iron finger with a powerful magnet attached to it (Figure 2.9). Water mixed with the sample was circulated through the magnet by a pump.

Magnetic particles collected by the magnet were dispersed in acetone using an ultrasonic bath before deposition onto lacey carbon/copper-mesh support grids. Conventional bright field diffraction contrast and high-resolution phase contrast imaging was acquired using a FEI Tecnai TEM operated at 200 kV (Centre for Electron Nanoscopy (CEN), Technical University of Denmark) and selected area electron diffraction (SAED) allowed for phase identification by Dr. Trevor Almeida of Imperial College London. High-angle annular dark-field (HAADF) imaging and complementary EDX analysis were performed using a Jeol JEM 2100F TEM (Imperial College London). HAADF images were formed by collecting high-angle scattered electrons with an annular dark-field detector in scanning TEM (STEM) mode, where contrast is strongly dependent on the average atomic number (Z) of the sample encountered by the incident probe.



Figure 2.9: In-house built magnetic extractor used to extract magnetic materials present in the samples.

2.2.3 Seismic interpretation

For this purpose of this study (Chapter 4), 58 two-dimensional seismic data sets were acquired, covering an area of approximately 1400 km^2 of onshore and offshore Wessex Basin, with a total length of 507.59 Km (Figure 4.1 and Table 4.1). The data was loaded into Petrel 2013 for interpretation. The quality of the 2D seismic data used in this project could be said to be generally acceptable even though only about 20% of the sections had available well tie data, and about 30% of the sections had unrecognisable reflections especially in areas where there are complex structures and steeply dipping surface strata, as a result of the Tertiary inversion (Hawkes *et al.*, 1998).

The 2D data quality is especially poor in the eastern part of my study area (Figure 1). Although the data quality was not perfect, there were still several strong reflectors through the whole section that can be interpreted over the region (Figure 4.1). Combined with the well data, the reflectors that can be clearly identified and mapped consist of the Top of the Chalk, Top Upper Greensand Formation (Base Chalk), Top Kimmeridge Clay Fm, Top Corallian Formation, Top Inferior Oolite, Top White Lias, Top Sherwood Sandstone and Top Permian (Figure 2.10). However, for sections below Jurassic strata, the reflections are weak, thus making it difficult to interpret with confidence except where there are well controls. Additionally, there were no synthetics due to the lack of relevant data.

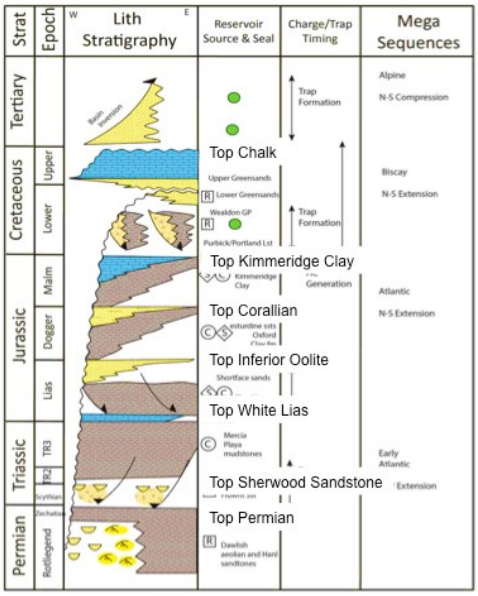


Figure 2.10: Wessex Basin tectonostratigraphy highlighting the key mapped seismic horizons. (Hawkes *et al* 1988)

In order to understand the general structural and depositional patterns in the Wessex Basin, major faults and horizons were interpreted using most of the 2D seismic data (Fig. 2.11). Those horizons, whose tops were mapped during this study are listed below:

- Top Chalk
- Top Kimmeridge Clay Fm
- Top Corallian
- Top Inferior Oolite
- Top White Lias
- Top Sherwood sandstone
- Top Permian

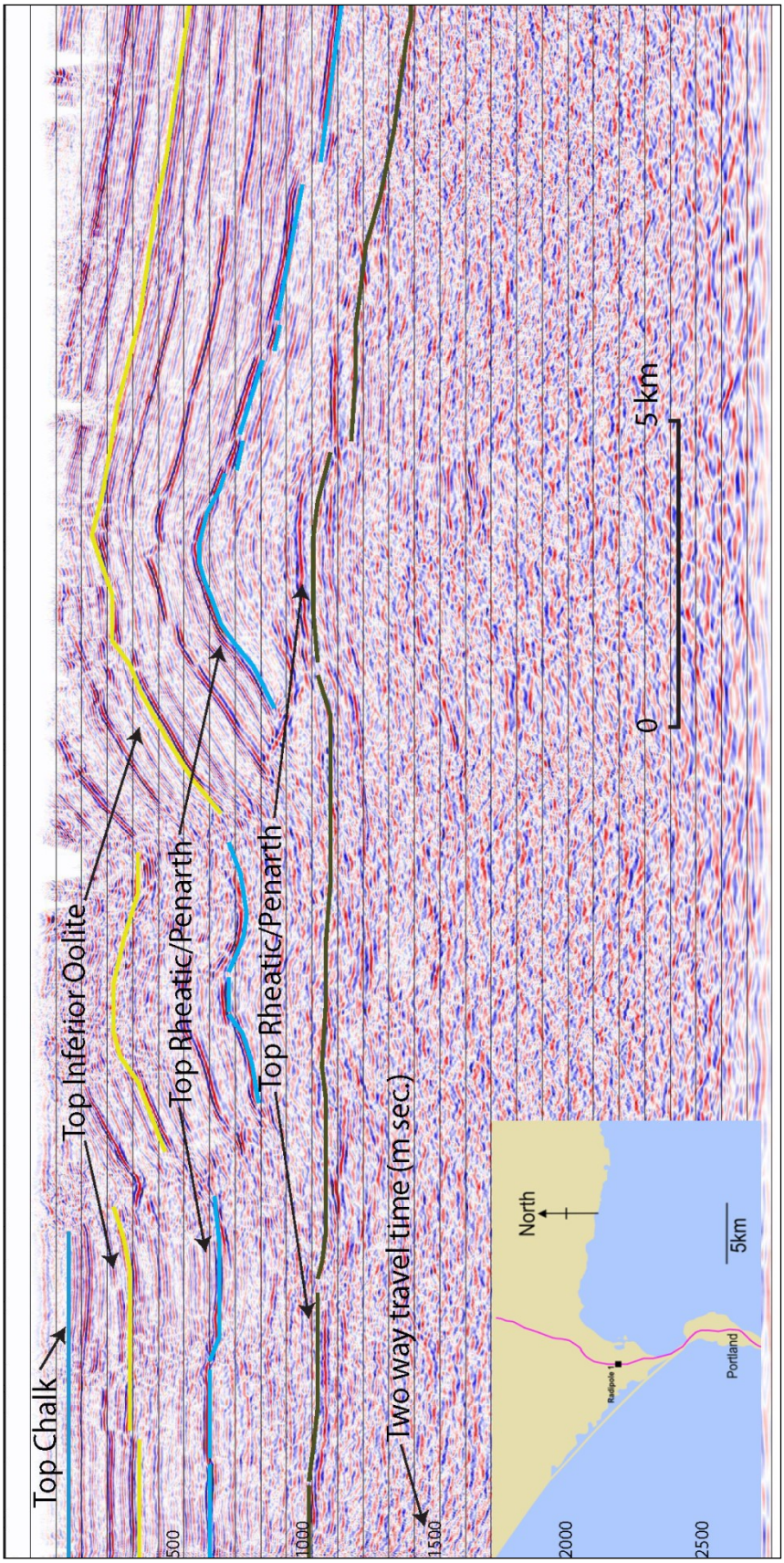


Figure 2.11: An image of section B92-40, showing the tops of the Chalk, Inferior Oolite, White Lias (Rheatic/Penarth) and Sherwood Sandstone as interpreted in this study.

2.2.4 Depth conversion and decompaction

For the purpose of generating surfaces of horizons of interest, depth conversion was carried out using two methods; 1) using calibrated depth-TWT time pairs data from 108 wells from my study area and 2) using the 2DMove software. Only top Inferior Oolite and White Lias surfaces were generated during this study, both the present day surface and the decompacted surface at the end of the Jurassic.

Chapter 3

Formation of magnetic minerals in hydrocarbon-generation conditions

3.1 Introduction

Diagenesis of clay minerals and carbonates during burial can lead to the formation of new magnetic minerals and phases in sedimentary successions; because this can also lead to remagnetisation and magnetic overprinting, these processes have been widely studied (Aubourg and Pozzi, 2010; Aubourg *et al.*, 2008a; Aubourg *et al.*, 2008b; Aubourg *et al.*, 2012; Banerjee *et al.*, 1997; Bjorlykke, 1998; Campos and Hallam, 1979; Chamley, 1994; Elmore *et al.*, 2001; Elmore *et al.*, 2012; Karlin, 1990; Kars *et al.*, 2012; Keller, 1963; McCabe and Elmore, 1989; McCabe *et al.*, 1987; McCabe *et al.*, 1983; Moreau *et al.*, 2005). When new minerals form post-rock formation, they acquire a remanent magnetisation in an ambient field, called a chemical (or crystallisation) remanent magnetisation (CRM) (Elmore *et al.*, 2012; McCabe and Elmore, 1989). New minerals are commonly formed due to: (1) action of external fluids, (2) changes in pressure, temperature and redox potential due to burial, (3) through maturation of organic material, (4) thermal metamorphism and (5) microbial actions (Elmore *et al.*, 2012).In this chapter, I am primarily concerned with the formation of the magnetic minerals, not the acquisition of CRM; however, CRM acquisition is an expression of magnetic mineral formation; therefore, I refer to both new magnetic mineral formation and CRM formation literature. Below is a review of generalised clay mineral diagenesis (section 3.1.1), followed by reviews of the formation of magnetic minerals under certain conditions (sections 3.1.2-3.1.7)

3.1.1 Clay mineral diagenesis

Clay mineral diagenesis begins with the elimination of Fe^{3+} from detrital clays to be replaced by Fe^{2+} in authigenic clays during burial and maturation of organic matter. For example, one of common routes clay mineral diagenesis reported involves the transformation of kaolinite to montmorillonite to smectite to illite and finally to chlorite (Keller, 1963). This process is argued to result in the release of iron, which leads to the formation of authigenic magnetic minerals (Curtis *et al.*, 1985; Katz *et al.*, 1998; Lu *et al.*, 1991; Moreau *et al.*, 2005; Tohver *et al.*, 2008). Illite and chlorite can carry primary magnetic susceptibility anisotropies comparable to those of titanomagnetites. For example, chlorite and hornblend minerals have been reported to be the primary magnetic carriers in studies of some greywackes and gabbros (Hounslow, 1985 and references therein). Similarly, laboratory investigations have confirmed that the transformation of iron-rich smectite into illite results in the formation of authigenic magnetic minerals (Hirt *et al.*, 1993).

Furthermore, microbial sulphate reduction, associated with biodegradation of organic matter during early diagenesis generates H_2S and/or HS^- that readily combines with dissolved iron, released during the illitization process to form pyrite (FeS_2) and its precursors such as greigite (Fe_3S_4) and makkinawite ($Fe_{1+x}S$) (Roberts and Weaver, 2005 and references therein), with greigite argued to be the main carrier of the initial, syn-depositional magnetisation in sediments (Roberts and Turner, 1993; Rowan *et al.*, 2009; Tric *et al.*, 1991).

At burial depths >2 km, or during heating in laboratories, greigite and pyrite are either oxidized to magnetite and haematite with traces of intermediary goethite or reduced to pyrrhotite and troilite (FeS) (Ahmed *et al.*, 2007; Aubourg and Pozzi, 2010; Aubourg *et al.*, 2008b; Aubourg *et al.*, 2012; Ibarra *et al.*, 1994). In addition, siderite ($FeCO_3$) could also form during deep burial in anoxic, non-sulphidic environments. For example, siderite forms when the interstitial water is saturated with dissolved iron, but cannot form any sulphides due to the non-availability of H_2S and/or HS^- species and the interstitial water is carbonate-rich (Roberts and Weaver, 2005).

Although greigite is thought to carry early, syn-depositional magnetisation (e.g., Roberts and Turner, 1993; Rowan *et al.*, 2009; Tric *et al.*, 1991), it is now known to carry late diagenic magnetisation (e.g., Horng *et al.*, 1998; Jiang *et al.*, 2001; Richter *et al.*, 1998). Greigite could form during late diagenesis from siderite if pore water chemistry becomes sulphidic (e.g., Roberts and Weaver, 2005; Sagnotti *et al.*, 2005). For example, Sagnotti *et al.* (2005) during a study of Miocene sediments discovered successive authigenic growth of pyrite, followed by siderite and then greigite. They argued that the magnetisation carried by the authigenic greigite is due to late diagenesis remagnetisation. Moreover, siderite and greigite have been reported to co-exist in sedimentary successions (Postma, 1977; Pye *et al.*, 1990), and greigite is now known to persist in geological records where all H_2S and/or HS^- produced during microbial biodegradation is removed due to high iron activity in interstitial pore waters. This could effectively retard or slowdown pyritisation process, thereby allowing greigite to persist in geological records (Kao *et al.*, 2004).

Several factors could influence the formation of magnetic minerals within sedimentary successions, below is a brief description of some of them.

3.1.2 Magnetic mineral formation due to external fluids

Magnetic minerals can form in a range of different fluids: hydrocarbons, basinal brines, orogenic and mineralising fluids (Elmore *et al*., 2012). This hypothesis is based on evidence such as temporal association between the timing of mineral formation – often determined through the CRM directions- and orogenesis (McCabe and Elmore, 1989). For example, mineral formation and remagnetisation in the Mississippian Barnet Shale, has been attributed to the action of migrating fluids from the Ouachita thrust front that forms the eastern part of the basin (Oliver, 1986, 1992).

Several studies have provided evidence or proposed models linking the presence of hydrocarbons and the formation of authigenic magnetic minerals, such as magnetite and pyrrhotite (e.g., Aldana *et al.*, 2003; Burton *et al.*, 1993; Costanzo-Alvarez, 2006; Elmore *et al.*, 1987; Elmore *et al.*, 1993; Machel, 1995; McCabe *et al.*, 1987). Donovan *et al.* (1979) were the first to associate hydrocarbon accumulation and magnetic enhancement. of magnetic signals, based on aeromagnetic data from Cement oil field in Oklahoma. Subsequent studies (e.g., Elmore and Crawford, 1990; Elmore *et al.*, 1987) have identified iron oxides and sulphides and pyrrhotite as primary carriers of CRM in hydrocarbon environment, others (e.g., Rijal *et al.*, 2010) have presented evidence for secondary magnetite as the CRM carrier.

Scanning electron microscopy (SEM) observations on near-surface samples revealed samples from oil fields are associated with spherical aggregates (framboids) of magnetic minerals (e.g., Aldana *et al.*, 2003; Aldana *et al.*, 1999; Costanzo-Alvarez, 2006; Costanzo-Alvarez *et al.*, 2000; Díaz *et al.*, 2000; González *et al.*, 2002);it has been argued that this points to an authigenic origin (e.g., Aldana *et al.*, 1999). Possible sources of iron atoms that could contribute to the authigenic magnetic mineral formation in hydrocarbon habitats, include:(1) the host rock (intrinsic) (Burton *et al.*, 1993; Machel, 1995; McCabe and Elmore, 1989), (2) the hydrocarbons themselves (e.g., Duyck *et al.*, 2002; Ellrich *et al.*, 1985; Sainbayar, 2012; Sundararaman *et al.*, 1993) and (3) fluids associated with hydrocarbons (Kharaka *et al.*, 1985). However, the presence of hydrocarbons can also be deleterious to magnetic mineralogy, either through microbial oxidation of magnetite or the dissolution of ferrimagnetic minerals (e.g., magnetite) and the precipitation of ferromagnetic (e.g., haematite) and/or paramagnetic ones (e.g., pyrite) (Emmerton *et al.*, 2013; Machel, 1995).

3.1.3 Magnetic mineral formation due to burial

It is known that burial can generate new magnetic minerals phases, and alter existing ones; there are many processes, which are very dependent on the environment (Elmore *et al.*, 2012).For example, greigite and pyrite, associated with biodegradation of organic matter during early diagenesis during burial to > 2 km, are either oxidized to magnetite and haematite with traces of intermediary goethite, or form pyrrhotite and troilite (FeS) depending on the environment (Ahmed *et al.*, 2007; Aubourg and Pozzi, 2010; Aubourg *et al.*, 2008b; Aubourg *et al.*, 2012; Ibarra *et al.*, 1994). It is also thought siderite ($FeCO_3$) can also form during deep burial in anoxic, non-sulphidic environments, if the interstitial water is saturated with dissolved iron, but cannot form any sulphides due to lack of H_2S and/or HS^-, (Roberts and Weaver, 2005). However, the formation mechanism of most magnetic minerals is non-unique. For example, the formation of greigite as described in section 3.1.2 above.

3.1.4 Organic formation of ferromagnetic minerals

Maturation of organic matter has also linked to magnetic mineral formation and remagnetisation in sediments (Elmore *et al.*, 2012 and references therein); the maturation process is often due to burial. For example, Banerjee *et al.* (1997) reported that the timing of CRM acquisition in the Belden Formation, Colorado, differs across the basin, but correlates well with modelled organic matter maturation time. Similarly, Blumstein *et al.* (2004) showed that the timing of a Jurassic CRM found in the Mississippian Desert Limestone and Chainman Shale (which are source rocks in western Utah), coincide with the timing of the maturation of organic matter in the basin. Many other studies have reported similar relationships between CRM and organic matter maturation (e.g., Cioppa *et al.*, 2002; Font *et al.*, 2006; Plaster-Kirk *et al.*, 1995).

3.1.5 Magnetic mineral formation and thermal metamorphism

Thermal metamorphism that happens as a result of spontaneous combustion, has also been suggested to cause strong remagnetisations in bituminous marine sediments, coals and hydrocarbon reservoirs (Cisowski and Fuller, 1987 and references therein). Studies of the Monterey and Sioquoc Formations in southern California, reveal a four orders of magnitude in increases in the natural remanent magnetization in the thermally metamorphosed sections, compared to the un metamorphosed ones (Cisowski and Fuller, 1987). It has been suggested that the heat needed for such spontaneous combustion could be provided from the low-

temperature oxidation of finely disseminated framboidal pyrites present in the sediments, or it can also be due to burial (Mathews and Bustin, 1984).

3.1.6 Microbial action

The biomineralisation of magnetic minerals have been well documented(Bazylinski, 1996). This biomineralisation can occur in one of two ways: 1) Iron biomineralisation by biologically induced mineralisation (BIM), where bacteria create reducing environments that allow for the intracellular transformation of Fe^{3+} to Fe^{2+} (e.g., Bell *et al*., 1987; Zhang *et al*., 1998; Bazylinski *et al*., 2007). 2) Biologically controlled mineralisation (BCM): bacteria produce magnetite extracellularly by various Fe^{3+} reducing bacteria within the bulk porewaters of sediments (Bazylinski *et al*. 2007).

3.1.7 Formation of magnetic minerals in hydrocarbon reservoirs

Various theories have been proposed in an attempt to explain the origin of the magnetic minerals found in association with hydrocarbon reservoir, two basic mechanisms have been proposed: (1) abiotic processes, for example, diagenetic processes (including maturation of organic matter) and physical-chemical changes brought about by the invading fluids (Aubourg and Pozzi, 2010; Burton *et al.*, 1993; Elmore *et al.*, 2012), and (2) microbial actions, for example, anaerobic microbial degradation of organic matter (Aldana *et al.*, 1999; Elmore *et al.*, 1987; Emmerton *et al.*, 2013). Burton *et al.* (1993) developed an abiotic thermodynamic model explaining how the magnetic response of magnetic minerals could be both increased or decreased depending on the local chemical environment, e.g., sulphur rich or not, and proximity to hydrocarbon plumes. Other authors (e.g., Emmerton *et al.*, 2013) reported a complex relationship between hydrocarbon and magnetic minerals: anaerobic biodegradation of oils (e.g., Bigge and Farrimond, 1998; Heider *et al.*, 1998)can lead to magnetic framboid formation, but the progression of biodegradation can also have a deleterious effect on magnetic nanoparticles reducing the overall magnetic susceptibility of the host rock. However, no data has been published yet, on the changes in magnetic mineralogy of oil source rocks that have generated and expelled oil; such oil source rocks are deeply buried and are very rarely targeted during exploratory drilling activities.

3.2 Samples

Three potential source rock samples from the Wessex Basin were obtained as described in section 2.2. The samples are the Kimmeridge Clay Fm from Kimmeridge Bay, Oxford Clay Fm from Chickerell and the Blue Lias Fm from Lyme Regis (Fig. 2.1). The non-carbonate

mineralogy of the Blue Lias Fm is reported to be composed of >50% illite, mixed layer illite/smectite >20%, kaolinite < 20% and chlorite <5%, while Oxford Clay Fm has a clay content composed of illite and mixed layer illite/smectite >60%, kaolinite and detrital chlorite of about 20 and 5% respectively (Hounslow, 1985 and references therein). The Kimmeridge Clay Fm non-carbonate content is composed mainly of mixed layer illite/smectite with minor amounts of kaolinite and chlorite (Scotchman, 1989). In terms of magnetic mineralogy, Hounslow (1985) reported the presence of titanomagnetite and titanohaematites in the Blue Lias Fm and Oxford Clay Fm.

In addition, magnetic studies carried on the Lias Group samples from St. Audrie's Bay, UK (Hounslow *et al.*, 2004), revealed the presence of iron oxides (magnetite and haematite) and sulphides. Hounslow *et al.* (2004) argued that the chemical remanent magnetisation (ChRM) from the Lias Group samples mainly resides in the sulphides and is of Brunhes age (<800 ka). Even though the St. Audrie's Bay is about 80 km north of my study area, Hounslow *et al.* (2004) is the only study to my knowledge that has estimated the timing of ChRM in the Lias Group, and to my knowledge, such studies have not been carried on the Kimmeridge Clay Fm nor on Oxford Clay Fm.

In this chapter, hydrous pyrolysis (artificial maturation) (Fig. 3.1) experiments similar to Aubourg and Pozzi (2010), but in anoxic environments and under constant hydration were carried out in order to investigate the effects of petroleum generation on magnetic mineralogy in the laboratory and to have a better understanding of the stoichiometry, type and abundance of magnetic minerals produced during the generation of oil and gas in the sub-surface. The three potential source rocks from the Wessex Basin, UK, were subjected to laboratory conditions similar to those experienced during catagenesis. This was done by means of pyrolysis in pressure vessels for 72 hours at different temperatures. For pyrolysis temperatures 300 °C and 320 °C, the pressure was 80 and 100 bar respectively; at depth the pressures are significantly higher for the given temperatures, but in terms of petroleum generation, heat is the most critical factor (Helgeson *et al.*, 2009; Pepper and Corvi, 1995; Stainforth, 2009). For example, at ~2 km depth, the temperature is typically ~50 °C with a pressure of ~ 150 bars, and at 6 km, the temperature is ~200 °C and the pressure ~600 bar (Machel, 1995).

The types of magnetic minerals formed during hydrous pyrolysis were characterised using a range of magnetic techniques. Transmission electron microscopy (TEM) combined with energy-dispersive X-ray (EDX) analysis of extracted magnetic minerals from the heated rocks

was also carried out in an attempt to identify the magnetic minerals generated. My findings will help to provide a better understanding of the magnetic minerals formed during oil generation and also in hydrocarbon-rich environment. These findings will help to interpret the often-problematical data generated by aeromagnetic surveys(e.g., Donovan *et al.*, 1979; LeSchack and Van Alstine, 2002).

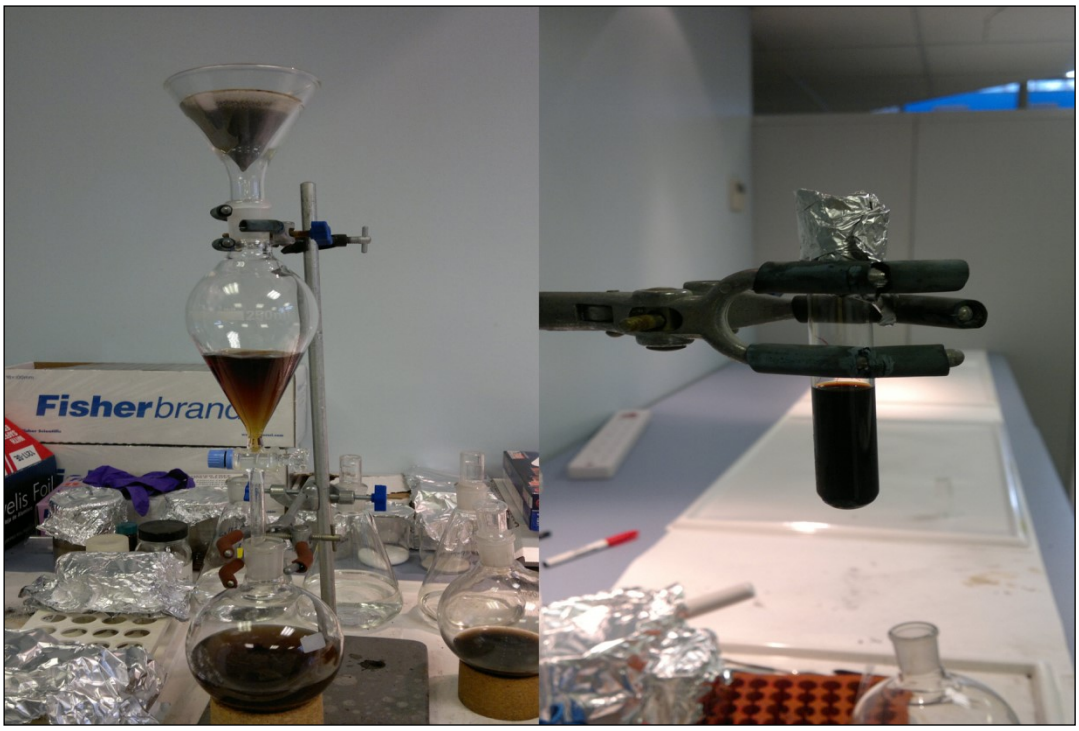


Figure 3.1: Crude oil generated from heating the Blue Lias Fm sample at 320 °C for 72 hrs. The other two samples (Kimmeridge and Oxford Clay Fms) heated at the same temperature for same duration also generated crude oil.

3.3 Magnetic characterisation of the rock samples

Both the pyrolysed (heated) and the non-pyrolysed (unheated) samples were characterised magnetically and the results are discussed below.

3.3.1 Magnetic hysteresis measurements

Room- and low-temperature magnetic hysteresis measurements were carried out on the samples using a Princeton VSM and a Quantum Design SQIUD VSM as described in section 2.2.2.

Room-temperature hysteresis measurements

Room-temperature magnetic hysteresis and backfield curves were measured on all the rock samples. The unheated samples all exhibited strong paramagnetic signals during hysteresis, with little or no evidence for a ferromagnetic (*sensulato*) signal (Fig. 3.2). That is, the three unheated samples have similar low saturation remanent magnetisation (M_{rs}) values (Table 3.1), though the Blue Lias Fm sample has a stronger paramagnetic response.

In contrast to the unheated samples the heated samples display significant ferromagnetic signals (Fig. 3.3-3.5). The shape of the curves (not slope corrected) changed from predominantly paramagnetic to ferromagnetic in character and the intensity of the magnetisation increased significantly. For example, the unheated Kimmeridge Clay Fm sample had a M_{rs} of 58 $\mu Am^2/kg$ at room-temperature, but Kimmeridge Clay Fm samples heated to 250-°C and 320 °C had M_{rs} values of 2510 $\mu Am^2/kg$ and 8150 $\mu Am^2/kg$ respectively (Fig. 3.3). Similarly, there is a significant increase in the saturation magnetization (M_s) from 550 $\mu Am^2/kg$ in unheated sample, to 6940 $\mu Am^2/kg$ and 34200 $\mu Am^2/kg$ for Kimmeridge Clay Fm heated at 250 °C and 320 °C respectively (Fig. 3.3 & Table 3.1). The Oxford Clay Fm also shows a similar trend where samples heated at 250 °C and 320 °C had M_s values of 28200 $\mu Am^2/kg$ and 11000-$\mu Am^2/kg$ respectively against 560 $\mu Am^2/kg$ for the immature sample, i.e., more than an order of magnitude increase with corresponding increase in the M_{rs} (Fig. 3.4 and Table 3.1). Similarly, the Blue Lias Fm showed a significant increase in magnetic grain sizes and abundance of magnetic materials after heating, with higher M_{rs} and M_s values compared to the unheated sample (Fig. 3.5).

A plot of M_s against pyrolysis temperature is shown in Figure 3.6a. Compared to the unheated starting materials, all three rocks displayed clear increases in concentration of magnetic materials. Also supporting the evidence for the alteration of the ferromagnetic contribution to the hysteresis response is an increase in B_c; all the heated rocks had higher coercivities than their unheated counterparts save for Kimmeridge Clay Fm 150 °C (Table 1 and Figure 3.6b). The high-field magnetic susceptibility (χ_{hf}), which measures the contribution of diamagnetic/paramagnetic material, varied across the three samples; all the heated Kimmeridge samples had less χ_{hf}than the unheated sample except for Kimmeridge Clay Fm heated at 250 °C with similar values to the unheated sample (Table 1). χ_{hf} values for the Oxford Clay Fm and the Blue Lias Fm were similar between the heated and the unheated samples (0.5-0.6 $\mu m^3/kg$) except for Oxford Clay Fm and Kimmeridge Clay Fm 320 °C which had lower values of about

0.002 $\mu m^3/kg$. The trend is similar with the Blue Lias Fm 250 °C much less paramagnetic contribution ($4 \times 10^{-11} m^3/kg$) and Blue Lias Fm 320 °C having a diamagnetic contribution of $-1 \times 10^{-10} m^3/kg$.

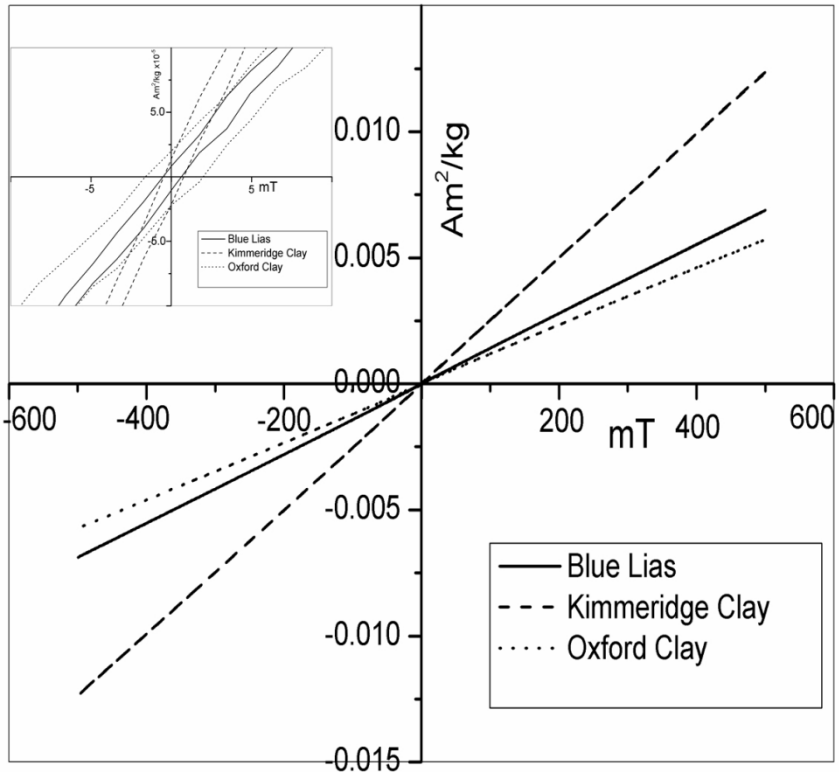


Figure 3.2: Hysteresis curves for the three unheated rock samples showing mainly paramagnetic behaviour. The curves are not slope corrected.

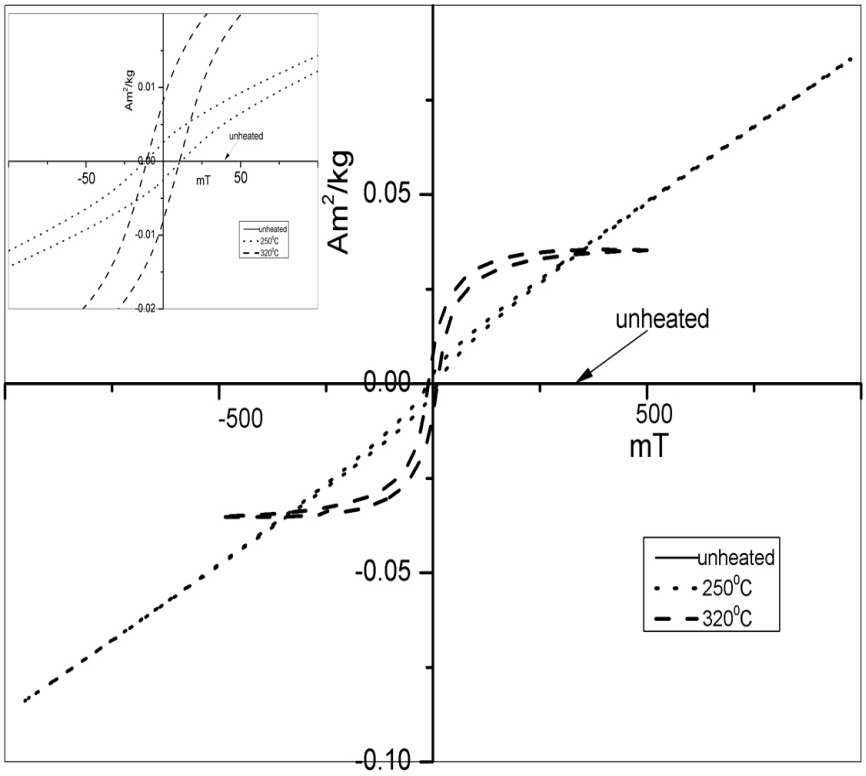


Figure 3.3: Magnetic hysteresis plots for the Kimmeridge Clay Fms heated (320 °C & 250 °C) and unheated showing changes in magnetic response after heating. The unheated sample response is almost flat and lies very close to the x-axis. The hysteresis loops do not have a paramagnetic correction.

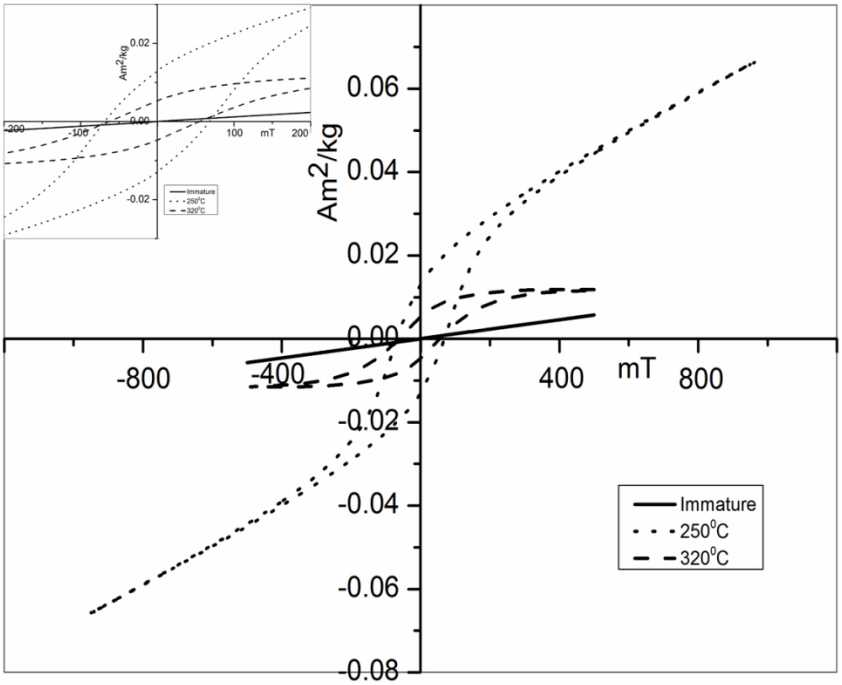


Figure 3.4: Magnetic hysteresis plots for Oxford Clay Fms heated (320 °C & 250 °C) and unheated showing changes in magnetic response after heating. The hysteresis loops do not have a paramagnetic correction.

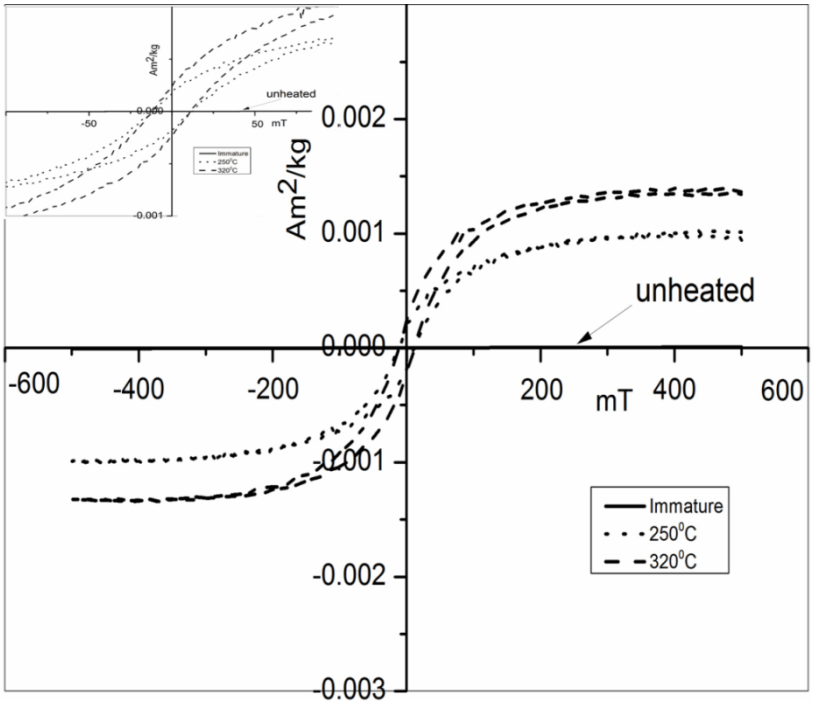


Figure 3.5: Magnetic hysteresis plots for Blue Lias Fm heated (320 °C & 250 °C) and unheated showing changes in magnetic response after heating. The immature sample response is almost flat and lies very close to the x-axis. The hysteresis loops do not have a paramagnetic correction.

Table 3.1: Room-temperature hysteresis parameters carried out on the three rock samples used in this study. χ_{hf}= high-field susceptibility, B_{cr}= remanent coercivity, B_c= Coercivity, M_{rs}= saturation remanent magnetization, M_{rs}/M_s= ratio of saturation remanent magnetization to saturation magnetisation, … = missing information due to instrument error.

Sample	B_c (mT)	B_{cr} (mT)	B_{cr}/B_c	M_{rs} ($\mu Am^2/kg$)	M_s ($\mu Am^2/kg$)	M_{rs}/M_s	χ_{hf} ($\times 10^{-7}$ m^3/kg)
Kimmeridge Clay immature	9.0	31	3.4	58	550	0.11	1
Kimmeridge Clay 150°	7.5	44	5.9	210	1530	0.14	0. 50
Kimmeridge Clay 200°C	16	35	2.2	240	1320	0.18	0. 50
Kimmeridge Clay 250°C	19	46	2.5	2510	6940	0.36	1
Kimmeridge Clay 300°C	34	120	3.5	540	2300	0.23	0. 50
Kimmeridge Clay 320°C	11	25	2.4	8150	34000	0.24	0.030
Oxford Clay immature	13	27	2.1	60	560	0.24	0. 50
Oxford Clay 150°C	13	47	3.5	140	660	0.21	0. 50
Oxford Clay 200°C	66	91	1.4	15100	27000	0.55	0. 60
Oxford Clay 250°C	83	110	1.4	12900	28000	0.57	0. 60
Oxford Clay 300°C	35	…	…	620	2670	0.24	0. 50
Oxford Clay 320°C	60	120	2.0	5030	11000	0.46	0.02
Blue Lias immature	7.1	…	…	36	280	0.20	0. 60
Blue Lias 150°C	22	14	0.64	140	900	0.15	0. 60
Blue Lias 200°C	13	40	3.0	400	2980	0.11	0. 60
Blue Lias 250°C	11	27	2.4	180	980	0.19	0.00040
Blue Lias 300°C	14	42	3.1	73	800	0.09	0. 5
Blue Lias 320°C	11	36	3.5	240	1380	0.17	-0.0010

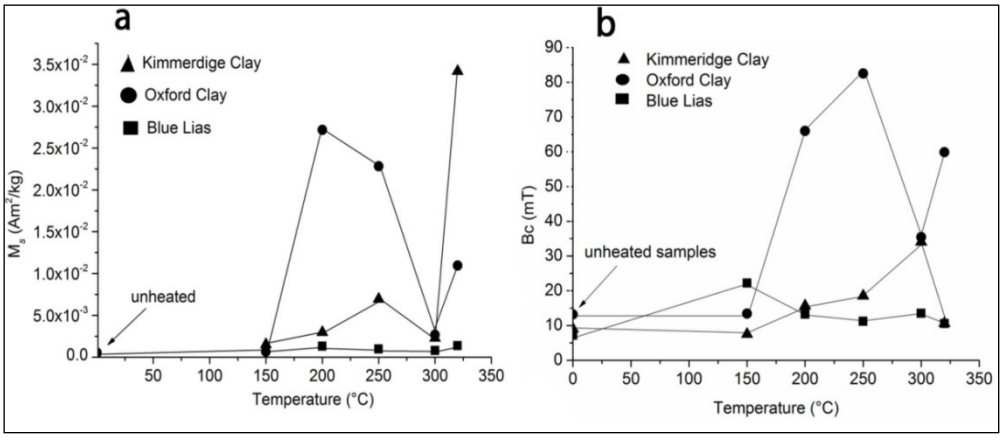


Figure 3.6: a) A plot of saturation remanent magnetization (M_s) versus pyrolysis temperature. Oxford Clay Fm showed a double peak M_s values first at 250 °C then a minimum at 300 °C and a secondary maximum at 320 °C. Kimmeridge Clay Fm showed the highest M_s at 320 °C pyrolysis temperature. b) Plot of the magnetic coercivity (B_c) against pyrolysis temperature for all three-source materials.

Low-temperature hysteresis measurements

A few magnetic hysteresis measurements were also carried out at 5 K on the heated rocks. Oxford Clay Fm 320 °C measured at 5 K had a M_{rs} value of 21400 μAm^2/kg whereas the same sample measured at room temperature had a M_{rs}value of 5030 μAm^2/kg, representing about a quadruple increase in magnetic remanence on cooling (Fig.3.7a). The Blue Lias Fm and Kimmeridge Clay Fm samples also show similar trends in variation between magnetic measurements performed at room temperature and those carried out at 5 K, exhibiting large increases in both M_s and M_{rs} (Fig. 3.7a-d).

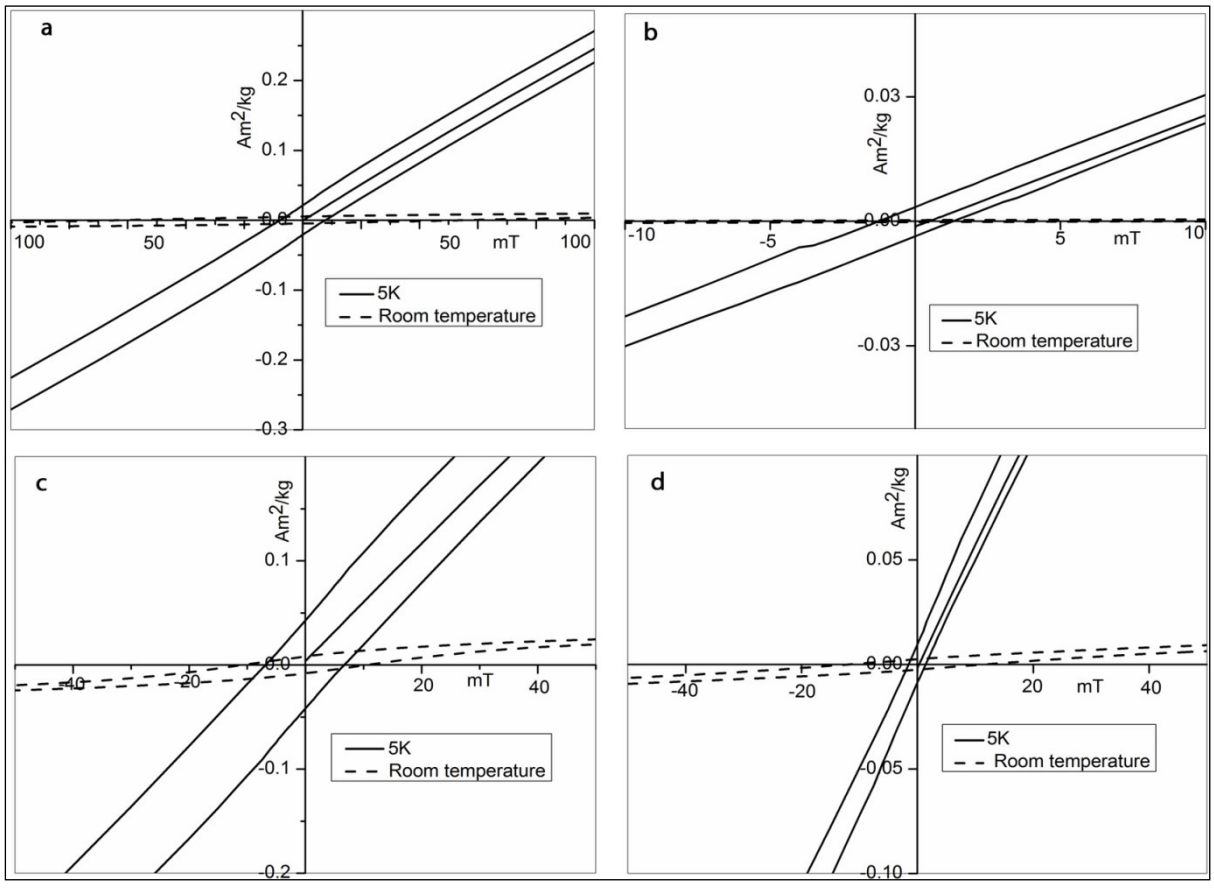


Figure 3.7: Comparison of hysteresis measurements carried out at 5 K and at room temperature of a) Oxford Clay Fm 320 °C b) Blue Lias Fm 320 °C c) Kimmeridge Clay Fm 320 °C and d) Kimmeridge Clay Fm 250 °C.

Room-temperature first-order reversal curves (FORC)

FORC measurements were carried out on samples with strong enough magnetic signal and it showed variability in magnetic mineral assemblages and grain size distributions (Fig. 3.8). FORC analysis of Oxford Clay Fm 200 °C indicated the presence pseudo-single domain particle (Roberts *et al.*, 2000) with narrow elongated contours that has a peak distribution at

about 60 mT (Fig. 3.8a). Kimmeridge Clay Fm 320 °C on the other hand, exhibited similar narrow contours but with a peak distribution near the origin (~10 mT) (Fig. 3.8b).

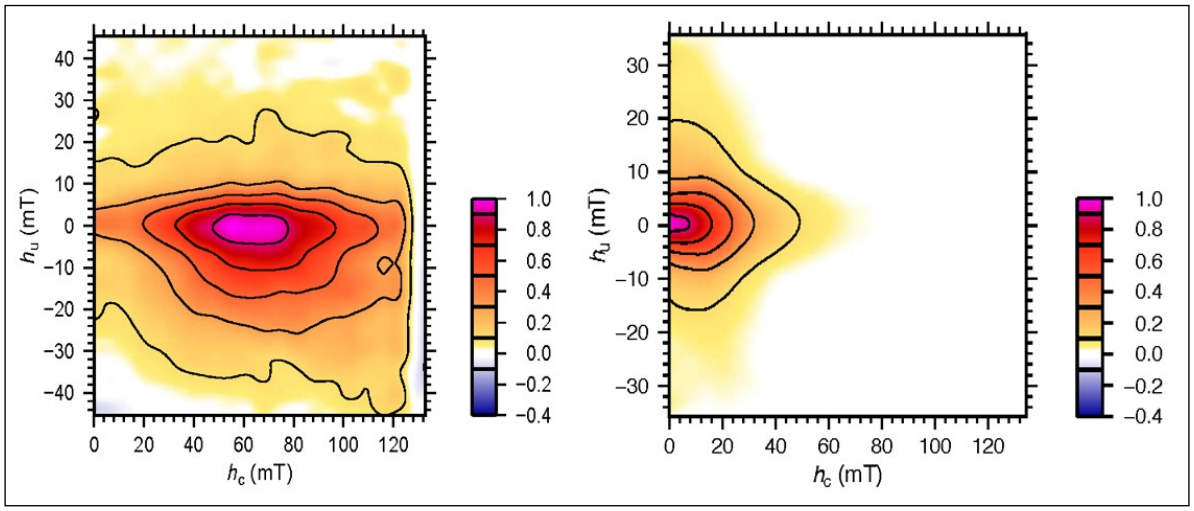


Figure 3.8: First-order reversal curves (FORC) diagrams for a) Oxford Clay Fm 200 °C showing narrow elongated contour distribution with peak at around 60 mT and b) Kimmeridge Clay Fm 320 °C showing narrow contour distribution with peak near the origin.

3.3.2 Thermomagnetic measurements

Thermomagnetic measurements were carried out on a selection of samples in order to investigate the type of magnetic mineralogy present in those samples. Two types of measurements were carried out: single and multicycle thermomagnetic curves to investigate alterations/transformation of magnetic phases present in the samples. The single thermomagnetic run curves showed irreversibility on cooling from 600 – 700 °C with all the samples showing various amount of decay in moment from about 330 °C (Figs. 3.9 a-f insets) with the 250 °C and 320 °C samples (Figs. 3.9 c-f insets) exhibiting a secondary increase in magnetic moment above 400 °C. All the samples had a higher moment on cooling from 650 °C except for Oxford Clay Fm 250 °C and 320 °C. Samples containing a mixture of magnetite and greigite show an inflection at temperatures between 200–300 °C during thermomagnetic experiments if heating was carried out in a reducing atmosphere and the sample will not show a marked minimum (Roberts *et al.*, 2011);this behaviour was observed in Oxford Clay Fm 320 °C (Fig. 3.9f inset).

The multicycle thermomagnetic curves are mostly irreversible for the two rock samples across all pyrolysis temperature ranges (Fig. 3.9). There is an increase of magnetic moment on cooling after heating to 300 °C in Oxford Clay Fm 250 °C (Fig. 3.9b), but the Kimmeridge Clay Fm 250 °C was nearly reversible on heating to the same temperature (Fig. 3.8b). There was a

general increase in magnetic moment after the 350 °C cycle in Kimmeridge Clay Fm (Fig. 3.8a) and a general decrease in moment after the 350 °C cycle Oxford Clay Fm (Fig. 3.9b). The 300 °C and 350 °C cycles produced nearly reversible curves for both Kimmeridge and Oxford Clay Formations 300 °C with a slight increase in magnetic moment on 350 °C cooling step (Figs. 3.9c & d) and a general increase in moment and similar behaviour between the two samples on the 500 °C and 650 °C cycles (Figs. 3.9e and f). Similarly, Kimmeridge and Oxford Clay Formations 320 °C show similar trends, with an initial increase in moment on both 300 °C and 350 °C cycles and a significant drop in magnetic moment in the 500 °C and 650 °C steps.

3.3.3 Low-temperature warming and cooling experiments

Two types of measurements were carried out here: 1) Warming curves of SIRMs induced at 5 K in a field of 7 T and warmed to room temperature (Figs. 3.10a-c). Two initial starting states were considered: after field-cooling (FC) from room temperature in field of 7 T and after zero-field cooling (ZFC) from room temperature. All the samples show a sharp drop in magnetization on heating, between 5 K and ~50 K, with a gradual decrease in magnetisation on warming ~50 K to room temperature. For all three samples the FC warming curves plotted above the ZFC data (Figs. 3.10a-c). During the warming experiments, initial magnetisation is seen to be much higher for the heated samples, compared to their unheated counterparts, providing further evidence for the production of magnetic minerals through pyrolysis. 2) Cooling curves of SIRMs at room temperature in a field of 7 T and cooled to 20 K was carried out on selected pyrolysed samples shown here in Figure 3.10d. No crystallographic transitions were observed in any of the experiments, suggesting that the demagnetisation observed on warming is due to the thermal relaxation of very small particles (~20-30 nm or finer) that are superparamagnetic at room temperature (Dunlop and Özdemir, 1997).

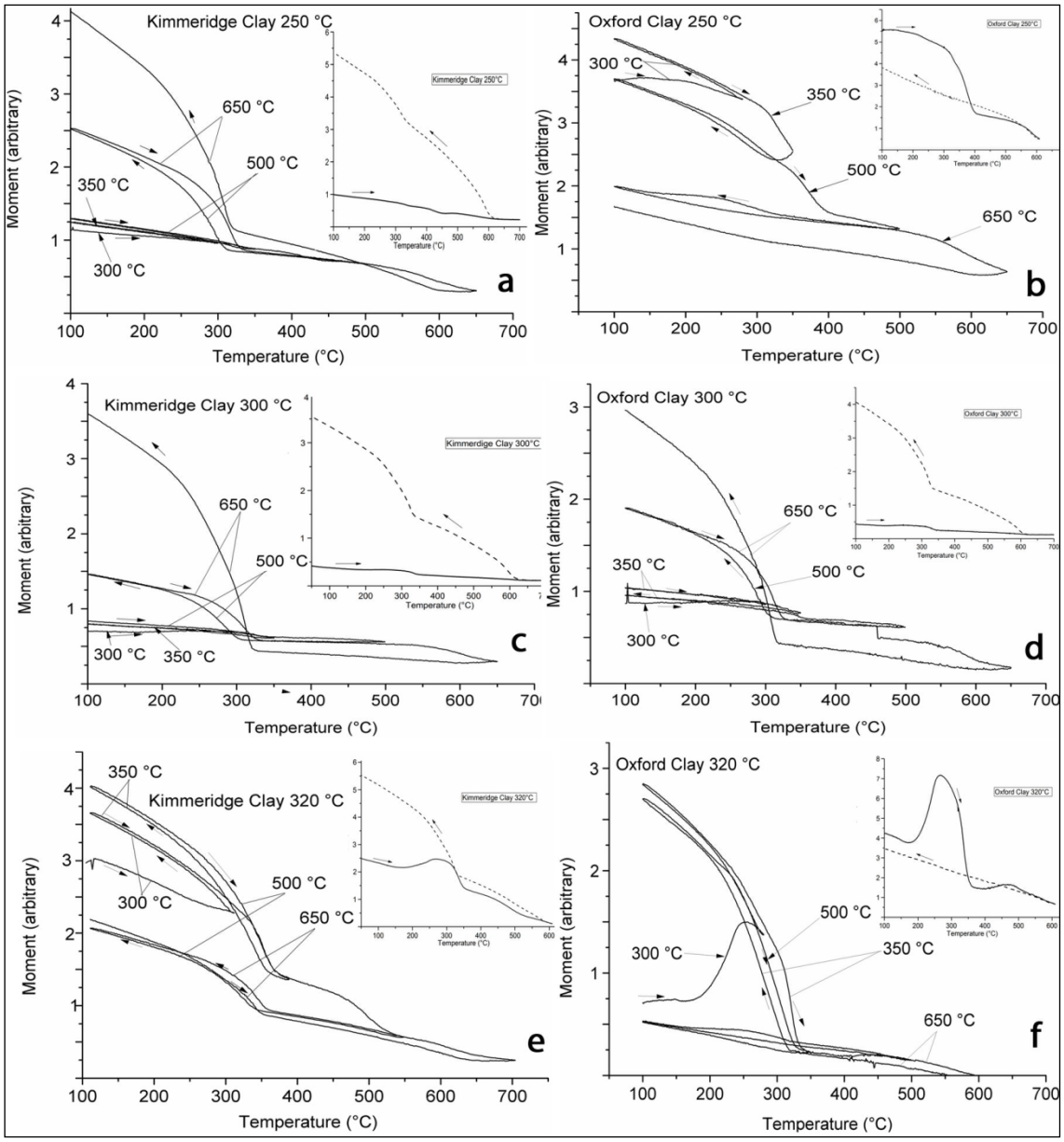


Figure 3.9: Multicycle thermomagnetic curves showing slight alteration and increase in magnetic moment (a, c & d) that indicates possible alterations from greigite and/or to possible magnetite. Panels b, e & f show an increase in moment after the first step, indicating alterations possibly to pyrrhotite and subsequent decrease in the moment in the 500 & 650 °C steps, indicating alterations to less magnetic mineral possibly pyrite and/or haematite. Insets: Continuous thermomagnetic curves indicating drop in magnetization on heating.a, b, d & e show drops of magnetization around 330 °C- 400 °C which might indicate the presence of pyrrhotite and at around 600 °C which indicates the presence of magnetite. c& f indicate the presence of 'mixed' pyrrhotite due to the shape of the curve and magnetite. All heating was carried out in helium atmosphere and a field of 100 mT.

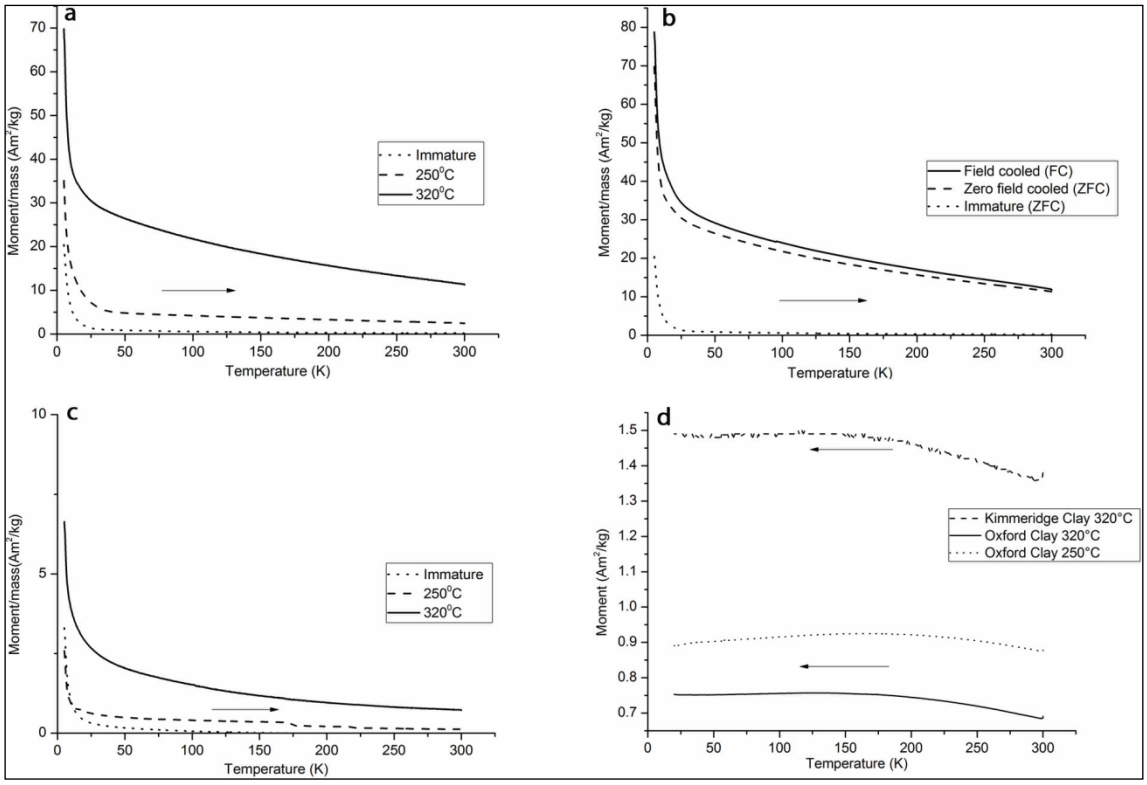


Figure 3.10: Warming curves for the Kimmeridge Clay Fm (a & b) and the Blue Lias Fm (c) imparted with a saturation isothermal remanence in field of 7 T at 5 K. Two initial states are considered, zero-field cooling (ZFC) and (FC). ZFC samples were demagnetised at room-temperature before cooling in zero field to 5 K. FC samples were cooled in a field of 7 T from room-temperature to 5 K. Note the difference in scale of the magnetisation of both samples. (d) Shows RT-SIRM with no obvious drop in magnetization on cooling.

3.4 Transmission electron microscopy (TEM)

For the purpose of imaging, magnetic particles were extracted as described in section 2.2.2. The TEM and EDX investigations provided high magnification imaging and chemical analysis of the magnetically extracted samples. Figure 3.11 presents Bright-field TEM images of the magnetic extracts of the heated Kimmeridge Clay Fm (320 °C). Large sheets are displayed in Figure 3.11a and the associated selected area electron diffraction (SAED) pattern (inset) is in good agreement with that of Fe(II–III) hydroxysalt green rusts (GR1) (Almeida *et al.*, 2012a). The high-magnification image of Figure 3.11b depicts a cluster of small particles (< 20-30 nm in diameter); in order to accurately identify the mineralogy present in this cluster (and others like it), the XRD and electron patterns were used to determine the lattice spacing and compared to published data. The measured lattice spacing d=3.54A (Fig. 3.11) matched closely with the reflection from d220 lattice of greigite, 3.49A; this was by far the closest fit compared to other likely minerals. The high-angle annular dark-field (HAADF) image of Figure 3.12a displays a group of GR1 sheets, and the associated EDX chemical maps (Figs.3.12b-h) depict the

corresponding elemental distribution of Al, C, Fe, K, Mg, O and Si, respectively. Figure 3.13 presents an HAADF image of an individual nanoparticle (~ 40 nm long, ~ 20 nm wide) and the associated EDX chemical maps show the elemental distribution of Fe (Fig. 3.13b) and O (Fig. 3.13c). The EDX spectrum of Figure 3.13d displays the elemental constituents of the nanoparticle shown in Figure 3.13a. No larger magnetic particles were observed, i.e., only of iron sulphide and iron oxide magnetic nanoparticles were detected.

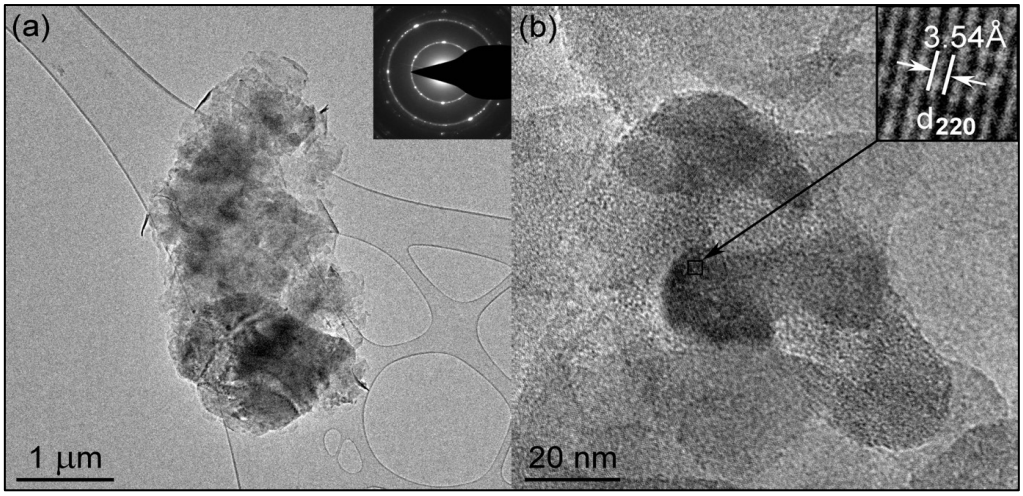


Figure 3.11:Bright-field TEM images of magnetic extract from Kimmeridge Clay Fm (320 °C) showing (a) sheets of green rust, as identified by selected area electron diffraction (SAED) (inset); and (b) clusters of nanoparticles (< 50nm), with characteristic lattice fringes consistent with the presence of Fe_3S_4 (inset).

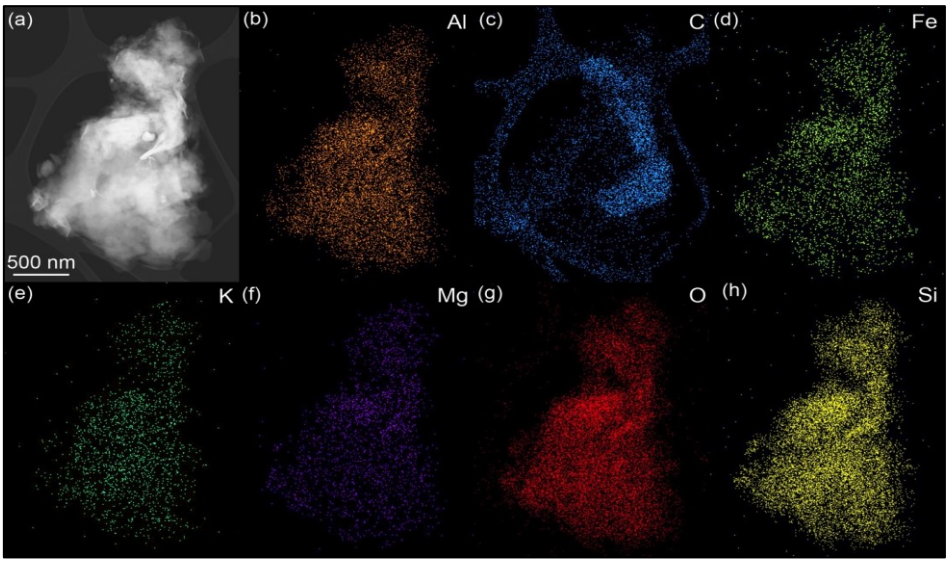


Figure 3.12:(a) HAADF image of magnetic extract from Kimmeridge Clay Fm (320 °C) showing sheets of green rust; and (b-h) EDX chemical maps showing (b) aluminium, (c) carbon, (d) iron, (e) potassium, (f) magnesium, (g) oxygen and (h) silicon content.

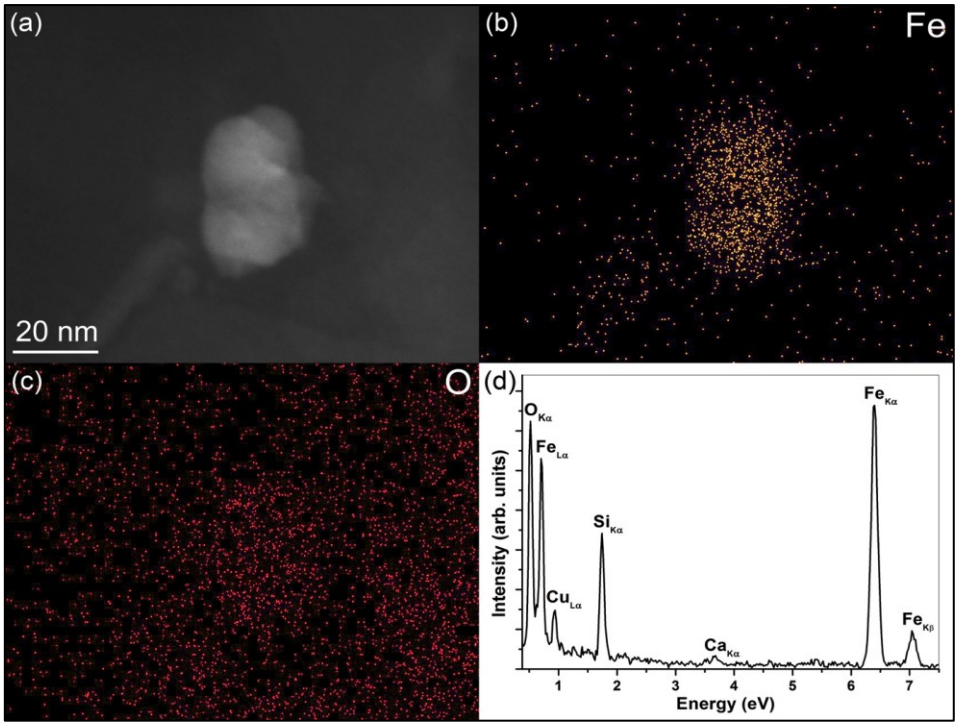


Figure 3.13: (a) HAADF image of magnetic extract from Kimmeridge Clay Fm (320 °C) showing an individual nanoparticle; and (b, c) EDX chemical maps showing (b) iron and (c) oxygen, content. (d) EDX spectrum acquired from the centre of the particle shown in (a).

3.5 Relationship between oil generation and production of magnetic minerals

The three unheated samples were all predominantly paramagnetic to varying degrees; the Blue Lias Fm had the weakest magnetic signal, presumably due to a smaller contribution of detrital chlorite than the Oxford Clay Fm and Kimmeridge Clay Fm rocks (Deconinck *et al.*, 2003; Hounslow, 1985).There is some evidence for the occurrence of ferromagnetic minerals, e.g., Hounslow (1985) reported titanomagnetite and titanohaematites in the Blue Lias Fm and Oxford Clay Fm (Hounslow, 1985), however, the ferromagnetic contribution was relatively very small.

Upon heating there is an increase in the amount of ferromagnetic material in the heated samples based on the saturation magnetization values (Table 3.1), confirming the formation of magnetic minerals as reported in similar heating experiments (e.g., Aubourg and Pozzi, 2010; Aubourg *et al.*, 2012; Kars *et al.*, 2012). Albeit it from a limited number of data points, two peaks of increase in M_s values were observed in all the three samples; a peak at pyrolysis temperature of 250 °C and another at pyrolysis temperature of 320 °C. An order to two orders of magnitude in magnetic signal strength was recorded in the Oxford Clay Fm and the Kimmeridge Clay Fm. This is in agreement with studies of thermally metamorphosed Monterey and Sisquoc

Formation, southern California, where increases in NRM of up to four orders of magnitude (Cisowski and Fuller, 1987).

There was evidence of increase in magnetic grain sizes based on the M_{rs}(Kono and Tanaka, 2007)values with double peaks also observed at 250 °C and 320 °C (Table 3.1). This double peak formation process is consistent with the model proposed by Aubourg *et al.* (2012) where they reported a peak for magnetite formation at about 200 °C to be gradually replaced by pyrrhotite until it is mainly pyrrhotite by about 300 °C. Also supporting the evidence of growth of magnetic grains is the overall increase in coercivities of the heated samples (Table 1). The reason for the observed drop in magnetisation in all the three samples heated at 300 °C might be due to the formation pyrite at this pyrolysis temperature. This is likely to occur under anoxic conditions (Karlin, 1990; Leslie *et al.*, 1990).

Magnetic measurements carried out at 5 K showed larger magnetizations than at room temperature, e.g., for Kimmeridge Clay Fm 250 °C M_{rs} = 9450 μAm^2/kg at 5 K compared with 2510 μAm^2/kg at room temperature. The Blue Lias Fm 320 °C had M_{rs}= 241 μAm^2/kg at 300 K and 336 μAm^2/kg at 5 K, and the Oxford Clay Fm 320 °C had M_{rs} = 21040 μAm^2/kg at 5 K compared to M_{rs} = 5030 μAm^2/kg at room temperature, indicating that the magnetic particles formed are ferromagnetic in nature but superparamagnetic at room temperature, i.e., small ferromagnetic particles are thermally unstable at room temperature and do not contribute to the ferromagnetic signal, but on cooling to 5 K become magnetically stable or 'blocked' and respond ferromagnetically(Nygård *et al.*, 2004). Quantitatively, as a first approximation the blocking volume of magnetite at room temperature is ~ 25 nm, but at 5 K is ~2 nm using data published in the literature (Dunlop, 1973) assuming a measurement time of 60 s. For greigite, under the same assumptions the value changes from ~18 nm at room temperature to ~5 nm at 5 K assuming that the magnetocrystalline anisotropy (-15 kJ/m^{-3} at room temperature) is temperature independent (Winklhofer *et al.*, 2014).

Warming curves plotted to investigate the thermal relaxation of the ferromagnetic particles in zero magnetic fields showed a sharp decrease in magnetization from about ~10-20 K for all the rock samples as they warmed to room-temperature (Fig. 3.10). This indicates that most of the magnetic enhancement is in very small ferromagnetic particles < 10 nm. The FC samples were slightly more magnetized than the ZFC samples (Fig. 3.10b) and the Blue Lias Fm had a much lower magnetic remanence both during the FC and ZFC compared with the Oxford Clay Fm and Kimmeridge Clay Fm (Fig. 3.10c). No phase transitions were observed in the warming

(Fig. 3.10a-c) and the RT-SIRM cooling curves (Fig. 3.10d), probably due to the sizes of magnetic grains present being too small to exhibit low-temperature crystallographic transitions(Dekkers, 1989). TEM investigations showed that the extracted ferromagnetic minerals are very small, less than < 20-30 nm, and occur in clusters overlapping one another. This makes imaging of any single crystal problematic (Fig. 3.11). Complementary EDX analysis revealed strong signals from Fe (Fig. 3.13), thus confirming the presence of elemental constituents needed for the formation of magnetic minerals found within the magnetic extracts.

3.6 Magnetic minerals formed in hydrocarbon-generation conditions

Attempts were made using various techniques in order to identify the magnetic mineral present at various pyrolysis temperatures in our samples. The multicycle thermomagnetic measurements revealed the presence of sulphides in all the samples (Fig. 3.9). The Kimmeridge Clay Fm 250 °C showed slight alterations during the initial thermomagnetic cycles, but a marked increase in moment after the 350 °C cycle suggesting a transformation of the sulphides present to possibly magnetite and/or the growth of pyrrhotite (Fig. 3.9a) (Dekkers, 1990; Nilsson *et al.*, 2013). Similar behaviour was observed in both Kimmeridge Clay Fm 300 °C and Oxford Clay Fm 300 °C (Fig. 3.9c & d). Conversely, Oxford Clay Fm 250 °C showed an initial alteration to a more magnetic phase, then a gradual decline in moment suggesting a partial alteration to pyrite above 350 °C to hematite (Fig. 3.9b) (Dekkers, 1990).

In summary, the continuous thermomagnetic curves indicated the presence of both iron sulphides and magnetite in the samples (Fig. 3.9 insets): The peaks around ~300 °C are likely due to iron sulphide phases, i.e., monoclinic pyrrhotite, the Curie temperature near ~600°Cis indicative of magnetite. On cooling significant volumes of iron sulphide appear to have been generated suggesting the initial material was abundant in a non-magnetic iron sulphide, i.e., pyrite. Kimmeridge and Oxford Clay Fms heated at 320 °C had a curve characteristic of an intergrowth of monoclinic and hexagonal (mixed) pyrrhotite (Figs. 3.9c & f insets) as reported by Schwarz (1975).In addition, the inflection observed in Oxford Clay Fm 320 °C, from around 200 °C of thermomagnetic experiment temperature suggests the presence of greigite(Fig. 3.9f inset) (Roberts *et al.*, 2011).

The absence of any low-temperature crystallographic transition could is likely because the dominant magnetic mineralogy is either hexagonal pyrrhotite and/or greigite, as they are reported not to show low-temperature transitions and are unstable to heating (Roberts *et al.*,

2011); monoclinic pyrrhotite has a transition at ~34 K, the 'Besnus transition' (Roberts *et al.*, 2011). The selection of greigite as a possible source may seem unusual as greigite is thought to be theoretically unstable at temperatures above 50 °C (Aubourg and Pozzi, 2010; Aubourg *et al.*, 2012), but Roberts *et al.* (2011) reported the occurrence of greigite hundreds/thousands of metres deep in sedimentary successions and argued greigite could occur as a stable mineral phase at these depths depending on oxygen fugacity, availability of organic matter and iron. Greigite have also been reported to occur in heating experiments of temperatures in excess of 350 °C when heating is carried out in a reducing atmosphere (Dekkers *et al.*, 2000), or during late-stage diagenesis (e.g., Jiang *et al.*, 2001; Roberts and Weaver, 2005; Sagnotti *et al.*, 2005). Lattice fringes observed in the TEM were consistent with greigite (Fig. 3.11);in addition, first order reversal curves (FORC) revealed the presence of a pseudo-single domain (PSD) behaviour with a peak coercivity around 60 mT, this suggests the presence of an iron sulphide, i.e., pyrrhotite and/or greigite, in Oxford Clay Fm 200 °C (Fig. 3.8a) (Roberts *et al.*, 2000). The distribution of contours from the Kimmeridge Clay Fm 320 °C FORC analysis around the origin is indicative of superparamagnetic (SP) behaviour, although it is difficult to identify the mineralogy.

My findings confirm the theoretical thermodynamic models of Burton *et al.* (1993) who proposed that the formation of magnetic minerals due to burial is strongly influenced by proximity to hydrocarbon generation and accumulation, species of aqueous sulphur (HS^-, H_2S, or SO_4^{2-}) and bicarbonate (HCO_3^-), pH and Eh conditions. Aubourg and Pozzi (2010); Aubourg *et al.* (2012) proposed a conceptual model that tried to explain the chemical remanent magnetization (CRM) acquired during clay burial based on laboratory experiments conducted both at atmospheric pressures and at 1000bar of pressure shielded from Earth's magnetic field with an applied vertical field of 2 mT, at temperatures of 50-250 °C. Kars *et al.* (2012) also made an attempt to fully characterise the magnetic mineralogy, grain size or origin of the CRM carriers in their study and they suggested that the process behind the neo-formed CRM is relatively short in geological timescale. In my experiments, I accelerated natural conditions by increasing the temperature in anoxic conditions to produce crude oil at 320 °C under constant hydration. My experiments differ from those of Aubourg and Pozzi (2010) in ways the chemical environments were controlled, i.e., anoxia and constant hydration.

3.7 Implications

I have established that magnetic minerals are abiotically and inorganically generated in conditions very similar to hydrocarbon generation conditions. In my experiments, I accelerated the rate of reaction: In petroleum systems in general, the oil generation 'window' varies widely depending on the activation energies of organofacies present from ~95-135°C and a gas generation window from ~135-155 °C, with heating rates varying ~0.5-2.0 °C Myr^{-1}(Pepper and Corvi, 1995); whereas in my experiments, I used a linear heating rate of 15 °C/minute which is far greater than what is observed under burial/heating conditions. It is problematic to accurately extrapolate my results to what is observable in geological records, but there is a long track record of using high temperature and pressure reactors to simulate geological reactions on laboratory timescales (Lewan, 1993; Lewan, 1998). The concept relies on the transformation rule in which the rate of chemical reaction is doubled for every 10 ˚C rise in temperature (Lewan, 1993; Lewan, 1998; Pepper and Corvi, 1995; Stainforth, 2009).

The abiotically generated magnetic particles are likely to be on average ≤ 10 nm, and have the potential to migrate along with crude oils since the sizes of pore-throats in sandstones range from 5 – 100 nm (Loucks, 2009; Nelson, 2009). Organic compounds found in crude oil reservoirs range from 4 – 100 nm in size (Loucks, 2009; Nelson, 2009) and assuming magnetic particles formed naturally are of similar sizes to those particles found in this study they could well migrate chelated to porphyrin molecules (through coordinate bonding) along with petroleum. There are reports of the occurrence of metals (e.g., Fe and Ni) in trace amount in crude oils from various regions (Alberdi-Genolet and Tocco, 1999; Duyck *et al.*, 2002; Shirey, 1931) and some studies have tied these chelated metallic constituents to their source rocks using various ratios of Fe, Ni and V. These ratios were reported to be constant from source to crude oil samples analysed (Didyk *et al.*, 1978; Mudiaga, 2011; Sundararaman *et al.*, 1993). It is possible, some of these metals are responsible for the positive magnetic contrast observed over oil fields (e.g., Donovan *et al.*, 1979; Ellrich *et al.*, 1985).

3.8 Conclusions

The research in this chapter has provided a better understanding of the formation of magnetic minerals in the subsurface through simulated burial and 'cooking' in the oil generation 'window'. I have shown that these processes produce significant – orders of magnitude greater – quantities of very small (< 10 nm) ferromagnetic minerals, thought to be greigite, pyrrhotite

and magnetite. It is likely that at least part of the magnetic anomalies observed during aeromagnetic studies of oil fields (e.g., Donovan *et al.*, 1979) or the magnetic minerals found in the studies of soil samples (Costanzo-Alvarez, 2006; Díaz *et al.*, 2000; Hounslow, 1985) are formed via the same burial processes explored in this research, i.e., they formed while petroleum is being generated thereby making it possible to use magnetism as a tool for oil and gas exploration.

Chapter 4

Seismic mapping and interpretation

4.1 Introduction

The Wessex Basin, located in Dorset, southern England (Fig. 4.1) was formed during the Late Permian and evolved throughout subsequent extensional and compressional tectonic events in the Mesozoic and Tertiary (e.g., Butler, 1998; Hawkes *et al.*, 1998; Underhill and Stoneley, 1998). These tectonic events controlled the formation and sedimentary fill of the basin, as summarized in Chapter 2. The Wessex Basin is an established hydrocarbon province with two recognised primary plays; the Triassic Sherwood Sandstone Group and the Jurassic Bridport Sandstone Formation. The Sherwood Sandstone Group lies stratigraphically below the generally accepted source rock in the basin; the Lower Lias mudrocks (Fig. 2.6) (Butler, 1998; Ebukanson and Kinghorn, 1986b; Hawkes *et al.*, 1998). In order to map out potential migration pathways, I focus my mapping and interpretations in this chapter on the potential source rock (Lias Clays) and the two potential reservoir intervals; the Sherwood Sandstone Group and the Bridport Sandstone Fm.

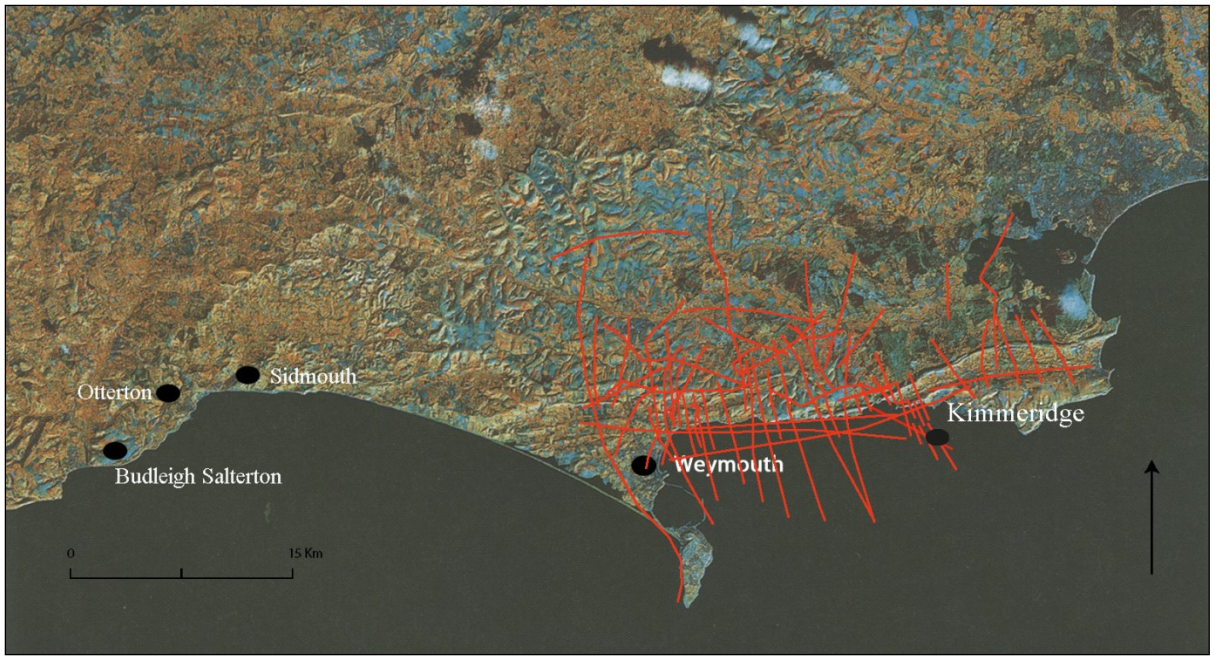


Figure 4.1: Satellite image of Dorset, showing the effects of the Tertiary inversion on the topography of the study area, key localities where source and reservoir rocks are exposed are shown in black dots while 2D seismic lines interpreted in this chapter are shown in red. Modified from Underhill and Stoneley (1998).

4.2 Hydrocarbon Plays

4.2.1 Sherwood Sandstone Group



Figure 4.2: Exposed section of the Sherwood Sandstone Group at Budleigh Salterton in Devon. (SY063817)

The Bridport Sandstone consists of clean, very fine to fine grained shallow marine sands of about ~70 m thick, deposited during the Early Jurassic (Fig. 2.6) (Buchanan, 1998; Underhill and Stoneley, 1998). It forms a diachronous unit and its deposition is structurally controlled in some areas within the Wessex Basin by the pre-existing extensional fault system, with main depocentres located south of the Purbeck Disturbance (Fig. 4.3) (Hawkes *et al.*, 1998; Jenkyns and Senior, 1991).Buchanan (1998) reported good reservoir properties for the Bridport Sandstone in the western part of the basin, where the unit is mainly composed of siliciclastic sediments, whereas in the eastern part of the Purbeck-Isle of Wight Basin (PWB), the unit has a high amount of calcite and mudstones. Overall, the Bridport Sandstone is generally less permeable than the Sherwood Sandstone Group, due to the presence of cemented layers even within the siliciclastic units, which limits the flow of hydrocarbons (Bjorkum and Walderhaug, 1993).

.

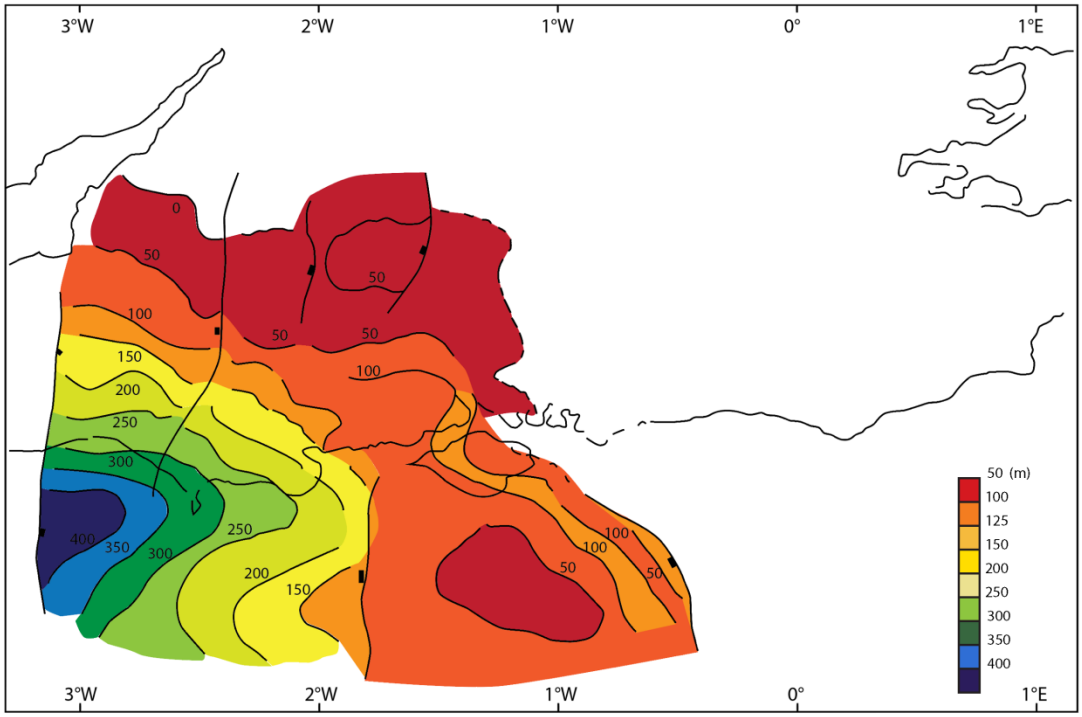


Figure 4.3: Gross isopach map for the Triassic Sherwood Sandstone Group. Modified from (Hawkes *et al.*, 1998).

The Sherwood Sandstone is overlain and sealed by the Murcia Mudstone Group (Fig. 2.6), which is thick unit (100-600+ m) of playa mudstones and evaporites, extensively developed throughout the Wessex Basin and provides an excellent topseal at Wytch Farm (Lott *et al.*, 1982).

4.2.2 Bridport Sandstone



Figure 4.4: Exposed Bridport Sandstone Formation section at West Bay in Dorset (SY463903).

The Bridport Sandstone consists of clean, very fine to fine grained shallow marine sands of about ~70 m thick, deposited during the Early Jurassic (Fig. 2.6) (Buchanan, 1998; Underhill and Stoneley, 1998). It forms a diachronous unit and its deposition is structurally controlled in some areas within the Wessex Basin by the pre-existing extensional fault system, with main depocentres located south of the Purbeck Disturbance (Fig. 4.3) (Hawkes *et al.*, 1998; Jenkyns and Senior, 1991).Buchanan (1998) reported good reservoir properties for the Bridport Sandstone in the western part of the basin, where the unit is mainly composed of siliciclastic sediments, whereas in the eastern part of the Purbeck-Isle of Wight Basin (PWB), the unit has a high amount of calcite and mudstones. Overall, the Bridport Sandstone is generally less permeable than the Sherwood Sandstone Group, due to the presence of cemented layers even within the siliciclastic units, which limits the flow of hydrocarbons (Bjorkum and Walderhaug, 1993).

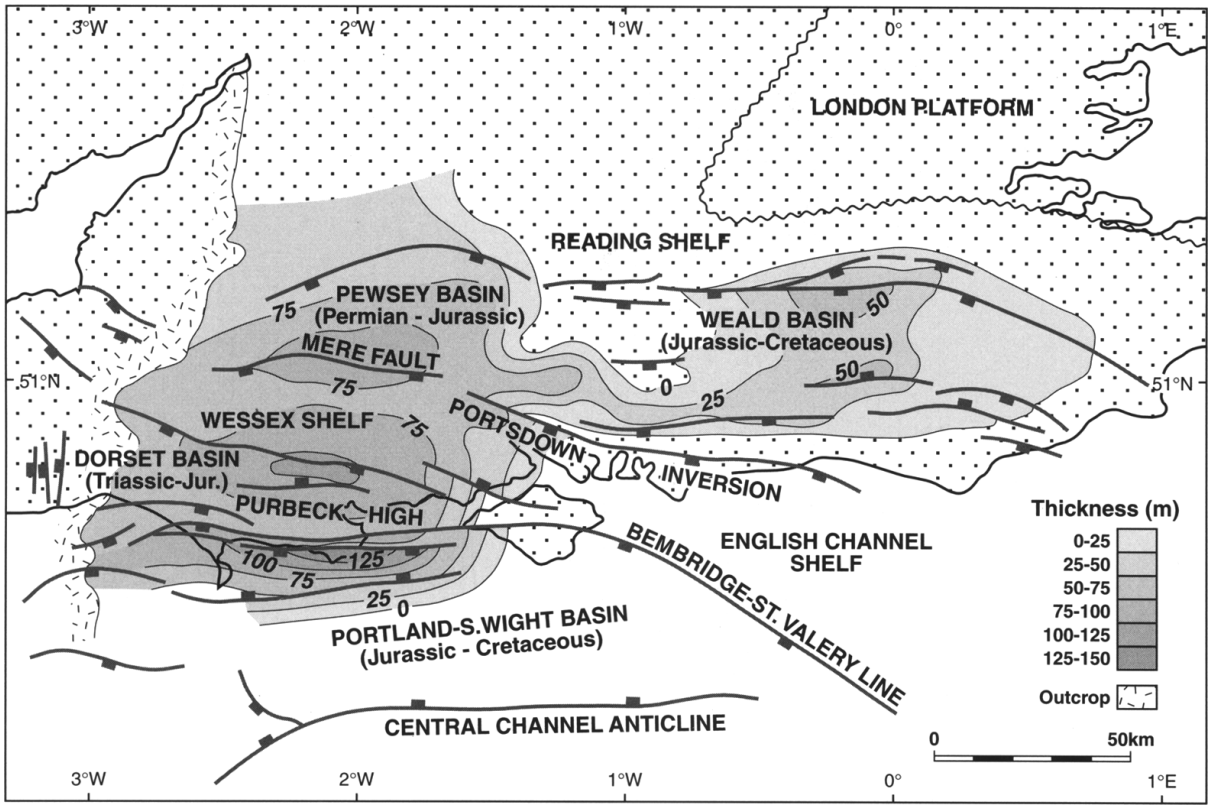


Figure 4.5: Gross isopach map for the Bridport Sandstone showing structural control of deposition by the extensional faults. From Hawkes *et al.* (1998).

The Bridport Sandstone is overlaid by a thin (1-5 m) carbonate bed of Inferior Oolite, which is in turn overlaid by thick (~ 190 m) mudstones of the Fuller's Earth Formation that acts as the top hydrocarbon seal (Buchanan, 1998; Hawkes *et al.*, 1998; Underhill and Stoneley, 1998).

4.2.3 Potential source rocks



Figure 4.6: Liassic – Monmouth Beach, Lyme Regis, Dorset; Oxford Clay Fm Formation– Weymouth Anticline, Dorset (SY703819); Kimmeridge Clay Fm Formation– Kimmeridge Bay, Dorset (SY909790).

There are three potential source rocks for the hydrocarbon generated in the Wessex Basin; the Liassic Mudstone Group, the Oxford Clay Fm Fm and the Kimmeridge Clay Fm Fm, which were deposited in the Lower, the Middle and the Upper Jurassic respectively (Underhill and Stoneley, 1998). In this chapter, I focus on the Liassic mudstone Groups as they are generally thought to be the main source of the hydrocarbon accumulations in the Wessex Basin as reported by many workers (e.g., Cornford *et al.*, 1988; Ebukanson and Kinghorn, 1986b), among others.

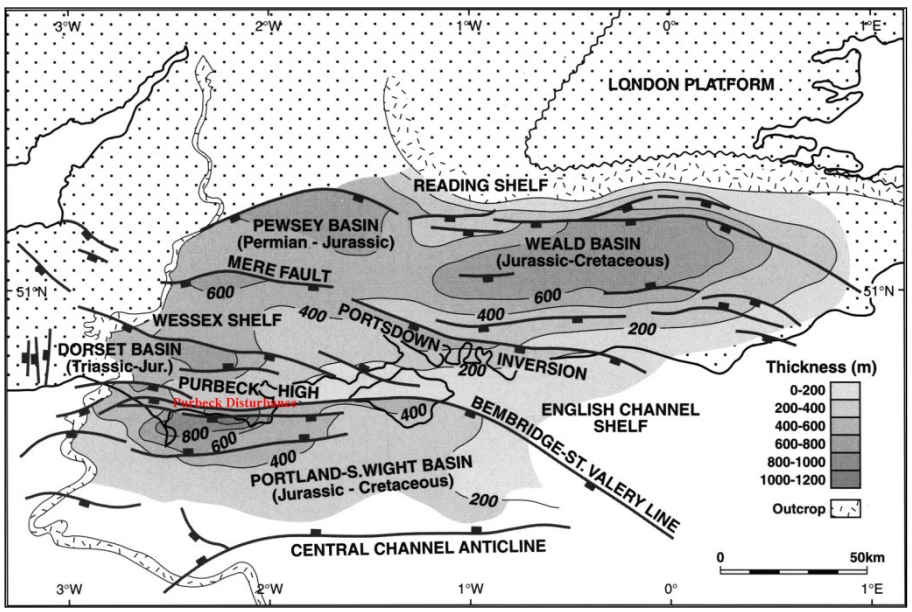


Figure 4.7: Gross isopach map for Early Jurassic Lias Group showing structural control on deposition. Modified from Hawkes *et al.* (1998).

Figure 4.7 shows gross isopach for the Early Jurassic Lias Group with deposition structurally controlled by east-west and northwest-southeast trending extensional faults. The main depocenter in the Wessex Basin is located to the south of the Purbeck Disturbance (Fig. 4.7), where the Lias shales are thought to have been mature and generated most of the oil found in the Wessex Basin (Cornford *et al.*, 1988; Ebukanson and Kinghorn, 1986a; McMahon and Turner, 1998; Penn *et al.*, 1986; Underhill and Stoneley, 1998). In exposures around Lyme Regis (Figs. 4.1 & 4.6), where samples were obtained for this study, the Lias is reported to be around 100 m thick (House, 1989) with estimated total organic carbon (TOC) and hydrogen index (HI) of 8.14% and 569 respectively (Akande, 2012a). The particular outcrop at Lyme Regis is located on the footwall of the main Portland-South Wight Basin fault and consequently is thought not to have achieved sufficient burial to have generated hydrocarbons (McMahon and Turner, 1998).

4.3 Hydrocarbon generation and the Tertiary Inversion

The Late Cretaceous-Tertiary inversion of the pre-existing east-west trending extensional faults has been identified throughout the Wessex Basin (Beeley and Norton, 1998; Bray *et al.*, 1998; Chadwick, 1993; Drummond, 1970; Lake and Karner, 1987; Law, 1998; Lott *et al.*, 1982; McMahon and Turner, 1998; Smith and Hatton, 1998; Stoneley, 1982; Underhill and Paterson, 1998) and there is evidence that suggests the inversion might have started as early as the Campanian (Drummond, 1970; Westhead and Woods, 1994). Plint (1982) reported significant uplift and erosion in the basin during the Eocene, but the most extensive inversion movement is argued to have occurred during the Miocene (Butler and Pullan, 1990; Chadwick, 1993). Furthermore, it is generally thought among workers that maturation and generation of hydrocarbons occurred uniquely on the hanging wall of the Abbotsbury-Ridgeway and the Purbeck-Isle of Wight fault systems during Late Cretaceous maximum burial prior to the Tertiary inversion, event. Hydrocarbons have likely migrated northwards into the footwall, either vertically along fault planes (e.g., Ebukanson and Kinghorn, 1986a; Penn *et al.*, 1986; Underhill and Stoneley, 1998) or laterally across the fault plane where sand-sand juxtaposition occurred. However, others believe there was at least some maturation of the Lias mudstones at Wytch Farm, even though that might not have resulted in any significant generation of hydrocarbons (Bray *et al.*, 1998; McMahon and Turner, 1998; Stoneley and Selley, 1986).

The generation of hydrocarbons in the Wessex and other adjacent basins in southern England was frozen by inversion events that took place at various intervals (chapter 2). Figure 4.5 shows areas affected by the uplift in the Wessex Basin. It can clearly be seen that the main axis of the inversion lies south of the Purbeck disturbance, in the Portland-South Wight Basin but the inversion was not restricted to this area. Localised and even major inversion axes are visible north of the Abbotsbury Ridgeway Fault and the Purbeck Disturbance. Similarly, Smith and Hatton (1998) conducted gravity and aeromagnetic studies of the basin in order to investigate the extensive effects of the inversion. A residual Bouguer gravity map reveals areas along both the Abbotsbury Ridgeway and the Purbeck Disturbance which show positive anomalies, suggesting denser, more compacted materials have been uplifted to shallower depths (Fig. 4.9).

In order to estimate the amount of shortening and uplift caused by the inversion, several theories have been proposed. Butler (1998), based on interval velocity mapping suggested there was about 900 m of shortening across the Portland – South Wight Trough (Fig. 4.8) due to compression and up to 1300 m of reverse displacement along the Purbeck – Isle of Wight Disturbance (Fig. 4.8). However, Sibson (1995) argued such reverse movements along listric faults could encounter significant frictional resistance and that footwall short-cut thrusts will develop. These short-cut thrusts were reported around the Kimmeridge area (Hawkes *et al.*, 1998), but, Butler (1998) argued that that frictional resistance could be have been overcome by a strike-slip component of the inversion. In additional, Law (1998) using sonic velocities estimated about 1200 m of missing section at Kimmeridge 5. Similarly, Beeley and Norton (1998), using seismic velocity forward models argued for about 1500 m of missing section for the along the Central Channel Anticline.

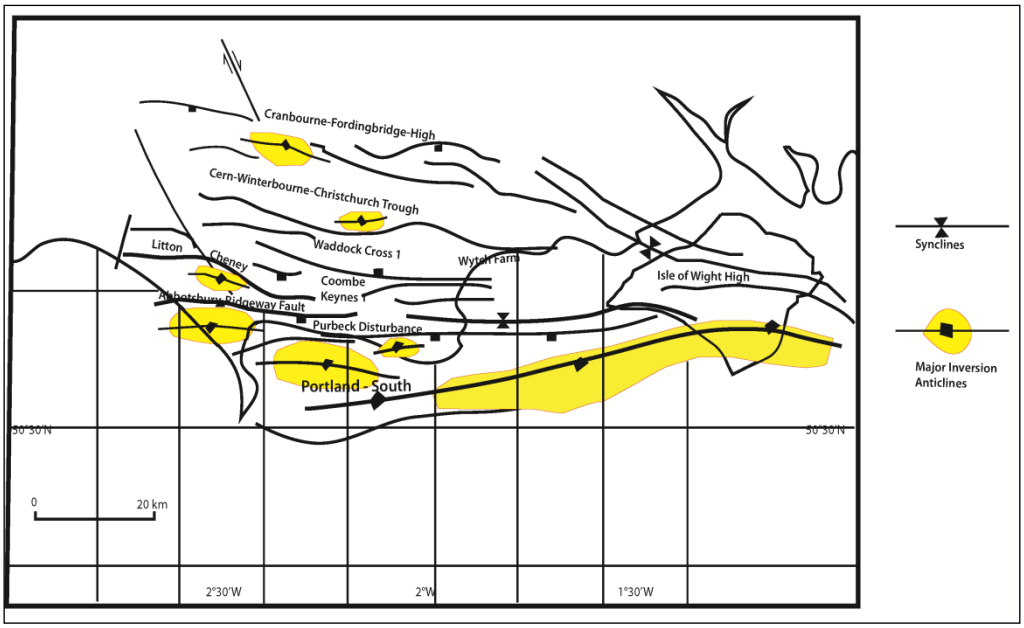


Figure 4.8: Map showing the Tertiary inversion elements in the Wessex Basin. Modified from Butler (1998).

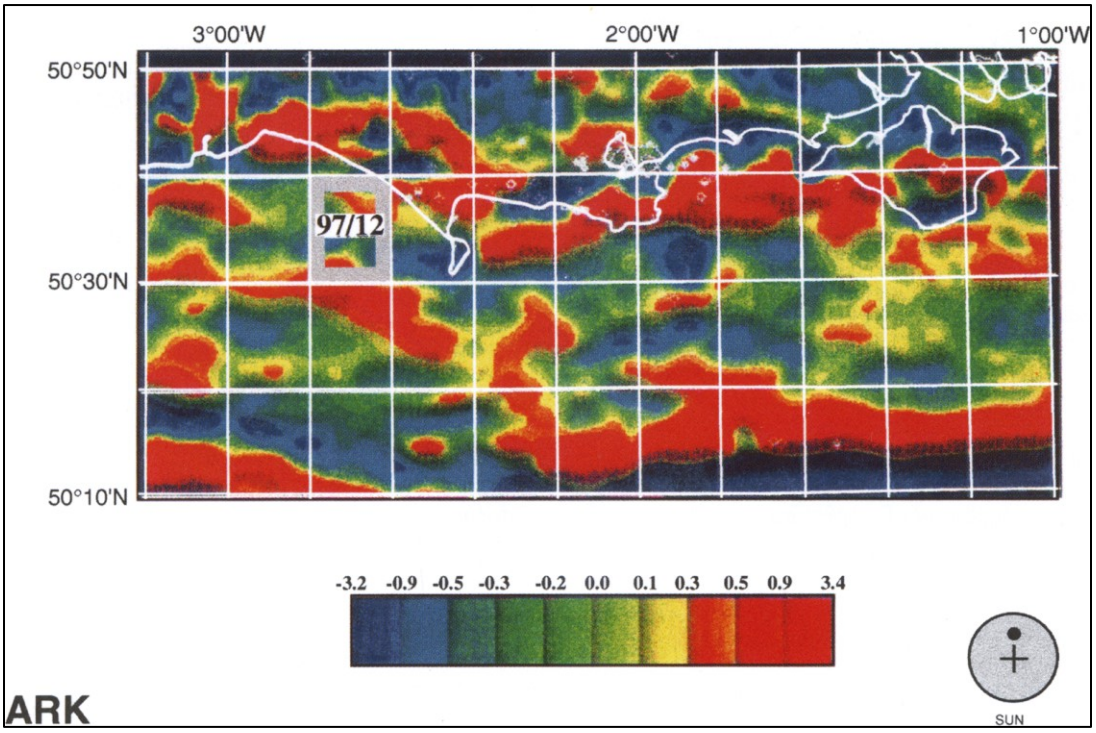


Figure 4.9: Residual Bouguer gravity map showing the Wessex Basin and the English Channel. From Smith and Hatton (1998).

Conversely, Bray *et al.* (1998) carried out burial reconstruction models using apatite fission track analysis (AFTA) and vitrinite reflectance data from the basin and estimated 2-3 km of missing section around the Kimmeridge area and 2.3 km in areas around Wytch Farm. They argued the Lias mudstones entered the oil generation window briefly at Wytch Farm during the

Late Jurassic/Early Cretaceous but never generated any significant amount of oil before cooling due to uplift (Fig. 4.10). However, the AFTA values for uplift at Wytch Farm are not consistent with vitrinite reflectance data and velocity analysis reported by Law 1998. Recent burial history reconstructions carried out at Imperial College using PetroMod^{TM} incorporating well data and Rock Eval data on a selection of wells from the Wessex by Brau (2015, unpublished) showed Wytch Farm K1-25 did not enter the oil window at any time (Fig. 4.11). This significantly, is in agreement with Law's estimates and it is argued that the main body of evidence indicates that the Lias source rocks at Wytch Farm never entered the oil window and that the billion barrels plus of hydrocarbons present in the field have to have been sourced from the mature kitchen some 10 km to the south (see Kimmeridge 5 burial model; Fig. 4.11).

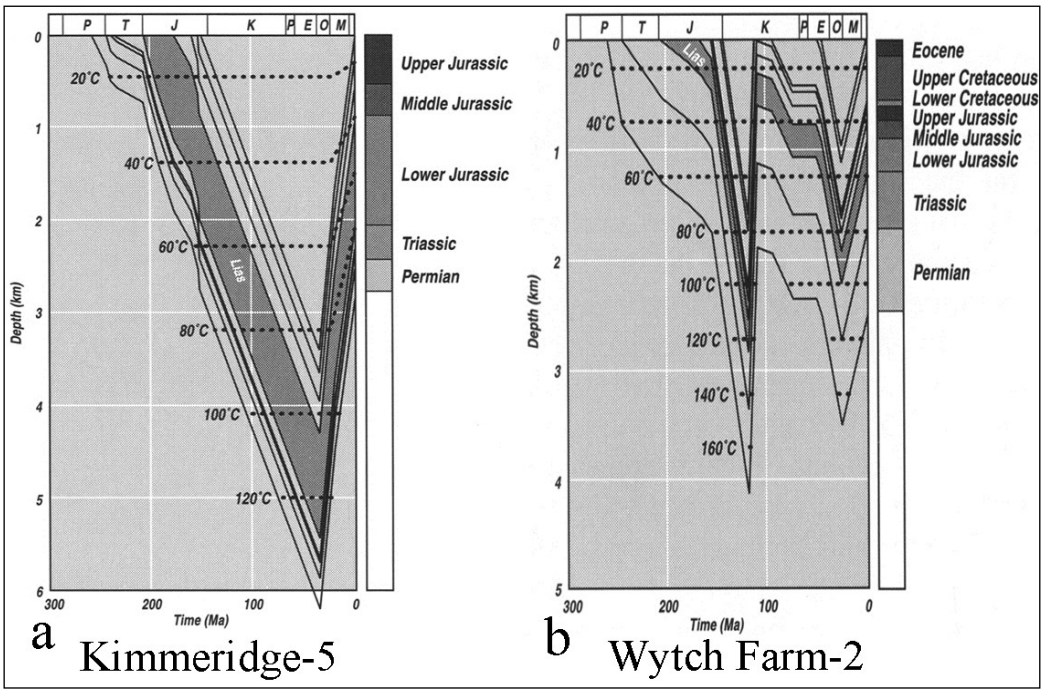


Figure 4.10: Burial reconstruction showing a) Kimmeridge 5 with the Lias entering the oil generation window during the Early Cretaceous before uplift in Oligocene, b) Wytch Farm-2 showing the Lias briefly entering the oil window in Mid. Jurassic before uplift in the Late Jurassic. From Bray *et al.* (1998)

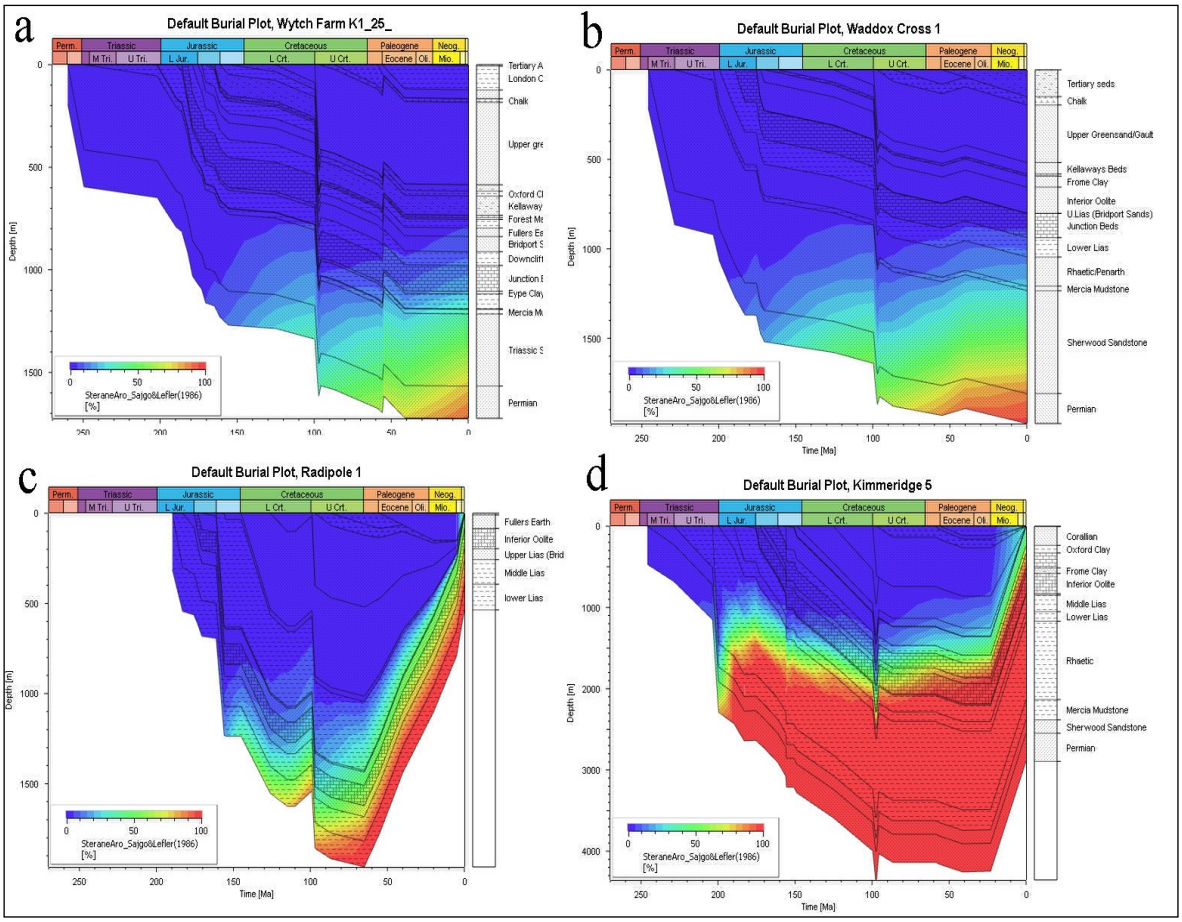


Figure 4.11: Burial reconstruction showing a) Wytch Farm K1-25 with the Lias immature, b) Waddock Cross-1 with the Lias Immature, c) Radipole-1 showing the Lias entering the oil window during mid. Cretaceous, and d) Kimmeridge 5 showing the Lias entering the oil window in the Early Cretaceous. From Brau, 2015.

4.4 Model

The main aim of this chapter is to produce an uplift and erosion map that will resolve the debate regarding hydrocarbon migration in the Wessex Basin. To achieve that, present day maps of top Chalk, Inferior Oolite and White Lias (Rheatic) and the base of the Wealden Group were mapped from 63, 2D seismic lines. These data were obtained from the UK Onshore Geophysical Library (UKOGL) through Lynx Geophysical. The data were mapped using Petrel 2013^{TM} software. Depth conversion and decompaction of these surfaces were also carried out using the Move 2015 ^{TM} software. Furthermore, geometrical restoration was carried out on a series of key selected sections (Table 4.2). Table 4.1 shows the 2D seismic lines used in this study.

Table 4.1: List of 2D seismic lines used to produce surfaces during this study.

Line	Record length (s)	Area	Date	Type	Length (km)	Polarity
AUK-94-AJ051	4	English Channel	1994	Mute & Stack	6.71	SEG
AUK-94-AJ052	4	English Channel	1994	Mute & Stack	13.44	SEG
AUK-94-AJ053	4	English Channel	1994	Mute & Stack	13.73	SEG
AUK-94-AJ054	4	English Channel	1994	Mute & Stack	11.7	SEG
AUK-94-AJ055	4	English Channel	1994	Mute & Stack	5.91	SEG
AUK-94-AJ056	4	English Channel	1994	Mute & Stack	10.13	SEG
AUK-94-AJ057	4	English Channel	1994	Mute & Stack	11.43	SEG
AUK-94-AJ059	4	English Channel	1994	Mute & Stack	10.38	SEG
AUK-94-AJ060	4	English Channel	1994	Mute & Stack	4.28	SEG
AUK-94-AJ061	4	English Channel	1994	Mute & Stack	5.82	SEG
AUK-94-AJ062	4	English Channel	1994	Mute & Stack	10.57	SEG
AUK-94-AJ063	4	English Channel	1994	Mute & Stack	17.94	SEG
AUK-94-AJ064	4	English Channel	1994	Mute & Stack	24.43	SEG
AUK-94-AJ066	4	English Channel	1994	Mute & Stack	23.64	SEG
AUK-94-AJ067	4	English Channel	1994	Mute & Stack	21.27	SEG
GC86-V30	3	Wareham, Dorset	1986	Migrated Stack	6.07	90 degree in advance of SEG
GC86-V33	3	Wareham, Dorset	1986	Migrated Stack	9.59	90 degree in advance of SEG
GC86-V34	3	Wareham, Dorset	1986	Migrated Stack	10.35	90 degree in advance of SEG
GC86-V36	3	Wareham, Dorset	1986	Migrated Stack	3.15	90 degree in advance of SEG
B90-32	3	Dorset	1990	Migrated Stack	11.82	SEGD
B90-33	3	Dorset	1990	Migrated Stack	14.52	SEGD
B90-37	3	Dorset	1990	Migrated Stack	14.16	SEGD
B92-38	3	SW Dorset	1991	Migrated Stack	5.28	SEGD
B92-39	3	SW Dorset	1991	Migrated Stack	8.24	SEGD
B92-40	3	SW Dorset	1991	Stack	24.83	SEGD
B92-41	3	SW Dorset	1991	Migrated Stack	8.08	SEGD
B92-42	3	SW Dorset	1991	Migrated Stack	5.71	SEGD
B92-43	3	SW Dorset	1991	Migrated Stack	13.51	SEGD
B92-44	3	SW Dorset	1991	Stack	14.79	SEGD
B92-54	3	SW Dorset	1991	Stack	7.95	SEGD
B92-55	3	SW Dorset	1991	Stack	8.44	SEGD
B92-56	3	SW Dorset	1991	Stack	14.83	SEGD
BV-00-01	3	Dorset	2000	Migrated	5.64	EXABYTE
BV-00-02	3	Dorset	2000	Migrated	4.44	EXABYTE
BV-00-03	3	Dorset	2001	Migrated	2.33	EXABYTE
BV-00-04	3	Dorset	2002	Migrated	3.71	EXABYTE
GC84-V181	2	Dorset	1984	Migrated Stack	8.99	SEGB
GC86-V27	3	Wareham, Dorset	1986	Migrated Stack	6.94	SEGB
GC86-V28	3	Wareham, Dorset	1986	Migrated Stack	5.67	SEGB
BP-82-80	3	Kimmeridge	1982	Migrated Stack	2.8	SEGB
BP-82-81	3	Kimmeridge	1982	Migrated Stack	3.38	SEGB
BP-82-82	3	Kimmeridge	1982	Migrated Stack	3.2	SEGB
BP-82-83	3	Kimmeridge	1982	Migrated Stack	3.67	SEGB
BP-83-056	5	Kimmeridge Bay	1983	Migrated Stack	2.01	SEGB
BP-83-058	5	Kimmeridge Bay	1983	Migrated Stack	2.14	SEGB
BP-83-058L	5	Kimmeridge Bay	1983	Migrated Stack	2.84	SEGB
BP-83-060	5	Kimmeridge Bay	1984	Migrated Stack	2.1	SEGB
BP-83-060L	5	Kimmeridge Bay	1985	Migrated Stack	2.64	SEGB
BP-83-062L	5	Kimmeridge Bay	1986	Migrated Stack	2.94	SEGB
BP85-02	3	Dorset	1988	Migrated	5.9	White trough
BP85-30	3	Dorset	1988	Migrated	7.16	White trough
BP-85-152	3	Bincombe	1986	Stack	5.99	SEGB
BP-85-153	4	Bincombe	1987	Stack	5.56	SEGB
BP91-201	3	Isle of Purbeck	1991	Stack	12.48	SEGD
BP91-202	3	Isle of Purbeck	1991	Stack	4.29	SEGD
BP91-203	3	Isle of Purbeck	1991	Stack	5.19	SEGD
BP91-204	3	Isle of Purbeck	1991	Stack	5.29	SEGD
BP91-205	3	Isle of Purbeck	1991	Stack	5.87	SEGD
BP91-206	3	Isle of Purbeck	1991	Stack	5.26	SEGD
BP91-207	3	Isle of Purbeck	1991	Stack	6.46	SEGD

The interpretation of the 2D seismic lines was carried out using well data and depth-TWT time pairs obtained from the UKOGL database. Figure 4.12 is a depth-TWT time-pairsplot for the Inferior Oolite, indicating a very strong linear correlation between depth and sonic velocity through the beds. In addition, depth converted and decompacted Inferior Oolite and White Lias present day surfaces were also generated. In addition, Figure 4.13 shows the interpretation of seismic line B92-40; all other sections were interpreted in the same way. Present day to top Inferior Oolite and White Lias surfaces were generated in the time domain and were converted

to depth using calibrated time/depth pairs from over a hundred wells obtained from the UKOGL website. Figures 4.14 and 4.15 show the different processes involved in generating depth converted and decompacted surfaces for seismic sections B90-32 and B90-37 respectively, with my study area decompacted prior to the Albian-Aptian erosional event. There were noticeable variations in thicknesses after the decompaction over some of the section, e.g., on line B90-32 there was an average increase in thickness of about 150 m from top Chalk to top Inferior Oolite after the decompaction, with similar increases in thickness observed from top Inferior Oolite to top White Lias (Fig. 4.14). In contrast however, a 100 m increase in thickness was observed on line B90-37 after decompaction in layers between top Chalk and top Inferior Oolite, while there was no observable increase in thickness in layers between top of Oolite and top of White Lias (Fig. 4.15). Similar decompaction processes were carried out on all seismic data in Table 4.1.

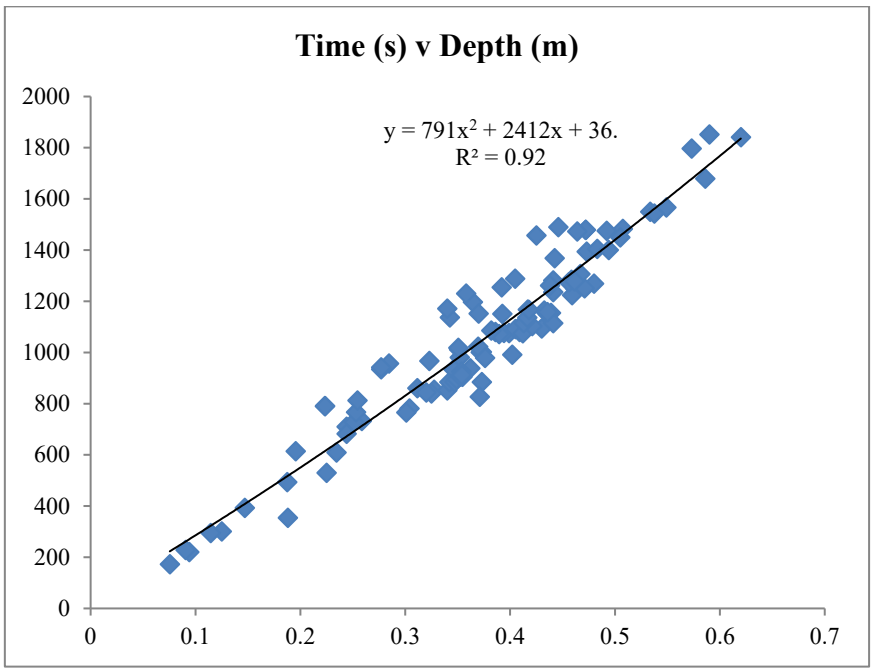


Figure 4.12: A multi-well one-way time (s) vs depth (m) showing a very strong correlation between the two.

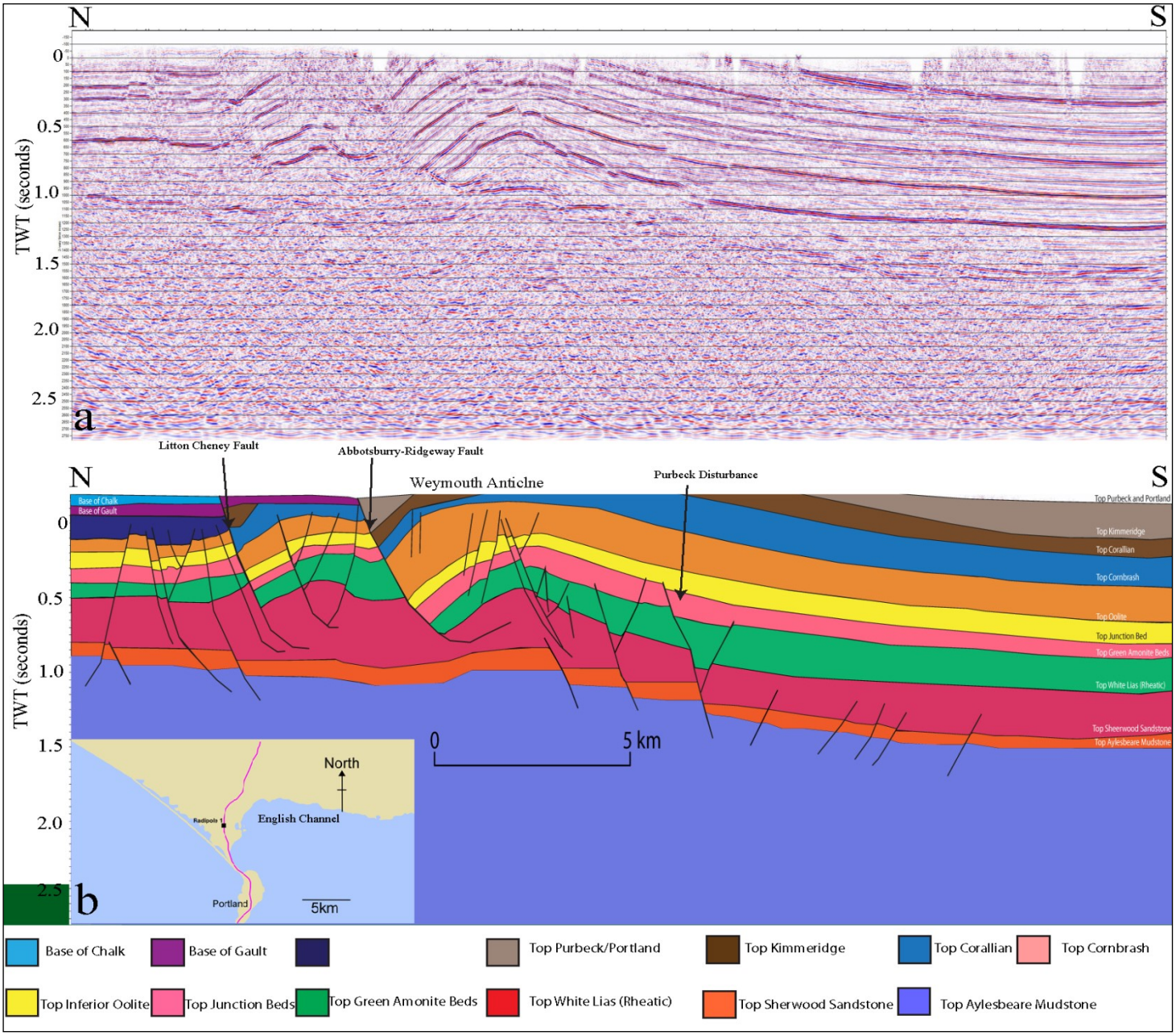


Figure 4.13: a) an image of seismic section B92-40, b) Interpretation of seismic section B92-40 showing tops of some of the geological formations identified and also the distribution and geometry of faults in the study area.

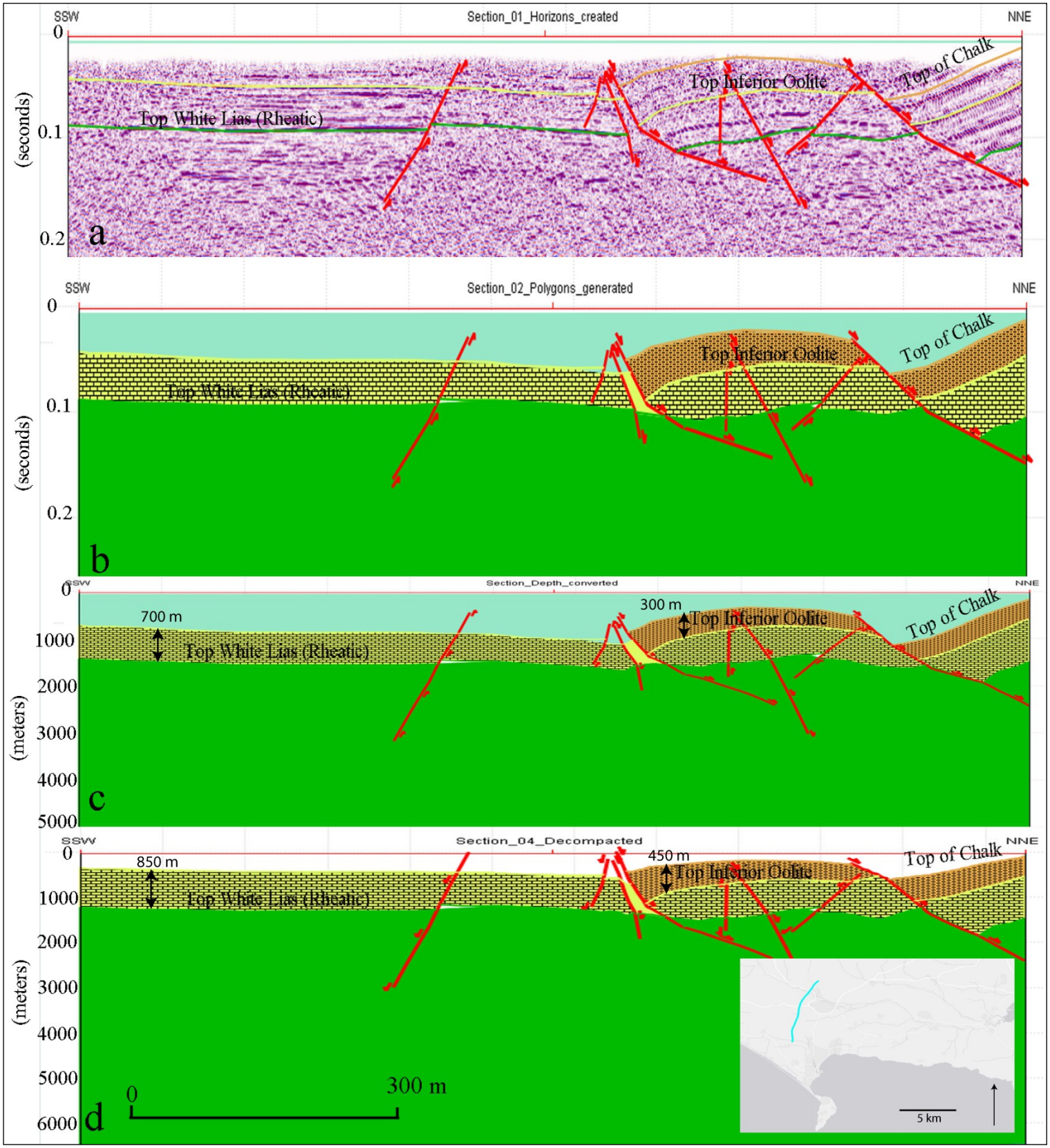


Figure 4.14: Seismic section B90-32 showing: a) Image of seismic section with faults and tops identified, b) Polygons generated using stratigraphic rock properties data, c) Depth converted and d) Decompacted section, note: an average of 150m increase in thickness.

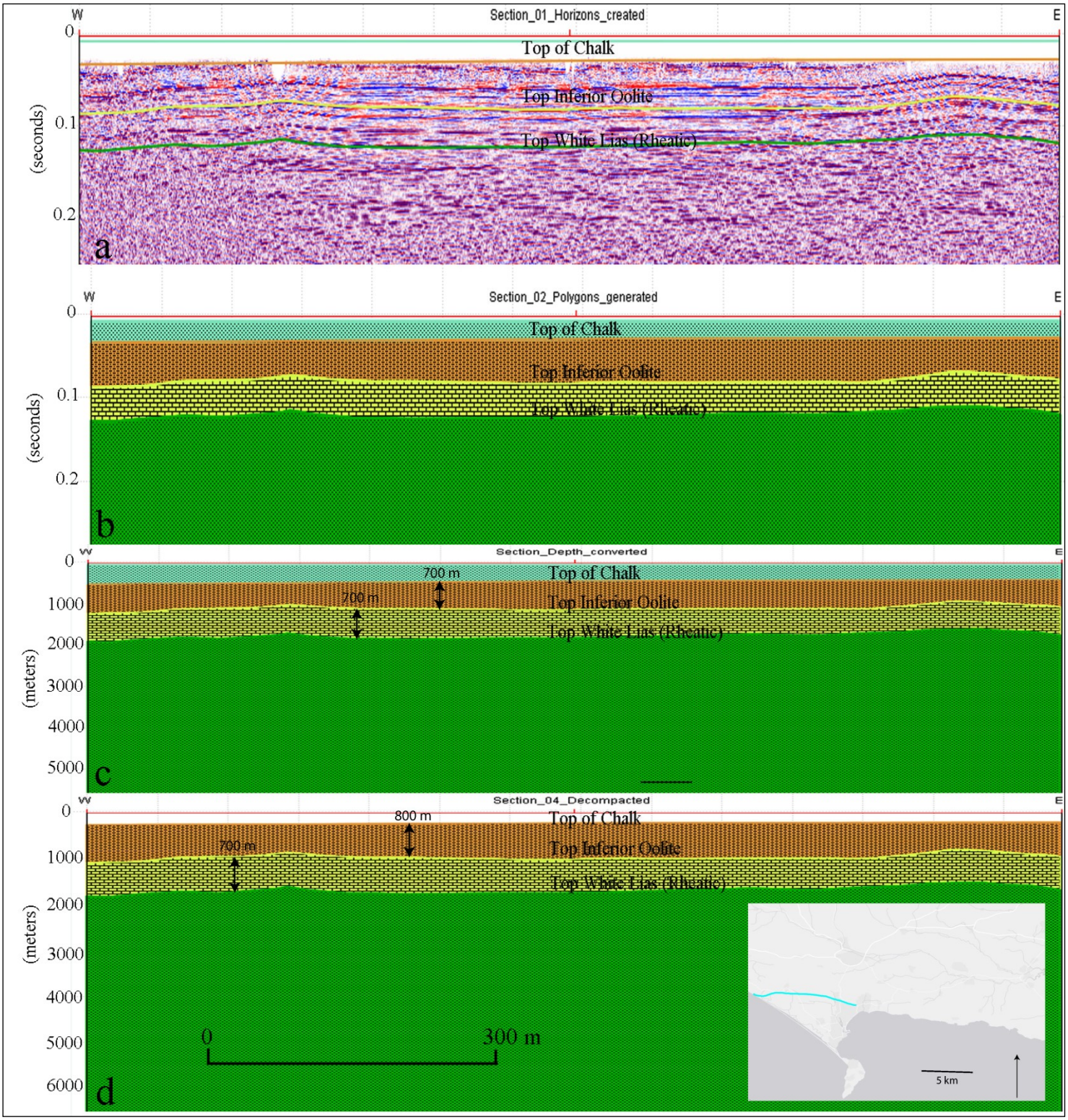


Figure 4.15: Seismic section B90-37 showing: a) Image of seismic section with tops identified, b) Polygons generated using stratigraphic rock properties data, c) Depth converted and d) Decompacted section.

In order to generate depth converted, decompacted surfaces, stratigraphic data, such as rock type, age and thickness were sourced from UKOGL well data base as well as from literature(Chadwick *et al.*, 2005). Similarly, for rock properties such as composition, porosity, velocity, grain size, and density, well logs (raster) were acquired from IHS Global for nine wells (Chapter 5) and the velocity was calculated from well tops data. During the decompaction process, all Tertiary to Recent sediments were removed (Figs. 4.11d and 4.12d) and horizons imported and appended in Petrel^{TM}.

Geometrical restoration was carried out on a selection of 2D seismic sections. Figure 4.14 is a composite south-north seismic section running from the offshore Portland–South Wight Basin to Wytch Farm and shows how the geometrical restoration was carried out. The missing sections were estimated from seismic lines B92-40 (Fig. 4.16) and a composite of BP-83-060L and 80-268, which passes through the Kimmeridge area.

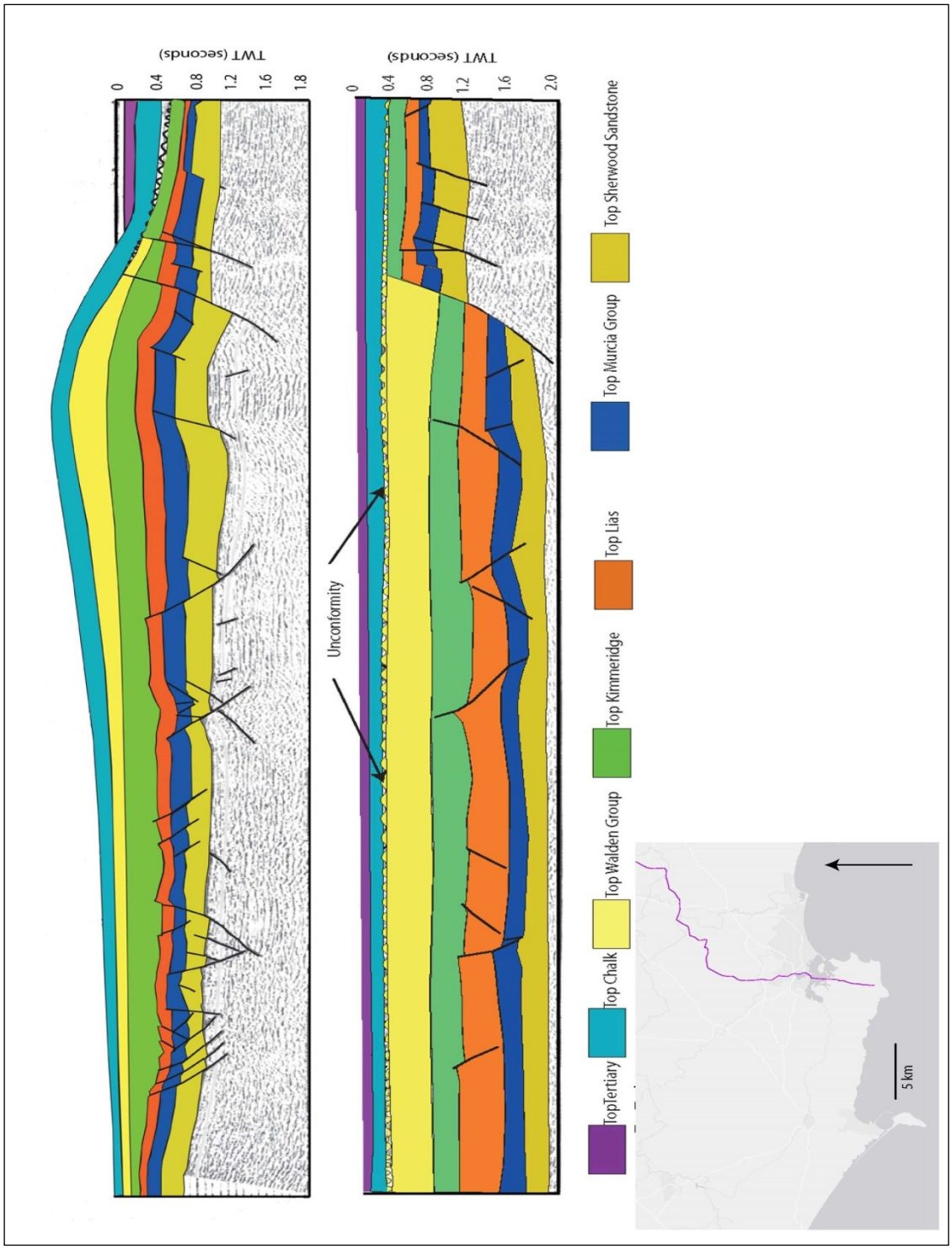


Figure 4.16: a) a composite section running from the offshore Portland –South Wight Basin to the Wytch Farm area showing the structures and the stratigraphy, b) a geometrically restored section with hanging wall restored prior toTertiary inversion.

The sections used to generate restored surfaces on the hanging walls of the Abbotsbury Ridgeway and the Purbeck-Isle of Wight faults are shown in Table 4.2, a total of 15 sections were used.

Table 4.2: A selection of 2D seismic sections used to generate geometrically restored surfaces

Line	Record length (s)	Area	Date	Type	Length (km)	Polarity
AUK-94-AJ052	4	English Channel	1994	Mute & Stack	13.44	SEG
AUK-94-AJ053	4	English Channel	1994	Mute & Stack	13.73	SEG
AUK-94-AJ054	4	English Channel	1994	Mute & Stack	11.7	SEG
AUK-94-AJ057	4	English Channel	1994	Mute & Stack	11.43	SEG
AUK-94-AJ059	4	English Channel	1994	Mute & Stack	10.38	SEG
B92-40	3	SW Dorset	1991	Stack	24.83	SEGD
BP-82-80	3	Kimmeridge	1982	Migrated Stack	2.8	SEGB
BP-82-81	3	Kimmeridge	1982	Migrated Stack	3.38	SEGB
BP-82-83	3	Kimmeridge	1982	Migrated Stack	3.67	SEGB
BP-83-060	5	Kimmeridge Bay	1984	Migrated Stack	2.1	SEGB
BP-83-060L	5	Kimmeridge Bay	1985	Migrated Stack	2.64	SEGB
BP85-30	3	Dorset	1988	Migrated	7.16	
BP91-202	3	Isle of Purbeck	1991	Stack	4.29	SEGD
BP91-203	3	Isle of Purbeck	1991	Stack	5.19	SEGD
BP91-204	3	Isle of Purbeck	1991	Stack	5.29	SEGD

Figure 4.17 shows a composite map, called the upheaval map, which consist of present day Inferior Oolite surface on the footwall of the Abbotsbury-Ridgeway and Purbeck faults, with the restored Inferior Oolite in the hanging wall superimposed on it (inset). The red arrows indicate potential hydrocarbon migration areas, i.e., Bridport Sandstone Fm– Bridport Sandstone Fm, from the hanging wall into the footwall. Similarly, upheaval map for the White Lias with restored Inferior Oolite superimposed on it is shown in Figure 4.18. Figure 4.18 is used to approximate the juxtaposition between Bridport Sandstone Fmin the hanging wall and Sherwood Sandstone Group on the footwall. Mapping Sherwood Sandstone Group directly was difficult due to very low amplitude resolution in most of the sections used in this study with depth. Instead, the top White Lias (Rhaetic/Penarth Group) was mapped and depths of 300-400 m was used to approximate depths to top Sherwood, based on well data from the Wytch Farm area. The red arrows in Figure 4.18 also indicate potential migration pathways around Kimmeridge-Creech, across the Purbeck-Isle of Wight Fault and Radipole.

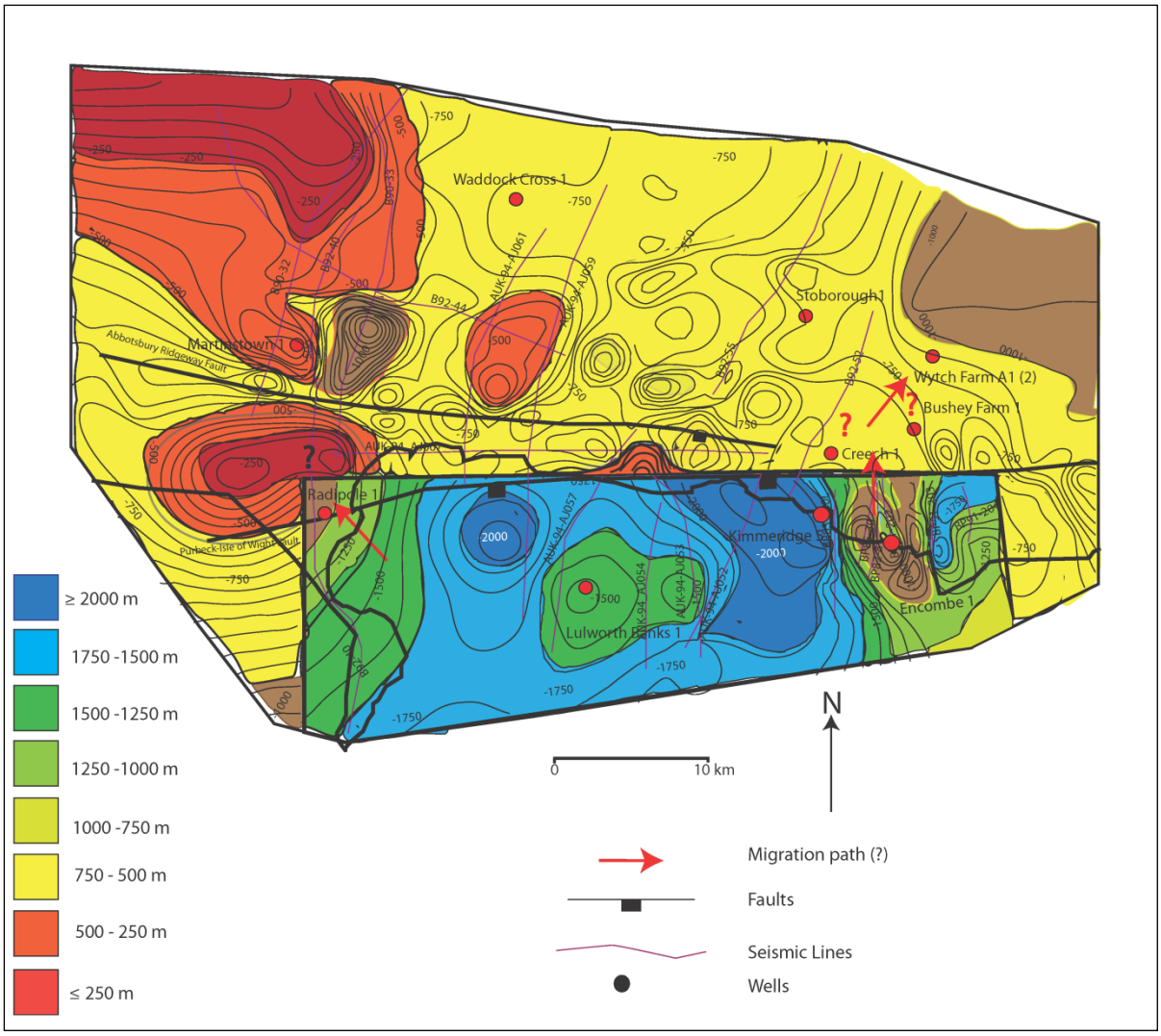


Figure 4.17: Upheaval map, consisting of present day Inferior Oolite surface on the footwall of the Abbotsbury-Ridgeway and Purbeck faults, with the restored Inferior Oolite in the hanging wall superimposed on in the lower section, showing potential migration routes.

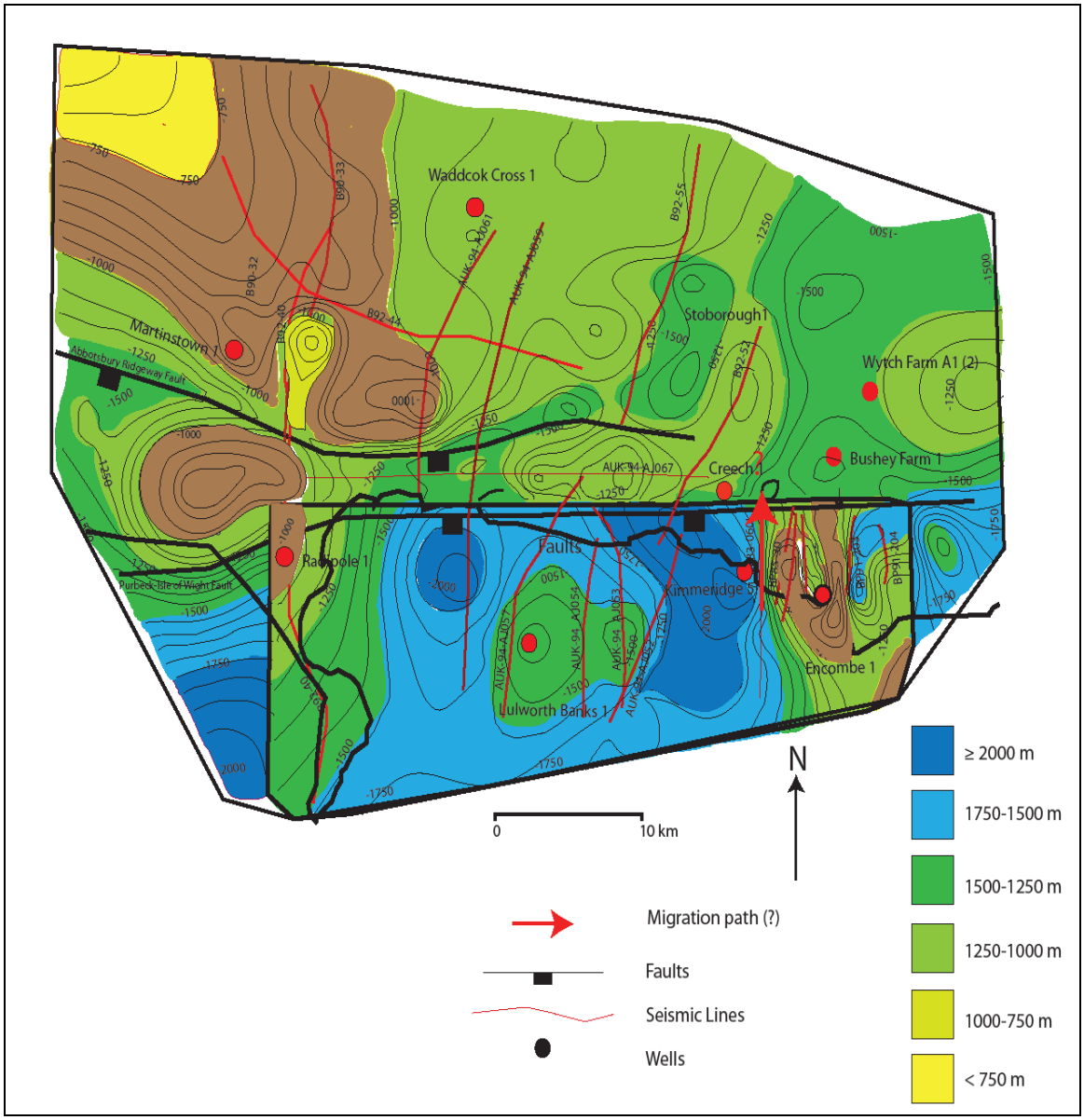


Figure 4.18: Upheaval map, consisting of present day Sherwood Group Surface (White Lias +300 m) surface on the footwall of the Abbotsbury-Ridgeway and Purbeck faults, with the restored Inferior Oolite in the hanging wall superimposed on it , showing potential migration route from Bridport Sandstone to Sherwood Sandstone via Creech.

4.5 Discussion

One of the key unresolved questions regarding the petroleum system of the Wessex Basin has been the apparent anomaly of over one billion barrels in place in the Sherwood Sandstone reservoir at Wytch Farm. A field that sits on the footwall of the Purbeck fault in an area that has been shown by geochemical and basin modeling data and studies to be too immature for oil generation in the Liassic source interval. Not only has the oil migrated laterally some ten kilometres it has also migrated stratigraphically downwards through over of 300 meters of Mercia Mudstone into the Sherwood Sandstone Group reservoir. The problem is compounded

by the reorganisation of the basin during Tertiary inversion and the lack of published maps that show the hanging wall and footwall cut-offs of the main carrier and reservoir horizons (e.g. Bridport & Sherwood sandstones)

I have restored the basin to its geometry during Late Cretaceous maximum burial by plotting the restored hanging wall of the Portland-South Wight and Abbotsbury-Ridgeway faults against the present day structure on the footwall. Clearly this is a simplification of the footwall geometry at the time of Late Cretaceous maximum burial as there has been some tilting of the basin up to the west during the Tertiary (e.g., Butler, 1998; Hawkes *et al.*, 1998). This tilt is best observed by spill of roughly two-thirds of the Wytch Farm field in a westerly direction during the Tertiary. This introduces a degree of uncertainty into the interpretation of footwall migration paths. Figure 4.17 shows a possible migration path for Wytch Farm oil within the Bridport Sandstone. Assuming the oil was generated at deep areas around Kimmeridge within the Portland – South Wight Basin, it could easily find its way to Wytch Farm via the Creech conduit, rather than through Bushey Farm (Fig. 4.17). The latter might seem the more obvious route, but I will present evidence in the next chapter, from magnetic and geochemical studies on core to suggest the Creech route to be more likely. The oil seeps encountered at Osmington Mills could easily reach the surface along the Purbeck Fault, as earlier proposed by Colter and Havard (1981). Similarly, oil found at Chickerell could have migrated up dip from the kitchen, via the Radipole conduit (Fig. 4.17).

Figure 4.18 shows the Bridport sandstone on the hanging wall, juxtaposed with Sherwood sandstone on the footwall providing a direct sand/sand hydrocarbon conduit. In areas around Kimmeridge, the restored Bridport Sandstone is about 1750-2000 m deep and the Sherwood across the fault around Creech is about 1500-1900 m deep. I argue that this point has the potential to serve as a migration path for the Sherwood oil found at Wytch Farm. Migration of oil along what is almost certainly a sealing fault (Underhill and Stoneley, 1998), is not required in this new model.

4.5.1 Assumptions and sensitivity of the model

Some assumptions were made in the model during depth conversions and decompactions (Figs. 4.14 and 4.15): it was assumed that the rock properties in the modelled formations (Inferior Oolite and White Lias) both in the footwall and the hanging wall, were uniform. A single average sonic velocity was also used based on calculated hanging wall sonic velocities (from various well data). In addition, rock property values (such as density and composition) were

calculated by the Move 2015 ™ software based on rock composition and depth data input (Section 4.4).

Similarly, assumptions were made during the geometrical restoration (Fig. 4.16) by simplifying the geometry of the faults in both the hanging and the footwall of the Abbotsbury-Ridgeway and Purbeck faults (Fig. 4.13). Tertiary Inversion uplift was estimated from missing sections of seismic lines B92-40 and a composite BP-83-060L and 80-268 (Table 4.2). Based on a published data (Beeley and Norton, 1998; Butler, 1998; Law, 1998), a maximum uplift of about 1500 m was assumed.

However, assumptions made in this Chapter will only drastically affect the model if the Tertiary Inversion is assumed to be less 800m in the hanging wall of the Abbotsbury-Ridgeway and Purbeck faults or the Tertiary Inversion has adversely affected the footwall of the Abbotsbury-Ridgeway and Purbeck faults. The former will lead to a model with little generated oil, probably not enough to migrate and accumulate in the footwalls of the Abbotsbury-Ridgeway and Purbeck faults, while the later will result in a model in which the oil found in Wytch Farm could probably have been generated at Wytch Farm. These two scenarios are unlikely and deviate from most of the published data from Wessex Basin (Hawkes *et al.*, 1998).

4.6 Conclusions

The constructed surface top of the White Lias and the upheaval maps for both the Bridport and the Sherwood reservoir/carrier beds (Figs. 4.17 and 4.18) provide insight into potential migration pathways for oils found in areas on the footwalls of both the Abbotsbury Ridgeway and the Purbeck-Isle of Wight Faults by indicating potential areas of sand/sand juxtaposition. Crude oil found within the Bridport Sandstone at Wytch Farm probably migrated through the Creech conduit, but less likely through Bushey Farm. Similarly, the most suitable position to juxtapose Bridport and Sherwood Sandstones is at Creech based on my mapping and analyses.

Questions still remain regarding the origins of the oils found at Chickerell, Martinstown and Waddock Cross. Perhaps a problem that will not be solved until the oil industry acquires blanket 3D seismic data across the region that will allow a more detailed set of migration maps to be generated.

Chapter 5

Hydrocarbon occurrence in the Wessex Basin and magnetic properties

5.1 Introduction

There have been reported cases of increased magnetic susceptibility (χ) within the vicinity of hydrocarbon accumulations due to the presence of framboidal iron oxides and sulphides (e.g., Emmerton *et al.*, 2013; Foote, 1986, 1992). An overview of this process has been discussed in Chapter 1. Magnetic measurements are not routinely carried out in the petroleum industry either on core samples or during downhole wireline logging. In the few cases where magnetic susceptibility measurements were performed, it was not to identify hydrocarbon bearing horizons but to delineate geologic horizons due to variations in magnetic mineral contents (Hounslow, 1985, 1987; Potter, 2008; Pozzi *et al.*, 1993) and/or to correlate between geological facies (Koptíková *et al.*, 2010).

In this chapter, an attempt has been made to map out the migration pathways of hydrocarbons in the Wessex Basin using magnetic and geochemical rock properties. For the purpose of this study, a total of 45 core samples were obtained from nine wells from the Wessex Basin, south England (Fig.5.1). The method for core logging is described in section2.2.2; cores were sampled either based on a high-magnetic susceptibility reading or visible evidence of oil staining. Sampling was restricted to the Inferior Oolite and Bridport Sandstone formations and the samples were characterized both magnetically and geochemically and the results of the findings are presented in this chapter.

To the best of my knowledge, there is only one (previously) published paper, Hounslow (1987) on the magnetic mineralogy of potential crude oil reservoirs in the Wessex Basin. Hounslow (1987) reported that the magnetic signal of the Bridport Sandstone from the Yeovil area of the Wessex Basin (about 20 km west of my study area. See Fig. 2.1) was dominated by paramagnetic minerals, such as chlorite and micas, with minor ferromagnetic (*sensu lato*) contributions from minerals such as ferrianilmanite and Fe-rich titanomagnetites. Clay mineral content within the Bridport Sandstone in the Wessex Basin varies; the lower part is dominated by silty mudstone, that graduate upward to very fine-grained sandstones (Hounslow, 1987).

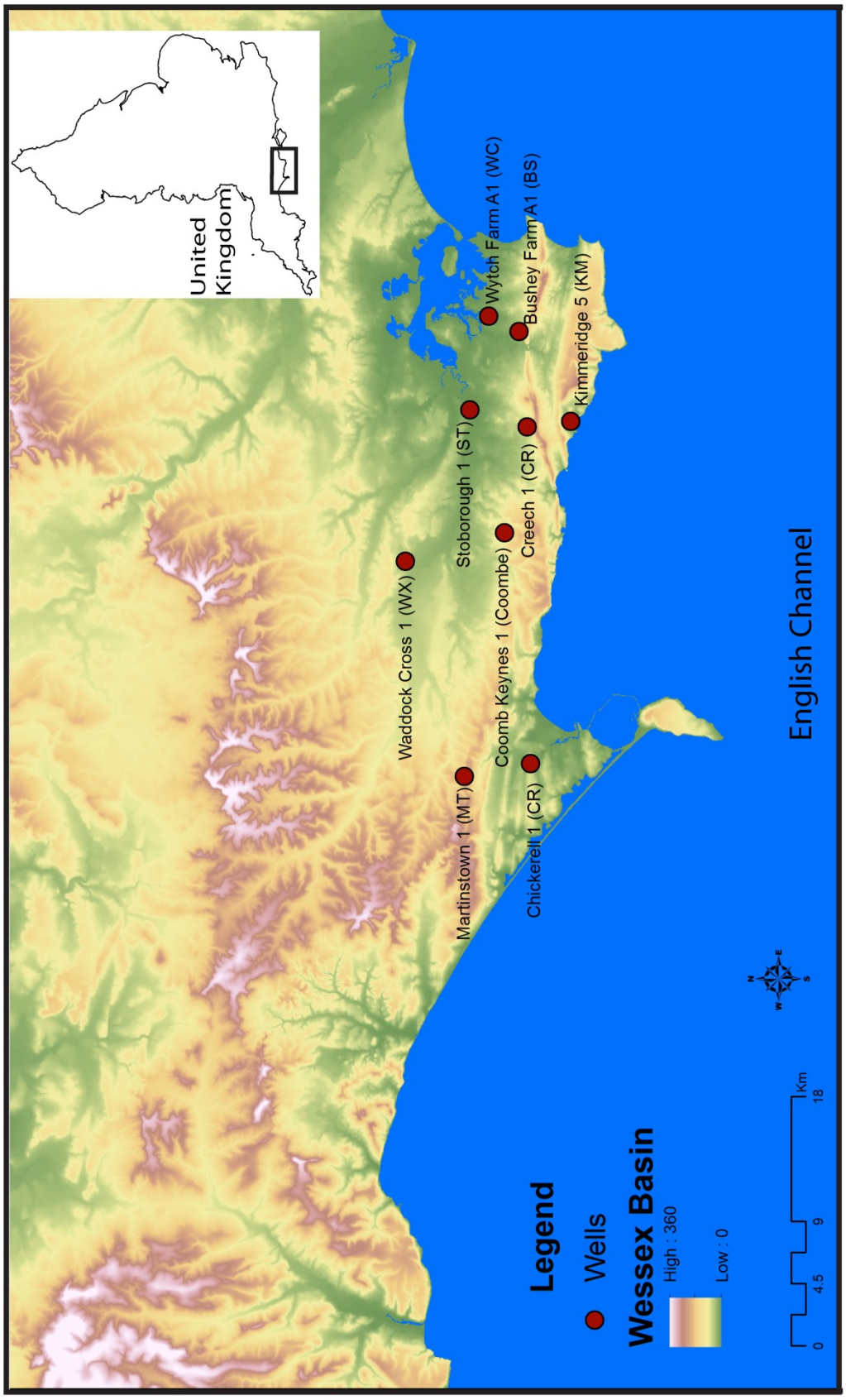


Figure 5.1: Map of Wessex Basin with location of the 9 sampled wells.

5.2 Geochemical characterization

The extraction of oil from the samples taken and fractionation of the extractible organic matter (EOM) into saturates, aromatics and polars was carried out using methods described in section 2.2.1. Not all samples contained sufficient amount of crude oil for geochemical extraction and analysis as sampling was carried out based on high-magnetic susceptibility readings, and/or visible oil staining, with a few randomly selected samples (section 2.2.2). It was difficult to classify the samples as 'oil-stained' and truly 'oil-free' because all the samples contain certain amount of hydrocarbon in them. Therefore, samples with what appears to be only contamination from drilling mud additives are marked 'poorly stained' (Figs. 5.2a-b), denoted by 'P', whereas samples with an appreciable amount of crude oil in them, i.e. enough for biomarker analysis (Figs. 5.2c-d), are marked 'oil-stained' denoted by 'O'. A summary of all the geochemical parameters investigated is shown in Table 5.1, while biomarkers used in this chapter and their interpretation is also shown in Table 5.2. Chromatograms of all fractions used for biomarker analysis carried out in this study are in Appendix 2.1.

5.2.1 Biomarkers

5.2.1.1 Environment of deposition

The following biomarkers were used to investigate the environment of deposition of the source rock, such as lacustrine, marine, anoxic, oxic conditions etc.

n-Alkanes and regular acyclic isoprenoids (pristane and phytane)

The m/z 57 allows for the visualization of alkanes and isoprenoid hydrocarbons and representative samples are displayed in Figure 5.2. The Pr/Ph ratios are relatively consistent but the alkane distribution varies; some (e.g., BS1 and KM3) show a unimodal distribution with a restricted range (C_{15} to C_{26}) and a relatively low molecular weight mode (n-C_{18}) (Figs. 5.2a & b), others (e.g., CH1 and WC3) have a unimodal distribution with a wide range (C_{15} to C_{37}) of compounds and a relatively high mode (n-C_{19} to n-C_{23}) (Figs. 5.2c & d). The alkane distribution observed in Figures 5.2a-b is characteristic of diesel-based drilling fluids.

A plot of the ratios of pristane (Pr) and phytane (Ph) was made to investigate the redox conditions at the time of source rock deposition (Fig. 5.3). Pr/Ph ratios < 1 indicate anoxic environment, Pr/Ph > 1, implying an oxic environment and Pr/Ph > 3 indicate terrigenous organic matter deposited in an oxic environment, but only high and low values can be reliably used (<0.5, >1.5) (Didyk *et al.*, 1978). Most of the samples plotted between 0.75 – 1.5, but Coomb1 and CH 6 had low values of 0.09 and 0.11 respectively and CR7 had a Pr/Ph ratio of

2.32 (Table 5.1). In addition, a plot of phytane/*n*-C_{18} against pristane/*n*-C_{17} that investigates biodegradation, organic matter source and environment of deposition is presented in Figure 5.4. Nearly all the samples plotted with the type II algal marine organic matter source, appear to have been deposited in strongly reducing environment, except for Coomb1, MT3 and CH6, which had anomalously low Pr/C_{17} values (Fig. 5.4 and Table 5.1).

Table 5.1: Distribution of gammacerane and homohopanes across all 45 samples analysed. See Table 2.1 for lithological and depth variations

Sample	Stain	Locality	Pr/Ph	Pr/C_{17}	Ph/C_{18}	$10G/(G+C_{30})$	$G/C_{31}R$	C_{30}/Ts	$C_{29}H/C_{30}H$	$C_{30}/29Ts$	29Ts/(29H+29Ts)	C_{35}/C_{34}	$C_{35}/(C_{31}-C_{35})$	$C_{31}R/C_{30}$	C_{29} ββ/(ββ +αα)	20S/(20S+20R)	Ts/Tm
BS1	P	Bushey Farm 1	1.0	0.5	0.5	--	--	--	--	--	--	--	--	--	--	--	--
BS2	P	Bushey Farm 1	1.2	0.5	0.5	--	--	--	--	--	--	--	--	--	--	--	--
BS3	P	Bushey Farm 1	1.0	0.6	0.5	--	--	--	--	--	--	--	--	--	--	--	--
BS4	P	Bushey Farm 1	1.5	0.6	0.5	--	--	--	--	--	--	--	--	--	--	--	--
BS5	P	Bushey Farm 1	1.0	0.6	0.5	--	--	--	--	--	--	--	--	--	--	--	--
BS6	P	Bushey Farm 1	1.6	0.7	0.5	--	--	--	--	--	--	--	--	--	--	--	--
BS7	P	Bushey Farm 1	1.3	0.6	0.5	--	--	--	--	--	--	--	--	--	--	--	--
BS8	P	Bushey Farm 1	1.4	0.6	0.5	--	--	--	--	--	--	--	--	--	--	--	--
BS9	P	Bushey Farm 1	1.2	0.8	1.1	--	--	--	1.1	--	--	--	--	0.3	--	--	1.0
BS10	P	Bushey Farm 1	--	--	--	--	--	--	--	--	--	--	--	--	--	--	--
COMB1	O	Coombe Keynes 1	0.1	0.2	0.8	--	--	--	0.3	--	--	0.5	0.3	0.4	52.5	48.7	1.5
COMB2	O	Coombe Keynes 1	1.1	0.7	0.8	--	--	--	0.5	--	--	--	--	0.4	--	--	1.2
COMB3	O	Coombe Keynes 1	1.0	0.9	1.0	--	--	--	0.8	--	--	--	--	0.3	30.0	8.0	1.2
COMB4	O	Coombe Keynes 1	1.0	0.9	1.0	--	--	3.3	--	3.6	0.2	--	--	0.4	90.2	79.1	0.9
MT1	P	Martinstown 1	1.1	0.5	0.6	--	--	--	0.4	--	--	--	--	0.5	--	--	0.9
MT2	O	Martinstown 1	1.7	0.6	0.5	--	--	--	--	1.2	1.0	---	--	--	--	--	--
MT3	O	Martinstown 1	0.4	0.1	0.5	--	--	--	--	--	--	--	--	0.6	--	--	0.8
MT4	P	Martinstown 1	1.3	0.8	0.8	--	--	--	--	--	--	--	--	--	--	--	--
ST1	P	Stoborough 1	1.0	0.6	0.7	--	--	--	0.8	--	--	--	--	--	40.4	21.6	1.1
ST2	P	Stoborough 1	1.0	0.7	0.7	--	--	--	0.8	--	--	--	--	0.3	52.0	77.2	1.1
ST3	O	Stoborough 1	0.3	0.5	0.8	--	--	6.5	0.3	--	--	0.4	0.3	0.3	62.2	49.9	2.1
ST4	O	Stoborough 1	0.9	0.7	0.6	--	--	5.1	0.8	--	--	--	--	0.3	33.3	40.4	1.2
WX1	O	Waddock Cross 1	0.7	1.0	1.5	--	--	5.8	0.3	--	--	0.6	0.5	0.3	57.6	38.3	2.0
WX2	O	Waddock Cross 1	1.3	0.9	1.1	3.7	1.4	--	0.5	--	--	--	--	0.4	82.7	36.3	0.9
WX3	O	Waddock Cross 1	0.6	1.1	1.5	--	--	5.9	0.3	--	--	0.6	0.5	0.3	52.6	57.2	2.3
CH1	O	Chickerell 1	0.8	1.4	1.6	2.4	0.9	3.9	0.3	3.6	0.6	--	--	0.4	68.1	22.4	3.2
CH2	O	Chickerell 1	1.0	1.5	1.6	2.5	0.8	4.0	0.3	3.7	0.6	--	--	0.4	56.2	27.1	3.1
CH3	O	Chickerell 1	0.8	1.0	1.0	2.3	0.8	3.6	0.3	3.3	0.6	--	--	0.4	38.9	20.8	3.8
CH4	O	Chickerell 1	0.7	1.2	1.1	2.3	0.8	3.7	0.2	3.5	0.6	--	--	0.4	68.1	57.9	3.2
CH5	O	Chickerell 1	0.9	1.2	1.3	2.5	0.9	3.8	0.3	3.5	0.6	--	--	0.4	82.8	75.1	3.5
CH6	O	Chickerell 1	0.1	0.2	1.2	2.5	0.9	4.0	0.2	3.5	0.6	--	--	0.4	63.4	63.5	3.1
CH7	O	Chickerell 1	1.4	0.8	0.7	--	--	3.8	0.5	--	--	--	--	0.5	--	--	0.9
CR1	O	Creech 1	1.6	0.6	0.6	--	--		1.5	1.3	0.6	--	--	0.6	89.9	72.4	0.8
CR2	P	Creech 1	1.0	0.6	0.5	--	--		--	--	--	--	--	--	63.3	41.5	1.1
CR3	O	Creech 1	0.8	0.8	0.6	2.1	0.7	7.4	0.3	4.6	0.5	0.5	0.2	0.4	49.1	31.1	0.7
CR4	O	Creech 1	1.0	0.8	0.7	2.0	0.6	7.9	0.3	5.0	0.5	0.6	0.3	0.4	49.0	42.2	1.3
CR5	O	Creech 1	1.0	0.7	0.6	2.2	0.7	7.4	0.3	4.6	0.5	0.4	0.3	0.4	55.2	51.8	1.5
CR6	O	Creech 1	0.8	0.8	0.6	1.9	0.6	7.8	0.3	4.8	0.5	0.7	0.3	0.4	41.0	41.0	1.2
CR7	P	Creech 1	2.3	0.6	0.5	--	--	--	--	--	--	--	--	--	--	--	--
KM1	O	Kimmeridge 5	1.0	0.8	0.9	--	--	--	--	--	--	--	--	0.4	--	--	0.9
KM2	P	Kimmeridge 5	0.7	0.7	1.0	--	--	--	0.5	--	--	--	--	0.3	--	--	0.9
KM3	P	Kimmeridge 5	1.2	0.7	0.7	--	--	--	0.4	--	--	--	--	0.3	--	--	0.7
KM4	O	Kimmeridge 5	1.1	0.6	0.6	--	--	--	0.4	--	--	--	--	0.2	--	--	1.0
WC1	O	Wytch Farm A1 (2)	1.2	0.6	0.5	2.1	1.0	4.5	0.3	4.5	0.6	0.4	0.2	0.3	63.0	30.8	1.7
WC2	O	Wytch Farm A1 (2)	1.1	0.6	0.5	2.1	0.7	4.4	0.3	4.4	0.5	0.7	0.3	0.4	96.2	59.1	1.8
WC3	O	Wytch Farm A1 (2)	1.2	0.6	0.5	2.5	1.0	4.2	0.3	4.2	0.5	0.5	0.2	0.3	59.9	55.7	1.7

Pr: Pristane
Ph: Phytane
10 x G/ (G+C_{30}): Gammacerane/ (gammacerane + C_{30} αβ hopane) x 10

G/C_{31}R: Gammacerane/ C_{31} hopane

C_{30}/Ts: C_{30} αβ hopane/ C_{27} 18α trisnorhopane
C_{30}/C_{29}Ts: C_{30} hopane/ C_{29} 18α norneohopane

C_{29}Ts/ (C_{29}αβ+C_{29}Ts): C_{29} 18α norneohopane/ (C_{29}αβ hopane + C_{29} 18α norneohopane)
C_{35}/C_{34}: C_{35} hopane/C_{34} hopane
C_{35}/ (C_{31}-C_{35}): C_{35} hopane/ (C_{31} hopane - C_{35} hopane)

C_{31}R/C_{30}: C_{31} hopane/ C_{30} αβ hopane
C_{29} ββ/ (ββ +αα): C_{29}steraneepimers ratio
20S/ (20S+20R): C_{29}steraneepimers ratio
O: oil-stained, P: poorly stained

Table 5.2: Summary of biomarkers and their interpretations used in this chapter

Biomarker	*m/z*	Interpretation	Reference
Pr/Ph	57	Anoxic (< 1), Oxic (> 1), Terrigenous (> 3) Reliable (< 0.5, > 1.5) Non-biodegraded =1.52 Slightly biodegraded = 1.29 Moderately biodegraded = 1.32 Heavily biodegraded = not present	(Didyk *et al.*, 1978)
Pr/C_{17}	57	Marine (<0.5), Terrigenous (> 0.6) Non-biodegraded = 0.63 Slightly biodegraded = 1.29 Moderately biodegraded = 4-5 Heavily biodegraded = not present	(Peters *et al.*, 2005) (Wenger *et al.*, 2002)
Ph/C_{18}	57	Shales (≤ 0.3), carbonates (≥ 0.3)	(Palacas)
10 × Gammacerane/(Gammacerane + C_{30})	191	Column stratification, sulphate-reducing, hypersaline.	(Damsté and De Leeuw, 1995)
Gammacerane/C_{31} R	191	Column stratification, sulphate-reducing, hypersaline.	(Damsté and De Leeuw, 1995)
C_{30}H/C_{29}Ts	191	High (>3), sub-oxic	(Peters *et al.*, 2005)
C_{29}/$C_{30\ H}$	191	Shales (≤ 1), carbonates (>1)	(Butler and Pullan, 1990; Haven and Rullkötter, 1988)
C_{29} Ts/(C_{29} H+C_{29}Ts)	191	Carbonates, evaporites	(Clark and Philp, 1989)
C_{35}/C_{34}	191	Shales (Low), Carbonates (High)	(Haven and Rullkötter, 1988; McKirdy and Powell, 1973)
C_{35}/(C_{31}-C_{35})	191	Shales (Low), Carbonates (High)	(Haven and Rullkötter, 1988)
C_{31}R/C_{30}	191	Presence indicates marine depositional environment	(Kolaczkowska *et al.*, 1990; Moldowan *et al.*, 1985)

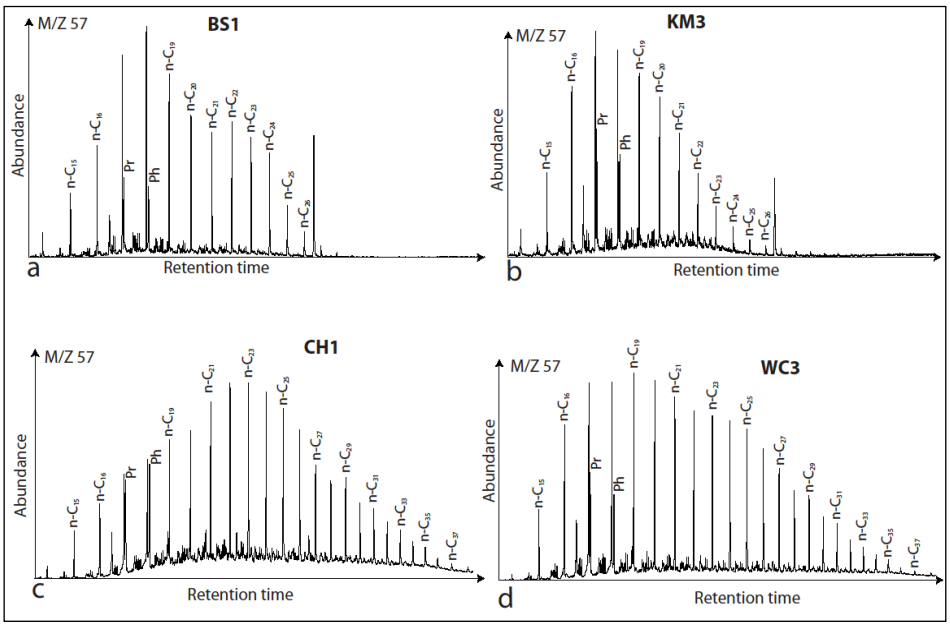


Figure 5.2: Mass chromatogram (m/z 57) of aliphatic fractions of a) and b) Bushey Farm A1 (3464) Kimmeridge 5 (872) respectively, stained probably by the drilling mud, these samples and others with similar geochemical signature are termed poorly-stained (P); c) and d) Chickerell 1 (262) and Wytch Farm A12 (2998) exhibiting typical n-Alkane distribution from crude oils these samples and others with similar geochemical signature are termed oily-stained (O).

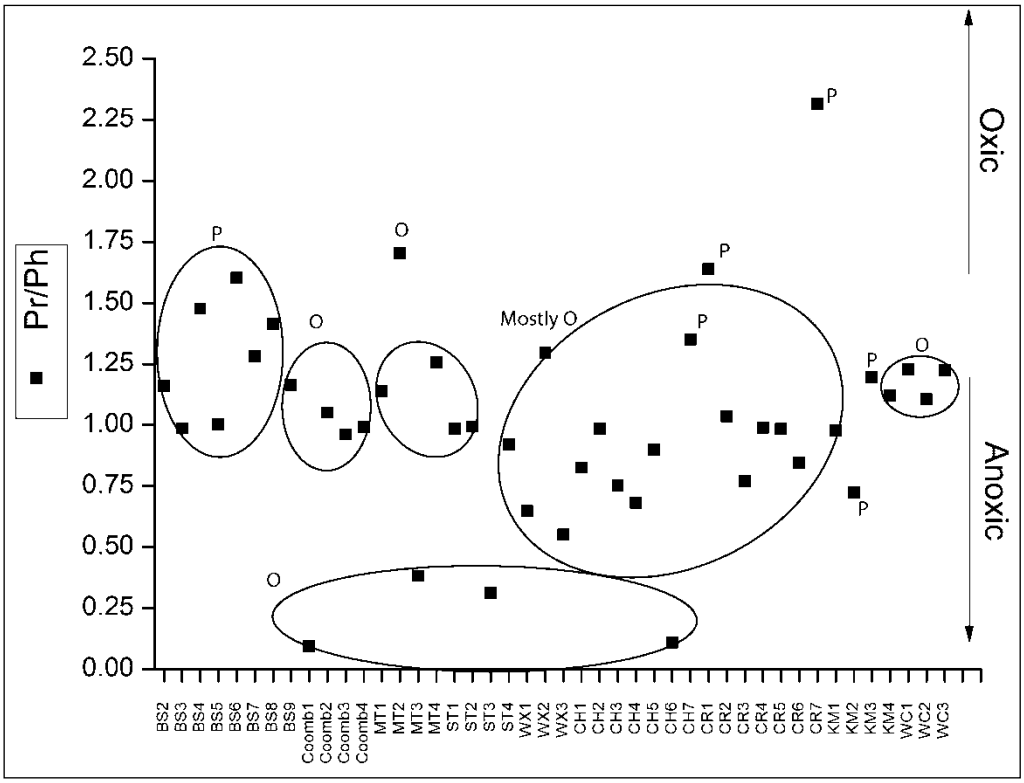


Figure 5.3: Ratios of pristane/phytane (Pr/Ph) plotted to investigate redox conditions at the time of source rock deposition. Samples Coomb1 and CH6 had anomalously low values, which could be as a result of instrument error. Cycles indicate grouping of Os and Ps.

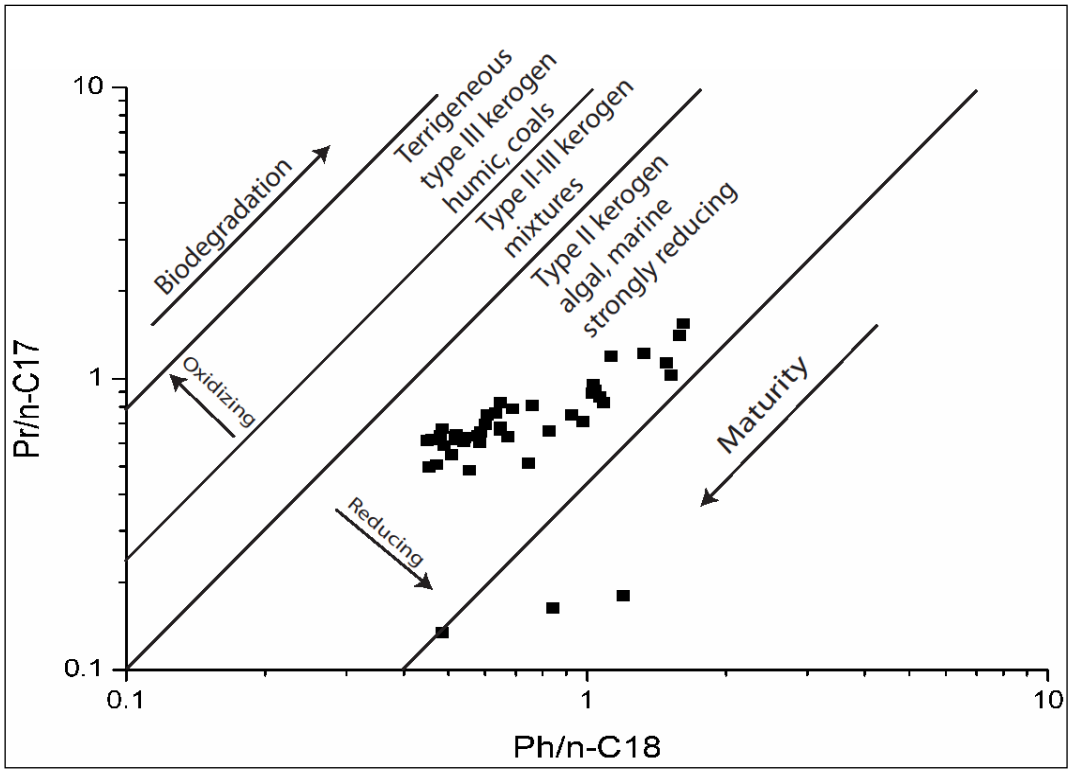


Figure 5.4: Ratios of Ph/C_{18}/Pr/C_{17} plotted in tandem to investigate organic matter type, and environments of deposition (Lijmbach, 1975); nearly all the samples plotted within the type II kerogen, from algal organic matter in a strongly reducing environment.

17α-Diahopane/ 18α-30-norneohopane (C_{30}/C_{29}Ts)

The *C_{30}H/C_{29}Ts* ratio was plotted to investigate a probable relationship between C_{30} hopane and oxic-suboxic/clay depositional environments. It was measured using the *m/z* 191 ion; however, not all samples had enough C_{29}Ts or C_{30} αβ hopane for analysis (Table 5.1). For example, Figure5.5 showed a selection of samples measured using the m/z 191 ion. Samples BS9 and KM3 had small amounts of terpanes in them (Figs.5.5a & b respectively) compared to CH1 and WC3, which had a full range of terpanes, up to C_{35}homohopane, with varying abundances (Figs.5.5 c & d).

A plot of C_{30} H/C_{29} Ts is presented in Figure 5.6. Two main groups can be seen: Coomb4 and the CH samples plot around 3.5 whereas CR and WC samples plot within the 4.0-5.0 range. The C_{30} H/C_{29} averages for all the wells (Table 5.3a) are plotted on a map and seem to show some structural control over the distribution of this biomarker; wells situated on or close to Abbotsbury Ridgeway and Purbeck faults have C_{30} H/C_{29} values >0, whereas wells located away from faults show a total absence of the biomarker except for Wytch Farm (Fig.5.7). Additionally a plot of C_{29} Ts/ (C_{29}H+ C_{29}Ts) can be used due to its abundance in crude oils as an oil maturity biomarker. A plot of C_{29} Ts/(C_{29} H+ C_{29} Ts) is shown in Figure 5.8, in which the samples plot in two distinct groups(Peters *et al.*, 2005); the CR and the WC samples plot between 0.5-0.55 whereas all the CH samples had values > 0.55 (Fig.5.8). The C_{29}Ts/(C_{29}H+ C_{29}Ts) average values for each of the wells was also plotted on a map of the study area and high values are evident on or near the Abbotsbury Ridgeway and Purbeck-Isle of Wight faults which display higher concentrations C_{29}Ts/(C_{29}H+ C_{29}Ts) except for Martinstown(Fig.5.9).

Homohopanes indices (C_{31}-C_{35})

The homohopanes are used as indicators for redox potential of the oil source rock during the time of deposition. They are usually visualised using the *m/z* 191 ion. Figure 5.10 shows a plot of C_{35}H/ (C_{31}H – C_{35}H). Samples BS9, ST4, CR3-CR6 and all the WC samples plotted between 0.2-0.35 while WX1 and WX3 have ratios >0.45. The C_{35}H/ (C_{31}H – C_{35}H) well averages (Table 5.3a) plotted on a map show C_{35}H/ (C_{31}H – C_{35}H) on the eastern part of the study area, with concentrations decliningfrom Waddock Cross southeastwards (Fig.5.11). The plot of the ratio of C_{35}/C_{34} and C_{29}/C_{30}, plotted in tandem (Fig.5.12), can be used to investigate the source facies of oil (Peters and Moldowan, 1991). The C_{35}/C_{34} parameter on the y axis shows variation among the samples, with values ranging from 0.35-0.7, whereas C_{29}/$C_{30}$was more or less constant at ~0.3 (Fig. 5.12).

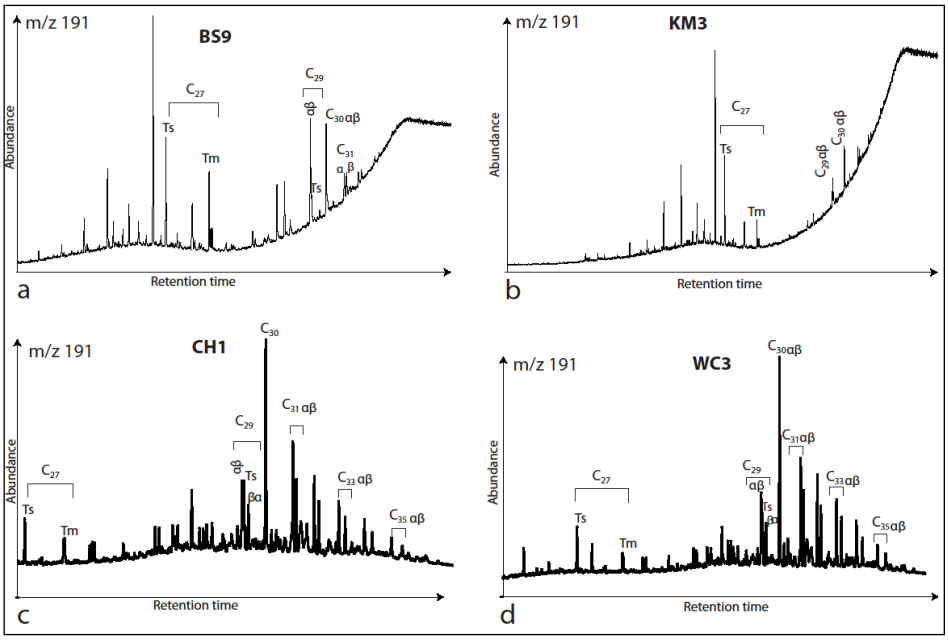


Figure 5.5: A selection of samples measured using *m/z* 191 ion. BS9 and KM3 (a and b respectively) had low concentration of hopanes (≤ C_{31} hopane), they belong to the 'P' marked group. CH1 and WC3 (c and d) on the other hand had a full suite of terpanes, up to C_{35}homohopane and they belong to the 'O' group.

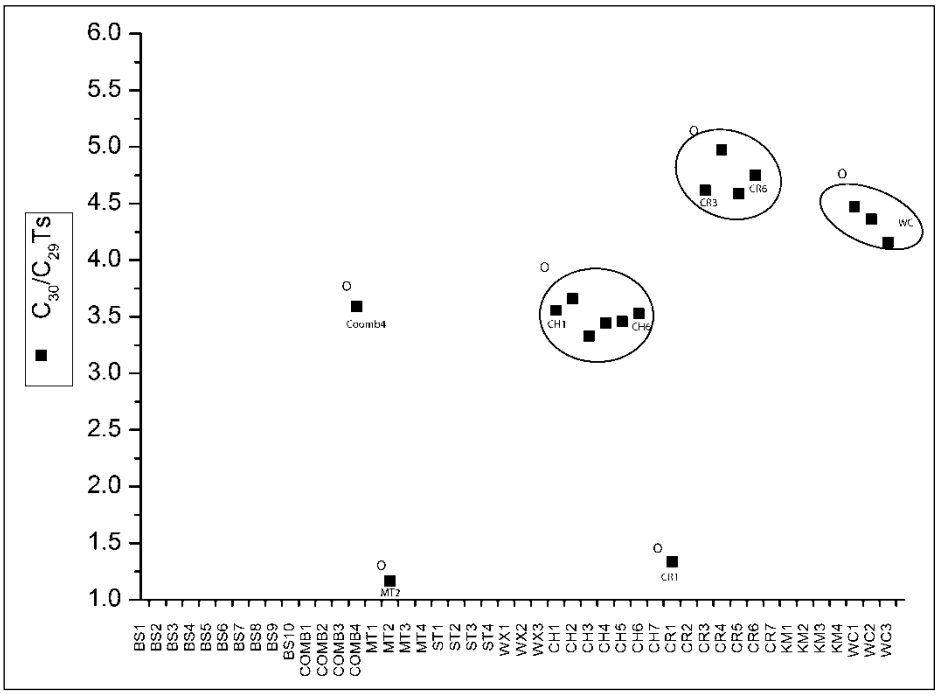


Figure 5.6: A plot of C_{30}/C_{29} Ts showing two distinct groups of oils; Coomb1 and the CH oils in one group, and CR and WC oils in another Comb oils and MT oils exhibit distinct responses. CR1 and MT2 are outliers.

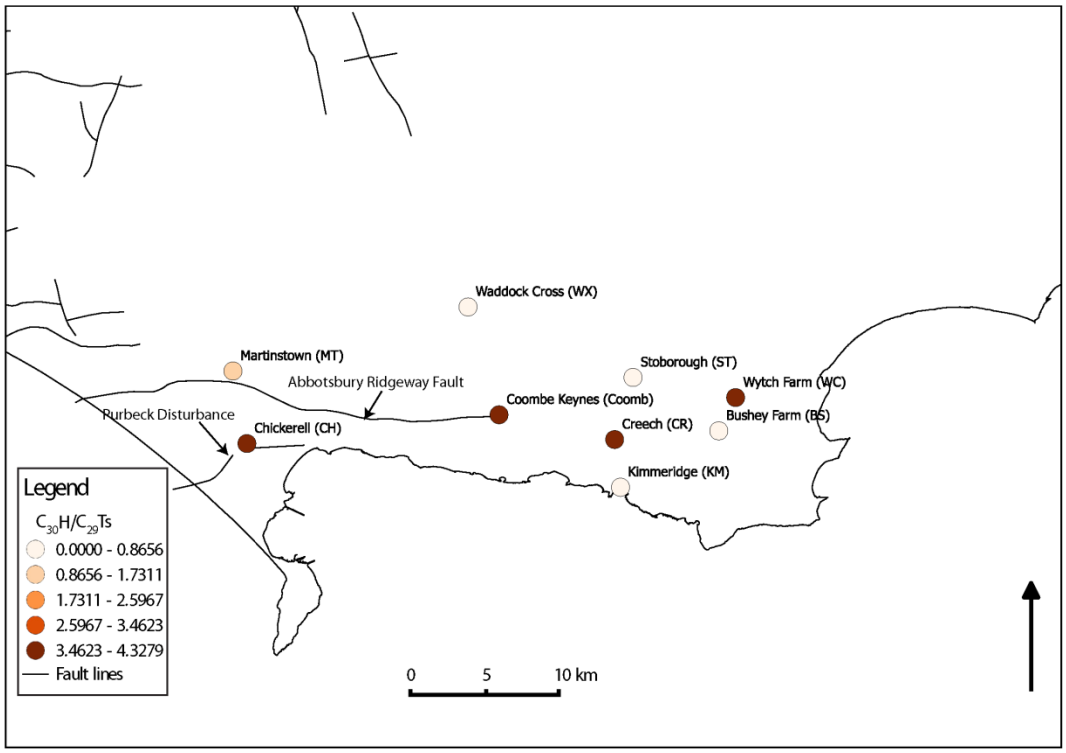


Figure 5.7: The distribution of well average values for C_{30}/C_{29} Ts, showing the biomarker mainly distributed along the main fault line of the study area.

Table 5.3a: mean, standard deviation and median of some of the biomarkers used in this Chapter.

	Pr/Ph			Pr/C17			Ph/C18			C35/(C31-C35)			C31R/C30			C29H/C30H		
Sample	mean	std dev	median	mean	std dev	median	mean	std dev	median	mean	std dev	median	mean	std dev	median	mean	std dev	median
Bushey Farm	1.2	0.2	1.2	0.6	0.1	0.6	0.6	0.2	0.5	-	-	-	0.3	-	0.3	1.1	-	1.1
Coombe Keynes	0.8	0.47	1	0.7	0.3	0.8	0.9	0.1	0.9	0.3	-	0.3	0.4	0.1	0.4	0.5	0.3	0.5
Martinstown	1.1	0.5	1.2	0.5	0.3	0.6	0.6	0.1	0.6	-	-		0.6	0.1	0.6	0.4	-	0.4
Stoborough	0.8	0.3	1	0.6	0.1	0.7	0.7	0.1	0.7	0.3	-	0.3	0.3	-	0.3	0.7	0.3	0.8
Waddock Cross	0.9	0.4	0.7	1	0.1	1	1.4	0.2	1.5	0.5	-	-	0.3	0.1	0.3	0.4	0.1	0.3
Chickerell	0.8	0.5	0.8	1	0.4	1.2	1.2	0.3	1.2	-	-	-	0.4	0.04	0.4	0.3	0.4	0.3
Creech	1.2	0.6	1	0.7	0.1	0.7	0.6	0.1	0.6	0.3	0.1	0.3	0.4	0.1	0.4	0.5	0.54-	0.3
Kimmeridge 5	1	0.2	1.1	0.7	0.1	0.7	0.8	0.2	0.8	-	-	-	0.3	0.1	0.3	0.4	0.1	0.4
Wytch Farm A1	1.2	0.1	1.2	0.6	-	0.6	0.5	-	0.5	0.2	0.1	0.2	0.3	0.1	0.3	0.3	-	0.3

Table 5.3a: mean, standard deviation and median of some of the biomarkers used in this Chapter.

	Ts/Tm			C29 ββ/(ββ +αα)			20S/(20S+20R)			10G/(G+C30)			G/C31R		
Sample	mean	std dev	median	mean	std dev	median	mean	std dev	median	mean	std dev	median	mean	std dev	median
Bushey Farm	1	-	1	-	-		0	-	-	-	-	-	-	-	-
Coombe Keynes	1.2	0.2	1.2	57.6	30.4	52.5	45.3	35.7	48.7	-	-	-	-	-	-
Martinstown	0.9	0.1	0.9	-	-	-			-	-	-	-	-	-	-
Stoborough	1.4	0.5	1.2	47	12.7	46.2	47.3	23.2	45.2	-	-	-	-	-	-
Waddock Cross	1.7	1	2	64.3	16.1	57.6	43.9	11.5	38.3	3.7	-	3.7	-	-	-
Chickerell	3	1	3.2	62.9	14.6	65.8	44.5	23.8	42.5	2.4	0.1	2.5	0.9	0.1	0.9
Creech	1.1	0.3	1.2	57.9	17.3	52.2	46.7	14.2	41.9	2.1	0.1	2.1	0.7	0.1	0.7
Kimmeridge 5	0.9	0.1	0.9	-	-			-	-	-	-	-	-	-	-
Wytch Farm A1	1.7	0.1	1.7	73.1	20.1	63	48.5	15. 5	55.7	2.2	0.2	2.1	0.9	0.2	1

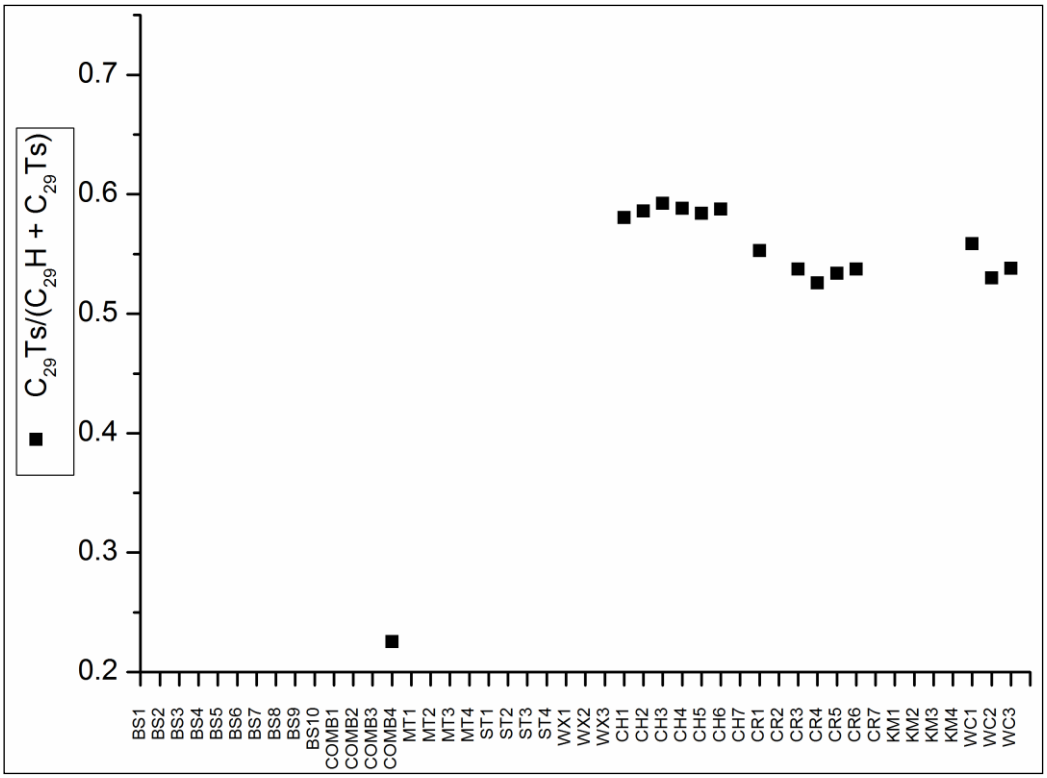


Figure 5.8: A plot of $C_{29}Ts/ (C_{29} H+C_{29} Ts)$ with the CH oils plotting differently from CR and WC. Values > 1 indicate carbonate/evaporite source. Low Coomb4 values could be instrument error.



Figure 5.9: The distribution of well average values for $C_{29}Ts/ (C_{29}H+ C_{29}Ts)$, showing the biomarker mainly distributed linearly along the main fault line of the study area.

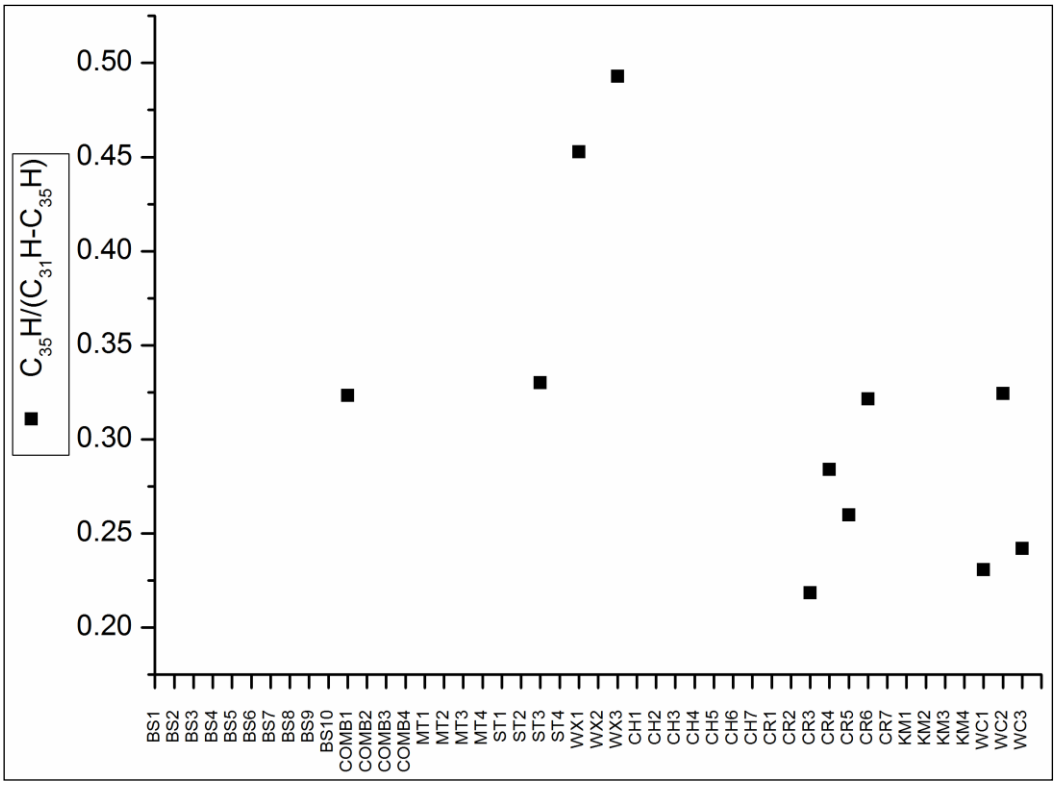


Figure 5.10: A plot of $C_{35}H/ (C_{31}H – C_{35}H)$ showing the WX samples plotting separate from the rest of the samples.

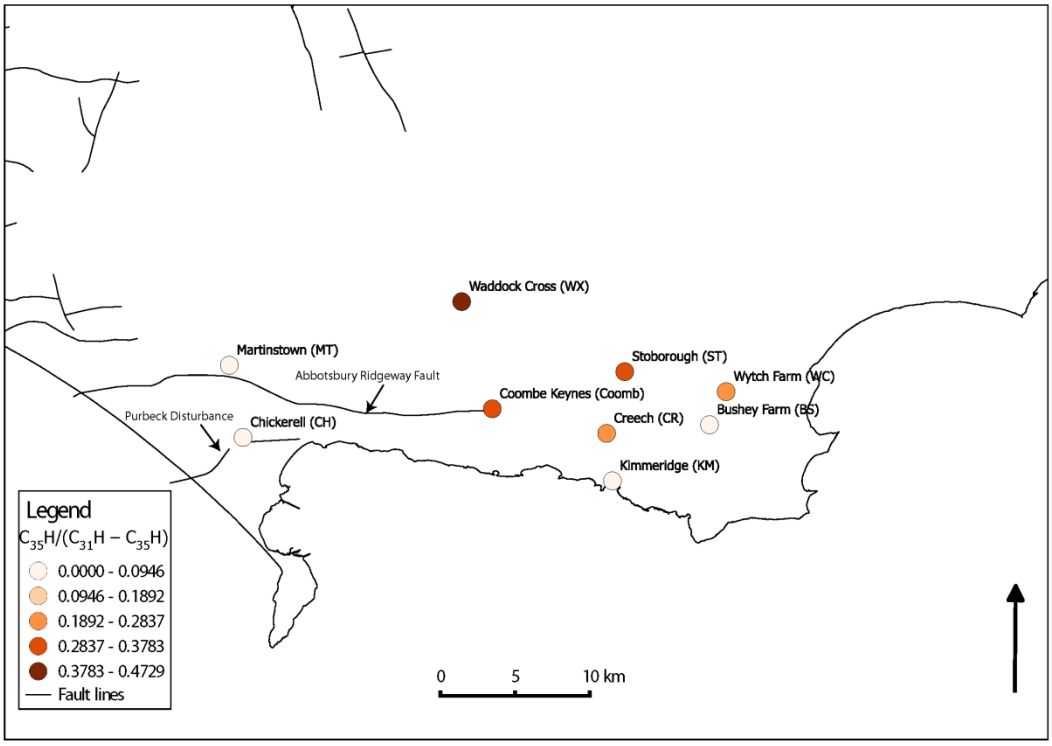


Figure 5.11: The distribution of well average values for $C_{35}H/ (C_{31}H – C_{35}H)$, showing the biomarker mainly distributed on the eastern section of the study area with concentration getting less from Waddock Cross south-eastwards.

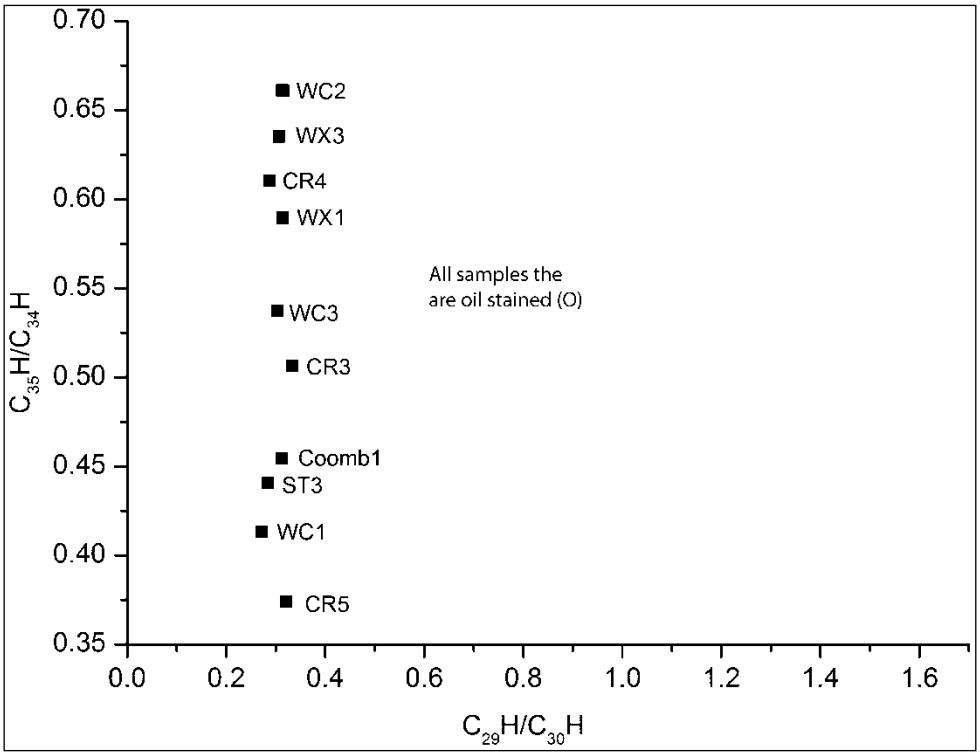


Figure 5.12: A plot $C_{35}H/C_{34}H$ showing no distinct groupings from the different oil samples.

C_{31}/C_{30}hopanes

A plot of the ratios of C_{31}/C_{30}hopanes is used to separate oils of marine from those of lacustrine deposited source rocks and is presented here in Figure 5.13, with most of the samples plotting between 0.3-0.45 and displaying some grouping; with CH, CR and WC samples mostly having similar values around 0.36, whereas ST and WX samples have ~0.33 (Fig. 5.13). The presence of $C_{31}H$ is generally in any crude sample is generally regarded as an indication for marine source (Peters *et al.*, 2005). A plot on map of the well average (Table 5.3a) values for C_{31}/C_{30} biomarker is shown in Figure 5.14, with no apparent pattern to the average distribution of the biomarker between the wells.

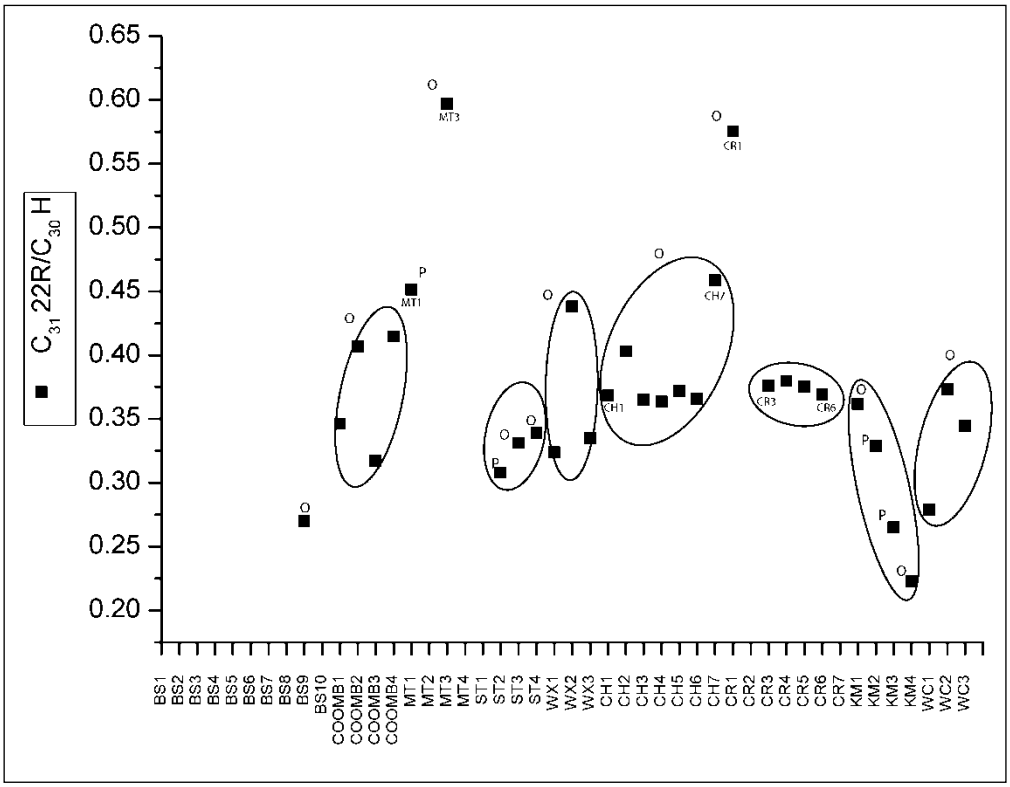


Figure 5.13: A plot of C_{31} 22R/C_{30} H showing ST and WX grouped on one hand, and CH, CR and WC on the other. Cycles indicate grouping of Os and Ps.

30- Norhopane/hopane index (C_{29} H/C_{30} H)

The *3*0-Norhopane/hopane (C_{29} H/C_{30} H) index is used to investigate oils generated from anoxic carbonate and/or marl source rocks (shales <1, carbonates/marl >1). It was measured using the *m/z* 191 fragment and the result is presented in Figure 5.15. No distinct grouping is observed as majority of the samples plotted between 0.2-0.5. The plot of (C_{29} H/C_{30} H) well average values is shown in Figure 5.16; it shows a fair average distribution of the biomarker across the study area without any apparent structural control on it (Fig.5.16)

5.2.1.2 Maturity parameters

Ts/Tm v C_{30} Hopane

A plot of Ts/Tm v C_{30} Hopane (absolute concentration of C_{30}H) was carried out to investigate thermal maturity in oils from a common source is shown in Figure 5.17. According to this classification, oil samples with low Ts/Tm ratio (< 1) and high C_{30}H values are characterised as immature (Waples and Machihara, 1991). Oils samples from Stoborough (ST), Kimmeridge (KM) and Martinstown plot in around Ts/Tm ratio of ~1, having very low C_{30}H concentration whereas most samples from Creech (CR), which had slightly higher concentration C_{30}H (Fig. 5.17). In addition, oils from Wytch Farm (WC) and Waddock Cross (WX) had similar Ts/Tm

ratios of about 1.5-2.0, but two samples from Waddock Cross (WX) had the highest $C_{30}H$ concentration, while oil samples from Chickerell (CH) had the highest Ts/Tm ratio and a relatively low $C_{30}H$ concentration (Fig. 5.17).

C_{29}Steraneepimer ratios

A plot of percentage of C_{29}epimerratios of αββ/ (αββ+ααα) versus (S/(S+R)) was also carried out in order to investigate further, variations in maturity among the oil samples studied. Ratios >0.4 for both biomarkers are considered to be in the oil window (Peters *et al.*, 2005). Figure 5.18 shows a percentage plot of C_{29} (αββ/ (αββ+ααα)) againstC_{29}(S/(S+R)). Most of the oil samples analysed in this study had values between 0.3-0.7 for both biomarkers, with few exception from 3 CH samples, that had C_{29} (αββ/ (αββ+ααα)) ratio of less than 0.3 (Fig. 5.18).

5.2.1.3 Water column stratification

Gammacerane indices

The gammacerane indices are used to investigate water column stratification caused mainly by hypersalinity during the source rock deposition (Damsté and De Leeuw, 1995)it is measured using the *m/z* 191 ion. A plot of 10 × gammacerane/ (gammacerane + $C_{30}H$) is presented in Figure 5.19, all samples analysed plotted within 1.5-2.5 interval. The plot of the biomarker well averages show that the biomarker is present in wells located on the hanging wall and the footwall of the basin, with low/zero concentration along the main fault lines (Fig.5.20). In addition, the gammacerane/C_{31} H (G/C_{31} H) index was also measured using same *m/z* ion and is presented in Figure 5.21. The ratios plotted in a similar pattern to those in Figure 5.19, with all ratios plotting within 0.6-1.0, with no distinct grouping. Similarly, the plot of the well average values for the biomarker shows it is also concentrated on the hanging and the footwall of the basin, with wells located on or near the Abbotsbury Ridgeway fault having low concentration of the biomarker (Fig.5.22).

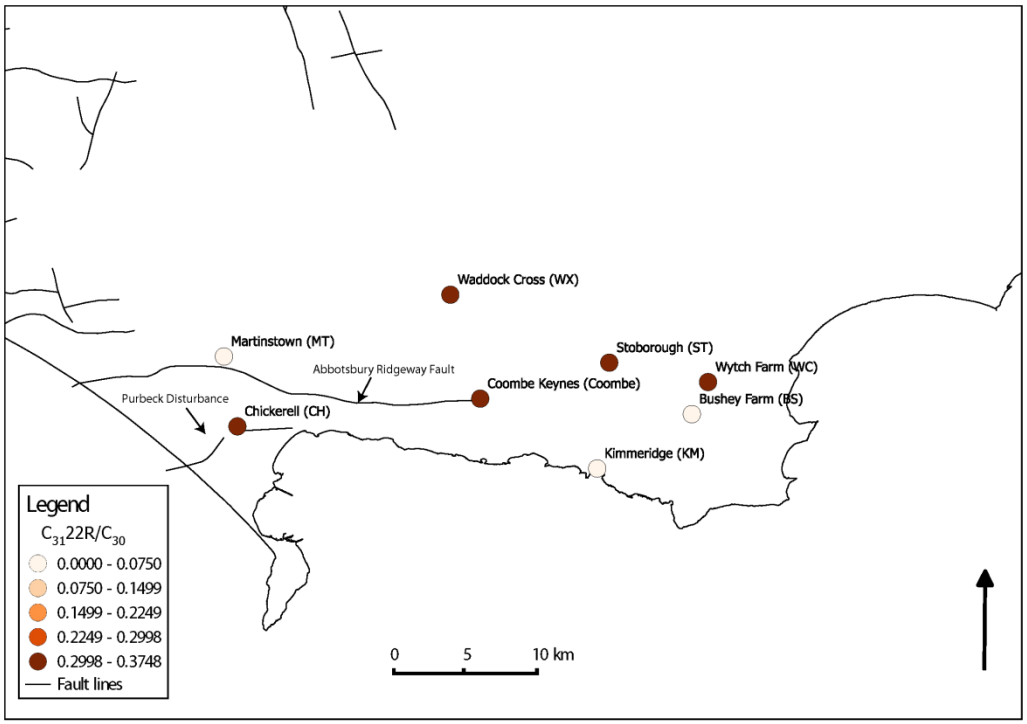


Figure 5.14: The distribution of well average values for C_{31} 22R/C_{30} H biomarker, showing no particular pattern of distribution.

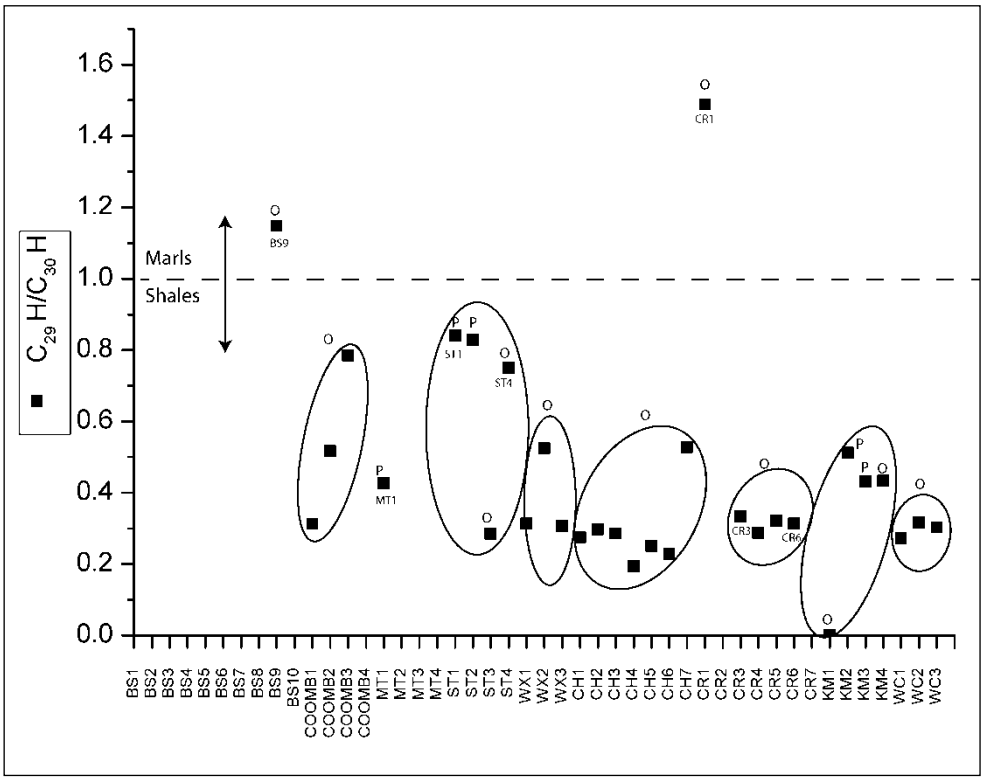


Figure 5.15: A plot of 30-Norhopane/hopane index also not showing any groupings of the oil samples measured.

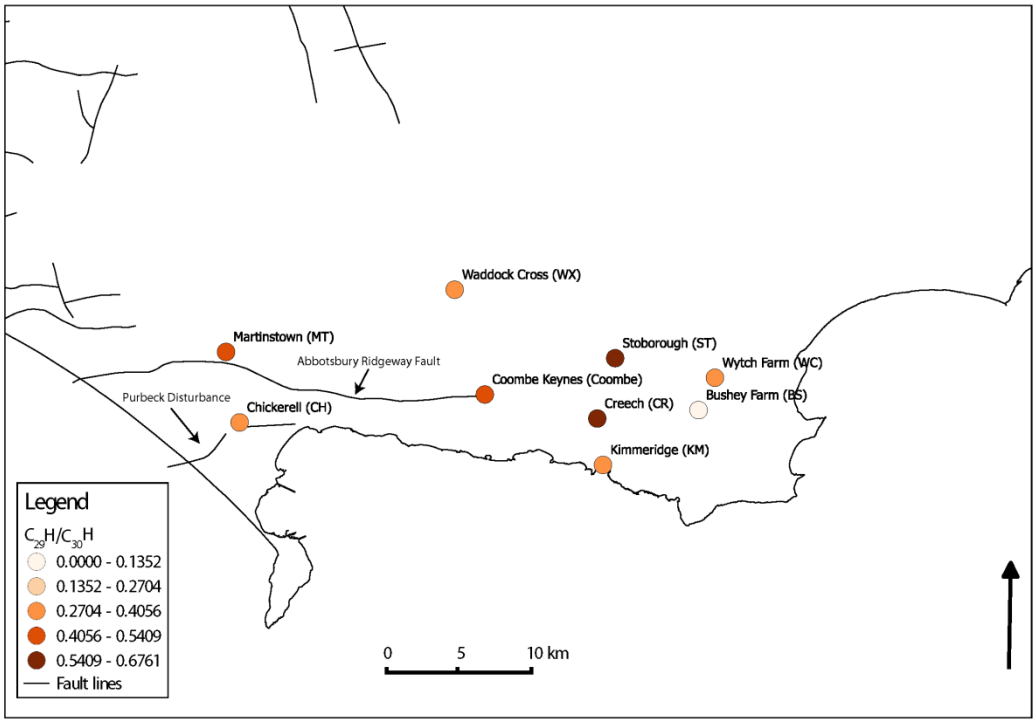


Figure 5.16: The distribution of well average values for C_{29} H/C_{30} H biomarker showing a fair distribution across all wells except for BThe distribution of well average values for C_{31} 22R/C_{30} H biomarker Bushey Farm (BS).

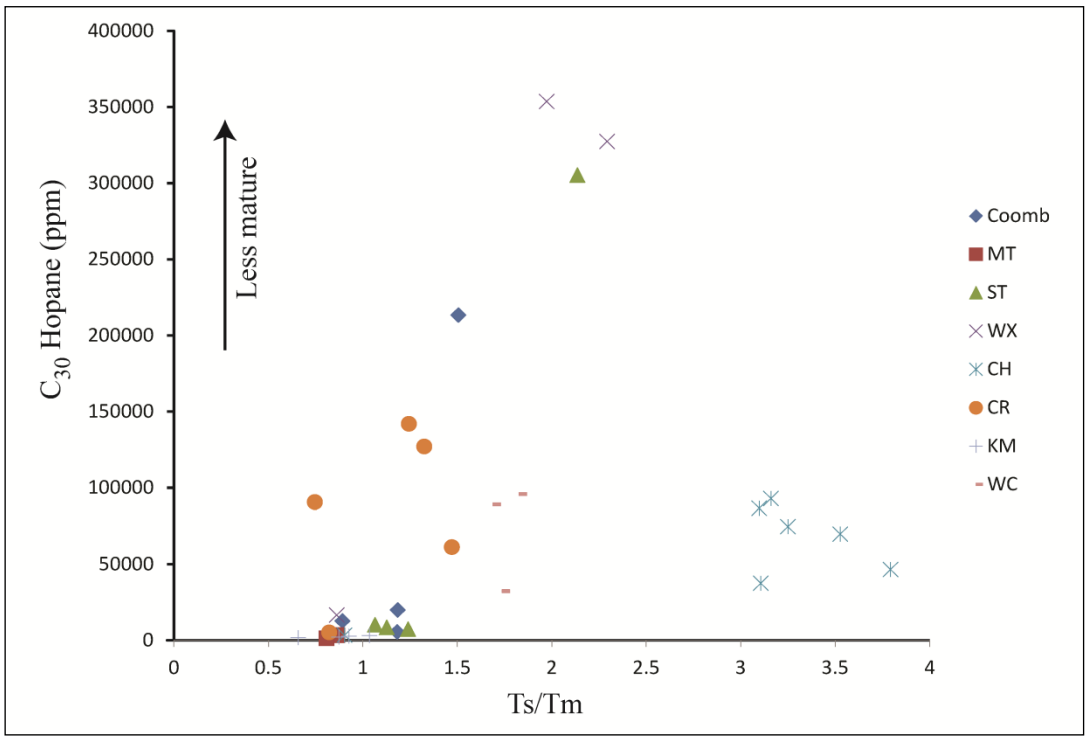


Figure 5.17: Plot of maturity biomarkers Ts/Tm versus C_{30}H.

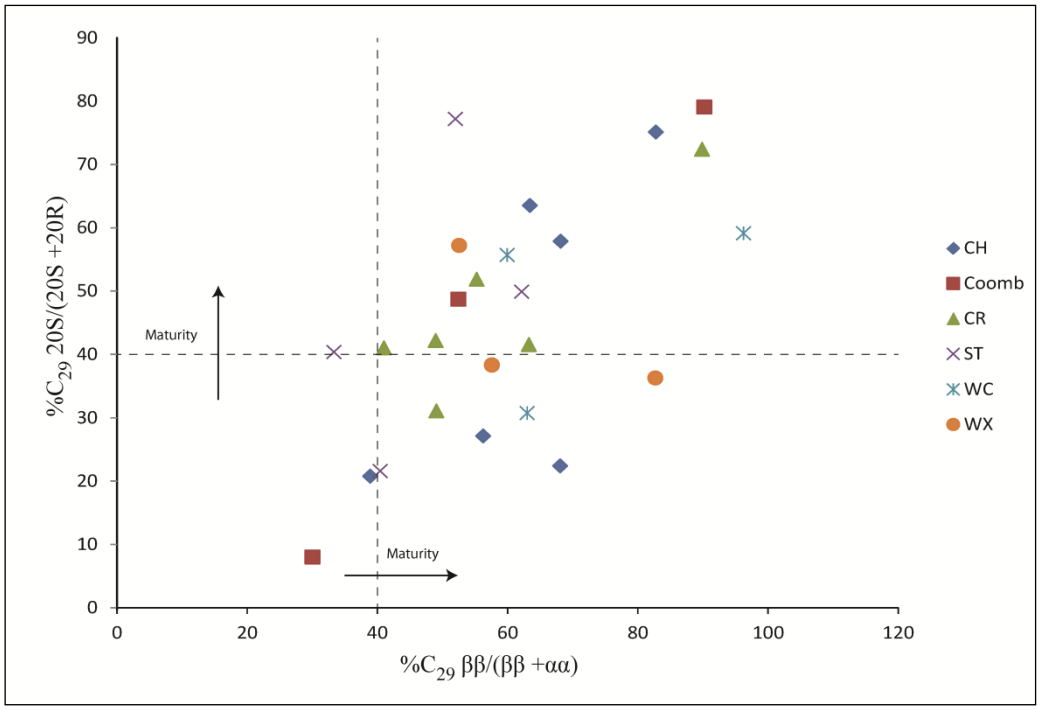


Figure 5.18: Plot of C_{29}steraneepimers, %αββ/ (αββ+ααα) versus %(S/(S+R)).

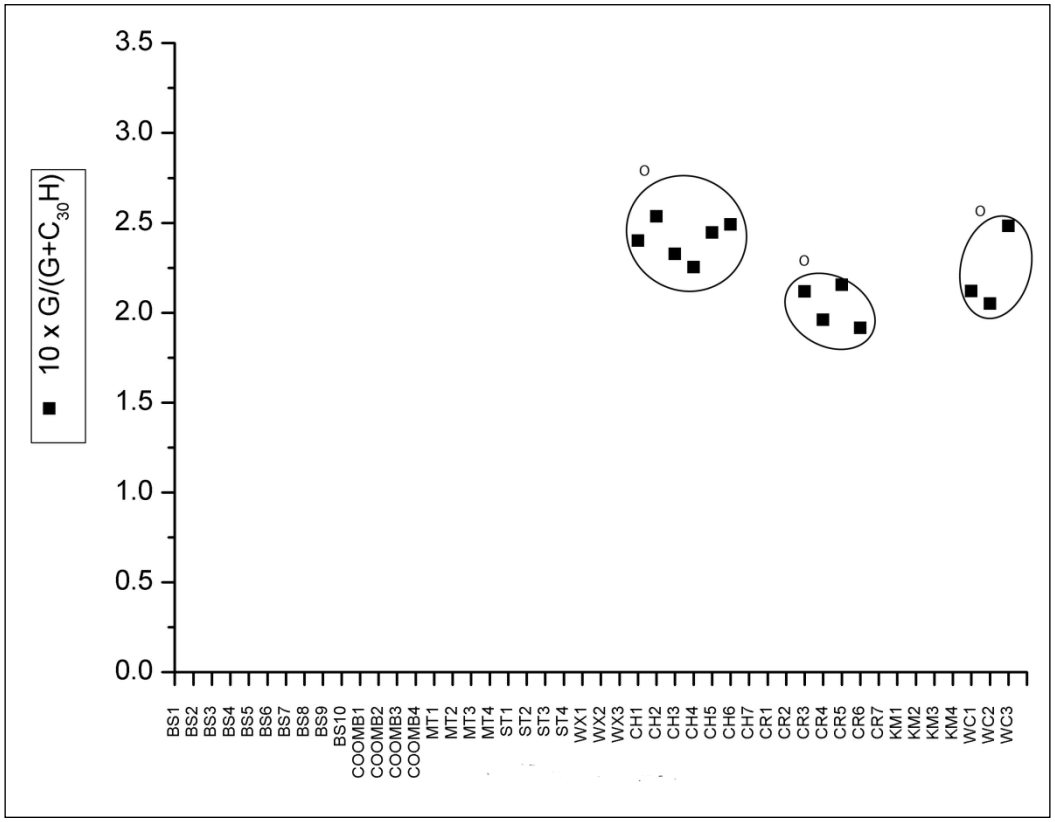


Figure 5.19: Gammacerane indices plotted to using 10 × G/ (G+C_{30} H) with all values plotting within 1.75 – 2.5.

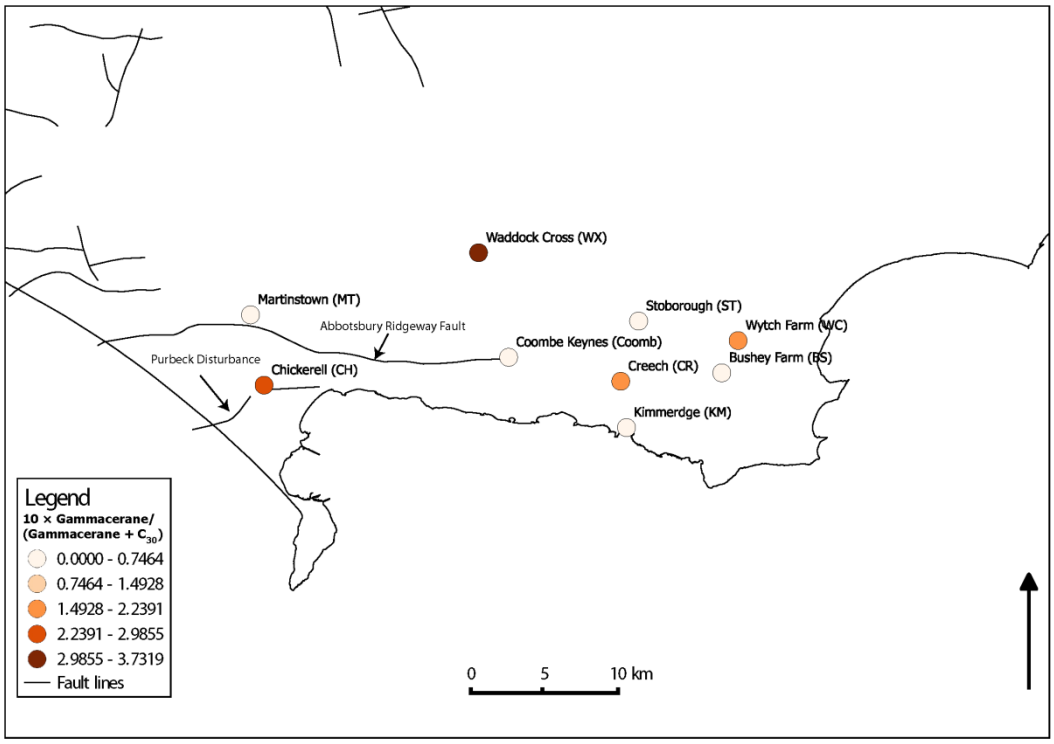


Figure 5.20: The distribution of 10 × G/ (G + C_{30}) biomarker, showing increasing concentration of the biomarker away from the main fault of the basin.

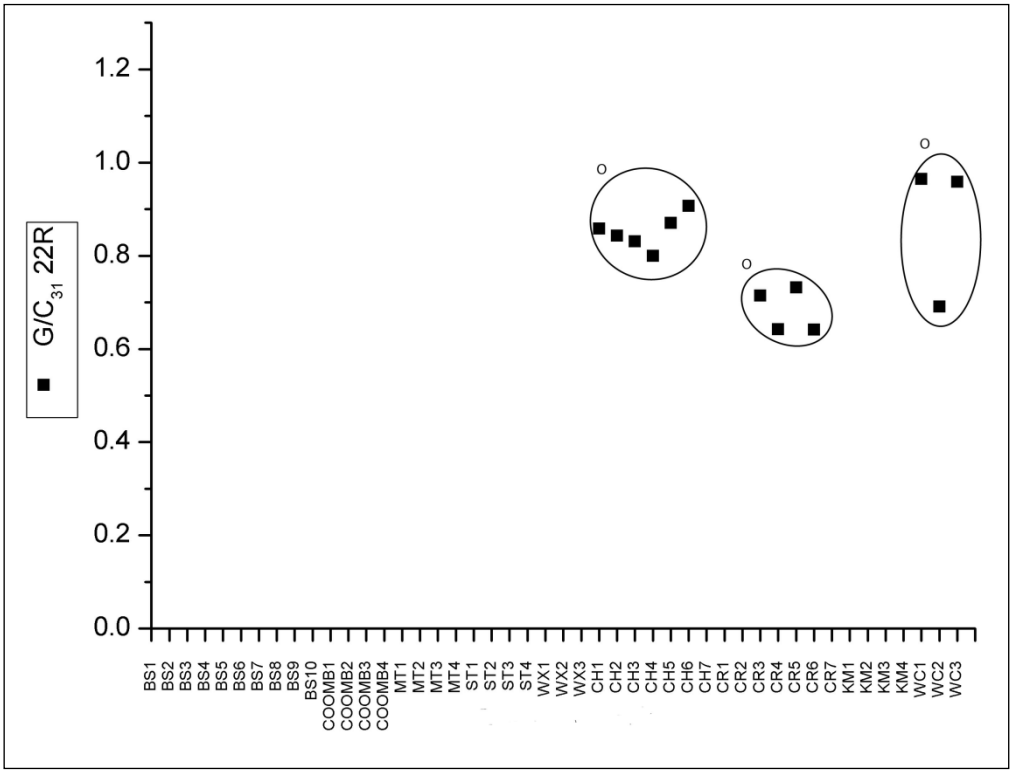


Figure 5.21: A plot of G/C_{31} 22R biomarker with WX, CH, CR and WC having values between 0.6-1.0, indicating rocks deposited in stratified water due to hypersalinity.

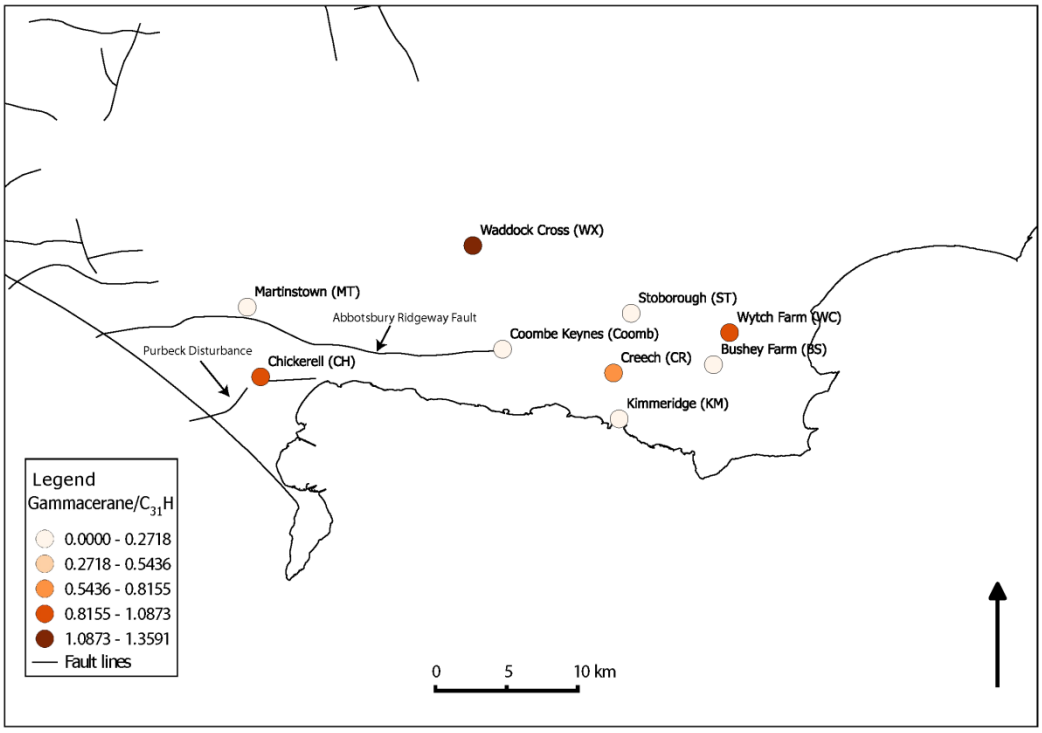


Figure 5.22: A plot of Gammacerane/C_{31} H, showing the concentration of the biomarker to the north and south of the main fault of the study area.

5.2.2 Are the oil samples genetically different?

5.2.2.1Environment of deposition and maturation

The Pr/Ph ratio is important in determining the environment of deposition: transformation of the phytyl side chain into phytane in anoxic environment or to pristane in oxicenvironments(McKirdy and Powell, 1973) (Chapter 2). Samples I analysed mostly had ratios between 0.5-1.5, i.e., within the oxic-suboxic region (Fig. 5.3);the use of Pr/Ph ratios have limitations in classifying depositional environments of oil samples, for example, Volkman (1988b) observed that the Pr/Ph ratios of the same oil vary with maturity;more thermally mature oils have higher Pr/Ph ratios. Kohnen (1991) and De Graaf *et al.* (1992) attributed this increase to the preferential cleaving of sulphur bound phytols from the source rocks during early oil maturation. Peters *et al.* (2005) also reported weakening of the ratios for oils or source rocks within the oil generation window, and suggest the Pr/Ph ratios should be used together with other geochemical parameters.

The Ph/*n*-C_{18} and Pr/*n*-C_{17} ratios, provide a more reliable classification of oils in terms of environment of deposition, organic matter type, oil maturity and biodegradation (Lijmbach, 1975). Nearly all the oil samples analysed in this study plot within the range of oils derived from Type II kerogen of algal marine origin that was deposited in a strongly reducing environment (Fig. 5.4). Furthermore, C_{30}/C_{29}Ts hopane ratios plotted to investigate source type

and environment of deposition (Moldowan *et al.*, 1985) shows source rocks that generated the Creech oils were deposited in an oxic-suboxic environment, Wytch Farm in suboxic-dysoxic environment and while Chickerell and Coombe Keynes oils in dysoxic-anoxic environment (Fig. 5.6), with some sort of lineament observed in the distribution of the biomarker, along the Abbotsbury Ridgeway-Purbeck faults (Fig. 5.7). However, Kolaczkowska *et al.* (1990) and Peters *et al.* (2005) argued that this ratio is also affected by oil maturity. Peters *et al.* (2005)suggest that the C_{30} hopane is thermally more stable than C_{29} Ts and the C_{30}/C_{29}Ts ratio could not be solely relied upon. In contrast, the C_{29}Ts/(C_{29}H + C_{29}Ts) shows all the oils present had slightly varying maturity levels, with oils from Creech and Wytch Farm being slightly more mature than the Chickerell oils (Moldowan *et al.*, 1985) (Fig. 5.8) and a similar distribution of the biomarker along the Abbotsbury Ridgeway and Purbeck-Isle of Wight fault lines (Fig. 5.9).

The homohopanes (C_{31} – C_{35}hopanes) contained in the samples analysed indicate that the source rocks that generated Wytch Farm and Creech samples were deposited in oxic-suboxic environment (Fig. 5.10) (Krooss *et al.*, 1991), this agrees with the C_{30}/C_{29}Ts ratios above (Fig. 5.6), while the Stoborough oils were sourced from rocks deposited in anoxic environments. In addition, Peters and Moldowan (1991) considered the presence of C_{35}hopanes in any oil sample as an indication that the source rocks were deposited in a highly reducing (-Eh) marine environment. The C_{35}/C_{34}homohopane ratios for the oils measured had values less than the predicted for oils derived from marine shales (>0.6), but most of the samples measured had values <0.6, this is indicative of oils sourced from coal/resin materials (Fig. 5.12). However, this ratio is also reported to be affected by oil maturity, e.g., Peters and Moldowan (1991)foundvalues of <0.6 in oils from Monterey Formation, California, which was neither sourced from coal nor resins. Conversely, the C_{29}H/C_{30}H plot (Fig. 5.15) shows nearly all the oils had ratios <1.0, which indicate the oils were not sourced from carbonate or marl, but shales in suboxic-anoxic conditions (Peters *et al.*, 2005). No obvious trend in the distribution of the C_{29}H/C_{30}H biomarker was observed as they plotted almost randomly (Fig. 5.16).

The C_{31}/C_{30}homohopane ratios are highly specific for distinguishing marine from lacustrine depositional conditions; samples measured in this study using this ratio had values > 0.25 (Fig. 5.13). This reaffirms the source rock for these oils was deposited in a marine environment (Johnson, 2006), with the biomarker fairly distributed around the study area (Fig. 5.14). Furthermore, the presence of gammacerane in some of the oils analyzed (Fig. 5.19 and Table 5.1) confirms those oil were sourced from hypersaline, semi restricted, water stratified environments (Damsté and De Leeuw, 1995). Moldowan *et al.* (1985) argued that the presence of gammacerane in oils confirms a highly reducing hypersaline environment of deposition.

In addition, biomarker analysis carried out to investigate maturity differences among the oil samples indicated varied maturity levels in oil samples from same wells and across the wells. A plot of Ts/Tm v $C_{30}H$ indicated that oil samples from Waddock Cross are generally less mature than oil samples from Creech, which in turn are less mature than oil samples from Wytch Farm (Fig. 5.17). Interestingly, oil samples from Chickerell seem to be the most mature base on Ts/Tm v $C_{30}H$ biomarker, with oils from Kimmeridge, Stoborough and Martinstown having similar maturities (Fig. 5.17). Oil samples from Waddock Cross are less mature than oils from Creech, which are in turn less mature than oils from Wytch Farm (Fig. 5.18).

5.2.3 Summary of geochemical characterisation

There is no evidence to suggest, based on the biomarker analysis carried out on the aliphatic fractions of the oil samples that they were not from a common source rock, i.e., all oils analysed in this study probably had the same source rock (Figs. 5.6 – 5.13). However, variations observed in some of the environment of deposition biomarkers, e.g., the C_{35}homohopane (Figs. 5.10 – 5.13) and the Ph/*n*-C_{18} and Pr/*n*-C_{17} (Fig. 5.4) might be due differences in oil thermal maturity, biodegradation (Appendix 2.1) or there were variations in conditions, during the deposition of the Lias. The deposition of the Lias took millions of years (Hawkes *et al.*, 1998), and it is probably incorrect to assume conditions were the constant throughout.

There is strong evidence to suggest oil maturity varies across the sampled wells.Oil samples from Kimmeridge are mature than samples from Creech (Fig. 5.17), with both being more mature than samples from Waddock Cross, but less mature Wytch Farm samples; Figure 5.18 also showing similar variations in oil maturities. It is possible to argue, based on biomarker analyses (this chapter), that oils found at different locations in Wessex Basin may have accumulated from various charge points, instead of a series of spill-chains as currently thought(Hawkes *et al.*, 1998).

5.3 Magnetic Characterisation

All the core samples were subjected to magnetic measurements in order to characterise their magnetic mineralogy, and the grain sizes and abundance of the magnetic minerals.

5.3.1 Magnetic mineral abundance

Hysteresis measurements were carried out on all samples at room-temperature (RT) and low temperature (LT). Hysteresis parameters that shed light on the abundance of magnetic materials, e.g., M_s, are discussed below.

I start by considering Kimmeridge5 (KM), as it is thought to be the closest charge point (Hawkes *et al., 1998)*. The Blue Lias M_s values were measured to investigate the abundance of magnetic material in the sample, show variation between the 'O' and the 'P' samples (Fig. 5.23a and Table 5.4), with 'P' samples having higher values. For example, KM2 and KM3, have 1.96 $\times 10^{-3}$ and 5.04 $\times 10^{-3}$ Am^2/kg respectively, while the 'O' samples, i.e., KM1 and KM4 had 5.2 $\times 10^{-4}$ and 1.27 $\times 10^{-3}$ Am^2/kg respectively. In contrast, variations in LT-M_s show the two 'O' samples having higher values than the corresponding 'P' samples. For example, KM1 and KM4 had 0.57 and 8.42 $\times 10^{-3}$ Am^2/kg respectively, while KM2 and KM3 had LT-M_s values of 0.4 and 0.5 Am^2/kg respectively (Fig. 5.23a and Table 5.4). In addition, high-field susceptibility (χ_{hf}) data, which measures the contribution made by paramagnetic and diamagnetic minerals, are shown in Figure 5.23b. In both the LT- and RT-χ_{hf}, the 'O' samples have higher values than the 'P' samples, e.g., RT-χ_{hf} values for KM1 and KM4 are 3.59 $\times 10^{-8}$ and 4.59 $\times 10^{-8}$ m^3/kg respectively, while KM2 and KM3 had 3.34 $\times 10^{-8}$ and 2.29 $\times 10^{-8}$ m^3/kg respectively (Fig. 5.23b and Table 5.4).

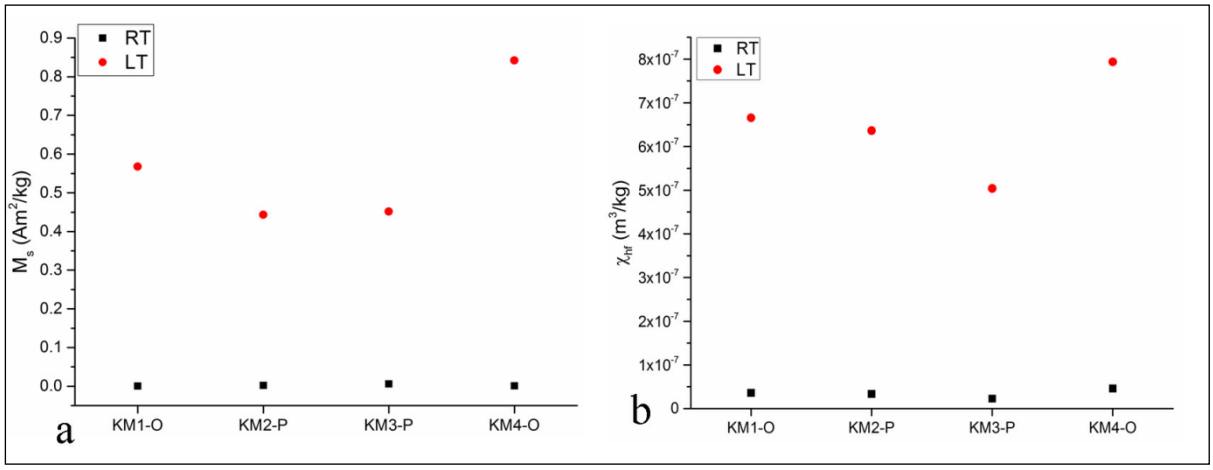


Figure 5.23: Kimmeridge: Plots of LT and RT magnetic hysteresis parameters showing plots of: a) $M_s$values, with 'O' samples having higher values than the 'P' samples in LT measurement, b) high-field susceptibility (χ_{hf}) showing the 'O' samples having larger paramagnetic contributions both at LT and RT.

The LT- and RT-M_s for the Bushey Farm (BS) samples are shown in Figure 5.24a. All the BS samples except for BS9 are marked 'P'. The LT- and RT-M_s values for the 'P' samples had higher LT-M_s than the 'O' sample (Fig. 5.24a and Table 5.4), with an overall decrease in the LT-M_s values with depth (Figs. 5.24a). Figure 5.24b shows a plot of LT- and RT-χ_{hf}, with the middlesamples having higher values.

In contrast, most of the Creech1 (CR) samples were classified as 'O'; CR1, CR2 and CR3 sampled from the Inferior Oolite Fm, while CR4– CR7 were sampled from the Bridport Sandstone Fm (Table 2.1). Figure 5.25a shows plots of LT-M_s data for the CR samples with

values varying generally. All the 'O' samples had higher values than CR2, but are all less than CR7 (P),. For example, CR7 has a higher LT-M_s value (0.89 Am^2/kg) compared to the other 'P' sample CR2(0.51 Am^2/kg), and with some of the 'O' samples, e.g., CR3 and CR4, that had LT-M_s 0.32 and 0.44 Am^2/kg respectively (Fig. 5.25a and Table 5.4); however, no such trend was observed in either the RT-M_s or LT- and RT-χ_{hf} data (Figs. 5.25a & b).

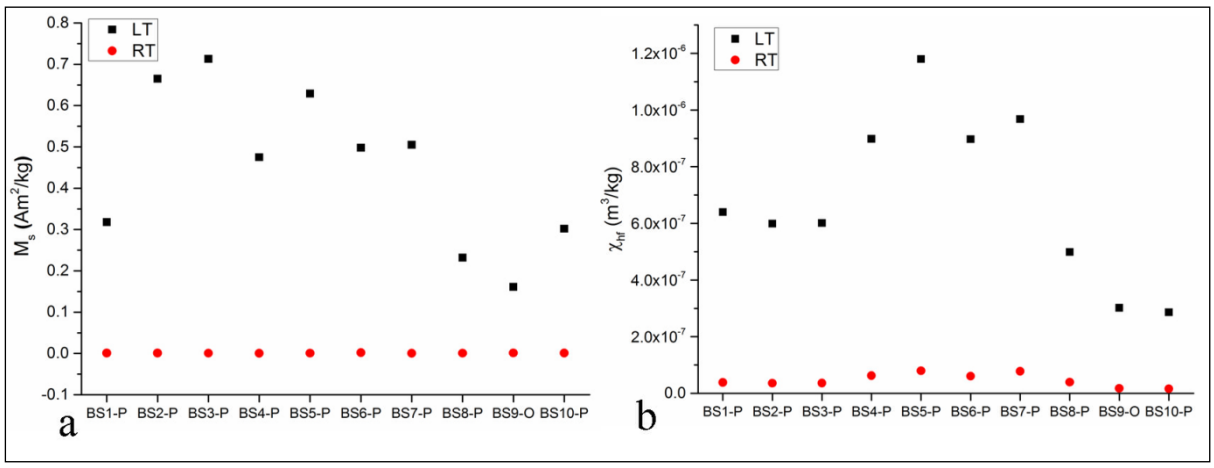


Figure 5.24: Bushey Farm: Plots of: a) LT- and RT-M_s values, showing lower LT value for BS9-O sample compared with the 'P' samples. b)) χ_{hf} values, showing no trend either with respect to oil staining or depth of sample.

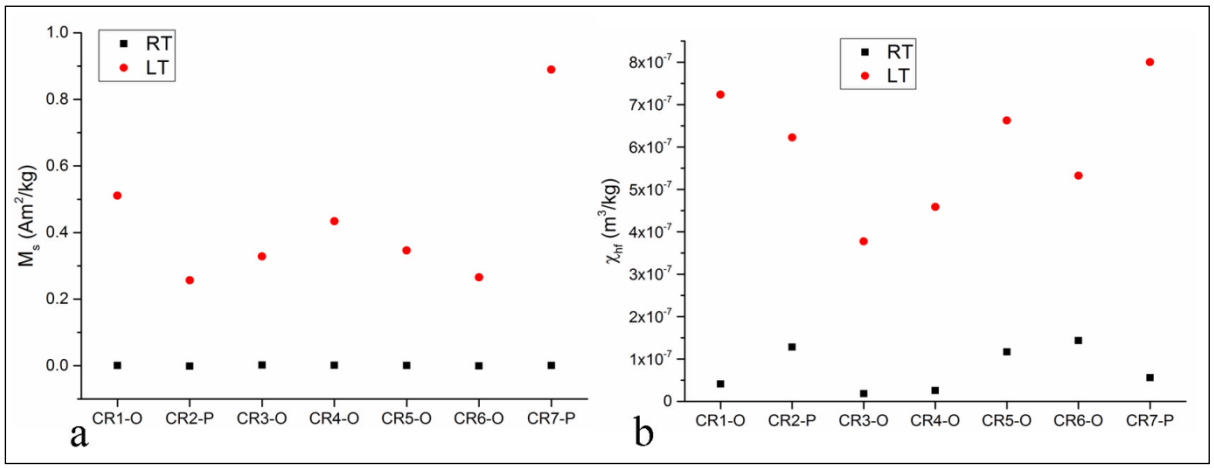


Figure 5.25: Creech: Plots of: a) LT- and RT-M_s showing that the 'O' samples having higher LT-M_s values, except for CR7 and negative values for RT CR2 and CR6. b) χhf, showing no particular pattern with respect to depth of sampling or oil stains.

Table 5.4: Low- (LT) and room-temperature (RT) hysteresis parameters for all samples analysed. See Table 2.1 for depth and lithological variations.

Sample Name	LT-M_s (Am^2/kg)	LT-M_{rs} $\times10^{-3}$(Am^2/kg)	LT-M_{rs}/M_s $\times10^{-2}$	LT-B_c (mT)	LT-$\chi_{hf}\times10^{-7}$(m^3/kg)	RT-M_s $\times10^{-4}$(Am^2/kg)	RT-$M_{rs}\times10^{-5}$(Am^2/kg)	RT-M_{rs}/M_s	RT-B_c (mT)	RT-$\chi_{hf}\times10^{-8}$(m^3/kg)
BS1-P	0.32	4.7	1.5	4.6	6.4	9.0	18.0	0.19	0.4	3.8
BS2-P	0.67	13.0	1.9	8	6.0	9.0	16.0	0.17	12.1	3.6
BS3-P	0.71	20.0	2.8	10.9	6.0	7.0	16.0	0.22	10.9	3.6
BS4-P	0.48	8.6	1.8	4.3	9.0	5.8	11.0	0.2	0.7	6.3
BS5-P	0.63	4.0	0.1	0.4	12.0	6.3	--	--	--	8.0
BS6-P	0.5	6.0	1.2	3.4	9.0	20.0	28.0	0.15	4	6.1
BS7-P	0.51	6.8	1.4	2	9.7	5.1	24.0	0.48	11.1	7.8
BS8-P	0.23	7.5	3.2	8.8	5.0	7.1	10.0	0.15	2.5	4.0
BS9-O	0.16	6.4	4.0	10.8	3.0	13.0	15.0	0.11	5.5	1.8
BS10-P	0.3	14.0	4.5	14.6	2.9	11.0	17.0	0.16	12.3	1.6
COOMB1-O	0.22	6.0	2.7	4.7	5.9	60.0	19.0	0.31	4	3.4
COOMB2-O	0.12	2.0	1.7	2.3	4.1	7.1	10.0	0.14	4.3	2.1
COOMB3-O	0.35	2.1	0.6	1.7	8.7	7.7	--	--	--	5.4
COOMB4-O	0.35	2.3	0.7	1.9	8.3	6.9	6.4	0.09	7.4	4.9
MT1-P	0.19	3.9	2.0	4	6.1	13.0	24.0	0.19	5.8	3.7
MT-O	0.17	3.6	2.1	4.5	4.9	36.0	62.0	0.17	12.1	2.9
MT3-O	0.4	6.4	1.6	5	5.5	12.0	19.0	0.16	5.4	3.5
MT4-P	0.11	2.2	2.0	4.2	3.8	9.7	16.0	0.16	6.8	1.9
ST1-P	0.33	2.7	0.8	1.9	7.2	13.0	11.0	0.81	2.4	4.3
ST2-P	0.98	2.3	2.3	3.8	4.0	7.3	13.0	0.18	5.6	2.0
ST3-O	0.23	5.1	2.2	6	5.4	49.0	37.0	0.75	6.6	3.1
ST4-O	0.69	3.6	0.5	1.7	13.0	32.0	33.0	0.1	3.3	9.0
WX1-O	0.56	4.2	0.7	2.1	8.3	55.0	52.0	0.94	6.5	4.8
WX2-O	0.12	4.0	0.3	0.6	21.0	21.0	18.0	0.86	1.6	13.0
WX3-O	0.35	6.7	1.9	5.1	6.8	14.0	27.0	0.2	6.3	4.0
CH1-O	0.4	3.0	0.7	5.1	8.7	4.7	8.8	0.19	12.7	3.6
CH2-O	0.5	3.5	0.7	4.8	6.2	7.3	9.8	0.13	12.3	3.2
CH3-O	0.47	3.5	0.8	4.7	7.3	7.1	11.0	0.15	10.9	3.9
CH4-O	0.57	4.1	0.7	4.8	8.1	5.4	9.2	0.17	11.8	4.4
CH5-O	0.47	3.5	0.7	4.5	6.2	6.1	11.0	0.17	13.4	3.2
CH6-O	0.48	5.1	1.1	5.9	7.5	5.2	11.0	0.22	11.8	4.3
CH7-P	0.46	6.8	1.2	7	9.8	7.8	78.0	0.1	10.7	5.7
CR1-O	0.51	2.3	0.5	3.4	7.2	9.5	14.0	0.15	8.9	4.1
CR2-P	0.26	2.7	1.0	7.9	6.2	-9.5	7.0	-0.73	21.6	13.0
CR3-O	0.33	15.0	4.5	15	3.8	17.0	25.0	0.15	11.2	1.9
CR4-O	0.43	20.0	4.6	15.1	4.6	15.0	25.0	0.17	14.1	2.6
CR5-O	0.35	18.0	5.1	18	6.6	4.3	21.0	0.49	16.9	12.0
CR6-O	0.27	15.0	5.6	15.2	5.3	-3.9	16.0	-0.39	14.7	14.0
CR7-P	0.89	18.0	2.0	7.7	8.0	9.3	19.0	0.21	13.6	5.6
KM1-O	0.67	1.0	0.2	1	6.7	4.3	8.5	0.2	9	3.6
KM2-P	0.44	1.3	0.3	2.2	6.4	20.0	27.0	0.14	9.7	3.3
KM3-P	0.45	1.1	0.2	1.6	5.0	57.0	28.0	0.48	5.6	2.3
KM4-O	0.84	1.5	0.2	1.1	7.9	13.0	20.0	0.16	5.2	4.6
WC1-O	0.64	19.0	3.0	11.5	5.7	14.0	20.0	0.13	8.9	4.3
WC2-O	0.65	18.0	2.8	11	5.6	7.5	15.0	0.2	14.7	4.1
WC3-O	0.82	9.0	1.2	3.8	7.1	3.9	9.1	0.23	13.8	5.7

Table 5.5: Field-cooled (FC) and zero-field cooled ratios of magnetisation at 30 K/15 K and 300 K/50 K

Sample Name	30K/15K (ZFC)	300K/50K (ZFC)	30K/15K (FC)	300K/50K (FC)
BS1-P	0.08	0.18	0.11	0.15
BS2-P	0.27	0.15	0.28	0.13
BS3-P	0.11	0.21	0.12	0.19
BS4-P	0.04	0.22	0.06	0.20
BS5-P	0.17	0.12	0.14	0.11
BS6-P	0.1	0.28	0.09	0.27
BS7-P	0.06	0.17	0.09	0.15
BS8-P	0.06	0.16	0.06	0.17
BS9-O	0.1	0.15	0.12	0.14
BS10-P	0.10	0.15	0.08	0.12
COOMB1-O	0.42	0.15	0.42	0.14
COOMB2-O	0.5	0.09	0.48	0.1
COOMB3-O	0.27	0.15	0.29	0.14
COOMB4-O	0.25	0.05	0.29	0.06
MT1-O	0.55	0.12	0.56	0.11
MT2-P	0.29	0.09	0.30	0.10
MT3-O	0.51	0.13	0.5	0.12
MT4-O	0.51	0.13	0.5	0.12
ST1-P	0.20	0.16	0.22	0.13
ST2-P	0.48	0.10	0.50	0.10
ST3-O	0.22	0.29	0.23	0.27
ST4-O	0.64	0.12	0.37	0.12
WX1-O	0.65	0.17	0.64	0.17
WX2-O	0.35	0.12	0.41	0.11
WX3-O	0.48	0.09	0.46	0.09
CH1-O	0.39	0.18	0.38	0.13
CH2-O	0.41	0.17	0.45	0.10
CH3-O	0.34	0.18	0.37	0.14
CH4-O	0.28	0.24	0.30	0.21
CH5-O	0.27	0.20	0.37	0.12
CH6-O	0.26	0.25	0.27	0.20
CH7-P	0.21	0.28	0.21	0.24
CR1-O	0.54	0.22	0.29	0.19
CR2-P	0.27	0.28	0.06	0.11
CR3-O	0.28	0.16	0.28	0.14
CR4-O	0.26	0.11	0.30	0.10
CR5-O	0.24	0.11	0.14	0.11
CR6-O	0.18	0.15	0.05	0.13
CR7-P	0.19	0.13	0.19	0.12
KM1-O	0.62	0.31	0.48	0.26
KM2-P	0.7	0.43	0.67	0.38
KM3-P	0.72	0.56	0.66	0.47
KM4-O	0.73	0.23	0.69	0.11
WC1-O	0.18	0.15	0.13	0.13
WC2-O	0.18	0.13	0.13	0.12
WC3-O	0.21	0.15	0.10	0.13

Table 5.6: mean, standard deviation and median for the low- and room-temperature magnetic measurements carried on the core samples

	LT-M_s (Am2/kg)			LT-M_{rs} $\times10^{-3}$(Am2/kg)			LT-$M_{rs}/M_s\times10^{-2}$			LT-B_c (mT)			LT-$\chi\times10^{-7}$ (m3/kg)		
Sample	**mean**	**std dev**	**median**	**mean**	**std dev**	**median**	**mean**	**std dev**	**median**	**mean**	**std dev**	**median**	**mean**	**std dev**	**median**
Bushey Farm	0.5	0.2	0.5	9.1	5.0	7.2	2.3	1.3	1.9	6.8	4.5	6.3	6.9	3	6.2
Coombe Keynes	0.3	0.1	0.3	3.1	1.9	2.2	1.4	0.9	1.2	2.7	1.4	2.1	6.8	2.2	7.1
Martinstown	0.2	0.1	0.2	4	1.8	3.8	1.9	0.2	2	4.4	0.4	4.4	5.1	1	5.2
Stoborough	0.6	0.3	0.5	3.4	1.2	3.2	1.4	0.9	1.5	3.4	2	2.9	7.4	4	6.3
Waddock Cross	0.3	0.2	0.4	4.9	1	4.2	0.9	0.8	0.8	2.6	2.3	2.1	1.2	7.8	8.3
Chickerell	0.5	0.1	0.5	4.2	1.3	3.5	0.9	0.2	0.8	5.3	1.5	4.8	7.7	1.3	7.5
Creech	0.4	0.2	0.4	13	7.4	15	3.3	2.1	4.5	11.7	5.4	15	6	1.5	6.2
Kimmeridge 5	0.6	0.2	0.6	1.2	0.2	1.2	0.2	0.1	0.2	1.5	0.6	1.4	6	1.2	6.6
Wytch Farm A1	0.7	0.1	0.7	16	5	18	2.3	0.9	2.8	8.8	4.3	11	6	0.1	5.7

	RT-M_s $\times10^{-3}$ (Am2/kg)			RT-M_{rs} $\times10^{-4}$ (Am2/kg)			RT-$M_{rs}/M_s\times10^{-1}$			RT-B_c (mT)			RT-$\chi\times10^{-8}$ (m3/kg)		
Sample	**mean**	**std dev**	**median**	**mean**	**std dev**	**median**	**mean**	**std dev**	**median**	**mean**	**std dev**	**median**	**mean**	**std dev**	**median**
Bushey Farm	0.1	0.1	0.1	1.5	0.8	1.6	0.2	1.1	0.2	6.6	5	5.5	4.3	2.1	3.8
Coombe Keynes	2	2.6	0.1	1.2	0.7	1	0.2	1.2	0.1	5.2	1.9	4.3	4	1.5	4.28
Martinstown	1.8	1.2	1.3	3	2.1	13	0.2	1	0.2	7.5	3.1	6.3	3	0.8	3.2
Stoborough	2.5	1.9	2.3	2.4	1.3	2.3	0.5	3.7	0.5	4.5	2	4.5	4.6	3.1	3.7
Waddock Cross	3	2.2	2.1	3.2	1.8	2.7	0.6	4.1	0.9	4.8	2.8	6.3	7.3	5	4.8
Chickerell	0.1	0.01	0.1	2	2.6	1.1	0.2	0.4	0.2	12	0.9	11.8	3.8	0.5	3.8
Creech	0.1	0.1	0.1	1.8	0.6	1.9	0.01	4.2	0.2	14.4	4.1	14.1	7.6	5.2	5.6
Kimmeridge 5	2.4	2.3	1.7	2.1	0.9	2.4	0.3	1.6	0.2	7.4	2.3	7.3	3.5	1	3.5
Wytch Farm A1	0.1	0.1	0.1	1.5	0.6	1.5	0.2	0.5	0.2	12.5	3.1	13.8	4.7	0.9	4.3

Figure 5.26 shows the plots of LT- and RT-hysteresis parameters for the Wytch Farm (WC) samples, all of which were oil stained. WC1 had lower LT-M_s values of 0.64 Am^2/kg compared to WC2 and WC3 that had 0.65 and 0.82 Am^2/kg respectively (Fig. 5.26a and Table 5.4). This indicates an increase in LT-M_s values with depth. Conversely, RT-M_s show decreasing values with depth, with WC1, WC2 and WC3 having 1.44 $\times10^{-3}$, 7.5 $\times10^{-4}$ and 3.9 $\times10^{-4}$ Am^2/kg respectively (Fig. 5.26a and Table 5.4). Both the LT- and RT- χ_{hf} show increasing paramagnetic contribution with sampling depth, e.g., WC1 and WC2 have nearly identical LT χ_{hf} values of 5.7 $\times10^{-7}$ and 5.6 $\times10^{-7}$ m^3/kg respectively, while WC3 had a slightly higher paramagnetic contribution of 7.1 $\times10^{-7}$ m^3/kg (Fig. 5.26b). Similarly, the RT-χ_{hf} data indicate that WC1 and WC2 have similar values of 4.3 $\times10^{-8}$ and 4.13 $\times10^{-8}$ respectively (Fig. 5.26b and Table 5.4), with WC3 having slightly higher value of 5.7 $\times10^{-8}$ (Table 5.4).

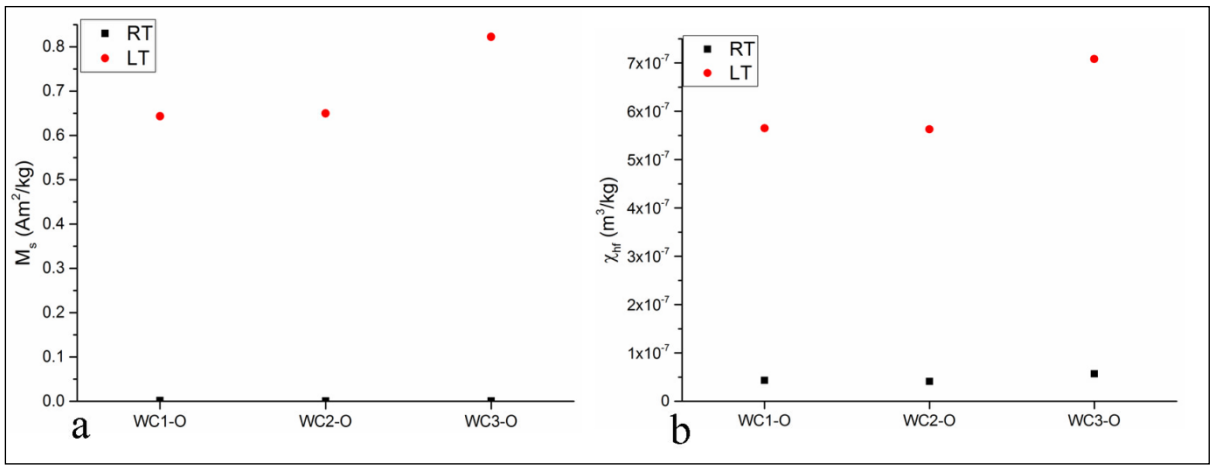


Figure 5.26: Waddock Cross: Plots of: a) LT- and RT-M_s values, showing increasing values for LT-M_s and decreasing values for RT-M_s with sampling depth. b) LT- and RT-χ_{hf} with WC1 and WC2 having about equal paramagnetic contributions and WC3 slightly higher contribution.

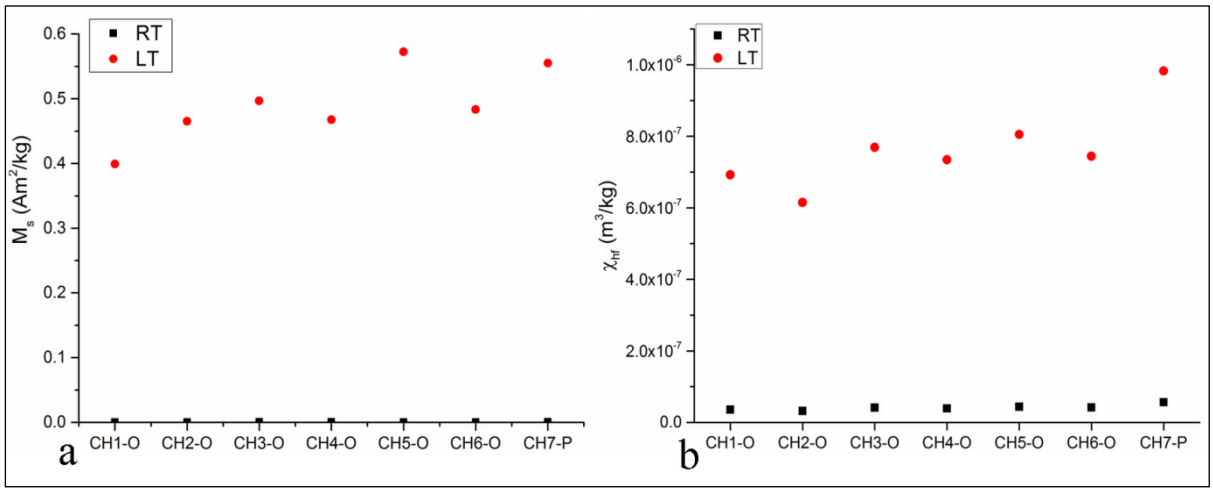


Figure 5.27: Chickerell: Plots of: a) LT- and RT-M_s, showing general increase in the LT-M_s values with depth of sampling, b) LT- and RT-χ_{hf} showing CH7 having the highest value.

The low- and room-temperature M_s data for the Chickerell (CH) data are shown in Figure 5.27a, with both datasets showing a slight increase with sampling depth (Table 5.4). In addition, LT- and RT-χ_{hf} plots are shown in Figure 5.27b, with the 'P' sample having the highest values (Fig. 5.27b and Table 5.4).

LT and RT-hysteresis parameters for the Stoborough (ST) samples are presented in Figure 5.28. No particular trend was observed in the LT-M_s data, e.g., ST1 and ST2 (both 'P') had 0.33 and 0.01 Am^2/kg respectively, while ST3 and ST4 (both 'O') had 0.23 and 0.70 Am^2/kg respectively (Fig. 5.28a and Table 5.4), with similar mixed trend in paramagnetic contribution observed based on the LT- and RT-χ_{hf} (Fig. 5.28b).

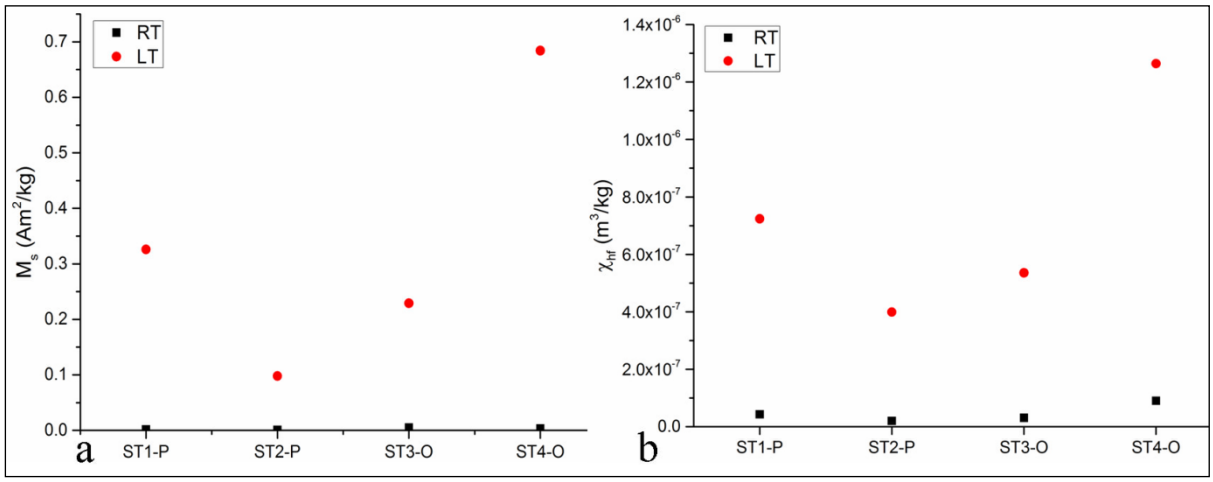


Figure 5.28:Stoborough: Plots of: a) LT- and RT-M_s,showing random variations, b)LT- and RT-χ_{hf}, showing no one particular trend in variations.

The sample WX2 from Waddock Cross (WX), had higher LT-$M_s$valuesthan WX1 and WX3 (Fig. 5.29a); however, the RT-M_s data shows a decrease in value with depth, e.g., WX1 had 5.9×10^{-3} Am^2/kg against 2.1×10^{-3} and 1.4×10^{-3} Am^2/kg for WX2 and WX3 respectively (Fig. 5.29b). WX2 had the highest LT- and RT-χ_{hf} values (Fig. 5.29b and Table 5.4). Both LT- and RT-M_s values for the Coombe Keynes (Coomb) samples vary randomly (Fig. 5.30a) with Coomb2 LT- and RT-χ_{hf} showing the lowest paramagnetic contribution (Fig. 5.30b).

Martinstown (MT) displayed no clear trend in the LT-M_s values between the 'P' and the 'O' samples (Fig. 5.31a). LT- and RT-χ_{hf} data show a slight decrease in value with depth although MT3 had higher values than MT2 (Fig. 5.31b).

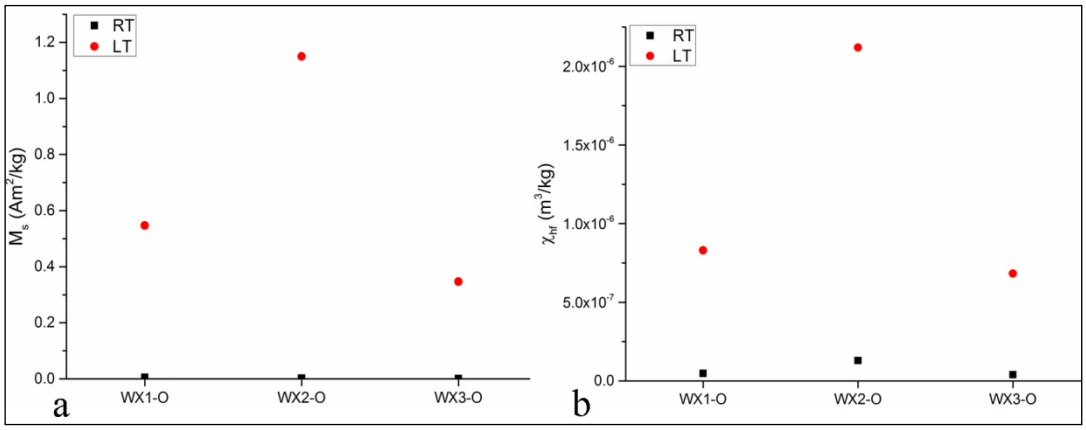


Figure 5.29: Wytch Farm: Plots of: a) LT- and RT-M_s showing WX2 having the value for the LT-M_s while decreasing with sampling depth for the RT-M_s, b) LT- and RT-χ_{hf}, showing WX2 having the largest paramagnetic contribution in both measurements.

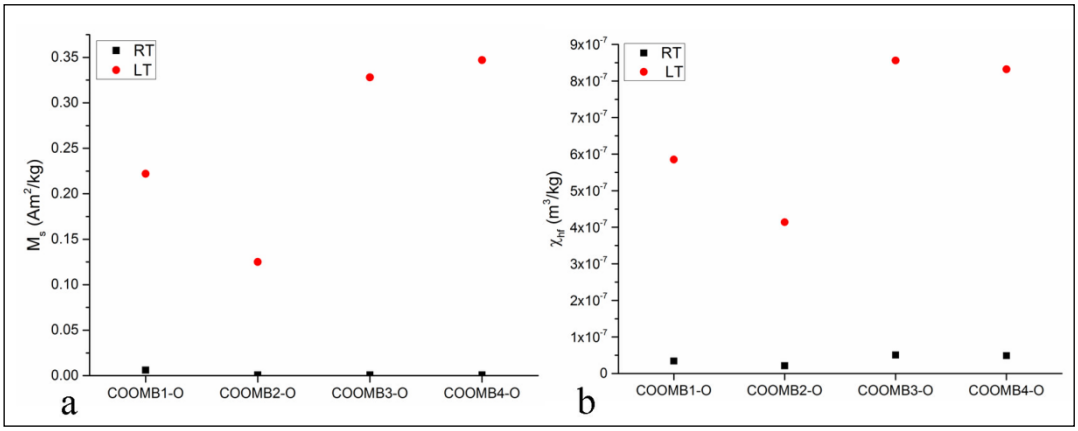


Figure 5.30: Coomb Keynes: Plots of: a) LT- and RT-$M_s$values, showing no variation with respect to depth of sampling, b) LT- and RT-χ_{hf} values showing no particular trend.

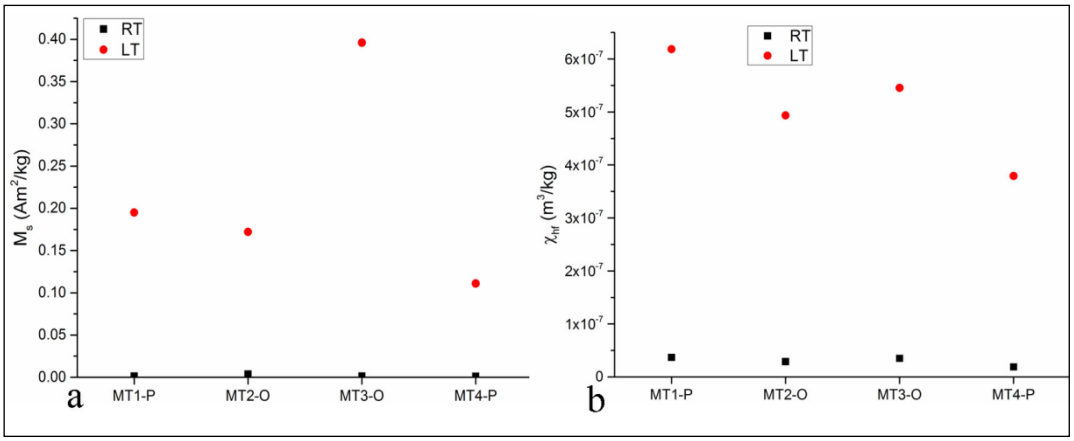


Figure 5.31: Martinstown: Plots of a) LT- and RT-M_s values, showing no clear trend in variation, b) LT- and RT-χ_{hf}, showing paramagnetic contribution generally decreasing with depth sampling, except for MT3.

Saturation remanence values for all the samples were compared to investigate for variation along possible hydrocarbon migration routes (see Chapter 4). Figure 5.32 shows LT-M_s values for all the samples, and well-average LT-M_s values are depicted in Figure 5.33. There is a mixed pattern in LT-M_s values from the Kimmeridge to Wytch Farm (Fig. 5.32). All the Creech samples, except for CR7, had lower LT-M_s values than Kimmeridge samples, while the Bushey

Farm samples mostly have higher LT-M_s values than the Kimmeridge samples (Fig.5.32). However, the Wytch Farm, the Waddock Cross and all the 'O' Stoborough samples had higher LT-M_s values than the Kimmeridge samples (Fig. 5.32).

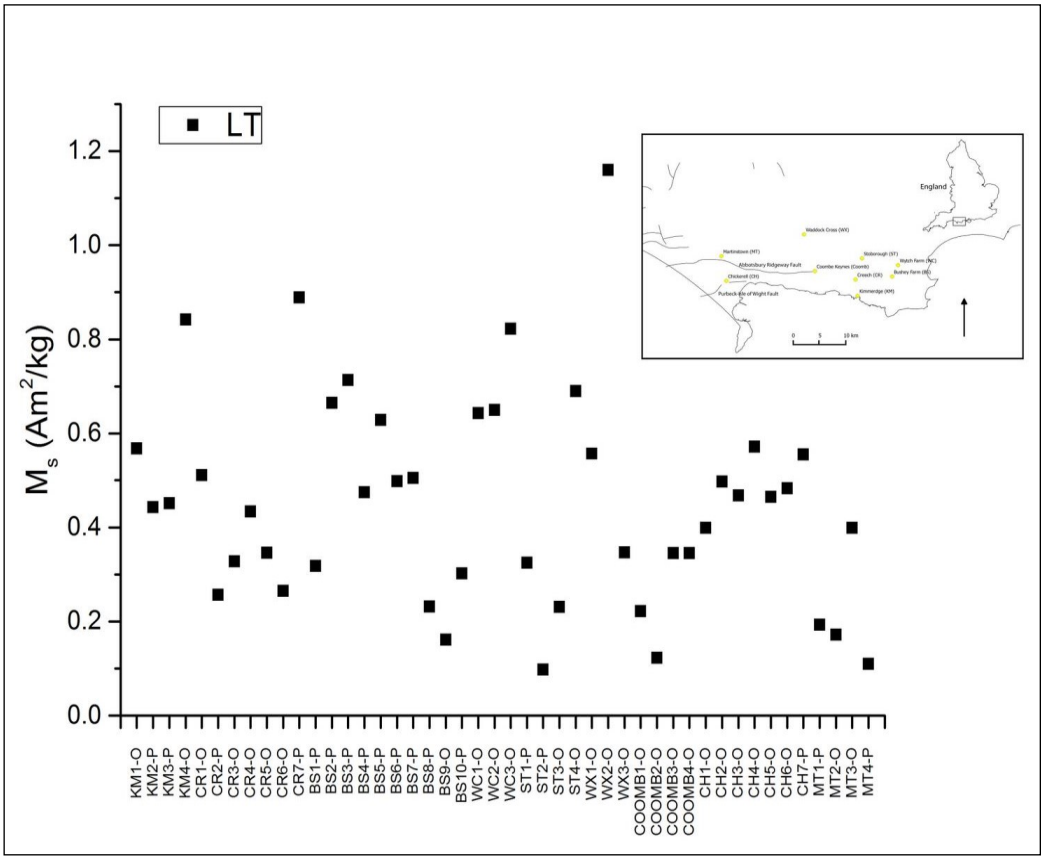


Figure 5.32: Plot of LT- showing variations across all the wells sampled.

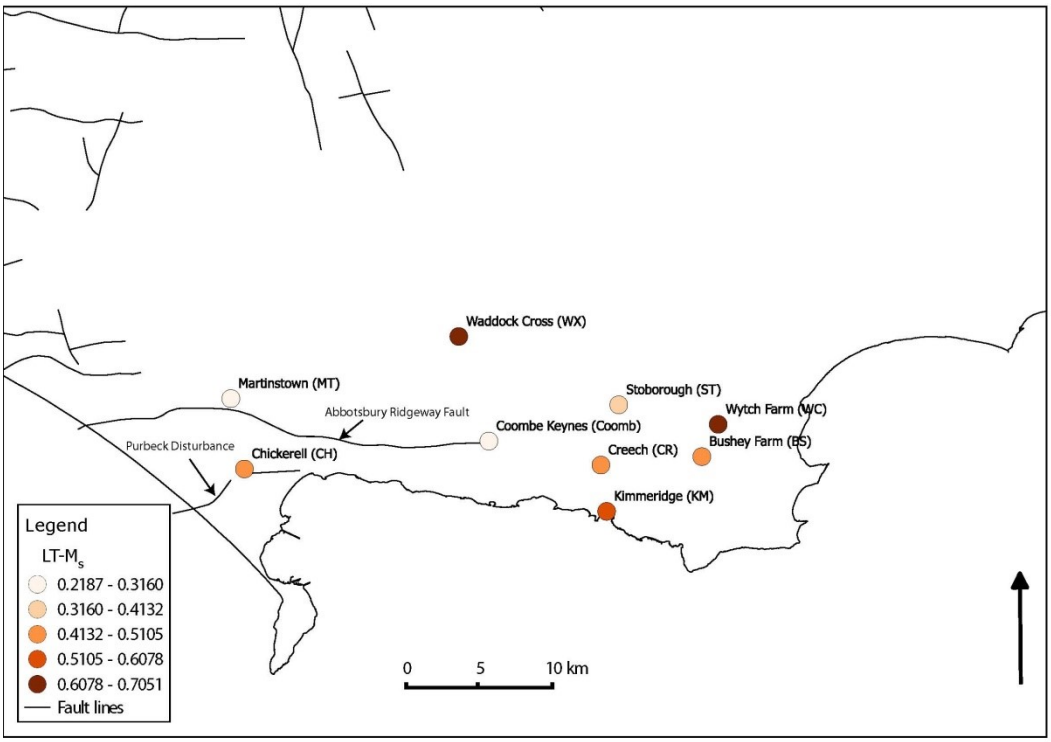


Figure 5.33: Plot of well LT-M_s average values, showing an increase well average from Kimmeridge to Wytch Farm and Waddock Cross, with Chickerell, Creech and Bushey Farm having similar averages. Legend units are Am^2/kg.

5.3.2 Magnetic mineral grain sizes and remanence carrying materials

Hysteresis parameters used to infer magnetic grain sizes such as coercivity (B_c) and the ratios of saturation remanence magnetisation to those of saturation magnetisation (M_{rs}/M_s) are discussed below.

RT-M_{rs} values for Kimmeridge5 (KM) samples show the 'P' samples have higher remanence than the O samples (M_{rs} is affected by abundance, mineralogy and grain-size), e.g., KM2 and KM3 have RT-M_{rs} values of 2.7 $\times 10^{-4}$ and 2.8 $\times 10^{-4}$ Am^2/kg respectively, whereas KM1 and KM4 had RT-M_{rs} values of 8.5 $\times 10^{-5}$ and 2.0 $\times 10^{-4}$ Am^2/kg respectively (Fig. 5.34a and Table 5.4). In contrast, the LT-M_{rs}/M_s showed opposite trend, with the 'O' samples having lower ratios than the 'P' samples (Table 5.4). Another grain-size parameter measured at both LT and RT was the coercivity (B_c) (Fig. 5.34b). In the LT-B_c measurement, the 'P' samples had higher values compared to their 'O' counterparts, for e.g., KM2 and KM3 had LT-B_c values of 2.2 and 1.6 mT respectively, whereas KM1 and KM4 had LT-B_c values of 1.0 and 1.1 mT respectively. However, the RT-B_c shows no clear trend (Fig. 5.334b). In addition, LT-M_{rs} for the Bushey Farm (BS) samples varied randomly with no clear trend (Fig. 5.35a), while the LT-M_{rs}/M_s and B_c data show that the intermediate samples (BS4-7) had lower values (Fig. 5.35b).

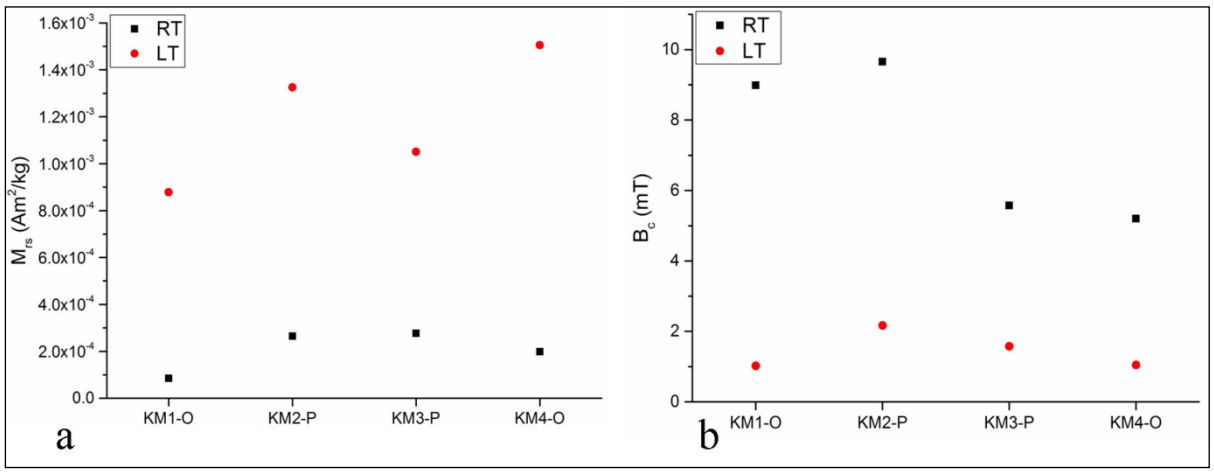


Figure 5.34: Kimmerdge: Plots of: a) LT and RT M_{rs}measurements, with 'O' samples having lower values than the 'P' samples in the RT measurement, b) lower Bc values for the 'O' samples in the LT measurement.

The LT-M_{rs} show mixed result for the Creech (CR) samples (Fig. 5.36): CR1 (O) was slightly lower than CR2 (P) with the other samples – including CR7 (P) - having as much higher LT-M_{rs} (Fig. 5.36a). The LT-B_c values for the 'O' samples were higher than for the 'P' samples, except for CR1. However, CR1 and CR2 sampled from the Inferior Oolite had lower remanence carrying materials and coercivity values compared to the rest of the Creech samples (Fig. 5.36 and Appendix 2.3).

Variation was also observed in the LT-M_{rs}/M_s, with all the 'P' samples having lower ratios than the 'O' samples (Fig. 5.36c and Table 5.4), but RT-M_{rs}/M_s show a random pattern, with CR2 and CR6 having negative ratios due to instrumental signal/noise ratios and no clear from among the rest of the samples (Fig. 5.36c). In addition both LT- and RT-M_{rs} data for the Wytch Farm (WC) samples show a decrease in remanence carrying materials with depth, e.g., WC1 had the highest LT-M_{rs} value with 1.9 $\times 10^{-2}$ Am^2/kg, followed by WC2 and WC3 with 1.8 $\times 10^{-2}$ Am^2/kg and 9.93 $\times 10^{-3}$ Am^2/kg respectively, while the RT-M_{rs} data show that WC1, WC2 and WC3 having 2.0 $\times 10^{-4}$, 1.5 $\times 10^{-4}$, and 9.1$\times 10^{-5}$ Am^2/kg respectively (Fig. 5.37a). LT-M_{rs}/M_s plots also show similar decreases in values with depth of sampling (Fig. 5.37c and Table 5.4), with RT- M_{rs}/M_s plots following an opposite trend of increasing ratios with depth (Fig. 5.37c and Table 5.4). However, no clear trend was observed in the RT-B_c data, but LT-B_c decreases with sampling depth, ranging from 3.8-11.5 mT (Fig. 5.37b and Table 5.4).

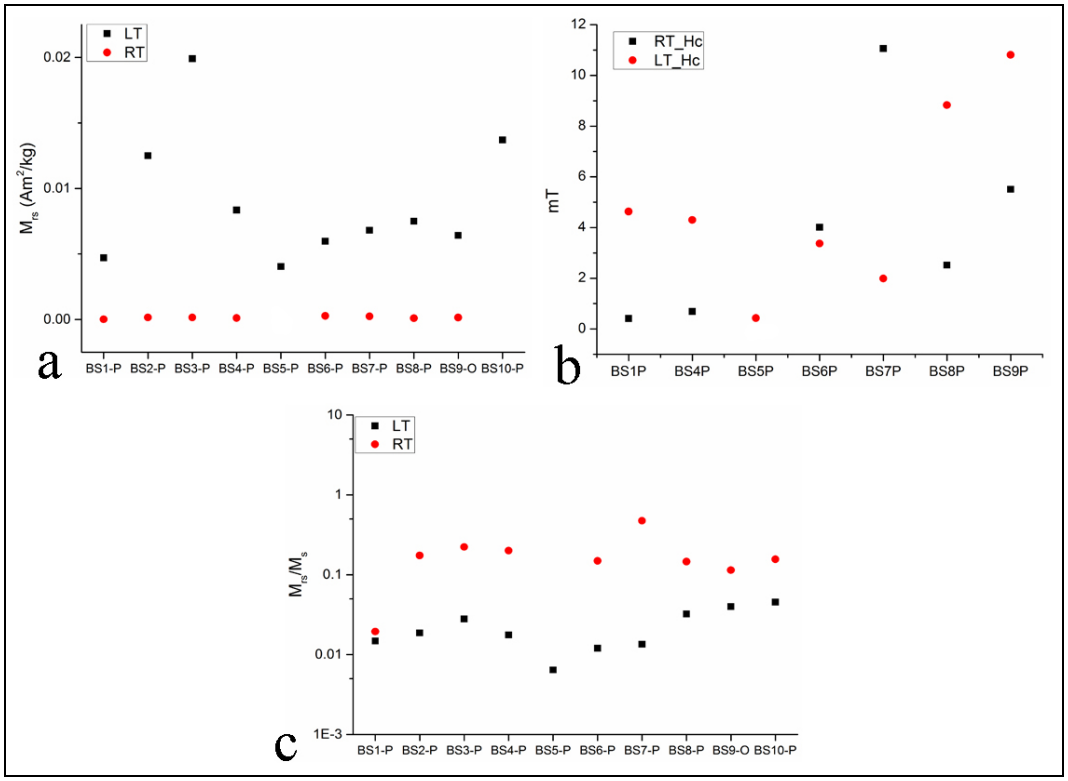


Figure 5.35: Bushey Farm: Plots of: a) LT and RT M_{rs} values showing no clear trend in variations, b) B_c showing no clear variation or trend, c) M_{rs}/M_s ratios, with no apparent differences between the 'P' and the 'O' samples. Note the absence of data for the BS5 sample in RT measurements. This was due to instrument error.

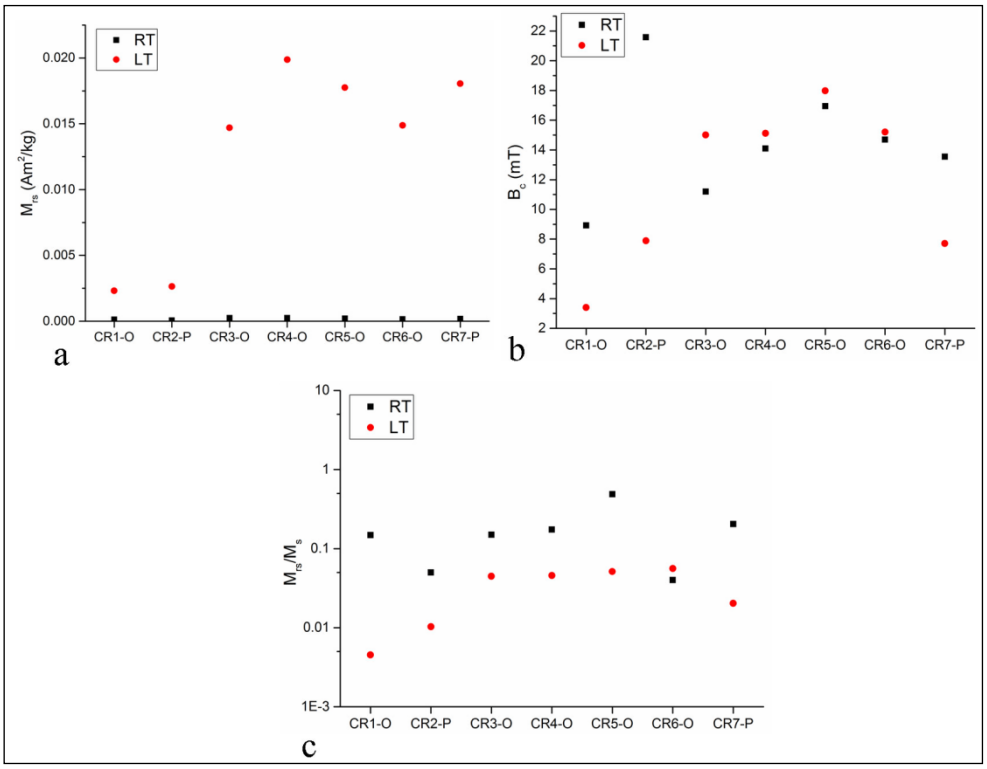


Figure 5.36: Creech: Plots of: a) LT-andRT-M_{rs} showing mixed results in LT-M_{rs} values with no clear trend. b) LT- and RT-B_c values with 'P' samples having lower LT-coercivity values than the 'O' samples except for CR1 and c) LT- and RT- M_{rs}/M_s with the 'P' samples having lower ratios in the LT-M_{rs}/M_s, CR2 and CR6 having negative ratios in the RT-M_{rs}/M_s due to low signal/noise ratios, with no apparent trend in the rest of the RT-M_{rs}/M_s ratios.

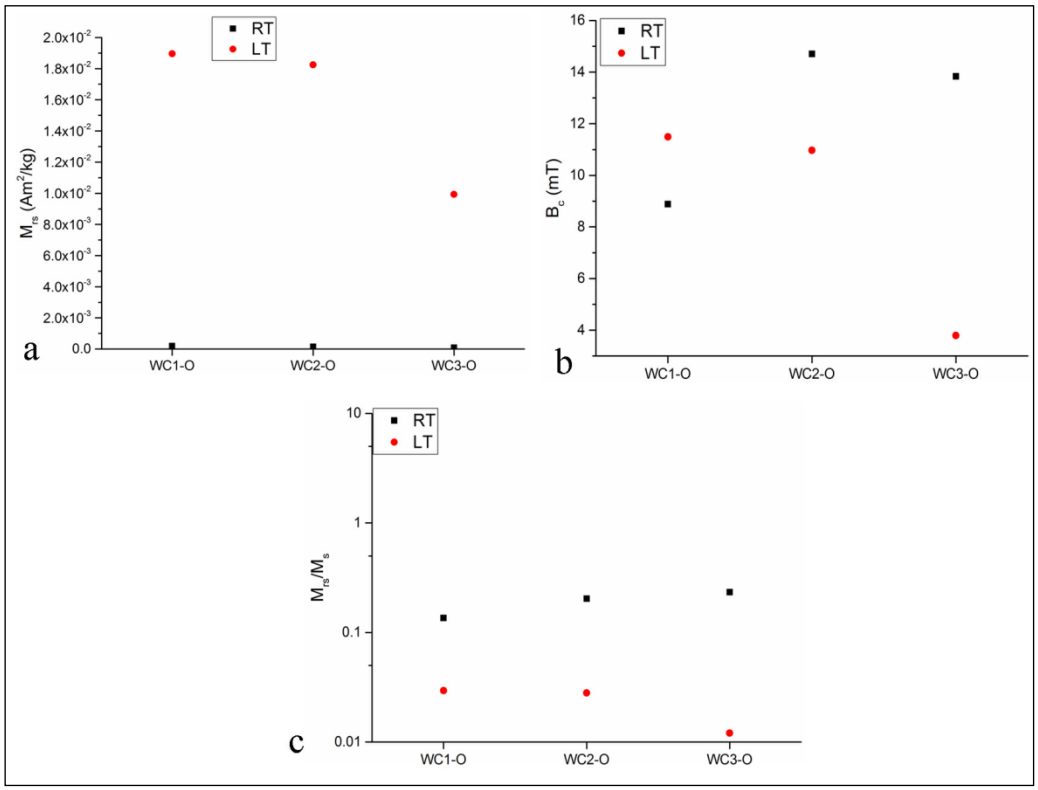


Figure 5.37: Wytch Farm: Plots of: a)LT- and RT-M_{rs} values showing decreasing values with sampling depth in both LT- and RT-M_{rs} values, b) LT- and RT-B_c values, showing decreasing trend in values with sampling depth in the LT-B_c and no clear trend in the RT-B_c, c) LT- and RT-M_{rs}/M_s showing decreasing values for LT-M_{rs}/M_s with increasing depth of sampling but increasing values for RT-M_{rs}/M_s with increasing sampling depth.

In contrast to Wytch Farm samples, the M_{rs} data from Chickerell (CH) showed an increase with depth, e.g., CH1, CH3 and CH7 had LT-M_{rs} values of 2.9 $\times 10^{-3}$, 3.5 $\times 10^{-3}$ and 6.78 $\times 10^{-3}$ Am^2/kg respectively; a similar trend was also observed in the RT-M_{rs} data (Fig. 5.38a and Table 5.4). The M_{rs}/M_s ratio also showed an increase with depth (Fig. 5.38c and Table 5.4). The LT -B_c values show a similar general increase in coercivity values with sampling depth, e.g., CH7 has the highest value of 7.0 mT, but the RT-B_c data did not show a clear trend (Fig. 5.38b and Table 5.4). Similarly, the LT- and RT-M_{rs} values for the Stoborough (ST) samples showed increases with oil staining. For example, ST3 and ST4 (the 'O' samples) had higher M_{rs} values than ST1 and ST2 (the 'P' samples) (Fig.5.39a). Figure 5.39b shows LT- and RT-B_c plots, it indicates increase in coercivity values with depth of sampling from ST1-ST3, but it decreases at ST4. Similar trend was observed in the LT- and RT-M_{rs}/M_s (Fig. 5.39c).

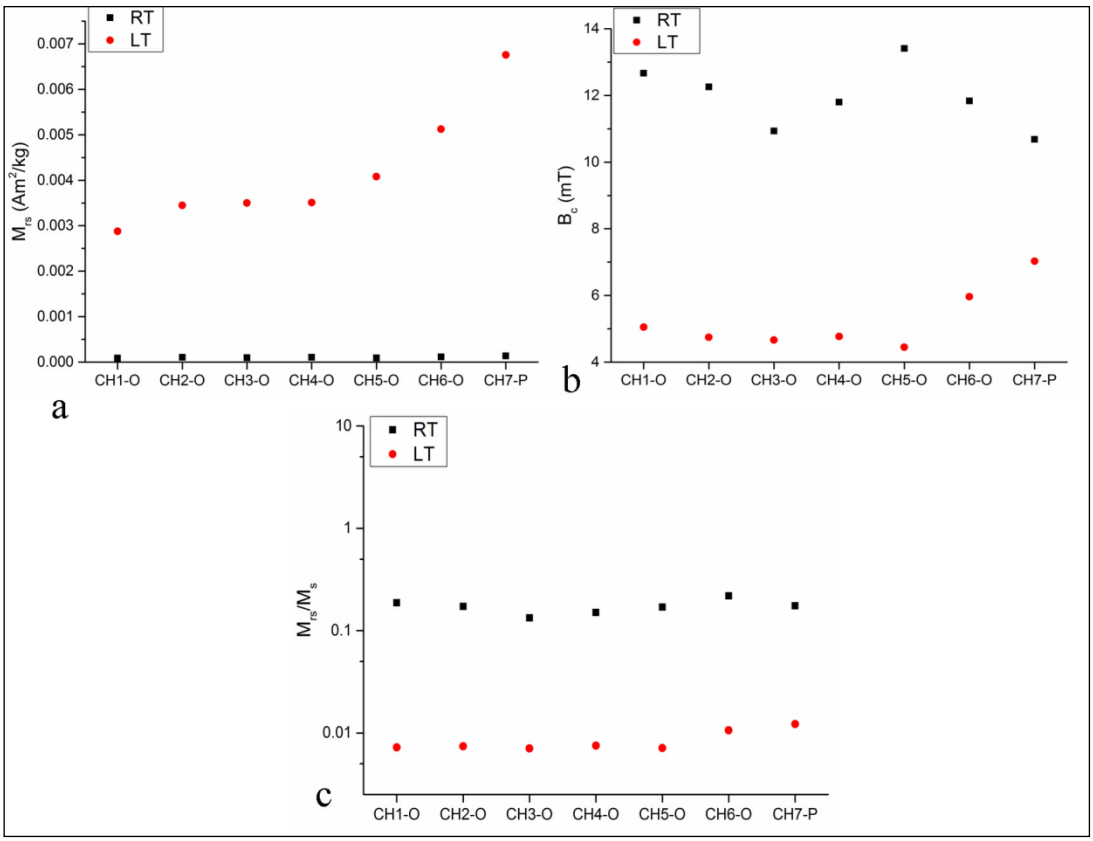


Figure 5.38: Chickerell: Plots of: a) LT- and RT-M_{rs}, showing CH7 having highest value in both cases, b) LT- and RT-B_c values showing no particular pattern, with CH7 having highest and lowest values in the LT- and RT-B_c respectively, c)LT- and RT-M_{rs}/M_s with CH7 having the highest value.

There is no clear pattern in the Waddock Cross (WX) samples' M_{rs} values (Fig. 5.40); e.g., both LT- and RT-M_{rs} show similar variations, with WX2 having the lowest value, but no depth related variations (Fig. 5.40a). In both LT- and RT-M_{rs}/M_s and B_c, WX2 again had the lowest values (Figs. 5.40b and c). The M_{rs}, B_c, M_{rs}/M_s data for the Coombe Keynes1 (Coomb) is shown in Figure 5.41. The grain-size dependent low-temperature data, i.e., LT-LT-M_{rs}/M_s and

LT-B_c, show a clear decrease with sampling depth; RT-B_c shows the opposite behaviour, however, the other data sets do not display a clear trend. (Fig. 5.41 and Table 5.4).

Data from Martinstown1 (MT) indicate that both the LT- and RT-M_{rs} showed no variation between the 'O' and the 'P' samples or with respect to sampling depth (Fig. 5.42a). However, RT-M_{rs}/M_s show a general decrease with depth (Fig. 5.42c).

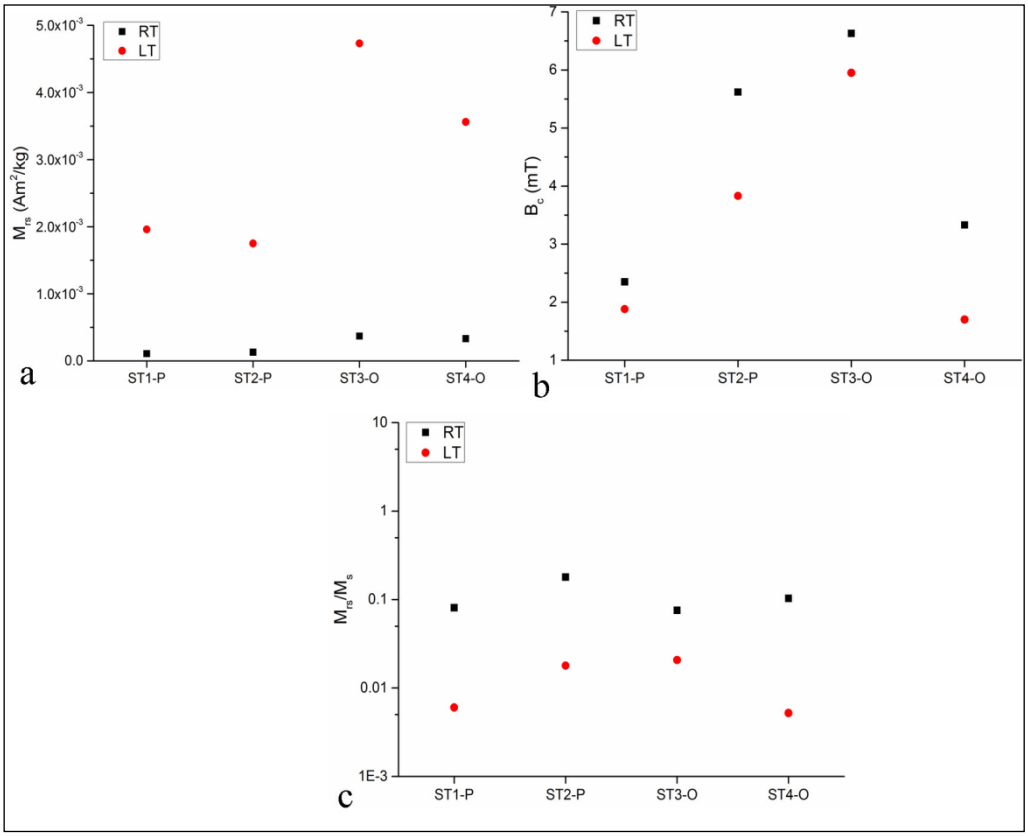


Figure 5.39: Stoborough:Plots of: a) LT- and RT-M_{rs}, with 'O' samples having higher M_{rs} values than their 'P' counterparts, b) LT- and RT-B_c, showing increase in B_c values for both measurements from ST1-ST3, with a decrease observed in ST4, c) LT- and RT-M_{rs}/M_s, with no one particular trend in both measurements.

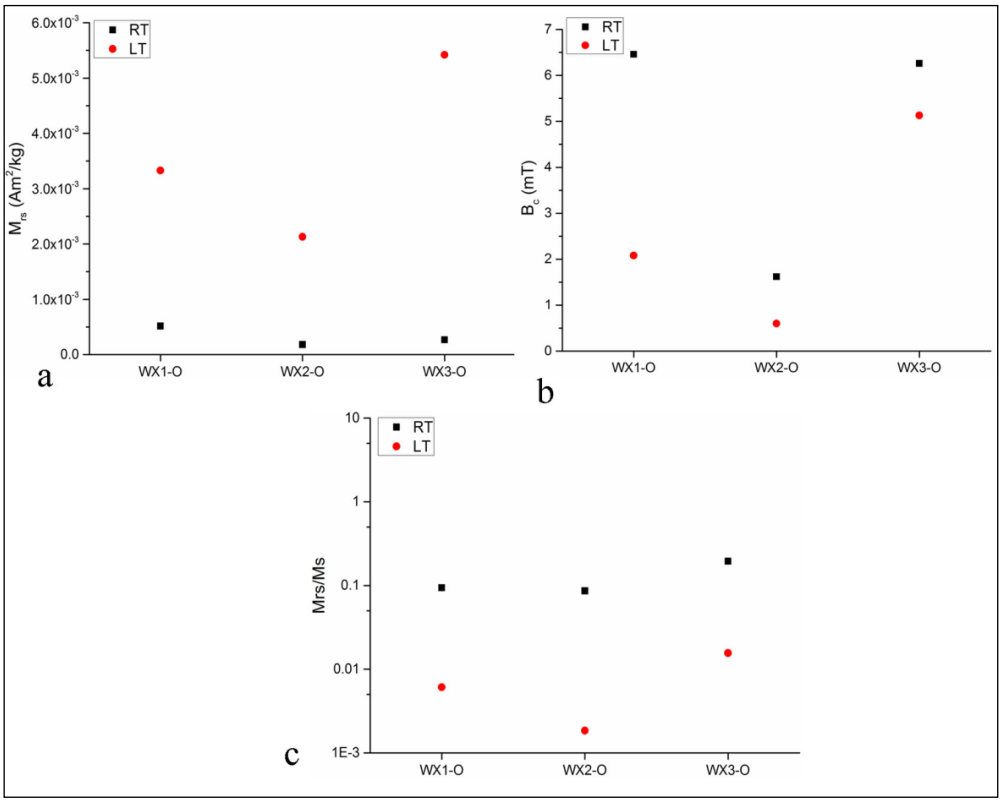


Figure 5.40: Waddock Cross: Plots of: a) LT- and RT-M_{rs}values, with WX2 having the lowest value in both measurements, b) LT- and RT-B_c with WX2 having the lowest coercivity values in both measurements, c) LT- and RT-M_{rs}/M_s ratios, with WX2 again having the lowest value.

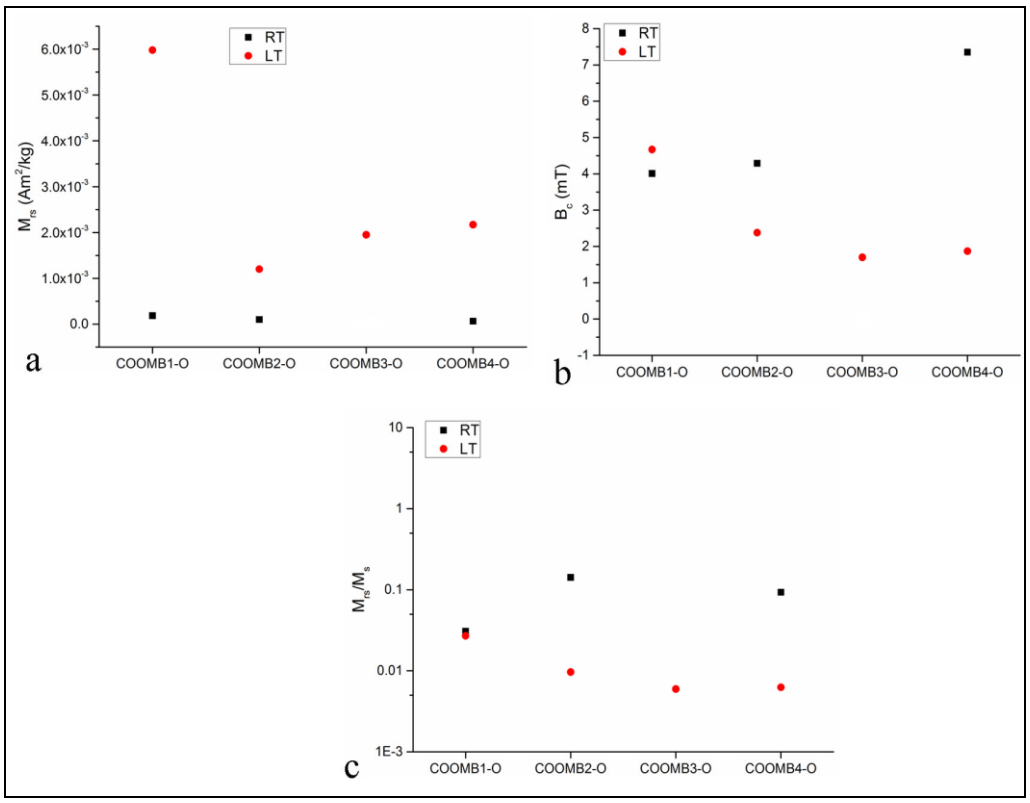


Figure 5.41: Coombe Keynes: Plots of: a) LT- and RT-M_{rs} values, the samples had near identical values in each of the measurements except for Coomb1 LT-M_{rs}, which is anomalously high, b) LT- and RT-B_c values, showing a general decrease in values with depth in the LT-M_{rs} but no particular trend in the RT-M_{rs}, c) LT- and RT-M_{rs}/M_s values showing a general decrease in value with sampling depth in the LT-M_{rs} values and no particular trend in the RT-M_{rs}. Note the absence of RT Coomb3 data. This was due to instrument error.

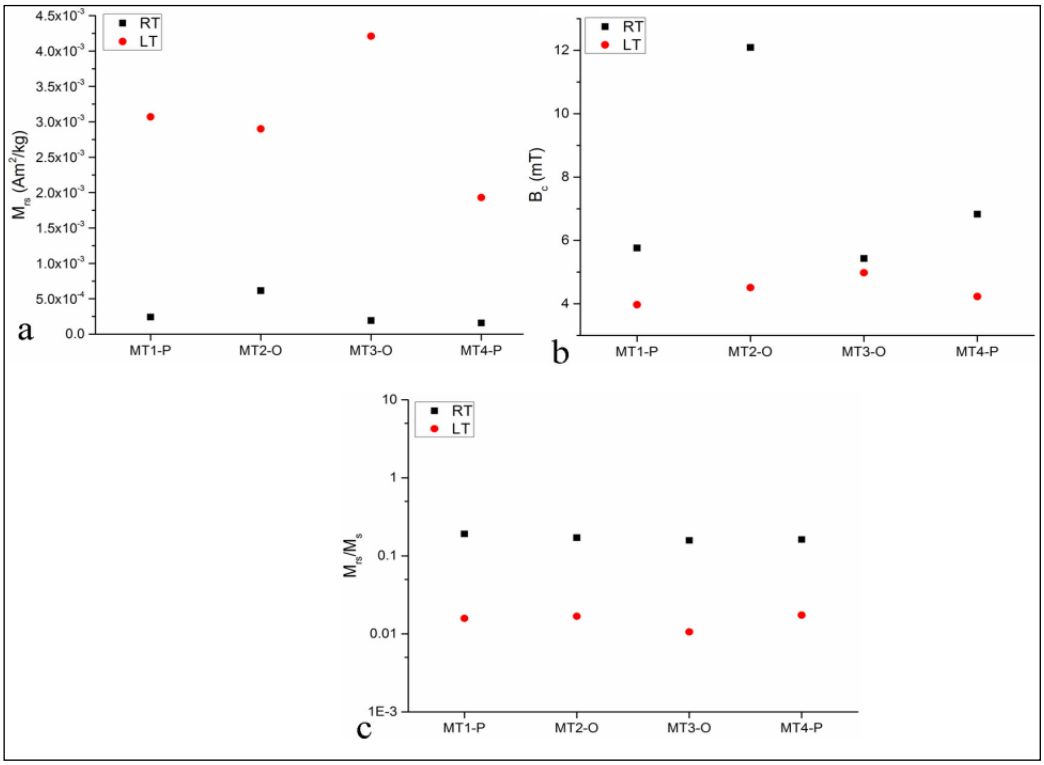


Figure 5.42: Martinstown: Plots of a) LT- and RT-M_{rs} values, showing MT2 having the highest value in the RT-M_{rs} value and no clear trend in the RT-M_{rs} values, b) LT- and RT-B_c values, with MT2 having the highest RT-B_c, c) LT- and RT-M_{rs}/M_s values, showing a general decrease in the RT-M_{rs}/M_s values with depth of sampling and MT2 having a higher LT-M_{rs}/M_s value.

LT-M_{rs} increased for all the samples from Kimmeridge to Wytch Farm through Bushey Farm and Creech (Fig.5.43), with Waddock Cross having higher average values (Table 5.6) than wells north of the Abbotsbury Ridgeway fault (Fig. 5.44).

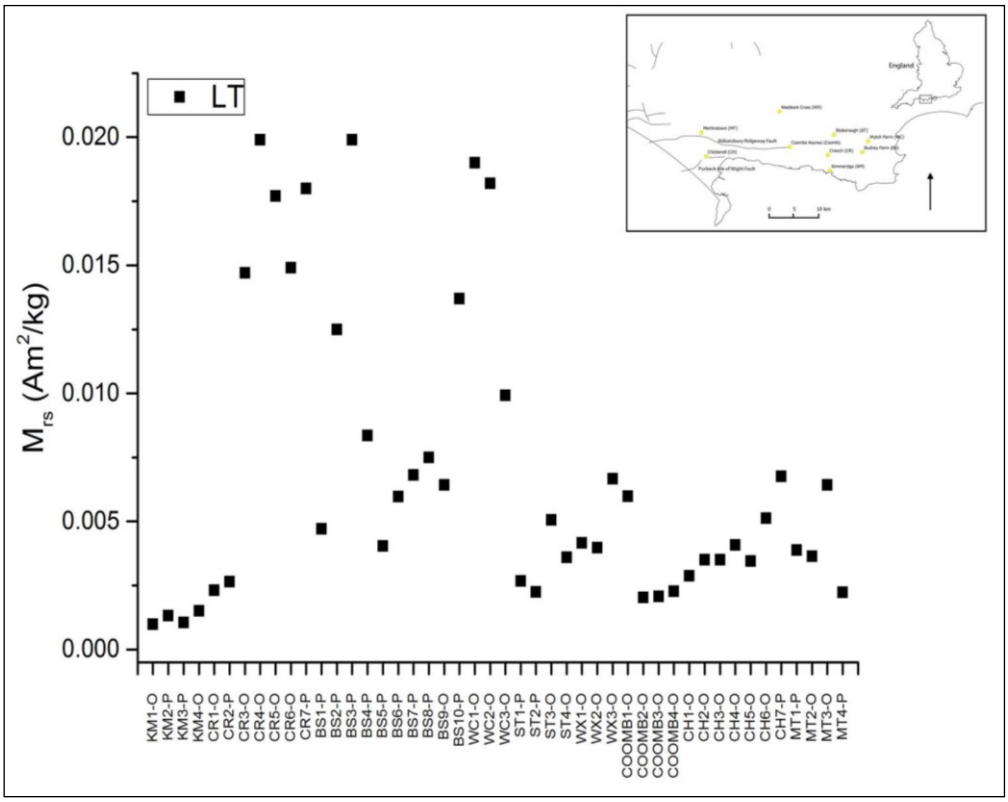


Figure 5.43: Plot of LT-M_{rs} for samples showing increase in values from Kimmeridge to Wytch Farm.

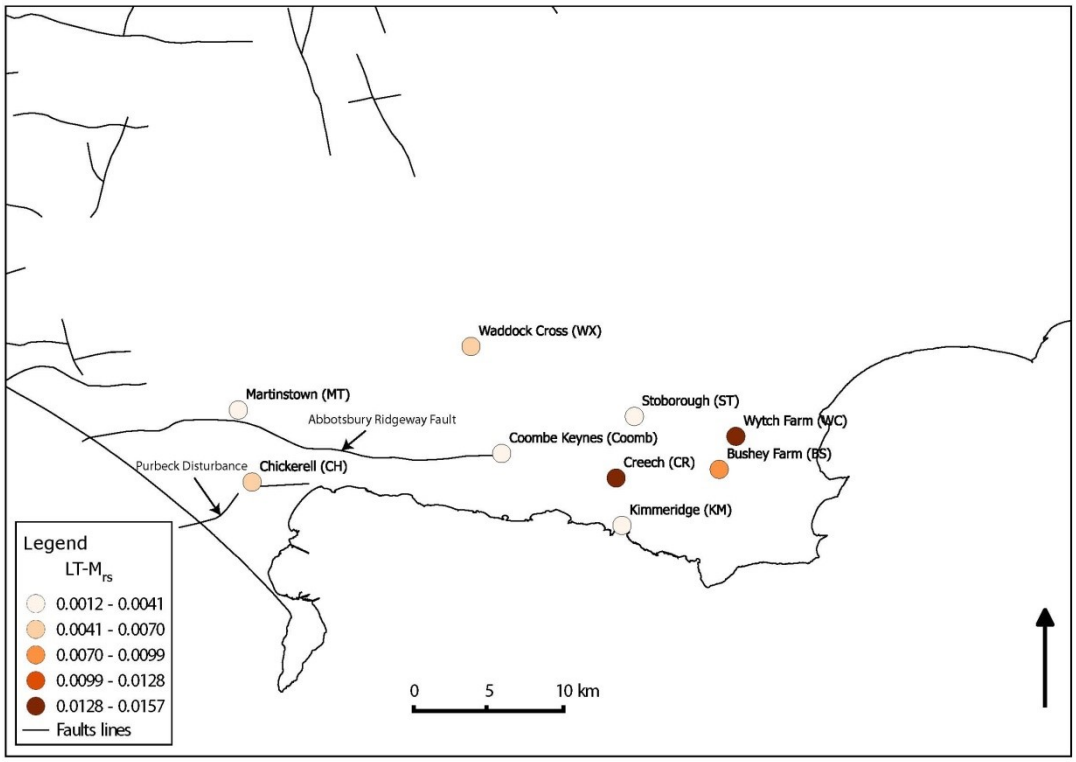


Figure 5.44: Plot of wells average LT-M_{rs} values, showing an increase from KM to WC through BS. Legend units are Am^2/kg.

Figure 5.45 shows plots of LT- and RT-M_{rs}/M_s ratios. Although Kimmeridge samples had the lowest LT-M_{rs}/M_s ratios (Fig. 5.45a) and CR had the highest; there was no clear trend (see Appendix 2.2). For most samples, the RT-M_{rs}/M_s ratio was ~ 0.2 (Fig. 5.45b). The LT-B_c values were lowest for Kimmeridge, but the RT-B_c values showed no clear trend (Fig. 5.46).

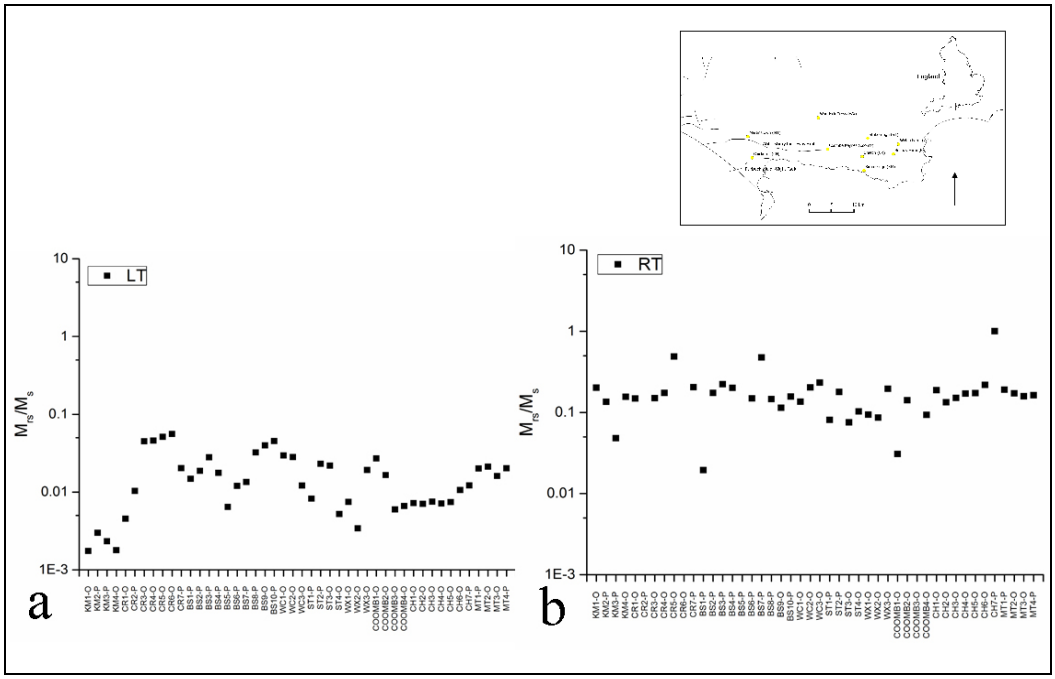


Figure 5.45: Plots of a) LT-M_{rs}/M_sshowing mixed relationship with 'O' samples and b) RT-M_{rs}/M_s nearly all samples had the same value.

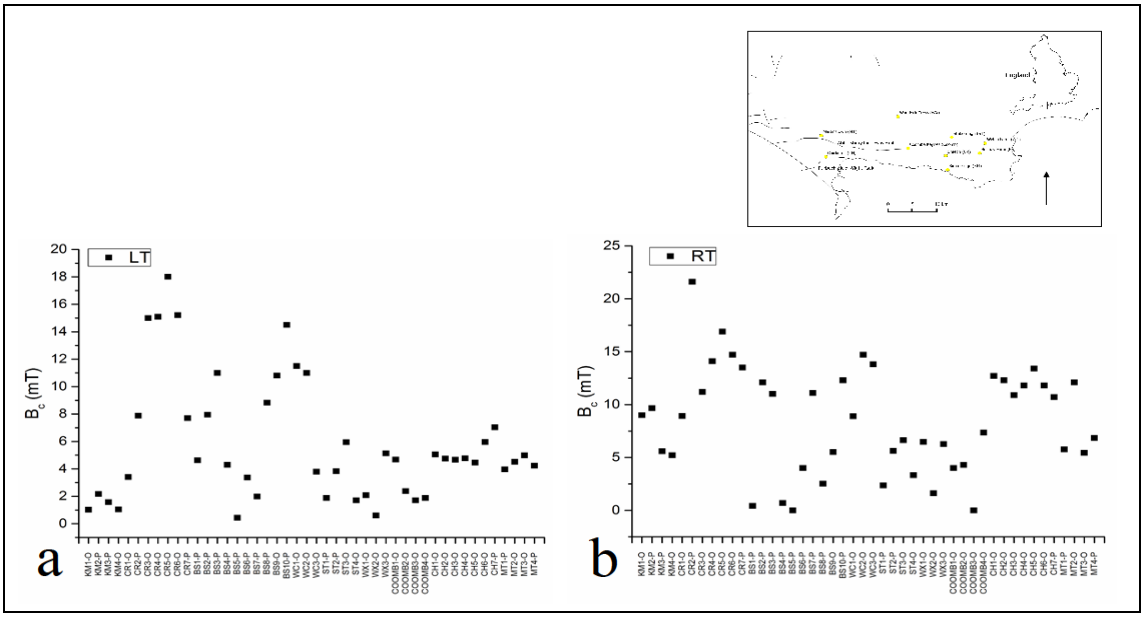


Figure 5.46: Plots of: a) LT-B_c, and b) RT-B_c values showing no clear trend in variations. Inset map shows the localities.

5.3.3 Determination of the magnetic mineralogy and grain size

Zero-field (ZFC) and field-cooled (FC) warming experiments were carried out to in order to investigate contributions from superparamagnetic and paramagnetic minerals and also to look

out for crystallographic transitions, such as Verwey Transition, which occurs ~120 K and is indicative of magnetite (Muxworthy and McClelland, 2000) and Besnus Transition, which occurs ~34 K and it is indicative of pyrrhotite (Besnus and Meyer, 1964). In addition, the ZFC-FC data were reduced and quantified, by taking two ratios of magnetisation: 1) 30 K divided by that at 15 K (30 K/15 K) to look at the presence of 'fine' ferromagnetic particles (~5-15 nm) and 2) at 300 K divided by 50 K (300 K/50 K) to look at the presence of 'larger' ferromagnetic particles (~ <30 nm). Although the 30 K/15 K data could be influenced not only by the abundance of superparamagnetic minerals, but also room-temperature paramagnetic minerals that become ferromagnetic at low temperatures.

All the Kimmeridge5 (KM) ZFC data had evidence for a Verwey transition in them in addition to a sharp decrease in magnetization observed in the range 10-30 K on warming (Fig. 5.47). This drop could be either due to unblocking and/or low-temperature Curie-temperature minerals. Figures 5.48 show the ZFC_FC ratios for the Kimmeridge5 samples, with no one particular trend either with respect to oil staining or sampling depth observed. However, the ZFC and FC warming curves for the Bushey Farm samples exhibit Besnus Transition, which is indicative of pyrrhotite (Fig. 5.49).

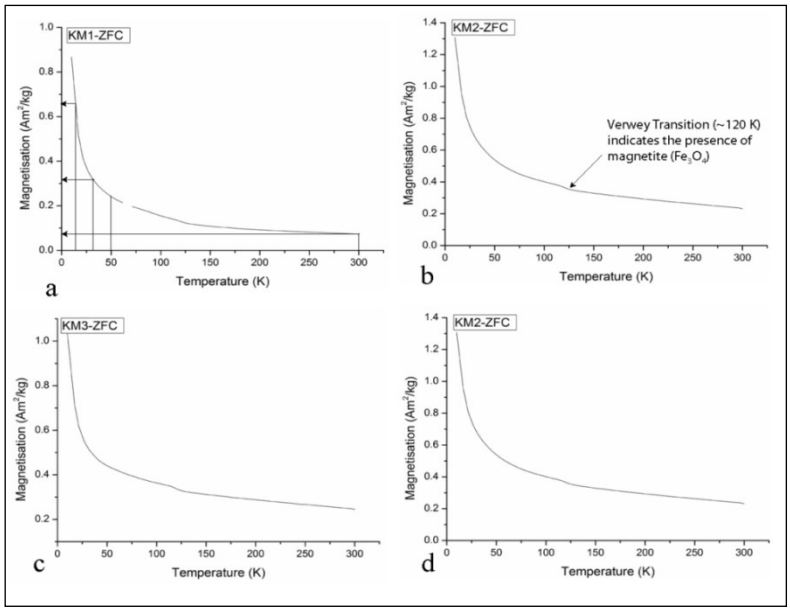


Figure 5.47: Kimmeridge: ZFC warming curves plot showing: a) KM1 with arrows showing magnetisations at 15, 30, 50 and 300 K whose ratios were used in this study to investigate the abundance of fine (<30 nm) and very fine (5-15 nm) ferromagnetic particles, b) KM2 showing higher magnetisation than KM1 with what appears to be a Verwey Transition at ~120 K, indicating the presence of magnetite in the sample, c) KM3 showing similar magnetisation to KM2 and possible Verwey Transition, d) KM4 showing a sharp drop in magnetisation around 120 K, which is indicative of magnetite.

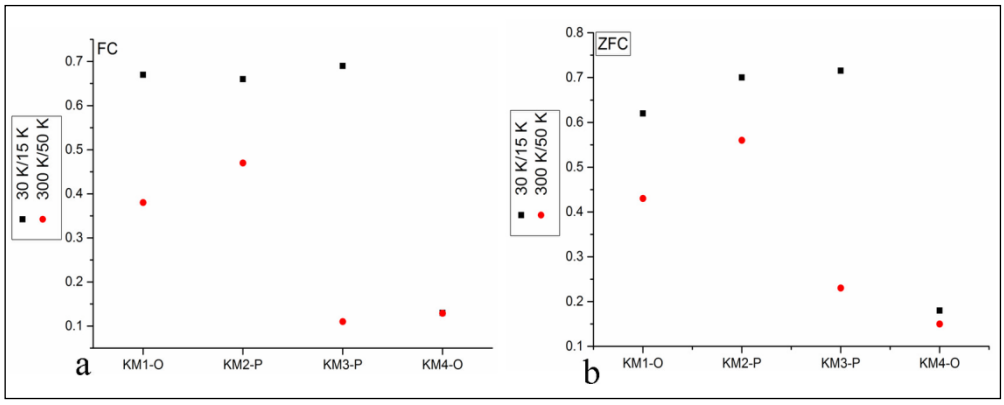


Figure 5.48: Kimmeridge: Plots of: and b) ratios of ZFC-FC LT-SIRM measurements showing the hyperfine magnetic ferromagnetic particles (30 K/15 K) showing no particular trend in variation and a decrease in 'larger' ferromagnetic particles (300 K/50 K) from KM1 to KM3 and then increasing again at KM4.

The ZFC-FC warming curves for the Creech1 (CR) and Wytch Farm (WC) samples are shown in Figures 5.50 and 5.51 respectively. No crystallographic transition was observed in any of the samples, this is possibly due to the absence of the magnetite or pyrrhotite, but could also be because the magnetic minerals present are too fine (Dekkers, 1989). The 'O' Creech samples' ZFC-FC 300 K/50 K ratios mostly have a higher concentration of the 'large' ferromagnetic particles than the 'P' samples (Table 5.5); there was no such distinction among the Wytch Farm samples as they are all oil stained. In contrast, ZFC-FC warming curves for the Chickerell1 (CH) samples exhibit a subtle Verwey Transition (Appendix 2.2) with the 'O' samples having a higher concentration of the 'large' ferromagnetic particles than the 'P' sample (Table 5.5).

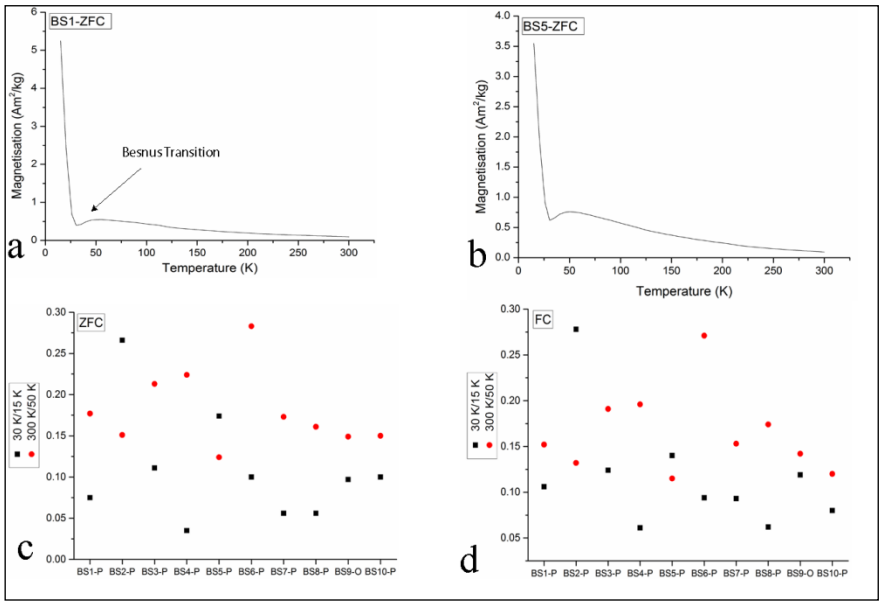


Figure 5.49: Bushey Farm: Plots of a & b) ZFC warming curves showing pyrrhotite as the dominant magnetic phase and c&d) ratios of ZFC and FC (30 K/ 15 K and 300 K/50 K).

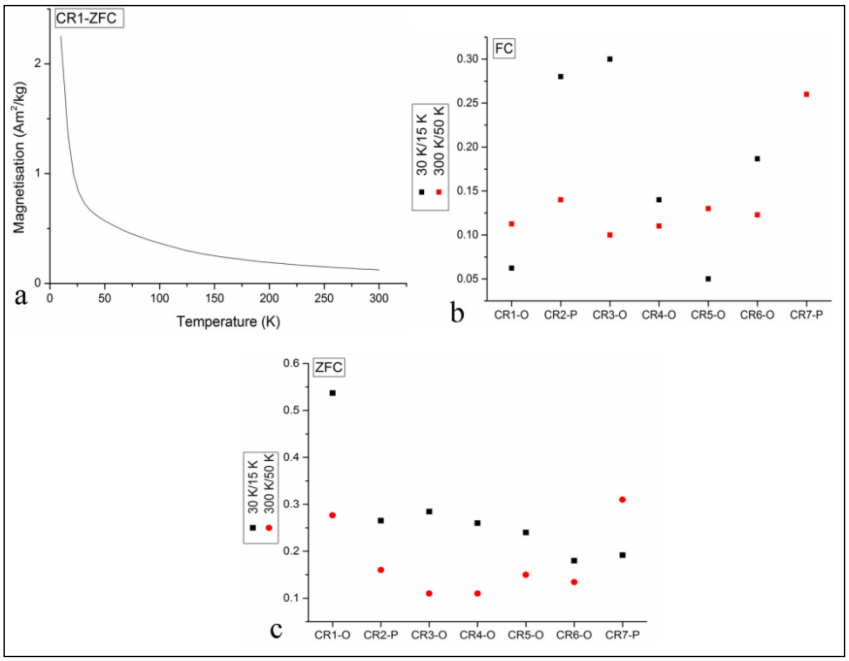


Figure 5.50: Creech: Plots of: a) ZFC warming curves for CR1, and b &c) ratios of FC and ZFC warming curves showing variation in amounts of 'large' grains with sampling depth and oil staining.

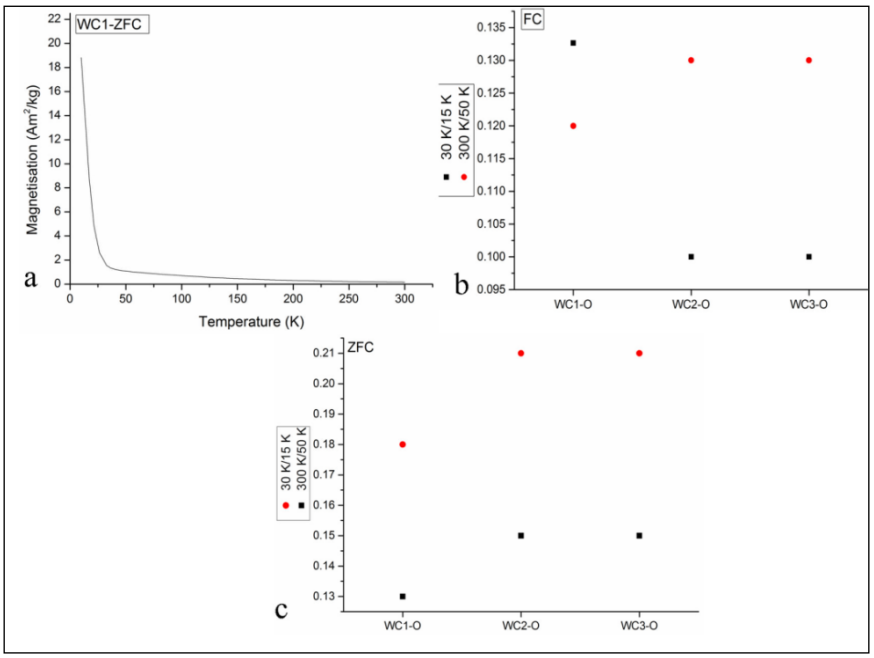


Figure 5.51: Wytch Farm: Plots of: a) ZFC warming curve for WC1, and b) & c) ratios of FC and ZFC warming curves showing variation in amounts of small/paramagnetic particles decreasing from WC1 to WC2 and increasing in WC3 in the FC curves (b).

ZFC data for Stoborough (ST), Waddock Cross (WX) Coombe Keynes (Coomb) and Martinstown (MT) all had double crystallographic transitions, i.e., Besnus and Verwey transitions (Fig. 5.52); this indicates these samples have both pyrrhotite and magnetite present in them.

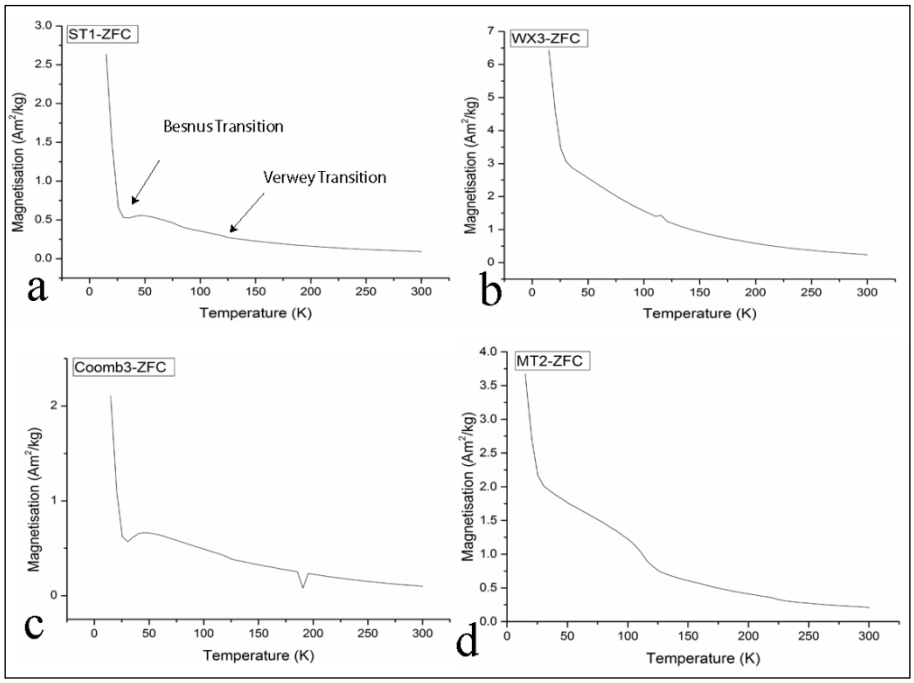


Figure 5.52: Plots of ZFC warming curve for Stoborough (ST), Waddock Cross (WX), Coombe Keynes (Coomb) and Martinstown (MT) all showing double crystallographic transitions (Besnus and Verwey) confirming the presence of pyrrhotite and magnetite in the samples. The kink at ~190 K in c) is most likely an instrument error.

The FC and ZFC 30 K/15 K ratios showed an increase from Kimmeridge to Wytch Farm, through Creech and Bushey Farm (Fig. 5.53a & b), and the ratios increased again from Stoborough. The ratios then gradually decrease through Waddock Cross, Coombe Keynes, Chickerell to Martinstown (Figs. 5.53a & b). The 300 K/50 K ratios in both the FC and ZFC did not show many consistent variations, though the Kimmeridge samples consistently had higher ratios indicating an abundance of nanoparticles less than ~30 nm (Figs. 5.53c & d).

Low-field volume susceptibility (pseudo-κ) measurements were carried out on core sections of seven from nine wells. It is referred to as 'pseudo-κ' because the volume was not very well constrained during the measurements; this was due to the nature of the core samples. The automated core logger described in Chapter 2 had a technical fault on my first visit to the BGS core store; all measurements record for Bushey Farm and Creech Samples were done manually. As a result, I sampled Kimmeridge and Chickerell without running them through the Bartington susceptibility meter. On my second visit however, the automation mechanism has been fixed and I was able to measure and sample give wells; this brings the total of measured wells to seven. Pseudo-κ values for the sampled intervals are presented here in Figure 5.54, with gaps at Kimmeridge and Chickerell positions. Continuous volume susceptibility (pseudo-κ) readings are included in Appendix 2.3. There was an increase in κ values of the Creech samples from 'P' to 'O' samples, similarly, the same trend was observed in both the Martinstown and the Stoborough samples, with the 'O' marked samples having higher κ values (Fig. 5.54). The

Bushey Farm samples – which were all poorly stained, with the exception of BS9 (Table 5.1) –had the lowest overall κ values (Fig. 5.54).

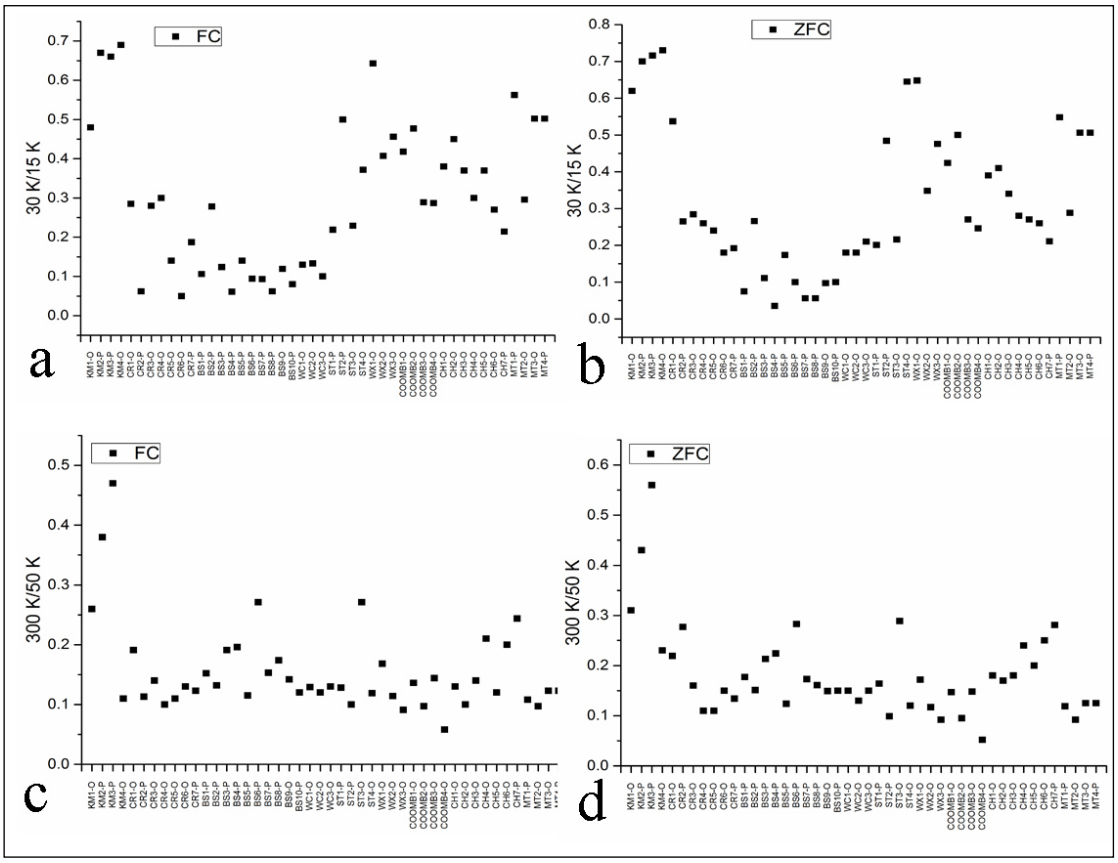


Figure 5.53: Plots of: a & b) 30 K/15 K FC and ZFC, values indicating two likely cycles of decrease in amounts of fine ferromagnetic particles from Kimmeridge to Wytch Farm and from Stoborough to Martinstown, c & d) 300 K/50 K FC and ZFC values showing no clear trend.

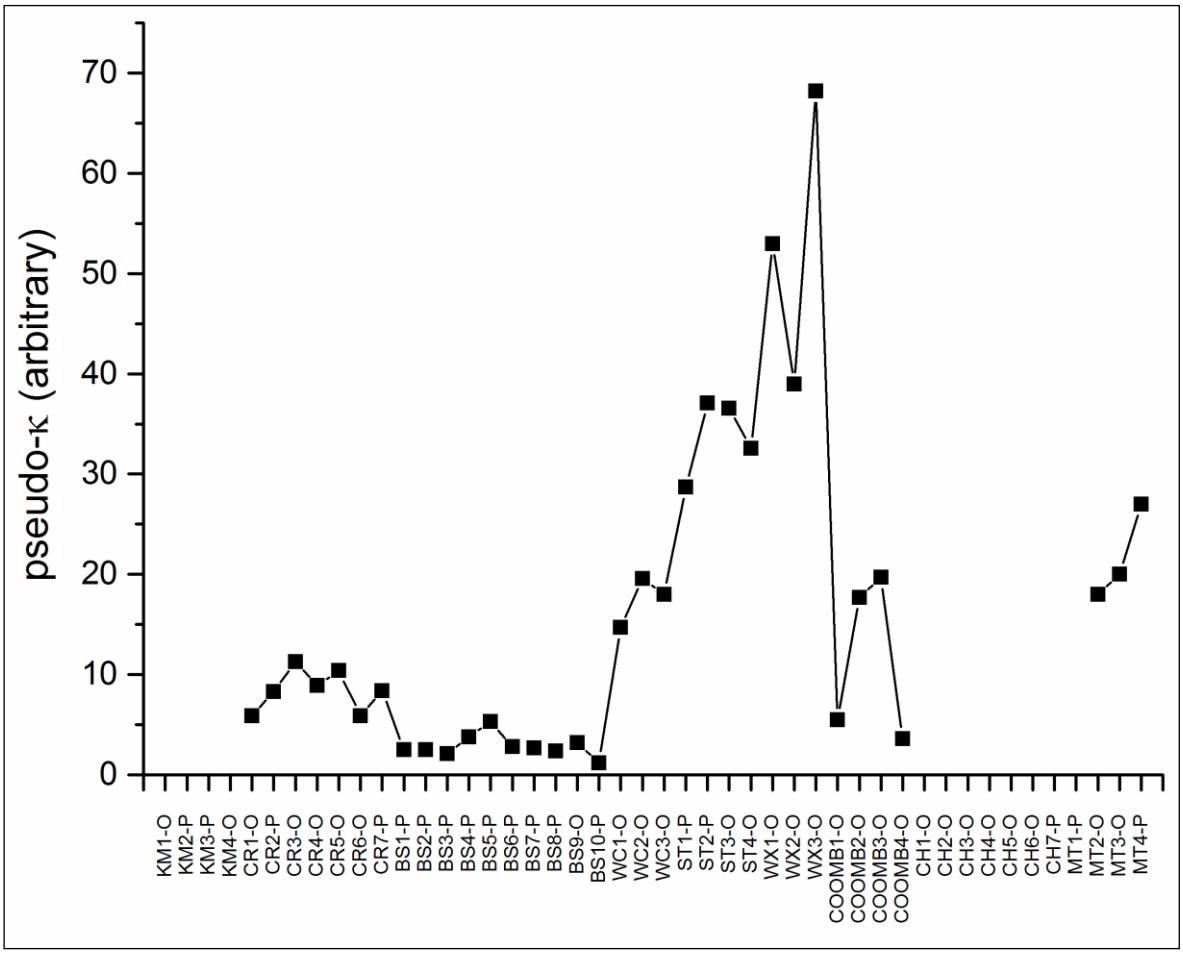


Figure 5.54: A plot of pseudo-κ values for the sampled intervals showing a fairly linear relationship between oil staining and low-field magnetic susceptibility. Note the gap at KM and CH is due to incomplete data.

5.4 Is there a relationship between oil staining and magnetism?

Variations in chemistry, abundance and grain size of the magnetic minerals in the studied wells and samples are here compared. Unravelling the true magnetic signal is complicated by most parameters being sensitive to several sources of variation, e.g., M_{rs} is sensitive to abundance and also grain size, as well as mineralogy, whereas M_s is only sensitive to abundance and mineralogy. It is seen below that most significant variations were found in the magnetic mineralogy; variations in grain-size and abundance were often conflicting. In addition, I investigate variations along the potential hydrocarbon migration routes (see Chapter 4).

5.4.1 Are there variations in ferromagnetic mineral abundance?

The abundance-dependent magnetic data, e.g., M_s and χ_{hf} (Table 5.4), suggest increases in abundance of magnetic materials in oil-stained (O) samples compared to the poorly-stained (P) ones, in the majority of the samples analysed; however, some of the data contradicts this model. For example, values for the Kimmeridge samples show increases in abundance of magnetic materials in the oil-stained samples, based on the LT-M_s and RT-χ_{hf} values (Figs. 5.23 and Table 5.4). Similarly, the oil-stained, Creech samples had higher concentration of magnetic materials than CR2 (P), but less than CR7 (P), albeit CR1 and CR2 were sampled in the Inferior Oolite intervals (Appendix 2.3). In addition, the oil-stained, Chickerell samples all had higher concentrations of magnetic materials based on LT-M_s values except for CH1 (Fig. 5.27 and Table 5.4). Samples from Wytch Farm, Chickerell and Coombe Keynes showed increasing abundance of magnetic materials with depth of sampling (Figs. 5.26, 5.27, 5.30 and Table 5.4), with some variations based on lithology also observed. For example, only CH1 was sampled from Inferior Oolite among the Chickerell (CH) samples (Table 2.1 and Appendix 2.3); it had the smallest concentration of magnetic materials compared to other Chickerell samples (Fig.5.27a and Table 5.4).

The χ_{hf} parameter (Table 5.4), that measures the contribution from paramagnetic minerals (*sensu lato*), i.e., superparamagnetic ferromagnetic particles (< 20-30 nm) and/or paramagnetic materials, indicates an increase in abundance of 'small' (superparamagnetic) and/or paramagnetic particles from the Kimmeridge (hydrocarbon 'kitchen' area) to Wytch Farm (hydrocarbon reservoir): If the signal is due to increased superparamagnetism (as supported by ZFC-FC data section 5.4.2), it is possible the small ferromagnetic particles are easier to transport and accumulate in Wytch Farm.

Figures 5.32 and 5.33 show the distribution of LT-M_s of the sampled wells from the study area; this parameter measures the total ferromagnetic contribution. The data indicates no significant variation in terms of absolute abundance along any of the migration pathways discussed in Chapter 4. In addition, low-field magnetic susceptibility (pseudo-κ) measurements carried out on the core sections sampled revealed samples without oil stain, e.g., Bushey Farm (BS), had lower values than oil-stained samples, e.g., Wytch Farm, Waddock Cross and Martinstown (Fig. 5.54).

Significant increases in LT-M_{rs} from Kimmeridge to Wytch Farm via Creech were observed, but the trend breaks down at Stoborough; this could be due to an increase in the total number of magnetic minerals, or growth of smaller magnetic minerals as M_{rs} is also affected by grain size. Based on average LT-M_{rs} values (Table 5.6), there appears to be growth of magnetic grains from the area around the hydrocarbon kitchen (Kimmeridge) to areas where currently there is an accumulation of oil (Wytch Farm) via Creech (CR) and Bushey Farm (BS) (Fig. 5.43).

5.4.2 Are there variations in ferromagnetic mineral grain sizes?

Magnetic grain-size proxies such as M_{rs}/M_s and B_c indicate grain-size variations between the samples. For example, M_{rs}/M_s and B_c values for Chickerell indicated increasing grain sizes with sampling depth (Fig. 5.38). Plots of M_{rs}/M_s (Fig. 5.45) and B_c (Fig. 4.46) all reaffirm increase in grain-size of magnetic minerals from Kimmeridge via Bushey Farm and Creech to Wytch Farm. Moreover, there appears to be increasing amount of remanence carrying materials from Stoborough – Coombe Keynes – Chickerell – Waddock Cross – Martinstown (in that order) (Figs. 5.43, 5.45 and 5.46), as supported by the LT-M_{rs} data (Table 5.6).

ZFC-FC ratios (300 K/50 K) indicate relative variations in both the ratio of small ferromagnetic particles ferromagnetic and/or low-temperature ferromagnetic materials (paramagnetic at room-temperature), i.e., the signal is a measure of grain size and magnetic mineralogy. Overall, the ZFC-FC data supports the χ_{hf}, data (Table 5.4), i.e., there is evidence for increasing abundance of 'small' and/or paramagnetic particles from the Kimmeridge to Wytch Farm (Fig. 5.53), i.e., even though the average grain-size appears to be increasing, the absolute number of small ferromagnetic particles increases also.

5.4.3 Are there variations in ferromagnetic mineralogy?

The ZFC-FC warming plots measured to investigate thermal relaxation and crystallographic transition of certain minerals (e.g., pyrrhotite) at low temperatures reveal the presence of mainly two magnetic phases: magnetite (Fe_3O_4) and pyrrhotite (Fe_7S_8). For example, samples from Bushey Farm Transition (at ~ 34 K), which indicates the presence of pyrrhotite as the predominant magnetic phase (Fig. 5.49). Samples from Stoborough, Waddock Cross, Coombe Keynes and Martinstown (Figs. 5.48) all exhibited double crystallographic transitions, i.e., Besnus (at ~34 K) and Verwey (at ~ 120 K) transitions, indicating the presence of both pyrrhotite and magnetite. Although other magnetic minerals, i.e., siderite and rhodochrosite, exhibit low-temperature crystallographic transitions similar to that of pyrrhotite (32-37 K), these minerals both show higher remanence during the field-cooled (FC) measurements than in the zero-field cooled (ZFC) measurements (Frederichs *et al.*, 2003); such variations in ZFC-FC measurements were not observed during my experiments. Some samples, e.g., from Creech (Fig. 5.50), Wytch (Fig. 5.51) and Chickerell, did not exhibit any crystallographic transitions. This absence could be due to: (1) lack of magnetite or pyrrhotite, (2) the magnetic grains being too small to exhibit low-temperature crystallographic transitions (Dekkers, 1989) or (3) non-stoichiometry of the phases.

Figure 5.55 shows an interpretive summary of magnetic mineral distribution in the study area; areas with appreciable amount of hydrocarbon in them (either reservoirs or carrier beds), e.g., Kimmeridge, Chickerell and Wytch Farm, had magnetite as the predominant magnetic mineralogy, while areas at the fringes of hydrocarbon accumulation had either mainly pyrrhotite, e.g., Bushey Farm, or a mixture of pyrrhotite and magnetite, e.g., Martinstown and Waddock Cross.

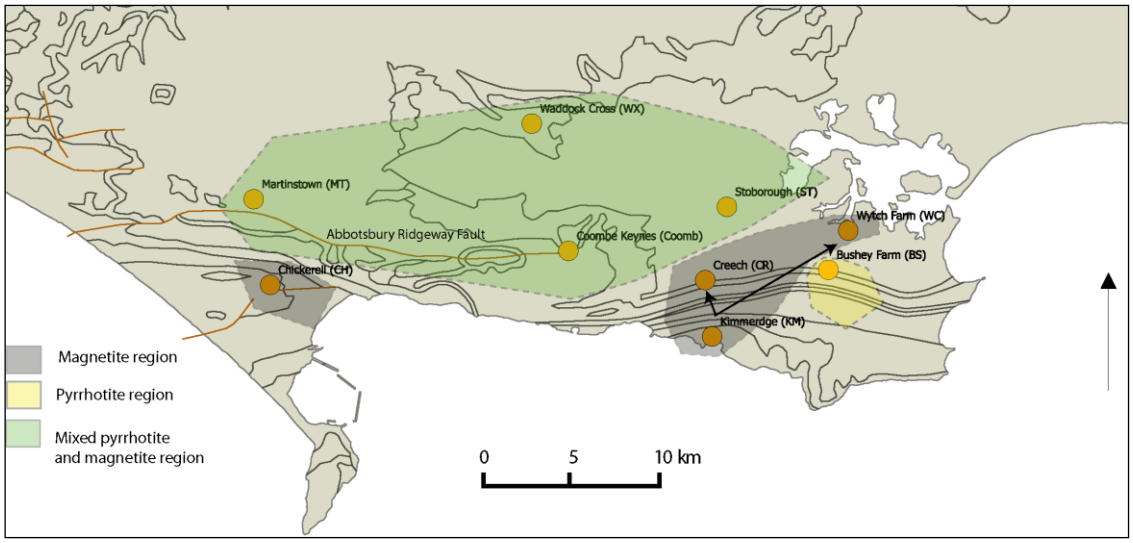


Figure 5.55: Map of study area showing my interpretation of the mineralogical changes along migration paths; from mainly magnetite in KM area with arrows showing direction of increasing magnetic grain size and pyrrhotite content; ST, WX and Coomb and MT areas have mixed magnetite and pyrrhotite while there was mainly magnetite around CH.

5.4.4 Are the variations in magnetic mineralogy affected by intrinsic magnetic contributions or contamination?

Hounslow (1987) reported that a relatively small ferromagnetic signal from the Bridport Sandstone saturated in a field of < 0.3 T. Hounslow (1987) claimed that the ferromagnetic signal is from detrital ferromagnetic ferrianilmanite (ilmenite with exsolved hematite), and to a lesser extent Fe-rich titanomagnetite. For the Bridport sand, (Hounslow, 1987) also reported the presence of paramagnetic chlorites and micas, plus pyrite and to a lesser extent goethite (from the weathering of pyrite). There are some significant methodological differences between the study of Hounslow (1987) and this one: (1) Hounslow (1987) sampled surface outcrops, not drill cuttings; the outcrops > 20 km to the west of the drill cuttings studied in this thesis; (2) Hounslow (1987) did not mention oil staining, and (3) grain sizes were determined using optical microscopy (i.e., > 300 nm); in this study low-temperature measurements accessed ferromagnetic particles < 30 nm in size. In this study I found no evidence for hematite, though magnetite and iron sulphide phases were present in both the oil-stained and poorly oil-stained samples, suggesting that these phases are intrinsic to the Bridport sand. Given the variation of the magnetic mineralogy within the samples studied in this study, and the distance to the samples of Hounslow (1987), it is difficult to infer a "true" background signal. I believe that the poorly oil-stained samples from the same wells as the oil-stained samples represent a better "true' background signal based on locality; though given that the absence of oil does not mean that oil was not formerly present, makes a unique and rigorous interpretation of a "true" background signal problematic: The poorly oil-stained samples can only be used as a guide to

the background signal. For reference, Hounslow (1985) also reported the presence of titanomagnetite and titanohaematites in the Blue Lias Fm and Oxford Clay Fm.

A possible source of sampling contamination in the analysed core samples was through additives from the drilling mud. Table 5.7 shows drilling mud type for each of the wells and its composition. Based on the well information available (Table 5.7), the only possible source of contamination will be from paramagnetic minerals, e.g., the chlorides. Paramagnetic contributions mostly affect the ZFC-FC 30 K/10 K parameter, which is a product of both the unblocking of 'small' particles (~5-15 nm) and also room-temperature paramagnetic materials with very low-temperature Curie temperatures. The ZFC-FC 30 K/10 K parameter did show variation between oil-stained and poorly-stained samples, suggesting that the variation was due to the presence of oil not the drilling process.

Table 5.7: Drilling mud types and composition for all the wells sampled (sourced from UKOGL website).

WELLS	TYPE OF FLUID IN HOLE	COMPOSITION OF FLUID
Bushey Farm	F/WATER BENTONITE POLYMER	fresh water, bentonite (20ppb), caustic soda (0.5ppb), soda ash (0.5ppb), carboxymethylcellulose (3.5ppb), barite (160ppb)
Coombe Keynes	WATER BASED,KCL/POLYMER/SATURATED	sea water,5% potassium chloride, 5-6% silicate
Martinstown	KCL/POLYMER	sea water,5% potassium chloride, 5-6% silicate
Stoborough	FRESHWATER GEL/RHEOSPERSE	fresh water, bentonite (20ppb), caustic soda (0.5ppb), soda ash (0.5ppb), carboxymethylcellulose (3.5ppb), barite (160ppb)
Waddock Cross	FRESHWATER GEL/RHEOSPERSE	fresh water, bentonite (20ppb), caustic soda (0.5ppb), soda ash (0.5ppb), carboxymethylcellulose (3.5ppb), barite (160ppb)
Chickerell	KCL/POLYMER-IDBOND, 38 KPPM CHLORITE	sea water,5% potassium chloride, 5-6% silicate
Creech	KCL/POLYMER	sea water,5% potassium chloride, 5-6% silicate
Kimmeridge5	SEA WATER/POLYMER	sea water,5% potassium chloride, 5-6% silicate
Wytch FarmA1	OBM (Mineral oil based)	base fluid (0.5bbl), viscosifeir (5ppb), emulsifier (0.5ppb), lime (5ppb), CaCl2 (30.2ppb), barite (167.9ppb)

ppb = parts per billion

5.5Proposed model

Previous hydrocarbon-focused, magnetic studies of soil or core samples (e.g., (Costanzo-Alvarez, 2006)) reported enhancement of magnetic signals (mainly magnetite) which is thought to have formed in the presence of crude oil. There are two ways through which the presence of hydrocarbon could enhance magnetic signal either:(1) through changes in the redox conditions

(-Eh) within its vicinity, which could lead to the reduction of non- or weakly magnetic iron or sulphide minerals, e.g., haematite and pyrite, to magnetic minerals, e.g., magnetite and pyrrhotite, or (2) through anaerobic microbial biodegradation of the hydrocarbons and the production of magnetite from Fe^{2+} and Fe^{3+} ions present (Burton *et al.*, 1993). Conversely, if the environment is aerobic the presence of hydrocarbons can be detrimental to the magnetic mineralogy, as aerobic microbial biodegradation generally oxidises thereby decreasing the overall magnetic signal (Emmerton *et al.* (2013). All oils extracted from samples studied in this chapter show no significant biodegradation as indicated by their Pr/C_{17} values (Table 5.1); and only some of the Chickerell samples fall within the slightly biodegraded range (Table 5.2). Therefore, biodegradation can be ruled out as the reason for the increase in magnetic signals observed from Kimmeridge through Creech and Bushey Farm to Wytch Farm.

This increase in the magnetic signal observed along the proposed oil-migration path from Kimmeridge to Wytch Farm is largely due to enhancement of particles < 30 nm identified through the low-temperature remanence and coercivity experiments (Figs. 5.47 – 5.51); as grains become larger and thermally blocked, i.e., no longer superparamagnetic, their coercivity increases; there is an overall increase in magnetic nanoparticles. This increase in nanoparticles could either be due to several mechanisms: (1) the conversion of haematite into magnetite and/or pyrrhotite, which occurs within hydrocarbon habitats (proximal plume) (Machel, 1995), (2) the accretion of nanometre sized ferromagnetic particles along the oil migration path, (3) accumulation of magnetic nanoparticles towards the end of the migration path. Mechanism (1) can be partially dismissed, as there is no or little evidence for haematite in the samples, though, as magnetite is magnetically much stronger than haematite only a small amount of haematite would need to be converted. Mechanism (2) also seems unlikely as the poorly oil-stained samples mostly have pyrrhotite in them. The predominance of pyrrhotite in the Bushey Farm samples for examples, could be due to partial conversion of magnetite to either pyrrhotite or siderite which occurs in near-distal plume environments (Machel, 1995), i.e., whilst the magnetite signal is enhanced along the migration path. Additionally, at shallow depths pyrrhotite is potentially enhanced at the expense of magnetite along the edges distal to the migration path. Samples from Stoborough, Waddock Cross, Coombe Keynes and Martinstown all had mixed pyrrhotite and magnetite, resulting in weaker magnetic signals compared to Creech and Wytch Farm (Fig. 5.55), suggesting there is not a large accumulation of oil around these areas, nor has migration been significant.

5.6 Summary

In this Chapter, I have interpreted magnetic data with the aim of establishing a relationship between hydrocarbon occurrence and formation of magnetic minerals. The hydrocarbons themselves where found to be relatively homogeneous with little evidence for biodegradation, and only small variations in oil maturity, i.e., it is likely the hydrocarbons all have a common source.

The magnetic signals were less homogeneous. I have established that the presence of hydrocarbon alters magnetic mineralogy and to some extent alters the grain size of the magnetic mineralogy. The magnetic signals of Kimmeridge, Creech, Wytch Farm and Chickerell are largely due to the presence of magnetite (Fig. 5.56). These are wells that contain appreciable amount of hydrocarbon or are located at carrier beds, along hydrocarbon migration paths (Table 5.1). Wells located at the fringes of large hydrocarbon accumulation had enhanced pyrrhotite-dominated magnetic signals, e.g., Bushey Farm.

This model is mainly based on the identified magnetic mineralogies rather than variations in magnetic abundance or grain sizes. It is argued in section 5.4.4 that neither the intrinsic magnetic properties of Bridport Sandstone nor contaminations drilling mud additives (Table 5.7) could have a significant effect on this interpretation (Fig. 5.55).

Chapter 6

Conclusions

6.1 Conclusion

6.1.1 Generation of magnetic materials in hydrocarbon-generation conditions

The relationship between the occurrence of petroleum and the generation of magnetic minerals have been investigated by many authors (e.g., Elmore *et al.*, 1993; Emmerton *et al.*, 2013; Machel, 1995) and the complexity of the relationship has been reported (e.g., Burton *et al.*, 1993; Emmerton *et al.*, 2013) among others. In this study, three (Blue Lias Fm, Kimmeridge Clay Fm and Oxford Clay Fm) potential source rocks from an oil-rich study area (Wessex Basin) were pyrolysed in conditions similar to those found in the hydrocarbon kitchen at various temperatures (150, 200, 250, 300 and 320 °C) and their magnetic properties measured, before and after the experiments. Although similar types of heating experiments have been carried out before (e.g., Aubourg and Pozzi, 2010; Aubourg *et al.*, 2012; Kars *et al.*, 2012), this study has allowed, for the first time, experimental investigation of the outcome of magnetic mineralogy during hydrocarbon generation (Chapter 3).

Magnetic characterisation of the pyrolysed rocks at low and room-temperature revealed a substantial increase in magnetic signals in the artificially-matured rocks, compared to unheated ones. For example, the unheated Kimmeridge Clay Fm sample had a saturation remanence magnetisation (M_{rs}) of 58 $\mu Am^2/kg$ at room-temperature, but Kimmeridge Clay Fm samples heated to 250 °C and 320 °C had M_{rs} values of 2510 $\mu Am^2/kg$ and 8150 $\mu Am^2/kg$ respectively, i.e., an order to two orders of magnitude increase in magnetic response. Similarly, there was a significant increase in the saturation magnetization (M_s) from 550 $\mu Am^2/kg$ in the unheated sample, to 6940 $\mu Am^2/kg$ and 34200 $\mu Am^2/kg$ for Kimmeridge Clay Fm heated at 250 °C and 320 °C respectively. Similar increases in abundance of magnetic remanence carrying materials was observed in the both the Blue Lias Fm and the Oxford Clay Fm.

Low-temperature magnetic measurements carried out on the unheated and pyrolysed and the unheated samples revealed the nature of the magnetic materials formed by the artificial-maturation. For example, Oxford Clay Fm 320 °C measured at 5 K had a M_{rs} value of 21400 $\mu Am^2/kg$ whereas the same sample measured at room temperature had a M_{rs}value of 5030 $\mu Am^2/kg$, representing about a four times increase in magnetic remanence. This suggests a large portion of the magnetic minerals formed during the pyrolysis experiments were super-paramagnetic at room temperature. This behaviour was observed in all of the three rocks studied. Moreover, zero-field cooling and field-cooling warming curves measurements carried out on the pyrolysed samples confirms that magnetic materials present in the samples are

superparamagnetic at room-temperature, but do not reveal any low-temperature crystallographic transition that is characteristic of some magnetic minerals (e.g., magnetite) probably because the magnetic grains present were too small (< 20 nm) to exhibit such a transition (Dekkers, 1989). High-temperature thermomagnetic measurements carried out on the pyrolysed samples revealed the presence of sulphides, with < 300 °C crystallographic transformations characteristic of hexagonal pyrrhotite (Dekkers, 1988) and T_c of ~580 °C, characteristic of magnetite.

Magnetic materials formed during the pyrolysis were extracted using an in-house magnetic extractor made by Stacey Emmerton for the purpose imaging. Transmission electron microscopy (TEM) and energy dispersive X-ray (EDX) analyses of the magnetic extracts reveal the presence of nanometre-sized cluster of particles. Identification of any magnetic minerals present was made difficult by the clustering of the particles and interference from acetone (solvent in which the magnetic particles were stored), and the only crystal whose lattice fringe was successfully measured was greigite. Even though it has been argued that greigite is unstable at temperatures exceeding 300 °C (e.g., Aubourg *et al.*, 2012), it has been reported to occur in trace amounts if heating is carried out in the absence of oxygen (Dekkers *et al.*, 2000).

These findings establish that magnetic minerals could be generated alongside hydrocarbons and have the potential to migrate alongside them based on their sizes. The migration of magnetic minerals has the potential to shed some light on the origin of magnetic anomalies observed over oil fields (e.g., Donovan *et al.*, 1979; Foote and Sobehrad, 1997; LeSchack, 1994).

6.1.2 Wessex Basin analysis

The Wessex Basin has been extensively studied (e.g., Butler, 1998; Law, 1998; Underhill and Stoneley, 1998), but unresolved questions remain on how crude oil generated on the hanging wall from the Lias mudrocks(Buchanan, 1998; Ebukanson and Kinghorn, 1986b) migrated into a stratigraphically older Sherwood Sandstone reservoir in the hanging wall, found at Wytch Farm (e.g., Bray *et al.*, 1998; Hawkes *et al.*, 1998).

I have answered some of the questions regarding the oil migration into Wytch Farm and other areas in the basin using three techniques; 1) seismic mapping and interpretations (Chapter 4), 2) geochemical studies of crude oil extracts from core materials obtained for the purpose of this study from the British Geological Society (BGS) core store (Chapter 5) and 3) magnetic characterisation of the core materials (Chapter 5).

The main aim of Chapter 4 was to produce an upheaval map. To achieve this, present day maps of top Chalk, Inferior Oolite and White Lias (Rheatic) and the base of the Wealden Group were mapped from 63, 2D seismic lines. These data were obtained from the UK Onshore Geophysical Library (UKOGL) through Lynx Geophysical. Geometrical restoration was also carried out on some selected 2D seismic lines, in which the hanging wall of the Abbotsbury Ridgeway and the Purbeck faults were restored prior to the Tertiary basin inversion.

The amount of uplift and subsequent erosion of materials in the hanging wall Abbotsbury Ridgeway and Purbeck-Isle of Wight fault system is estimated to be around 1500 km (Law, 1998) or more (Bray *et al.*, 1998) based on various studies carried out. In this study, 2D seismic lines B92-40 and a composite of BP-83-060 L and 80-268, which passes through the Kimmeridge area, were used to estimate the thicknesses of the missing sections in order to carry out the geometric restoration.

A map of present day top Inferior Oolite and Sherwood Sandstone (White Lias + 300m) surface was juxtaposed against the restored inferior Oolite surface to create the upheaval maps. These maps shed light on potential migration paths for oil seeps found at Osmington Mills and Mupe Bay, which is probably along the Purbeck Disturbance, as previously argued by Underhill and Stoneley (1998), possible migration routes through Creech into Wytch Farm and subsequent westward spilling into Stoborough and possibly Waddock Cross, due to eastward tilting of the basin. A potential migration route into Chickerell was also identified via Radipole was identified in this chapter.

6.1.3 Hydrocarbon and magnetic properties

For the third part of this study, a total of 49 core materials from nine wells from the study area were characterised geochemically and magnetically, to investigate patterns along the possible migration pathways (Chapter 5). The sampling interval was restricted to Inferior Oolite and Bridport Sandstone. For the purpose of geochemical analysis, extractible organic matter (EOM), extracted from the core materials using solvents was fractionated and the aliphatic fractions were run in a Gas Chromatography – Mass Spectrometry (GC-MS).

Biomarker analysis reveals that all oils studied have probably came from a common source-rock; type II algal, marine shale deposited mostly in a strongly reducing environment. However, the maturity levels among the oil vary. For example, based on the Ts/Tm v $C_{30}H$

biomarker parameter, oils from Waddock Cross are generally less mature than oil samples from Creech, which is in turn less mature than oil samples from Wytch Farm, while oils from Chickerell are the most mature.

A plot $C_{29}\alpha\beta\beta/(\alpha\beta\beta+\alpha\alpha\alpha)$ versus $C_{29}(S/(S+R))$ also shows samples from Chickerell being some of the most mature in the area, with Waddock Cross and Creech oil being generally less mature than oil from Wytch Farm. Because of the eastward tilting of the reservoir at Wytch Farm, it is expected that the oil will spill from the top of the reservoir, thereby making oils found along the spill-chain, less mature. This explains why oil from Stoborough and Waddock Cross are generally less mature than oil from Wytch Farm. Oil from Creech is less mature than oil from Wytch Farm, this could suggest a different system of oil spill, whereby the less mature oil was trapped at Creech and the later generated oil found a route to migrate and accumulate at Wytch Farm.

Magnetic characterisation of the core materials revealed differences between the oil-stained samples (O) and the poorlystained samples (P) (Chapter 5). Measurements carried out include low-field magnetic susceptibility (κ), low- and room-temperature hysteresis measurements and zero-field cooled (ZFC) and field-cooled (FC) warming curves. Pseudo-κ measurements carried out on core sections reveal cores with oil staining had higher magnetic volume susceptibility than cores that are poorly stained. Data from the hysteresis measurements indicate increases in low-temperature saturation remanence magnetisation (LT-M_{rs}) s from Kimmeridge (the 'kitchen area') to Wytch Farm and Waddock Cross (reservoir areas), with similar pattern of increasing values from Kimmeridge to Wytch Farm also observed for the LT-M_{rs}/M_s ratio and the LT- and RT-coercivity values (B_c). In addition, ratios of magnetisation at 300 K/50 K and 30 K/15 K from the ZFC and FC warming curve experiments were computed to investigate the abundance of larger (~ <30 nm) and smaller (~ <20 nm) respectively. Both FC and ZFC ratios show an increase in the abundance of smaller particles (30 K/15 K) from Kimmeridge to Wytch Farm; with no obvious relationship observed in 300 K/50 K ratios.

I argue, based on the results of chapter 5, that in areas with significant hydrocarbon accumulation, such as Kimmeridge, Creech and Wytch Farm (Figure 5.55) magnetite will be stable and will be the predominant magnetic phase. I also argue, in areas along the fringes of such hydrocarbon accumulation, e.g., Stoborough, Coombe Keynes, Martinstown and Waddock Cross (Figure 5.55), a mixed pyrrhotite-magnetite equilibrium is established, while

in areas with a marginal hydrocarbon presence, e.g., Bushey Farm, pyrrhotite is the predominant magnetic phase (Figure 5.55).

In summary, there was evidence for the enhancement of magnetic signals from Kimmeridge to Wytch Farm (Figure 5.55), due to the conversion of non-magnetic minerals to magnetic minerals with higher M_{rs} and coercivities and/or the accretion of nano-metre sized magnetic minerals. Some magnetic measurements carried out in this study indicate staining from oil could enhance magnetic signals, as previously reported (e.g., Machel, 1995), but crucially, I have shown that mineral magnetic methods have the potential to map out oil migration pathways.

6.2 Future work

Enhancement of magnetic signals around hydrocarbon accumulation is complex (Machel, 1995) and the studies of soil or core samples alone may not be able to provide all the answers. The low-field volume magnetic susceptibility (κ) measurements provides a quick and inexpensive way that could be incorporated easily during well logging, coupled with techniques such as UV fluorescence that could identify hydrocarbon stained areas down-hole. Soil and core magnetic studies could also be carried out together with ground magnetic and radiometric studies, as these have proven to be successful in identifying areas of hydrocarbon accumulations (e.g., LeSchack, 1997; LeSchack and Van Alstine, 2002). Higher quality 2D, and where possible 3D, seismic data should be acquired from potential target areas to generate better surfaces that will help resolve most oil migration issues. Future work could also be combined with aeromagnetic and high-resolution ground magnetic data.

References

Ahmed, M.A., Blesa, M.J., Moliner, R., 2007. Chemical Decomposition of Iron in Spanish Coal Pyrolysis Identified by Mossbauer Spectroscopy at Different Temperatures. Energy Sources, Part A: Recovery, Utilization, and Environmental Effects 29, 1443-1456.

Akande, W.G., 2012a. Evaluation of hydrocarbon generation potential of the Mesozoic organic-rich rocks using TOC and Rock-Eval pyrolysis techniques. Geosci. **2**, 164-170.

Alberdi-Genolet, M., Tocco, R., 1999. Trace metals and organic geochemistry of the Machiques Member (Aptian–Albian) and La Luna Formation (Cenomanian–Campanian), Venezuela. Chem. Geol. 160, 19-38.

Aldana, M., Costanzo-Alvarez, V., Díaz, M., 2003. Magnetic and mineralogical studies to characterize oil reservoirs in Venezuela. The Lead. Ed. 22, 526-529.

Aldana, M., Costanzo-Alvarez, V., Gomez, G., Vitiello, D., Colmenares, L., 1999. Framboidal magnetic minerlas and their possible association to hydrocarbons: La Victoria oil field, southwestern Venezuela. Geof. Int. **38**, 137-152.

Almeida, T.P., Fay, M., Zhu, Y., Brown, P.D., 2012a. Controlling role of pH and temperature on $CoFe_2O_4$ nanostructures produced by hydrothermal synthesis. Journal of nanoscience and nanotechnology 12, 8801-8805.

Aubourg, C., Pozzi, J.-P., 2010. Toward a new 250 °C pyrrhotite–magnetite geothermometer for claystones. Earth and Plan. Sci. Lett. 294, 47-57.

Aubourg, C., Pozzi, J.-P., Janots, D., Sarahoui, L., 2008a. Imprinting chemical remanent magnetization in claystones at 95C. Earth and Plan. Sci. Lett. 272, 9.

Aubourg, C., Pozzi, J.P., Janots, D., Sahraoui, L., 2008b. Imprinting chemical remanent magnetization in claystones at 95 °C. Earth and Plan. Sci. Lett. 272, 172-180.

Aubourg, C., Pozzi, J.P., Kars, M., 2012. Burial, claystones remagnetization and some consequences for magnetostratigraphy. Geol. Soc. Lon. Sp. Pub. (Eds.) R. D. Elmore, A. R. Muxworthy, M. M. Aldana and M. Mena 371, 181-188.

Banerjee, S., Elmore, R.D., Engel, M.H., 1997. Chemical remagnetization and burial diagenesis: Testing the hypothesis in the Pennsylvanian Belden Formation, Colorado. Journ. Geophys. Res. 102, 24825-24842.

Banerjee, S., Moskowitz, B., 1985. Ferrimagnetic Properties of Magnetite, in: Kirschvink, J., Jones, D., MacFadden, B. (Eds.), Magnetite Biomineralization and Magnetoreception in Organisms. Springer US, pp. 17-41.

Bazylinski, D.A., 1996. Controlled biomineralization of magnetic minerals by magnetotactic bacteria. Chemical Geology 132, 191-198.

Beeley, H.S., Norton, M.G., 1998. The structural development of the Central English Channel High — constraints from section restoration. Geo. Soc., Lon. Sp. Pub. (Eds.) J. R. Underhill 133, 283-298.

Besnus, M.J., Meyer, A.J., 1964. Nouvelles donnees experimentales sur le magnetisme de la pyrrhotine naturelle, 507-511 ed.

Bigge, M.A., Farrimond, P., 1998. Biodegradation of seep oils in the Wessex Basin — a complication for correlation. Geo. Soc., Lon. Sp. Pub. (Eds.) J. R. Underhill 133, 373-386.

Bjorkum, P.A., Walderhaug, O., 1993. Isotopic composition of a calcite-cemented layer in the Lower Jurassic Birdport Sands, southern England; implications for formation of laterally extensive calcite-cemented layers. Jour. Sed. Res. 63, 678-682.

Bjorlykke, K., 1998. Clay mineral diagenesis in sedimentary basins - a key to the prediction of rock properties. Examples from the North Sea Basin. Clay Min. 33, 15-34.

Blumstein, A.M., Elmore, R.D., Engel, M.H., Elliot, C., Basu, A., 2004. Paleomagnetic dating of burial diagenesis in Mississippian carbonates, Utah. Jour. Geophys Res. 109, 144-160.

Bray, R.J., Duddy, I.R., Green, P.F., 1998. Multiple heating episodes in the Wessex Basin: implications for geological evolution and hydrocarbon generation. Geo. Soc., Lon. Sp. Pub. (Eds.) J. R. Underhill 133, 199-213.

Breger, I., 1966. Geochemistry of lipids. Journ. Am. Oil Chem. Soc. 43, 197-202.

Buchanan, J.G., 1998. The exploration history and controls on hydrocarbon prospectivity in the Wessex basins, southern England, UK. Geo. Soc., Lon. Sp. Pub. (Eds.) J. R. Underhill 133, 19-37.
Burton, E.A., G., M.H., Qi, J., 1993. Thermodynamic constrain on anomalous magnetization in shallow and deep hydrocarbon seepape environments. Soc. Sed. Geol. 49, 15.
Butler, M., 1998. The geological history of the southern Wessex Basin — a review of new information from oil exploration. Geol.l Soc. Lon. Sp. Pub. (Eds.) J. R. Underhill 133, 67-86.
Butler, M., Pullan, C.P., 1990. Tertiary structures and hydrocarbon entrapment in the Weald Basin of southern England. Geological Society, London, Special Publications. (Eds.) R. F. P. Hardman 55, 371-391.
Butler, R.F., 1992. Paleomagnetism: Magnetic domains to geological terrains. Boston; Oxford: Blackwell Scientific.
Campos, H.S., Hallam, A., 1979. Diagenesis of English Lower Jurassic limestones as inferred from oxygen and carbon isotope analysis. Earth and Planetary Science Letters 45, 23-31.
Chadwick, R.A., 1993. Aspects of basin inversion in southern Britain. Journ. Geol. Soc. 150, 311-322.
Chadwick, R.A., Chadwick, R.A., Evans, D.J., 2005. A Seismic Atlas of Southern Britain: Images of Subsurface Structure. Brit. Geo. Sur.
Chamley, H., 1994. Clay Mineral Diagenesis, in: Parker, A., Sellwood, B. (Eds.), Quantitative Diagenesis: Recent Developments and Applications to Reservoir Geology. Springer Netherlands, pp. 161-188.
Cioppa, M.T., Symons, D.T.A., Flore, M., 2002. Initial analysis of the Jurassic "Nordegg Member", Fernie Formation: using paleomagnetism to date source rock thermal maturation. Physics and Chemistry of the Earth, Parts A/B/C 27, 1161-1168.
Cisowski, S.M., Fuller, M., 1987. The generation of magnetic anomalies by combustion metamorphism of sedimentary rock, and its significance to hydrocarbon exploration. Geol. Soc. Am. Bull. 99, 21-29.
Clark, J.P., Philp, R.P., 1989. Geochemical characterization of evaporite and carbonate depositional environments and correlation of associated crude oils in the Black Creek basin, Alberta. Bull. Can. Pet. Geol. 37, 401-416.
Colter, V., Havard, D., 1981. The Wytch Farm Oil Field, Dorset, Petroleum Geology of the Continental Shelf of North-West Europe. Heyden London, pp. 494-503.
Cornford, C., Christie, O., Endresen, U., Jensen, P., Myhr, M.-B., 1988. Source rock and seep oil maturity in Dorset, Southern England. Org. Geochem. 13, 399-409.
Costanzo-Alvarez, V., Aldana, M., Aristeguieta, O., Marcano, M.C., Aconcha, E., 2000. Study of magnetic contrasts in the Guafita oil field (south-western Venezuela). Phys. and Chem. of the Earth, Part A: Solid Earth and Geodesy 25, 437-445.
Costanzo-Alvarez, V., Aldana M., Bayona, G. & Ayala C., 2006. Hydrocarbon-induced magnetic contrasts in some Venezuelan and Columbian oil wells. Earth Plan. Space **58**, 1401-1410.
Curtis, C.D., Murchison, D.G., Berner, R.A., Shaw, H., Sarnthein, M., Durand, B., Eglinton, G., Mackenzie, A.S., Surdam, R.C., 1985. Clay Mineral Precipitation and Transformation during Burial Diagenesis [and Discussion]. Philosophical Transactions of the Royal Society of London A: Mathematical, Physical and Engineering Sciences 315, 91-105.
Damsté, J.S.S., De Leeuw, J.W., 1995. Comments on "Biomarkers or not biomarkers. A new hypothesis for the origin of pristane involving derivation from methyltrimethyltridecylchromans (MTTCs) formed during diagenesis from chlorophyll and alkylphenols" from M. Li, S. R. Larter, P. Taylor, D. M. Jones, B. Bowler and M. Bjorøy. Org. Geochem. 23, 1085-1087.
De Graaf, W., Damsté, J.S.S., de Leeuw, J.W., 1992. Laboratory simulation of natural sulphurization: I. Formation of monomeric and oligomeric isoprenoid polysulphides by low-temperature reactions of inorganic polysulphides with phytol and phytadienes. Geochim. et Cosmo. Acta 56, 4321-4328.
Deconinck, J.-F., Hesselbo, S., Debuisser, N., Averbuch, O., Baudin, F., Bessa, J., 2003. Environmental controls on clay mineralogy of an Early Jurassic mudrock (Blue Lias Formation, southern England). Int. Journ. Earth Sci. 92, 255-266.
Dekkers, M.J., 1988. Magnetic properties of natural pyrrhotite Part I: Behaviour of initial susceptibility and saturation-magnetization-related rock-magnetic parameters in a grain-size dependent framework. Phys. Earth and Plan. Int. 52, 376-393.
Dekkers, M.J., 1989. Magnetic properties of natural pyrrhotite. II. High- and low-temperature behaviour of Jrs and TRM as function of grain size. Phys. Earth and Plan. Int. 57, 266-283.

Dekkers, M.J., 1990. Magnetic monitoring of pyrrhotite alteration during thermal demagnetization. Geophys. Res. Lett. 17, 779-782.
Dekkers, M.J., Passier, H.F., Schoonen, M.A.A., 2000. Magnetic properties of hydrothermally synthesized greigite (Fe3S4)—II. High- and low-temperature characteristics. Geophys. Journ. Int. 141, 809-819.
Díaz, M., Aldana, M., Costanzo-Alvarez, V., Silva, P., Pérez, A., 2000. EPR and magnetic susceptibility studies in well samples from some Venezuelan oil fields. Phys. Chem. of the Earth, Part A: Solid Earth and Geodesy 25, 447-453.
Didyk, B.M., Simoneit, B.R.T., Brassell, S.C., Eglinton, G., 1978. Organic geochemical indicators of palaeoenvironmental conditions of sedimentation. Nature 272, 216-222.
Donovan, T.J., Forgey, R.L., Roberts, A.A., 1979. Aeromagnetic detection of diagenetic magnetite over oil fields. AAPG Bulletin 63, 245-248.
Donovan, T.J., Hendricks, J.D., Roberts, A.A., Eliason, P.T., 1984. Low-altitude aeromagnetic reconnaissance for petroleum in the Arctic National Wildlife Refuge, Alaska. Geophysics 49, 1338-1353.
Drummond, P.V.O., 1970. The Mid-Dorset Swell. Evidence of Albian—Cenomanian movements in Wessex. Proceedings of the Geologists' Association 81, 679-714.
Dunlop, D.J., 1973. Superparamagnetic and single-domain threshold sizes in magnetite. Journ. Geophys. Res. 78, 1780-1793.
Dunlop, D.J., Özdemir, O., 1997. Rock magnetism. Fundamentals and frontiers. Cambridge studies in magnetism series: Cambridge University Press. . **135**, 287-300.
Duyck, C., Miekeley, N., Porto da Silveira, C.L., Szatmari, P., 2002. Trace element determination in crude oil and its fractions by inductively coupled plasma mass spectrometry using ultrasonic nebulization of toluene solutions. Spectrochimica Acta Part B: Atom. Spect. 57, 1979-1990.
Ebukanson, E.J., Kinghorn, R.R.F., 1985. Kerogen facies in the major jurassic mudrock formations of southern england and the implication on the depositional environments of their precursors. Journ. Pet. Geol. 8, 435-462.
Ebukanson, E.J., Kinghorn, R.R.F., 1986a. Maturity of organic maiter in the jurassic of southern england and its relation to the burial history of the sediments. Journ. Pet. Geol. 9, 259-280.
Ebukanson, E.J., Kinghorn, R.R.F., 1986b. Oil and gas accumulations and their possible source rocks in southern england. Journ. Pet. Geol. 9, 413-427.
Ellrich, J., Hirner, A., Stärk, H., 1985. Distribution of trace elements in crude oils from southern Germany. Chemical Geology 48, 313-323.
Ellwood, B.B., Crick, R.E., 1988. Paleomagnetism of paleozoic asphaltic deposits in southern Oklahoma, USA. Geophysical Research Letters 15, 436-439.
Ellwood, B.B., Pemberton, S.G., 1984. Some magnetic properties of Athabasca Oil Sand samples, Alberta, Canada. Can. Journ.of Earth Sci. 21, 278-283.
Elmore, R.D., Cates, K., Gao, G., Land, L., 1994. Geochemical constraints on the origin of secondary magnetizations in the Cambro-Ordovician Royer Dolomite, Arbuckle Mountains, southern Oklahoma. Phys. Earth and Plan. Int. 85, 3-13.
Elmore, R.D., Crawford, L., 1990. Remanence in authigenic magnetite: Testing the hydrocarbon-magnetite hypothesis. Journ.of Geophy. Res. 95, 4539-4549.
Elmore, R.D., Engel, M.H., Crawford, L., Nick, K., Imbus, S., Sofer, Z., 1987. Evidence for a relationship between hydrocarbons and authigenic magnetite. Nature 325, 428-430.
Elmore, R.D., Imbus, S.W., Engel, M.H., Fruit, D., 1993. Hydrocarbons and magnetizations in magnetite. Applications of Paleomagnetism to Sedimenatry Geology. Soc. Sed. Geol. Special pub No. 49, 181-191.
Elmore, R.D., Kelley, J., Evans, M., Lewchuk, M.T., 2001. Remagnetization and orogenic fluids: testing the hypothesis in the central Appalachians. Geophysical Journal International 144, 568-576.
Elmore, R.D., Muxworthy, A.R., Aldana, M., 2012. Remagnetization and chemical alteration of sedimentary rocks. Geol. Soc. London, Sp. Pub. (Eds.) R. D. Elmore, A. R. Muxworthy, M. M. Aldana and M. Mena 371.
Emmerton, S., Muxworthy, A.R., Sephton, M.A., Aldana, M., Costanzo-Alvarez, V., Bayona, G., Williams, W., 2013. Correlating biodegradation to magnetization in oil bearing sedimentary rocks. Geochimica et Cosmochimica Acta 112, 146-165.

Evans, M.E., Heller, F., 2003. Preface, in: Michael, E.E., Friedrich, H. (Eds.), International Geophysics. Academic Press, pp. xi-xii.
Farrimond, P., 2005. Book Review: The Biomarker Guide, Volumes 1 and 2 by K.E. Peters, C.C. Walters and J.M. Moldowan, 2005, 1155 pp. Cambridge University Press, Cambridge. . J. Paleolimnol 34, 539-540.
Filby, R.H., 1994. Origin and nature of trace element species in crude oils, bitumens and kerogens: implications for correlation and other geochemical studies. Geological Society, London, Special Publications 78, 203-219.
Font, E., Trindade, R.I.F., Nédélec, A., 2006. Remagnetization in bituminous limestones of the Neoproterozoic Araras Group (Amazon craton): Hydrocarbon maturation, burial diagenesis, or both? Journal of Geophysical Research: Solid Earth 111, n/a-n/a.
Foote, R.S., 1986. Integrating airbone and surface magnetic data, Remote Sensing for Exploration Geology, pp. 233-247.
Foote, R.S., 1992. Use of magnetic field aids oil search. Oil & Gas Journal, 137-142.
Foote, R.S.N.R., Sobehrad, J., 1997. Aeromagnetic near-surface profiling as an exploration tool, in Applications of emerging technologies: Unconventional methods in exploration for petroleum and natural gas. Dallas Southern Methodist University Press, 183-193.
Frederichs, T., von Dobeneck, T., Bleil, U., Dekkers, M.J., 2003. Towards the identification of siderite, rhodochrosite, and vivianite in sediments by their low-temperature magnetic properties. Physics and Chemistry of the Earth, Parts A/B/C 28, 669-679.
Garden, I.R., Guscott, S.C., Burley, S.D., Foxford, K.A., Walsh, J.J., Marshall, J., 2001. An exhumed palaeo-hydrocarbon migration fairway in a faulted carrier system, Entrada Sandstone of SE Utah, USA. Geofluids 1, 195-213.
Gong, Z., Dekkers, M.J., Heslop, D., Mullender, T.A.T., 2009. End-member modelling of isothermal remanent magnetization (IRM) acquisition curves: a novel appraoch to diagnose remagnetization. Geophysical Journal International **178**, 693-701.
González, F., Aldana, M., Costanzo-Álvarez, V., Díaz, M., Romero, I., 2002. An integrated rock magnetic and EPR study in soil samples from a hydrocarbon prospective area. Physics and Chemistry of the Earth, Parts A/B/C 27, 1311-1317.
Guzmán, O., Costanzo-Álvarez, V., Aldana, M., Díaz, M., 2011. Study of magnetic contrasts applied to hydrocarbon exploration in the Maturín Sub-Basin (eastern Venezuela). Stud Geophys Geod **55**, 359-376.
Haven, H.L.t., Rullkötter, J., 1988. The diagenetic fate of taraxer-14-ene and oleanene isomers. Geochimica et Cosmochimica Acta 52, 2543-2548.
Hawkes, P.W., Fraser, A.J., Einchcomb, C.C.G., 1998. The tectono-stratigraphic development and exploration history of the Weald and Wessex basins, Southern England, UK. Geo. Soc., Lon. Sp. Pub. (Eds.) J. R. Underhill 133, 39-65.
Heider, F., Dunlop, D.J., 1987. Two types of chemical remanent magnetization during the oxidation of magnetite. Physics of the Earth and Planetary Interiors 46, 24-45.
Heider, J., Spormann, A.M., Beller, H.R., Widdel, F., 1998. Anaerobic bacterial metabolism of hydrocarbons. FEMS Microbiology Reviews 22, 459-473.
Helgeson, H.C., Richard, L., McKenzie, W.F., Norton, D.L., Schmitt, A., 2009. A chemical and thermodynamic model of oil generation in hydrocarbon source rocks. Geochimica et Cosmochimica Acta 73, 594-695.
Hirt, A.M., Banin, A., Gehring, A.U., 1993. Thermal generation of ferromagnetic minerals from iron-enriched smectites. Geophysical Journal International 115, 1161-1168.
Horng, C.-S., Torii, M., Shea, K.-S., Kao, S.-J., 1998. Inconsistent magnetic polarities between greigite- and pyrrhotite/magnetite-bearing marine sediments from the Tsailiao-chi section, southwestern Taiwan. Earth and Planetary Science Letters 164, 467-481.
Hounslow, M.W., 1985. Magnetic fabric arising from paramagnetic phyllosilicate minerals in mudrocks. Journal of the Geological Society 142, 995-1006.
Hounslow, M.W., 1987. Magnetic fabric characteristics of bioturbated wave-produced grain orientation in the Bridport-Yeovil Sands (Lower Jurassic) of Southern England. Sedimentology 34, 117-128.

Hounslow, M.W., Posen, P.E., Warrington, G., 2004. Magnetostratigraphy and biostratigraphy of the Upper Triassic and lowermost Jurassic succession, St. Audrie's Bay, UK. Palaeogeography, Palaeoclimatology, Palaeoecology 213, 331-358.
House, M.R., 1989. Geology of the Dorset coast. Geol. Ass. Lon.
Ibarra, J., Palacios, J., Moliner, R., Bonet, A.J., 1994. Coal Utilization and the EnvironmentEvidence of reciprocal organic matter-pyrite interactions affecting sulfur removal during coal pyrolysis. Fuel 73, 1046-1050.
Jenkyns, H.C., Senior, J.R., 1991. Geological evidence for intra-Jurassic faulting in the Wessex Basin and its margins. Journal of the Geological Society 148, 245-260.
Jiang, W.-T., Horng, C.-S., Roberts, A.P., Peacor, D.R., 2001. Contradictory magnetic polarities in sediments and variable timing of neoformation of authigenic greigite. Earth and Planetary Science Letters 193, 1-12.
Johnson, W.C., 2006. The biomarker guide, volumes 1 & 2. Geoarchaeology 21, 515-517.
Kao, S.-J., Horng, C.-S., Roberts, A.P., Liu, K.-K., 2004. Carbon–sulfur–iron relationships in sedimentary rocks from southwestern Taiwan: influence of geochemical environment on greigite and pyrrhotite formation. Chemical Geology 203, 153-168.
Karlin, R., 1990. Magnetite diagenesis in marine sediments from the Oregon continental margin. Journal of Geophysical Research: Solid Earth 95, 4405-4419.
Kars, M., Aubourg, C., Pozzi, J.-P., Janots, D., 2012. Continuous production of nanosized magnetite through low grade burial. Geochemistry, Geophysics, Geosystems 13, Q08Z48.
Katz, B., Elmore, R.D., Cogoini, M., Ferry, S., 1998. Widespread chemical remagnetization: Orogenic fluids or burial diagenesis of clays? Geology 26, 603-606.
Keller, W., 1963. Diagenesis in clay minerals—a review. Clays and clay minerals 13, 136-157.
Kharaka, Y.K., Hull, R.W., Carothers, W.W., 1985. Water-rock interactions in sedimentary basins, in relationship of organic matter and mineral diagenenesis. SEPM Short Course 17, 79-176.
Killops, S., Killops, V., 2004. Introduction to Organic Geochemistry. Blackwell Publishing Ltd., pp. 325-362.
Kittel, C., 1949. Physical Theory of Ferromagnetic Domains. Reviews of Modern Physics 21, 541-583.
Kittel, C., 1967. Introduction to Solid State Physics Third ed. John Wiley & Sons, Inc. New York.
Kohnen, M.E.L., 1991. Sulphurised lipids in sediments: the key to reconstruct palaeobiochemicals and their origin.
Kolaczkowska, E., Slougui, N.-E., Watt, D.S., Maruca, R.E., Michael Moldowan, J., 1990. Thermodynamic stability of various alkylated, dealkylated and rearranged 17α- and 17β-hopane isomers using molecular mechanics calculations. Organic Geochemistry 16, 1033-1038.
Kono, M., Tanaka, H., 2007. Perspectives of Geomagnetism: Geodynamo, Paleomagnetism and Rock Magnetism ; Tribute to Prof. Masaru Kono. Terra Scientific Publishing Company.
Koptíková, L., Bábek, O., Hladil, J., Kalvoda, J., Slavík, L., 2010. Stratigraphic significance and resolution of spectral reflectance logs in Lower Devonian carbonates of the Barrandian area, Czech Republic; a correlation with magnetic susceptibility and gamma-ray logs. Sedimentary Geology 225, 83-98.
Krooss, B.M., Brothers, L., Engel, M.H., 1991. Geochromatography in petroleum migration: a review. Geological Society, London, Special Publications 59, 149-163.
Lake, S.D., Karner, G.D., 1987. The structure and evolution of the Wessex Basin, southern England: an example of inversion tectonics. Tectonophysics 137, 347-378.
Law, A., 1998. Regional uplift in the English Channel: Quantification using sonic velocity. Geo. Soc., Lon. Sp. Pub. (Eds.) J. R. Underhill 133, 187-197.
Leblanc, G.E., Morris, W.A., 1999. Aeromagnetics of southern Alberta within areas of hydrocarbon accumulation. Bulletin of Canadian Petroleum Geology 47, 439-454.
LeSchack, L.A., 1994. Ground-based magnetic horizontal gradient intensity and radiometric surveys, a cost-effective hydrocarbon exploration tool: Three case histories in Western Canada. Canadian Society of Exploration Geophysicists Recorder 19, 7-13.
LeSchack, L.A., 1997. Results of magnetic HGI and radiometric surveys in W. Canada. Oil & Gas Journ. **95** 20, 84-89.
LeSchack, L.A., Jackson, J.R., 2003. Airborne Measurement of Transient Pulses Locates Hydrocarbon Reservoirs. AAPG Ann. Conv. Texas.

LeSchack, L.A., Van Alstine, D.R., 2002. High-resolution Ground-magnetic (HRGM) and Radiometric Surveys for Hydrocarbon Exploration: Six Case Histories in Western Canada. in Surface exploration case histories: Application of geochemistry, magnetics and remote sensing, D. Schumacher and L. A. LeSchack, eds; AAPG in Geology 48, 67-156.
Leslie, B.W., Lund, S.P., Hammond, D.E., 1990. Rock magnetic evidence for the dissolution and authigenic growth of magnetic minerals within anoxic marine sediments of the California continental borderland. Jour. of Geophys. Res. 95, 4437-4452.
Lewan, M.D., 1984. Factors controlling the proportionality of vanadium to nickel in crude oils. Geochimica et Cosmochimica Acta 48, 2231-2238.
Lewan, M.D., 1993. Laboratory Simulation of Petroleum Formation, in: Engel, M., Macko, S. (Eds.), Organic Geochemistry. Springer US, pp. 419-442.
Lewan, M.D., 1998. Sulphur-radical control on petroleum formation rates. Nature 391, 164-166.
Lijmbach, G.W., 1975. On the origin of petroleum. In: Applied Science Publishers Proceedings of the 9th World Petroleum Congress, London., 357-369.
Liu, Q., Liu, Q., Chan, L., Li, H., Xia, X., Cheng, T., Wang, F., Zhang, S., 2004. Relationship between magnetic anomalies and hydrocarbon microseepage above gas field, Ordos basin, China. Journal of Petroleum Science and Engineering 88, 241-251.
Liu, Q., Liu, Q., Chan, L., Yang, T., Xia, X., Cheng, T., 2006. Magnetic enhancement caused by hydrocarbon migration in the Mawangmiao Oil Field, Jianghan Basin, China. Journal of Petroleum Science and Engineering 53, 25-33.
Liu, Q., Liu, S., 1999. Magnetic and mineralogical characteristics of reservoir rocks in the Yakela oil field, northern Ta rim Basin and their implications for magnetic detection of oil and gas accumulations. Chin. Sci. Bull. 44, 174-177.
Lord, C.J., 1991. Determination of trace metals in crude oil by inductively coupled plasma mass spectrometry with microemulsion sample introduction. Analytical Chemistry 63, 1594-1599.
Lott, G., Sobey, R., Warrington, G., Whittaker, A., 1982. The Mercia Mudstone Group (Triassic) in the western Wessex Basin. Proceedings of the Ussher Society 5, 340-346.
Loucks, R.G., Reed, R.M. Ruppel, S.C. and Jarvie, D.M, 2009. Morphology, genesis and distribution of nanometer-scale pores in siliceous mudstones of the Mississippian Barnett shale. Jour. Sed. Res. **79**, 848-861.
Lu, G., Marshak, S. & Kent, D. V., 1990. Characteristics of magnetic carriers responsible for late Paleozoic remagnetization in carbonate strata of the Mid-continent, U.S.A. Earth & Plan. Sci. Lett. **99**, 351-361.
Lu, G., McCabe, C., Hanor, J.S., Ferrell, R.E., 1991. A genetic link between remagnetization and potassic metasomatism in the Devonian Onondaga Formation, Northern Appalachian Basin. Geophysical Research Letters 18, 2047-2050.
Machel, H.G., 1995. Magnetic mineral assemblages and magnetic contrasts in diagenetic environments with implications for studies of palaeomagnetism, hydrocarbon migration and exploration. Geological Society, London, Special Publications **98**, 9-29.
Mathews, W.H., Bustin, R.M., 1984. Why do the Smoking Hills smoke? Canadian Journal of Earth Sciences 21, 737-742.
McCabe, C., Elmore, R.D., 1989. The occurrence and origin of Late Paleozoic remagnetization in the sedimentary rocks of North America. Reviews of Geophysics 27, 471-494.
McCabe, C., Sassen, R., Saffer, B., 1987. Occurrence of secondary magnetite within biodegraded oil. Geology 15, 7-10.
McCabe, C., Van der Voo, R., Peacor, D.R., Scotese, C.R., Freeman, R., 1983. Diagenetic magnetite carries ancient yet secondary remanence in some Paleozoic sedimentary carbonates. Geology 11, 221-223.
McElhinny, M.W., 1973. Paleomagnetism and Plate Tectonics. Cambridge University Press, Cambridge.
McKirdy, D.M., Aldridge, A.K., Ypma, P.J.M., 1983. A geochemical comprison of some crude oils from pre-Ordovician carbonate rocks. Adv. Org. Geochem. Abu Dhabi Pet. Conf., 99-107.
McKirdy, D.M., Powell, T.G., 1973. Relationship between pristane to phytane ratio, crude oil composition, and geological environment in Australia, in: Austral., G. (Ed.). Bureau of Mineral Resources, Geology and Geophysics.

McMahon, N.A., Turner, J., 1998. The documentation of a latest Jurassic-earliest Cretaceous uplift throughout southern England and adjacent offshore areas. Geol. Soc. Lon. Sp. Pub. (eds.) J. R. Underhill 133, 215-240.
Moldowan, J.M., Seifert, W.K., Gallegos, E.J., 1985. Relationship between petroleum composition and depositional environment of petroleum source rocks. AAPG Bulletin 69, 1255-1268.
Moreau, M.G., Ader, M., Enkin, R.J., 2005. The magnetization of clay-rich rocks in sedimentary basins: low-temperature experimental formation of magnetic carriers in natural samples. Earth and Planetary Science Letters 230, 193-210.
Mudiaga, O.C., Oforka, N.C. and Osuji, L.C., 2011. Trace metals geochemistry of crude oils from Umutu/Bomu fields in south west Niger Delta Nigeria. Energy & Environent Reserach 1, 139-146.
Muxworthy, A.R., McClelland, E., 2000. Review of the low-temperature magnetic properties of magnetite from a rock magnetic perspective. Geophysical Journal International 140, 101-114.
Nelson, P.H., 2009. Pore-throat sizes in sandstones, tight sandstones, and shales. AAPG Bulletin 93, 329-340.
Nilsson, A., Lee, Y.S., Snowball, I., Hill, M., 2013. Magnetostratigraphic importance of secondary chemical remanent magnetizations carried by greigite (Fe3S4) in Miocene sediments, New Jersey shelf (IODP Expedition 313). Geosphere 9, 510-520.
Nygård, R., Gutierrez, M., Høeg, K., Bjørlykke, K., 2004. Influence of burial history on microstructure and compaction behaviour of Kimmeridge clay. Petroleum Geoscience 10, 259-270.
Oliver, J., 1986. Fluids expelled tectonically from orogenic belts: Their role in hydrocarbon migration and other geologic phenomena. Geology 14, 99-102.
Oliver, J., 1992. The spots and stains of plate tectonics. Earth-Science Reviews 32, 77-106.
Ourisson, G., Rohmer, M., Poralla, K., 1987. Prokaryotic Hopanoids and other Polyterpenoid Sterol Surrogates. Annual Review of Microbiology 41, 301-333.
Palacas, J.G., 1983. Carbonate Rocks as Sources of Petroleum: Geological and Chemical Characteristics and Oil-Source Correlations. World Petroleum Congress.
Peirce, J.W., Goussev, S.A., Charters, R.A., Abercrombie, H.J., DePaoli, G.R., 1998. Intrasedimentary magnetization by vertical fluid flow and exotic geochemistry. The Leading Edge 17, 89-92.
Penn, I.E., Chadwick, R.A., Holloway, S., Roberts, G., Pharaoh, T.C., Allsop, J.M., Hulbert, A.G., Burns, I.M., 1986. Principal Features of the Hydrocarbon Prospectivity of the Wessex-Channel Basin, U.K: Proceedings of the 3rd Conference on Petroleum Geology of N.W. Europe. Graham & Trotman.
Pepper, A.S., Corvi, P.J., 1995. Simple kinetic models of petroleum formation. Part I: oil and gas generation from kerogen. Marine and Petroleum Geology 12, 291-319.
Peters, K.E., Moldowan, J.M., 1991. Effects of source, thermal maturity, and biodegradation on the distribution and isomerization of homohopanes in petroleum. Organic Geochemistry 17, 47-61.
Peters, K.E., Walters, C.C., Moldowan, J.M., 2005. The Biomarker Guide: Volume 2, Biomarkers and Isotopes in Petroleum Systems and Earth History. Cambridge University Press.
Plaster-Kirk, L.E., Elmore, R.D., Engel, M.H., Imbus, S.W., 1995. Palaeomagnetic investigation of organic-rich lacustrine deposits, Middle Old Red Sandstone, Scotland. Scottish Journal of Geology 31, 97-105.
Plint, A.G., 1982. Eocene sedimentation and tectonics in the Hampshire Basin. Journal of the Geological Society 139, 249-254.
Postma, D., 1977. The occurrence and chemical composition of Recent Fe-rich mixed carbonates in a river bog. Journal of Sedimentary Research 47, 1089-1098.
Potter, D., 2008. Method and apparatus for rock sample analysis using magnetic susceptibility. Google Patents, Harriot-Watt University.
Pozzi, J.P., Barthès, V., Thibal, J., Pocachard, J., Lim, M., Thomas, T., Pages, G., 1993. Downhole magnetostratigraphy in sediments: Comparison with the paleomagnetism of a core. Journ. Geophys. Res. **98**, 7939-7957.
Pye, K., Dickson, J.A.D., Schiavon, N., Coleman, M.L., Cox, M., 1990. Formation of siderite-Mg-calcite-iron sulphide concretions in intertidal marsh and sandflat sediments, north Norfolk, England. Sedimentology 37, 325-343.
Reynolds, R.L., Fishman, N.S., Hudson, M.R., 1991. Sources of aeromagnetic anomallies over Cement oil field (Oklahoma), Simpson oil field (Alaska) and the Wyoming-Idaho-Utah thrust belt. Geophysics 56, 606-617.

Richardson, K.G., Noltimier, H.C., 1980. Paleomagnetic study of the Mahogany Oil Shale, Uinta Basin, Utah. Am. Geophys. Un., abs, 215-216.
Richter, C., Roberts, A.P., Stoner, J.S., Benning, L.D., Chi, C.T., 1998. Magnetostratigraphy of Pliocene-Pleistocene sediments from the eastern Mediterranean Sea, in: Robertson, A.H.F., Emeis, K.C., Richter, C., Camerlenghi, A. (Eds.), Procs of ODP Scientific Results. Vol.160. Mediterranean I: covering Leg 160 of the cruises of the Drilling Vessel "Joides Resolution", Las Palmas, Gran Canaria, to Naples, Italy, Sites 963-973, 7 March - 3 May 1995. Texas A & M University Ocean Drilling Program, pp. 61-73.
Rijal, M.L., Appel, E., Petrovský, E., Blaha, U., 2010. Change of magnetic properties due to fluctuations of hydrocarbon contaminated groundwater in unconsolidated sediments. Environmental Pollution 158, 1756-1762.
Roberts, A.P., Chang, L., Rowan, C.J., Horng, C.-S., Florindo, F., 2011. Magnetic properties of sedimentary greigite (Fe3S4): An update. Rev. Geophy. 49, 227-236.
Roberts, A.P., Pike, C.R., Verosub, K.L., 2000. First-order reversal curve diagrams: A new tool for characterizing the magnetic properties of natural samples. Jour. Geophy. Res. **105**, 28461-28475.
Roberts, A.P., Turner, G.M., 1993. Diagenetic formation of ferrimagnetic iron sulphide minerals in rapidly deposited marine sediments, South Island, New Zealand. Earth and Planetary Science Letters 115, 16.
Roberts, A.P., Weaver, R., 2005. Multiple mechanisms of remagnetization involving sedimentary greigite (Fe3S4). Earth and Planetary Science Letters 231, 263-277.
Rowan, C.J., Roberts, A.P., Broadbent, T., 2009. Reductive diagenesis, magnetite dissolution, greigite growth and paleomagnetic smoothing in marine sediments: A new view. Earth and Planetary Science Letters 277, 223-235.
Sagnotti, L., Roberts, A.P., Weaver, R., Verosub, K.L., Florindo, F., Pike, C.R., Clayton, T., Wilson, G.S., 2005. Apparent magnetic polarity reversals due to remagnetization resulting from late diagenetic growth of greigite from siderite. Geophysical Journal International 160, 89-100.
Sainbayar, J., Monkhoobor, D. & Budeebazar, A., 2012. Determination of trace elements in the Tamsagbulag and Tagaan Els crude oils and their distillation fractions by using ICP-OES. Adv. Chem. Eng. & Sci 2, 113-117.
Sassen, R., 1980. Biodegradation of crude oil and mineral deposition in a shallow Gulf Coast salt dome. Organic Geochemistry 2, 153-166.
Saunders, D.F., Burson, K.R., Thompson, C.K., 1991. Observed relation of soil magnetic susceptibility and soil gas hydrocarbon analyses to subsurface hydrocarbon accumulations. AAPG Bulletin 75, 389-408.
Schwartz, W., 1980. B. P. Tissot and D. H. Welte, Petroleum Formation and Occurrence. A new Approach to Oil and Gas Exploration. Springer-Verlag. Berlin. Heidelberg. New York. Zeitschrift für allgemeine Mikrobiologie **20**, pp 428.
Schwarz, E.J., 1975. Magnetic properties of Pyrrhotite & their use in applied geology & geophysics. Geological Survey, Canada.

.
Scotchman, I.C., 1989. Diagenesis of the Kimmeridge Clay Formation, onshore UK. Journal of the Geological Society 146, 285-303.
Shirey, W.B., 1931. Metallic constituents of cude petroleum. Industrial & Engineering Chemistry 23, 1151-1153.
Sibson, R.H., 1995. Selective fault reactivation during basin inversion: potential for fluid redistribution through fault-valve action. Geological Society, London, Special Publications 88, 3-19.
Smith, C., Hatton, I.R., 1998. Inversion tectonics in the Lyme Bay-West Dorset area of the Wessex Basin, UK. Geological Society, London, Special Publications 133, 267-281.
Stainforth, J.G., 2009. Practical kinetic modeling of petroleum generation and expulsion. Marine and Petroleum Geology 26, 552-572.

Stone, V.C.A., Fairhead, J.D., Oterdoom, W.H., 2004. Micromagnetic seep detection in the Sudan. The Leading Edge 23, 734-737.
Stoneley, R., 1982. The structural development of the Wessex Basin. Journal of the Geological Society 139, 543-554.
Stoneley, R., Selley, R.C., 1986. A field guide to the petroleum geology of the Wessex Basin. Department of Geology, Imperial College London.
Suk, D., Peacor, D.R., der Voo, R.V., 1990. Replacement of pyrite framboids by magnetite in limestone and implications for palaeomagnetism. Nature 345, 611-613.
Sundararaman, P., Raedeke, D., L., 1993. Vanadyl porphyrins in exploration: Maturity indicators for source rocks and oils. Elsevier, Kidlington, UK.
Taylor, G.K., Tauxe, L., 2010. Essentials of Paleomagnetism. 489 pp. University of California Press. .
Tipler, P.A., 1999. Physics for Scientists and Engineers. W. H. Freeman/Worth Publishers (New York). .
Tissot, B.P., Welte, D.H., 1984. Petroleum formation and occurrence. Springer-Verlag. Berlin. New York.
Tohver, E., Weil, A.B., Solum, J.G., Hall, C.M., 2008. Direct dating of carbonate remagnetization by 40Ar/39Ar analysis of the smectite–illite transformation. Earth and Planetary Science Letters 274, 524-530.
Tric, E., Laj, C., Jéhanno, C., Valet, J.-P., Kissel, C., Mazaud, A., Iaccarino, S., 1991. High-resolution record of the Upper Olduvai transition from Po Valley (Italy) sediments: support for dipolar transition geometry? Physics of the Earth and Planetary Interiors 65, 319-336.
Tyson, R., 2005. The" productivity versus preservation" controversy: cause, flaws, and resolution. Sp. pub.-sepm. (eds.) N. B. Harris 82, 17-33.
Tyson, R.V., 1987. The genesis and palynofacies characteristics of marine petroleum source rocks. Geological Society, London, Special Publications 26, 47-67.
Underhill, J.R., Paterson, S., 1998. Genesis of tectonic inversion structures: seismic evidence for the development of key structures along the Purbeck–Isle of Wight Disturbance. Journal of the Geological Society 155, 975-992.
Underhill, J.R., Stoneley, R., 1998. Introduction to the development, evolution and petroleum geology of the Wessex Basin. Geol. Soc. Lon. Sp. Pub. (eds.) J. R. Underhill 133, 1-18.
Volkman, J.K., 1988a. Biological marker compounds as indicators of the depositional environments of petroleum source rocks. Geological Society, London, Special Publications 40, 103-122.
Volkman, J.K., 1988b. Biological marker compounds as indicators of the depositional environments of petroleum source rocks. Geol. Soc. Lon. Sp. Pub. (eds.) J. R. Underhill 40, 103-122.
Walden, J., Oldfield, F., Smith, J., 1999. Environmental magnetism: A practical guide. Tech. guide No.6 London: Quaternary Research Association.
Waples, D.W., Machihara, T., 1991. Biomarkers for Geologists: a practical guide to the application of steranes and triterpanes in petroleum exploration. Tulsa: AAPG, pp 91.
Wenger, L.M., Davis, C.L., Isaksen, G.H., 2002. Multiple Controls on Petroleum Biodegradation and Impact on Oil Quality.
Westhead, R.K., Woods, M.A., 1994. Anomalous Turonian-Campanian Chalk deposition in south Dorset; the influence of inherited pre-Albian structures. Proceedings of the Geologists' Association 105, 81-89.
Williams, W., Muxworthy, A.R., 2006. Configurational anisotropy in single-domain and pseudosingle-domain grains of magnetite. Jour. Geophy. Res. **111**.
Winklhofer, M., Chang, L., Eder, S.H.K., 2014. On the magnetocrystalline anisotropy of greigite (Fe3S4). Geochemistry, Geophysics, Geosystems 15, 1558-1579.
Wisniowiecki, M.J., Van der Voo, R., McCabe, C., Kelly, W.C., 1983. A Pennsylvanian paleomagnetic pole from the mineralized Late Cambrian Bonneterre Formation, southeast Missouri. Jour. Geophys. Res. **88**, 6540-6548.

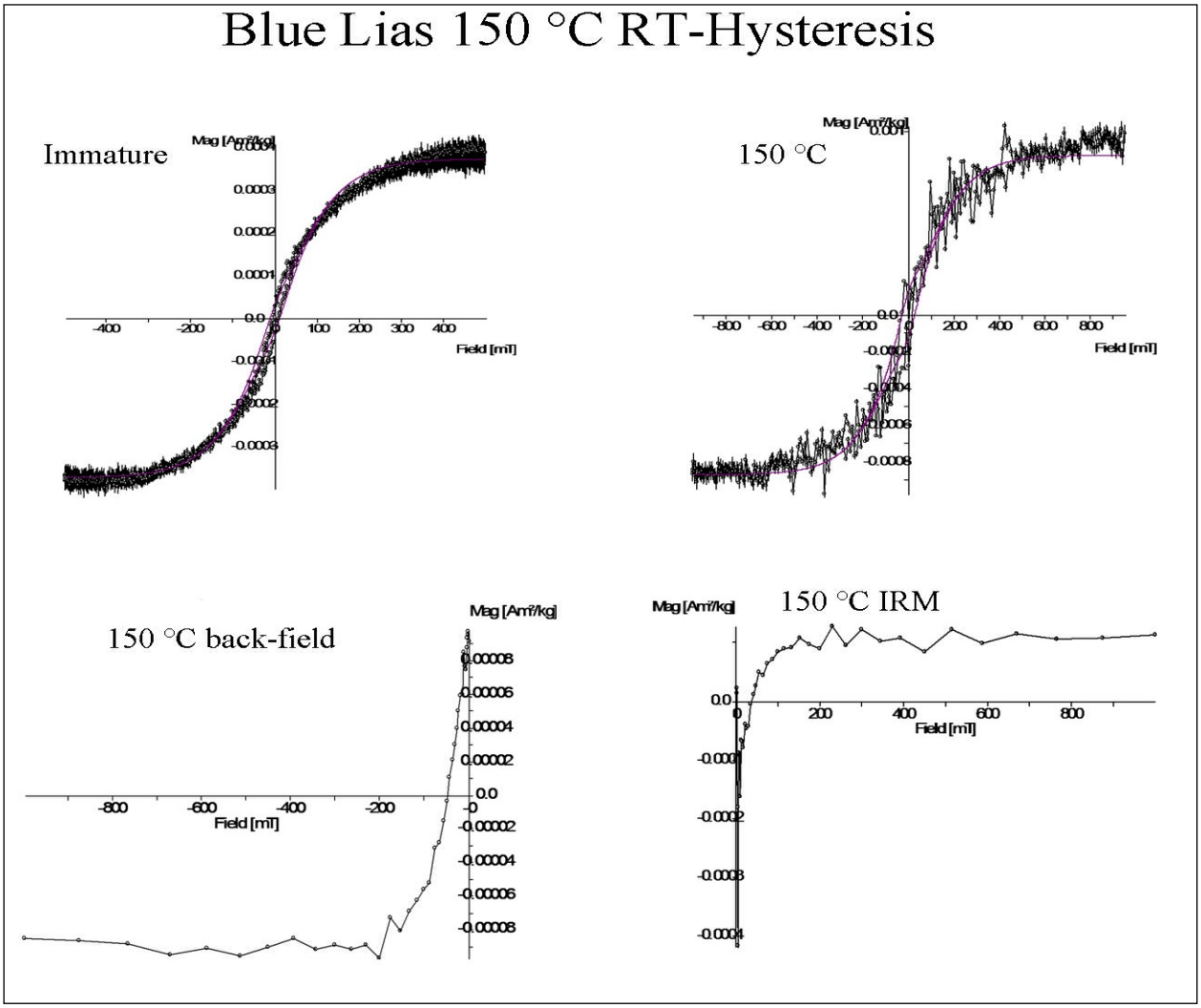
Appendix 1

Magnetic measurements

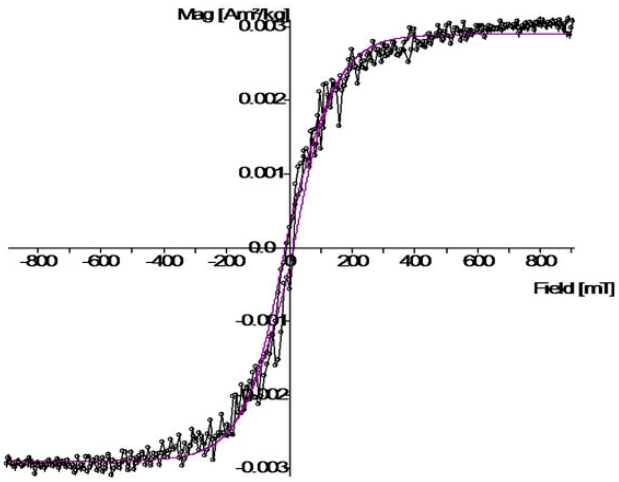
1) RT-Hysteresis measurements
    a) Hysteresis curves
    b) IRM acquisition curves
    c) Back-field acquisition curves
2) LT-Hysteresis measurements
    a) Hysteresis curves
3) Warming curves
    a) Zero-field cooled (ZFC)
    b) Field-cooled (FC)

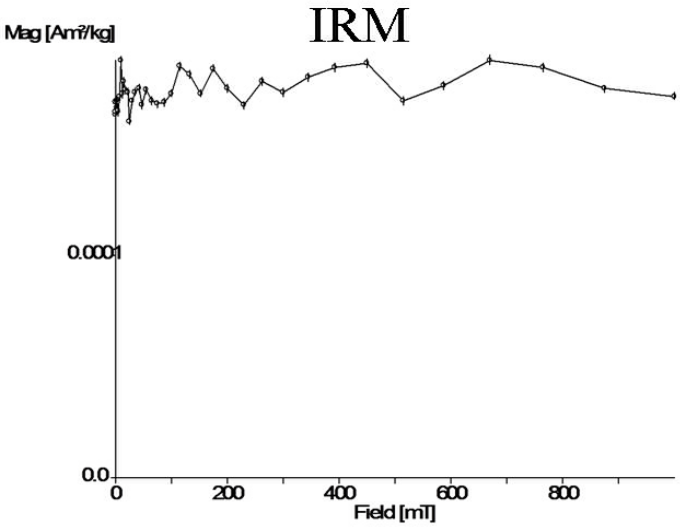
RT-Hysteresis

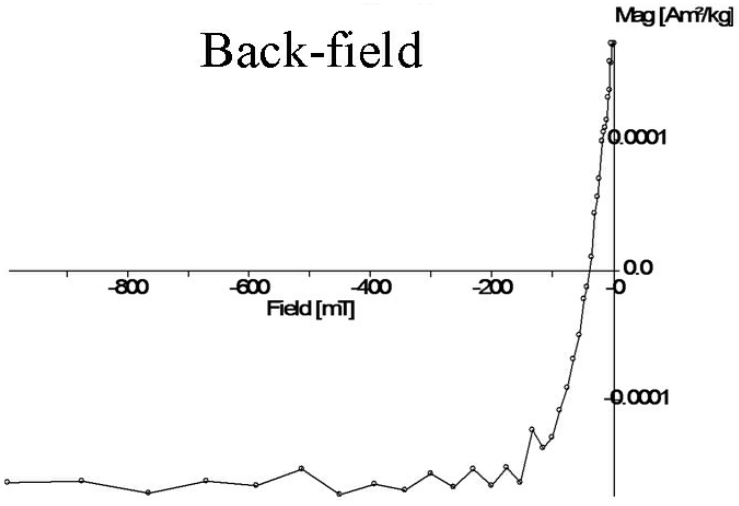
RT-Hysteresis experiments carried out in on three potential source rocks are presented below.



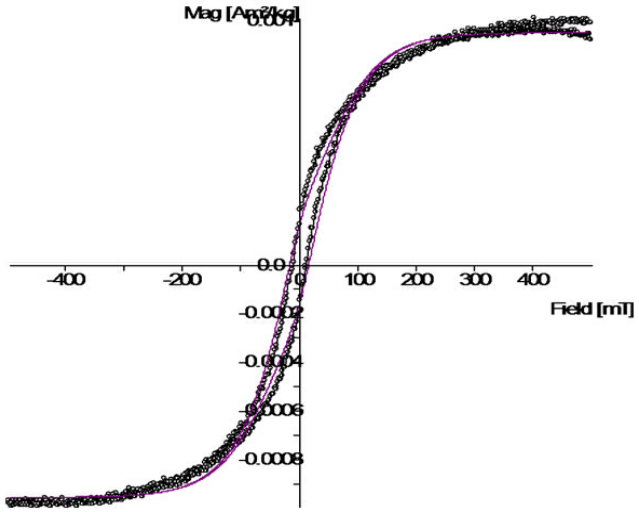
Blue Lias 200 °C RT-Hysteresis



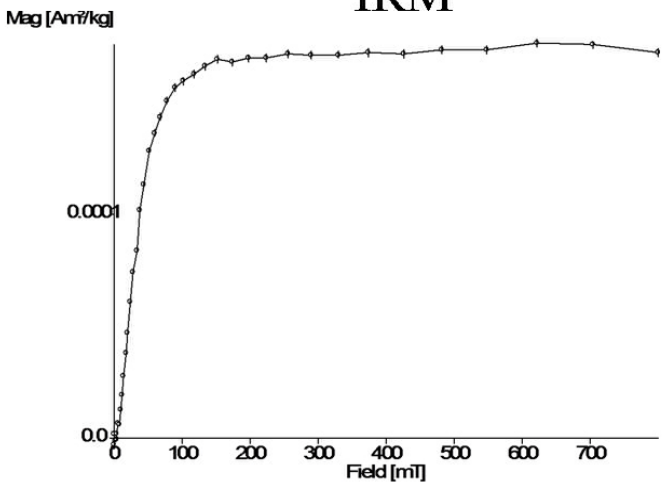




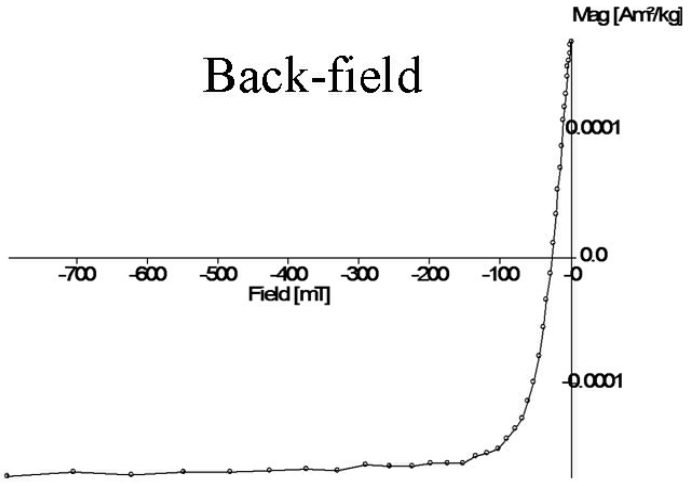
Blue Lias 250 °C RT-Hysteresis



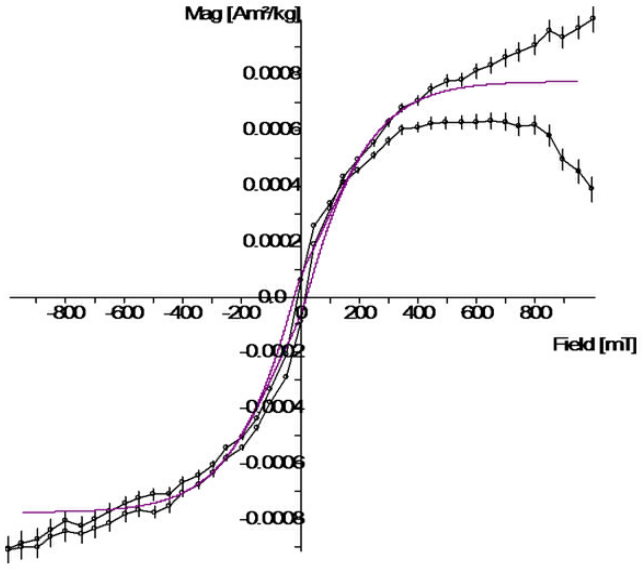
IRM

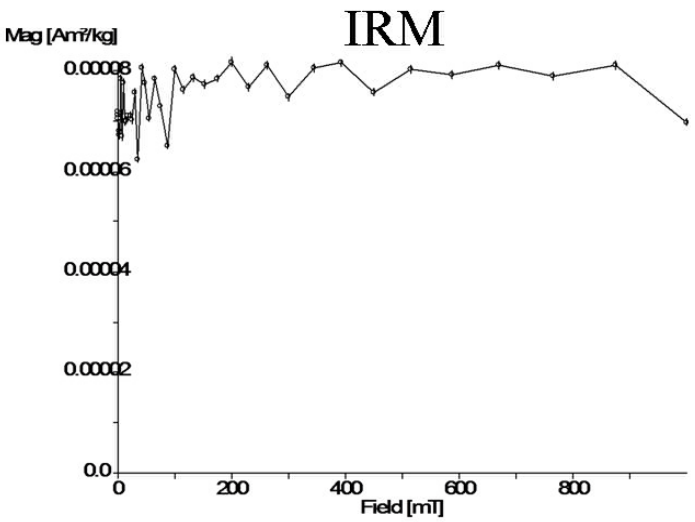


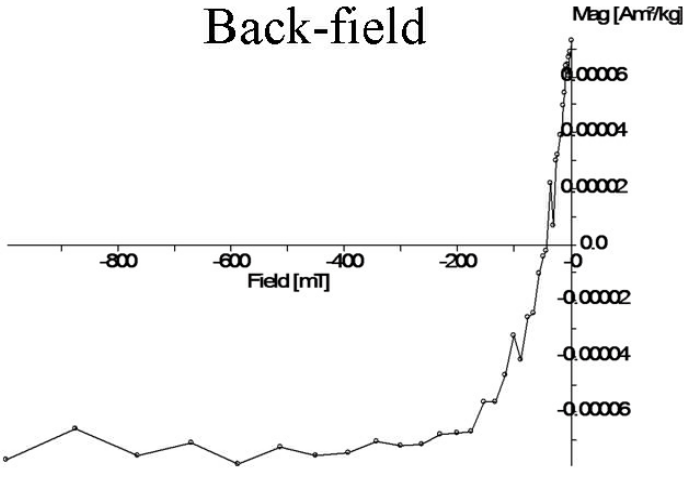
Back-field



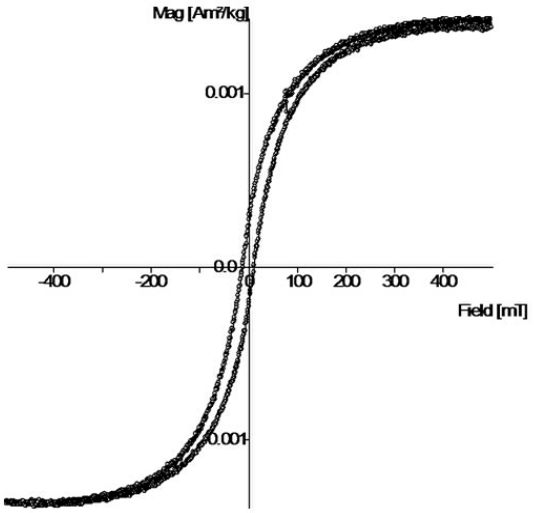
Blue Lias 300 °C RT-Hysteresis



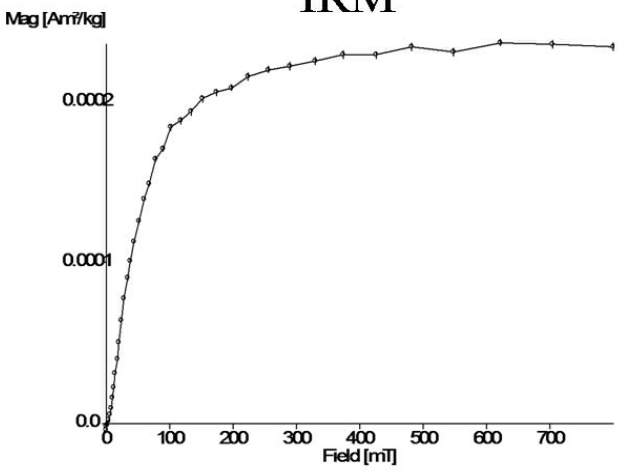




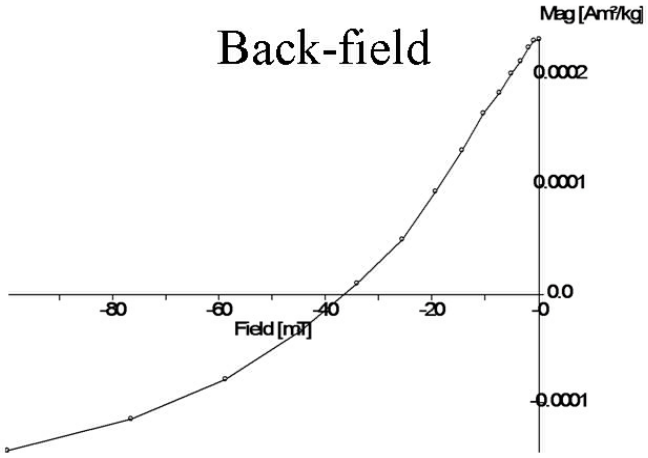
Blue Lias 320 °C RT-Hysteresis



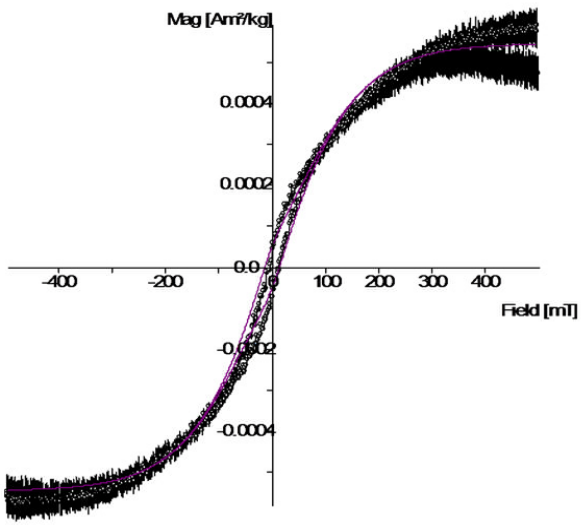
IRM

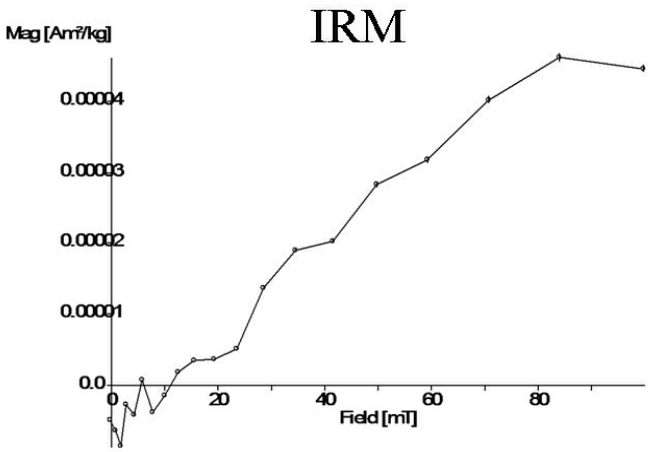


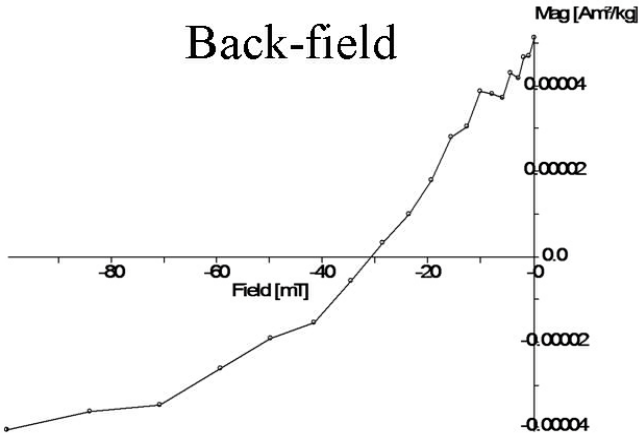
Back-field



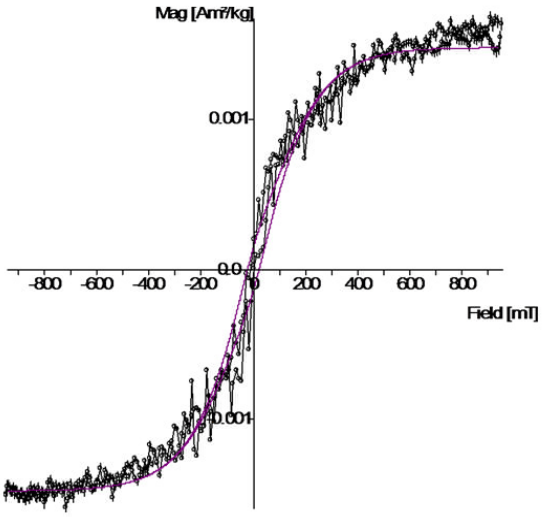
Kimmeridge Clay immature RT-Hysteresis



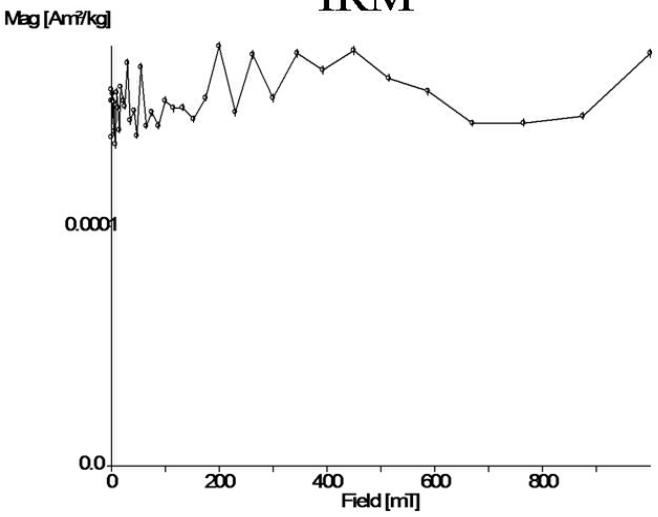




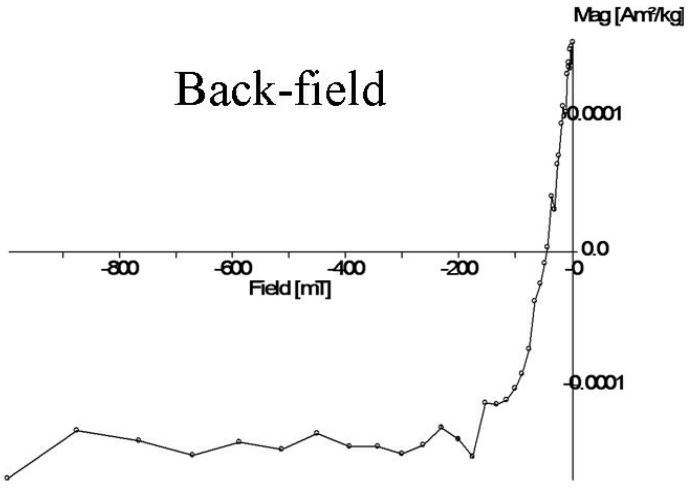
Kimmeridge Clay 150 °C RT-Hysteresis



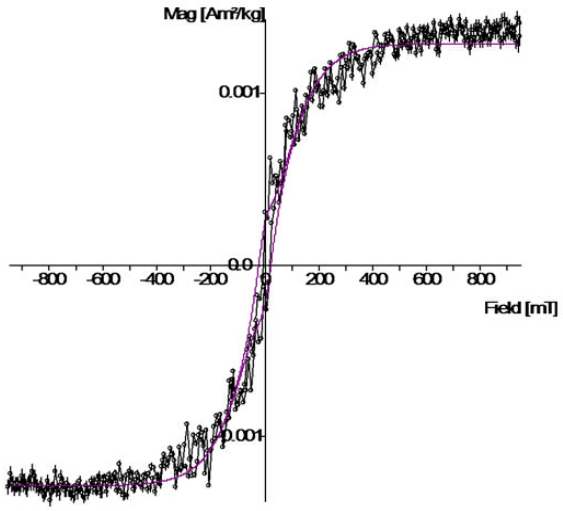
IRM

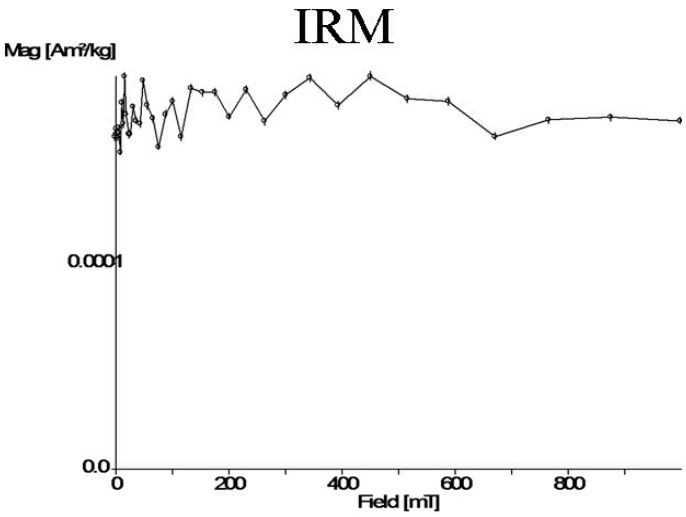


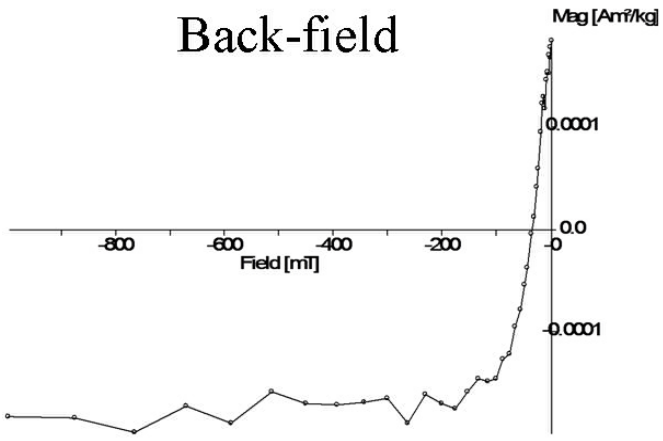
Back-field



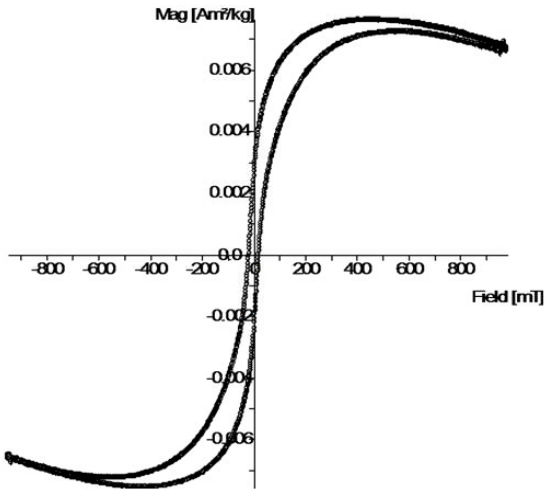
Kimmeridge Clay 200 °C RT-Hysteresis

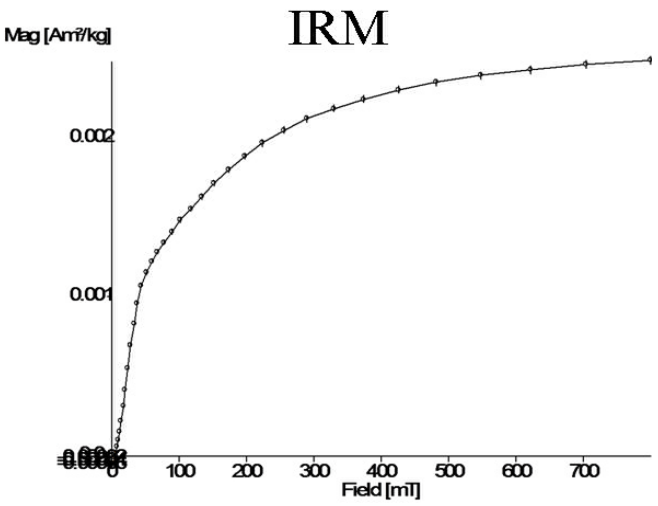


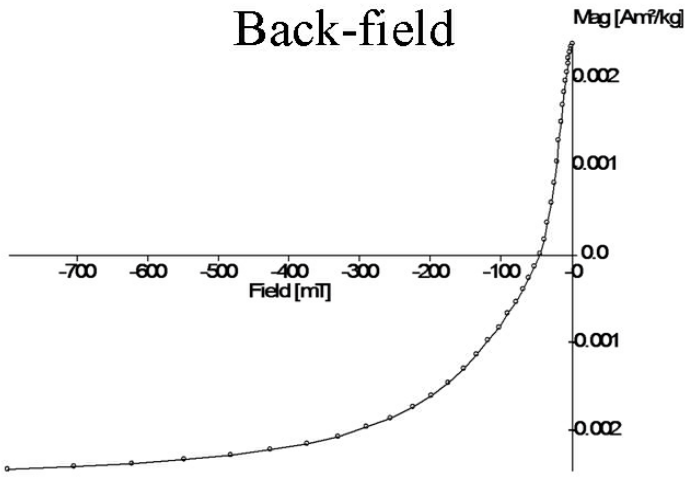




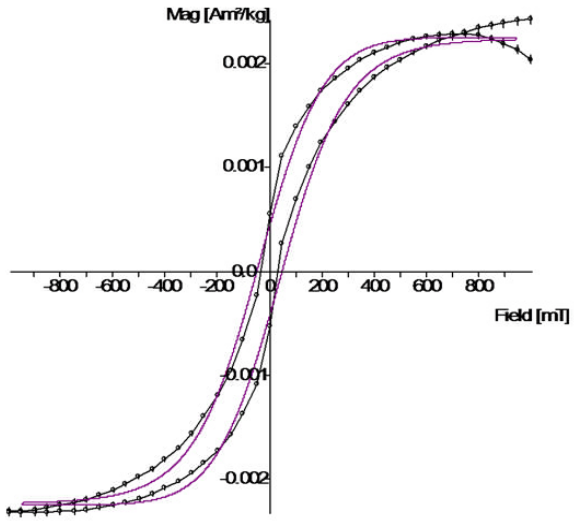
Kimmeridge Clay 250 °C RT-Hysteresis

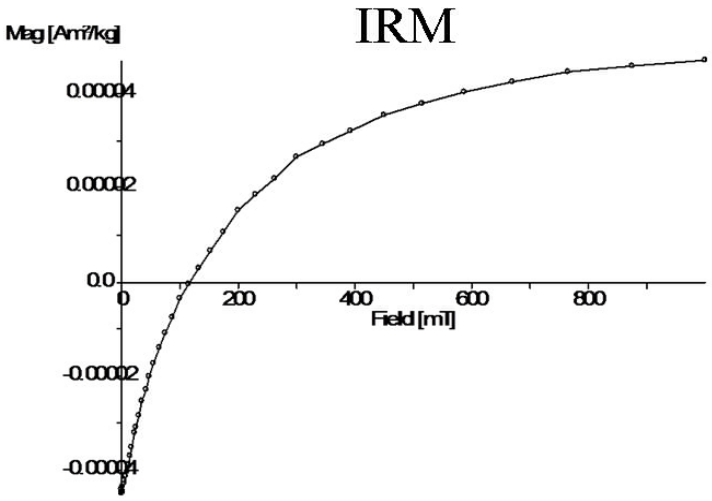


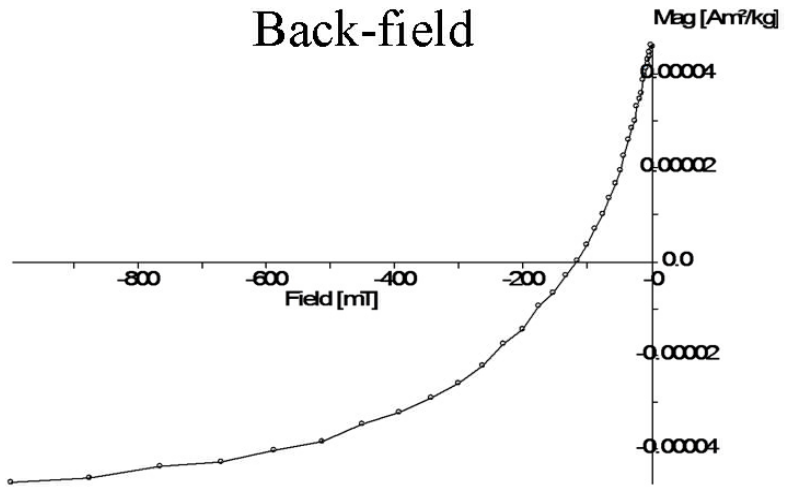




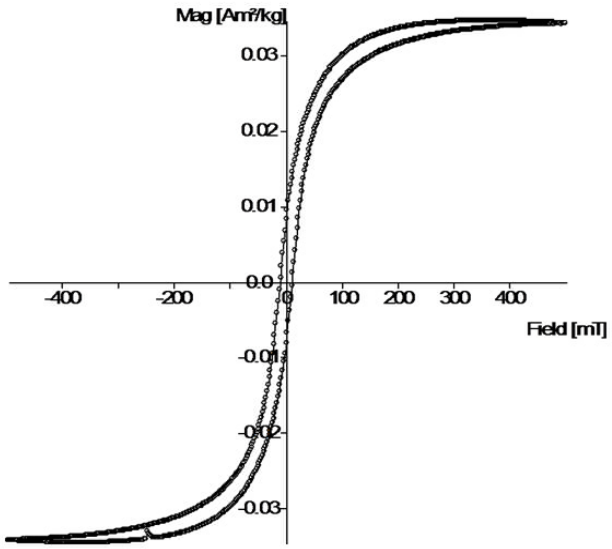
Kimmeridge Clay 300 °C RT-Hysteresis



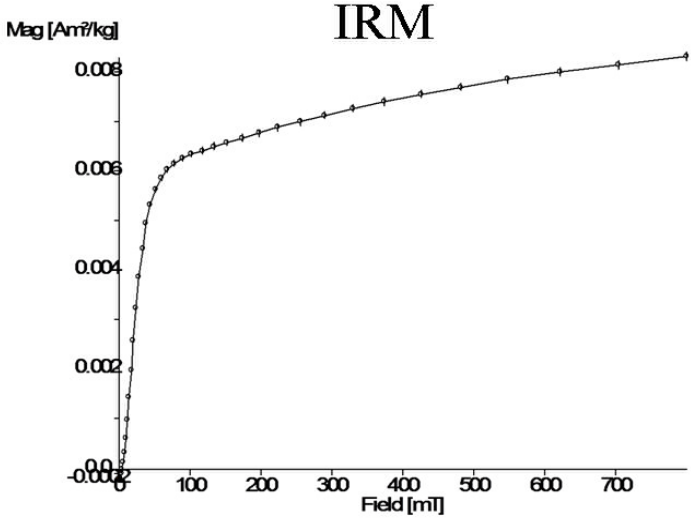




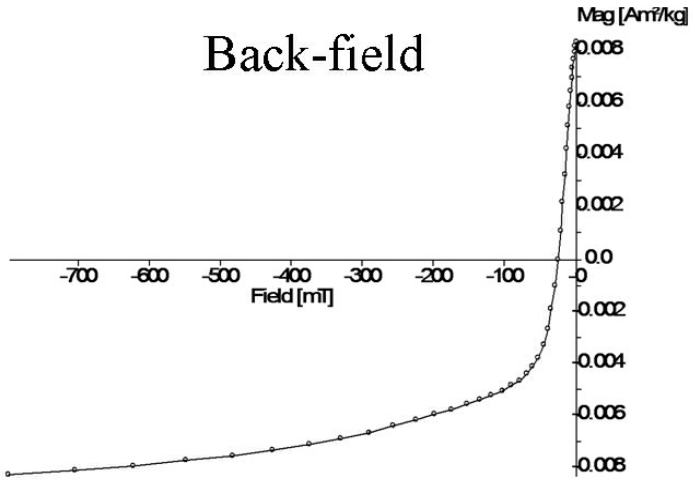
Kimmeridge Clay 320 °C RT-Hysteresis



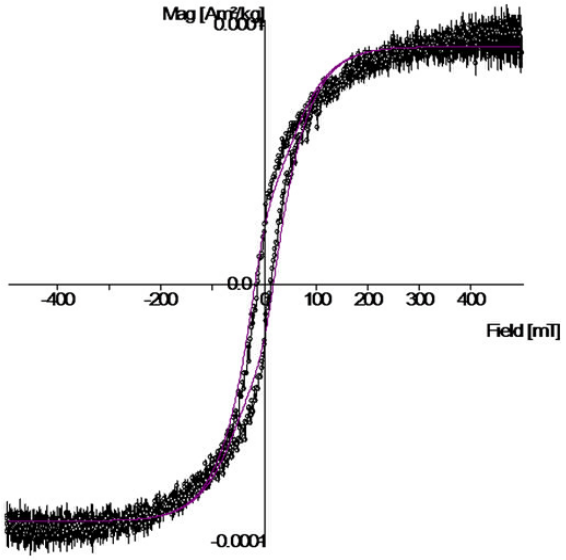
IRM

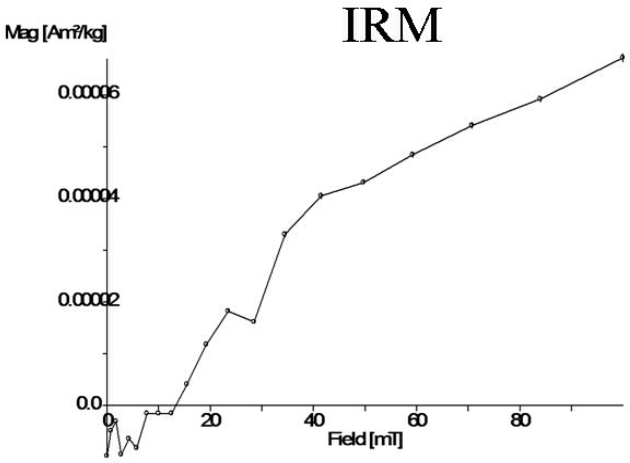


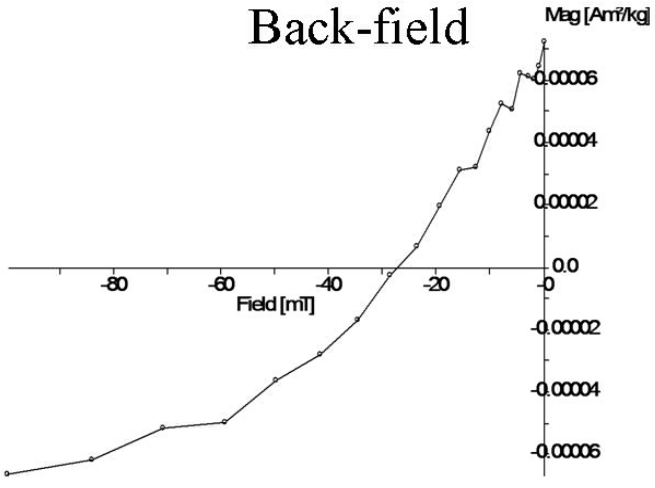
Back-field



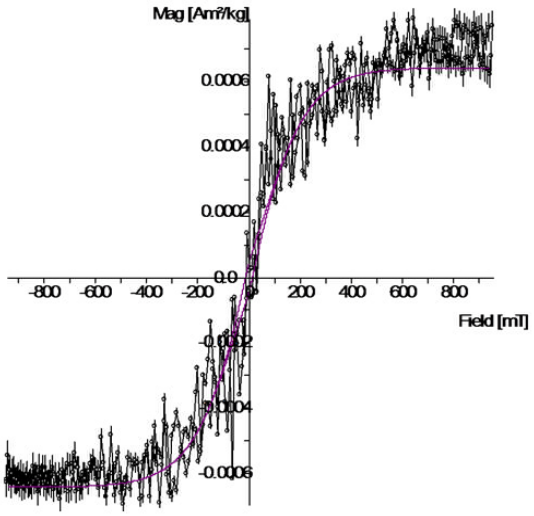
Oxford Clay immature RT-Hysteresis



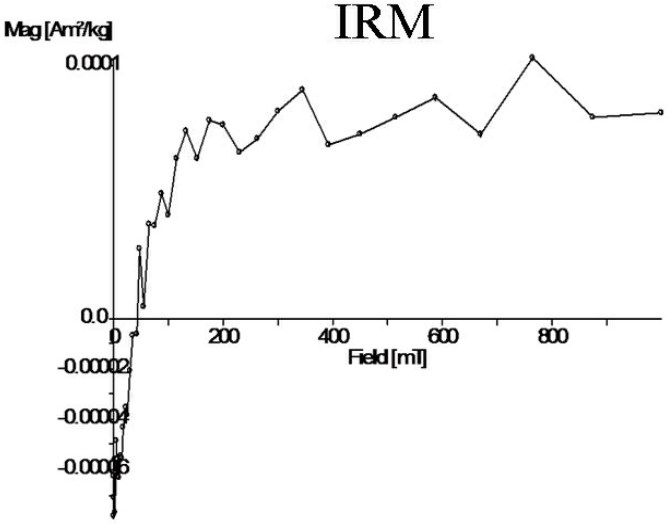




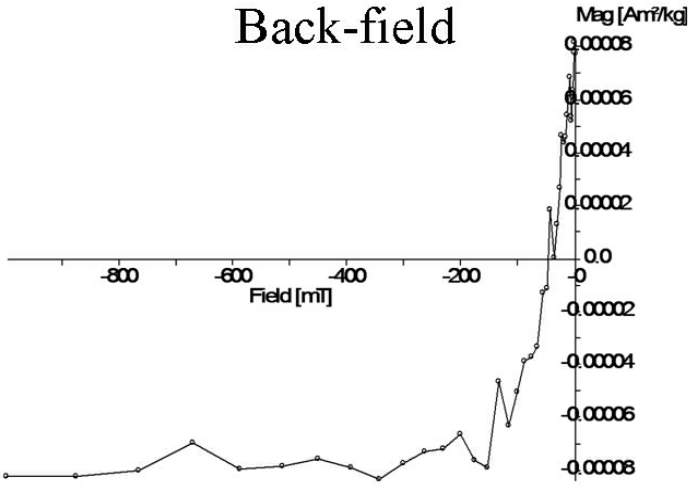
Oxford Clay 150 °C RT-Hysteresis

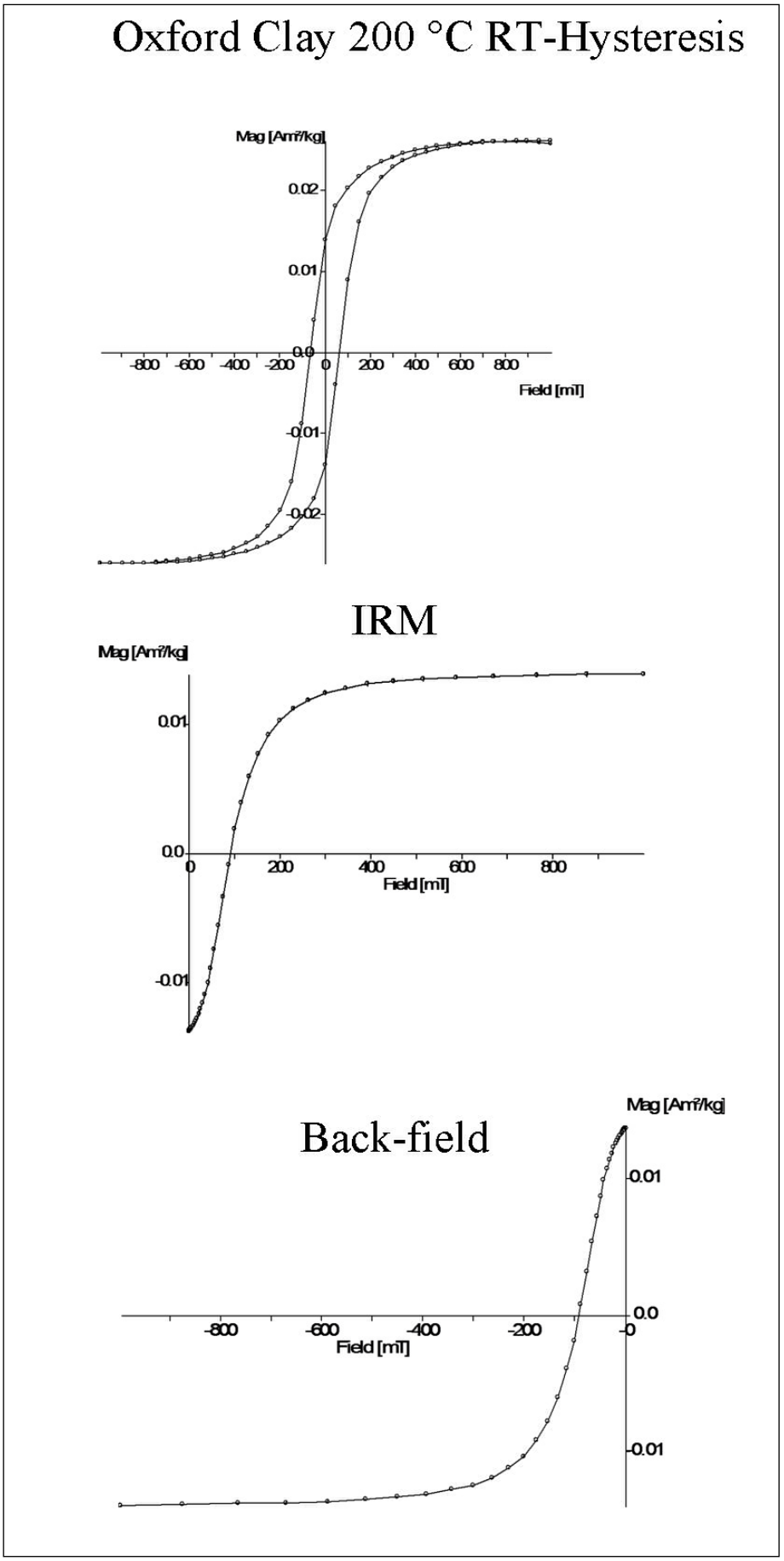


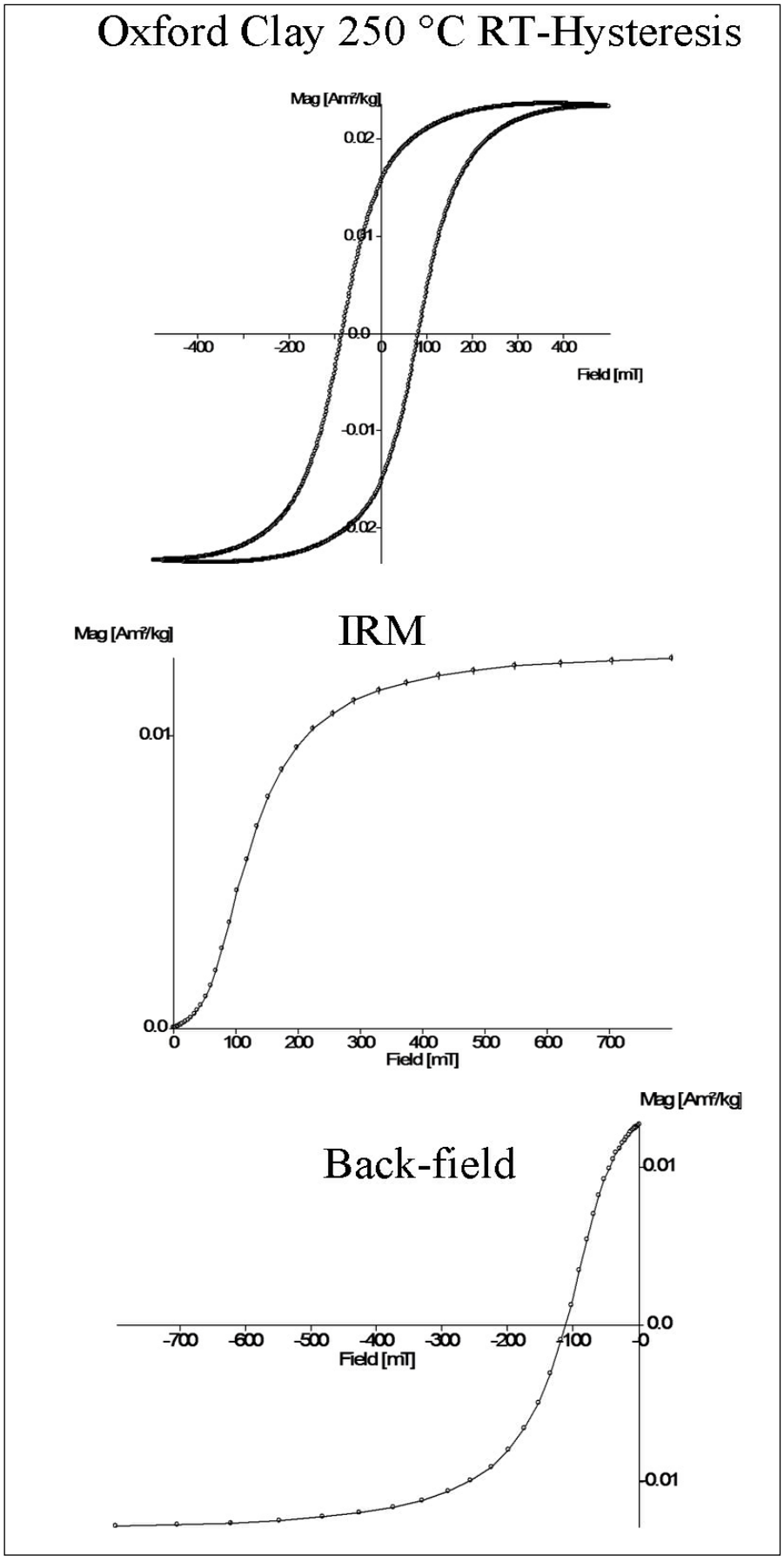
IRM

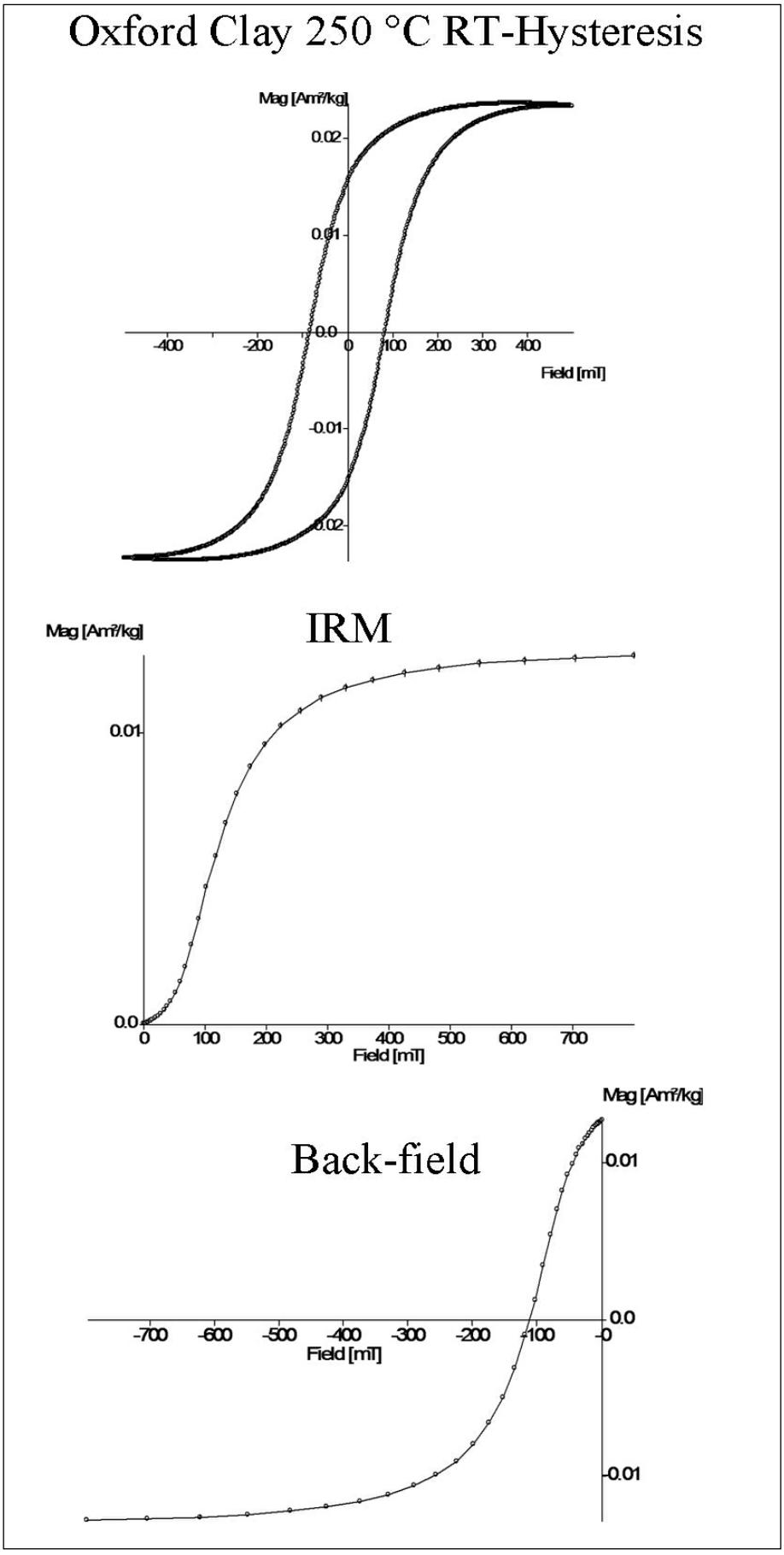


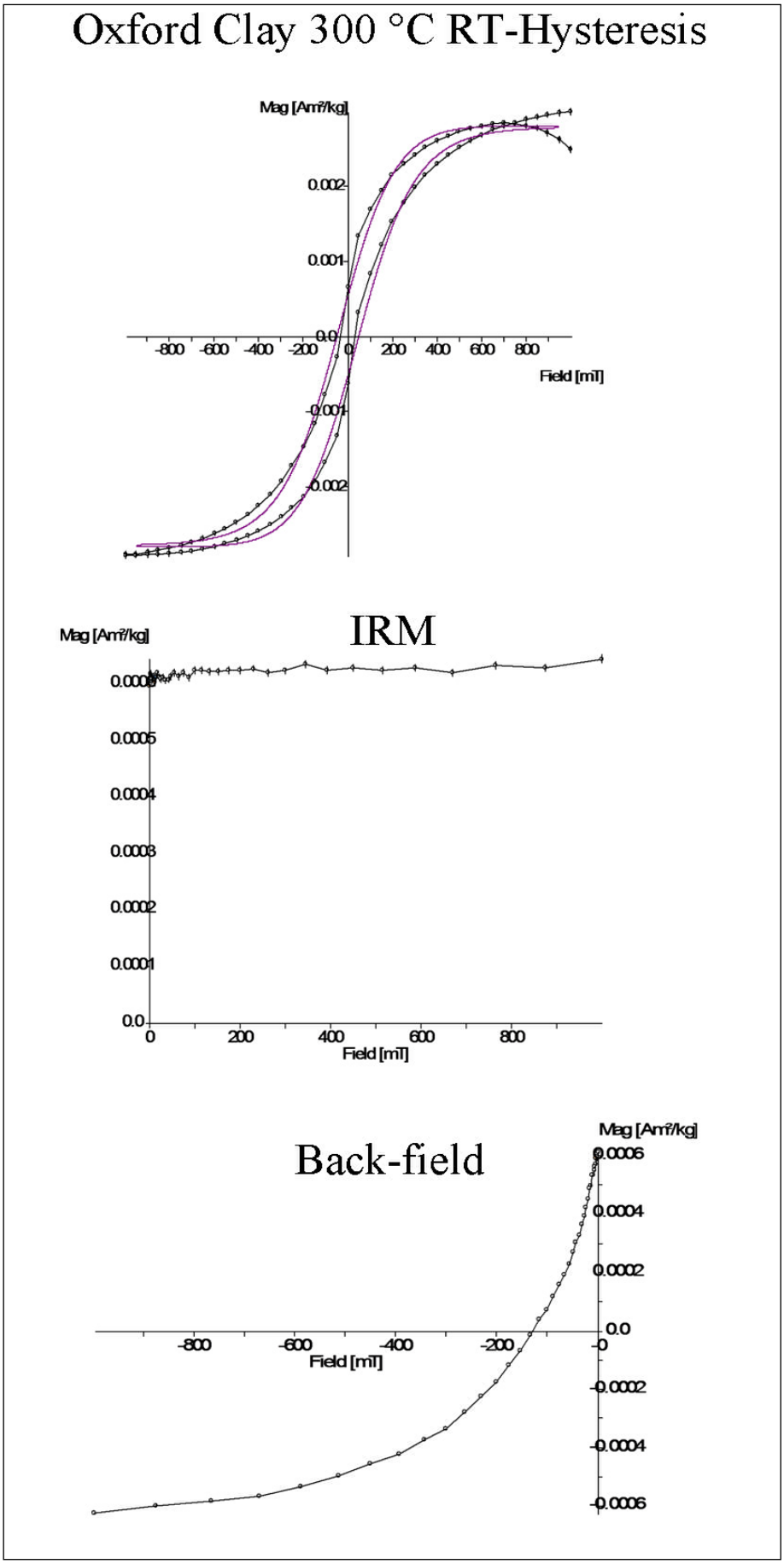
Back-field

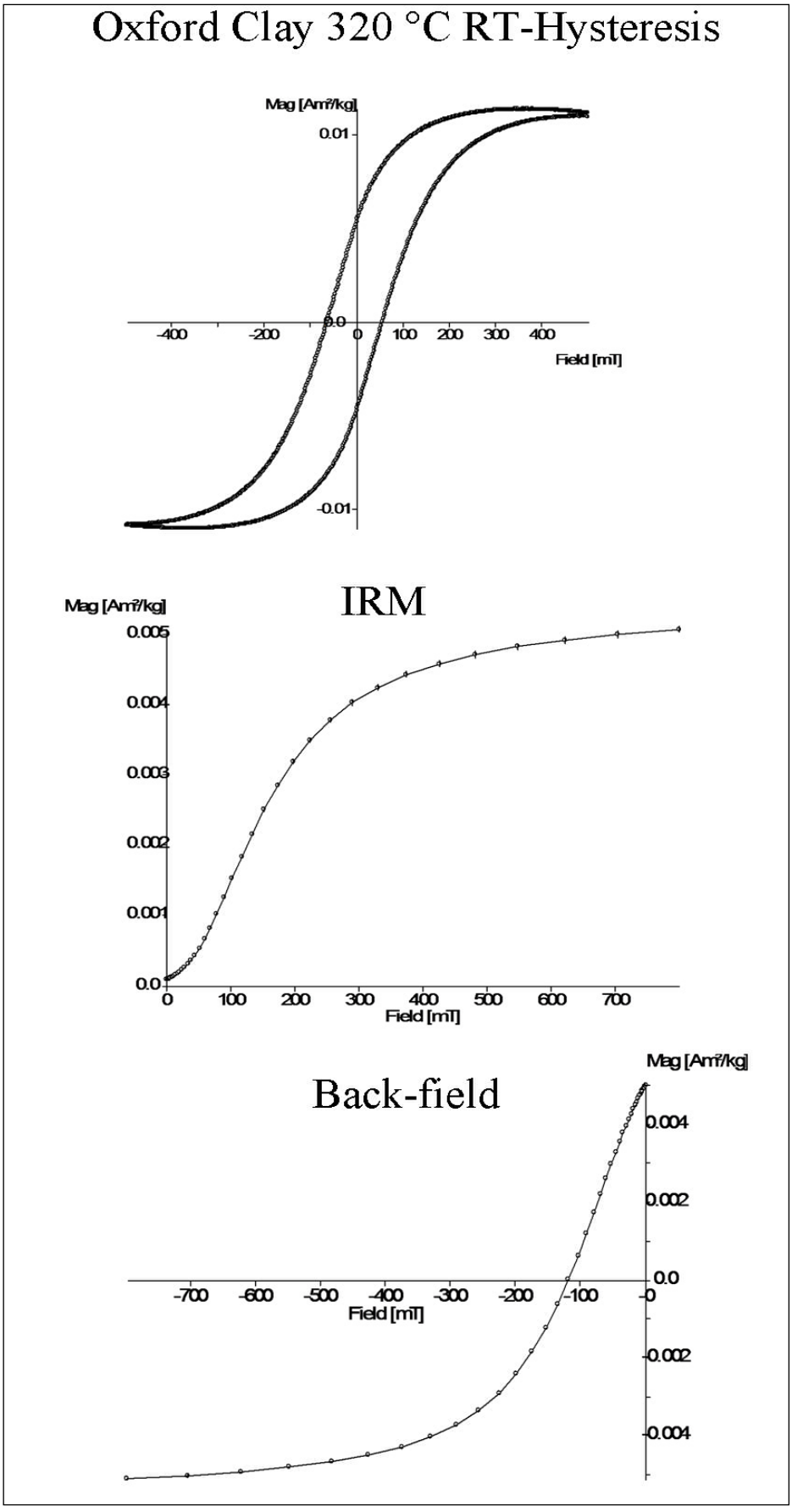



Oxford Clay 200 °C RT-Hysteresis
Mag [Am²/kg]
0.02
0.01
0.0
-0.01
-0.02
-800 -600 -400 -200 0 200 400 600 800
Field [mT]
IRM
Mag [Am²/kg]
0.01
0.0
-0.01
0 200 400 600 800
Field [mT]
Back-field
Mag [Am²/kg]
0.01
0.0
-0.01
-800 -600 -400 -200 -0
Field [mT]

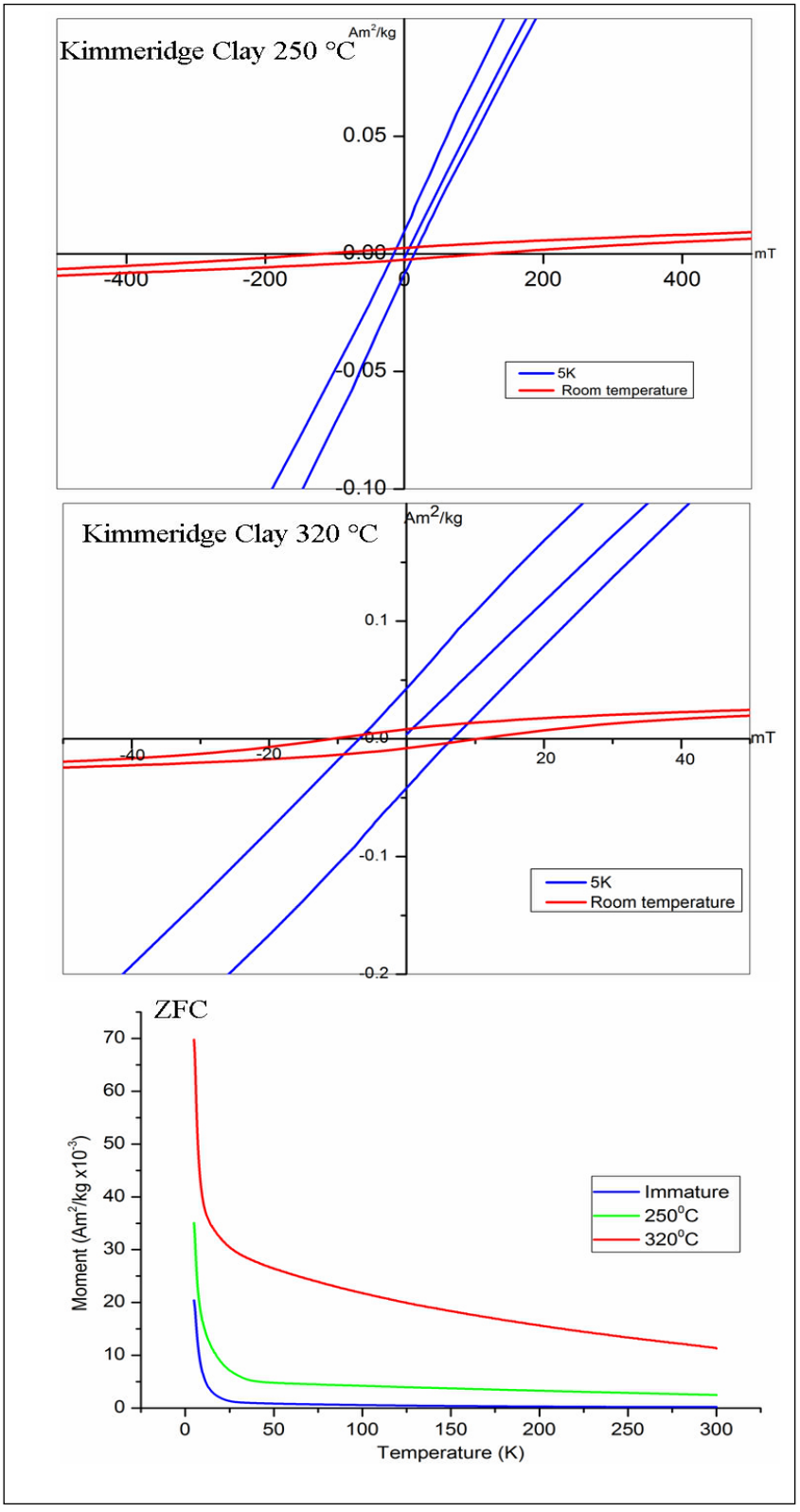

Oxford Clay 250 °C RT-Hysteresis
Mag [Am²/kg]
0.02
0.01
0.0
-0.01
-0.02
-400
-200
0
100
200
300
400
Field [mT]
IRM
Mag [Am²/kg]
0.01
0.0
0
100
200
300
400
500
600
700
Field [mT]
Back-field
Mag [Am²/kg]
0.01
0.0
-0.01
-700
-600
-500
-400
-300
-200
-100
-0
Field [mT]

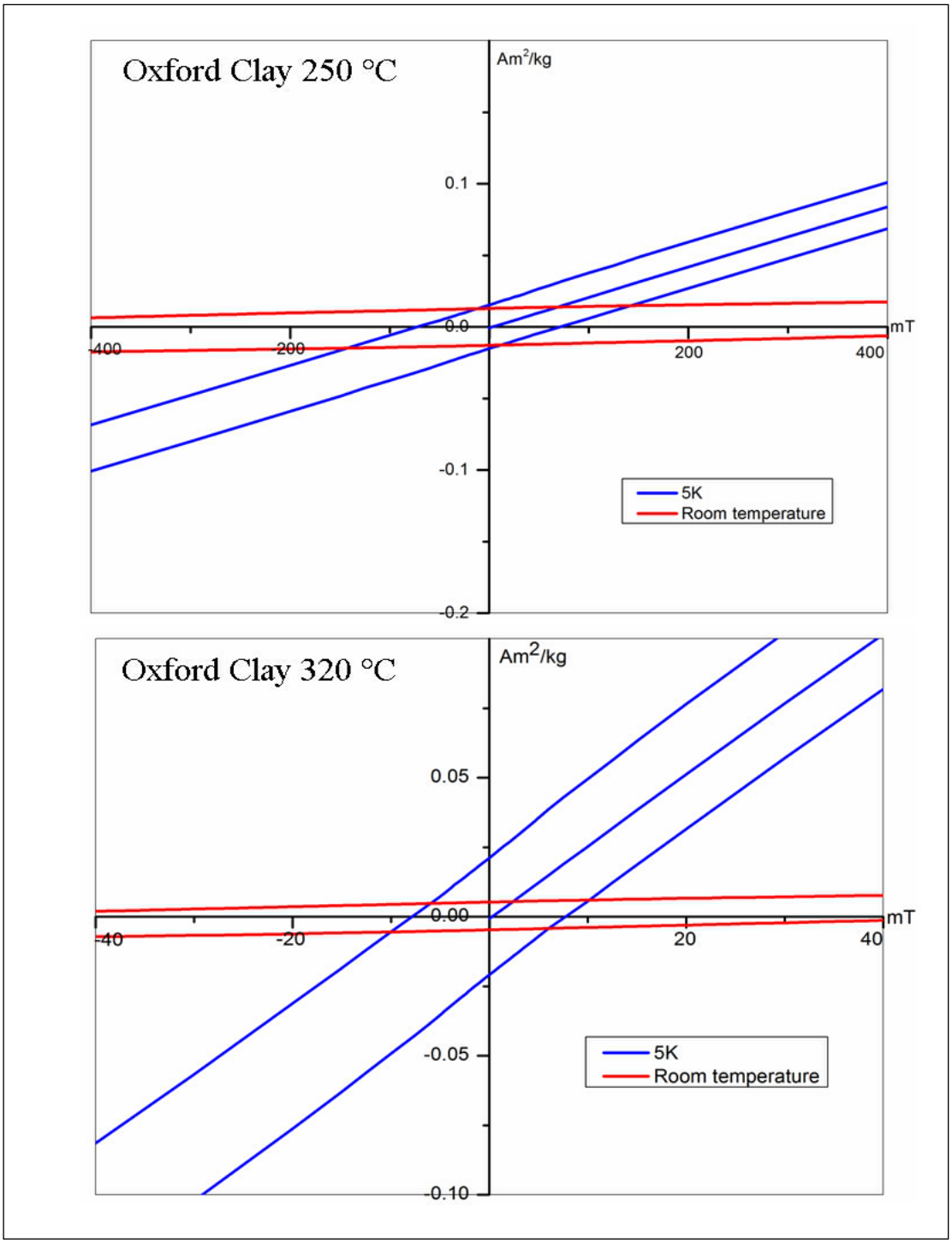

Oxford Clay 250 °C RT-Hysteresis
Mag [Am²/kg]
0.02
0.01
0.0
-0.01
-0.02
-400
-200
0
100
200
300
400
Field [mT]
IRM
Mag [Am²/kg]
0.01
0.0
0
100
200
300
400
500
600
700
Field [mT]
Back-field
Mag [Am²/kg]
0.01
0.0
-0.01
-700
-600
-500
-400
-300
-200
-100
-0
Field [mT]

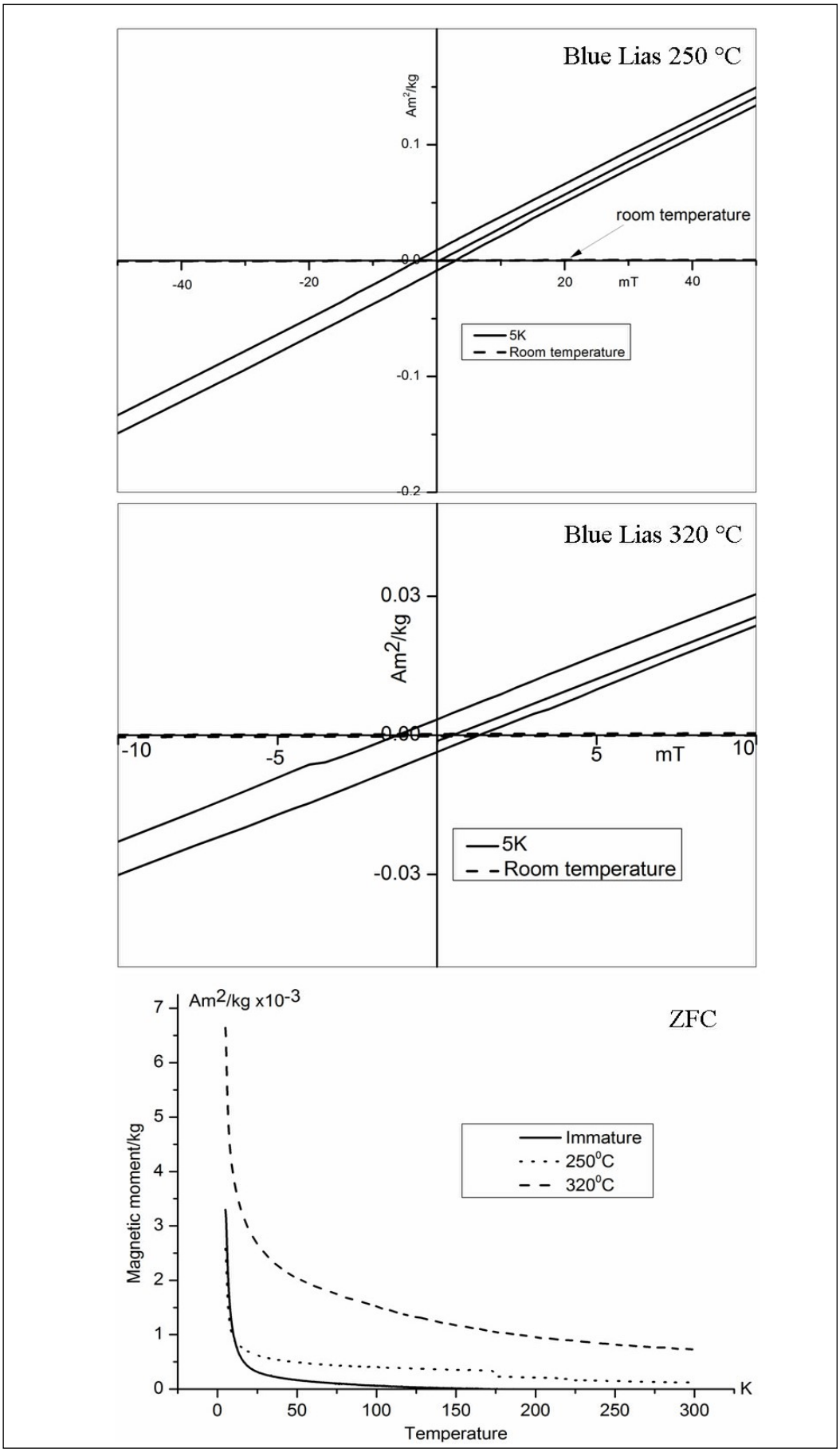

Oxford Clay 300 °C RT-Hysteresis
Mag [Am²/kg]
0.002
0.001
0.0
-0.001
-0.002
-800 -600 -400 -200 0 200 400 600 800
Field [mT]
IRM
Mag [Am²/kg]
0.0006
0.0005
0.0004
0.0003
0.0002
0.0001
0.0
0 200 400 600 800
Field [mT]
Back-field
Mag [Am²/kg]
0.0006
0.0004
0.0002
0.0
-0.0002
-0.0004
-0.0006
-800 -600 -400 -200 -0
Field [mT]


Oxford Clay 320 °C RT-Hysteresis
Mag [Am²/kg]
0.01
-0.01
-400
-200
0.0
0
100
200
300
400
Field [mT]
IRM
Mag [Am²/kg]
0.005
0.004
0.003
0.002
0.001
0.0
0
100
200
300
400
500
600
700
Field [mT]
Back-field
Mag [Am²/kg]
0.004
0.002
0.0
-0.002
-0.004
-700
-600
-500
-400
-300
-200
-100
-0
Field [mT]

LT-Hysteresis and ZFC warming experiments

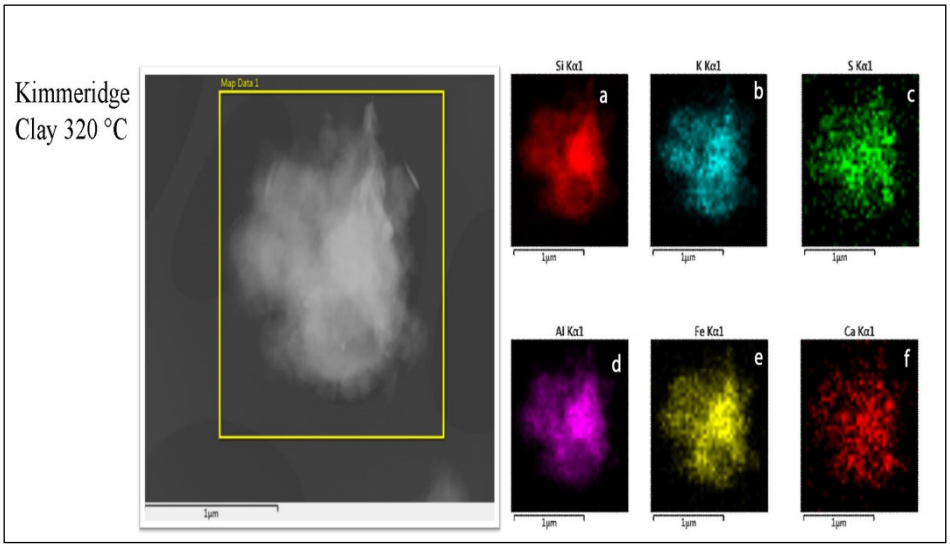


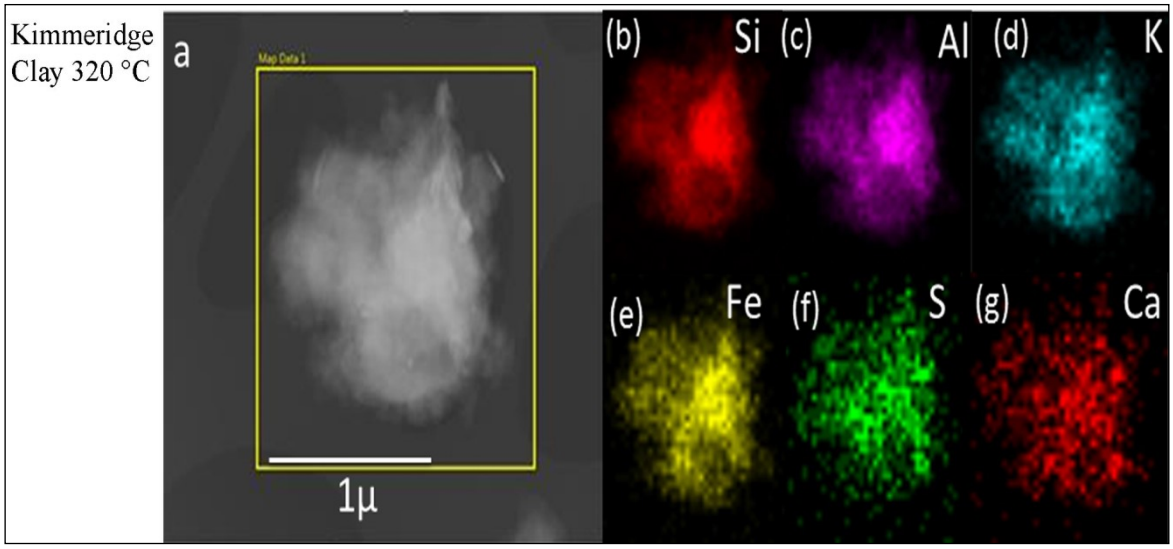

Oxford Clay 250 °C
Am²/kg
0.1
0.0
-0.1
-0.2
-400
-200
200
400
mT
5K
Room temperature
Oxford Clay 320 °C
Am²/kg
0.05
0.00
-0.05
-0.10
-40
-20
20
40
mT
5K
Room temperature


Blue Lias 250 °C
Am²/kg
0.1
0.0
-0.1
-0.2
-40
-20
20
mT
40
room temperature
5K
Room temperature
Blue Lias 320 °C
0.03
Am²/kg
0.00
-0.03
-10
-5
5
mT
10
5K
Room temperature
Am²/kg x10⁻³
ZFC
Magnetic moment/kg
7
6
5
4
3
2
1
0
0
50
100
150
200
250
300
K
Temperature
Immature
250°C
320°C

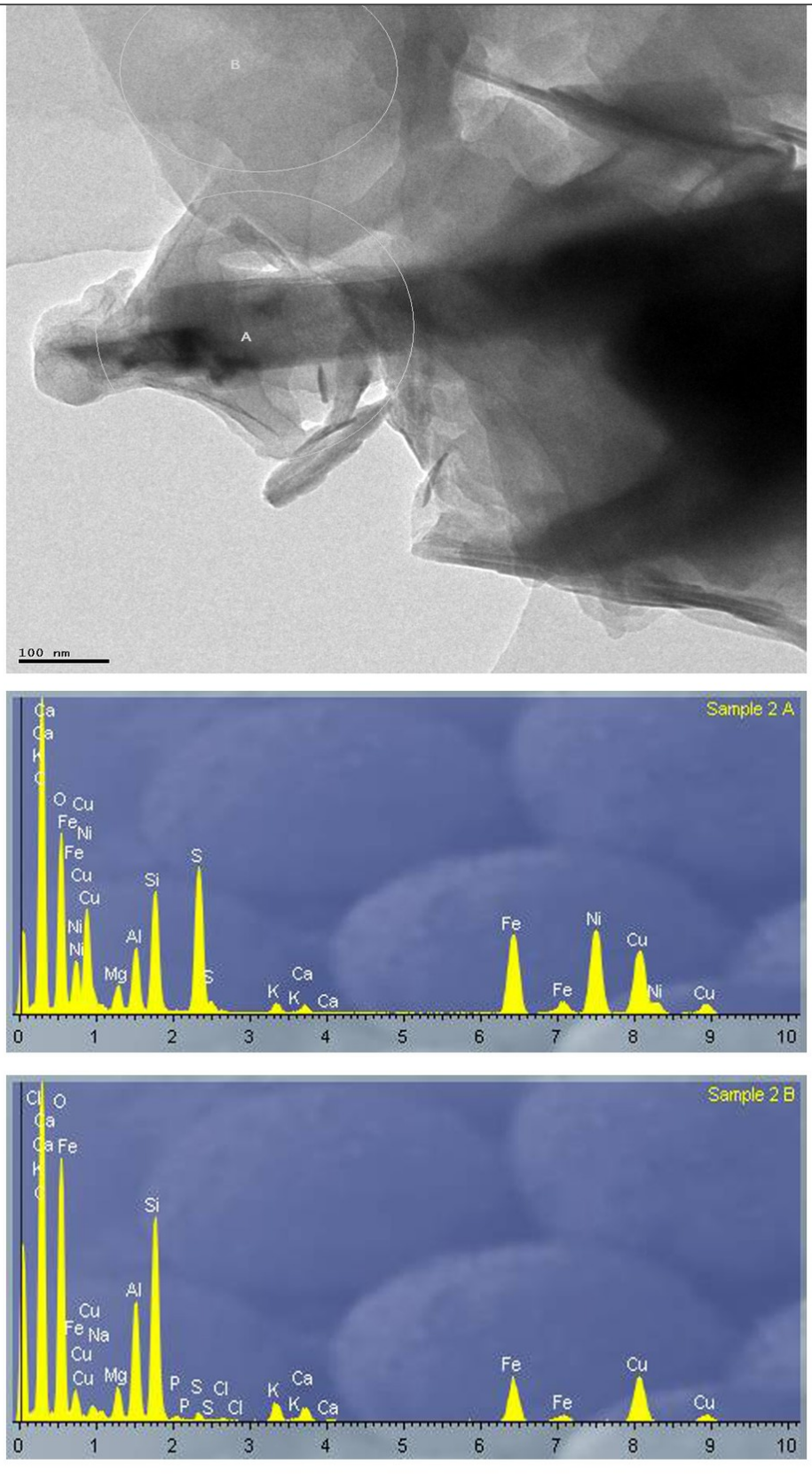
Appendix 1.2

TEM and EDX images acquired for the study in chapter 3 are presented below.





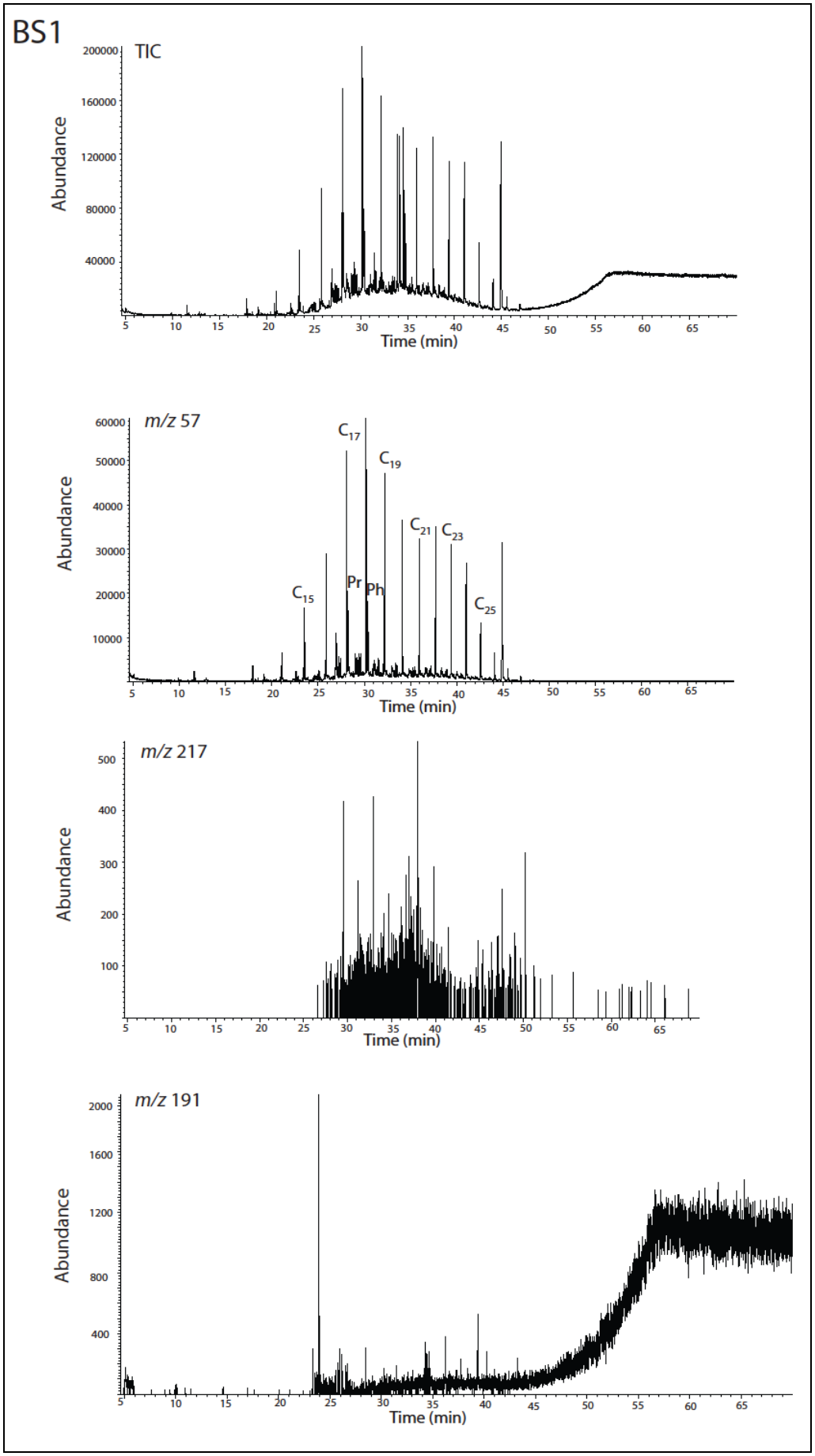
Kimmeridge 320 °C magnetic extracts and EDX

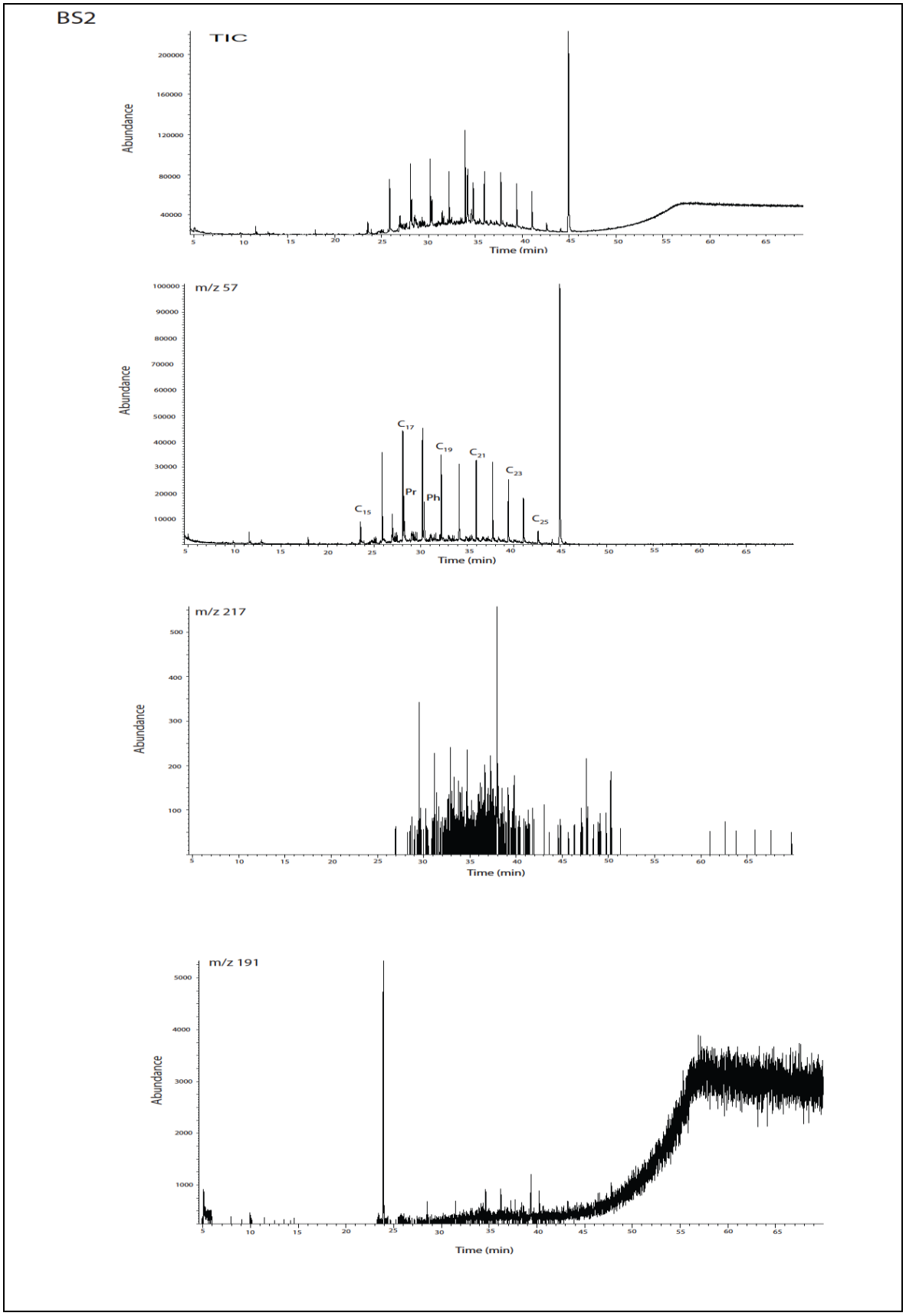


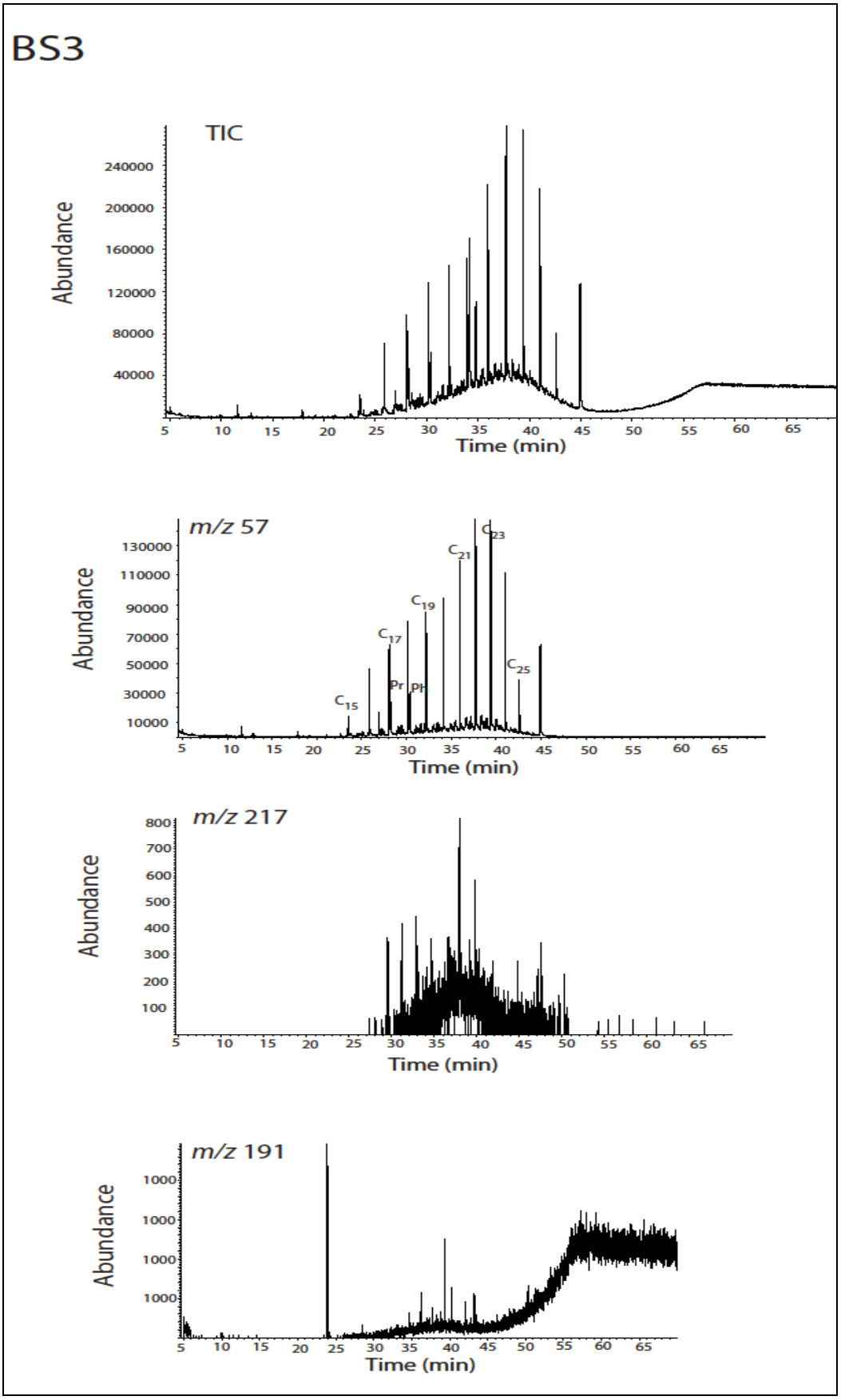
Appendix 2

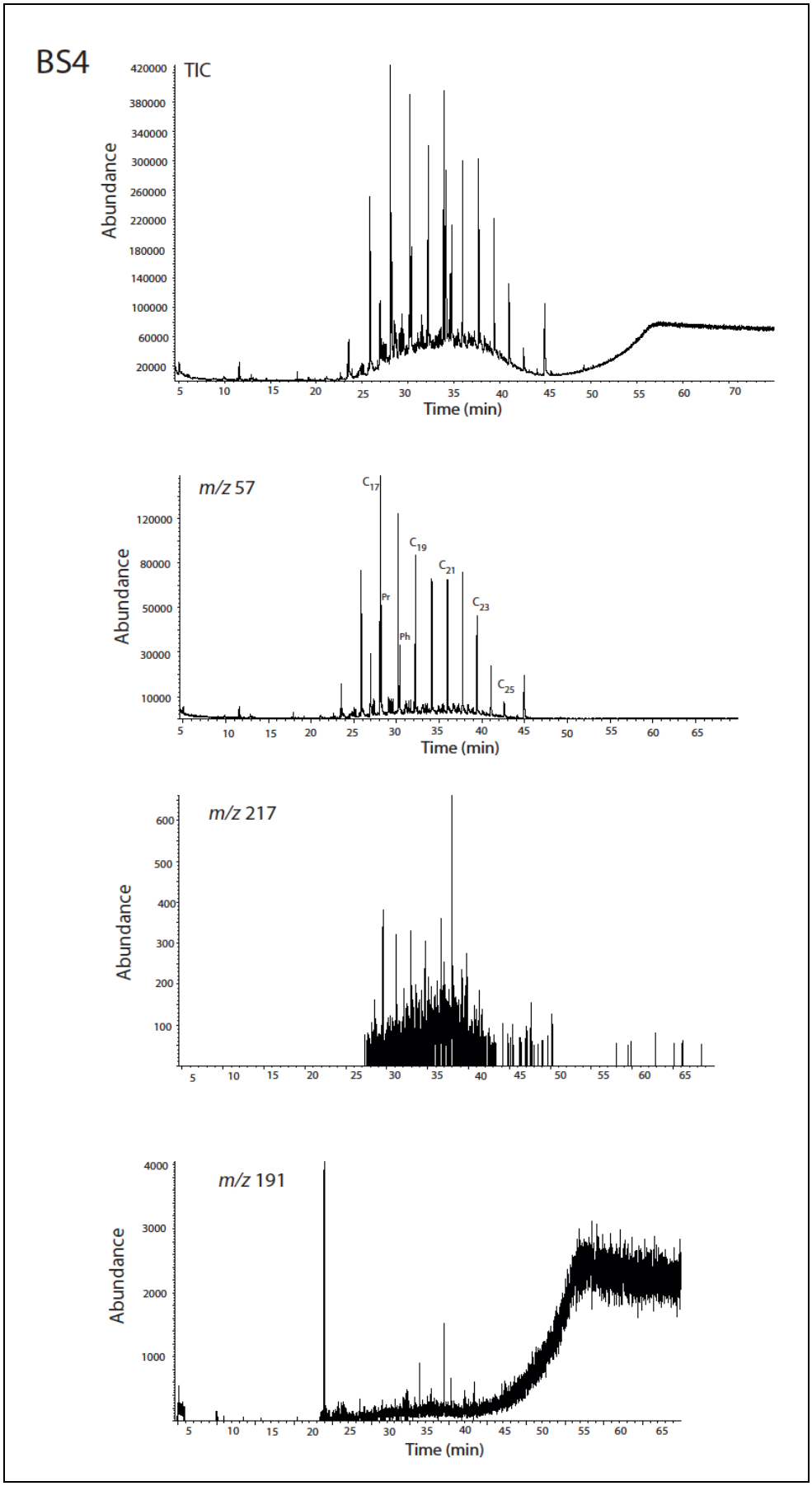
Appendix 2.1

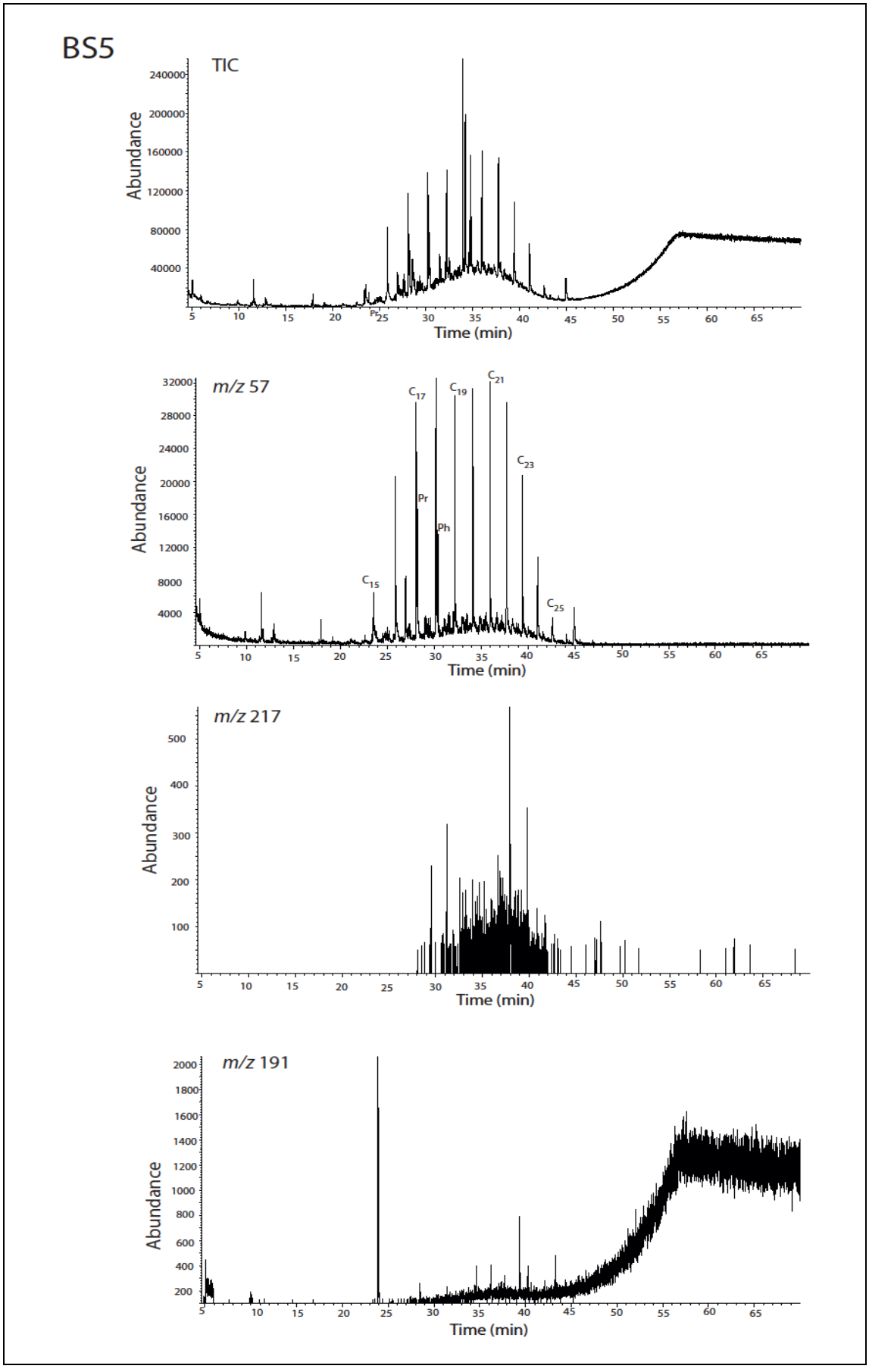
1) Geochemical analysis
    a. **TIC chromatogram:** Total Ion Current chromatogram of the aliphatic extract.
    b. **m/z 191 chromatogram:** Ion extraction 191 to identify hopanes within the aliphatic fractions.
    c. **m/z 217 chromatogram:** Ion extraction 217 to identify steranes within the aliphaticfractions.
    d. **m/z 57 chromatogram:** Ion extraction 57 to identify n-alkanes within the aliphaticfractions.

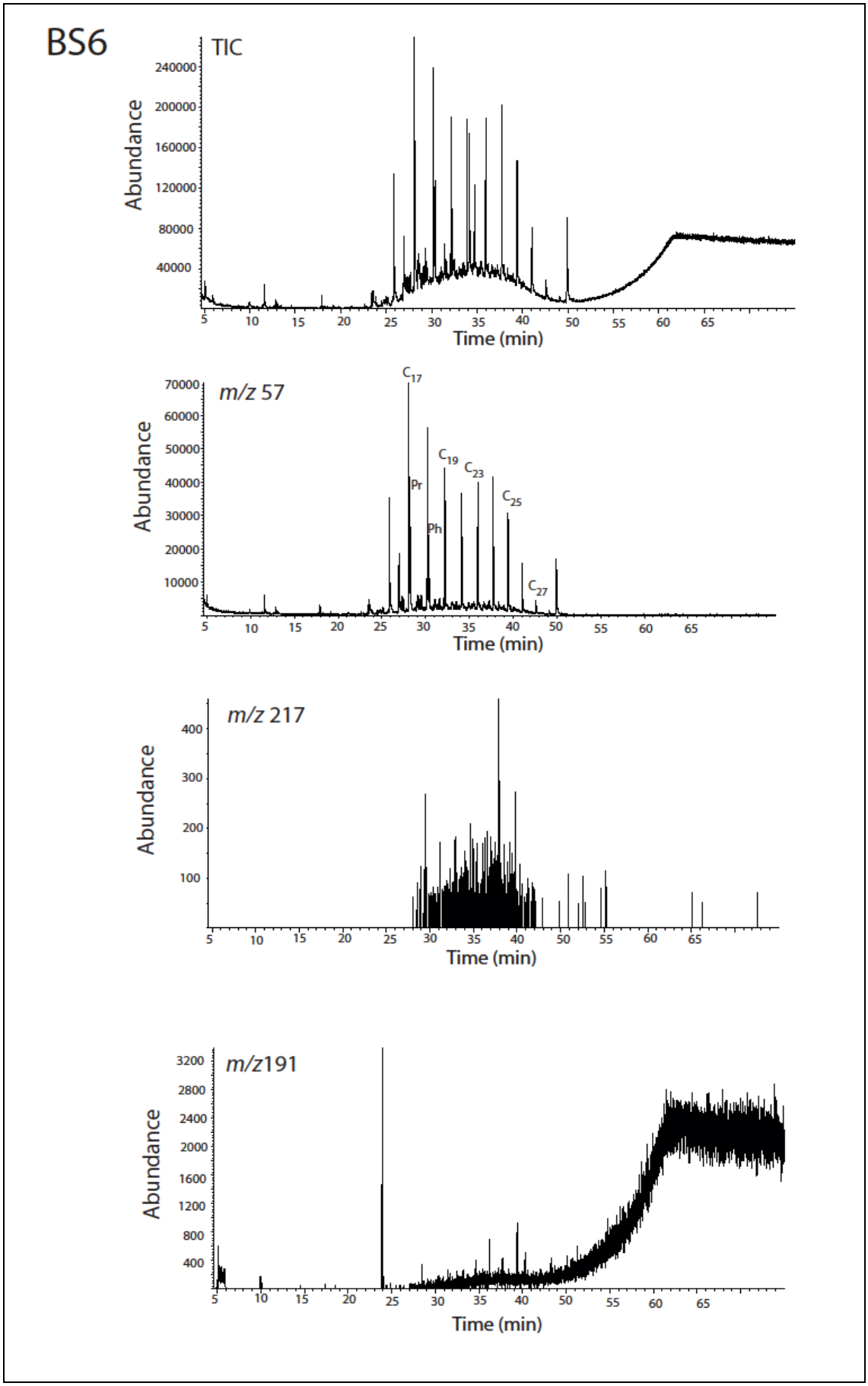

BS1
TIC
Abundance
Time (min)
m/z 57
C17
C19
C21
C23
C15
Pr
Ph
C25
m/z 217
m/z 191

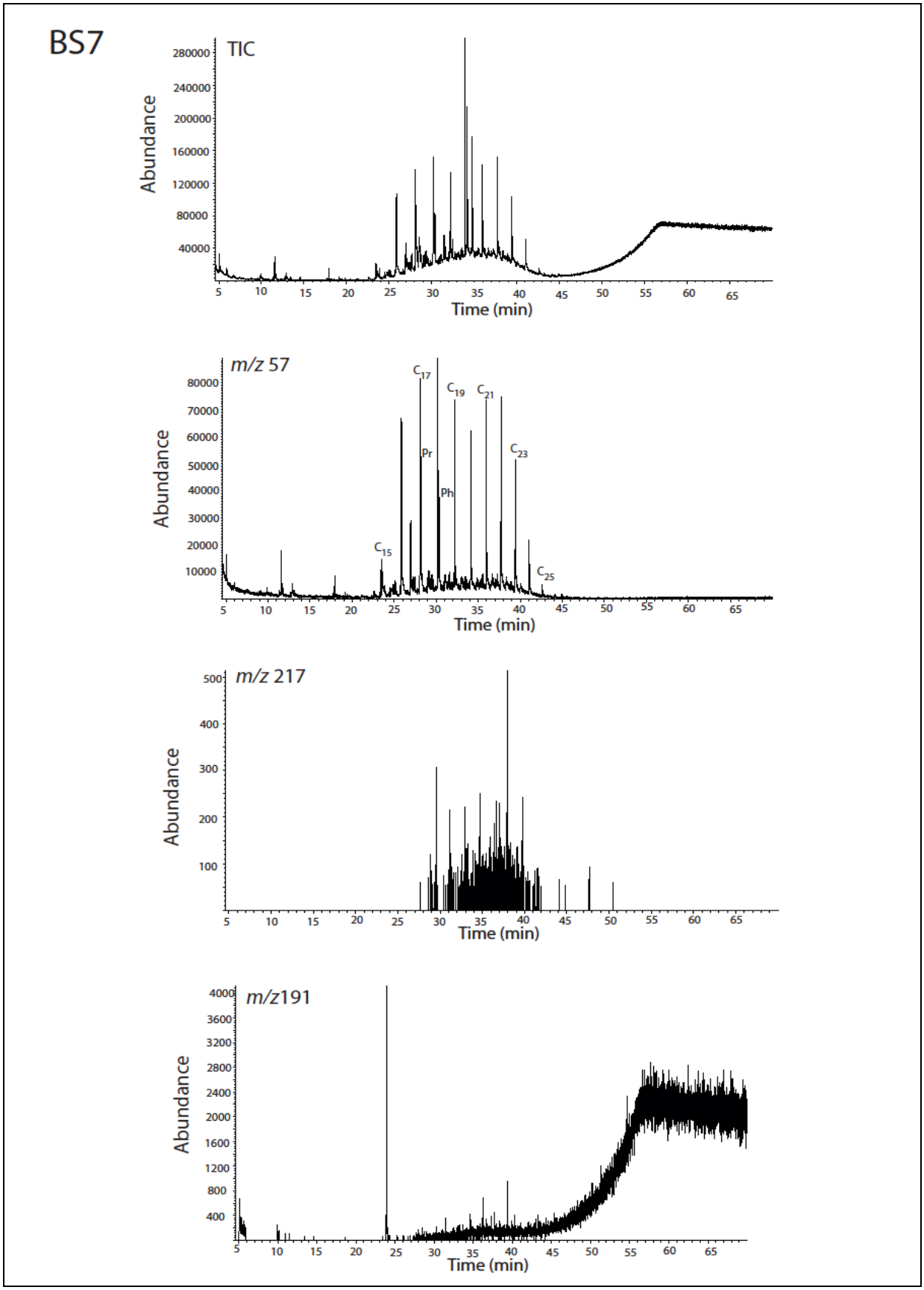

BS2
TIC
Abundance
Time (min)
m/z 57
C15
C17
Pr
Ph
C19
C21
C23
C25
m/z 217
m/z 191

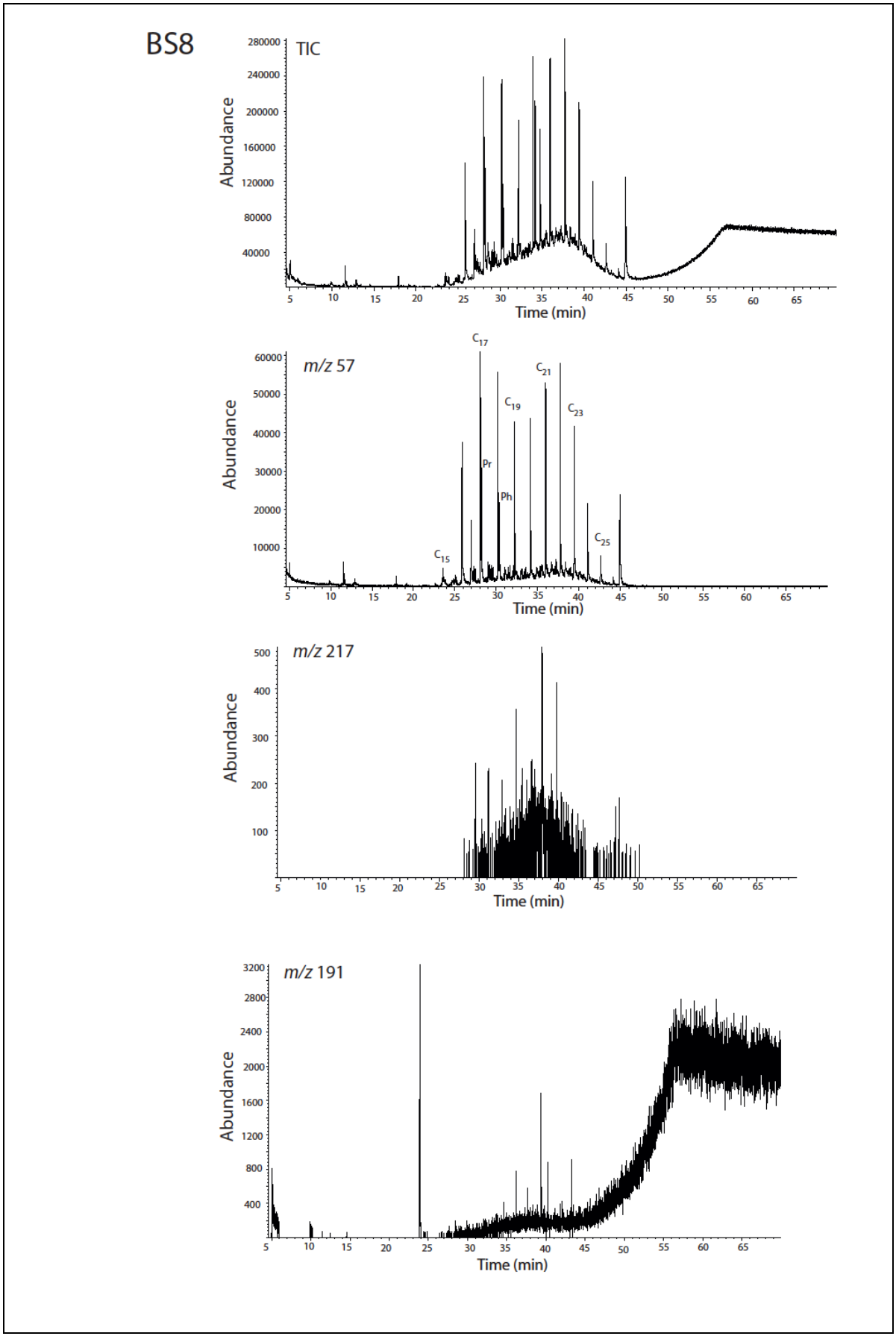

BS3
TIC
Abundance
240000
200000
160000
120000
80000
40000
5 10 15 20 25 30 35 40 45 50 55 60 65
Time (min)
m/z 57
Abundance
130000
110000
90000
70000
50000
30000
10000
C15
C17
Pr
Ph
C19
C21
C23
C25
5 10 15 20 25 30 35 40 45 50 55 60 65
Time (min)
m/z 217
Abundance
800
700
600
500
400
300
200
100
5 10 15 20 25 30 35 40 45 50 55 60 65
Time (min)
m/z 191
Abundance
1000
1000
1000
1000
5 10 15 20 25 30 35 40 45 50 55 60 65
Time (min)

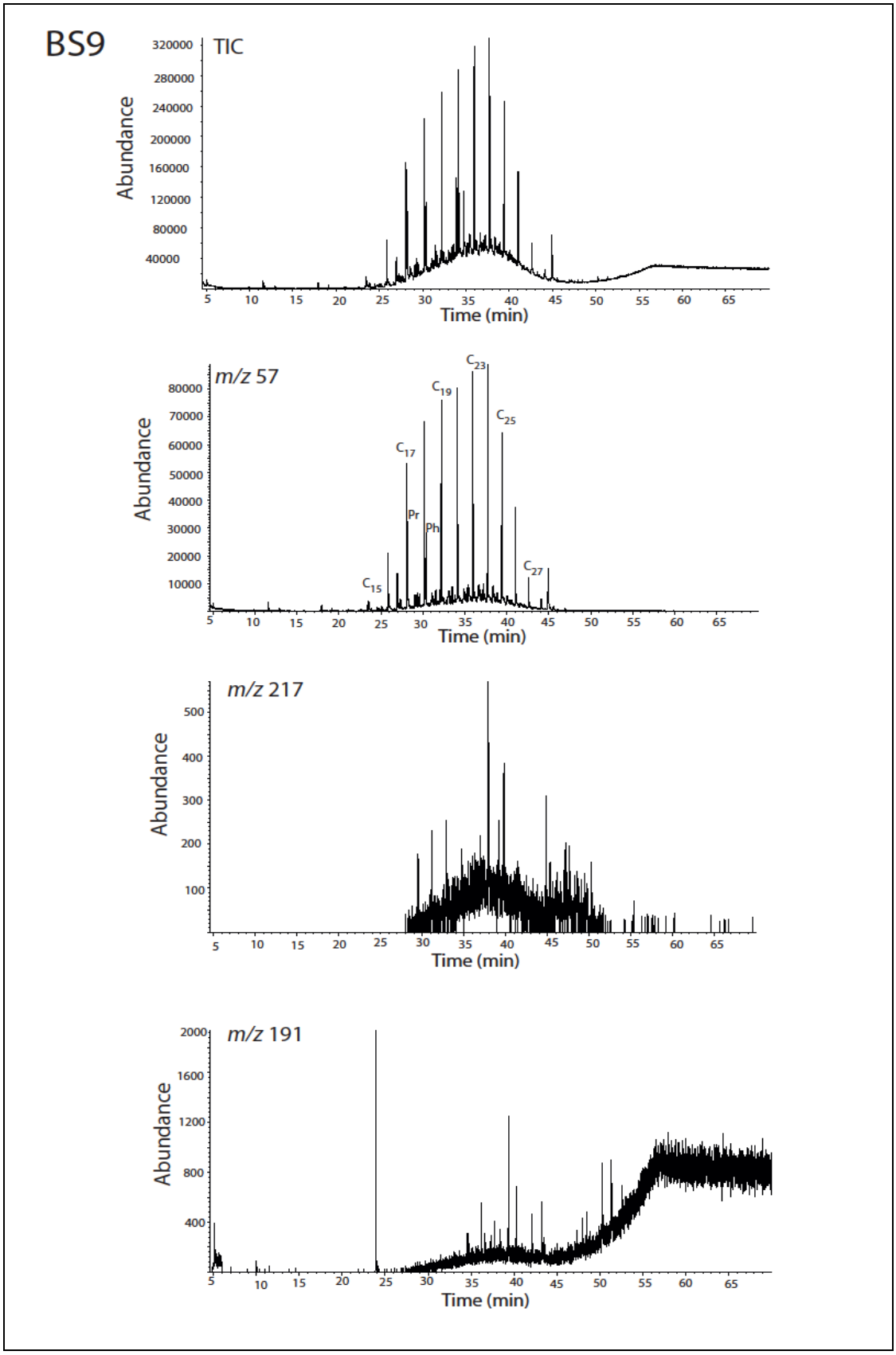

BS4
TIC
Abundance
Time (min)
m/z 57
C17
C19
C21
C23
C25
Pr
Ph
m/z 217
m/z 191

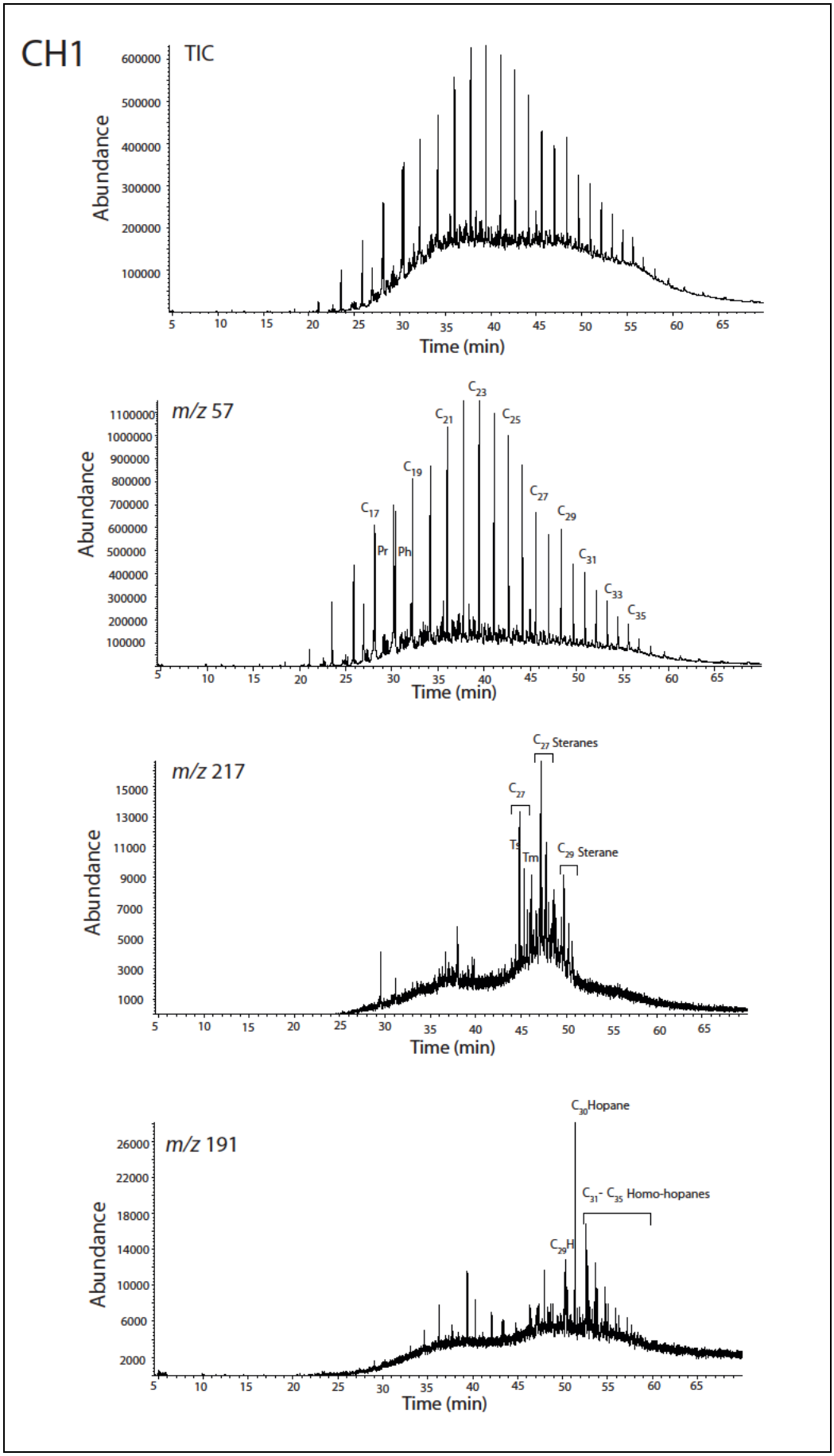

BS5
TIC
Abundance
Time (min)
m/z 57
C17
C19
C21
C23
C15
C25
Pr
Ph
m/z 217
m/z 191

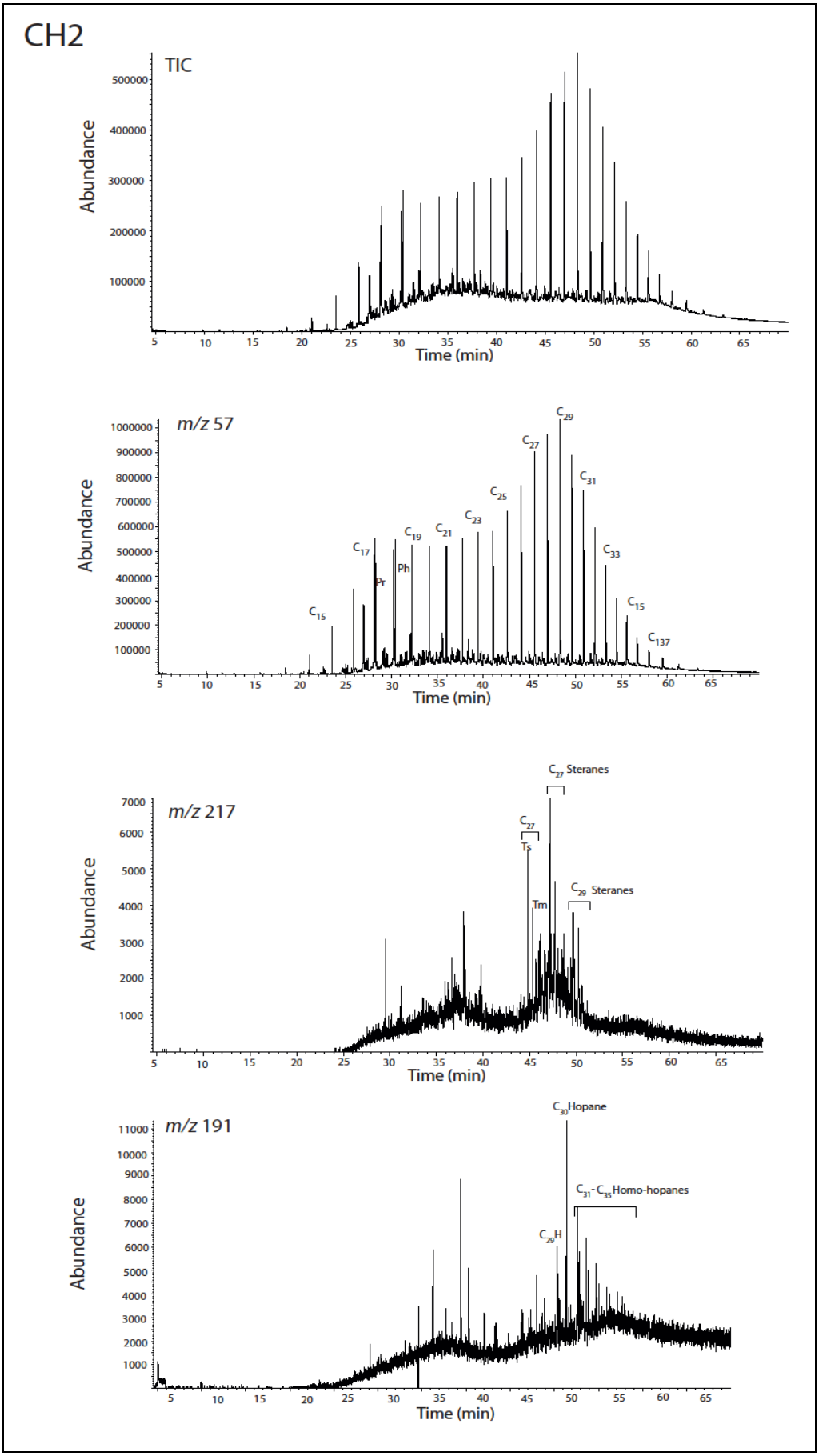

BS6
TIC
Abundance
Time (min)
m/z 57
C17
Pr
C19
Ph
C23
C25
C27
m/z 217
m/z191

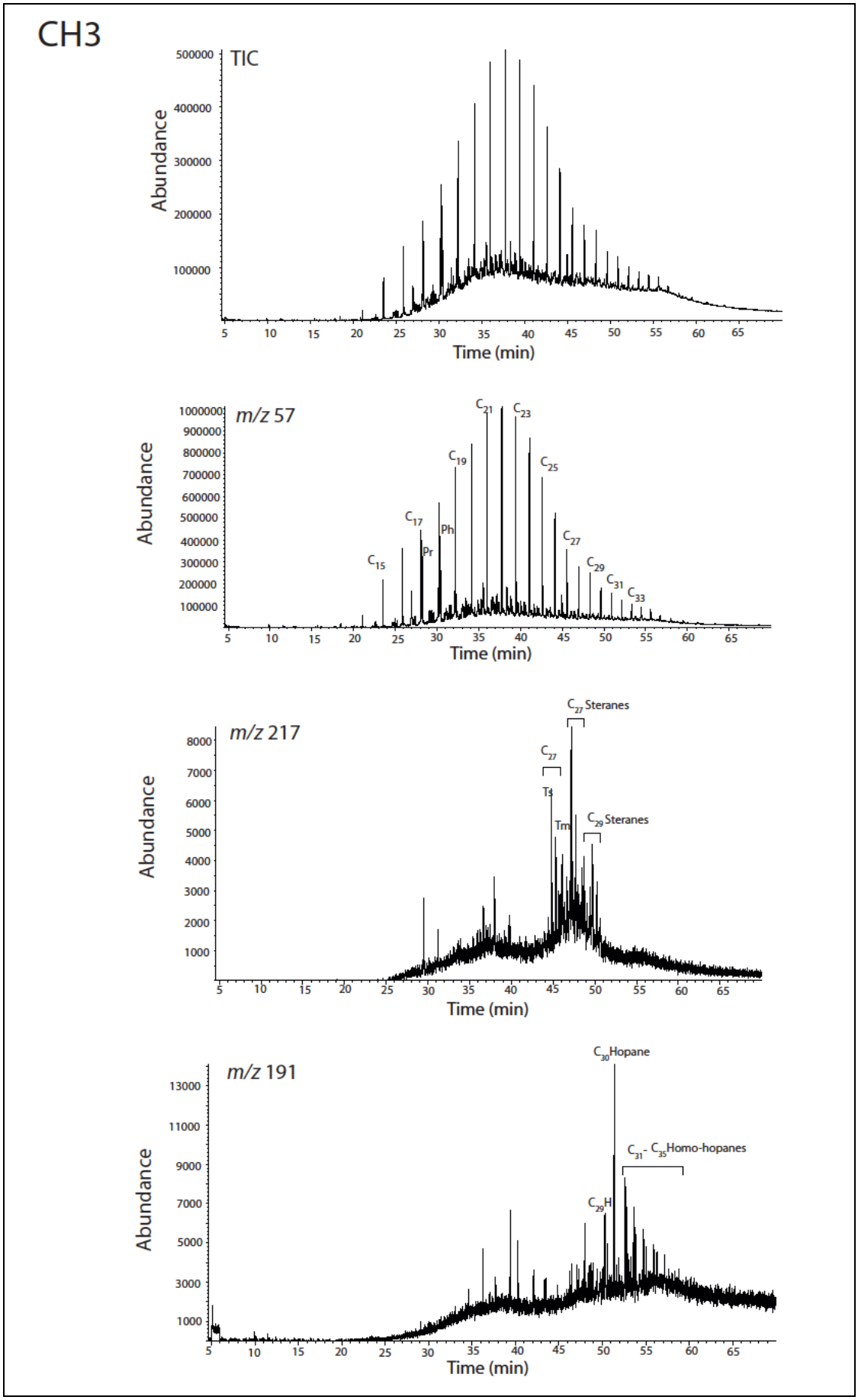

BS7
TIC
Abundance
Time (min)
m/z 57
C17
C19
C21
C23
C25
Pr
Ph
C15
m/z 217
m/z191

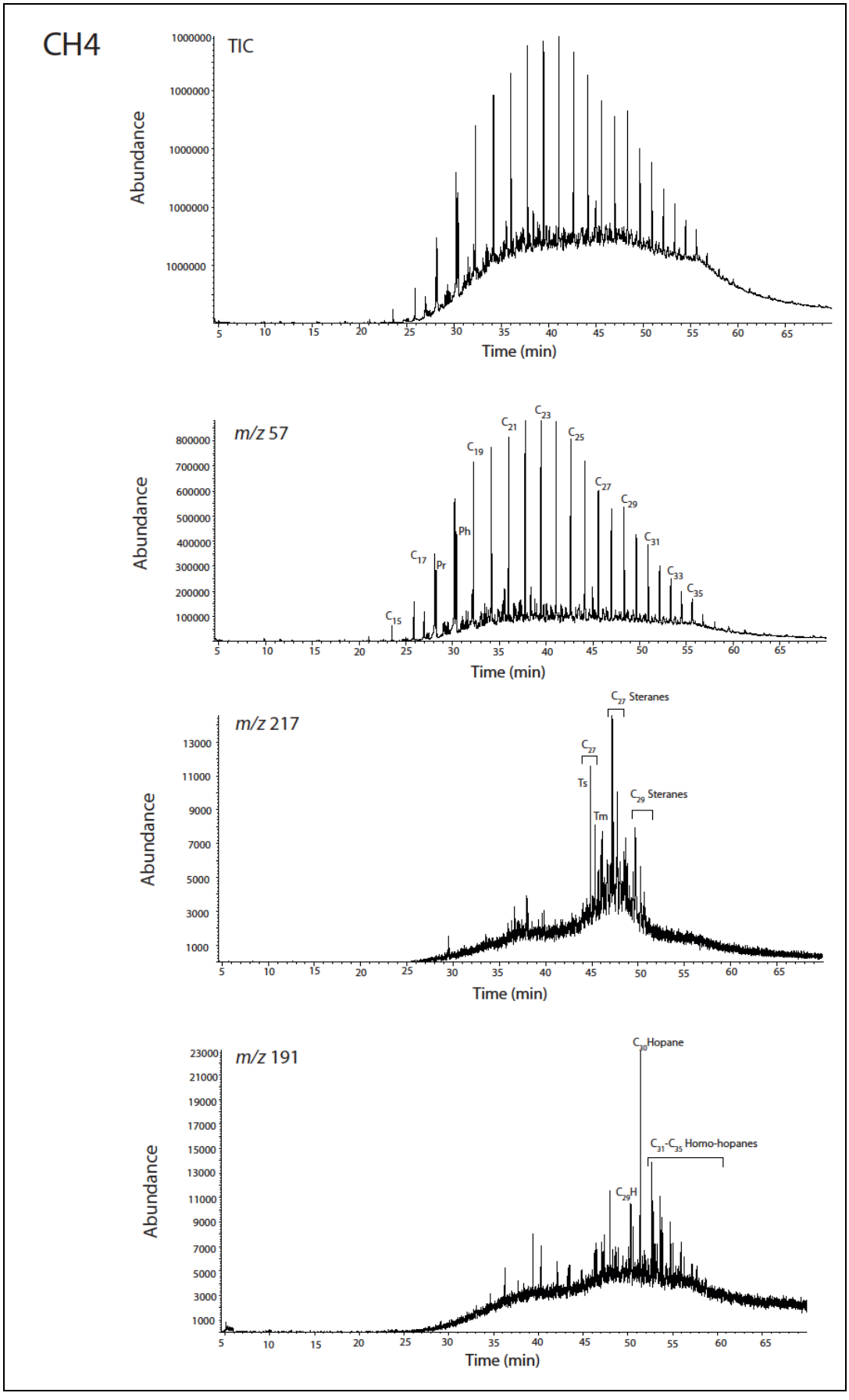

BS8
TIC
Abundance
Time (min)
m/z 57
C17
C21
C19
C23
Pr
Ph
C15
C25
m/z 217
m/z 191

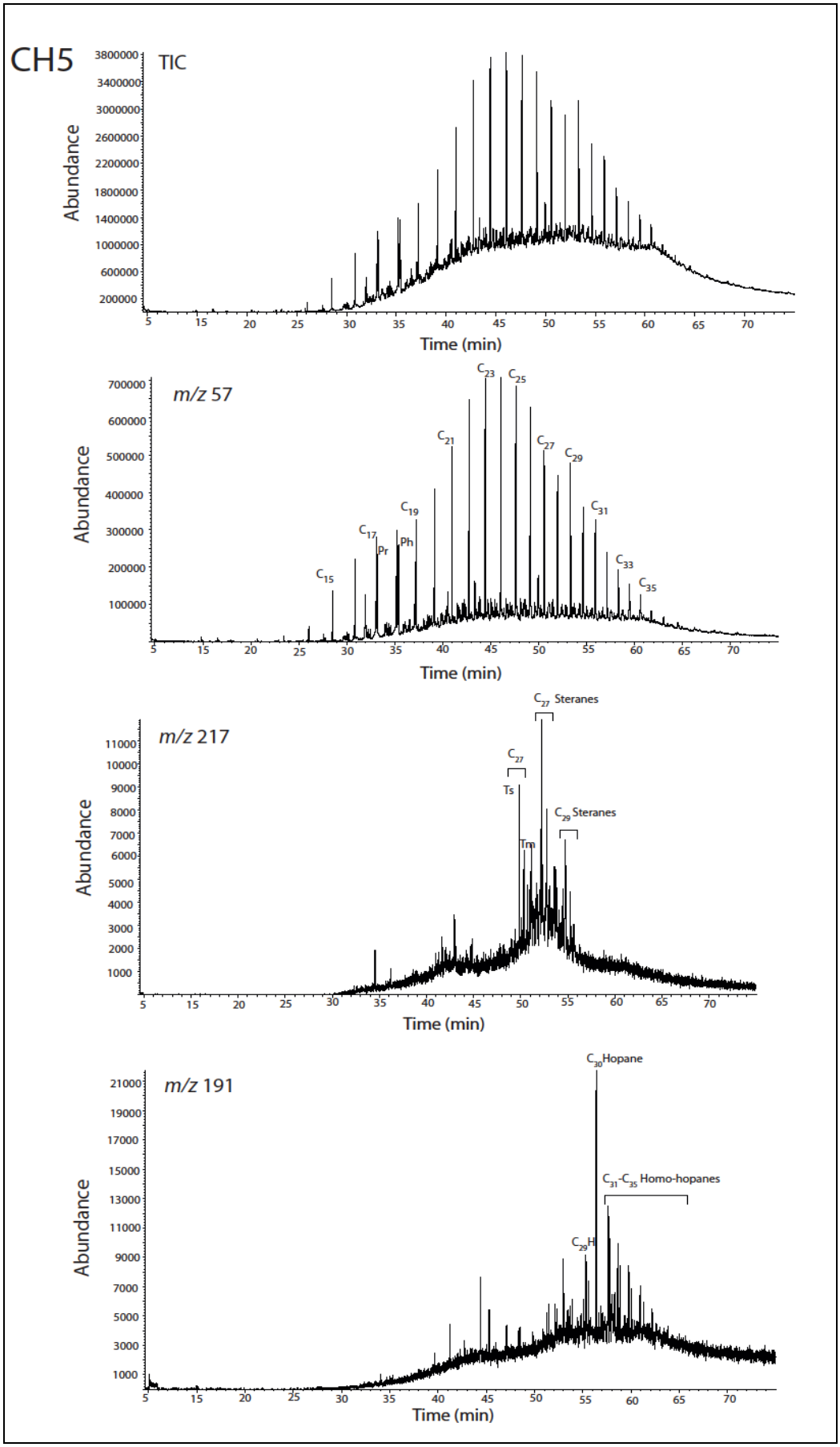

BS9
TIC
Abundance
Time (min)
m/z 57
C15
C17
Pr
Ph
C19
C23
C25
C27
m/z 217
m/z 191


CH1
TIC
Abundance
Time (min)
m/z 57
C17
Pr
Ph
C19
C21
C23
C25
C27
C29
C31
C33
C35
m/z 217
C27 Steranes
C27
Ts
Tm
C29 Sterane
m/z 191
C30Hopane
C31- C35 Homo-hopanes
C29H

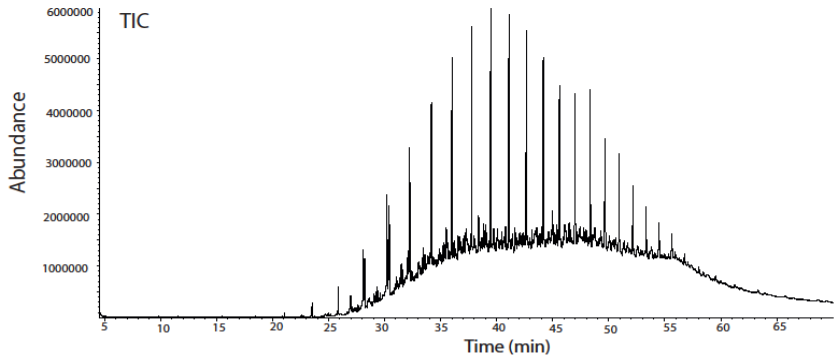

CH2
TIC
Abundance
Time (min)
m/z 57
C15
C17
Pr
Ph
C19
C21
C23
C25
C27
C29
C31
C33
C15
C137
m/z 217
C27 Steranes
C27 Ts
Tm
C29 Steranes
m/z 191
C30Hopane
C31-C35Homo-hopanes
C29H

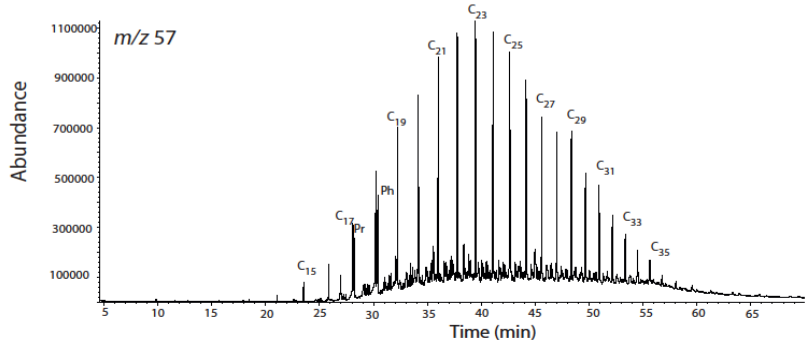

CH3
TIC
Abundance
Time (min)
m/z 57
C15
Pr
Ph
C17
C19
C21
C23
C25
C27
C29
C31
C33
m/z 217
C27 Steranes
C27
Ts
Tm
C29 Steranes
m/z 191
C30Hopane
C31 - C35Homo-hopanes
C29H

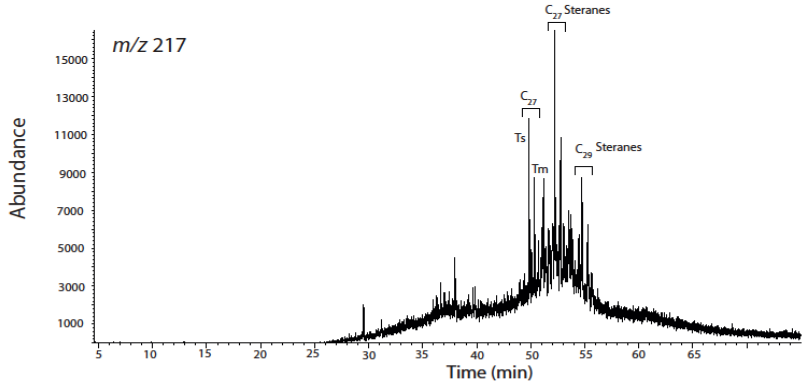

CH4
TIC
Abundance
Time (min)
m/z 57
C15
C17
Pr
Ph
C19
C21
C23
C25
C27
C29
C31
C33
C35
m/z 217
C27 Steranes
C27
Ts
Tm
C29 Steranes
m/z 191
C30Hopane
C31-C35 Homo-hopanes
C29H

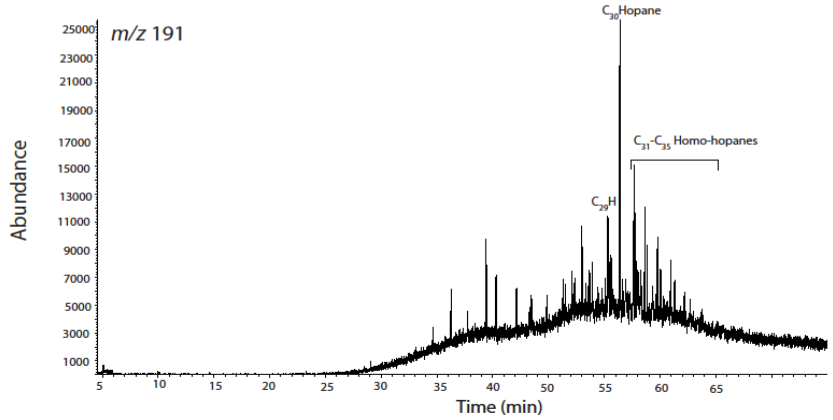

CH5
TIC
Abundance
Time (min)
m/z 57
C15
C17
Pr
Ph
C19
C21
C23
C25
C27
C29
C31
C33
C35
m/z 217
C27 Steranes
C27
Ts
Tm
C29 Steranes
m/z 191
C30Hopane
C31-C35 Homo-hopanes
C29H

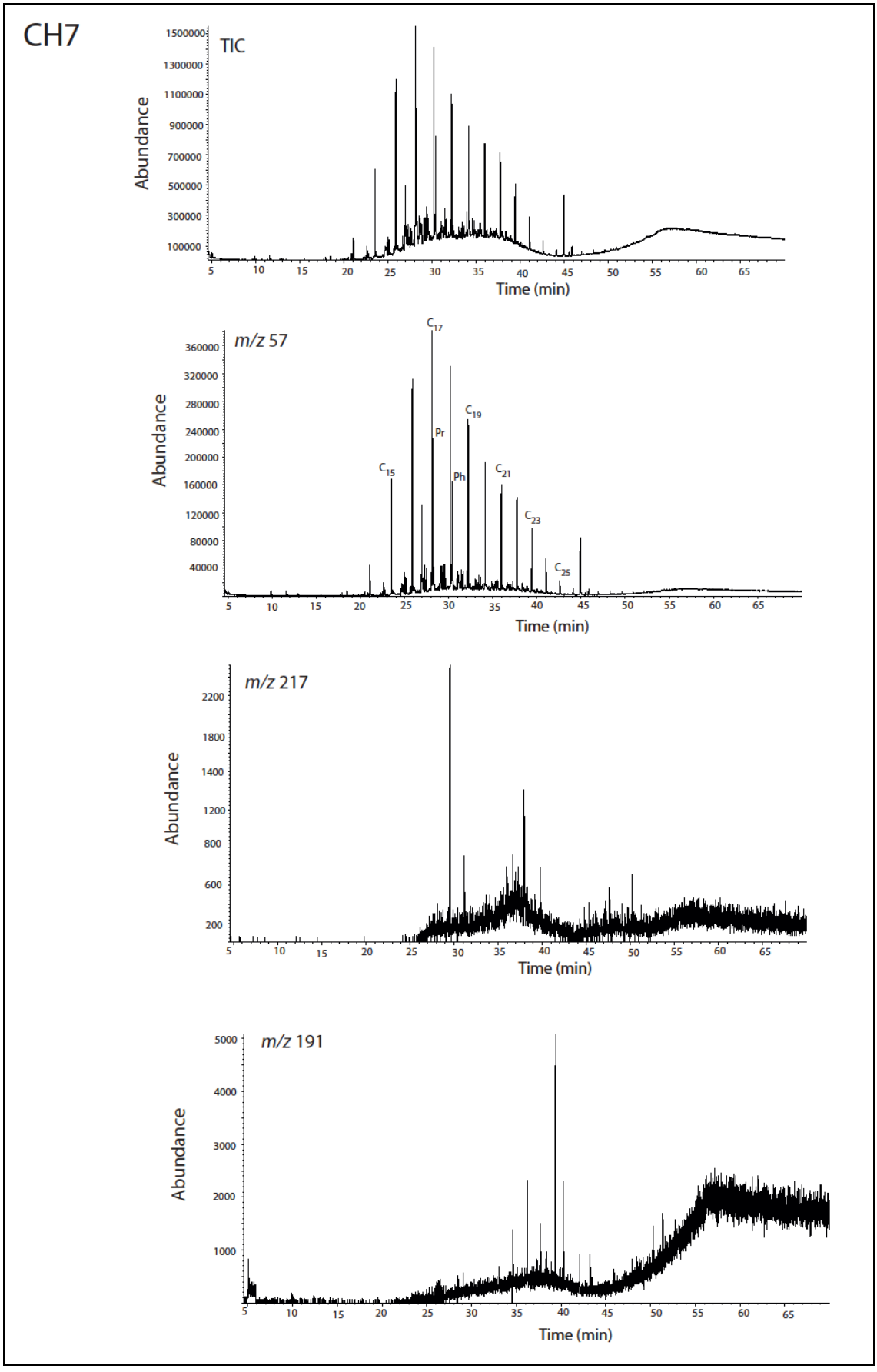
CH6


TIC
Abundance
Time (min)

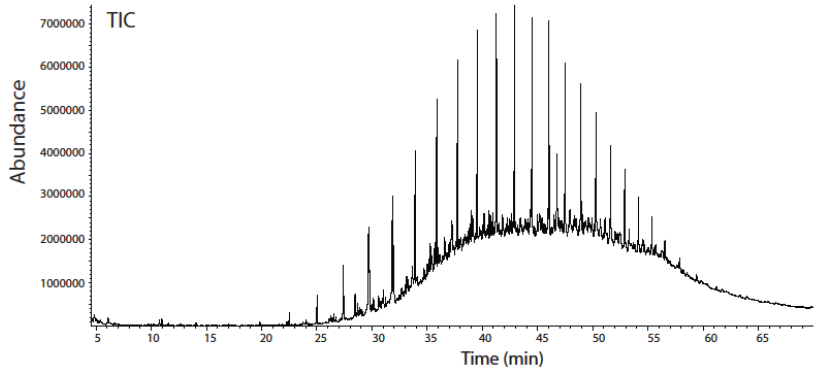

m/z 57
Abundance
Time (min)
C15
C17
Pr
Ph
C19
C21
C23
C25
C27
C29
C31
C33
C35

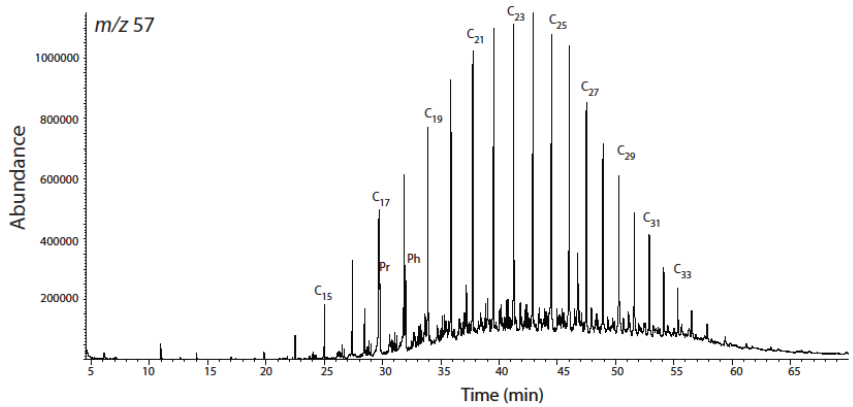

m/z 217
Abundance
Time (min)
C27 Steranes
C27
Ts
Tm
C29 Steranes

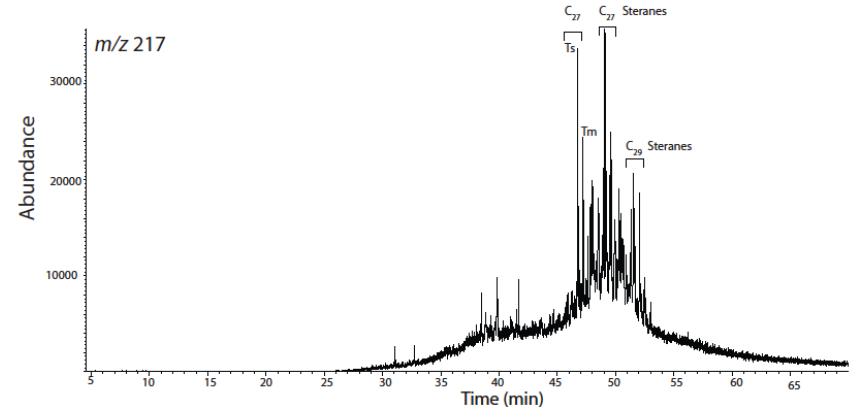

m/z 191
Abundance
Time (min)
C30 Hopane
C31-C35 Homo-hopanes
C29H

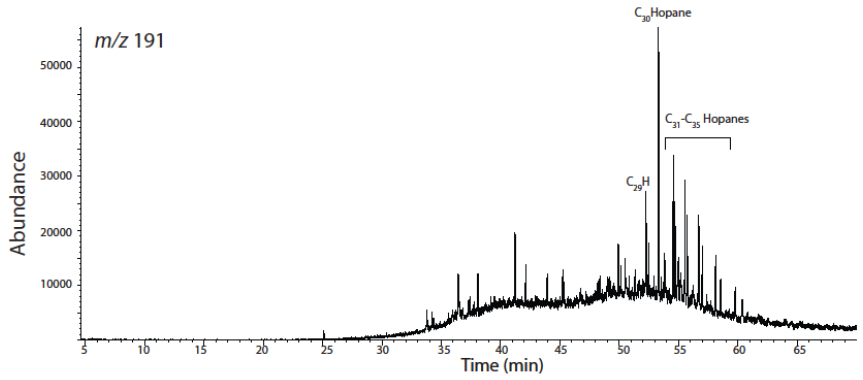

CH7
TIC
Abundance
Time (min)
m/z 57
C17
Pr
C19
Ph
C15
C21
C23
C25
m/z 217
m/z 191

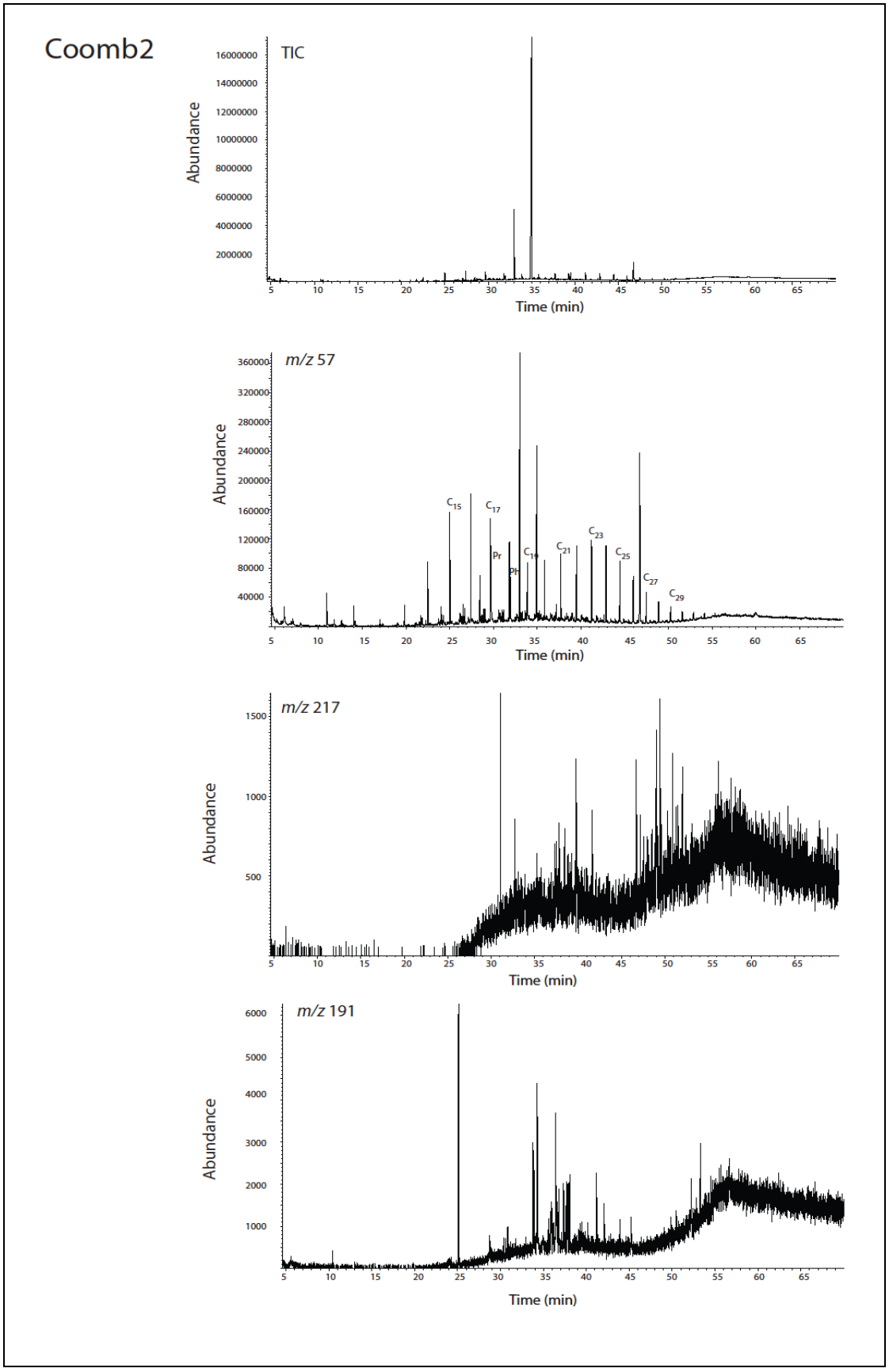
Coomb1

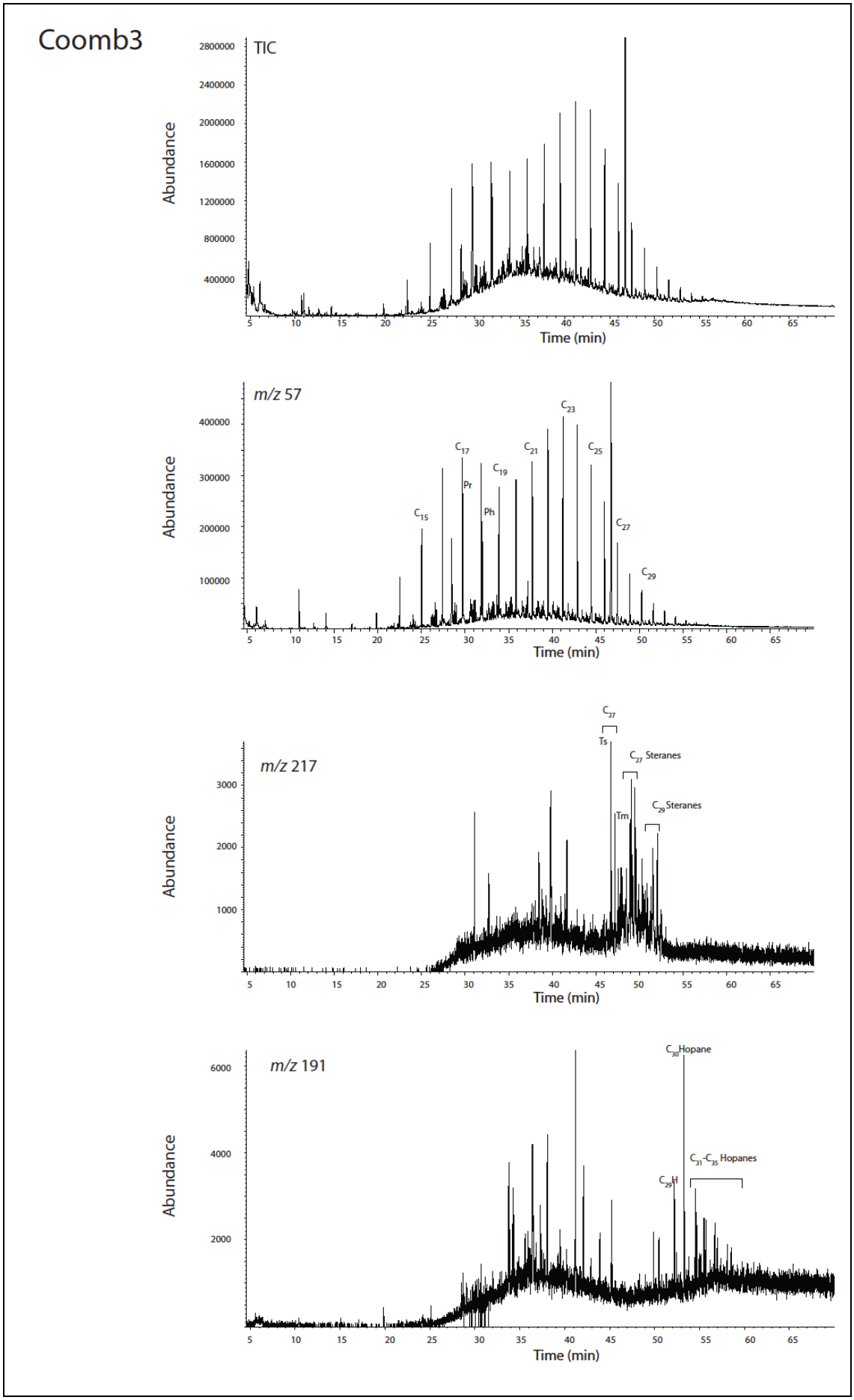

TIC
Abundance
Time (min)

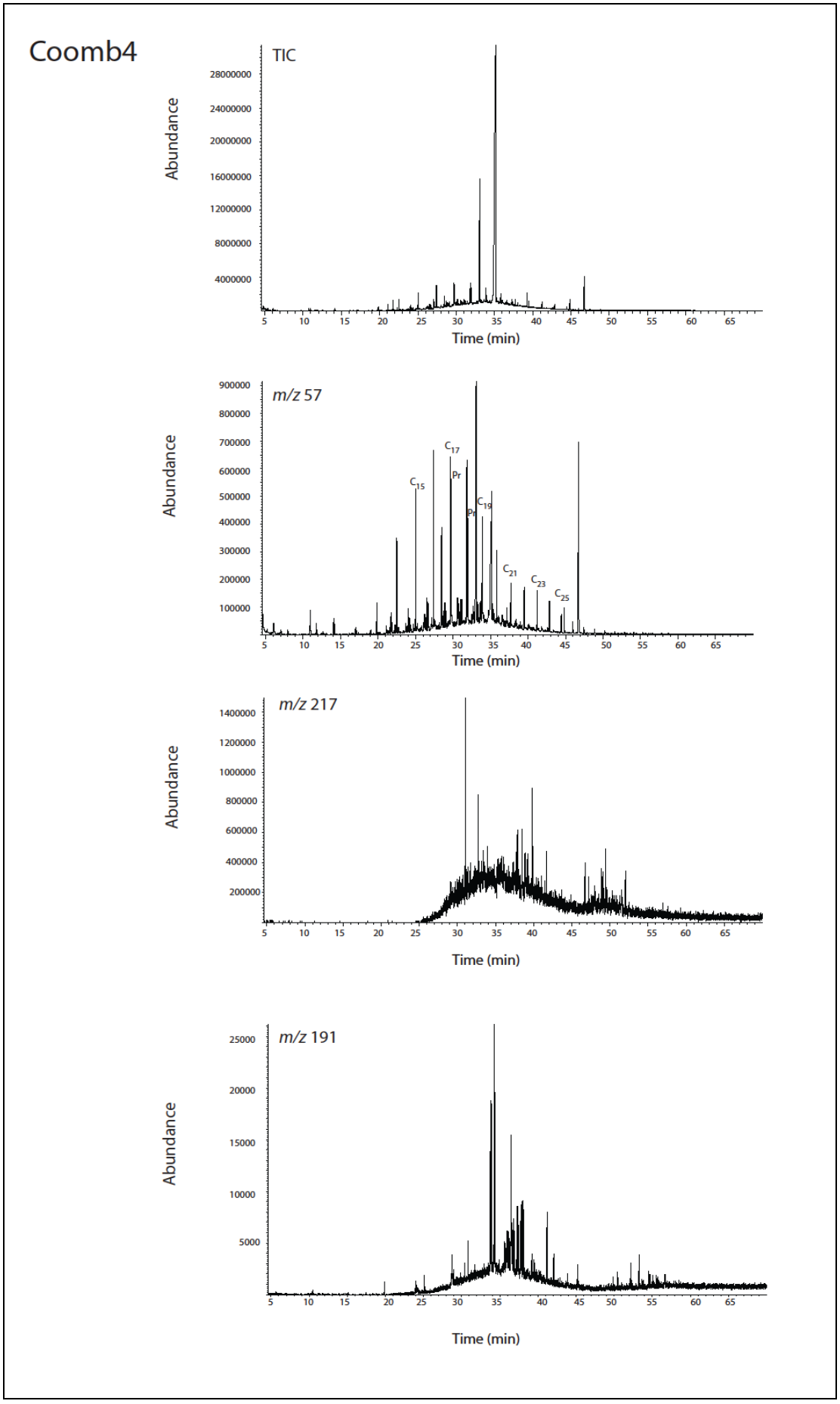

m/z 57
Abundance
Time (min)
C15
C17
Pr
Ph
C19
C21
C23
C25
C27
C29
C31
C33

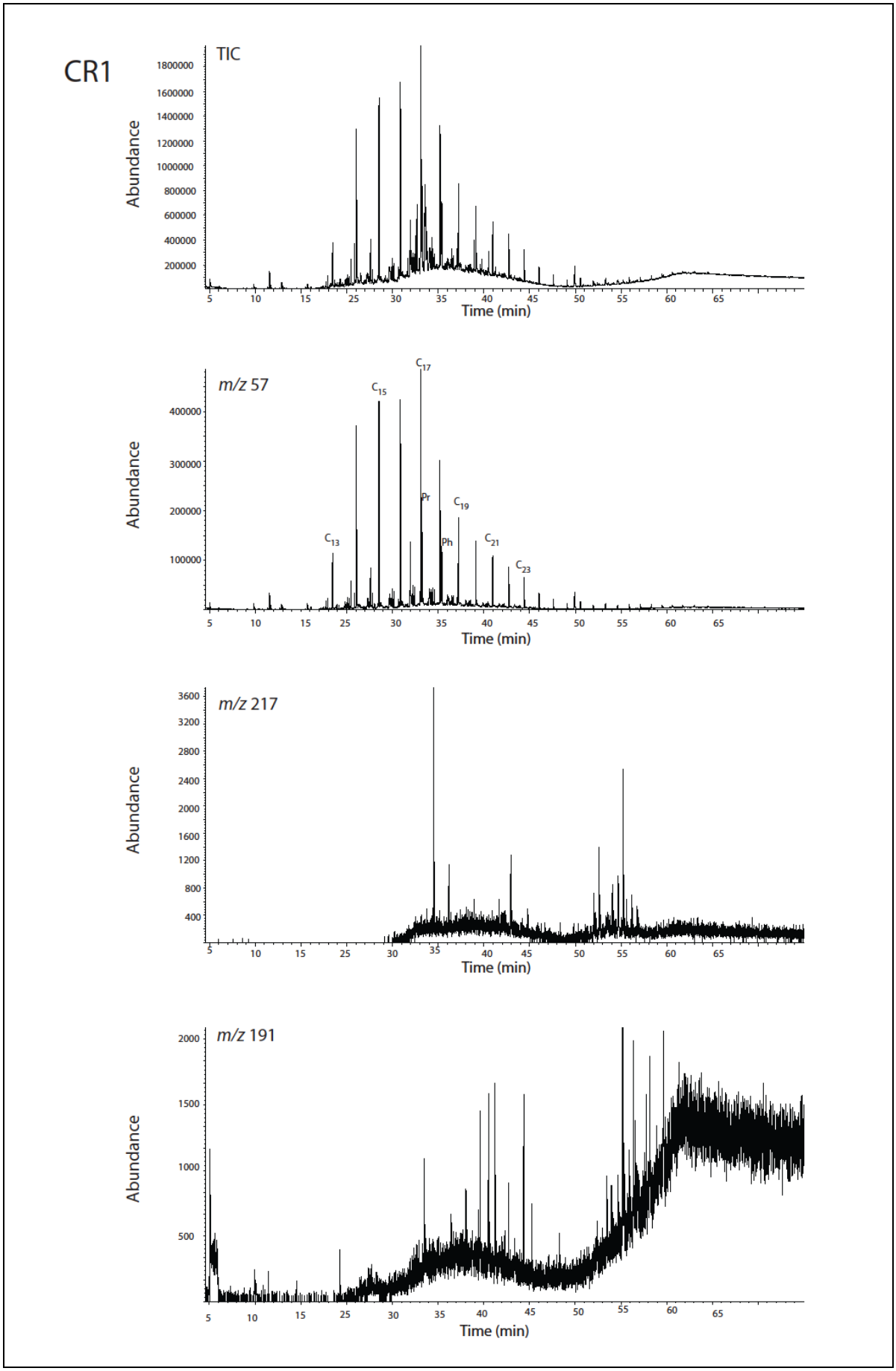

m/z 217
Abundance
Time (min)
C27 Ts
C27 Steranes
Tm
C29 Steranes

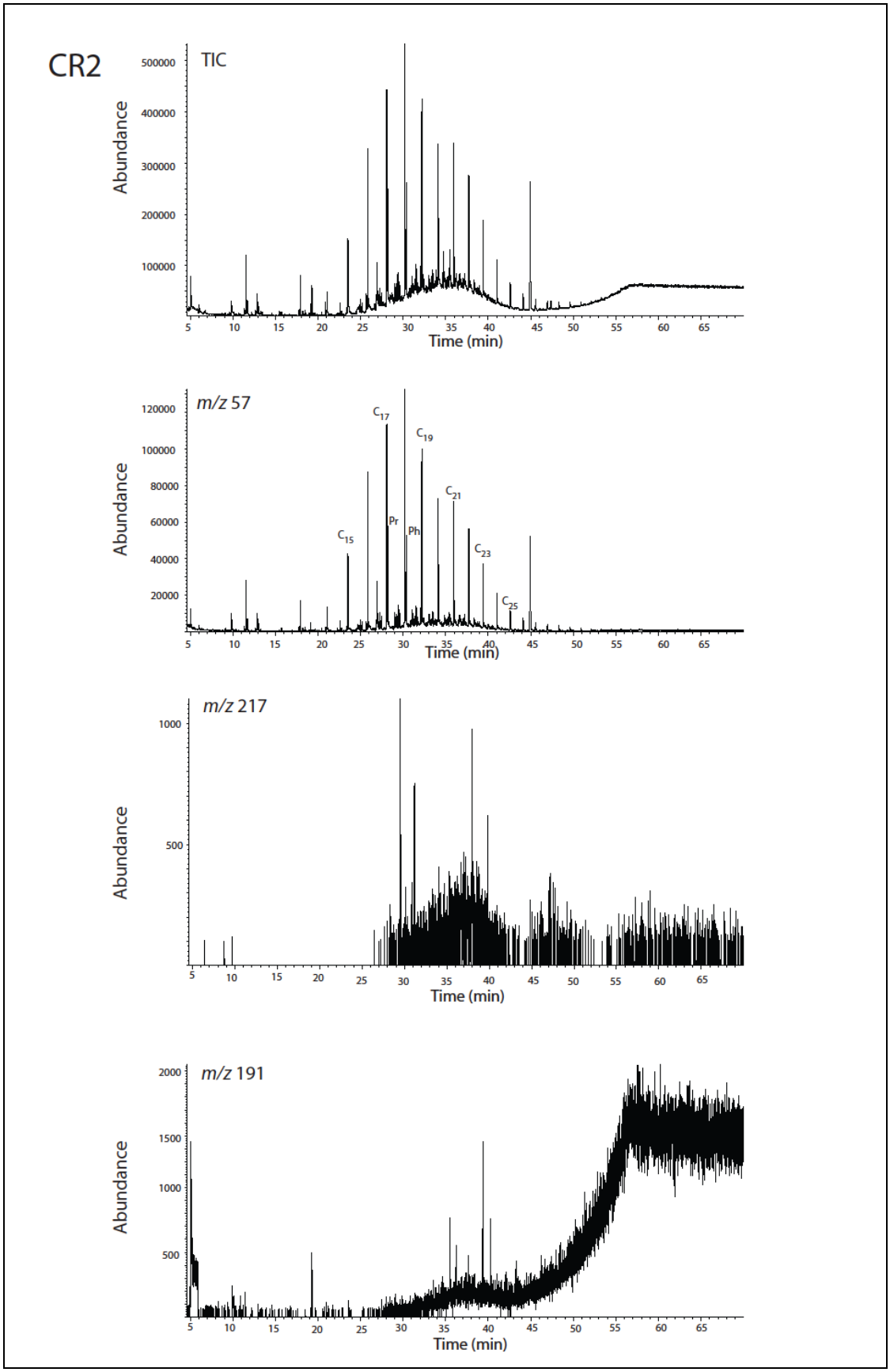

m/z 191
Abundance
Time (min)
C30 Hopane
C31-C35 Hopanes
C29H

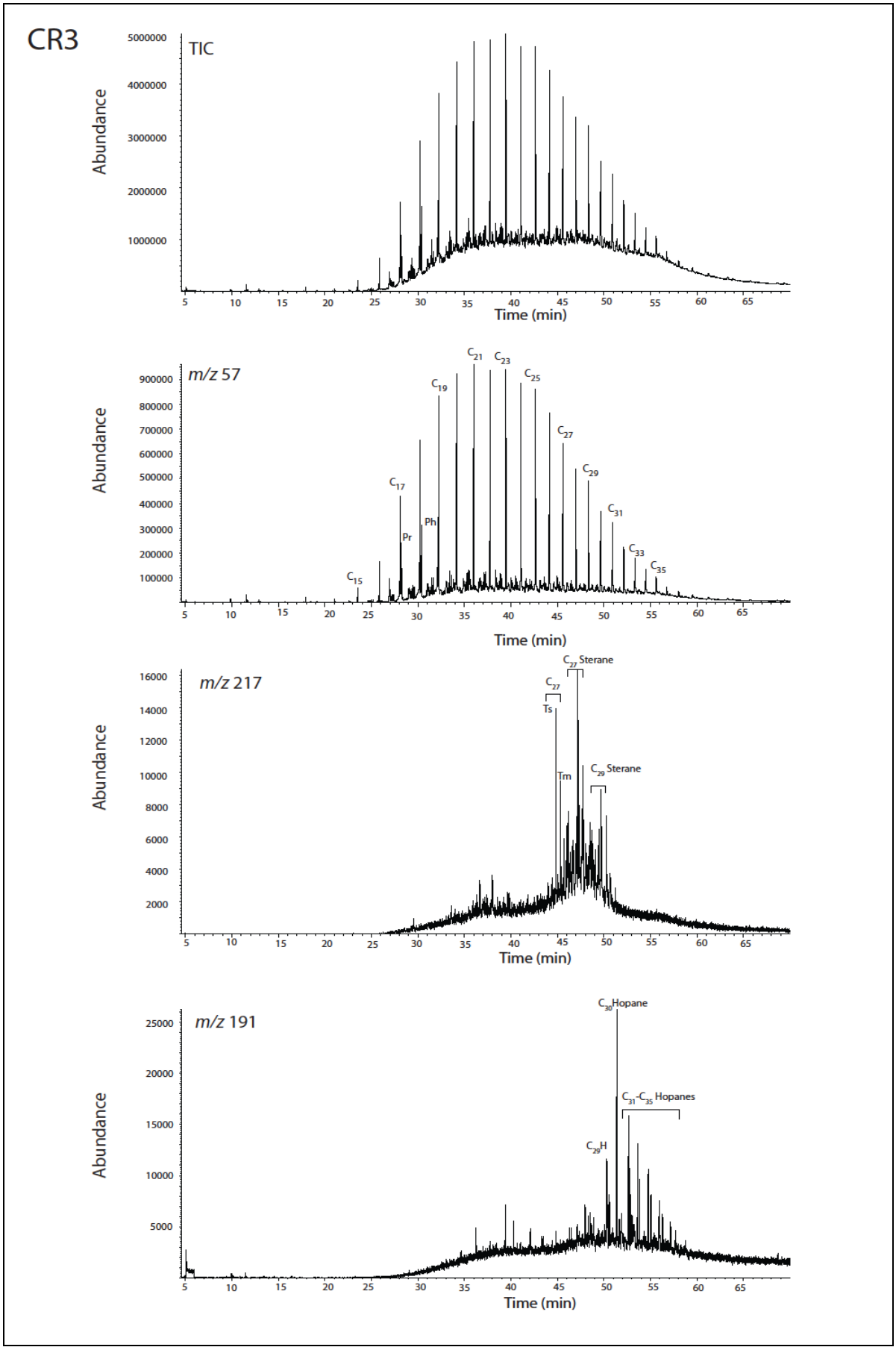

Coomb2
TIC
Abundance
Time (min)
m/z 57
C15
C17
Pr
Ph
C19
C21
C23
C25
C27
C29
m/z 217
m/z 191

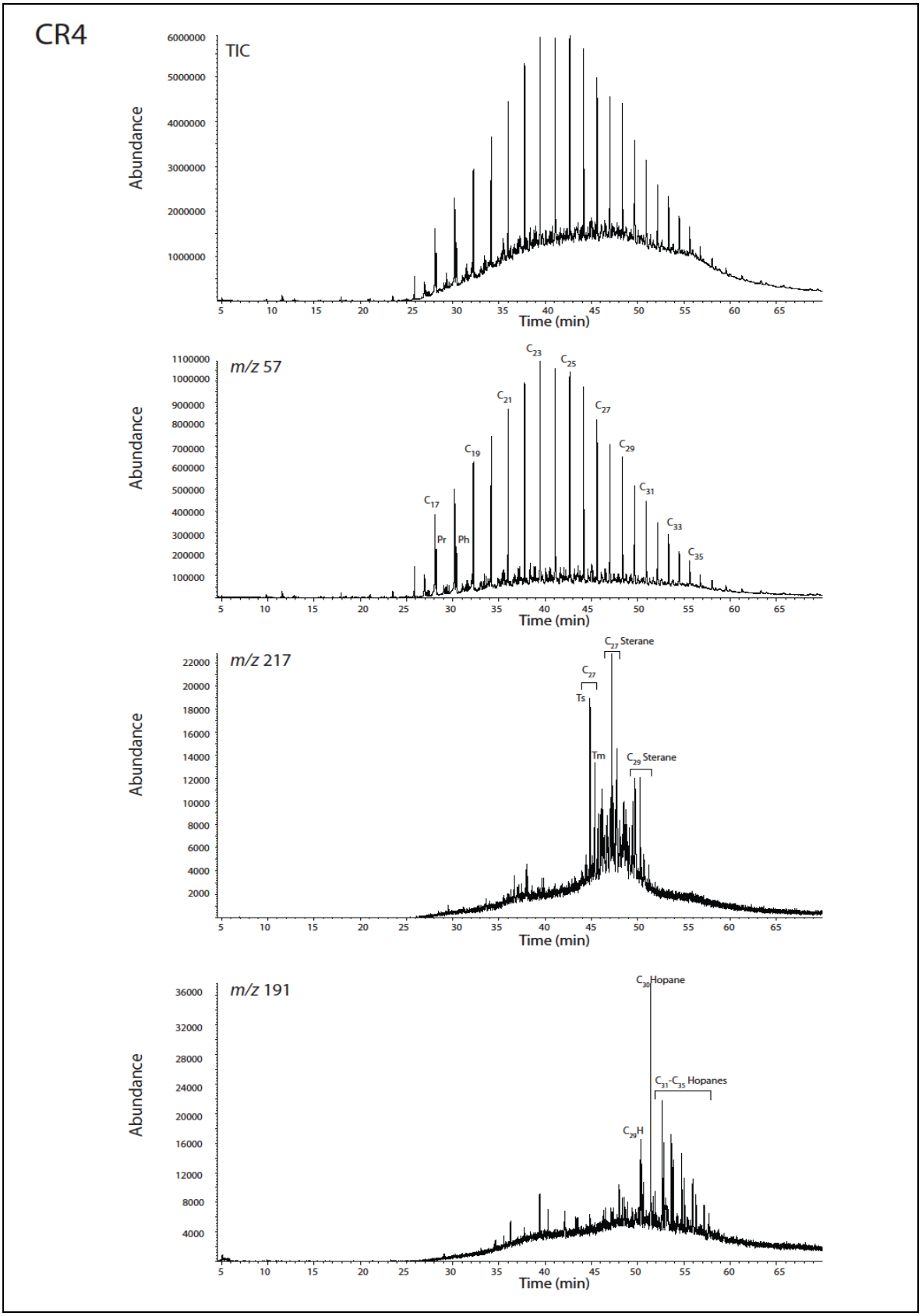

Coomb3
TIC
Abundance
Time (min)
m/z 57
C15
C17
Pr
Ph
C19
C21
C23
C25
C27
C29
m/z 217
C27 Ts
C27 Steranes
Tm
C29 Steranes
m/z 191
C30 Hopane
C29H
C31-C35 Hopanes

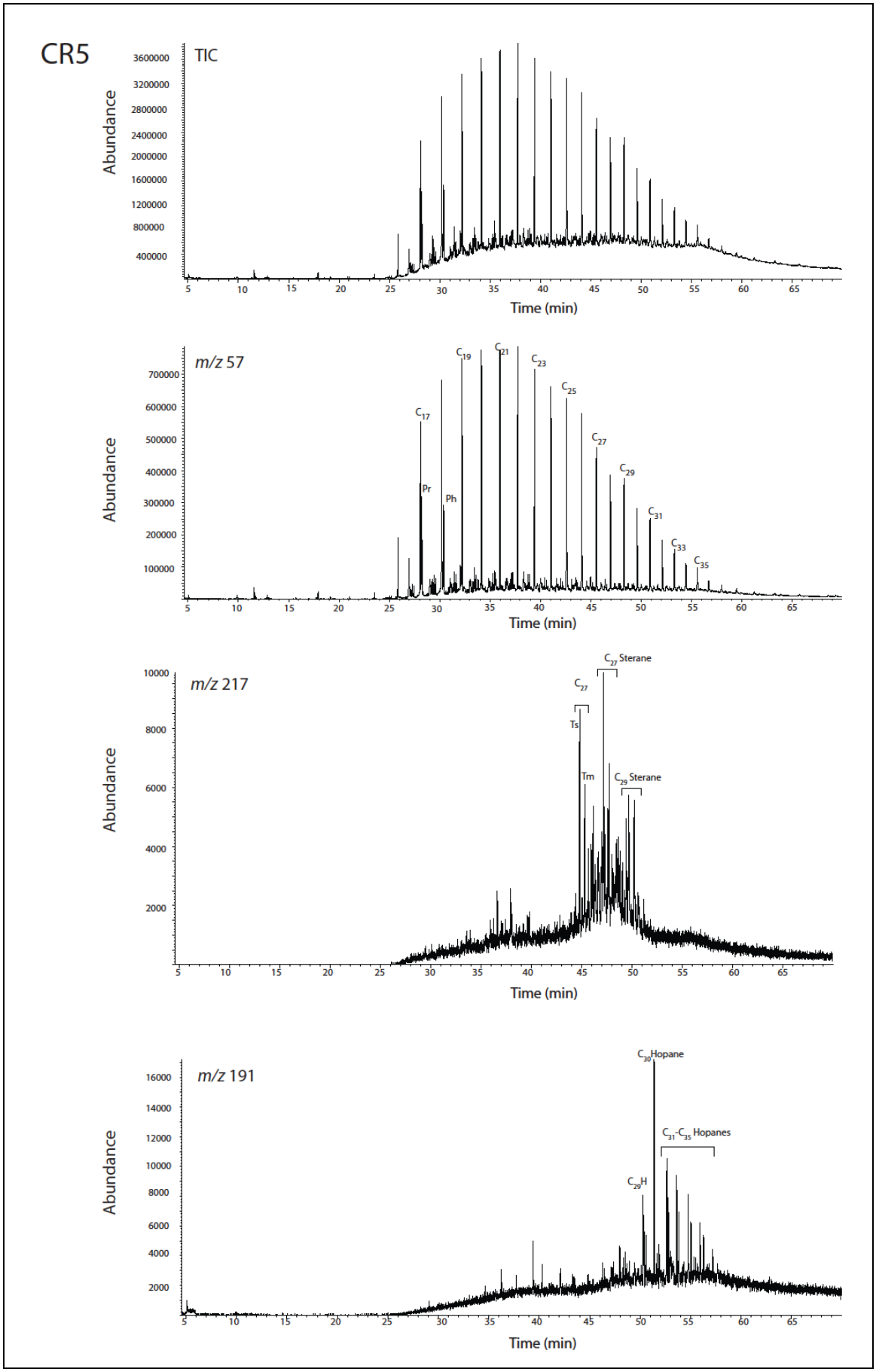

Coomb4
TIC
Abundance
Time (min)
m/z 57
C15
C17
Pr
Ph
C19
C21
C23
C25
m/z 217
m/z 191

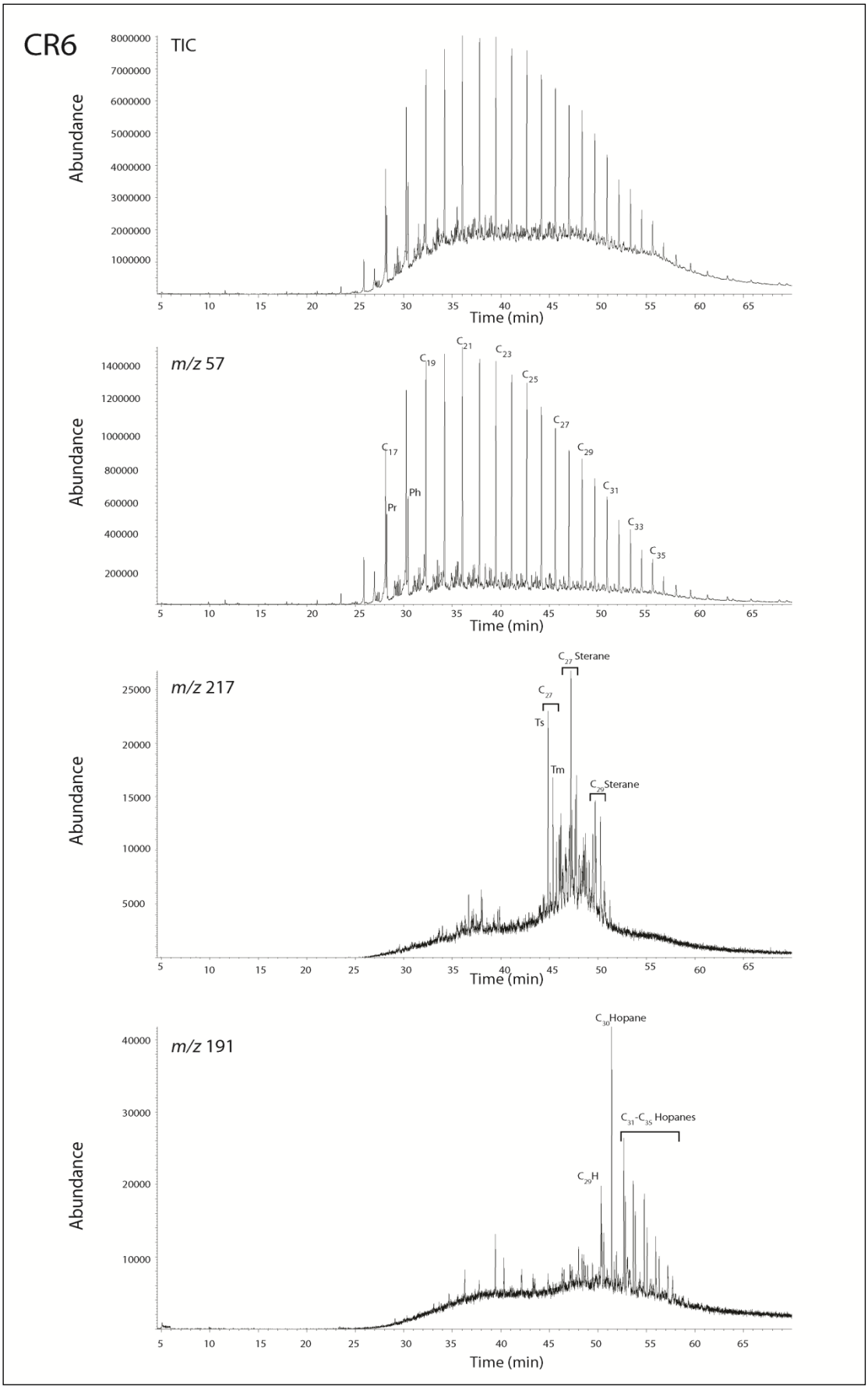

CR1
TIC
Abundance
Time (min)
m/z 57
C13
C15
C17
Pr
C19
Ph
C21
C23
m/z 217
m/z 191

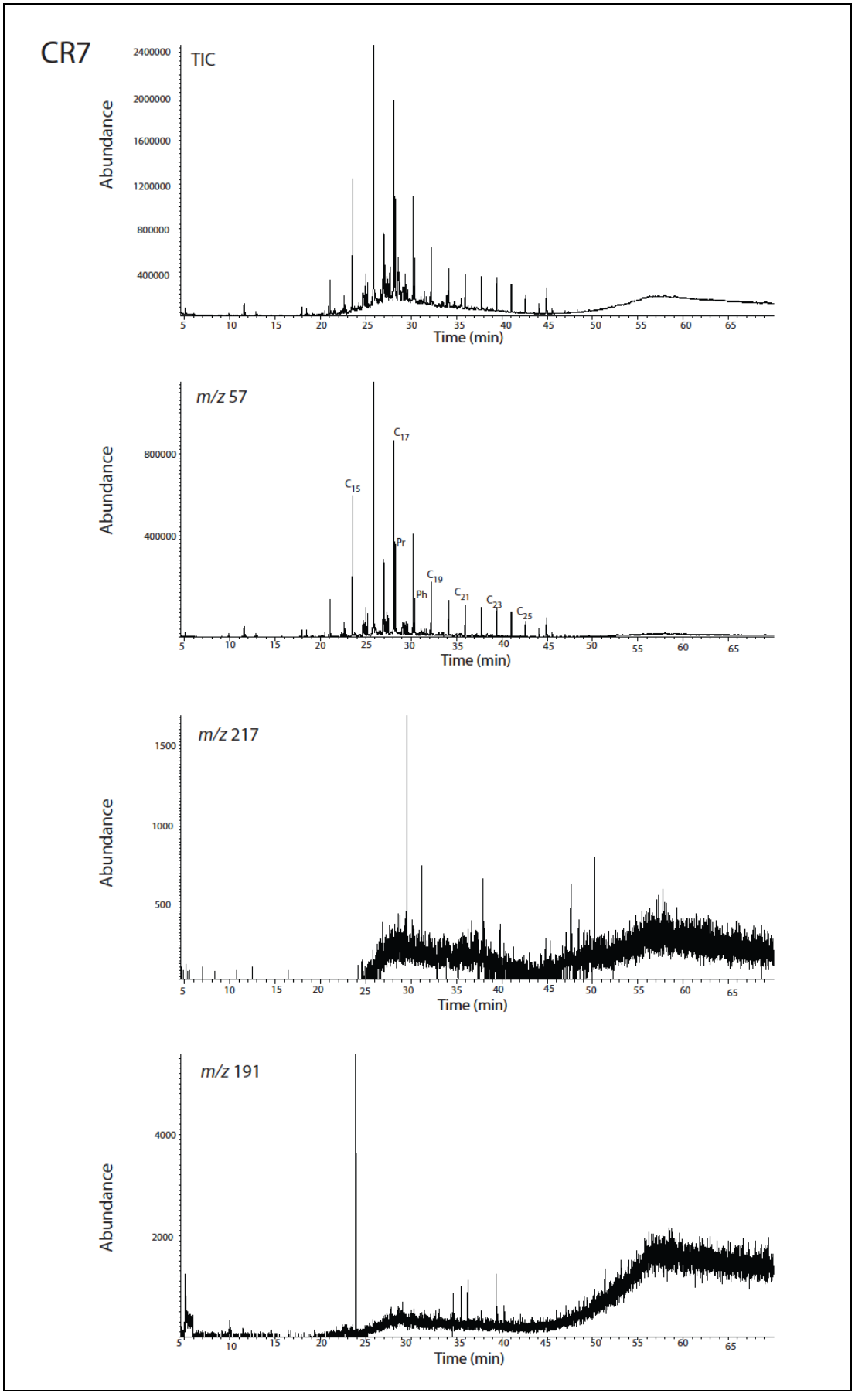

CR2
TIC
Abundance
Time (min)
m/z 57
C17
C19
C21
C15
Pr
Ph
C23
C25
m/z 217
m/z 191


CR3
TIC
Abundance
Time (min)
m/z 57
C15
C17
Pr
Ph
C19
C21
C23
C25
C27
C29
C31
C33
C35
m/z 217
C27 Ts
C27 Sterane
Tm
C29 Sterane
m/z 191
C30 Hopane
C31-C35 Hopanes
C29H

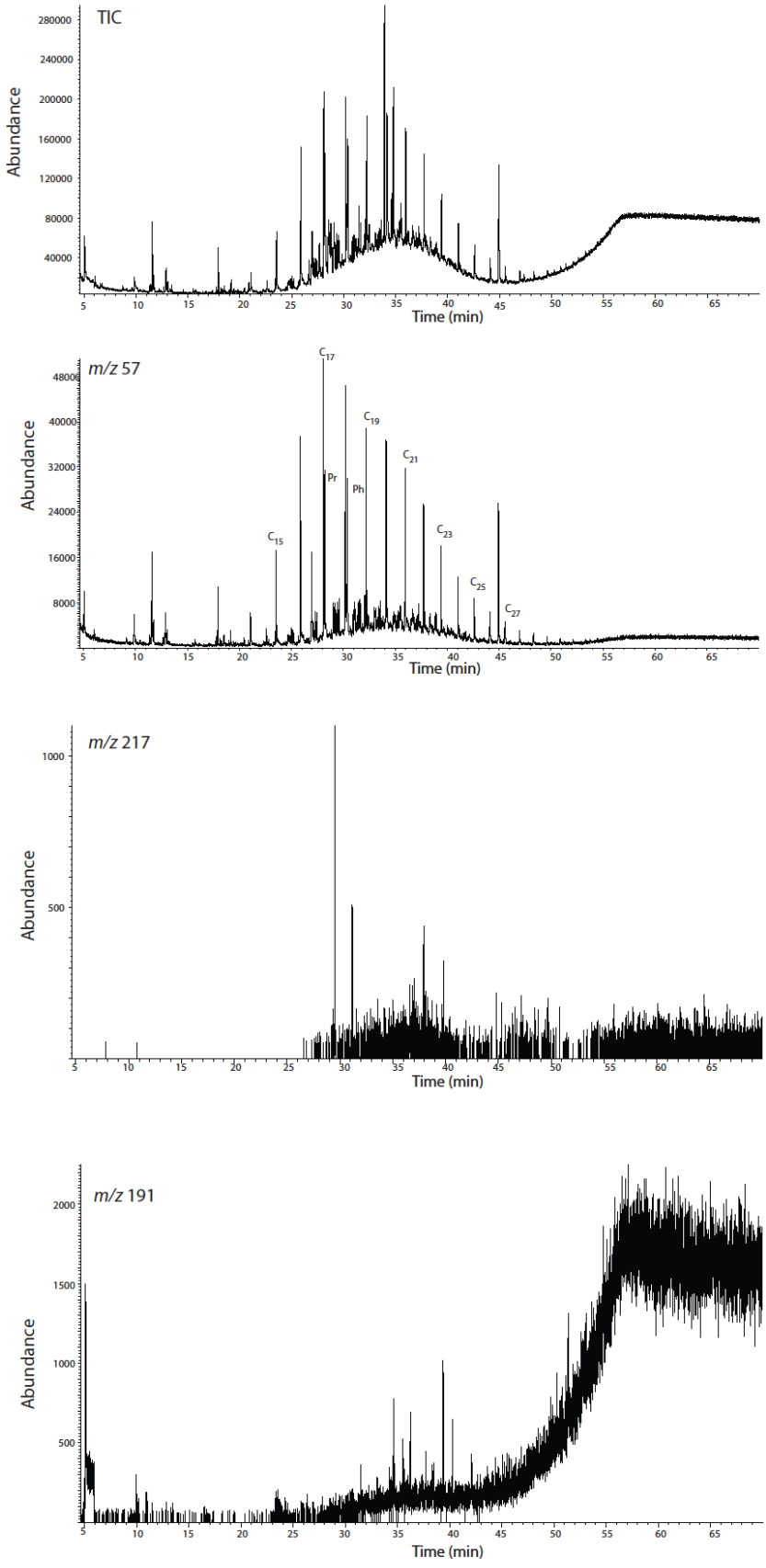

CR4
TIC
Abundance
Time (min)
m/z 57
C17
Pr
Ph
C19
C21
C23
C25
C27
C29
C31
C33
C35
m/z 217
C27 Sterane
C27 Ts
Tm
C29 Sterane
m/z 191
C30 Hopane
C31-C35 Hopanes
C29H

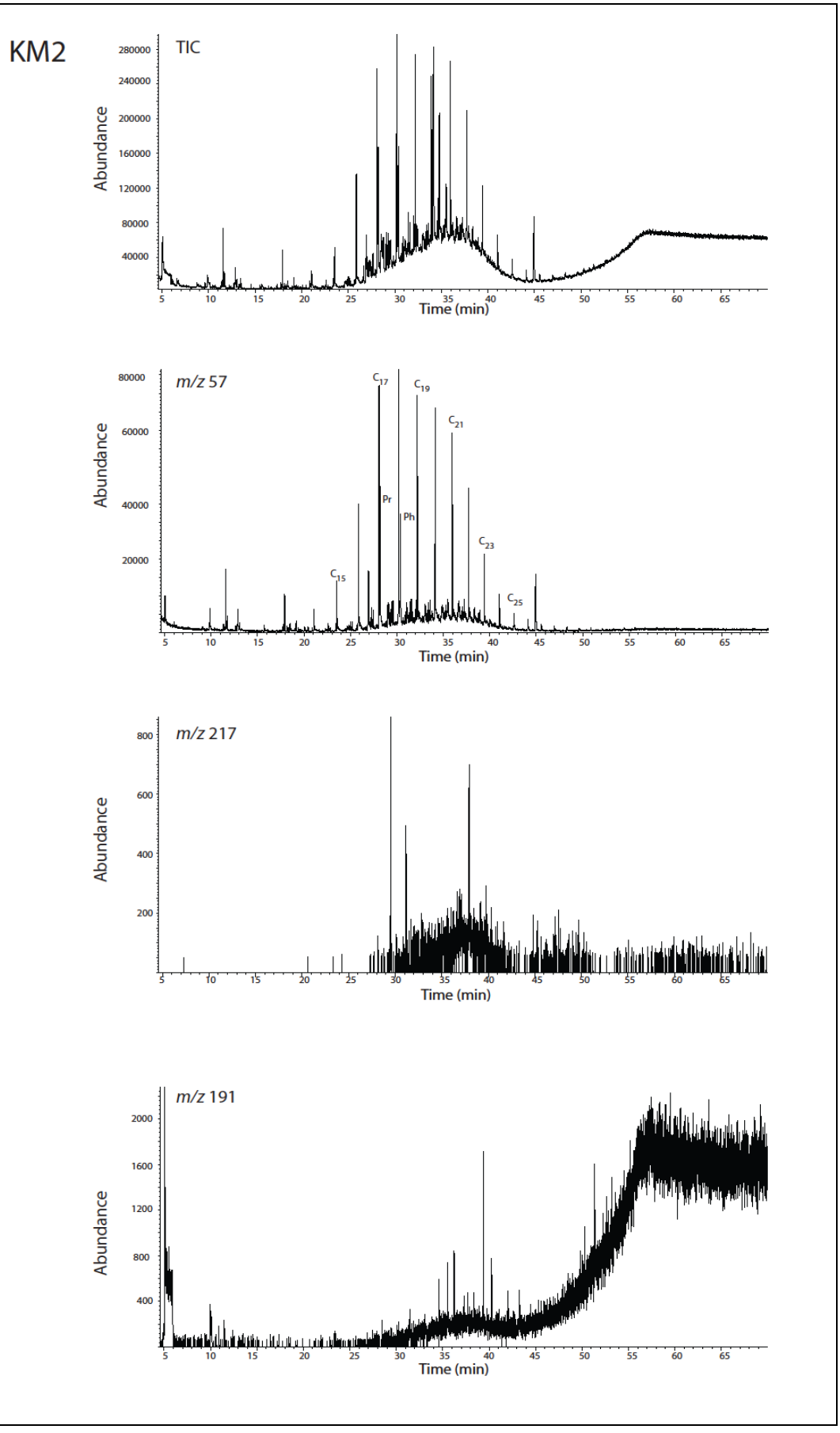

CR5
TIC
Abundance
Time (min)
m/z 57
C17
Pr
Ph
C19
C21
C23
C25
C27
C29
C31
C33
C35
m/z 217
C27
Ts
Tm
C27 Sterane
C29 Sterane
m/z 191
C30 Hopane
C31-C35 Hopanes
C29H

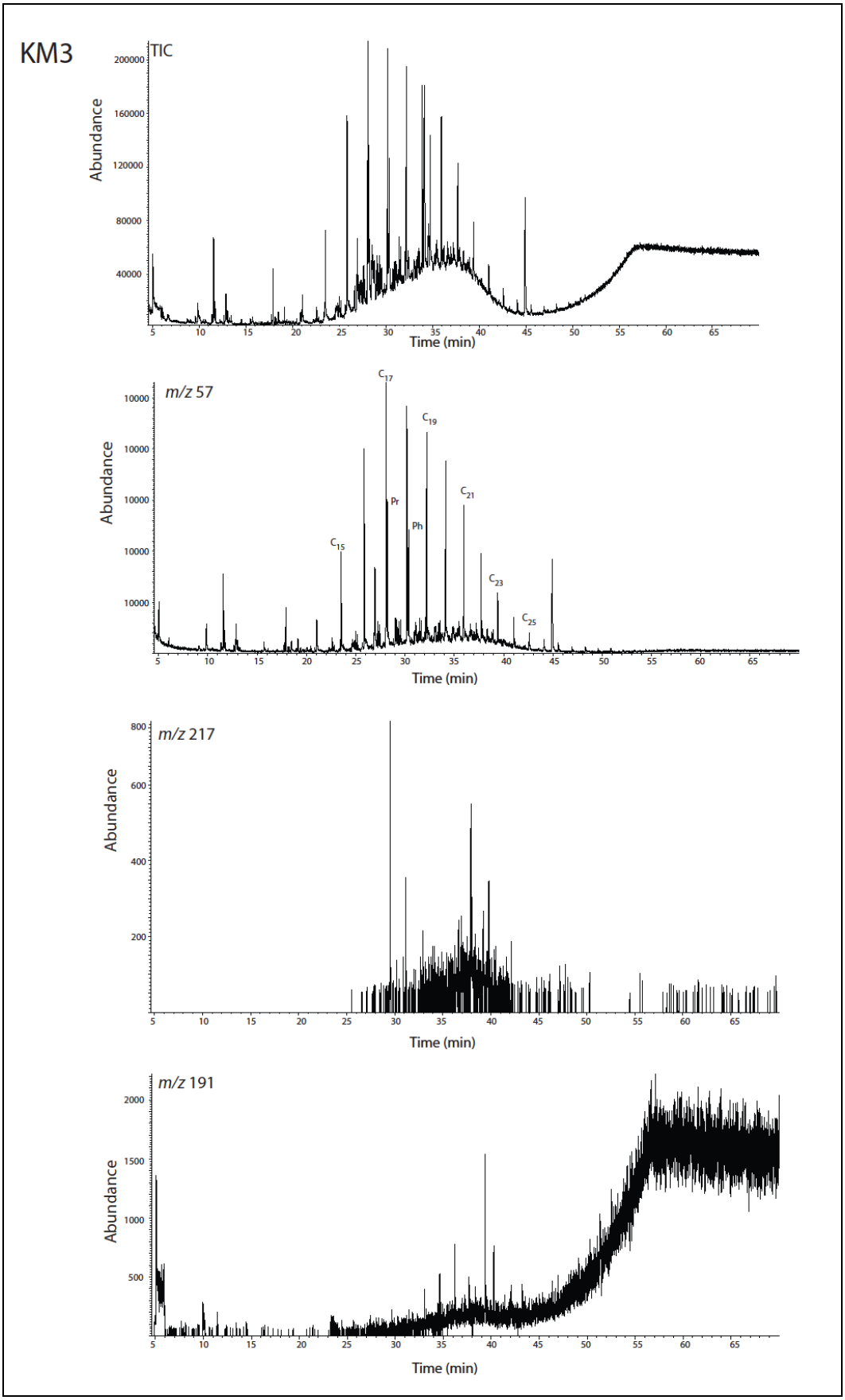

CR6
TIC
Abundance
Time (min)
m/z 57
C17
Pr
Ph
C19
C21
C23
C25
C27
C29
C31
C33
C35
m/z 217
C27 Sterane
C27
Ts
Tm
C29 Sterane
m/z 191
C30 Hopane
C31-C35 Hopanes
C29H

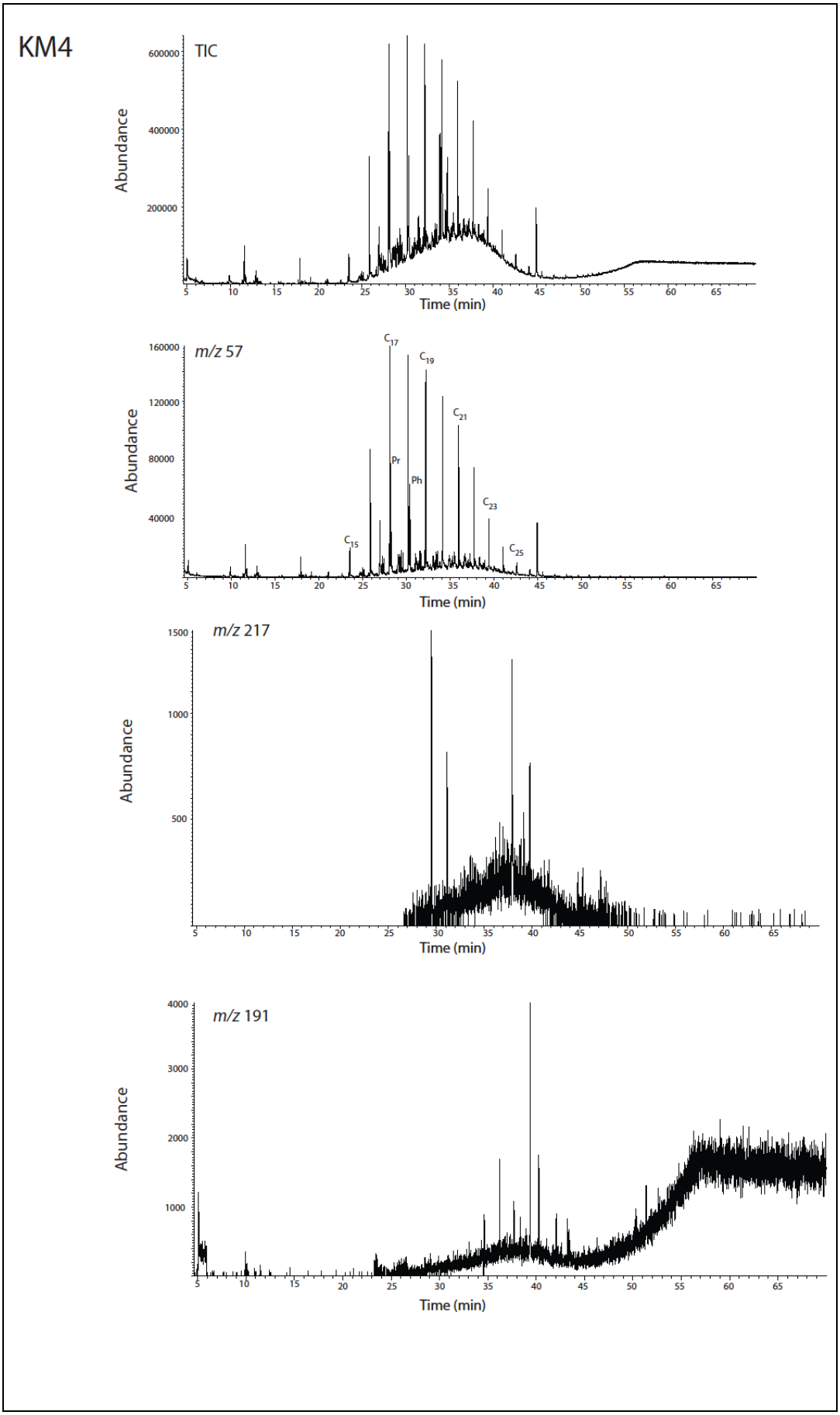

CR7
TIC
Abundance
Time (min)
m/z 57
C15
C17
Pr
Ph
C19
C21
C23
C25
m/z 217
m/z 191

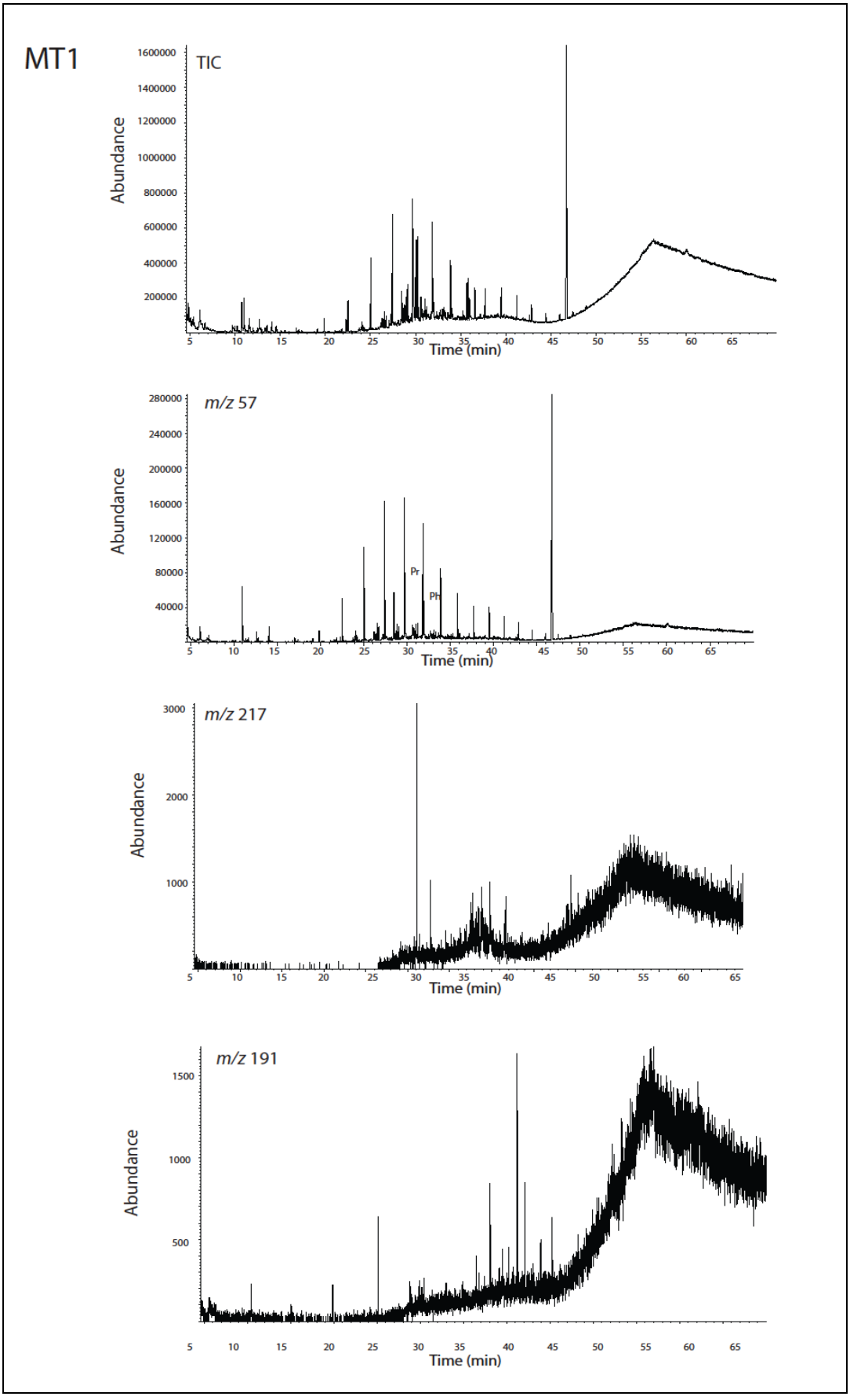
KM1


TIC
Abundance
Time (min)
m/z 57
C17
C19
C21
C23
C25
C27
Pr
Ph
C15
m/z 217
m/z 191

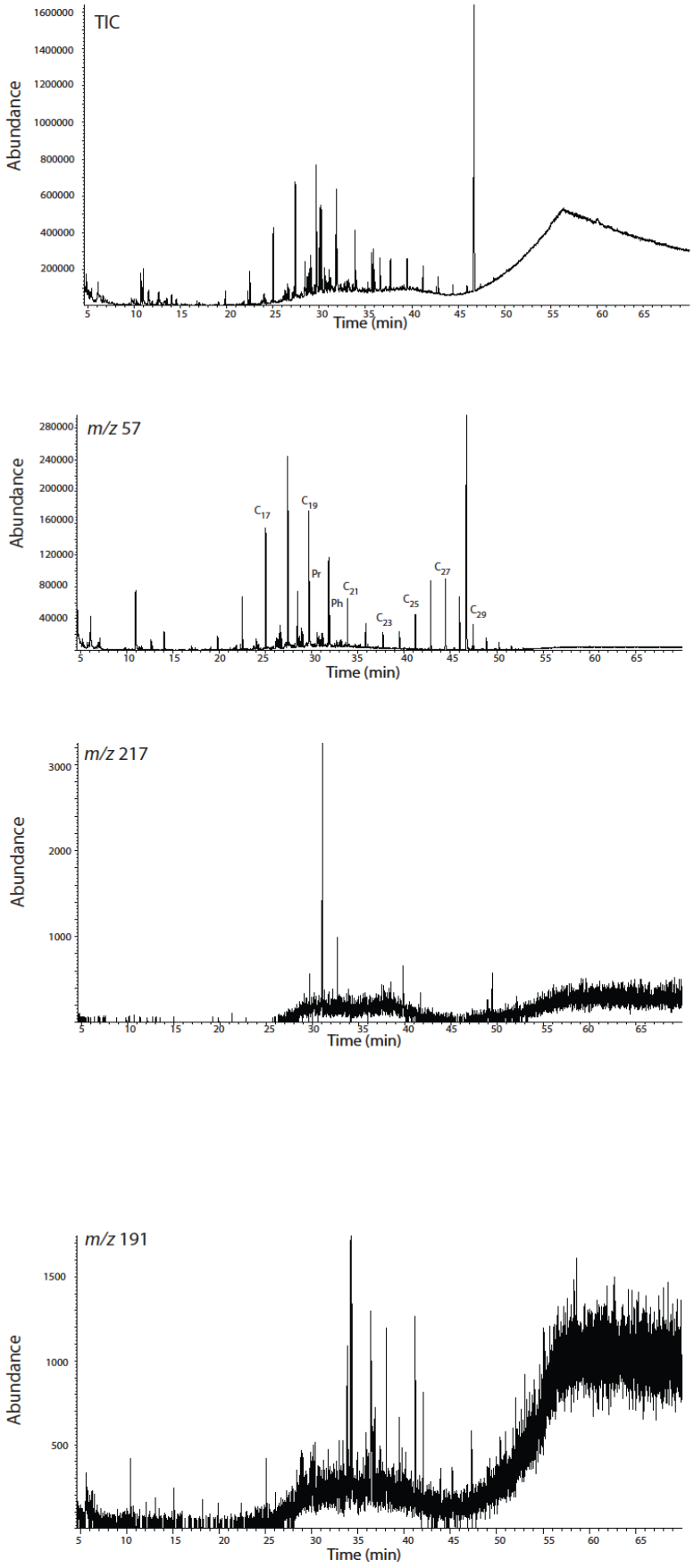

KM2
TIC
Abundance
Time (min)
m/z 57
C17
C19
C21
Pr
Ph
C23
C15
C25
m/z 217
m/z 191

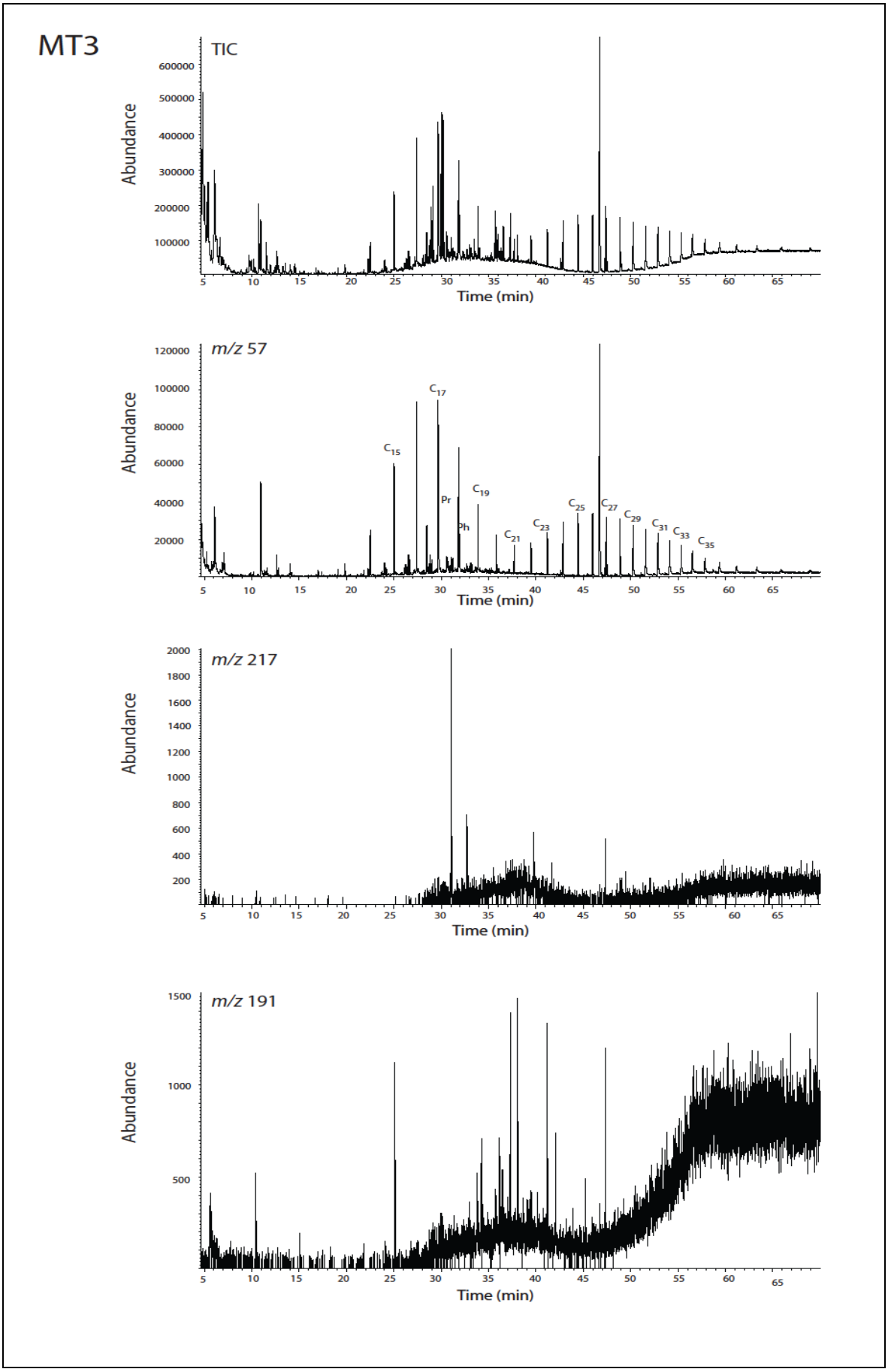

KM3
TIC
Abundance
Time (min)
m/z 57
C17
C19
C21
C23
C25
Pr
Ph
C15
m/z 217
m/z 191

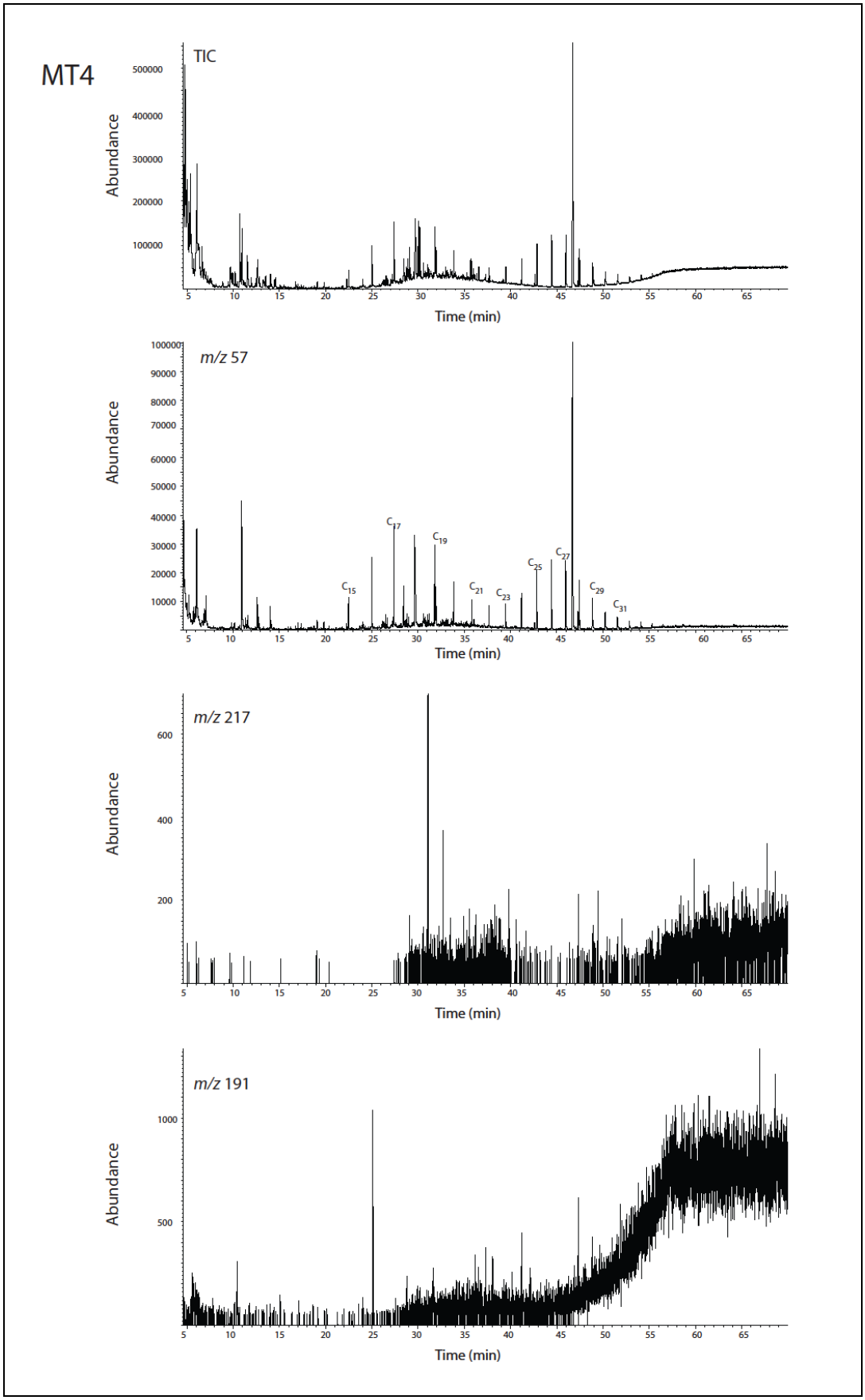

KM4
TIC
Abundance
Time (min)
m/z 57
C17
C19
C21
C23
C25
Pr
Ph
C15
m/z 217
m/z 191

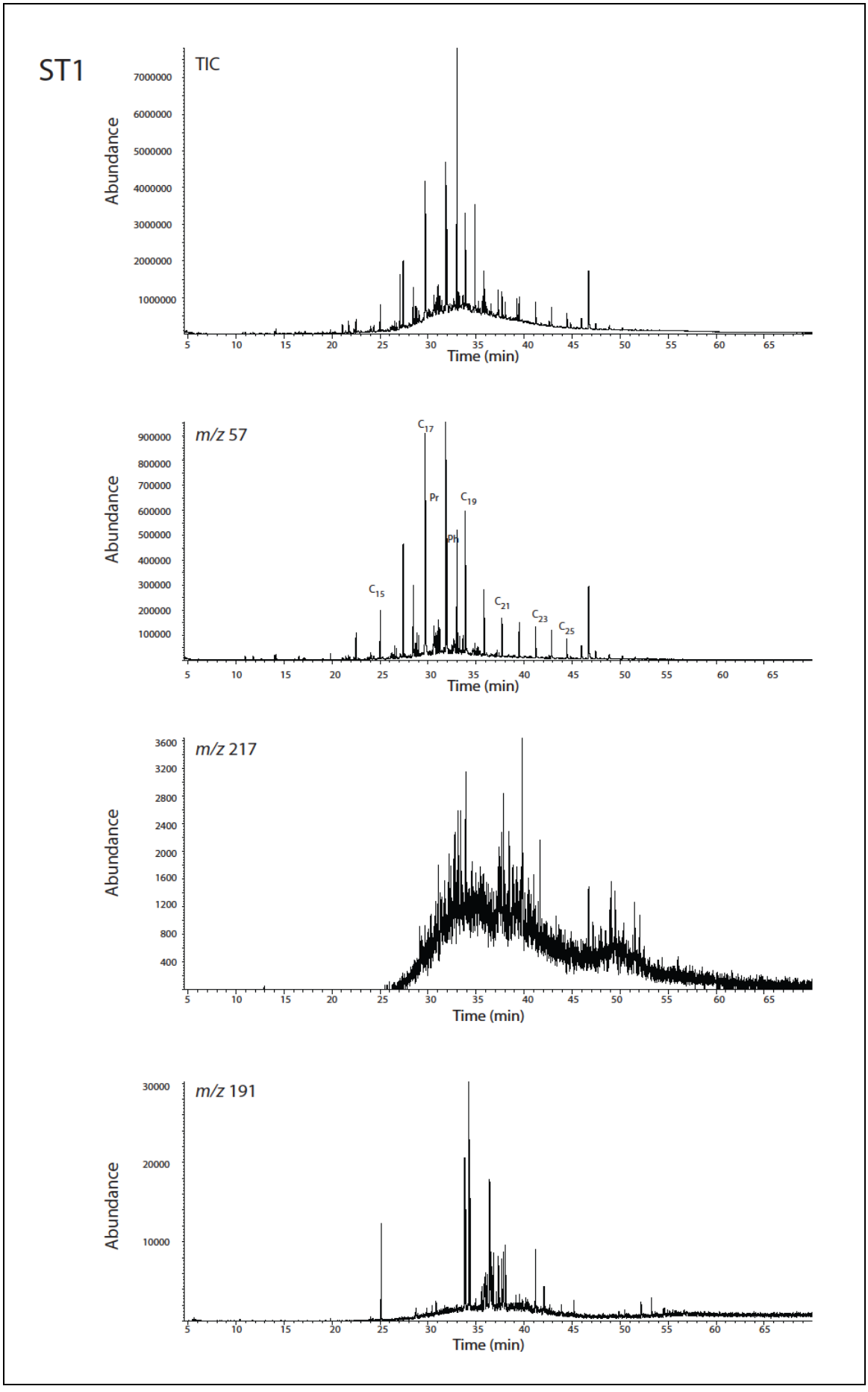

MT1
TIC
Abundance
Time (min)
m/z 57
Pr
Ph
m/z 217
m/z 191

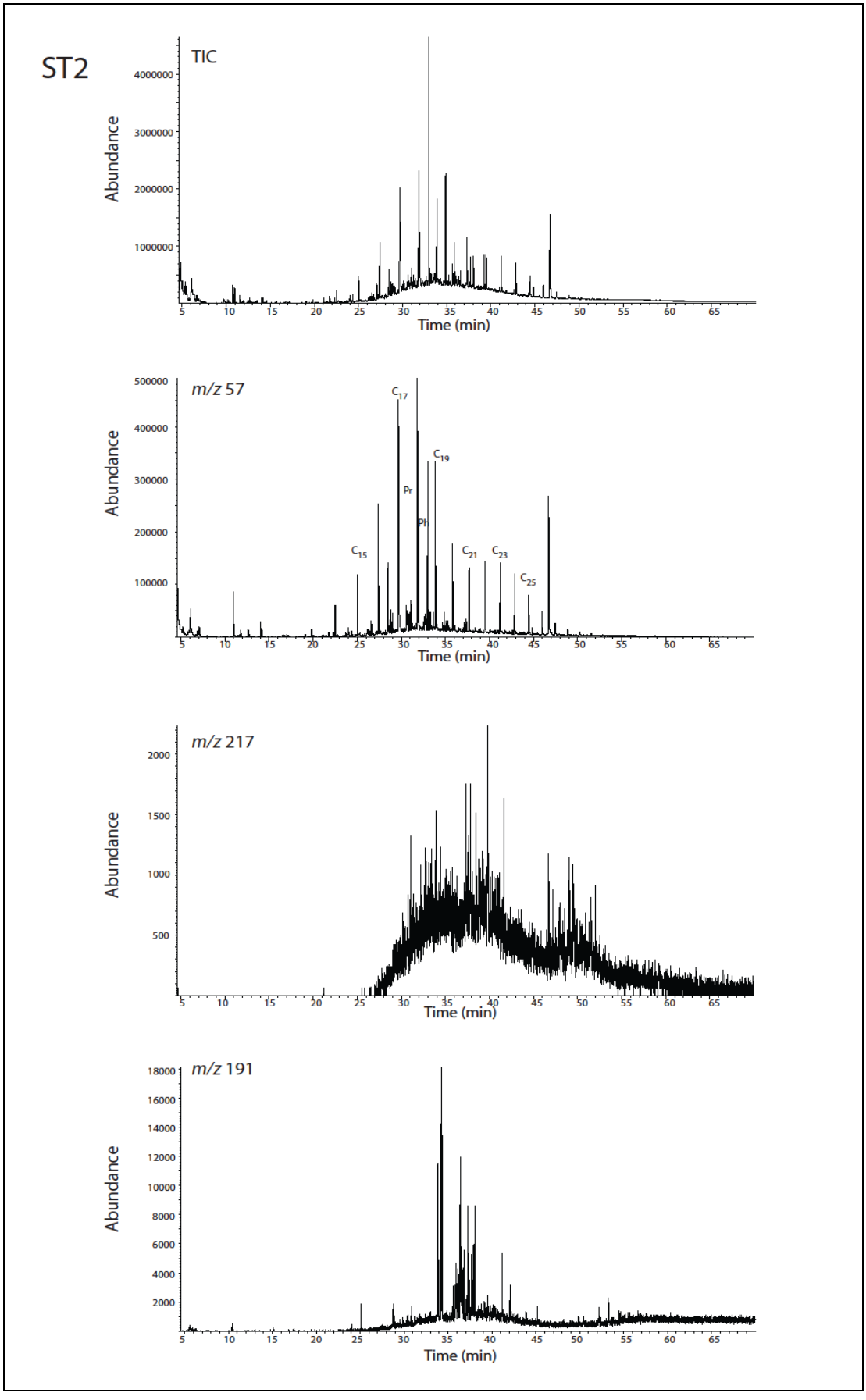
MT2

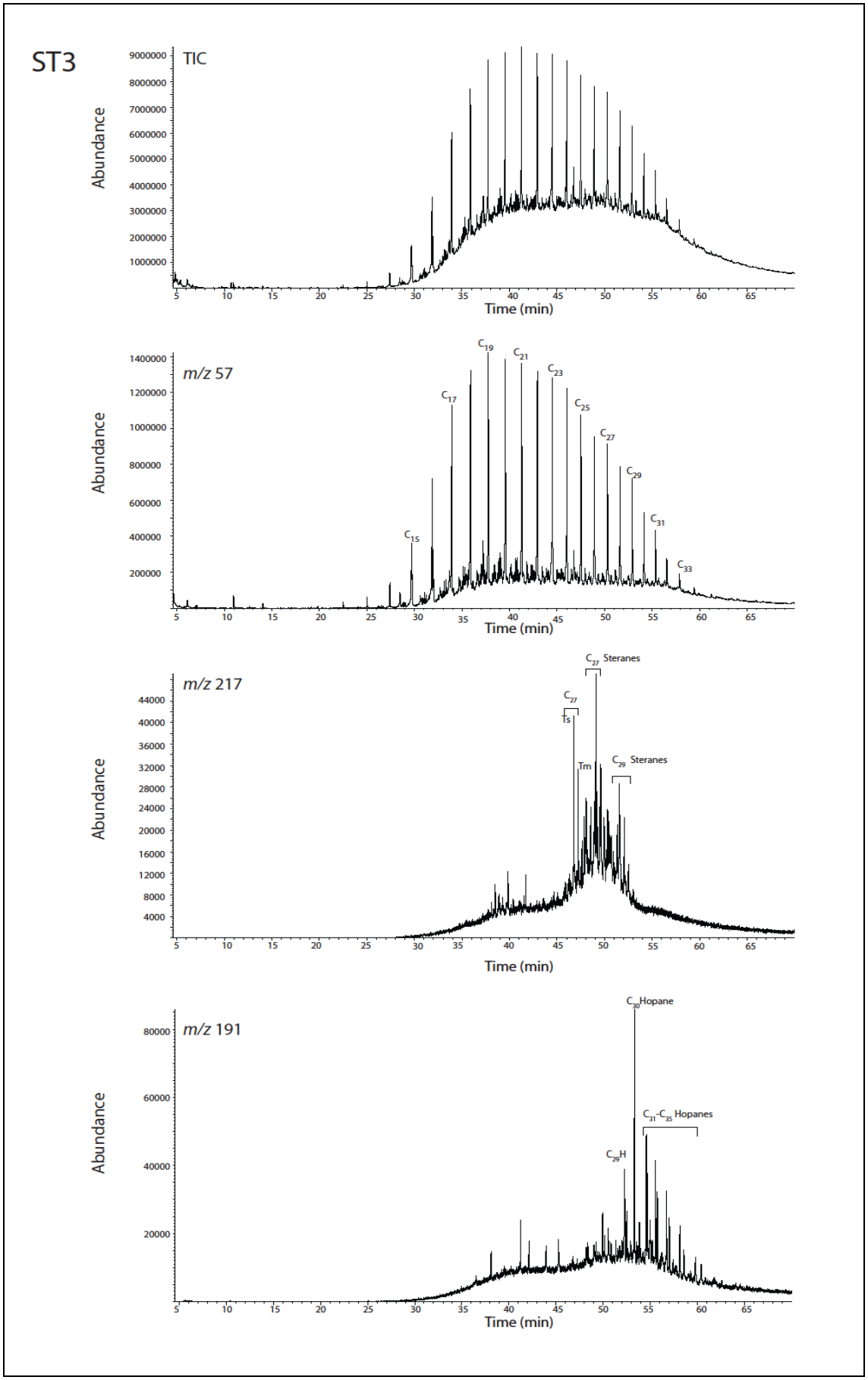

TIC
Abundance
Time (min)
m/z 57
C17
C19
Pr
C21
Ph
C23
C25
C27
C29
m/z 217
m/z 191

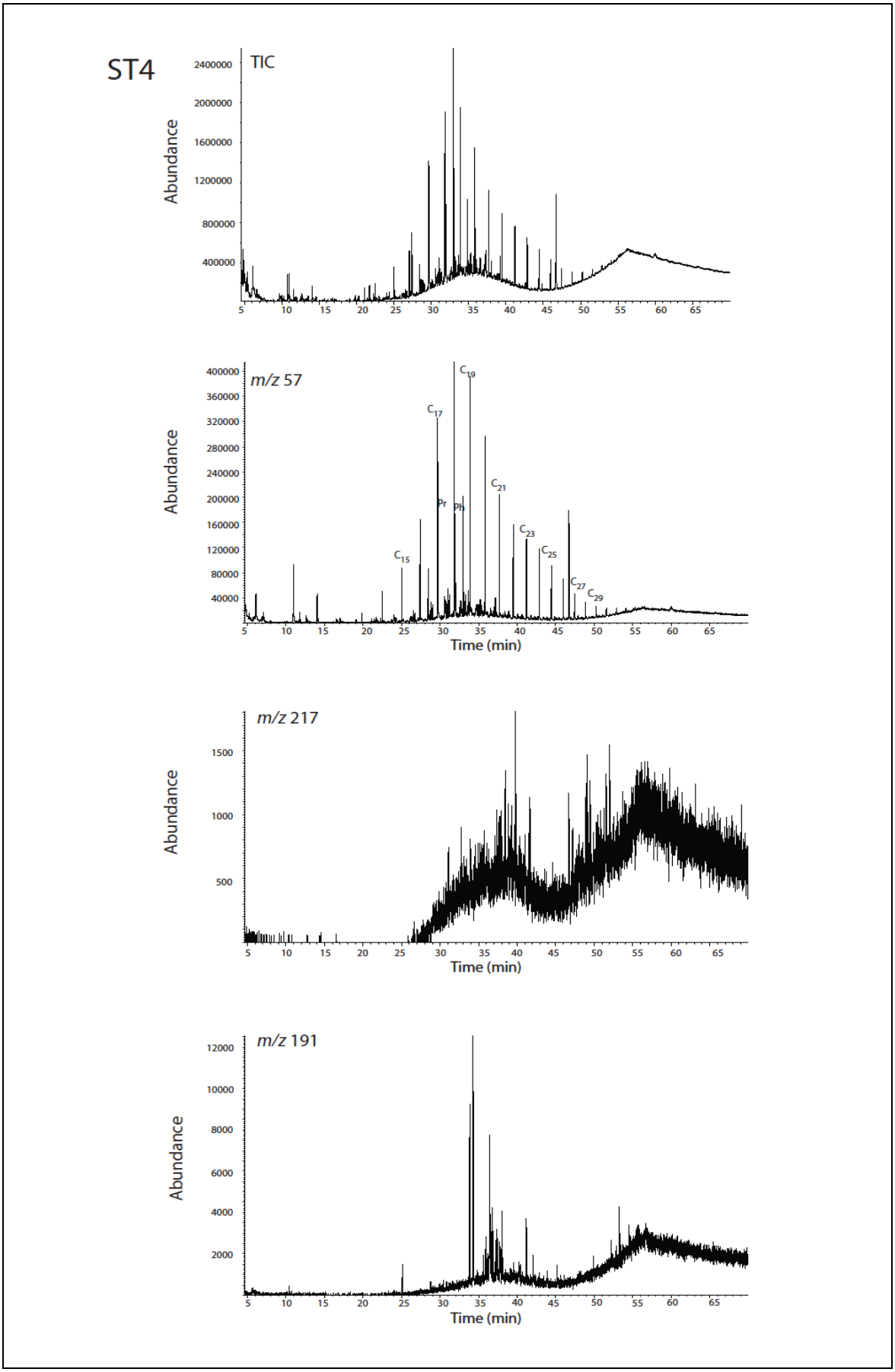

MT3
TIC
Abundance
Time (min)
m/z 57
C15
C17
Pr
Ph
C19
C21
C23
C25
C27
C29
C31
C33
C35
m/z 217
m/z 191

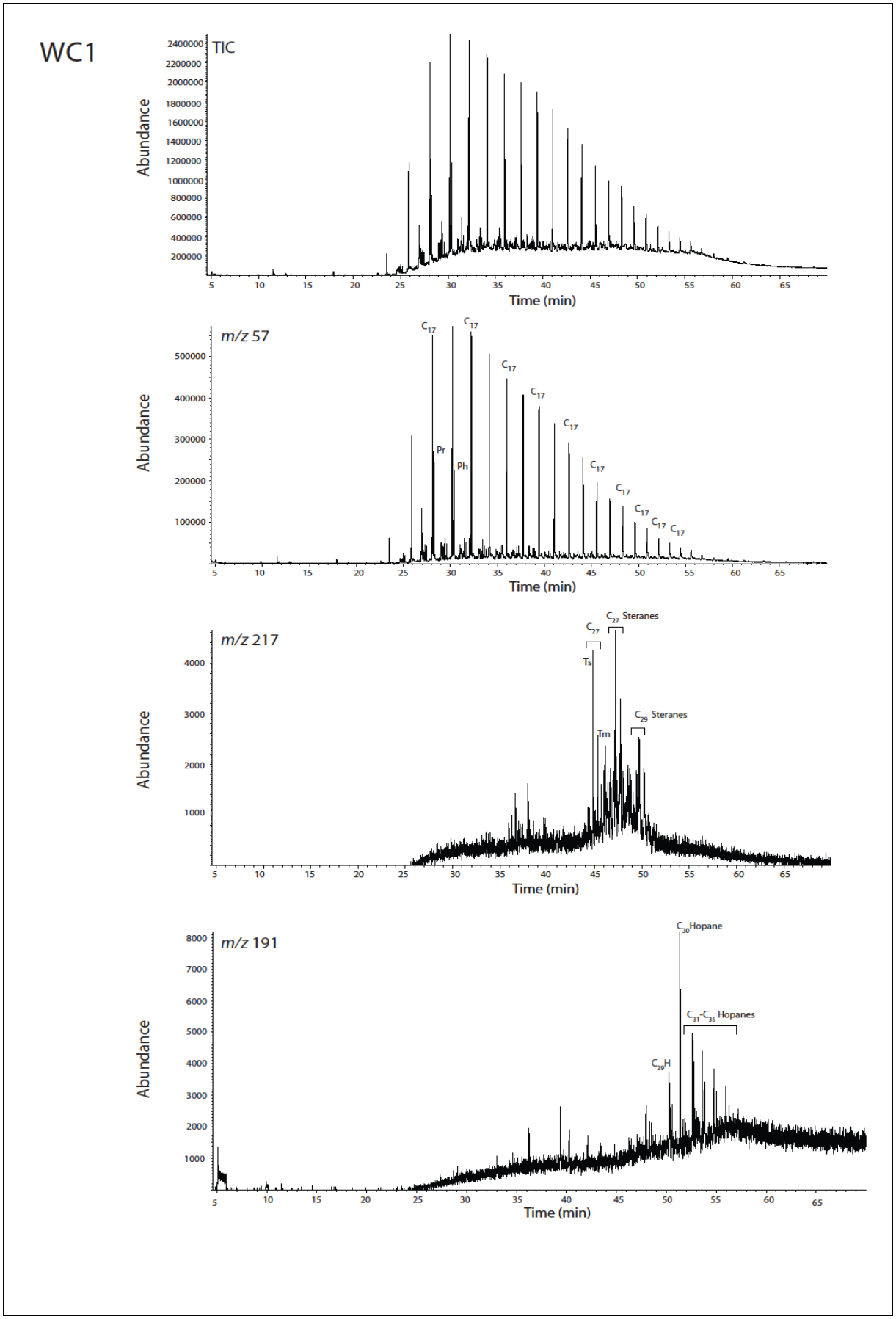

MT4
TIC
Abundance
Time (min)
m/z 57
C15
C17
C19
C21
C23
C25
C27
C29
C31
m/z 217
m/z 191


ST1
TIC
Abundance
Time (min)
m/z 57
C17
Pr
C19
Ph
C15
C21
C23
C25
m/z 217
m/z 191

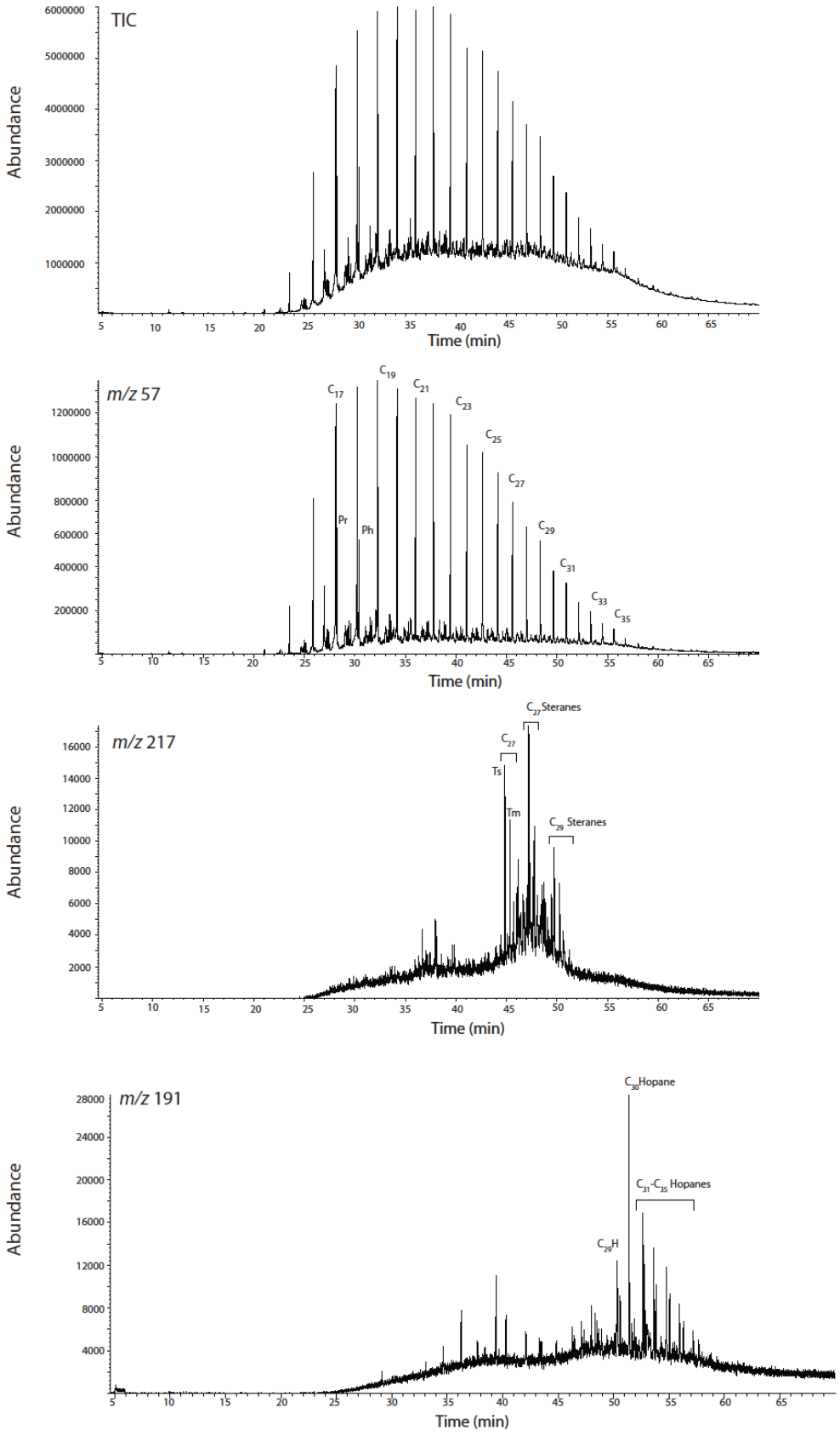

ST2
TIC
Abundance
Time (min)
m/z 57
C17
C19
Pr
Ph
C15
C21
C23
C25
m/z 217
m/z 191

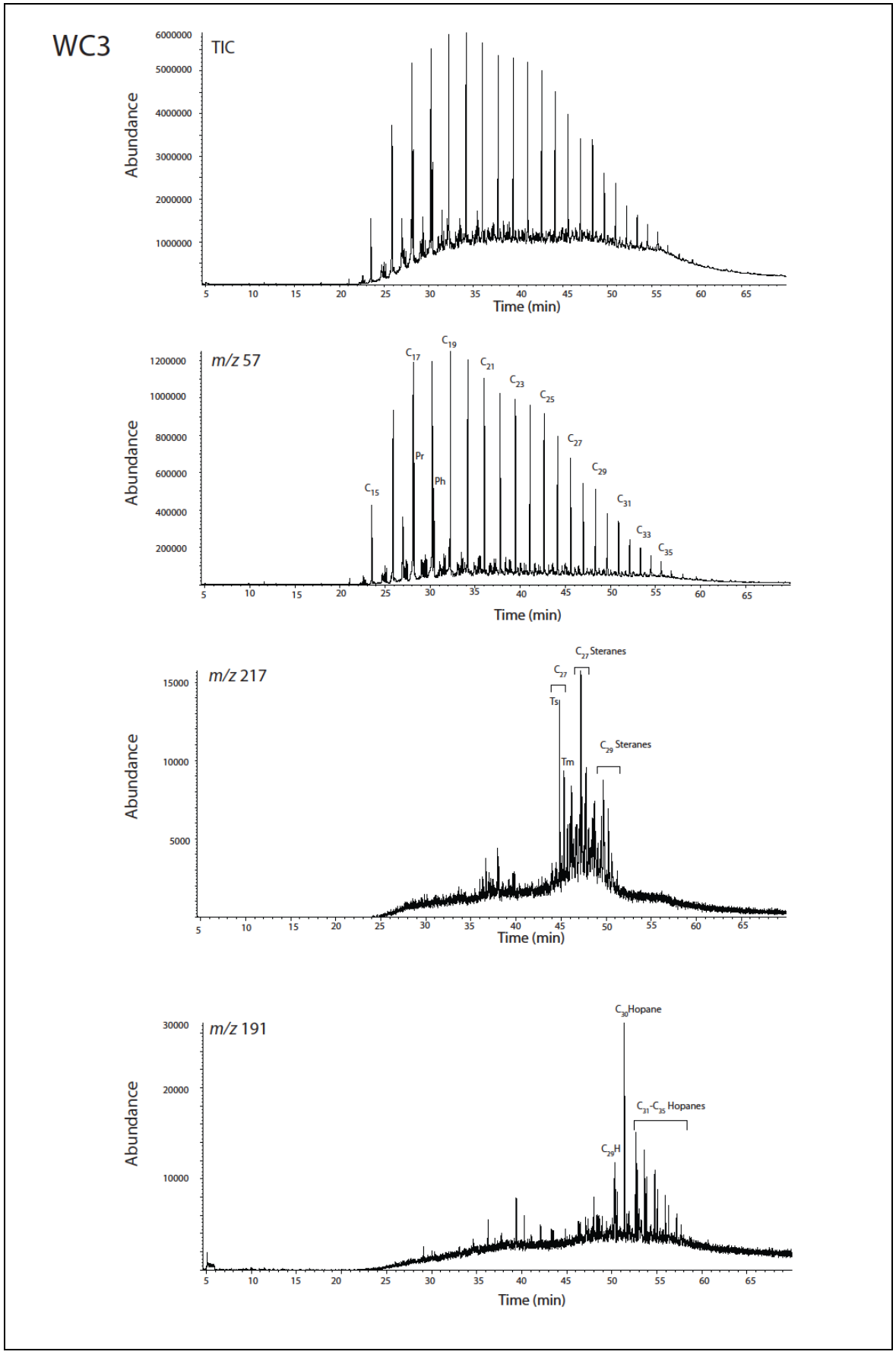

ST3
TIC
Abundance
Time (min)
m/z 57
C15
C17
C19
C21
C23
C25
C27
C29
C31
C33
m/z 217
C27 Steranes
C27 Ts
Tm
C29 Steranes
m/z 191
C30Hopane
C31-C35 Hopanes
C29H

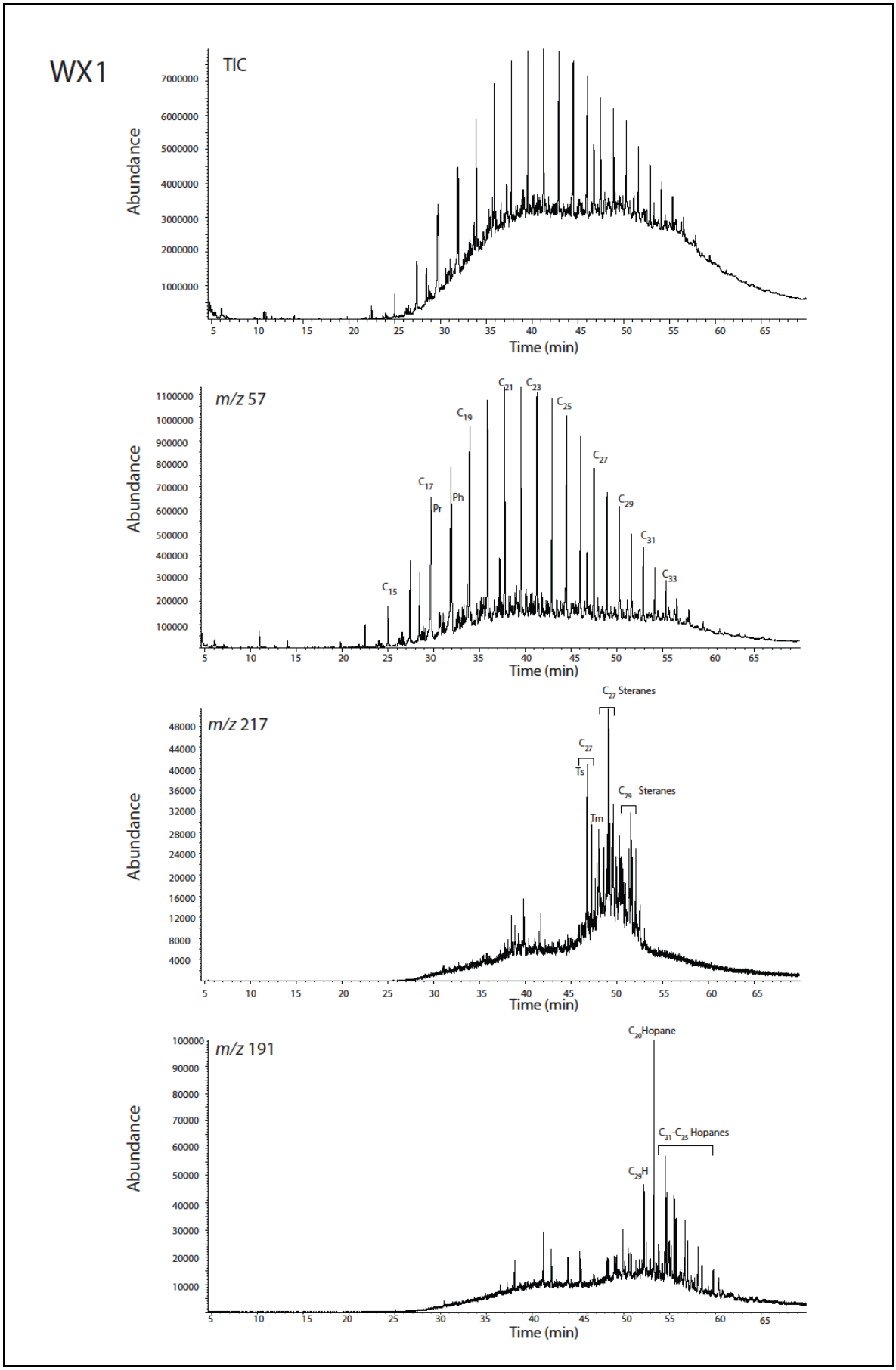

ST4
TIC
Abundance
2400000
2000000
1600000
1200000
800000
400000
m/z 57
C19
C17
C21
Pr
Ph
C23
C25
C15
C27
C29
Time (min)
m/z 217
1500
1000
500
m/z 191
12000
10000
8000
6000
4000
2000
5 10 15 20 25 30 35 40 45 50 55 60 65

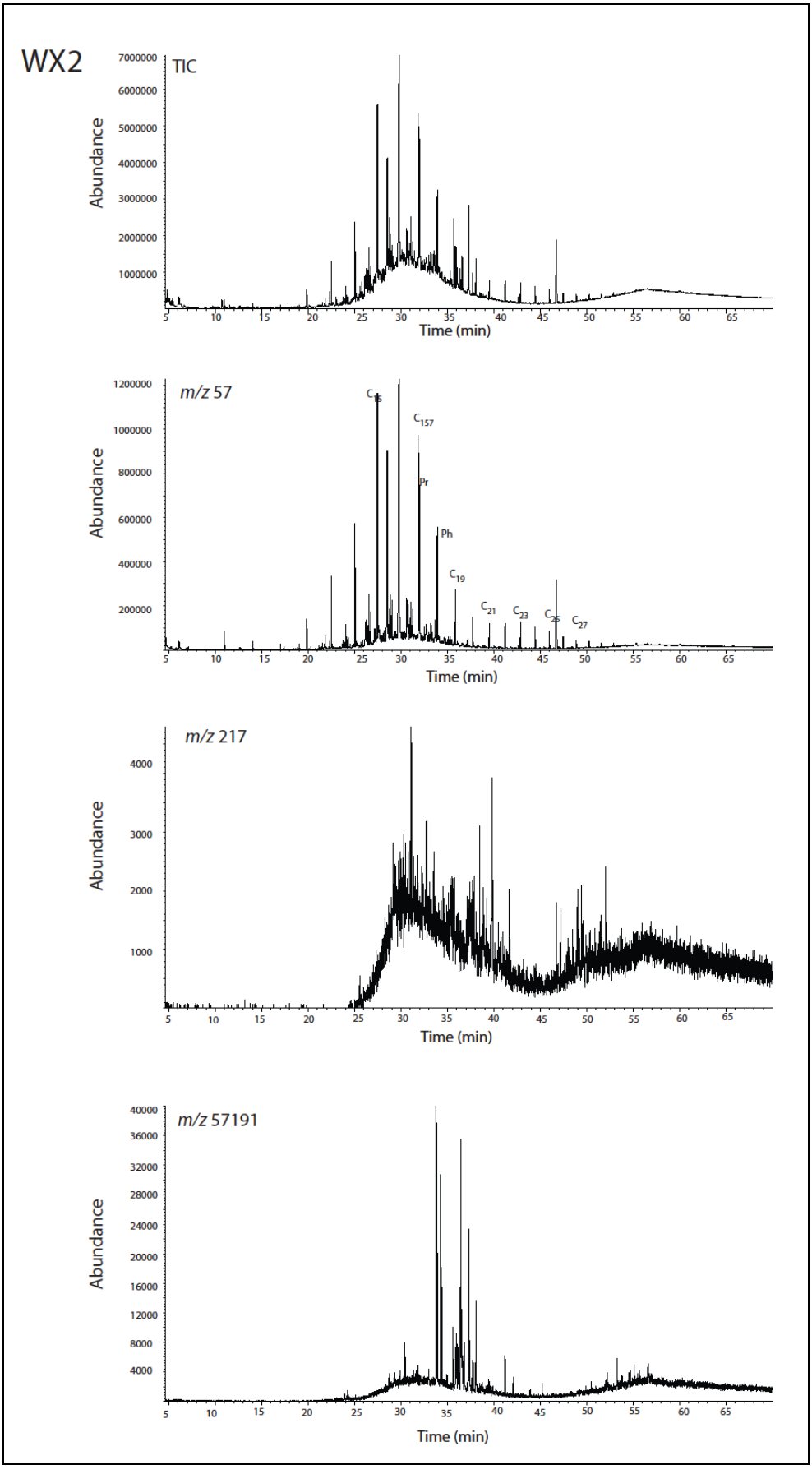

WC1
TIC
Abundance
Time (min)
m/z 57
C17
Pr
Ph
m/z 217
C27
C27 Steranes
Ts
Tm
C29 Steranes
m/z 191
C30Hopane
C21-C25 Hopanes
C29H

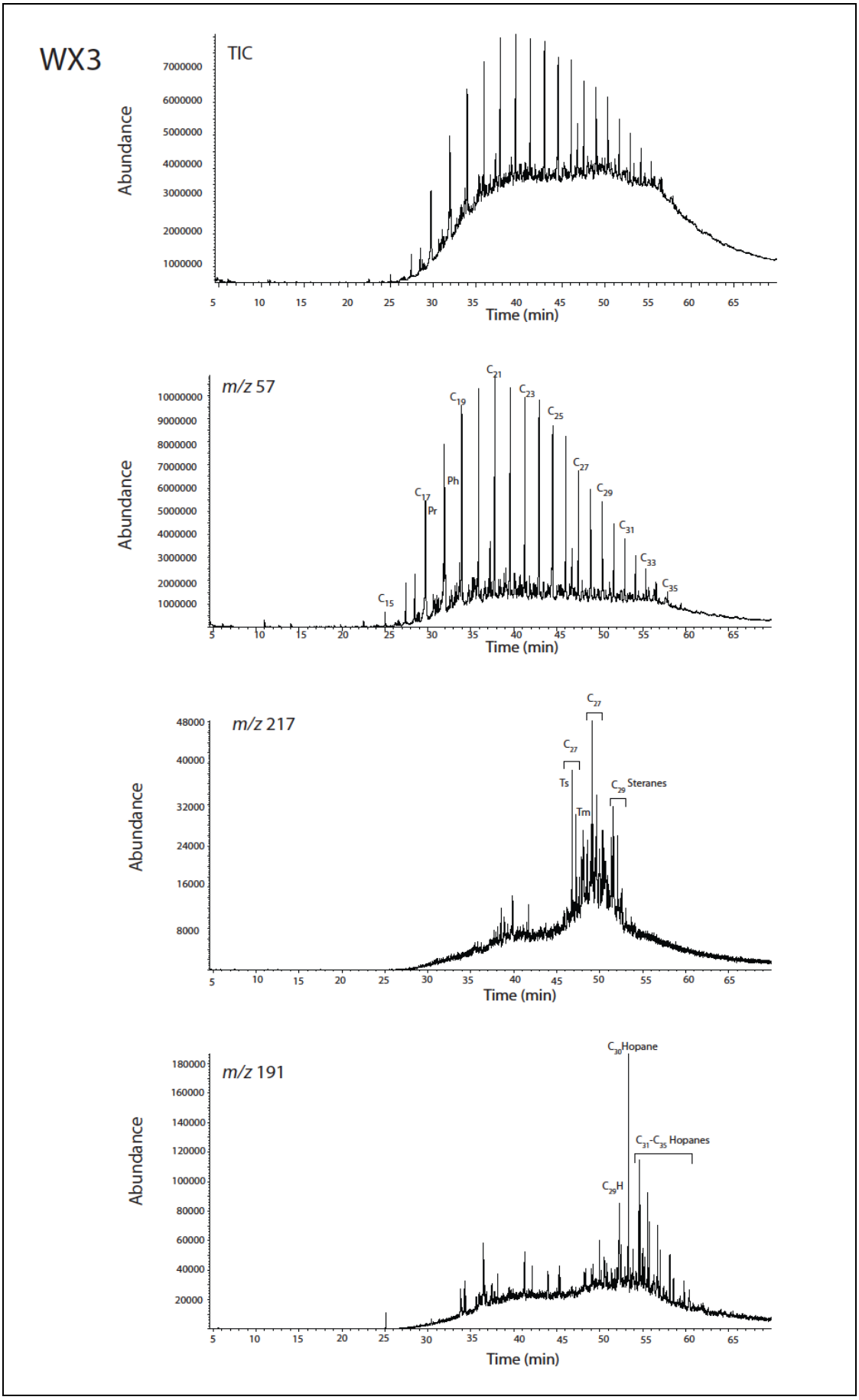
WC2


TIC
Abundance
Time (min)
m/z 57
C17
Pr
Ph
C19
C21
C23
C25
C27
C29
C31
C33
C35
m/z 217
C27 Steranes
C27
Ts
Tm
C29 Steranes
m/z 191
C30Hopane
C31-C35 Hopanes
C29H


WC3
TIC
Abundance
Time (min)
m/z 57
C15
C17
Pr
Ph
C19
C21
C23
C25
C27
C29
C31
C33
C35
m/z 217
C27
Ts
Tm
C27 Steranes
C29 Steranes
m/z 191
C30Hopane
C31-C35 Hopanes
C29H

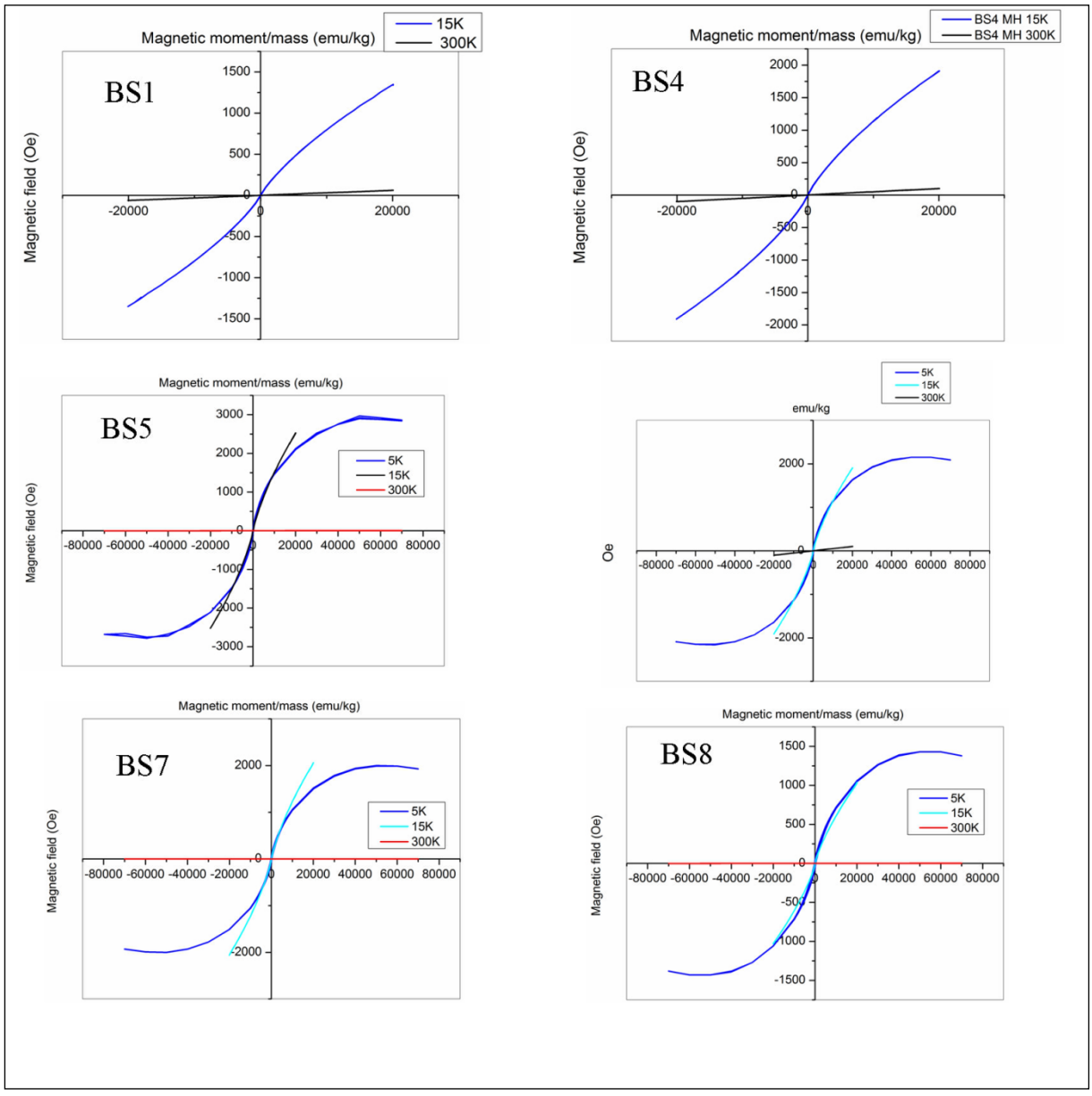

WX1
TIC
Abundance
Time (min)
m/z 57
C15
C17
Pr
Ph
C19
C21
C23
C25
C27
C29
C31
C33
m/z 217
C27 Steranes
C27 Ts
Tm
C29 Steranes
m/z 191
C30Hopane
C31-C35 Hopanes
C29H

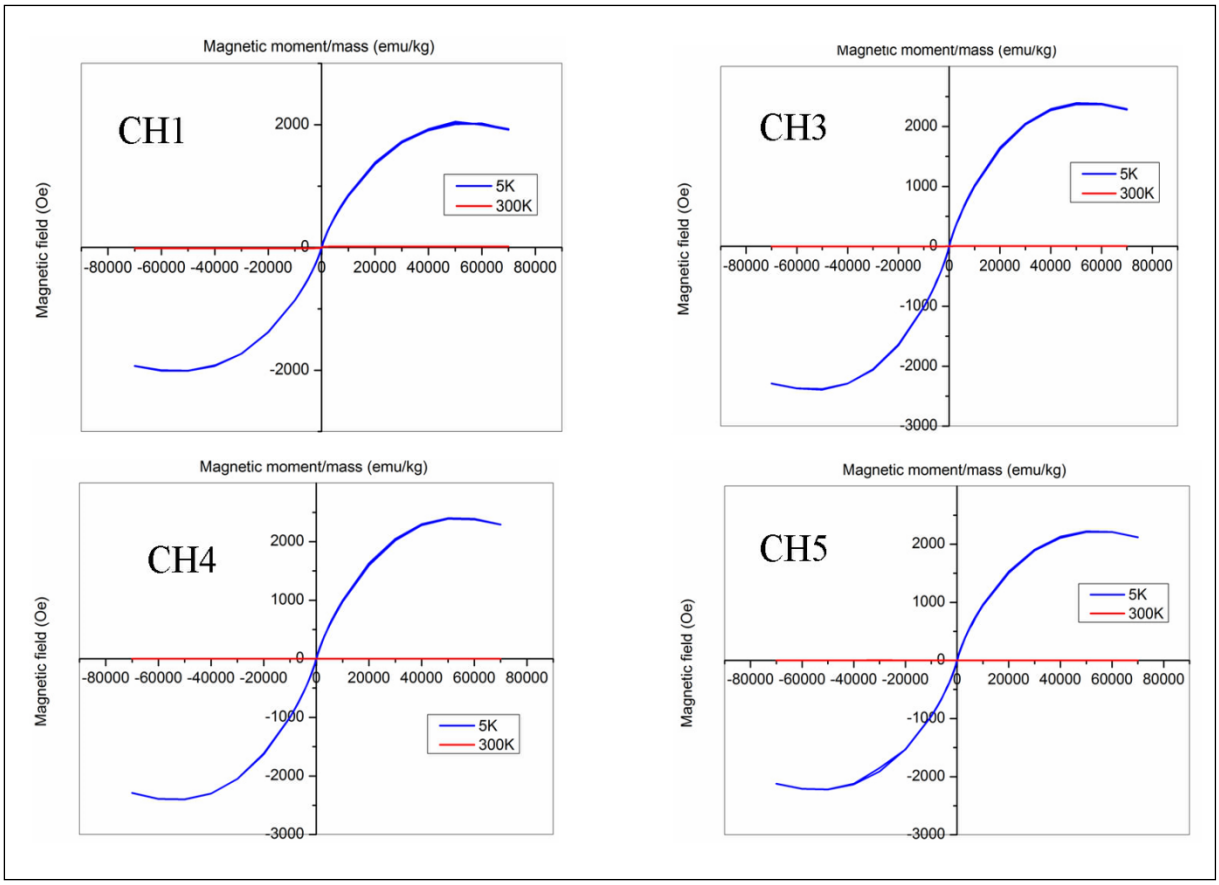

WX2
TIC
Abundance
Time (min)
m/z 57
C15
C157
Pr
Ph
C19
C21
C23
C25
C27
m/z 217
m/z 57191

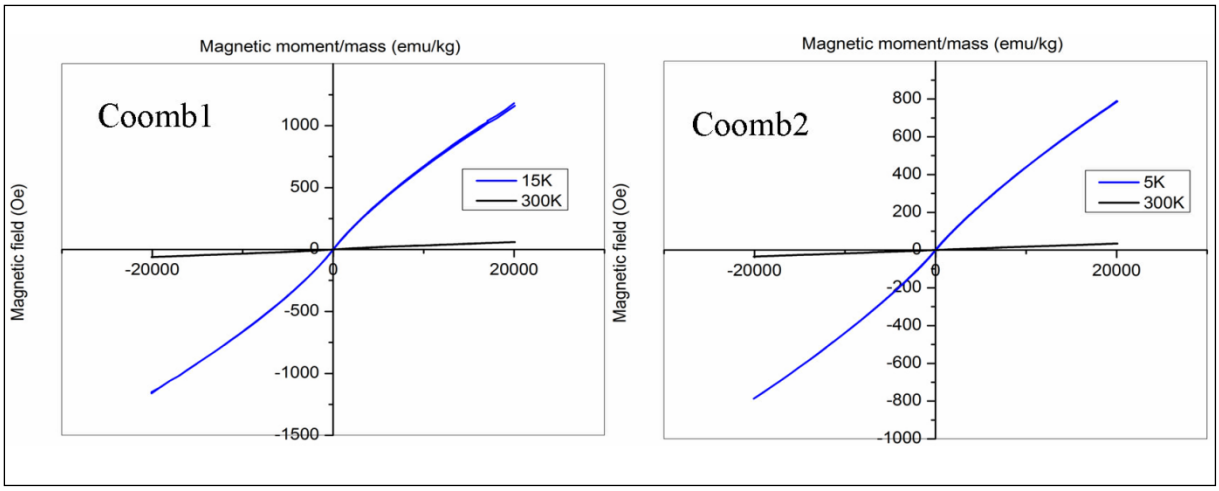

WX3
TIC
Abundance
Time (min)
m/z 57
C15
C17
Pr
Ph
C19
C21
C23
C25
C27
C29
C31
C33
C35
m/z 217
C27
Ts
Tm
C27
C29 Steranes
m/z 191
C30 Hopane
C31-C35 Hopanes
C29H

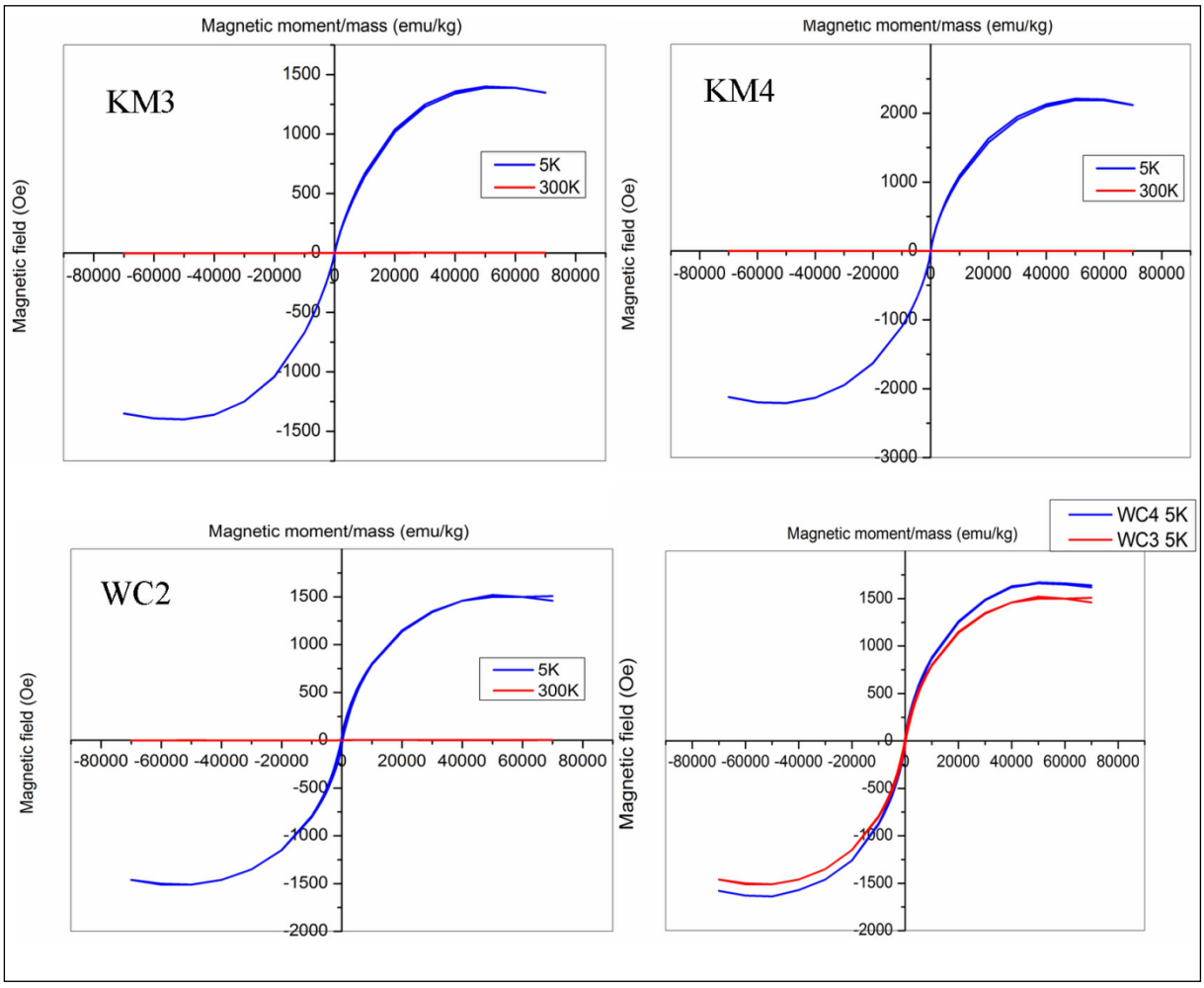
Appendix 2.2

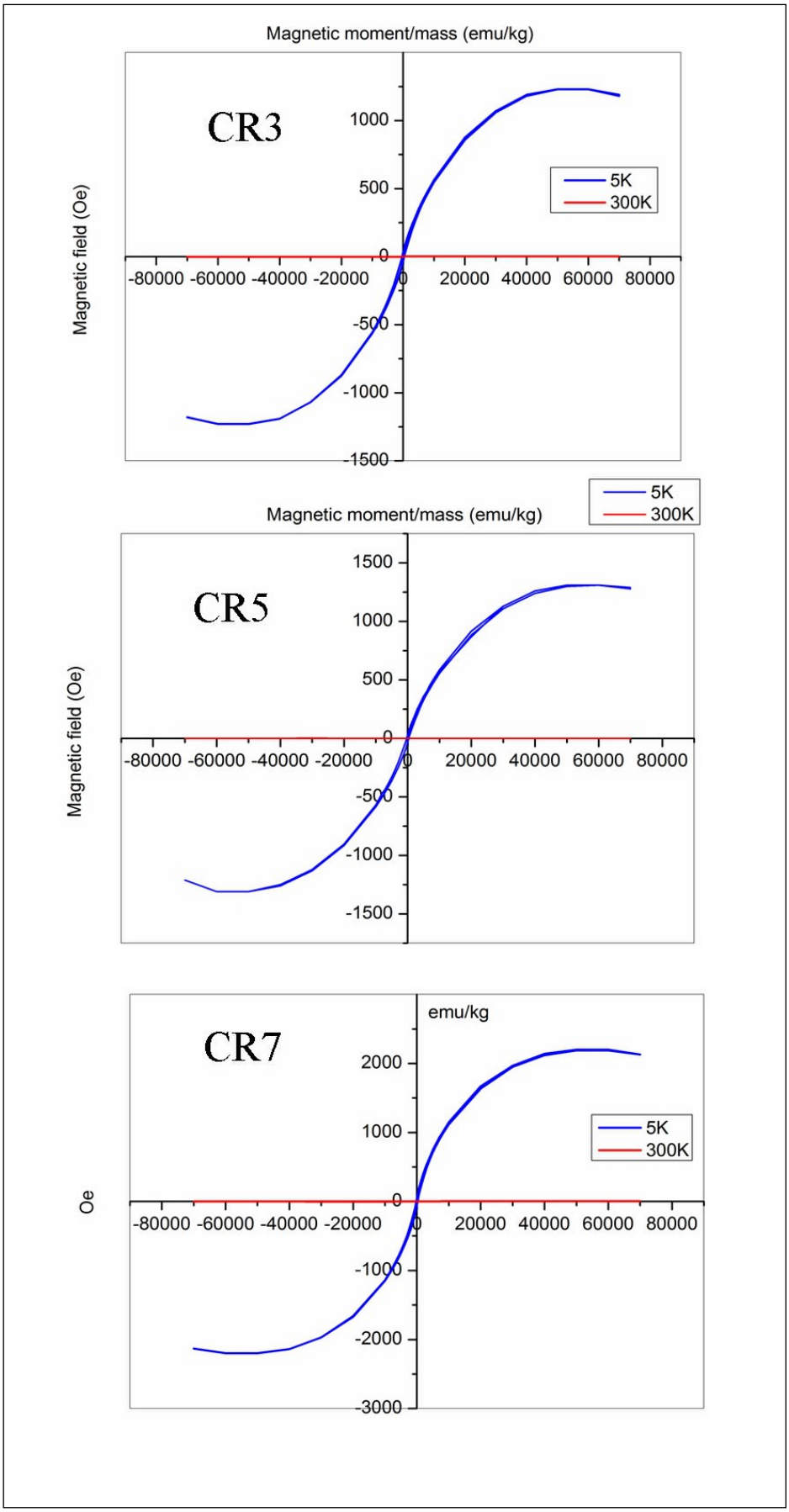
Magnetic hysteresis and ZFC experiments carried out in chapter 5 are presented below.

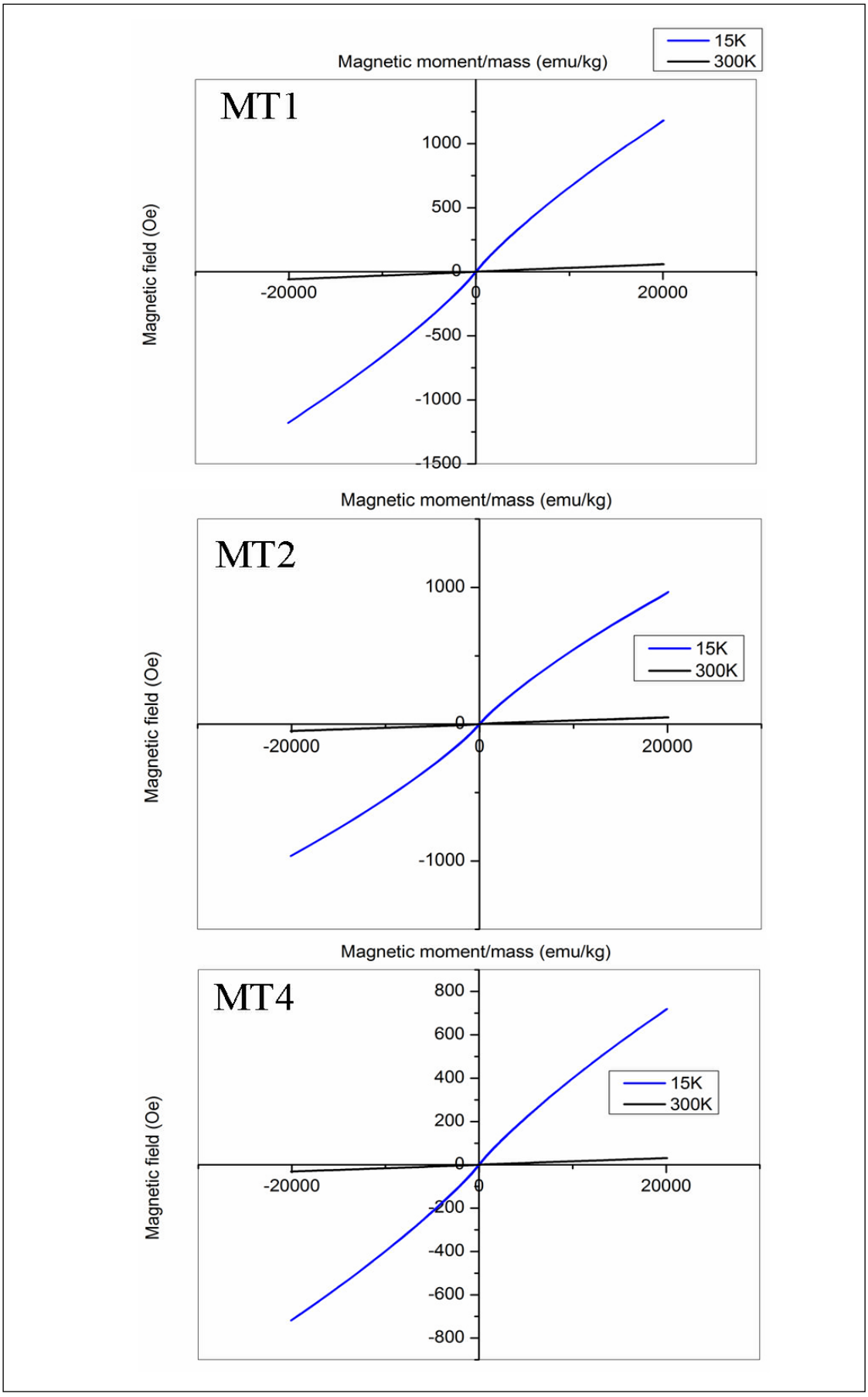


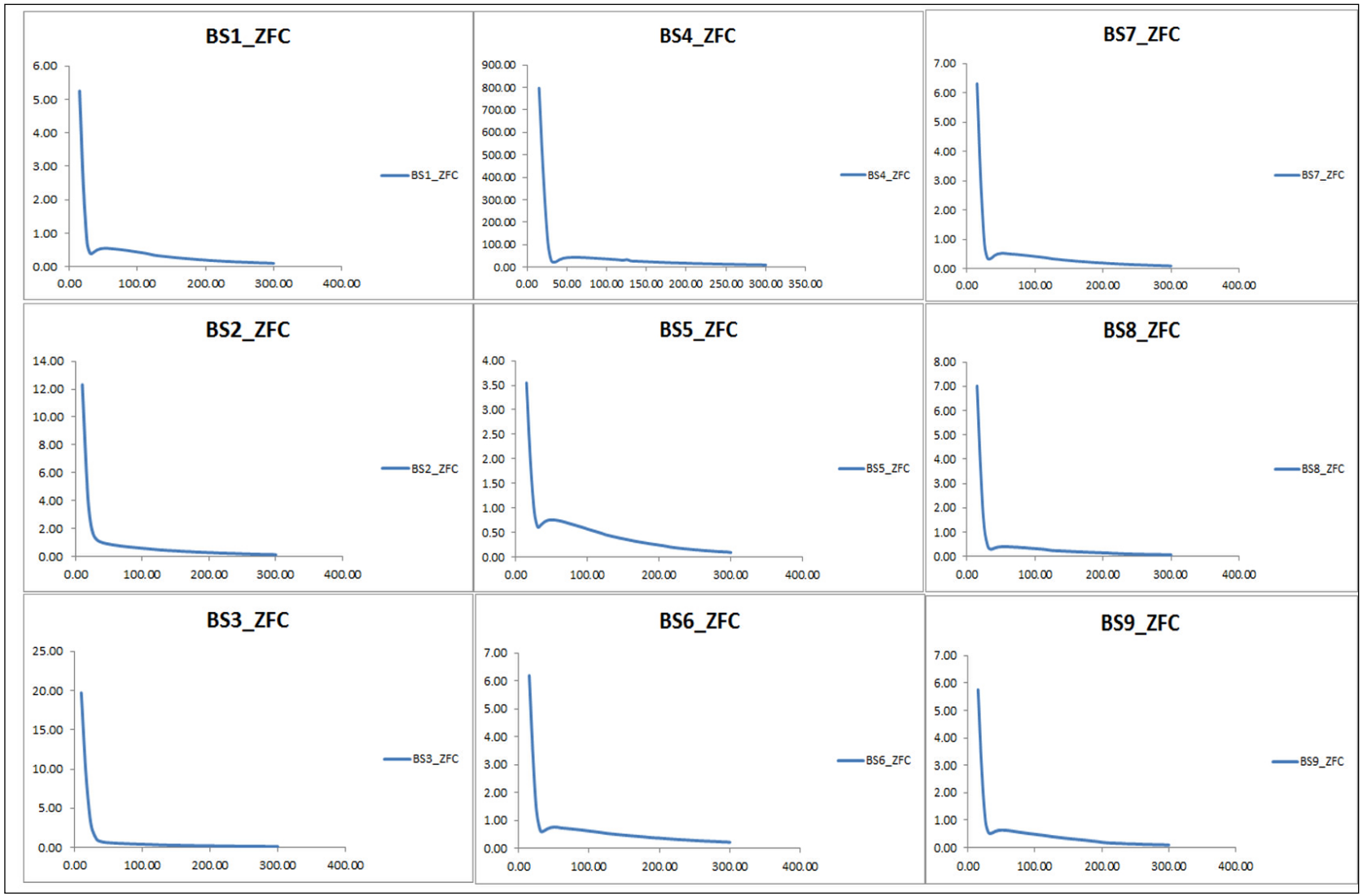

CH1
Magnetic moment/mass (emu/kg)
Magnetic field (Oe)
5K
300K
CH3
Magnetic moment/mass (emu/kg)
Magnetic field (Oe)
5K
300K
CH4
Magnetic moment/mass (emu/kg)
Magnetic field (Oe)
5K
300K
CH5
Magnetic moment/mass (emu/kg)
Magnetic field (Oe)
5K
300K

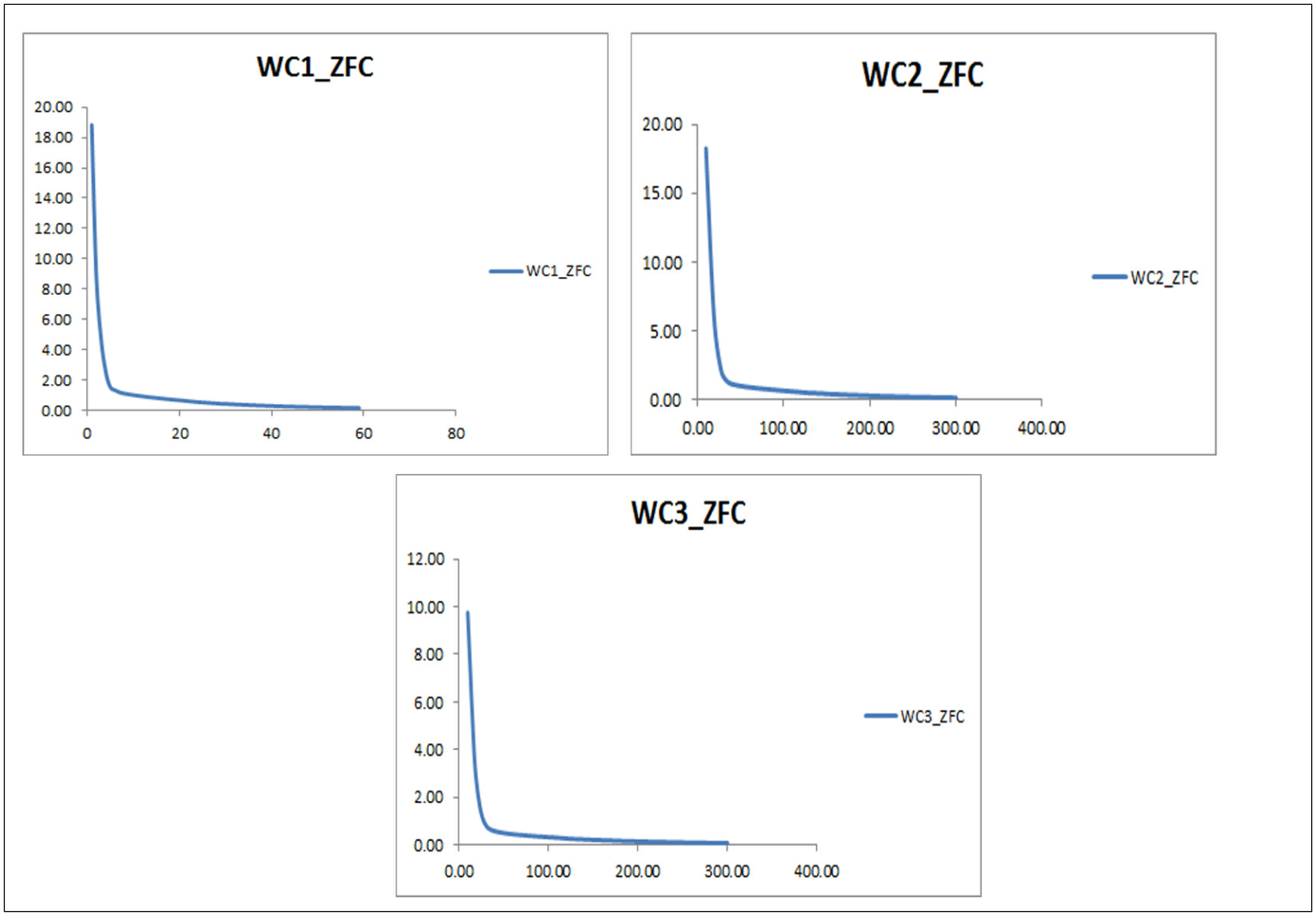

Coomb1
Magnetic moment/mass (emu/kg)
Magnetic field (Oe)
15K
300K
Coomb2
Magnetic moment/mass (emu/kg)
Magnetic field (Oe)
5K
300K

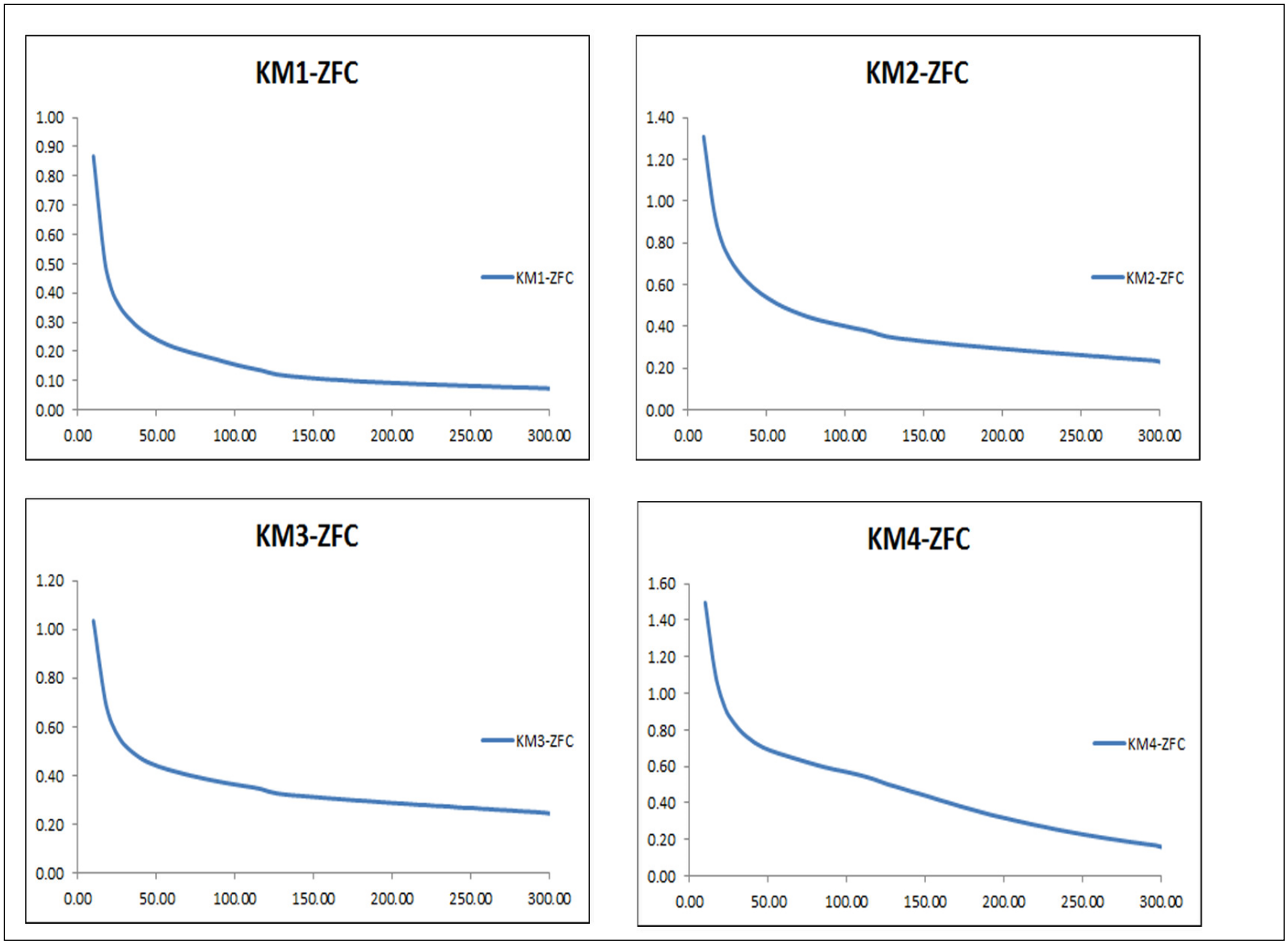

KM3
Magnetic moment/mass (emu/kg)
Magnetic field (Oe)
5K
300K
KM4
Magnetic moment/mass (emu/kg)
Magnetic field (Oe)
5K
300K
WC2
Magnetic moment/mass (emu/kg)
Magnetic field (Oe)
5K
300K
Magnetic moment/mass (emu/kg)
Magnetic field (Oe)
WC4 5K
WC3 5K

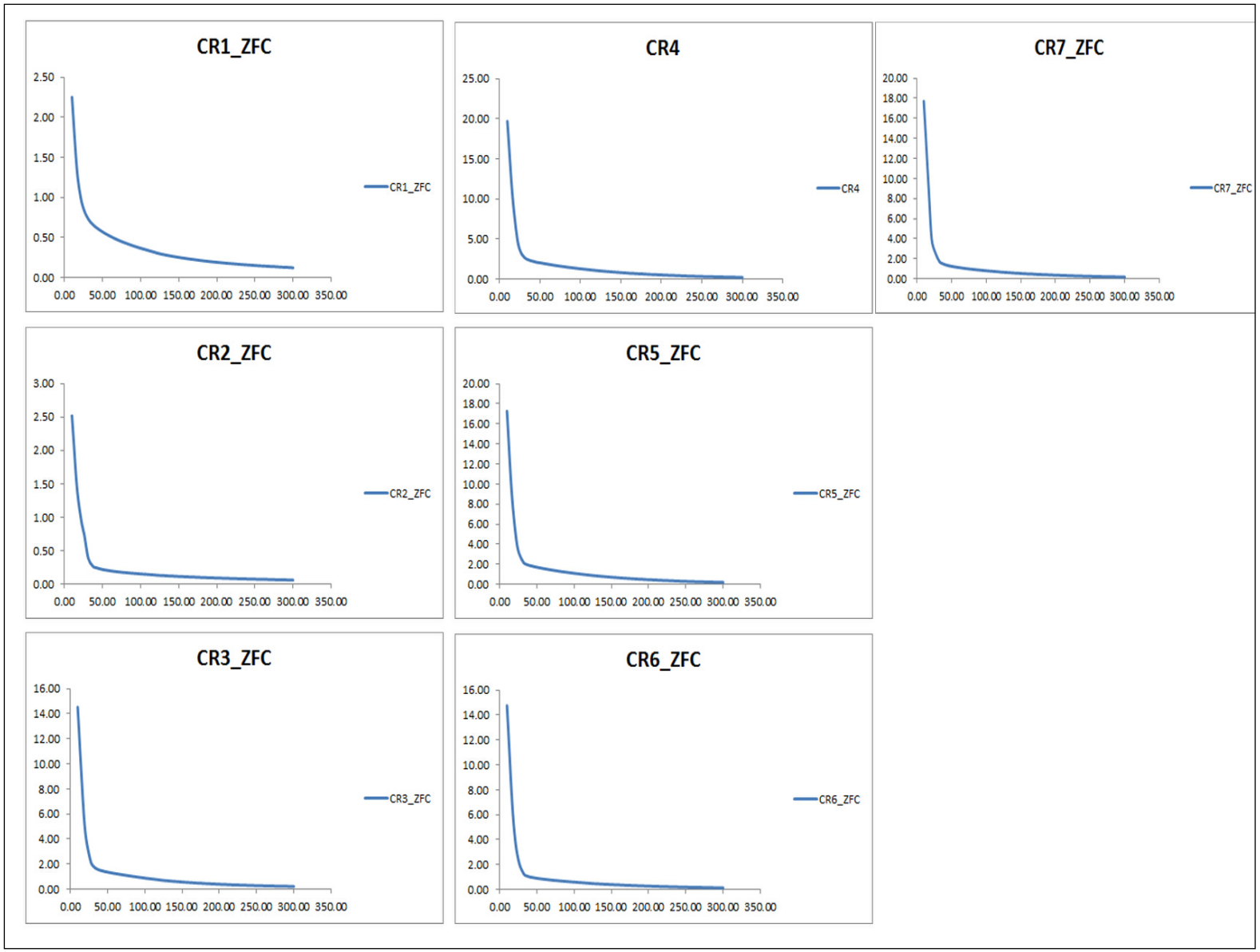

Magnetic moment/mass (emu/kg)
CR3
Magnetic field (Oe)
1000
500
0
-500
-1000
-1500
-80000 -60000 -40000 -20000 0 20000 40000 60000 80000
5K
300K
Magnetic moment/mass (emu/kg)
CR5
Magnetic field (Oe)
1500
1000
500
0
-500
-1000
-1500
-80000 -60000 -40000 -20000 0 20000 40000 60000 80000
5K
300K
emu/kg
CR7
Oe
2000
1000
0
-1000
-2000
-3000
-80000 -60000 -40000 -20000 0 20000 40000 60000 80000
5K
300K

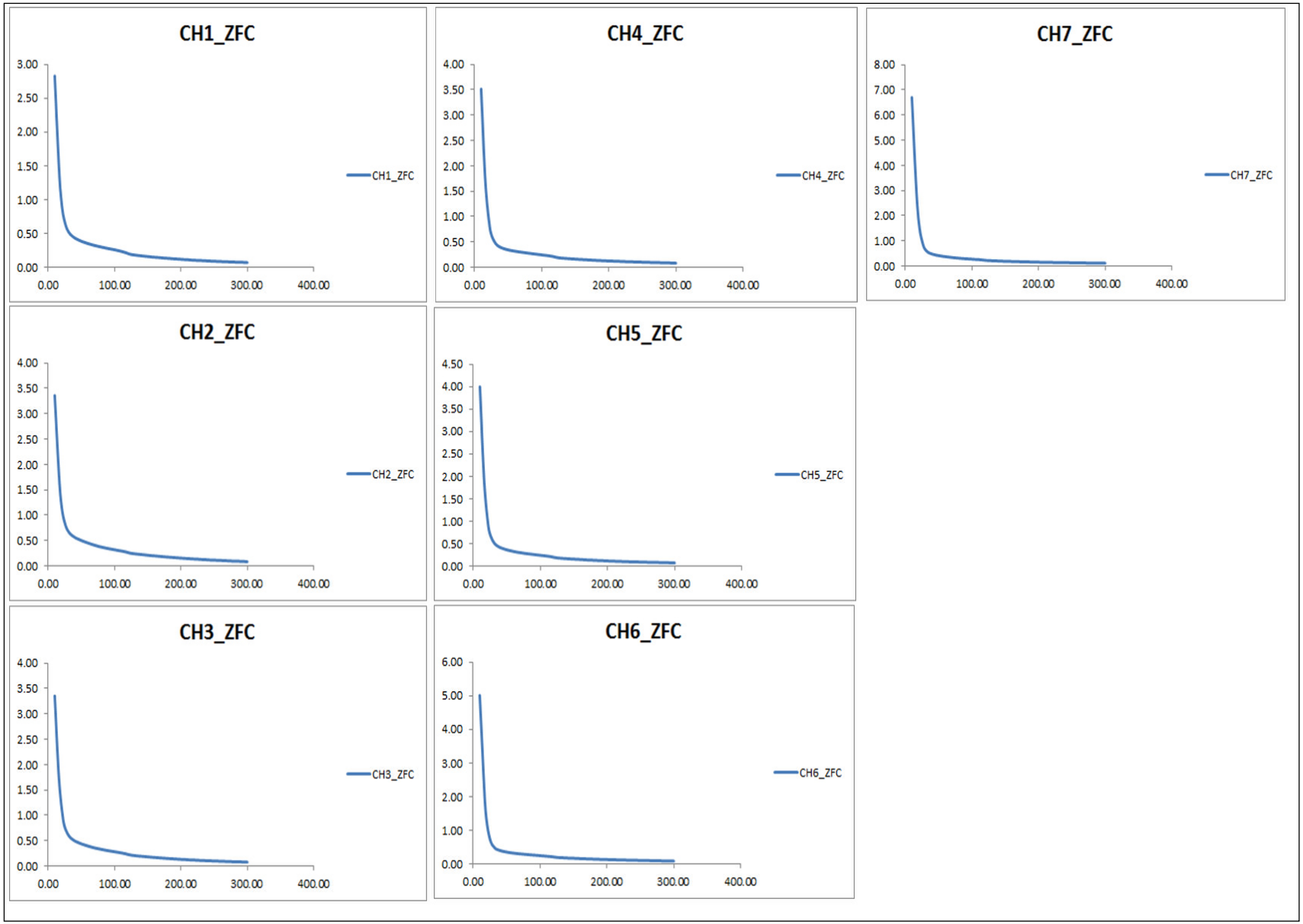

MT1
15K
300K
Magnetic moment/mass (emu/kg)
Magnetic field (Oe)
1000
500
0
-500
-1000
-1500
-20000
0
20000
MT2
15K
300K
Magnetic moment/mass (emu/kg)
Magnetic field (Oe)
1000
0
-1000
-20000
0
20000
MT4
15K
300K
Magnetic moment/mass (emu/kg)
Magnetic field (Oe)
800
600
400
200
0
-200
-400
-600
-800
-20000
0
20000

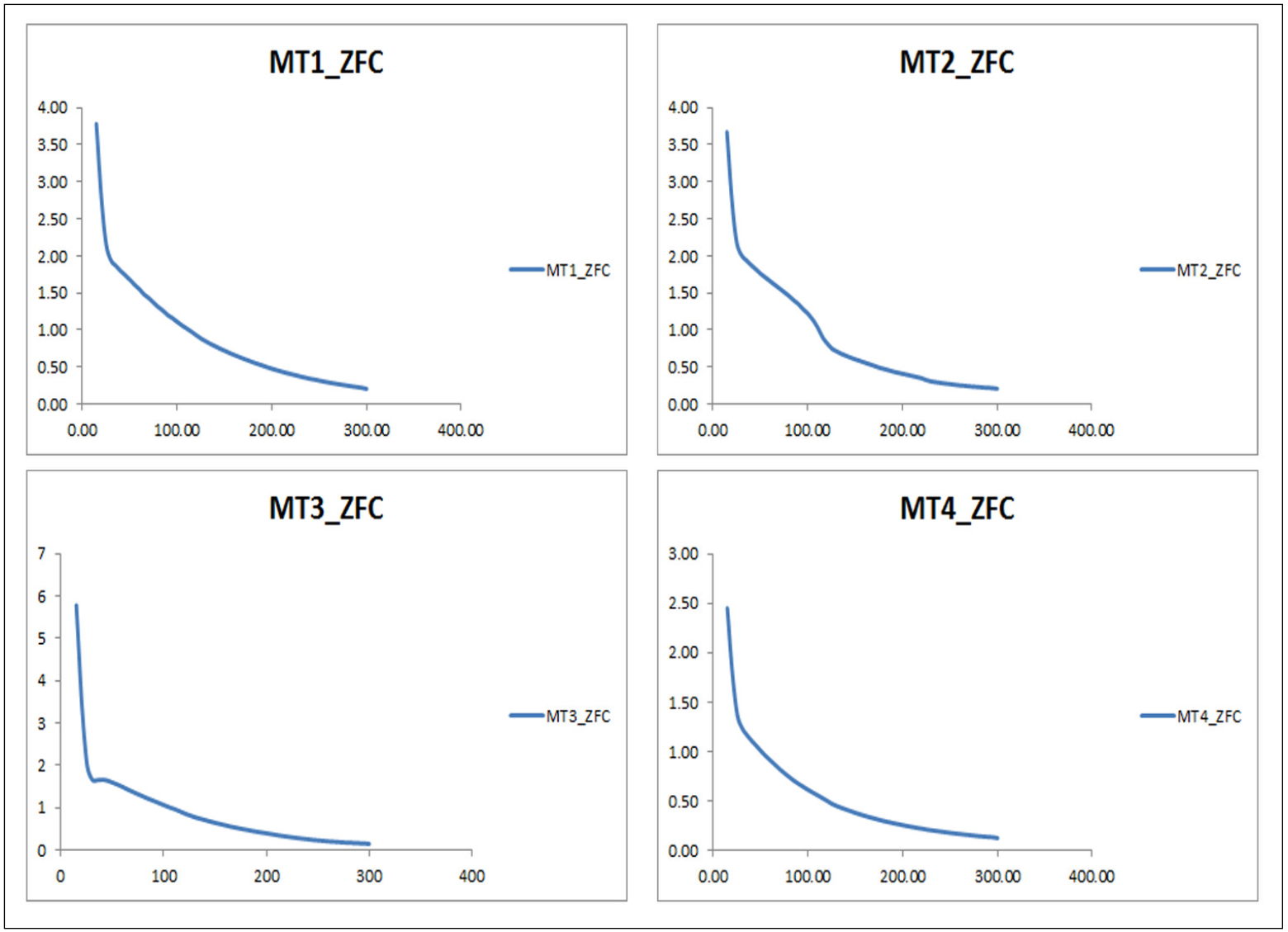

BS1_ZFC
BS1_ZFC
BS4_ZFC
BS4_ZFC
BS7_ZFC
BS7_ZFC
BS2_ZFC
BS2_ZFC
BS5_ZFC
BS5_ZFC
BS8_ZFC
BS8_ZFC
BS3_ZFC
BS3_ZFC
BS6_ZFC
BS6_ZFC
BS9_ZFC
BS9_ZFC

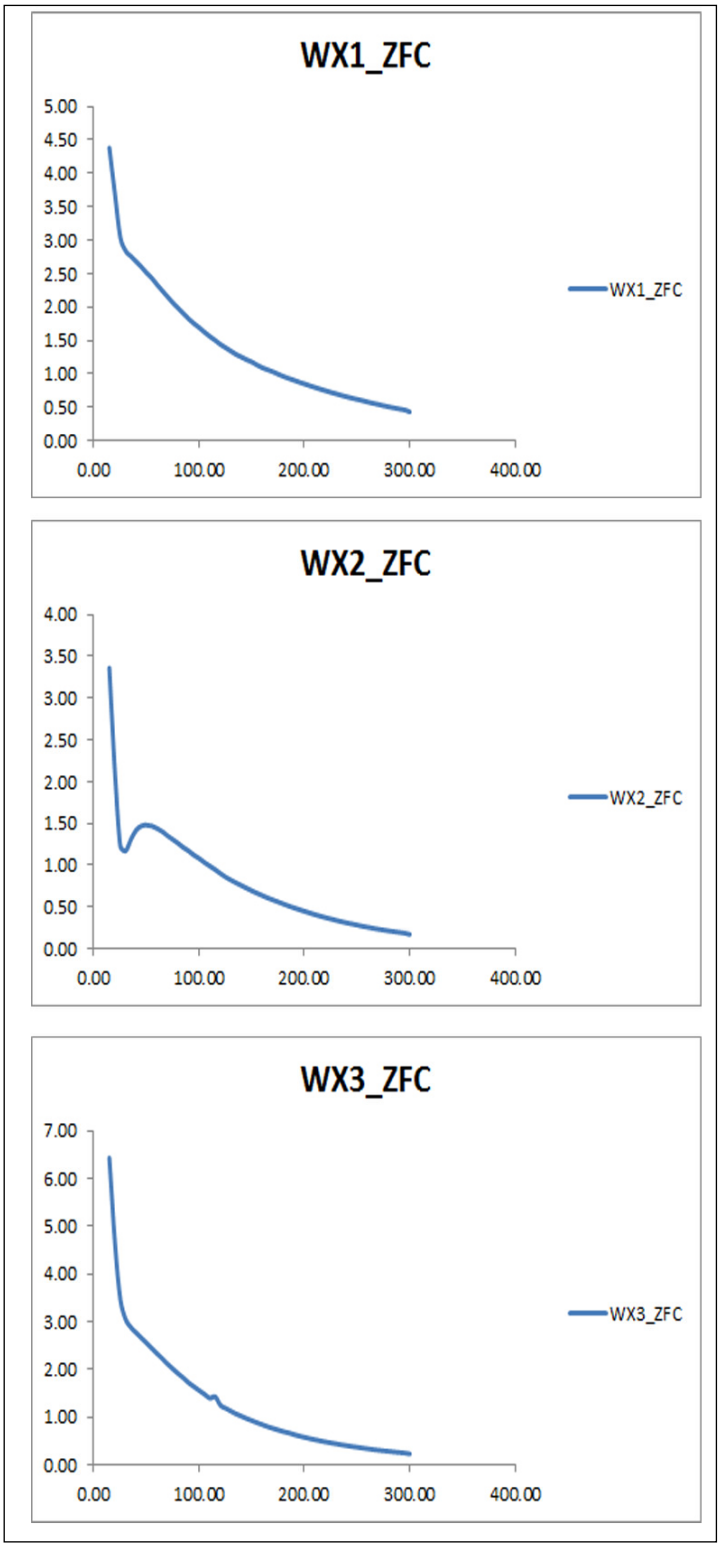

WC1_ZFC
20.00
18.00
16.00
14.00
12.00
10.00
8.00
6.00
4.00
2.00
0.00
0
20
40
60
80
WC1_ZFC
WC2_ZFC
20.00
15.00
10.00
5.00
0.00
0.00
100.00
200.00
300.00
400.00
WC2_ZFC
WC3_ZFC
12.00
10.00
8.00
6.00
4.00
2.00
0.00
0.00
100.00
200.00
300.00
400.00
WC3_ZFC

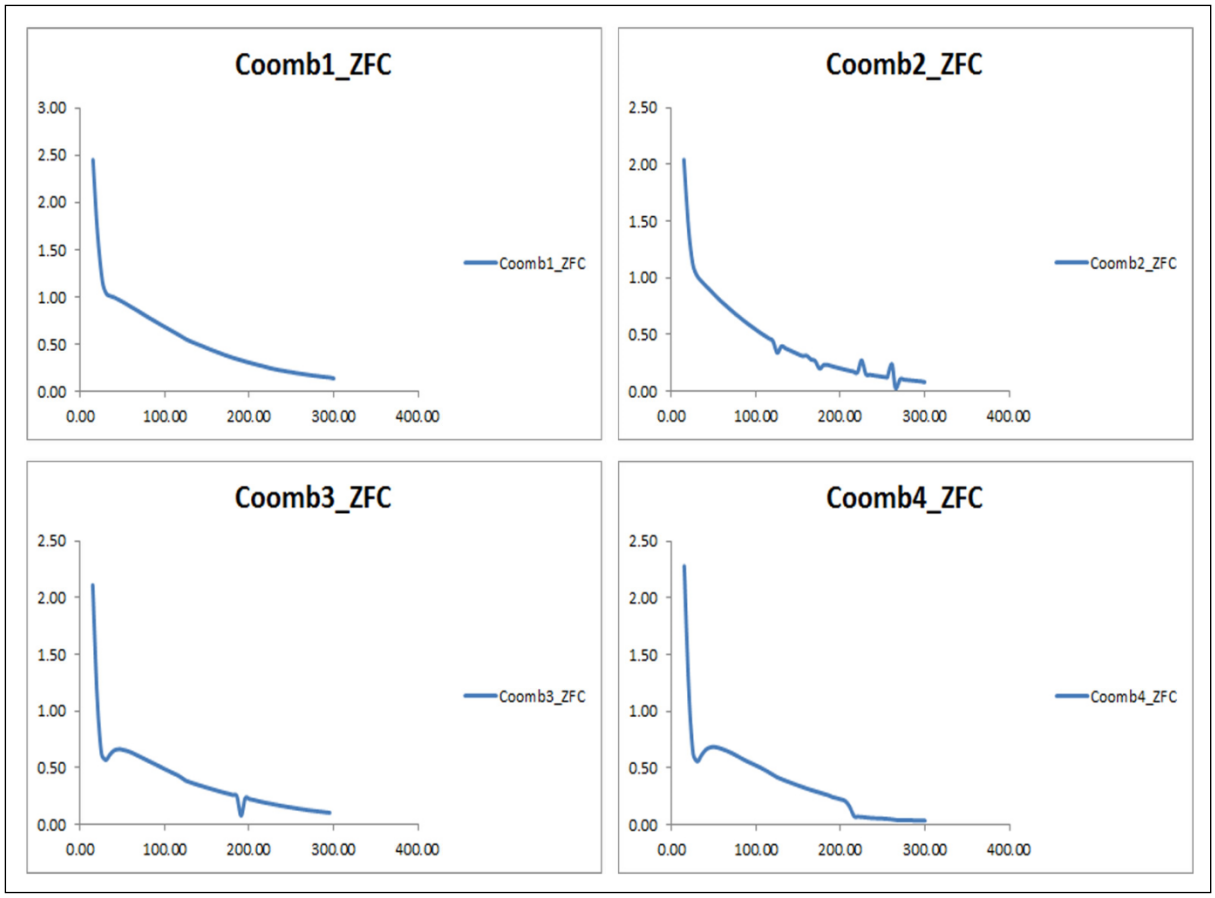

KM1-ZFC
1.00
0.90
0.80
0.70
0.60
0.50
0.40
0.30
0.20
0.10
0.00
0.00
50.00
100.00
150.00
200.00
250.00
300.00
KM1-ZFC
KM2-ZFC
1.40
1.20
1.00
0.80
0.60
0.40
0.20
0.00
0.00
50.00
100.00
150.00
200.00
250.00
300.00
KM2-ZFC
KM3-ZFC
1.20
1.00
0.80
0.60
0.40
0.20
0.00
0.00
50.00
100.00
150.00
200.00
250.00
300.00
KM3-ZFC
KM4-ZFC
1.60
1.40
1.20
1.00
0.80
0.60
0.40
0.20
0.00
0.00
50.00
100.00
150.00
200.00
250.00
300.00
KM4-ZFC

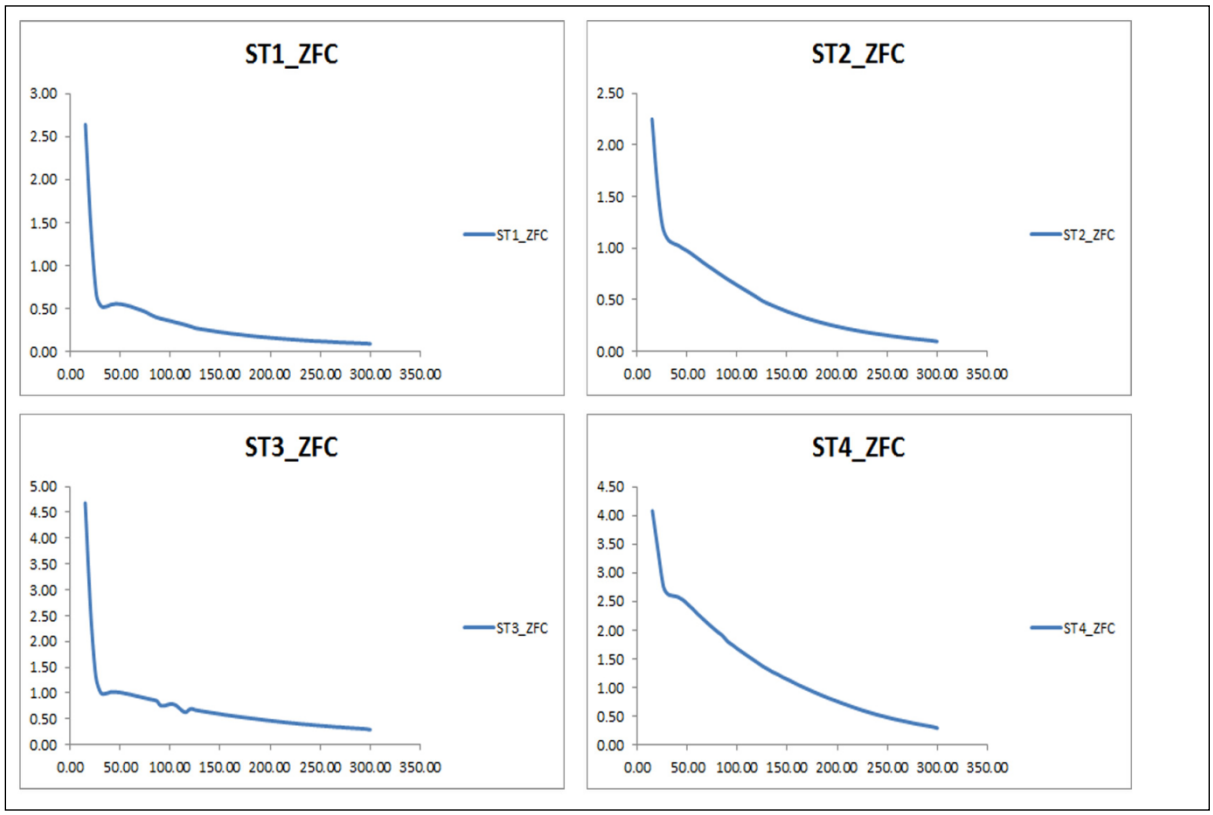

CR1_ZFC
2.50
2.00
1.50
1.00
0.50
0.00
0.00 50.00 100.00 150.00 200.00 250.00 300.00 350.00
CR1_ZFC
CR4
25.00
20.00
15.00
10.00
5.00
0.00
0.00 50.00 100.00 150.00 200.00 250.00 300.00 350.00
CR4
CR7_ZFC
20.00
18.00
16.00
14.00
12.00
10.00
8.00
6.00
4.00
2.00
0.00
0.00 50.00 100.00 150.00 200.00 250.00 300.00 350.00
CR7_ZFC
CR2_ZFC
3.00
2.50
2.00
1.50
1.00
0.50
0.00
0.00 50.00 100.00 150.00 200.00 250.00 300.00 350.00
CR2_ZFC
CR5_ZFC
20.00
18.00
16.00
14.00
12.00
10.00
8.00
6.00
4.00
2.00
0.00
0.00 50.00 100.00 150.00 200.00 250.00 300.00 350.00
CR5_ZFC
CR3_ZFC
16.00
14.00
12.00
10.00
8.00
6.00
4.00
2.00
0.00
0.00 50.00 100.00 150.00 200.00 250.00 300.00 350.00
CR3_ZFC
CR6_ZFC
16.00
14.00
12.00
10.00
8.00
6.00
4.00
2.00
0.00
0.00 50.00 100.00 150.00 200.00 250.00 300.00 350.00
CR6_ZFC


CH1_ZFC
3.00
2.50
2.00
1.50
1.00
0.50
0.00
0.00
100.00
200.00
300.00
400.00
CH1_ZFC
CH4_ZFC
4.00
3.50
3.00
2.50
2.00
1.50
1.00
0.50
0.00
0.00
100.00
200.00
300.00
400.00
CH4_ZFC
CH7_ZFC
8.00
7.00
6.00
5.00
4.00
3.00
2.00
1.00
0.00
0.00
100.00
200.00
300.00
400.00
CH7_ZFC
CH2_ZFC
4.00
3.50
3.00
2.50
2.00
1.50
1.00
0.50
0.00
0.00
100.00
200.00
300.00
400.00
CH2_ZFC
CH5_ZFC
4.50
4.00
3.50
3.00
2.50
2.00
1.50
1.00
0.50
0.00
0.00
100.00
200.00
300.00
400.00
CH5_ZFC
CH3_ZFC
4.00
3.50
3.00
2.50
2.00
1.50
1.00
0.50
0.00
0.00
100.00
200.00
300.00
400.00
CH3_ZFC
CH6_ZFC
6.00
5.00
4.00
3.00
2.00
1.00
0.00
0.00
100.00
200.00
300.00
400.00
CH6_ZFC


MT1_ZFC
4.00
3.50
3.00
2.50
2.00
1.50
1.00
0.50
0.00
0.00
100.00
200.00
300.00
400.00
MT1_ZFC
MT2_ZFC
4.00
3.50
3.00
2.50
2.00
1.50
1.00
0.50
0.00
0.00
100.00
200.00
300.00
400.00
MT2_ZFC
MT3_ZFC
7
6
5
4
3
2
1
0
0
100
200
300
400
MT3_ZFC
MT4_ZFC
3.00
2.50
2.00
1.50
1.00
0.50
0.00
0.00
100.00
200.00
300.00
400.00
MT4_ZFC

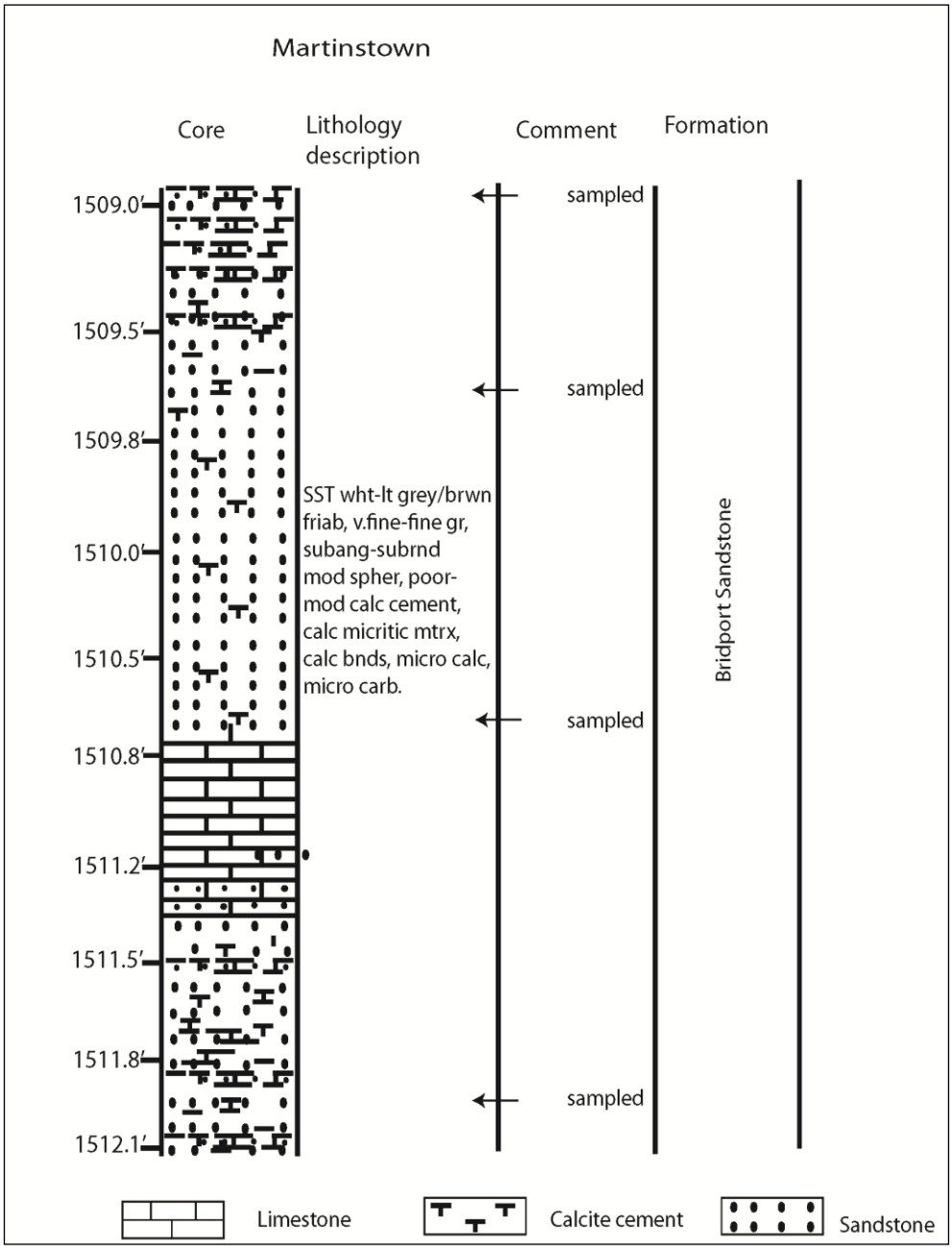

WX1_ZFC
5.00
4.50
4.00
3.50
3.00
2.50
2.00
1.50
1.00
0.50
0.00
0.00
100.00
200.00
300.00
400.00
WX1_ZFC
WX2_ZFC
4.00
3.50
3.00
2.50
2.00
1.50
1.00
0.50
0.00
0.00
100.00
200.00
300.00
400.00
WX2_ZFC
WX3_ZFC
7.00
6.00
5.00
4.00
3.00
2.00
1.00
0.00
0.00
100.00
200.00
300.00
400.00
WX3_ZFC

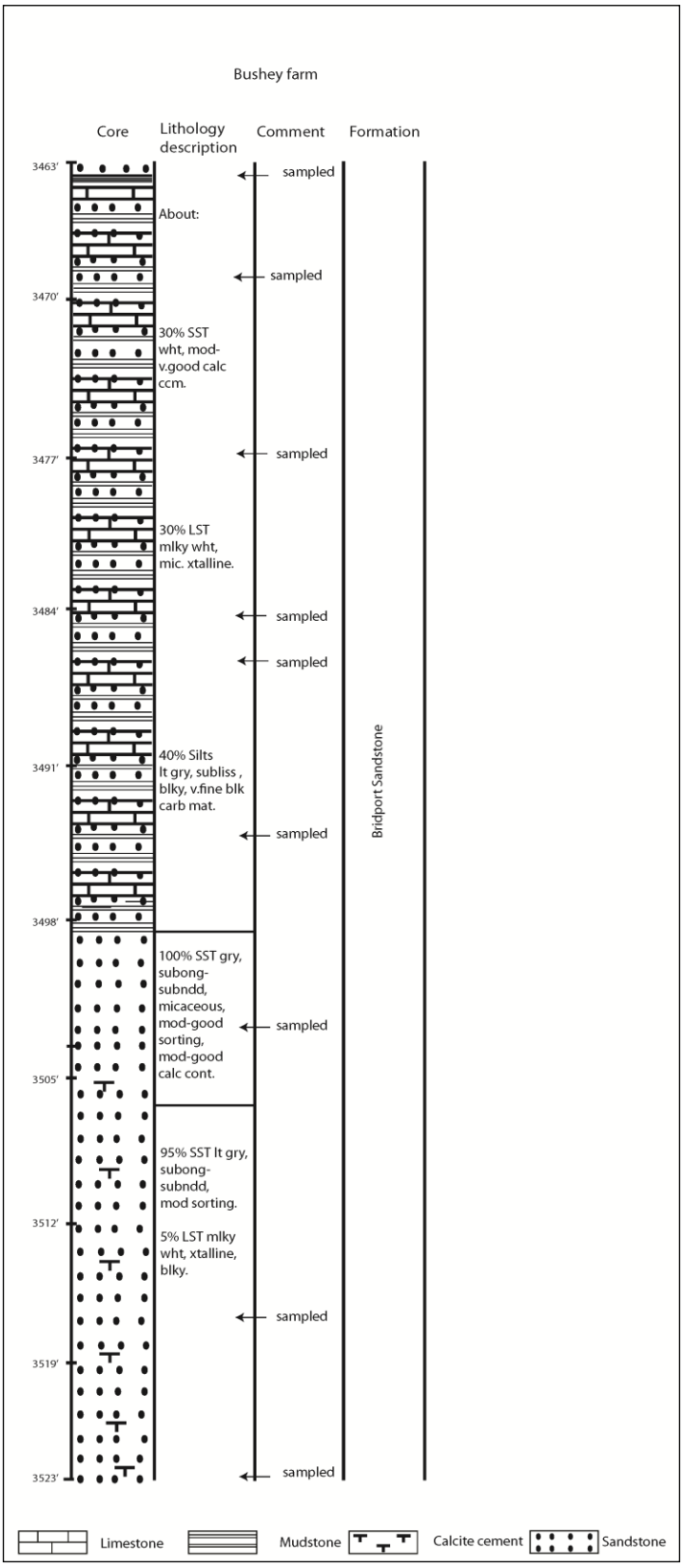

Coomb1_ZFC
3.00
2.50
2.00
1.50
1.00
0.50
0.00
0.00
100.00
200.00
300.00
400.00
Coomb1_ZFC
Coomb2_ZFC
2.50
2.00
1.50
1.00
0.50
0.00
0.00
100.00
200.00
300.00
400.00
Coomb2_ZFC
Coomb3_ZFC
2.50
2.00
1.50
1.00
0.50
0.00
0.00
100.00
200.00
300.00
400.00
Coomb3_ZFC
Coomb4_ZFC
2.50
2.00
1.50
1.00
0.50
0.00
0.00
100.00
200.00
300.00
400.00
Coomb4_ZFC

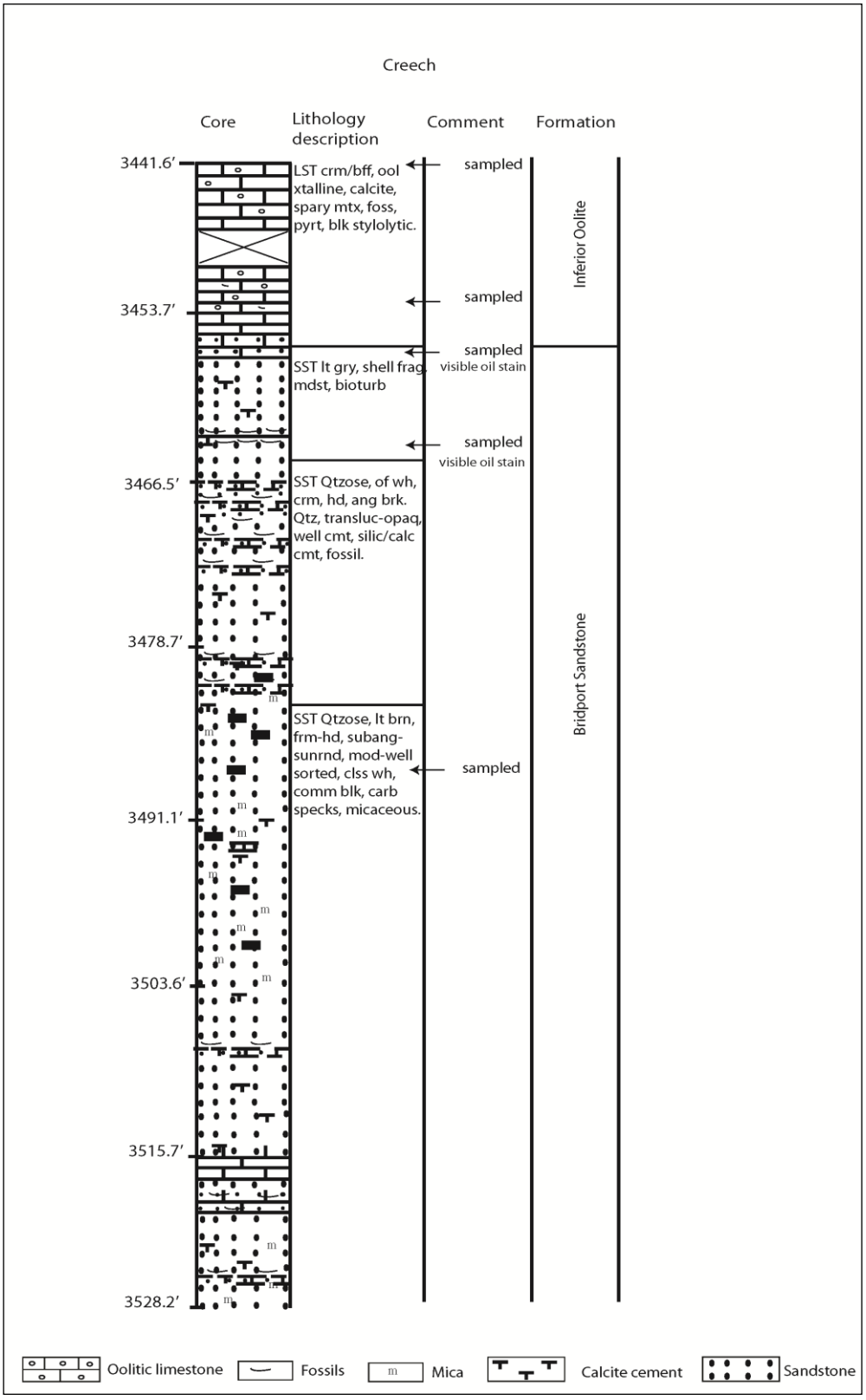

ST1_ZFC
3.00
2.50
2.00
1.50
1.00
0.50
0.00
0.00
50.00
100.00
150.00
200.00
250.00
300.00
350.00
ST1_ZFC
ST2_ZFC
2.50
2.00
1.50
1.00
0.50
0.00
0.00
50.00
100.00
150.00
200.00
250.00
300.00
350.00
ST2_ZFC
ST3_ZFC
5.00
4.50
4.00
3.50
3.00
2.50
2.00
1.50
1.00
0.50
0.00
0.00
50.00
100.00
150.00
200.00
250.00
300.00
350.00
ST3_ZFC
ST4_ZFC
4.50
4.00
3.50
3.00
2.50
2.00
1.50
1.00
0.50
0.00
0.00
50.00
100.00
150.00
200.00
250.00
300.00
350.00
ST4_ZFC

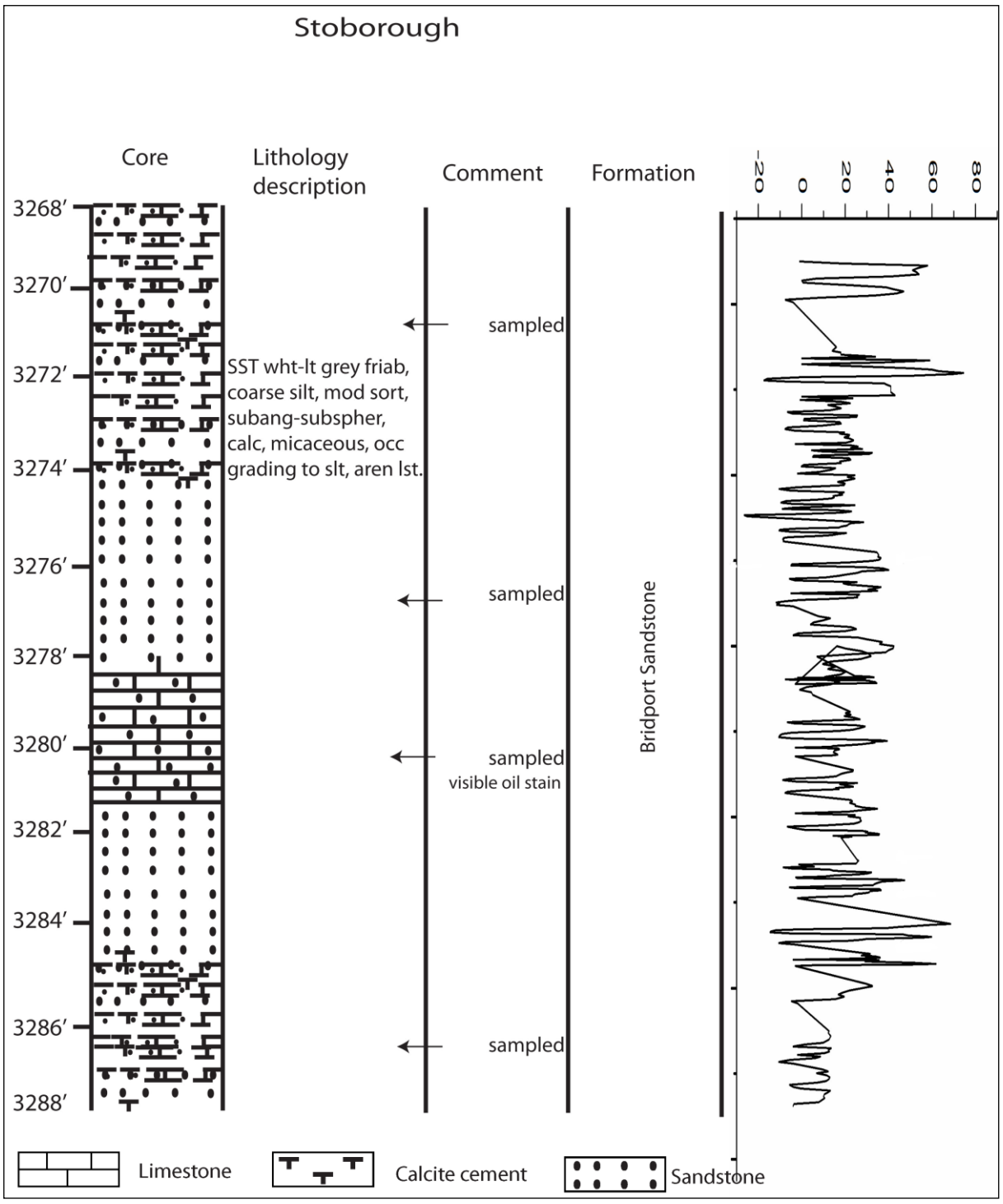
Appendix 2.3

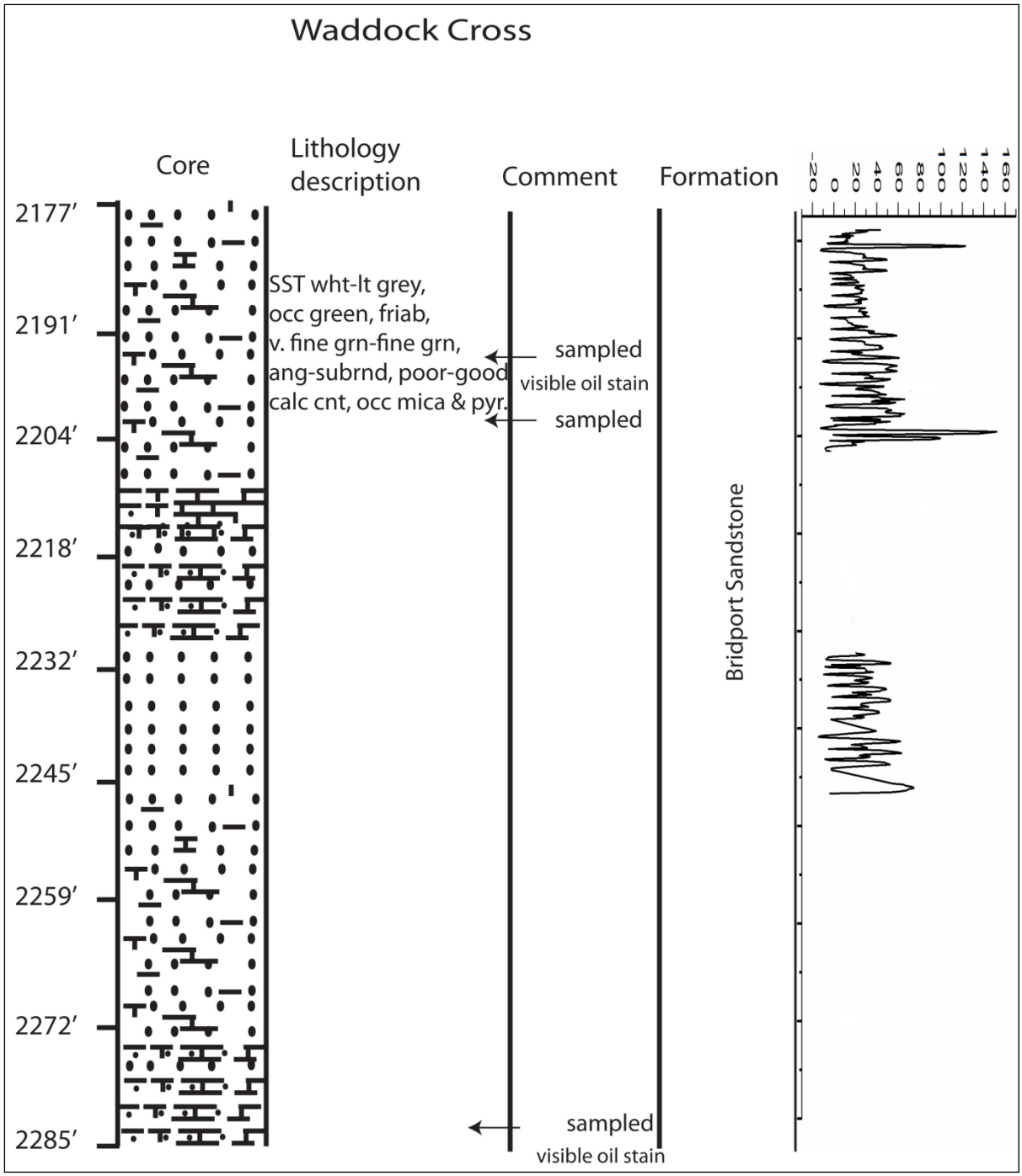
Core logs, lithology descriptions and low-field magnetic susceptibility measurements.

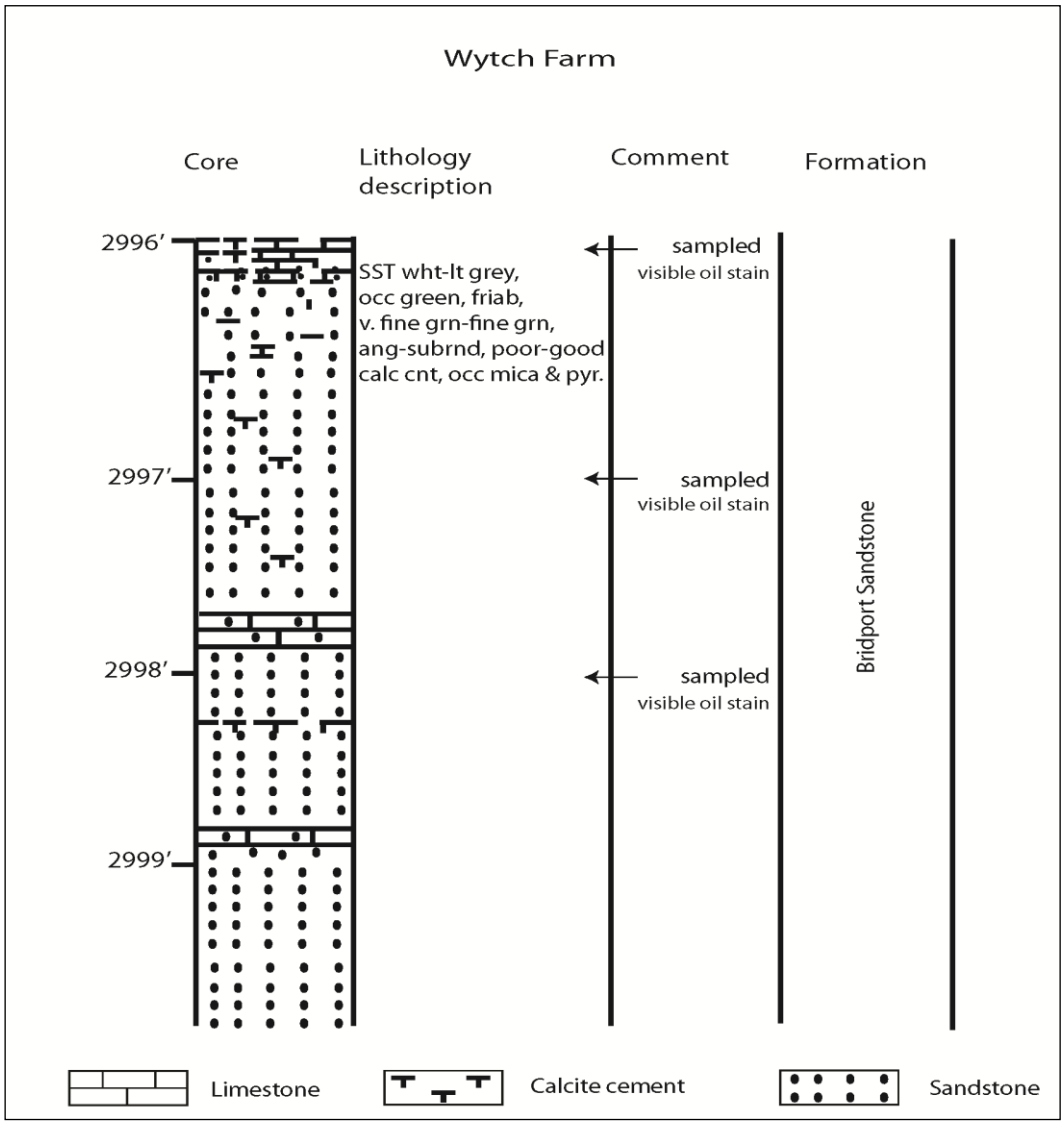


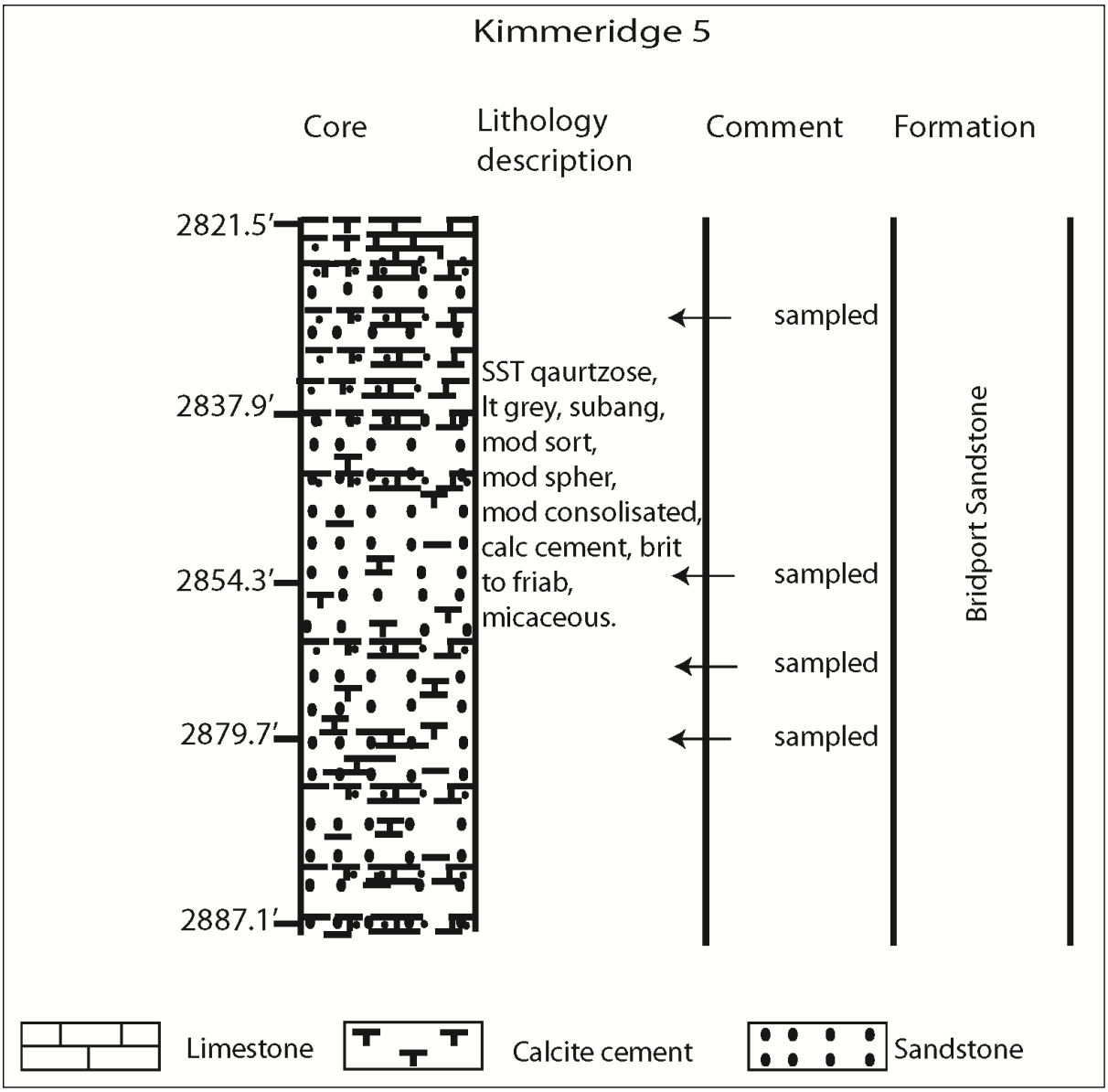

Bushey farm
Core
Lithology description
Comment
Formation
3463'
3470'
3477'
3484'
3491'
3498'
3505'
3512'
3519'
3523'
About:
30% SST wht, mod-v.good calc ccm.
30% LST mlky wht, mic. xtalline.
40% Silts lt gry, subliss , blky, v.fine blk carb mat.
100% SST gry, subong-subndd, micaceous, mod-good sorting, mod-good calc cont.
95% SST lt gry, subong-subndd, mod sorting.
5% LST mlky wht, xtalline, blky.
sampled
Bridport Sandstone
Limestone
Mudstone
Calcite cement
Sandstone

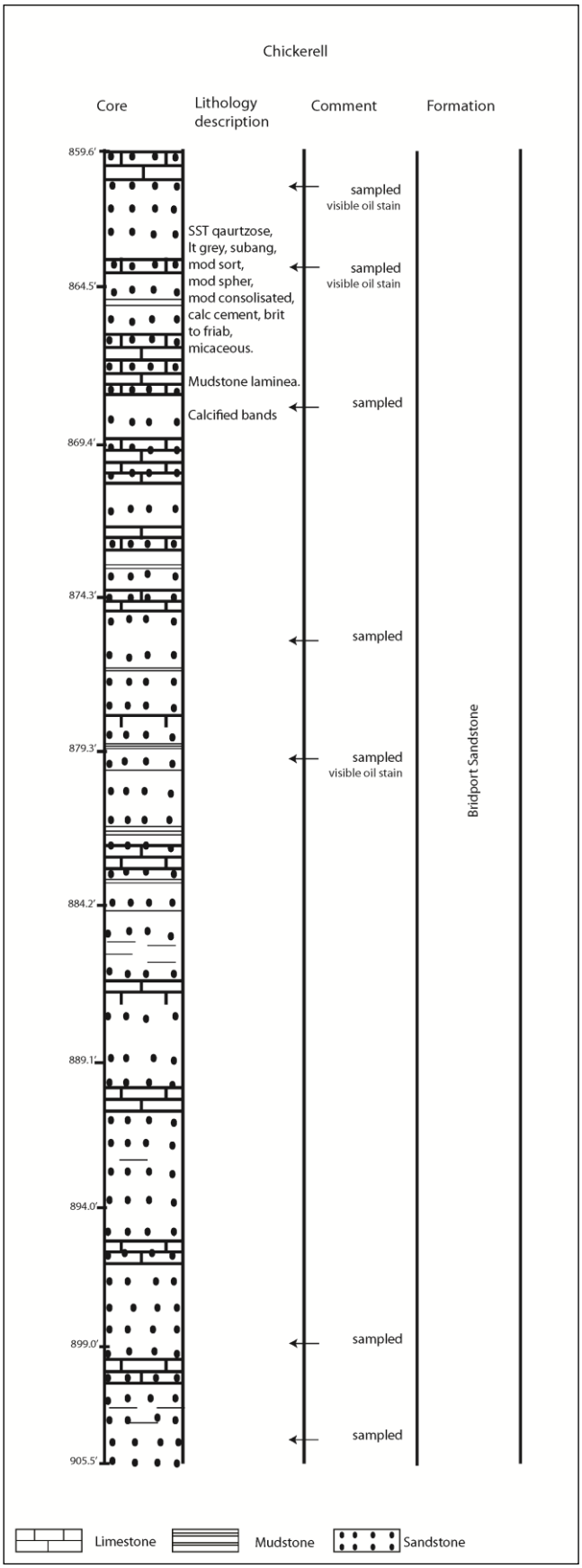

Creech
Core
Lithology description
Comment
Formation
3441.6′
3453.7′
3466.5′
3478.7′
3491.1′
3503.6′
3515.7′
3528.2′
LST crm/bff, ool xtalline, calcite, spary mtx, foss, pyrt, blk stylolytic.
SST lt gry, shell frag, mdst, bioturb
SST Qtzose, of wh, crm, hd, ang brk. Qtz, transluc-opaq, well cmt, silic/calc cmt, fossil.
SST Qtzose, lt brn, frm-hd, subang-sunrnd, mod-well sorted, clss wh, comm blk, carb specks, micaceous.
sampled
sampled
sampled
visible oil stain
sampled
visible oil stain
sampled
Inferior Oolite
Bridport Sandstone
Oolitic limestone
Fossils
m
Mica
Calcite cement
Sandstone


Stoborough
Core
Lithology description
Comment
Formation
-20
0
20
40
60
80
3268′
3270′
3272′
3274′
3276′
3278′
3280′
3282′
3284′
3286′
3288′
SST wht-lt grey friab, coarse silt, mod sort, subang-subspher, calc, micaceous, occ grading to slt, aren lst.
sampled
sampled
sampled
visible oil stain
sampled
Bridport Sandstone
Limestone
Calcite cement
Sandstone


Waddock Cross
Core
Lithology description
Comment
Formation
2177′
2191′
2204′
2218′
2232′
2245′
2259′
2272′
2285′
SST wht-lt grey, occ green, friab, v. fine grn-fine grn, ang-subrnd, poor-good calc cnt, occ mica & pyr.
sampled
visible oil stain
sampled
sampled
visible oil stain
Bridport Sandstone
-20
0
20
40
60
80
100
120
140
160


Wytch Farm
Core
Lithology description
Comment
Formation
2996′
2997′
2998′
2999′
SST wht-lt grey,
occ green, friab,
v. fine grn-fine grn,
ang-subrnd, poor-good
calc cnt, occ mica & pyr.
sampled
visible oil stain
sampled
visible oil stain
sampled
visible oil stain
Bridport Sandstone
Limestone
Calcite cement
Sandstone


Kimmeridge 5
Core
Lithology description
Comment
Formation
2821.5'
2837.9'
2854.3'
2879.7'
2887.1'
SST qaurtzose, lt grey, subang, mod sort, mod spher, mod consolisated, calc cement, brit to friab, micaceous.
sampled
sampled
sampled
sampled
Bridport Sandstone
Limestone
Calcite cement
Sandstone


Chickerell
Core
Lithology description
Comment
Formation
859.6'
864.5'
869.4'
874.3'
879.3'
884.2'
889.1'
894.0'
899.0'
905.5'
SST qaurtzose, lt grey, subang, mod sort, mod spher, mod consolisated, calc cement, brit to friab, micaceous.
Mudstone laminea.
Calcified bands
sampled
visible oil stain
sampled
visible oil stain
sampled
sampled
sampled
visible oil stain
sampled
sampled
Bridport Sandstone
Limestone
Mudstone
Sandstone